

Thermal Stability of Hydrocarbon Radicals

Wing Tsang
National Institute of Standards and Technology
Gaithersburg, MD 20899

ABSTRACT

This paper reviews the present state of knowledge regarding the stability of hydrocarbon radicals. We will begin with some definitions regarding thermodynamic and kinetic stability and general comments justifying our interest. A number of the important issues dealing with the accurate determination of these properties will be discussed. This will be followed by a survey of some of the problems and controversies regarding correct values. Finally, thermodynamic and kinetic data bearing on the stability of the radicals will be summarized.

BACKGROUND

The reactions of hydrocarbons in the gas phase and non-polar media frequently proceed through free radical mechanisms. Quantitative understanding of the temporal behavior of such processes depends on knowledge of the thermodynamic and kinetic properties of the radicals. The thermodynamic stability of any compound can most conveniently be expressed in a quantitative sense in terms of its free energy or equilibrium constant of formation. This can be expressed as,

$$\Delta F = \Delta H - T\Delta S = -RT \ln K_p \quad [1]$$

$$K_p = k_f/k_r(RT)^n \quad [2]$$

where the reference state is for the elements at 1 bar and 298 K, k_f and k_r are the rate constants in the two directions and n represent the order of the reaction. Thermodynamic properties serve as limits for kinetics and the basis for the estimation and evaluation of kinetic information. A particularly important application is its use for the calculation of the rate constant in one direction if that for the reverse reaction is known. Alternatively, when the rates in both directions have been measured, the reproduction of the equilibrium property serves as an important check of the validity of the data. Thermodynamic properties of radicals are not only important for their own sake but can be used to infer the chemical stability and reactivity of the compounds formed by any two radicals. This is largely due to the fact that radical combination rate constants do not vary greatly.

Enthalpy and entropy define the properties of a molecule in terms of energetics and structure (1). Traditionally, they form the basis for estimation (2). Modern day computational packages (3) permit their direct calculation from ab initio quantum mechanics. Such methods work quite well for small radicals and are in general more reliable with respect to structural or entropic factors than the energies. In time, these methods will play an ever more important role in defining the properties of radicals. In the meantime dependence must remain with experimental determinations. A key role for accurate measurements is as a means of validating calculations. A combination of group additivity and small molecule calculational results should in principal give all the information necessary for the determination of the thermodynamic properties of larger entities.

As suggested above, the thermodynamic properties of radicals can be determined through the measurement of the equilibrium constant (1). From measurements at one temperature enthalpies can be determined if entropies can be estimated. This is usually known as the 3rd law method. Alternatively, from determinations of the equilibrium constant as a function of temperature, the enthalpy of the process can be determined from the slope or

$$d[\ln K_p]/d(1/T) = -\Delta H/R. \quad [3]$$

This is known as the second law method. Substituting back into Eq 1 then leads to a determination of the entropy. In order to determine the property of a radical the thermodynamic properties of the other compounds for the reaction must be known and if reactions are carried out at temperatures different than 298 K heat capacity corrections must be made.

Much effort has been devoted to determining the enthalpies of free radicals (4,5). They are directly related to the bond dissociation energies of the molecular entity from which the radicals are formed and is a convenient marker for molecular stability or reactivity. Many measurement methods lead only to the determination of the energies. If one applies the second

law method, then a slope can be determined without the need for an absolute value of the equilibrium constant, if the calibration factor does not vary over the temperature range used and assumptions can be made about the reverse process. Complete quantitative description in the context of molecular stability will also require knowledge of the entropy. Our knowledge and understanding of radical structure and vibrational frequencies are such that for the less complex radicals, measurements exist or they can be estimated with considerable accuracy. There remains uncertainties for larger species. This is particularly the case for the molecular motions associated with low frequency vibrations. Unfortunately, these are also the largest contributors to the entropies. In the case of simple hydrocarbon radicals, the important issues are the frequency of the umbrella motion at the radical site. It is in fact uncertain as to whether they can be represented in the simple harmonic oscillator approximation. Another issue is the barrier to internal rotation of rotors at the radical site.

Kinetic stability(6) can most readily be defined in terms of the rate expressions for decomposition of radicals or the parent hydrocarbon,

$$k = A_{\infty} T^n \exp(-E_{\infty}/RT) s^{-1} \quad [4]$$

where we have chosen to write the rate expression in the modified Arrhenius form. Over short ranges, data can be written in the regular Arrhenius form where $n=0$. The infinities are given to define the results in terms of the rate constant in the limiting high pressure region. This means the results are for a system where the distribution function for the molecule is Boltzmann. High pressure rate expression for decomposition is a fundamental property of a molecule and is given in this form in order to differentiate it from the more general case where the distribution function are perturbed when the chemical lifetimes become shorter than energy transfer times, leading to a distorting of the Boltzmann distribution. The high pressure rate expressions are one of the fundamental inputs for the understanding of many complex reaction systems. They define the non-reactive lifetimes of the radicals and play a key role in the evolution of such systems. Even for the cases where energy transfer is important, the high pressure rate expression is the basis upon which estimates for energy transfer effects are made. As suggested earlier, these rate expressions can be used to derive or be derived from the thermodynamics.

EXPERIMENTAL METHODS

All experimental procedures for determining the thermodynamic and kinetic stability of radicals involve quantitative measurement of some property associated with their generation or destruction. Kinetic measurements in both directions is a prime method for determining equilibrium constants of formation. The reliable values that are now available owe much to the understanding of how to carry out accurate kinetic measurements. The first prerequisite is to find systems that are mechanistically unambiguous. This requirement is aided by the sensitivity of modern detection methods. It is thus possible to work under conditions where there are no ambiguity regarding the process being studied. Table 1 summarizes a variety of kinetic methods that have made significant contributions to the determination of the thermodynamic properties of hydrocarbon radicals. In general, the thermal decomposition reactions are carried out at the highest temperatures, the radical decompositions at intermediate temperatures while the metathesis and ion-molecule reactions are at the lowest or ambient temperatures. The choice of a technique is highly dependent on the availability of a suitable precursor. This is particularly true at the lower temperatures. At the higher temperatures more channels are opened up. However this can lead to mechanistic complications.

An alternative approach is to subject a molecule to some form of physical excitation such as a photon or electron which leads to the formation of the radical in question and then observing their formation and deducing the energetics on the basis of an energy balance. Since molecules have a distribution of energies an important issue has always been the proper selection of reaction thresholds. As with the kinetic methods, the availability of an appropriate precursor is an important determinant of what can be measured. Since this is a physical method, the most reliable numbers are for the smaller species. Furthermore, as with kinetic methods, earlier workers were much too optimistic regarding measurement accuracy. The tendency has been to reproduce the kinetic results that are now known to be in error. Here again improvements in understanding and techniques are leading to more accurate determinations.

RESULTS

A: Thermodynamic Stability: Table 2 contains a summary of data on bond dissociation energies that can be derived from heats of formation data. These have largely been derived from the methods summarized in Table 1. Also included in Table 2 are the recommendations of

Table 1: Kinetic procedures and methods used in determining the thermodynamic properties of organic radicals.(8,9)

Process	Method	Reaction Type (example)
Thermal Decomposition	Single Pulse Shock Tube Flow and Static systems. Detection of stable products	$R_1-R_2 \rightleftharpoons R_1+R_2$ $((tC_4H_9)_2 \rightleftharpoons 2 tC_4H_9)$
Radical Combination	Photolytic generation of Radicals and spectroscopic Detection	
Radical Decomposition	Photolytic and thermal generation of radicals. Detection of stable products or decay of radicals	$R \rightleftharpoons H/CH_3 + \text{olefin}$ $nC_3H_7 \rightleftharpoons C_2H_4 + CH_3$
Radical Addition	Decay of photolytically generated small radicals	
Metathesis of halogenated organics	Photolytic generation of radicals Followed by their decay	$X + RH \rightleftharpoons R + HX$ $Br + tC_4H_9$
Ion-molecule equilibria	Metathesis reaction involving ions in flow system. Mass spectrometric detection of reactants and products	$C_3H_6 + CH_3O \rightleftharpoons$ $C_3H_5 + CH_3OH$

McMillen and Golden(4) published in 1982 which are based largely on iodination results. It can be seen that in all cases except for methyl, for which the best results are from physical approaches, there have been significant increases in the heats of formation. This is surprising to those who are not intimately acquainted with the field. Since much of chemistry is involved in the breaking or forming of bonds, there is a natural attempt to interpret experimental observations in terms of bond dissociation energies. Unfortunately, it is now clear that earlier investigators were much too optimistic regarding the accuracy of their estimates.

The following contains a brief historical sketch of the sequence of studies of which the data in Table 2 represent hopefully the final correct values. The first systematic investigation of the thermodynamic properties of hydrocarbon radicals were the studies of Butler et al (9) where the kinetics of the decomposition of the alkyl iodides was interpreted in terms of the breaking of the carbon-iodine bond. Subsequent analysis revealed that the decomposition reaction is in fact a radical chain process with the additional possibility of a molecular decomposition channel. A few years later, Szwarc and coworkers (10) studied inhibited decomposition of simple hydrocarbons in flow systems. Radical processes were suppressed by the addition of the radical inhibitor, toluene. It is now clear that the conditions in the flow reactor were very poorly defined. The consequence was that the rate expressions are all now known to be characterized by low A-factors and activation energies. Several years later Benson and coworkers(1) used iodination kinetics to determine bond energies. The specific reactions used in their work were largely those involving the bimolecular attack of iodine atom on alkyl iodide to form the hydrocarbon radical and the iodine molecule or the reverse. A number of major errors were corrected leading once again to large increases in the measured heats of formation.

These results which first appeared in the early 1960s were summarized in a 1982 article in Annual Reviews of Physical Chemistry (4) and for many years represented the generally accepted values. However beginning with the single pulse shock tube work in the late 1960s(11) it became increasingly difficult to fit experimental results with such heats of formation. Some of the consequences are summarized in Table 2 and represent a further increase of 10-20 kJ/mol. The correctness of these numbers is attested by the large volume of experimental data that can now reproduce the thermodynamic properties of the radicals. Indeed, if errors are substantially larger than the estimated uncertainties, this will call into question much that is believed to be understood about experimental gas phase kinetics. Actually, of all the numbers given in Table 2, only that for t-butyl radical is still subject to any controversy. It should also be noted that there may also be uncertainties of the order of several kJ/mol in the heats of formation of the larger alkanes (12). This will of course be directly reflected in the errors of the radicals.

The ultimate importance of data such as summarized in Table 2 is as a basis for estimation. It is of interest to consider the consequences of errors in such values. If they are directly reflected in the rate or equilibrium constants, then an error of 5.5 kJ/mol will lead to an

Table 2: Heats of formation for some hydrocarbon radicals and their corresponding bond dissociation energies. (7,8) Heats of formation in italics are from McMillen and Golden (4)

R1/R2 (kJ/mol)	(Ref 4)	H	CH ₃ 147 ± 1	C ₂ H ₅ 119 ± 2	i-C ₃ H ₇ 90 ± 2	t-C ₄ H ₉ 48 ± 3
CH ₃ (147 ± 1)	<i>(147±1)</i>	440	378	370	370	360
C ₂ H ₅ (119 ± 2)	<i>(108±4)</i>	422	370	364	362	352
n-C ₃ H ₇ (100 ± 2)	<i>(88±4)</i>	422	373	365	362	353
i-C ₃ H ₇ (90 ± 2)	<i>(76±4)</i>	412	372	364	361	343
s-C ₄ H ₉ (69 ± 2)	<i>(54±8)</i>	413	370	362	356	336
i-C ₄ H ₉ (70 ± 2)		422	371	363	360	341
t-C ₄ H ₉ (48 ± 3)	<i>(39±4)</i>	400	360	352	341	321
t-C ₅ H ₁₁ (28 ± 3)		402	361	354	334	314
C ₃ H ₅ (allyl)(171 ± 3)	<i>(164±6)</i>	368	318	311	309	302
C ₃ H ₅ (propenyl)(267 ± 3)		465	421	414		
C ₄ H ₇ (isobutenyl)(138 ± 3)		373				
C ₄ H ₇ (methylallyl)(158 ± 3)		375				
C ₃ H ₃ (propargyl)(351 ± 2)		384	333	326	322	
C ₄ H ₅ (methylpropargyl)(313 ± 2)		385				
C ₆ H ₅ (phenyl)(341 ± 4)		475	436	428	423	408
C ₆ H ₅ CH ₂ (benzyl)(207 ± 4)	<i>(200± 6)</i>	375	324	318	317	309

error of a factor of 10 in these quantities at room temperature and a factor of 2 at 1000 K. Correspondingly an error of 21 kJ/mol will lead to an error of 4 orders of magnitude at room temperature and a factor of 10 at 1000 K. This is a direct reflection of the logarithmic dependence of the rate and equilibrium constants on the thermodynamic functions. It is clear that the accuracy that are now attainable is probably sufficient for higher temperature applications but is still somewhat unsatisfactory for room temperature use.

B: Kinetic Stability: The kinetic stability of hydrocarbon molecules and radicals that are consistent with the thermodynamics are summarized in Tables 3-4. Table 3 contains experimental data on the decomposition of a number of simple alkanes and alkynes and are the results of single pulse shock tube studies. They have been a major factor in the development of the results given in Table 2. Some noteworthy factors are the following: (a) It can be seen that at the high temperature end of the experimental studies, for a particular type of reaction the A-factors do not vary greatly except for the influence of reaction path degeneracy and differences in rate constants are largely due to activation energy changes. (b) It is possible to discern a difference in the A-factors for the cases where alkyl radicals are formed as opposed to the formation of a resonance stabilized radical. This difference is explicable in terms of the stiffer structure of the latter. (c) Over the entire temperature range, for the bond breaking reaction of alkanes there is a negative curvature of the Arrhenius plot. This is much larger for the most highly substituted hydrocarbon. Actually, the lowest temperature results are derived from the conversion of the combination rate constants to the dissociation values through the equilibrium

Table 3: Summary of rate expressions for the decomposition of some alkanes and alkynes

Reaction	Rate Expressions
Alkanes 1000-1200K	
k(iC ₃ H ₇ -tC ₄ H ₉) => iC ₃ H ₇ + tC ₄ H ₉	2.5x10 ¹⁶ exp(-36800/T)s ⁻¹
k(iCH ₃ -tC ₄ H ₉) => CH ₃ + tC ₄ H ₉	1x10 ¹⁷ exp(-41100/T)s ⁻¹
k(C ₂ H ₅ tC ₅ H ₁₁) => C ₂ H ₅ + tC ₅ H ₁₁	6x10 ¹⁶ exp(-38800/T)s ⁻¹
k(iC ₃ H ₇ -tC ₅ H ₁₁) => iC ₃ H ₇ + tC ₅ H ₁₁	2.3x10 ¹⁶ exp(-35900/T)s ⁻¹
k(sC ₄ H ₉ -tC ₄ H ₉) => sC ₄ H ₉ + tC ₄ H ₉	3x10 ¹⁶ exp(-36400/T)s ⁻¹
k(sC ₄ H ₉ -sC ₄ H ₉) => sC ₄ H ₉ + sC ₄ H ₉	3.5x10 ¹⁶ exp(-37900/T)s ⁻¹
k(C ₆ H ₁₁ -tC ₄ H ₉) => C ₆ H ₁₁ + tC ₄ H ₉	3x10 ¹⁶ exp(-37400/T)s ⁻¹
k(tC ₄ H ₉ -tC ₄ H ₉) => tC ₄ H ₉ + tC ₄ H ₉	3x10 ¹⁶ exp(-34500/T)s ⁻¹
Alkynes 1000-1200 K	
k(HCCCH ₂ -nC ₃ H ₇) => HCCCH ₂ + nC ₃ H ₇	8x10 ¹⁵ exp(-36300/T) s ⁻¹
k(HCCCH ₂ -iC ₄ H ₉) => HCCCH ₂ + iC ₄ H ₉	1.2x10 ¹⁶ exp(-36700/T) s ⁻¹
k(CH ₃ CCCH ₂ -nC ₃ H ₇) => CH ₃ CCCH ₂ + nC ₃ H ₇	1.5x10 ¹⁶ exp(-36800/T) s ⁻¹
k(HCCCH ₂ -sC ₄ H ₉) => HCCCH ₂ + sC ₄ H ₉	8x10 ¹⁵ exp(-35000/T) s ⁻¹
k(HCCCH ₂ -iC ₃ H ₇) => HCCCH ₂ + iC ₃ H ₇	5x10 ¹⁵ exp(-34800/T) s ⁻¹
Alkanes 300 - 1200 K	
k(C ₂ H ₅ -C ₂ H ₅) => 2 C ₂ H ₅	4.4x10 ²⁵ (1/T) ^{2.7} exp(-44441/T)s ⁻¹
k(iC ₃ H ₇ -iC ₃ H ₇) => 2 iC ₃ H ₇	1.6x10 ³¹ (1/T) ^{4.2} exp(-43897/T)s ⁻¹
k(tC ₄ H ₉ -tC ₄ H ₉) => 2tC ₄ H ₉	5.5x10 ³⁸ (1/T) ^{6.45} exp(-41065/T)s ⁻¹

Table 4: Derived rate expressions for radical decomposition, based on thermodynamics and rate constant for addition 300–900 K

Reaction	Rate Expressions s ⁻¹	Rate Constants at 750 K s ⁻¹
nC ₃ H ₇ = C ₂ H ₄ + CH ₃	1.2x10 ¹³ exp(-15260/T)	1.8x10 ³
sC ₄ H ₉ = C ₃ H ₆ + CH ₃	9x10 ¹² exp(-14770/T)	2.5x10 ⁴
iC ₃ H ₇ = C ₃ H ₆ + H	2.6x10 ¹³ exp(-18730/T)	3.7x10 ²
sC ₄ H ₉ = 1-C ₄ H ₈ + H	1.3x10 ¹³ exp(-18320/T)	3.2x10 ²
sC ₄ H ₉ = c-C ₄ H ₈ + H	4.2x10 ¹² exp(-17500/T)	3.1x10 ²
sC ₄ H ₉ = t-C ₄ H ₈ + H	4.7x10 ¹² exp(-17100/T)	5.8 x10 ²
tC ₄ H ₉ = C ₄ H ₈ + H	8.5x10 ¹³ exp(-18900/T)	9.7 x10 ²

constant. Rate constants are in fact so small that they are not measurable and thus physically meaningful. The relative invariance of the A-factor at the higher temperatures is in contrast to the situation at the lower temperatures. The consequence is that with the existing data base on thermodynamics and decomposition kinetics it should be fairly straightforward to predict rate constants for decomposition of simple hydrocarbons.

Table 4 contains rate expressions for the decomposition of a number of alkyl radicals(12). The experimental data set of rate expressions for the decomposition of the larger alkyl radicals are unsatisfactory. Even for the same system rate expressions can be widely divergent. The situation is much better regarding rate constants. For such studies radicals must be generated in situ. Furthermore it is likely that many of the studies are in the region where energy transfer effects make significant contributions. However at somewhat lower temperatures there exist very good data on radical addition to olefins or the reverse of the decomposition reaction. Combination of this data with the equilibrium constants leads to rate expressions for decomposition. A check is offered through a match of the rate constants for decomposition at the experimental decomposition temperature. The results on H-bond cleavage is indicative of the effect of methyl substitution. Reaction pathway degeneracy must also be considered. We have also found that the effect of methyl substitution on C-C bond cleavage is very similar to that for the stable compounds (13).

CONCLUSION

Experimental studies have now led to highly accurate values for the thermodynamic and kinetic stability of a large number of hydrocarbon radicals. The techniques that have been employed are extensible to other systems. There is the need for such measurements for many of the larger highly unsaturated radicals with or without resonance stabilization. The increased accuracy requirements under ambient conditions mean that there is still a need to reduce uncertainty limits in all cases. In combination with rapidly developing theory, the expectation is for increasingly accurate predictions of the properties of reactive hydrocarbon systems.

REFERENCES

- O'Neal, H. E., Benson, S. W., "Thermochemistry of Free Radicals" in "Free Radicals" (Kochi, J., ed.) John Wiley and Sons, New York, 1973
- Benson, S. W., "Thermochemical Kinetics", John Wiley and Sons, New York, 1974
- Frisch, M. J.; Trucks, G. W.; Head-Gordon, M.; Gill, P. M. W.; Wong, M. W.; Foresman, J. B.; Johnson, B. G.; Schlegel, H. B.; Robb, M. A.; Replogle, E.S.; Gomperts, R.; Andres, J. L.; Raghavachari, K.; Binkley, J. S.; Gonzalez, C.; Martin, R. L.; Fox, D. J.; Defrees, D. J.; Baker, J.; Stewart, J. J. P.; Pople, J. A. Gaussian 92, revision F.4; Gaussian, Inc.: Pittsburgh, PA, 1992.
- McMillen, D. E. and Golden, D. M., (1982), *Annu. Rev. Phys. Chem.*, 33, 493-532
- Berkowitz, J., Ellison, G. B., and Gutman, D., *J. Phys. Chem.*, 98, 2744, 1995
- Tsang, W. and Kiefer, J. H., "Unimolecular Reactions over Extended Pressure and Temperature Ranges" in *Dynamics and Kinetics of Small Radicals*, ed. K. Liu and A. Wagner. World Scientific Company, Singapore, 1995, 59.
- Tsang, W., "Heats of Formation of Organic Free Radicals by Kinetic Methods" in "Energetics of Free Radicals" (A. Greenberg and J. Liebman, ed.) Blackie Academic and Professional, 1996 , 22
- Ellison G. B., Davico, G. E., Bierbaum, V., and DePuy, C., *Int. J. Mass Spec.* 1996, 156, 109
- Butler, E. T., Mandel, E. and Polanyi, M., *Trans. Faraday Soc.*, 41, 298, 1945
- Szwarc, M., *Chem. Rev.*, 47, 1675, 1950
- Stull, D. R., Westrum, E. F., and Sinke, G. R., (1969) "The Chemical Thermodynamics of Organic Compounds", John Wiley and Sons, New York, NY
- Tsang, W., *J. Amer. Chem. Soc.*, 107, 2872, 1985
- Tsang, W., unpublished results

CLIMBING MOUNT PSI: THE LEVEL OF THEORY NEEDED TO OBTAIN 1 KCAL/MOL
ACCURACY IN THERMOCHEMICAL PROPERTIES

David Feller
Environmental Molecular Sciences Laboratory,
Pacific Northwest National Laboratory, MS K1-96
P.O. Box 999, Richland, Washington 99352

ABSTRACT

A variety of molecular properties, including atomization energies, bond lengths and harmonic vibrational frequencies were computed for more than 80 experimentally well-characterized molecules, many of which were taken from the Gaussian-2 and G2/97 collections. This body of data was stored in the Environmental Molecular Sciences Laboratory Computational Results Database and was subsequently analyzed to determine the sensitivity of each property towards the electron correlation treatment and the quality of the underlying Gaussian basis set. In light of the importance of the basis set in limiting the ultimate accuracy of the theoretical predictions, a wide range of correlation consistent basis sets (including, in some cases, up through aug-cc-pV6Z) was used. These were combined with five popular levels of theory, ranging from simple Hartree-Fock theory up through coupled cluster theory. The importance of core/valence, scalar relativistic, atomic spin-orbital effects and more extensive correlation recovery were also examined in terms of their impact on agreement with experiment. All of these effects can contribute on the order of 1 - 2 kcal/mol or more to quantities such as a heat of formation.

I. INTRODUCTION

The accuracy of five widely-used electronic structure methods in reproducing experimental atomization energies (ΣD_e), electron affinities, proton affinities, ionization potentials, vibrational frequencies and geometries were recently examined by Feller and Peterson.¹ Methods included Hartree-Fock (HF) theory, second- and fourth-order Møller-Plesset perturbation theory (MP2 and MP4), coupled cluster theory with single and double excitations (CCSD) and coupled cluster theory with a quasiperturbative treatment of triples (CCSD(T)). In addition to the raw errors resulting from each specific (method/ basis set) pair, an attempt was made to assess a given method's *intrinsic* error, i.e. the deviation with respect to experiment in the limit of a complete 1-particle basis set.

Throughout the development of quantum chemistry, up until the early 1990s, the primary sources of error in most electronic structure calculations were more-or-less evenly attributable to relatively poor quality basis sets and an inadequate treatment of the electron correlation problem. However, following the development of the correlation consistent basis sets²⁻⁵ it became possible to exploit the regularity of these basis sets to perform an effective extrapolation to the complete basis set (CBS) limit. This was accomplished by fitting results obtained from successively larger and larger basis sets with one of a number of simple functional forms. Feller and Peterson examined three extrapolations. The first of these is the empirically motivated exponential form, given for total energies by the expression:

$$E(x) = E_{\text{CBS}} + b e^{-cx} \quad (1)$$

where x is an index associated with each basis set, $x=2$ (DZ), 3(TZ), 4(QZ), etc.⁶⁻¹⁰ The second is a combined Gaussian/exponential function:^{11,12}

$$E(x) = E_{\text{CBS}} + b e^{-(x-1)} + c e^{-(x-1)**2} \quad (2)$$

And, the final expression is:

$$E(\ell_{\text{max}}) = E_{\text{CBS}} + b/(\ell_{\text{max}} + 1)^4 \quad (2)$$

where ℓ_{max} is the maximum angular momentum present in the basis set.¹³ For second and third row correlation consistent basis sets, x (eq. 1) = ℓ_{max} (eq. 2).

II. PROCEDURE

Most geometries were optimized with a gradient convergence criterion of $1.5 \times 10^{-5} E_h/a_0$, corresponding to the "tight" criterion defined in Gaussian-94,¹⁴ using the same level of theory as was used in evaluating the desired property. For example, CCSD(T) thermochemical properties were evaluated at the optimal CCSD(T) geometries. A looser convergence criterion of $1.0 \times 10^{-4} E_h/a_0$ was necessary for the largest basis set CCSD(T) optimizations.

Unless otherwise noted, open shell energies were based on unrestricted Hartree-Fock (UHF) zeroth order wavefunctions and were performed with the Gaussian-94 program.¹⁴ Orbital symmetry and equivalence restrictions were not imposed in atomic calculations. Closed shell CCSD(T) calculations were performed with MOLPRO-97¹⁵ and Gaussian-94. CCSDT calculations were obtained from ACES II.¹⁶ All calculations were performed on a 16 processor Silicon Graphics, Inc. PowerChallenge, a 32 processor SGI Origin 2000 or an SGI/Cray J90 at D.O.E.'s National Energy Research Supercomputing Center. The largest CCSD(T) calculation reported in this study included 734 functions. As in the previous study, results were stored and analyzed using the Environmental Molecular Sciences Laboratory (EMSL) Computational Results Database,¹⁷ which currently contains over 32,000 entries.

Atomization energies were corrected for the effects of core/valence (CV) correlation (which is not included in normal frozen core calculations run with programs like Gaussian) by performing all electron calculations with the cc-pCVQZ basis sets, which are specially designed for this purpose. The 1s pairs of electrons for third period elements was treated as frozen cores.

Atomic spin-orbit and molecular/atomic scalar relativistic corrections were also appended to our nonrelativistic atomization energies and are denoted ΔE_{SO} and ΔE_{SR} , respectively. The former account

for the improper description of the atomic asymptotes, since atomic energies determined by our calculations correspond to an average over the possible spin multiplets. In some cases, such as the 2Π states of molecules like CH and OH, there is an additional *molecular* spin-orbit correction due to the splitting of the $2\Pi_1$ and $2\Pi_j$ states. Spin-orbit corrections were taken from the atomic and molecular values reported by Dunning and coworkers,^{10,12} which are based on the experimental values of Herzberg¹⁸ and Moore.¹⁹ Scalar relativistic corrections were obtained from configuration interaction wavefunctions including single and double excitations (CISD) using the cc-pVTZ basis set. The CISD(FC) wavefunction was used to evaluate the dominant 1-electron Darwin and mass-velocity terms in the Breit-Pauli Hamiltonian.

Our results will be compared to experimental atomization energies extrapolated to 0 K, both with and without zero point energies (ZPEs), i.e. $\Sigma D_0(0K)$ and $\Sigma D_e(0K)$, respectively. A majority of the experimental data used in this report was taken from the NIST-JANAF Tables (4th. Edition)²⁰ and Huber and Herberg.²¹ Our zero point energies were based on harmonic CCSD(T) frequencies.

III. RESULTS

Table 1 contains representative comparisons between CCSD(T) values of ΣD_0 and the corresponding, best available experimental values. The three right-most columns contain the differences with respect to experiment for the three CBS estimates, eqs. 1 - 3. For most of the 80 molecules the convergence in the frozen core binding energies is slow enough that fairly large basis sets are required. Of all the methods tested, only CCSD(T) shows continuous improvement in the level of agreement with experiment as the basis set size increases. If a double zeta basis set is largest that can be afforded, MP2 actually gives better statistical agreement with experiment.

In general, the errors arising from the use of $ZPE = 1\Sigma\omega$, where ω are harmonic frequencies obtained from CCSD(T) calculations, is relatively small. The mean absolute deviation with respect to experiment, ϵ_{MAD} , for frozen core CCSD(T) is ~ 1.5 kcal/mol, with worse case errors as large as 4.5 kcal/mol. This value includes adjustments for atomic spin-orbit effects. Core/valence corrections range from essentially zero to as much as 7.1 kcal/mol, and can be of either sign. By including core/valence corrections ϵ_{MAD} , drops into the 0.7 - 0.8 kcal/mol range. Relativistic corrections produce no *overall* change in ϵ_{MAD} , but did reduce the maximum errors. Although scalar relativistic corrections tend to decrease the binding energy, they can be of either sign and vary from near zero to 2.4 kcal/mol.

A correction should also be applied for the difference between CCSD(T) and full CI. Very little is known about this difference because CCSD(T) recovers such a large percentage of the correlation energy that determining energies with even greater accuracy is a very difficult task. We recently examined the impact of higher order correlation effects on the dissociation energies of HF, N₂ and CO. Among the higher order methods examined were two variations of coupled cluster theory (CCSDT and CCSD(TQ)) and two approximations to full configuration interaction. Again, basis sets were chosen from the correlation consistent family of basis sets, with the largest being the aug-cc-pVQZ set. Polarized valence double zeta quality basis sets were found to yield corrections that differed substantially from larger basis set results. At the double zeta level, higher order corrections increased the binding energies, whereas calculations with triple and quadruple zeta basis sets gave the opposite effect. Although the absolute magnitude of the higher order corrections was small for these diatomics, they were nonetheless significant in light of a target accuracy of ± 1 kcal/mol. Among molecules composed of first-through-third period elements, such as those in the G2 and G2/97 collections, the contribution to ΣD_0 from higher order correlation effects could easily exceed 1 kcal/mol. CCSD(TQ) often overestimated the higher order correction, sometimes exceeding the estimated full configuration interaction result by a factor of three.

Normally, because CCSD(T) is based on only a single reference configuration, it would not be expected to describe transition states very well. However, for some transition states, where the Hartree-Fock configuration still constitutes a significant component in the transition state wavefunction, CCSD(T) may perform as well as explicit multireference methods like configuration interaction (CI). The transition state for the reaction $H_2CO \rightarrow H_2 + CO$ has been obtained with a wide assortment of theoretical methods. Compared to complete active space CI, CCSD(T) does a good job of predicting the barrier height and is far less costly.

VII. CONCLUSIONS

CCSD(T) atomization energies were computed for a set of 80 molecules with reliable experimental data. Basis sets were taken from the augmented correlation consistent family and represent some of the largest Gaussian basis sets currently available. By using any of the three complete basis set extrapolations (eqns. 1 - 3), it is possible to enter a regime where core/valence, scalar relativistic, atomic spin-orbit, anharmonic ZPE effects or higher order correlation effects can become as important as the remaining error due to the use of finite basis set. Failure to account for any one of these effects can lead to errors on the order of several kcal/mol or more in particularly troublesome cases. On the other hand, in fortunate cases some of these corrections can nearly cancel. The overall mean absolute deviation is below 1 kcal/mol.

Although CCSD(T) suffers from some of the same limitations as other single-reference methods, it is currently the most accurate *ab initio* electronic structure technique that can be applied with large basis sets to small molecules. Coupled cluster theory *without* the inclusion of triple excitations was found to be frequently less accurate for atomization energies than second order perturbation theory. CCSD(T) is not capable of describing large regions of most potential energy surfaces, but nonetheless it may do quite well for certain transition states.

ACKNOWLEDGMENTS

This research was supported by the U. S. Department of Energy under Contract No. DE-AC06-76RLO 1830. The Pacific Northwest National Laboratory is a multiprogram national laboratory operated by Battelle Memorial Institute.

REFERENCES

- (1) Feller, D.; Peterson, K. A. *J. Chem. Phys.* **1998**, *108*, 154.
- (2) Dunning, T. H., Jr. *J. Chem. Phys.* **1989**, *90*, 1007.
- (3) Woon, D. E.; Peterson, K. A.; Dunning, T. H., Jr. **to be published**.
- (4) Wilson, A. K.; Mourik, T. v.; Dunning, T. H., Jr. *J. Mol. Struct. (Theochem)* **1996**, *388*, 339.
- (5) van Mourik, T.; Dunning, T. H., Jr. *Theor. Chem. Acc.* **to be published**.
- (6) Feller, D. *J. Chem. Phys.* **1992**, *96*, 6104.
- (7) Xantheas, S. S.; Dunning, T. H., Jr. *J. Phys. Chem.* **1993**, *97*, 18.
- (8) Feller, D. *J. Chem. Phys.* **1993**, *98*, 7059.
- (9) Woon, D. E.; Dunning, T. H., Jr. *J. Chem. Phys.* **1993**, *99*, 1914.
- (10) Peterson, K. A.; Kendall, R. A.; Dunning, T. H., Jr. *J. Chem. Phys.* **1993**, *99*, 1930.
- (11) Peterson, K. A.; Woon, D. E.; Dunning, T. H., Jr. *J. Chem. Phys.* **1994**, *100*, 7410.
- (12) Woon, D. E.; Dunning, T. H., Jr. *J. Chem. Phys.* **1994**, *101*, 8877.
- (13) Martin, J. M. L. *Chem. Phys. Lett.* **1996**, *259*, 679.
- (14) Frisch, M. J.; Trucks, G. W.; Schlegel, H. B.; Gill, P. M. W.; Johnson, B. G.; Robb, M. A.; Cheeseman, J. R.; Keith, T. A.; Petersson, G. A.; Montgomery, J. A.; Raghavachari, K.; Al-Laham, M. A.; Zakrzewski, V. G.; Ortiz, J. V.; Foresman, J. B.; Cioslowski, J.; Stefanov, B. B.; Nanayakkara, A.; Challacombe, M.; Peng, C. Y.; Ayala, P. Y.; Chen, W.; Wong, M. W.; Andreas, J. L.; Replogle, E. S.; Gomperts, R.; Martin, R. L.; Fox, D. J.; Binkley, J. S.; Defrees, D. J.; Baker, J.; Stewart, J. J. P.; Head-Gordon, M.; Gonzalez, C.; Pople, J. A. Gaussian 94, E.3, Gaussian, Inc. Pittsburg PA, 1996.
- (15) Werner, H. J.; Knowles, P. J.; Almlöf, J.; Amos, R. D.; Berning, A.; Cooper, D. L.; Deegan, M. J. O.; Dobbyn, A. J.; Eckert, F.; Elbert, S. T.; Hampel, C.; Lindh, R.; Lloyd, A. W.; Meyer, W.; Nicklass, A.; Peterson, K. A.; Pitzer, R. M.; Stone, A. J.; Taylor, P. R.; Mura, M. E.; Pulay, P.; Schütz, M.; Stoll, H.; Thorsteinsson, T. MOLPRO, Universität Stüttgart, Stüttgart, Germany, University of Sussex, Falmer, Brighton, England, 1997.
- (16) Stanton, J. F.; Gauss, J.; Watts, J. D.; Nooijen, M.; Oliphant, N.; Perera, S. A.; Szalay, P. G.; Lauderdale, W. J.; Gwaltney, S. R.; Beck, S.; Balkova, A.; Bernholdt, D. E.; Baeck, K.-K.; Rozyczko, P.; Sekino, H.; Hober, C.; Bartlett, R. J.; Almlöf, J.; Taylor, P. R.; Helgaker, T.; Jensen, H. J. A.; Jørgensen, P.; Olsen, J. ACES II, University of Florida, 1998.
- (17) Feller, D. *J. Comp. Chem.* **1996**, *17*, 1571.
- (18) Herzberg, G. *Molecular Spectra and Molecular Structure I. Spectra of Diatomic Molecules*; Van Nostrand Reinhold Co., Inc.: New York, 1950.
- (19) Moore, C. E. *Atomic Energy Levels* Washington, D.C., 1949; Vol. U.S. National Bureau of Standards Circular 467, NBS.
- (20) Chase, M. W., Jr. *NIST-JANAF Tables (4th Edition)*, *J. Phys. Chem. Ref. Data*, **1998**, *Mono. 9*, Suppl. 1.
- (21) Huber, K. P.; Herzberg, G. *Molecular Spectra and Molecular Structure: Constants of Diatomic Molecules*; Van Nostrand Reinhold Co. Inc.: New York, 1979; Vol. 4.

Table 1. Contributions to CCSD(T) Atomization Energies (kcal/mol) for a Selected Subset of the G2 Molecules.^a

Molecule	ΣD_e	ZPE Expt.			Atom. Expt. ΣD_0			Erro r	w.r.t. Mixed Exp.	Expt. ℓ_{\max}
		$1\Sigma_{\omega_1}$	ZPE	ΔE_{CV}	ΔE_{SR}	ΔE_{SO}	(0K)			
CH ₄ (¹ A ₁)	418.9	27.8	27.6	1.3	-0.2	-0.1	392.5 ± 0.1	-0.4	-0.4	-0.3
H ₂ O (¹ A ₁)	232.5	13.5	13.3	0.5	-0.3	-0.2	219.35 ± 0.01	-0.4	-0.6	-0.4
HF (¹ Σ^+)	141.4	5.9	5.9	0.2	-0.2	-0.4	135.2 ± 0.2	-0.1	-0.1	-0.1
SiH ₂ (¹ A ₁)	153.6	7.3	7.3	0.0	-0.2	-0.4	144.4 ± 0.7	1.3	1.3	1.5
HCl (¹ Σ^+)	107.0	4.3	4.2	0.3	-0.2	-0.8	102.24 ± 0.5	-0.2	0.0	0.1
CO (¹ Σ^+)	258.2	3.1	3.1	0.9	-0.2	-0.3	256.2 ± 0.2	-0.7	-0.7	-0.5
N ₂ (¹ Σ_g^+)	226.1	3.4	3.4	1.0	-0.1	0.0	225.1 ± 0.4	-1.5	-1.1	-0.8
SO ₂ (¹ A ₁)	257.6	3.9	4.4	1.0	-0.9	-1.0	254.0 ± 0.2	-1.2	-0.3	0.4
Cl ₂ (¹ Σ_g^+)	58.8	0.8	0.8	0.2	+0.7	-1.7	57.18 ± 0.01	0.0	0.4	0.7

^aThe atomic asymptotes were described with the UCCSD(T) method. The column labeled " ΣD_e " contains complete basis set estimates based on aug-cc-pVTZ through aug-cc-pV6Z basis sets. Theoretical zero point energies were obtained from CCSD(T) calculations. Errors for the exponential, mixed and $1/\ell_{\max}$ CBS atomization energies (ΣD_0), which appear in the three right-most columns, were computed as the difference between the theoretical value, defined as: $E[\text{CCSD(T)}(\text{FC})/\text{CBS}] - 1\Sigma_{\nu_1} + \text{CV} + \text{scalar relativistic} + \text{atomic/molecular S.O.}$ and the bolded experimental value. For diatomics with a nonzero molecular spin-orbit contribution, e.g. OH (² Π), the sum of the atomic and molecular contributions is included in ΔE_{SO} .

REVERSE RADICAL DISPROPORTIONATION: A MECHANISTIC STUDY

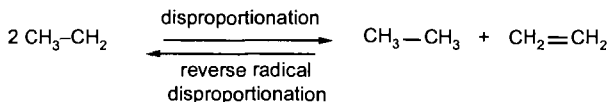
Christoph Rüchardt

Institut für Organische Chemie und Biochemie, Universität Freiburg
Albertstr. 21, D-79104 Freiburg, Germany
E-Mail: ruechardt@oca.chemie.uni-freiburg.de

Keywords: Retro-disproportionation, hydrogen transfer, thermochemistry, free radicals

INTRODUCTION

Radical disproportionations are well known radical destroying processes. The reverse reaction, accordingly, generates free radicals e.g. from an alkene and a hydrocarbon:



Despite a few early references (1) the scope and the mechanistic details of reverse radical disproportionations (retrodisproportionations) have been investigated only recently. In this context it was suggested that reverse disproportionations are important components to the complex network of reactions which are responsible for coal liquefaction processes (2) but also to synthetic dehydrogenations by quinones (3) or nitro compounds (4). In addition there is evidence which supports the assumption that NAD(P)H-reductions in the cell are initiated by reverse disproportionation (1,3).

EXPERIMENTAL

The methodology and the materials were described previously in detail (5).

RESULTS AND DISCUSSION

The mechanistic study which was performed in our laboratory concentrated in the beginning on the reactions of 9,10-dihydroanthracene (DHA), xanthene, acridane and N-methylacridane and a series of similarly structured hydrocarbons with weak C-H-bonds and α -methylstyrene as hydrogen acceptor. Then, in addition, a series of substituted styrene, cyclic dienes and aromatic hydrocarbons like azulene or polyacenes were included. These reactions are performed generally in the temperature range from 200 – 350° C. The reactions lead usually to quantitative transformations of starting materials. From this investigation, which will be reviewed briefly in this preprint, the three-step non chain radical mechanism of Scheme 1 was suggested

If the radicals formed from the donor in step 1 cannot disproportionate, alternative termination reactions are observed, frequently by participation of the solvent. In the case of styrene as an acceptor the DHA-derived radicals do add to another styrene molecule and a formal addition product of DHA to styrene is isolated (an-reaction) (6).

The following results support the suggested mechanism:

1. When the H-donors are varied, $\log k$ decreases proportionally with the increasing C-H-bond strength (Polanyi-relationship)
2. The activation enthalpies ΔH^\ddagger are a few kcal smaller than the reaction enthalpies of the rate determining retrodisproportionation step and they correlate linearly with each other (thermochemical kinetics) (7).
3. Solvent effects are small (<factor 10) and they do not correlate with solvent polarity.
4. Polar substituents in the acceptor (subst. α -methylstyrenes) or donor (xanthene or acridane vs. DHA or substituted DHA) are also small (< factor 10).
5. When deuterated donors are used no deuterium incorporation into the starting acceptor is found in most examples proving that step 1 is irreversible. The kinetic isotope effects

in these experiments $k(H)/k(D)$ are close to the maximal expected values at a given temperature.

6. The observation of an *isokinetic relationship* over a wide range of reactivity supports the assumption that no change of mechanism is occurring within this series.
7. The existence of free radical intermediates and their structures are shown by epr, by spin trapping, by radical clock experiments and by the observation of other radical rearrangements e.g. the azulene - naphthalene rearrangement (8).

A phenomenon which may be of importance in coal liquefaction processes is the observation that the H-transfer reaction of e.g. DHA to α -methylstyrene is strongly enhanced by the addition of a hydrocarbon with a weaker C-H bond (e.g. 7H-benz(de)anthracene) which is not used up during the overall reaction. This reaction, therefore, can be performed at temperatures as low as 200 – 230° C instead of 300° C when a „catalyst“ of this type is added (9). Fullerenes like C_{60} or C_{70} are transfer hydrogenated with DHA in a specific way to the partially hydrogenated products $C_{60}H_{16}$, $C_{60}H_{36}$ and $C_{70}H_{36}$ (10). The mechanistic criteria discussed above apply also to quinone oxidations of acridanes or N-subst.-nicotinamides. This suggests, that biochemicals NAD(P)H-reductions are also initiated by retrodisproportionation.

CONCLUSIONS

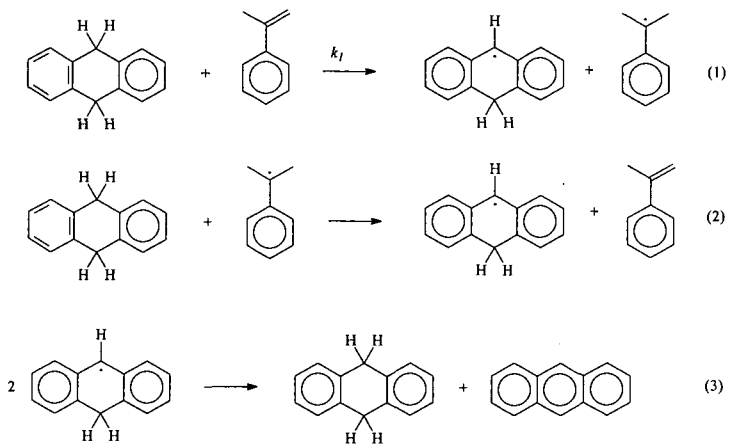
Retrodisproportionations are a class of important free radical reactions which have been unduly neglected for a long time. They are responsible in particular for high temperature hydrogen transfer reactions e.g. in coal liquefaction processes and their mechanisms are well understood now. The quantitative kinetic investigations should allow predictions for simulations of complex high temperature radical reactions of hydrocarbons.

ACKNOWLEDGEMENT

The contributions of a large group of coworkers, whose names are mentioned in the references, are gratefully acknowledged. The research reported in this paper was generously supported by the State of Baden - Württemberg, Deutsche Forschungsgemeinschaft and the Fonds der Chemischen Industrie.

REFERENCES

- (1) For a recent review and for references see C. Rüchardt, M. Gerst, J. Ebenhoch, *Angew. Chem. Int. Ed. Engl.* **1997**, 36, 1406 - 1430.
- (2) see e.g. M. L. Poutsma, *Energy and Fuel*, **1990**, 4, 113 - 131.
- (3) C. Hoefler, C. Rüchardt, *Liebigs Ann.* **1996**, 183 - 188.
- (4) M. Coellen, C. Rüchardt, *Chem. Eur. J.* **1995**, 1, 564 - 571.
- (5) see ref. and literature quoted there.
- (6) J. O. Metzger, F. Bangert, *Chem. Ber.* **1994**, 127, 673 - 675.
J.O.Metzger in Houben-Weyl, *Methoden der Organischen Chemie*, 4th. Edition, (M. Regitz, B. Giese Ed.), Vol E 19a/part1, p. 60.
- (7) S. W. Benson, *Thermochemical Kinetics*, 2nd. ed., Wiley, New York, 1976.
- (8) F. Keller, H.-D. Beckhaus, C. Rüchardt, *Liebigs Ann.* **1997**, 2055 - 2063.
- (9) M. Gerst, J. Morgenthaler, C. Rüchardt, *Chem. Ber.* **1994**, 127, 1039 - 1045.
J.Morgenthaler, C.Rüchardt, *Eur.J.Org.Chem.* **1999**, (in print).
- (10) R. Bini, J. Ebenhoch, M. Fantì, P. W. Fowler, S. Leach, G. Orlandi, C. Rüchardt, J. P. B. Sandall, F. Zerbetto, *Chem. Phys.* **1998**, 232, 75 - 84, and references given there.



Scheme 1. Mechanism Proposed for Transfer Hydrogenation with DHA.

HYDROGEN ATOM ABSTRACTION BY TRANSITION METAL COMPLEXES

James M. Mayer, Justine P. Roth, Mark A. Lockwood, Kun Wang
Department of Chemistry
University of Washington, Box 351700
Seattle, Washington 98195

ABSTRACT

A key step in many oxidation reactions is hydrogen atom abstraction by a metal-containing reactive site. We have examined oxidations of alkanes and alkylaromatic compounds by metal-oxo compounds and metal coordination complexes, including chromyl chloride (CrO_2Cl_2), permanganate, manganese μ -oxo dimers, copper(III) compounds, and iron(II)-diimine complexes. The data indicate that many of the reactions proceed by initial hydrogen atom abstraction to give the hydrocarbyl radical. Addition of $\text{H}\cdot$ to the metal complex occurs with protonation of a ligand and one-electron reduction of the metal center. For example, $\{(\text{phen})_2\text{Mn}(\mu\text{-O})_2\text{Mn}(\text{phen})_2\}^{3+}$ is reduced first to $\{(\text{phen})_2\text{Mn}(\mu\text{-O})(\mu\text{-OH})\text{Mn}(\text{phen})_2\}^{3+}$ with protonation of a bridging oxo group. The rates at which these reagents abstract $\text{H}\cdot$ are quantitatively related to their thermodynamic affinity for $\text{H}\cdot$ (in other words, the strength of the O-H or N-H bond they form). On this basis, there are strong analogies to well-known organic radical chemistry, even though the oxidants may not have any radical character. In efforts toward a more detailed understanding of H-atom transfer, studies are ongoing of hydrogen-atom self exchange rates.

INTRODUCTION

The oxidation of hydrocarbons often involves initial abstraction of a hydrogen atom to form a carbon radical (eq 1). This occurs in combustion reactions and in a range of industrial partial oxidation processes, many of which are done on an enormous scale. Hydrogen atom abstraction is also implicated in a variety of biochemical processes and is increasingly valuable in organic synthesis. The abstracting agent in H-atom transfer reactions is typically a reactive main group radical, a species with at least one unpaired electron spin. For this reason, H-atom transfer is classified as a "radical reaction."



The current understanding of rates of hydrogen abstraction by radicals is based not on radical character but on the enthalpy of reaction.¹ This was first enunciated by Evans and Polanyi in the 1930s. The enthalpy change (ΔH) for reaction 1 is simply the difference between the strength of the R-H bond being cleaved and the strength of the H-X bond formed. Activation energies E_a (and rate constants $\log k$) correlate closely with ΔH when comparing similar radicals. This is reminiscent of the Marcus-Hush theory of electron transfer, in which rates correlate with driving force as long as reagents of similar intrinsic barriers are compared. Different classes of radicals fall on different correlation lines. The standard explanation for this is termed polar effects, a result of the overlap of the half-occupied frontier orbital of the radical with the HOMO and LUMO of the C-H bond.

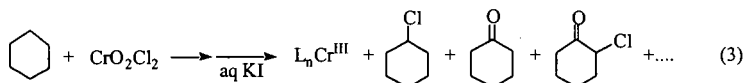
We have been exploring hydrocarbon oxidations by transition metal complexes, many of which proceed by $\text{H}\cdot$ transfer to a ligand on the transition metal (eq 2). The presence or absence



of unpaired electrons in such complexes does not correlate with reactivity and therefore cannot be used to understand $\text{H}\cdot$ transfer. So instead of looking at the spin state of the metal complex $\text{M}(\text{X})\text{L}_n$, it has often been assumed that there is a requirement for radical character at the ligand that accepts the H (X in eq 2). We find that the metal reactions are predominantly influenced by the ground state thermodynamics (the ΔH) rather than by radical character. Similar conclusions have recently been reached for hydrogen atom transfer between alkanes and alkenes (and related reactions).² We are now beginning to explore what is meant by the phrase *similar radicals* when the abstractor is not a radical. [An experimental section is not included here; the reader is referred to the original, peer-reviewed literature for such information.^{5,7,8}]

RESULTS AND DISCUSSION

The oxidation of alkanes by chromyl chloride, CrO_2Cl_2 (e.g., eq 3), is known as the Étard reaction and dates from the nineteenth century. In the 1960s, Wiberg and co-workers argued convincingly for organic radical intermediates (though other mechanisms have been discussed).³ Organic radicals have also been implicated in the oxidations of alkylaromatic compounds by permanganate.⁴ Detailed mechanistic studies in our labs⁵ have indicated that both types of reactions occur by initial hydrogen atom transfer (e.g., eq 4).



Hydrogen atom abstraction by CrO_2Cl_2 and permanganate was at first surprising because these are d^0 , closed-shell species, with no unpaired spin density. Their reactions are better explained on the basis of the strength of the bond they can make to $\text{H}\cdot$, which can be calculated by a thermochemical cycle (Scheme 1).^{5,6} For permanganate, the value derived is 80 kcal/mol. As shown in Figure 1, the rate constant for hydrogen abstraction from toluene for permanganate is close to what would be predicted based on the Polanyi correlation of rates with driving force.

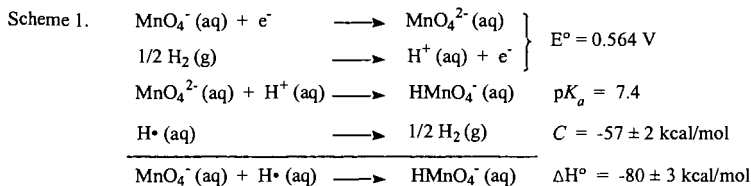
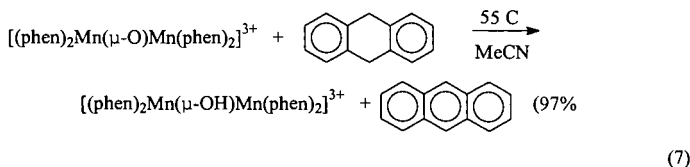
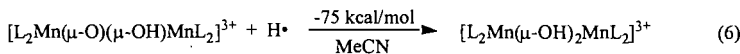
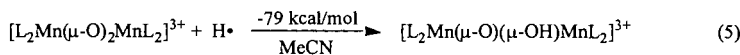


Figure 1 $\log k$ vs. O-H bond strength for reactions of toluene with ${}^n\text{Bu}_4\text{NMnO}_4$ and $\text{RO}\cdot$.

In principle, any active site with affinity for $\text{H}\cdot$ (that is, an affinity for both an electron and a proton) should be able to abstract hydrogen atoms from a substrate. And the rate constant for H-atom transfer should be roughly predictable from the Polanyi correlation illustrated in Figure 1. Our first efforts in this direction involved the dimanganese di- μ -oxo complex $[\text{Mn}_2(\mu\text{-O})_2(\text{phen})_4]^{3+}$.⁷ Redox potential and $\text{p}K_a$ measurements yielded the O-H bond strengths in eqs 5 and 6 (using a variant of Scheme 1). As predicted from this bond strength, $[\text{Mn}_2(\mu\text{-O})_2(\text{phen})_4]^{3+}$ oxidizes dihydroanthracene (DHA) to anthracene in high yield over 11 h at 55 °C (eq 7; traces of anthrone and anthraquinone are also formed). Kinetic and mechanistic studies⁷ indicate a pathway of initial hydrogen atom abstraction from the weak C-H bond, with a deuterium isotope effect $k_{\text{DHA}}/k_{d_{12}\text{-DHA}}$ of 4.2 ± 0.3 at 55 °C and formation of bifluorenyl and 9-fluorenone from fluorene.



Hydrogen atom abstraction has also been observed for an iron(III) complex,⁸ as shown in equation 8. Complex 1 has an affinity for an electron, because the Fe³⁺ center is oxidizing, and an affinity for a proton, because one of the biimidazole ligands is deprotonated. The measured *E* and p*K_a* values translate into an affinity for H• of 76 ± 2 kcal/mol. H-atom abstraction reactivity is perhaps surprising in this case because the proton accepting site is three bonds removed from the redox active iron.

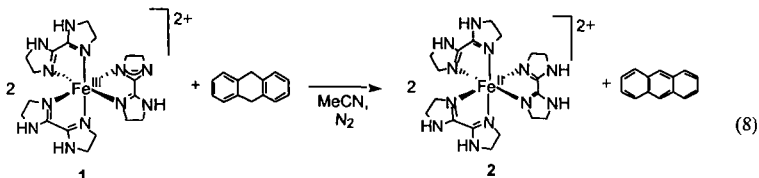


Figure 2 plots the rate constants for hydrogen abstraction from DHA versus the strength of the O–H or N–H bond formed for oxygen radicals, permanganate, the manganese μ -oxo dimers, and the iron complex 1. Remarkably, the rate constants for the metal complexes are within a factor of 10² of the values predicted by linear extrapolation of the values for ^tBuO• and ^{sec}BuOO• (Figure 2). This is a one-parameter fit of the rate constants, based only on the ground state affinity of the oxidant for H•. While it is not yet known how general a result this will be, it seems clear that analyzing a hydrogen transfer reaction should start with the relevant bond strengths.

Figure 2. log*k* vs. X–H bond strength for H-atom abstraction from dihydroanthracene.

Viewed from another perspective, the rough success of the correlation in Figure 2 indicates that ^tBuO•, ^{sec}BuO₂•, and the four metal complexes behave as “similar radicals.” We are now trying to understand what makes these oxidants are similar. A frontier orbital/polar effect argument is difficult to make, as the orbital patterns of the metal complexes are varied and quite different from that of the oxygen radicals. A polar effect rationale would also incorrectly predict that the iron complex would not correlate with the others, because it has a nitrogen rather than an oxygen as the atom that receives the hydrogen. An alternative possibility, following Marcus theory, is that these reagents are similar because they have similar intrinsic barriers. To explore this view, we have been studying the possible hydrogen atom self-exchange reaction between iron complexes 1 and 2. The oral presentation will describe recent results, and discuss the possibility that intrinsic barriers and polar effects are both needed to understand H-atom transfer reactions.

ACKNOWLEDGMENTS.

We want to thank those who have been involved in this effort in addition to the authors: Dr. Jerry Cook, Dr. Kim Gardner, Teresa Blubaugh, Andrea Collier, and Linda Kuehnert. We are also grateful the National Institutes of Health for the primary funding for this work, with early support from the donors of the Petroleum Research Fund, administered by the American Chemical Society, the National Science Foundation, Union Carbide, Chevron Research, BP America, DuPont, and the Exxon Education Foundation.

REFERENCES

- (1) Ingold, K. U. Chapter 2, pp. 69ff and Russell, G. A. Chapter 7, pp. 283-293 in *Free Radicals* Kochi, J. K., Ed.; Wiley: New York, 1973. Tedder, J. M. *Angew. Chem., Int. Ed. Engl.* **1982**, *21*, 401.
- (2) Richardt, C.; Gerst, M.; Ebenhoch, J. *Angew. Chem., Int. Ed.* **1997**, *36*, 1406-1430.
- (3) Wiberg, K. B. in *Oxidation in Organic Chemistry Part A*: K. B. Wiberg, Ed., Academic, New York, 1965, pp. 69-184. Freeman, F. in *Organic Syntheses by Oxidation with Metal Compounds* W. J. Mijs, C. R. H. I. de Jonge, Eds., Plenum, New York, 1986, Chapter 2. Nenitzescu, C. D. *Bull. Soc. Chim. Fr.* **1968**, *4*, 1349. Rappé, A. K.; Goddard, W. A., III *J. Am. Chem. Soc.* **1982**, *104*, 3287.
- (4) Waters, W. A. *Quart. Rev. (London)* **1958**, *277*. Stewart, R. *Oxidation Mechanisms*; Benjamin: New York, 1964. Fatiadi, A. J. *Synthesis (Stuttgart)* **1987**, 85.
- (5) Cook, G. K.; Mayer, J. M. *J. Am. Chem. Soc.* **1994**, *116*, 1855. Cook, G. K.; Mayer, J. M. *ibid* **1995**, *117*, 7139. Wang, K.; Mayer, J. M. *J. Org. Chem.* **1997**, *62*, 4248. Gardner, K. A.; Kuehnert, L. L.; Mayer, J. M. *Inorg. Chem.* **1997**, *36*, 2069. Mayer, J. M. *Acc. Chem. Res.* **1998**, *31*, 441-50.
- (6) Leading references: Bordwell, F. G. *et al. J. Am. Chem. Soc.* **1991**, *113*, 9790; **1996**, *118*, 8777. Parker, V. D. *ibid.* **1992**, *114*, 7458 & **1993**, *115*, 1201. Tilset, M.; Parker, V. D. *ibid.* **1989**, *111*, 6711 & *ibid.* **1990**, *112*, 2843. Parker, V. D.; Handoo, K. L.; Roness, F.; Tilset, M. *ibid.* **1991**, *113*, 7493. Wayne, D. D. M.; Luszytky, E.; Page, D.; Ingold, K. U.; Mulder, P.; Laarhoven, L. J. J.; Aldrich, H. S. *ibid.* **1995**, *117*, 8737.
- (7) Wang, K.; Mayer, J. M. *J. Am. Chem. Soc.* **1997**, *119*, 1470.
- (8) Roth, J. P.; Mayer, J. M. *Inorg. Chem.*, in press.

THERMODYNAMIC AND KINETIC STUDIES OF REACTIONS OF THIOLS, DISULFIDES,
SULFUR, AND HYDROGEN SULFIDE

Carl D. Hoff
Department of Chemistry,
University of Miami
Coral Gables, Florida 33124

ABSTRACT

A range of SAT [sulfur atom transfer] enthalpies have been determined for reactions involving both main group and transition metal compounds. These include sulfur atom transfer reactions to phosphine, arsine and stibine¹, carbene², and stannylene³ compounds as well as insertion of sulfur into metal-hydrogen⁴ and metal-metal bonds⁵. Kinetic and thermodynamic studies of reactions of thiols⁶, disulfides⁷, hydrogen sulfide⁸, and sulfur⁹ with complexes of chromium, molybdenum, and tungsten, have also been performed. The choice of mechanism appears to depend primarily on the strength of the sulfur-sulfur or sulfur-hydrogen bond that is broken, but also can be changed by ligand donor ability of the sulfur compound.

I. INTRODUCTION

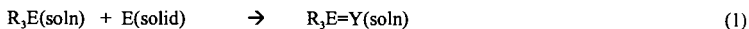
The chemistry of transition metal sulfur complexes is important to a number of industrial and biochemical processes.¹⁰ Oxidative addition of the sulfur-sulfur and sulfur hydrogen bond to metals play a fundamental role in these reactions. Thermochemical data for these reactions are rare in spite of their importance. In addition, there are relatively few mechanistic studies of reactions with transition metal complexes in solution of the simple sulfur reactants H₂S and S₈.¹¹ The mechanisms and energetics of these reactions may lend some insight into possible heterogeneous reactions of the same substrates.

II. PROCEDURE

Enthalpies of reaction have been measured by reaction calorimetry using either a Setaram Calvet Calorimeter or Guild Solution Calorimeter using techniques described in detail elsewhere.¹ Kinetic studies were performed using a flow through FT-IR microscope/reactor system that has also been described in the literature¹². Reagents, solvents, and gases were all carefully purified using standard techniques.

III. RESULTS

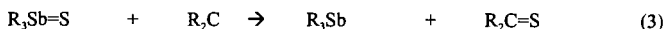
The enthalpies of reaction with chalcogen donors [Y = S, Se, Te] have been measured for a range of R₃E complexes [E = P, As, Sb] according to eqn. (1) in toluene solution at room temperature:



For 1/8 S₈ these data span over 32 kcal/mole depending on R and E. The heavier donor atoms As and Sb are labile enough to measure directly sulfur atom transfers such as those shown in eqn.(2):



These data provide additional checks on the thermochemical data. They also provide a basis for direct measure of single S atom transfer reactions using R3Sb=S or R3As=S which in some cases are more selective than sulfur, as discovered by Jason¹³. The organostannylene complexes LSn [L = Me₃taa = octamethylidibenzotetraaza[14]annulene] prepared by Kuchta and Parkin¹⁴ also react directly with chalcogens and chalcogen atom transfer reagents to form the LSn=Y complexes. Enthalpies of addition to and subtraction from chalcogens at the Sn(II) center are in the expected order Se < S. The stable carbenes prepared by Arduengo and coworkers¹⁵ also undergo clean S atom transfer:



The enthalpies of S atom transfer to the carbene carbon are more exothermic than to the stannylene tin. The crystal structures of two of the R₂C=S complexes have been determined. There is a correlation between the structures, the enthalpies of sulfurization, and also the enthalpies of binding to metals of the carbene and stannylene ligands.

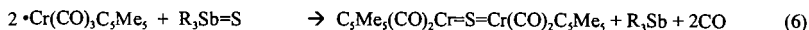
The enthalpies of insertion of a single sulfur atom into the metal-hydrogen bonds have been determined as shown in eqn. (4):



These data allow estimation of the M-SH bond strength which follows the order Cr < Mo < W. Desulfurization by phosphines of the metal sulphydryl complexes occurs in some cases as shown in eqn.(5), in keeping with thermochemical predictions:



Reaction (6) between two moles of the 17 electron stable chromium centered radical and triphenyl antimony sulfide occurs cleanly as shown:

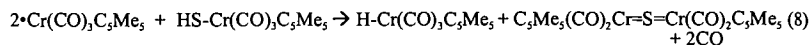


The enthalpy of reaction (6) has been measured and used to estimate the energy of "embedding" a single S atom in the multiply bonded bridging sulfido complex.

The stable transition metal radical $\bullet\text{Cr}[\bullet\text{Cr} = \bullet\text{Cr}(\text{CO})_3\text{C}_3\text{Me}_5]$ provides a good area for study of the mechanisms of reaction of a transition metal radical fragment with organosulfur substrates. Earlier work has shown a variety of mechanisms for reactions of thiols⁶ and disulfides⁷. This work has been extended to include H_2S and S_8 . Reaction of hydrogen sulfide with the radical species is much faster than analogous reactions of thiols. Initial oxidative addition of one sulfur-hydrogen bond occurs as shown in eqn. (7):



The metal sulphydryl complex formed in the first step can be further attacked by two moles of radical:

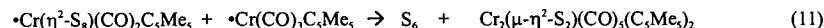


The mechanism of reaction (7) follows two pathways. Under pressure of carbon monoxide a third order rate law is obeyed [first order in hydrogen sulfide and second order in metal radical]. At low pressures of carbon monoxide, at higher temperatures, or under argon atmosphere, a second order rate law is obeyed [first order in hydrogen sulfide and first order in metal radical]. Rate and activation parameters as well as CO dependence are all consistent with rate determining ligand substitution to form the hydrogen sulfide substituted radical complex shown in eqn. (9):



In spite of the fact that the equilibrium in eqn. (9) lies to the left, the hydrogen sulfide substituted radical complex once formed can undergo rapid attack by a second mole of metal radical. Under appropriate conditions the rate of oxidative addition occurs at the rate of ligand substitution itself. The small size of hydrogen sulfide probably accounts for its increased ability, relative to thiols, to compete with carbon monoxide as a ligand.

In a similar way, S_8 also shows a complex reactivity pattern with the chromium radical and depends on carbon monoxide pressure. Kinetic evidence supports a pathway under argon atmosphere involving steps shown in eqn.(10) and (11):



Formation of $\text{Cr}_2(\mu\text{-}\eta^2\text{-S}_2)(\text{CO})_3(\text{C}_3\text{Me}_5)_2$ is clean under appropriate conditions and its enthalpy of formation as well as desulfurization to $\text{Cr}_2(\mu\text{-S})(\text{CO})_4(\text{C}_3\text{Me}_5)_2$ have been measured.

VII. CONCLUSIONS

Some insight into factors determining the enthalpies of sulfur atom transfer and insertion as well as the rates and mechanisms of related reactions have been determined. Considerable additional work is needed before the understanding of inorganic sulfur reactions achieves the level of understanding currently present in organic sulfur chemistry.

ACKNOWLEDGMENT

This research was supported by the Petroleum Research Fund administered by the American Chemical Society as well as the National Science Foundation.

REFERENCES

- (1) Capps, K. B.; Wixmerten, B.; Bauer, A.; Hoff, C. D. *Inorg. Chem.* **1998**, *37*, 2861.
- (2) Huang, J.; Schanz, H. J.; Nolan, S. P.; Bauer, A.; Capps, K. B.; Hoff, C. D.; **to be published.**
- (3) Parkin, G.; Kuchta, M. C.; Capps, K. B.; Wixmerten, B.; Bauer, A.; Hoff, C. D. **to be published.**
- (4) Bauer, A.; Capps, K. B.; Wixmerten, B.; Abboud, K. A.; Hoff, C. D. *Inorg. Chem.* **1999**, *38*, 2136.
- (5) Capps, K. B.; Bauer, A.; Hoff, C. D.; **to be published.**
- (6) Ju, T. D.; Capps, Lang, R. F.; Roper, G. C.; Hoff, C. D. *J. Am. Chem. Soc.* **1996**, *118*, 5328.
- (7) Ju, T. D.; Capps, K. B.; Lang, R. F.; Roper, G. C.; Hoff, C. D.; *Inorg. Chem.* **1997**, *36*, 614.
- (8) Capps, K. B.; Bauer, A.; Hoff, C. D.; *Inorg. Chem.* **submitted for publication.**
- (9) Capps, K. B.; Bauer, A.; Hoff, C. D.; **to be published.**
- (10) Transition Metal-Sulfur Chemistry. *ACS Symp. Ser.* **1996**, *653*.
- (11) James, B. R. *Pure and Appl. Chem.* **1997**, *69*, 2213.
- (12) Ju, T. D.; Capps, K. B.; Roper, G. C.; Lang, R. F.; Hoff, C. D.; *Inorg. Chim. Acta.* **1998**, *270*, 488.
- (13) Jason, M. E.; *Inorg. Chem.* **1997**, *36*, 241.
- (14) Kuchta, M. C.; Parkin, G.; *J. Amer. Chem. Soc.* **1994**, *116*, 8372.
- (15) Arduengo, A. J. III, Harlow, R. L.; Kline, M.; *J. Am. Chem. Soc.* **1991**, *113*, 361.

HYDROGEN TRANSFER FROM CATALYST INTERMEDIATE PROTOTYPES TO STABILIZED RADICALS

James A. Franz, Douglas S. Kolwaite, John C. Linehan and Jerome C. Birnbaum
Pacific Northwest National Laboratory
Richland, Washington 99352

Edward Rosenberg
University of Montana
Missoula, MT 59812

Keywords: Free Radicals, Organometallic Hydrides, Hydrogen Transfer, Kinetics, Benzyl Radical, Absolute Rates

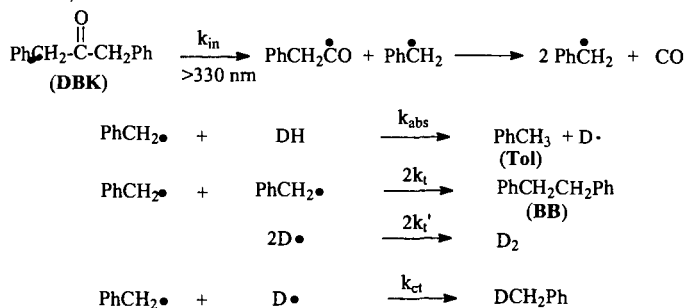
INTRODUCTION

The transfer of hydrogen from metal-hydrogen bonds (M-H) to closed-shell molecules or free radicals, from metal-activated organic structure (MC-H) and from metal-activated heteroatom-hydrogen bonds (MS-H) are primary processes involved in catalytic hydroxypropylolysis of organic structure. The characterization of the reactivity of transition metal hydride μ - and σ -bonds and agostic M-H₂ bonds in fundamental catalysis steps is of wide interest. Whereas a substantial body of data now exists describing the kinetics of reactions of alkyl organic free radicals with main group hydrides (e.g., S-H¹, Se-H², Sn-H and Si-H³), few kinetic studies of the reactions of transition metal hydrides⁴, and particularly hydrides involving novel metal bonding arrangements, exist. Relatively few kinetic studies of the reaction of benzylic radicals with either main group or transition metal hydrides exist. In previous work we have determined families of basis rate expressions for abstraction of hydrogen atom by alkyl and benzylic radicals from a variety of hydrogen donors for use in competition kinetic studies to measure rate constants for homolytic molecular rearrangements related to coal and biomass hydroxypropylolysis.⁵ Recently, we have carried out kinetic studies to determine the homolytic hydrogen transfer properties of hydrogen bonded in novel arrangements in metal clusters and other catalyst related systems. In this paper, we review recent results from application of competition kinetic methods to determination of absolute rates of abstraction of hydrogen atom from M-H, C-H and S-H bonds to the benzyl radical, where M = Mo, Os, Ru, Ir, and Rh.

KINETIC APPROACH

The kinetic method used in studies in this laboratory to determine rates of reaction of stabilized organic free radicals makes use of the competition of self-termination of the radical of interest with abstraction of hydrogen from the donor (DH) of interest. The competition of self-termination of benzyl radical to form bibenzyl (BB) versus hydrogen abstraction to form toluene (Tol) is depicted in Scheme 1. Thus, photolysis of a convenient photoprecursor (DBK) to form benzyl radical under conditions of constant rate of photolysis of DBK is followed by abstraction of hydrogen to form toluene (k_{abs}) versus self-termination ($2k_t$) to form bibenzyl.

Scheme 1



The rate of formation of bibenzyl and toluene are given by the differential equations ($[PhCH_2\bullet] = [B\bullet]$):

$$\frac{d[Tol(t)]}{dt} = k_{abs}[DH(t)][B\bullet] \quad (1)$$

$$\frac{d[BB(t)]}{dt} = k_t[B\bullet]^2 \quad (2)$$

Note that for constant benzyl radical concentration and short extent of consumption of donor, DH, integration of eq 1 and eq 2 yield expressions that are linear in toluene and bibenzyl with time.

Combining eqs 1 and 2, for $DH(t) = DH(0) - Tol(t)$ leads to eqs 3 and 4:

$$\int \left(\frac{d[Tol(t)]}{[DH(0)] - [Tol(t)]} \right) = k_{abs} \sqrt{\frac{1}{k_t} [BB] \Delta t} \quad (3)$$

$$Tol(t) = DH_0 \left(1 - e^{-\frac{k_{abs}(\sqrt{BB} \sqrt{\Delta t})}{\sqrt{k_t}}} \right) \quad (4)$$

Eq. 4 provides the time dependence of formation of toluene in terms of self-termination product, bibenzyl (BB), the elapsed time of the photolysis in seconds (Δt), the initial hydrogen donor concentration, DH_0 , and the rate constants for abstraction, k_{abs} , and self-termination, k_t .

At short extent of conversion of the donor, DH, and DBK, the exponent in eq 4 is small and the expression reduces to:

$$Tol(t) = DH_{av} \left(\frac{k_{abs}}{\sqrt{k_t}} (\sqrt{BB(t)} \sqrt{\Delta t}) \right) \quad (5)$$

or

$$k_{abs} = \frac{[Tol]}{[DH_{av}] \sqrt{BB} \sqrt{\Delta t}} \sqrt{k_t} \quad (6)$$

Short extent of conversion of photoprecursor, DBK, and hydrogen donor DH, results in constant benzyl radical concentration and linear formation of toluene and bibenzyl with duration of photolysis. If DBK is photolyzed at a constant rate of photolysis to short extent of conversion, but the donor DH is appreciably consumed, the time dependence of toluene and bibenzyl production will exhibit curvature described by eq 4. Providing values of k_t are available for a given solvent system, the method is a particularly convenient method for the determination of rate constants for abstraction, k_{abs} , by stabilized radicals from donors.

Experimental rate constants for self-termination of organic free radicals are available from the work of Fischer and coworkers.⁶ Rate constants can be estimated using the empirical method recommended by Fischer using the von Smoluchowski equation (eq 7) with diffusion coefficients derived from the Spornol-Wirtz modification of the Debye-Einstein equation (eq 8), or estimated by measurement of the diffusion coefficient of a model of the radical of interest (e.g., toluene for benzyl radical) in the solvent of interest by the Taylor method.⁷

$$2k_t = (8\pi / 1000) \sigma \rho D_{AB} N \quad (7)$$

$$D_{AB} = kT / 6\pi\eta r_f \quad (8)$$

In eq 7, N is Avogadro's number, D_{AB} is the diffusion coefficient of the radical A in solvent B, σ is a spin statistical factor describing the percent of singlet radical encounter pairs formed (1/4) and ρ is the diameter of the diffusing radical. Eq. 8 is the Spornol-Wirtz (SW)⁸ modification of the Debye Einstein equation ($f = SW$ microfriction factor, η is the viscosity of the solvent). A number of the assumptions inherent in this semiempirical approximation are subject to challenge. The assumption that 100% of singlet encounter radical pairs react in the solvent cage, and the assumption that the diffusion constants for the parent hydride can be used as a model⁹ for the radical can be challenged. Empirically it has been established by Fischer and coworkers that self-termination rate constants k_t for small carbon-centered radicals in non-associating solvents

can be estimated with errors less than about 20%. For benzyl radical in alkanes and in toluene, the errors in estimation of the rate constant for self termination of benzyl are less than 15%. Details of the procedure for estimation of values of k_t have been presented elsewhere. For self-termination of benzyl radical in benzene, the procedure provides the expression:

$$\ln(2k_t/M^{-1}s^{-1}) = 26.94 - 2733/RT, \text{ RT in calories.} \quad (9)$$

The competition kinetic method is most suitable for rate constants in the range 10^3 - 10^6 $M^{-1}s^{-1}$.

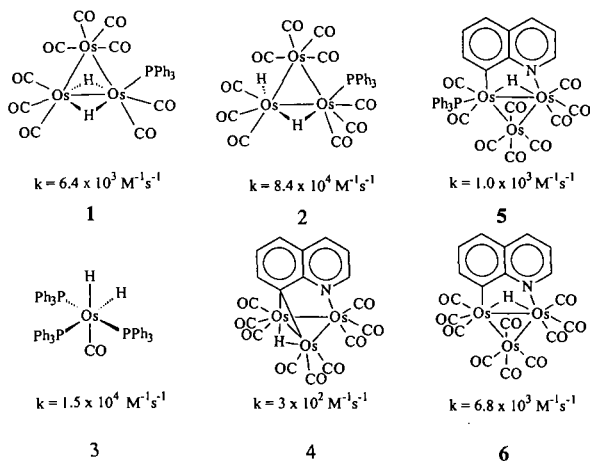
EXPERIMENTAL APPROACH

Samples of dibenzyl ketone (DBK), ~ 0.01 M, hydrogen donor, 10^{-4} - 10^{-2} M, and internal gas chromatography standard are dissolved in benzene in 5-mm x 6-cm diameter pyrex tubes. The solutions are freeze-thaw degassed in three cycles and sealed on a vacuum line. The samples are temperature-equilibrated in an aluminum block equipped with thermocouples in a temperature-controlled oven equipped with a quartz window to allow photolysis. The samples are photolyzed with the water-filtered light of a 1-kW Hanovia high pressure xenon arc lamp for periods of 0.5 second to typically 30 seconds, to short extent (e.g., < 1-2%) of conversion of DBK and donor. Samples are opened and the yields of toluene and bibenzyl are determined by gas chromatography. Care is taken to ensure that the temperature of the sample remains constant during the photolysis. To verify that equation (6) is appropriate, the time dependence of production of toluene and bibenzyl is measured using constant lamp power levels and carefully reproducible sample positioning. The use of eq 6 is appropriate for linear production of toluene and bibenzyl, as predicted by eqs 1 and 2, where benzyl radical concentration is a constant. For extensive conversion of donor, but constant photolysis rate of the photoprecursor, eq. 4 may be employed. For very fast donors, where significant consumption of donor occurs, very short photolysis times are necessary to operate in the linear range of toluene/bibenzyl concentration. A Uniblitz computer-controlled optical shutter was employed to allow accurate, short photolysis times. Hydrides were synthesized or purchased from Strem Chemical.¹⁰

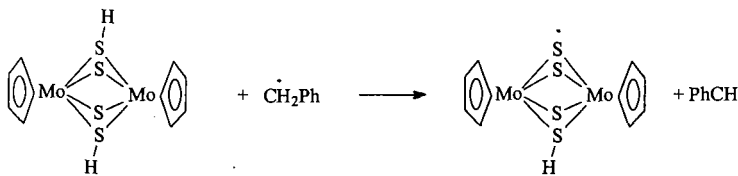
RESULTS AND DISCUSSION

Rate expressions for hydrogen atom abstraction from a selection of osmium mono- and trimetallic clusters were determined, as well as rate constants for ruthenium and rhodium hydrides have been examined. Rate constants for reaction of benzyl radical with metal hydrides in benzene are shown in Figure 1. The immediate observation is that μ -bonding does not render the hydrogen atom inaccessible to abstraction by benzyl radical. Structure 1 is only 2-10 times less reactive than σ dihydride 3, and only a factor of ten slower than mixed σ - and μ -hydride 2.

Figure 1. Hydrogen Abstraction from Mono- and Triosmium hydrides. Rate constants are in benzene at 298K.



The highly congested and electron deficient structure of 4 results in a rate constant an order of magnitude less than 1. This rate constant is near the practical lower limit of the



11

The results illustrate the surprising effects on homolytic reactivity that can be imparted by incorporation of the heteroatom function in the Mo_2S_4 cluster.

CONCLUSIONS

We have presented a preliminary account of characterization of the homolytic kinetic reactivity of a selection of transition metal hydrides, including a selection of trisium clusters that include σ - and μ -bonding of hydrogen to electron-deficient and electron-precise (18-electron) trimetallic clusters, and we have presented new rate constants for reaction of rhodium, ruthenium, iridium and molybdenum hydrides. The results show that μ -bonded hydrogen is reduced only moderately in reactivity compared to σ -bonded hydrides for non-fluorinated systems, in which migration of the hydrogen about the trisium skeleton appears to be slow. The rate constants are sensitive to steric bulk about the cluster, and are sensitive to the degree of electron-deficiency or lack thereof. Work to characterize the reactivity of homolytic intermediates arising from mononuclear and cluster organometallics is underway. Finally, this work has provided quantitative insight into the homolytic reactivity of metal-hydrogen bonding configurations in catalyst intermediates and a view of the enhancement of heteroatom reactivity resulting from incorporation in small clusters.

ACKNOWLEDGEMENT

This work was supported by the Office of Science, Office of Basic Energy Sciences, U.S. Department of Energy, under contract DE-ACO6-76RLO 1830.

REFERENCES

- 1 Franz, J.A.; Bushaw, B.A.; and Alnajjar, M.S. *J. Am. Chem. Soc.* **1989**, *111*, 268
- 2 Newcomb, M.; Choi, S.-Y.; Horner, J. H. *J. Org. Chem.* **1999**, *In press*
- 3 (a) Curran, D. P. *Synthesis* **1988**, *6*, 417-39, (b) Baguley, P. A.; Walton, J. C. *Angew. Chem. Int. Ed.* **1998**, *37*, 3072-3082, (c) Davies, A. G. *Organotin Chemistry*; WILEY-VCH: Weinheim, 1997.
- 4 For examples, see (a) Bakac, A. *Inorg. Chem.* **1998**, *37*, 3548-3552, (b) Ash, E. A.; Hurd, P. W.; Darenbourg, M. Y.; Newcomb, M. J. *J. Am. Chem. Soc.* **1987**, *109*, 3313-3317, (c) Bullock, R. M.; Samsel, E. G. *J. Am. Chem. Soc.* **1990**, *112*, 6886-6898, (d) Eisenberg, D. C.; Lawrie, C. J. C.; Moody, A. E.; Norton, J. R. *J. Am. Chem. Soc.* **1991**, *113*, 4888-4895, (e) Eisenberg, D. C.; Norton, J. R. *Isr. J. Chem.* **1991**, *31*, 55-66, (f) Kinney, R. J.; Jones, W. D.; Bergman, R. G. *J. Am. Chem. Soc.* **1978**, *100*, 7902-7915.
- 5 See, e.g. (a) Alnajjar, M.S. and Franz, J.A. *J. Am. Chem. Soc.* **1992**, *114*, 1052, (b) Autrey, S.T.; Alnajjar, M.S.; Nelson, D.A.; and Franz, J.A. *J. Org. Chem.* **1991**, *56*, 2197.
- 6 (a) Fischer, H.; Paul, H. *Acc. Chem. Res.* **1987**, *20*, 200-266, (b) Lehni, M.; Schuh, H.; Fischer, H. *Int. J. Chem. Kinet.* **1979**, *11*, 705-713. (c) Claridge, R. F. C.; Fischer, H. *J. Phys. Chem.* **1983**, *87*, 1960-1967, (d) Huggenberger, C.; Fischer, H. *Helv. Chim. Acta* **1981**, *64*, 338-353.
- 7 See ref. 5b for a detailed description of the procedure for obtaining von Smoluchowski rate expressions.
- 8 Spemol, A.; Wirtz, K., *Z. Naturforsch.* **1953**, *8a*, 522.
- 9 Polarizable radicals may not be well served by this assumption, but benzyl radical is well-behaved: (a) Okamoto, K.; Hirota, N.; and Terazima, M. *J. Chem. Soc. Far. Trans.* **1998**, *94(2)*, 185 and *J. Phys. Chem. A.* **1997**, *101*, 5269.
- 10 Compounds **1** and **2**: (a) Deeming, A.J.; Hasso, S. J., *J. Organomet. Chem.*, **1975**, *88*, C21. (b) Shaply, J.R., Keister, J.B.; Churchill, M.R., *J. Am. Chem. Soc.*, **1975**, *97*, 4145. (c) Deeming, A.J.; Hasso, S. J., *J. Organomet. Chem.*, **1976**, *114*, 313. Compounds **4,5**, and **6**: Kabir, S.E.; Kolwaite, D.S.; Rosenberg, E.; Hardcastle, K.; Creswell, W.; Gringstaff, J., *Organometallics*, **1995**, *14*, 3611. Arcia, E.; Kolwaite, D.S.; Rosenberg, E.; Hardcastle, K.; Ciurash, J.; Duque, R.; Osella, D.; Gogetto, R.; Milone, L., *Organometallics*, **1998**, *17*, 415. Compound **3**: Ahmad, N.; Levison, J. J.; Robenson, S. D.; Uttley, M. F.; Parshall, G. W. ed., *Inorganic Synthesis*, **1974**, *15*, 54-56. Compound **7**: Ahmad, N.; Levison, J. J.; Robenson, S. D.; Uttley, M. F.; Parshall, G. W. ed., *Inorganic Synthesis*, **1974**, *15*, 48-50. Compounds **8** and **10** purchased from Strem Chemicals.
- 11 Franz, J.A.; Linehan, J.C.; Birnbaum, J.C.; Hicks, K.S.; and Alnajjar, M.S. *J. Am. Chem. Soc.*, submitted.
- 12 Rakowski DuBois, M.; VanDerveer, M.C.; DuBois, D.L.; Haltiwanger, R.C. and Miller, W.K. *J. Am. Chem. Soc.* **1980**, *102*, 7456.

EXPERIMENTAL APPROACHES TO MEASURE THE CHEMICAL AND PHYSICAL
PROPERTIES OF RADICAL INTERMEDIATES; TIME-RESOLVED PHOTOACOUSTIC
CALORIMETRY WITH THE LAYERED PRISM CELL.

Tom Autrey and Nancy Foster-Mills

Pacific Northwest National Laboratory
Environmental Health Sciences Division
Richland, WA 99352

KEYWORDS

Thermochemistry, kinetics, radical intermediates

ABSTRACT.

Mechanistic kinetic modeling has been successfully used to elucidate the contributions of strong bond scission by various competing hydrogen transfer pathways as a function of the reaction conditions. The success of the MKM approach is limited by the availability and quality of kinetic and thermodynamic data derived from either experimental and/or theoretical methods. New and improved experimental methods to obtain quantitative information regarding the thermochemical and kinetic properties of reactive intermediates in condensed phases will facilitate the development new and improved mechanistic kinetic models. We have used time-resolved photoacoustic calorimetry, employing the Layered Prism Cell (LPC), to measure the chemical and physical properties of short-lived reactive intermediates in solution. The lifetimes and thermochemical properties of reactive radicals in the presence of various hydrogen atom donors will be presented and comparisons will be drawn to the literature.

INTRODUCTION.

Mechanistic Kinetic Modeling (MKM) is a useful experimental approach to quantify and understand the important reaction pathways occurring in a complex reaction scheme. MKM combined with traditional experimental and semi-empirical approaches have been used to investigate high temperature (> 600 K) hydrogen atom transfer pathways between hydroaromatic structures.¹⁻¹⁷ The approach is develop a model inclusive of the important reaction pathways that will "predict" (or fit) experimental observations. However, the quality of the model is limited by inclusion of the important reaction steps and the availability of thermochemical kinetic parameters to provide temperature dependent rate data. The models have evolved with enhanced methods to predict contributing reaction pathways and improvements in measuring or calculating heats of formation of transient radical intermediates. For example, inclusion of the reverse hydrogen transfer step for a thermal neutral hydrogen transfer yields a model that fits the experimental data without the need to invoke the controversial radical hydrogen transfer pathway.⁷ In another example, it was shown that varying the barrier for the initiation step for hydrogen transfer between alkyl pyrenes by less a few kcal/mol resulted in a model that fits the experimental data without the need to invoke the rht pathway.² Even the observed experimental selectivity of bond scission could be explained by a change in reaction pathways (hydrogen atoms and/or molecular assisted homolysis) with a change in solvent composition.¹

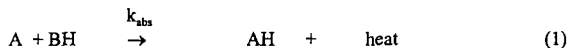
One of the goals of our research is to use experimental and theoretical approaches to measure or calculate the heats of formation of organic free radicals and to measure rate constants of reactions of reactive transient species. In this symposium new methods using time-resolved photoacoustic calorimetry to obtain rate constants for hydrogen atom transfer reactions and determinations of heats of formation of transient species will be presented.

APPROACH.

Time-resolved photoacoustic calorimetry has been used to obtain both chemical and physical properties of photo-generated reactive intermediates. Absorption of electromagnetic energy (hv) by a molecule in solution generates an electronically/vibrational excited meta-stable intermediate. The excess energy can be released from the excited state by a combination of emission, internal conversion (IC) and/or *chemical pathways*. The release of heat by either IC or chemical pathways generates an acoustic pressure pulse that can be detected with an ultrasonic transducer. The mathematical solutions describing the events leading to formation of the acoustic pressure pulse and the subsequent detection with piezoelectric transducers to yield a

photoacoustic signal,¹⁸⁻²⁰ and the methods to analyze the photoacoustic signals to obtain information on the chemical and physical properties of short-lived reactive intermediates have been studied in detail.²¹⁻²⁷

A model is useful to illustrate the time dependent response, $M(t)$, provided by an ultrasonic transducer for a simple scheme involving the reaction of a reactive intermediate A to AH as shown in equation 1. In this example A is a photo-generated reactive intermediate and B is a hydrogen donor. $M(t)$ is adequately described by a convolution (*) of the exponential release of heat $H(t)$ with a model instrument response function, $S(t)$. In our model $S(t)$ is a dampened sine wave, where ν is the resonant frequency, τ_c is the dampening constant of the transducer and K is an instrument constant. Using our model instrument response function we can demonstrate that for τ_A , ($\tau_A = 1/k_{abs}$, rate of abstraction) in $H(t)$, varied between 100 ns and 10 μ s result in a calculated response $M(t)$ that is distinguishable in shape from model instrument response $S(t)$ as shown in Figure 1.



$$M(t) = H(t) * S(t) \quad (2)$$

$$H(t) = \phi_{abs} \exp(-t/\tau_A) \quad (3)$$

$$S(t) \sim K [\exp(-t/\tau_c) \sin(\nu t)] \quad (4)$$

The experimental instrument response $R(t)$ can be obtained with a photoacoustic standard, where $\phi = 1$, and $\tau \ll \nu$. The experimentally observed photoacoustic signal $E(t)$ is therefore the convolution of $H(t)$ with the experimental instrument response $R(t)$ as shown in equation 5.

$$E(t) = H(t) * R(t) \quad (5)$$

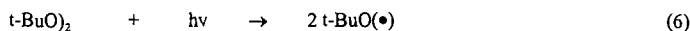
From the *shape* and *amplitude* of the experimental photoacoustic waveform, $E(t)$, we can obtain a description of the events that occurred as a consequence of the absorption of energy to generate radical intermediate A. The exponential release of heat $H(t)$ is comprised of two separable parameters, ϕ_{abs} the fraction of absorbed energy released as heat in the conversion of A \rightarrow AH, and τ_A , the lifetime of reactive intermediate A. This is an important point, the *amplitude* of the photoacoustic waveform is directly proportional to the magnitude of the fraction of absorbed energy released as heat, and the *shape* of the photoacoustic waveform is proportional to the rate of decay of A \rightarrow AH.

Deconvolution of the experimental waveform $E(t)$, with the experimentally measured instrument response, $R(t)$ can provide quantitative information regarding both the quantity of energy released in the transformation of A \rightarrow AH and the rate at which the process occurs. Both ϕ_{abs} and τ_A depend on the concentration and properties of the hydrogen atom donor BH. Importantly, these two parameters can be treated independently. Specifically, sources of heat (or volume changes) contributing to the amplitude of the photoacoustic signal need not be quantitatively discriminated if a kinetic analysis is all that is desired.

In our laboratory we have been developing methods to improve the sensitivity, enhance the time-resolution and increase experimental flexibility.²⁸⁻³¹ We have taken an approach to treat the kinetic and thermodynamic components of the experiment separately when necessary. Using optical transparent (thin) samples the kinetic information (τ) can be obtained from the shape of the waveform, even if the thermodynamic and volumetric components contributing to the amplitude of the signals are still difficult to quantify.

RESULTS.

Pulsed photolysis of di-t-butylperoxide in the uv generates a pair of reactive t-butoxyl radicals. The lifetime of the radicals is solvent dependent. The reaction scheme shown in equations 6-7 can be modeled as a sequential two step reaction pathway.



In previous work²⁸ we demonstrated the capability to obtain the lifetime of the t-butoxyl radical in binary solvent mixtures containing methanol and ethanol. Using the layered PA cell permits the a direct measure of the rate of hydrogen abstraction by measuring the volume change induced by the reaction of the alkoxyl radical with the solvent (even when the thermodynamic properties of the sample and reference solutions are not matched).

To obtain quantitative thermochemical estimates a reasonable understanding of both thermal and volumetric contributions to the PA amplitude must be evaluated. There has been some effort undertaken to separate the enthalpic and volumetric contributions in organic solvents using both photoacoustic and transient grating approaches. Another potential hindrance is thermal changes brought about by changes in heats of solvation. In order to separate the ΔV_{rxn} and $\Delta \Delta H_{\text{soliv}}$ terms from the experimentally measured amplitude a few groups have used correction terms. The approach is to use a standard hydrogen donor, e.g., cyclohexadiene and assume the difference between the gas phase literature value and the experimental PA signal is constant. Then the difference between gas phase values and observed value (a correction term) can be subtracted from experimental value to arrive at an experimental measurement of the BDE. One of the assumptions used in the correction term approach is the equivalency of the solvent quality factors for an organic solvent with and without significant concentrations of peroxide. For unmatched solvents there can be a substantial difference. Additionally correction factors must be determined for each experimental condition, i.e., irradiation in a 30% peroxide solution will yield a different correction term need for a 6% peroxide solution and different corrections are necessary for various excitation wavelengths, i.e., 308 nm will yield a different magnitude correction than 355 nm.

The advantage of the layered prism cell is that a direct measure can be possible because the reaction volume change, due to peroxide bond scission, can be separated from the thermal volume change, due to an exothermic hydrogen atom abstraction, in a time-resolved manner. Unfortunately interpretation of thermochemistry data obtained in the layered cell can suffer from the same difficulties experienced with the traditional cuvette geometry in solvents where the contribution due to enthalpies of solvation of the different species can be significant. An accurate evaluation of the thermochemistry requires equivalent thermoelastic properties ($\beta/\alpha\rho C_p$) for both the sample and reference solution and the ability to separate the ΔV_{rxn} and $\Delta \Delta H_{\text{soliv}}$ from the amplitude of the signal. Results for some of our energy determinations are shown in Table 1. The lower limits determined for the BDE in polar solvents is likely due to the contribution differences in enthalpy of solvation between the alkoxyl radical/donor pair and the t-BuOH/donor radical pair. The benefits and limitations of time-resolved photoacoustic calorimetry with the layered prism cell will be presented.

ACKNOWLEDGMENTS.

This work was supported by the U.S. Department of Energy, Office of Basic Energy Research, Chemical Sciences Division, Process and Techniques Branch. The work was conducted at Pacific Northwest Laboratory, which is operated for the U. S. Department of Energy under Contract DE-ACO6-76RL0 1830. Support for NFM was provided through AWU-NW under grant DE-FG06-89ER-75522 with the U.S. Department of Energy.

REFERENCES.

- (1) Autrey, T.; Albom, E. A.; Franz, J. A.; Camaioni, D. M. *Energy Fuels* 1995, 9, 420-8.
- (2) Autrey, T.; Powers, T.; Albom, E. A.; Camaioni, D. M.; Franz, J. A. *Coal Sci. Technol.* 1995, 24, 1431-4.
- (3) Autrey, T.; Albom-Cleveland, E.; Camaioni, D. M.; Franz, J. A. *Prepr. Pap. - Am. Chem. Soc., Div. Fuel Chem.* 1994, 39, 627-31.
- (4) Autrey, S. T.; Camaioni, D. M.; Ferris, K. F.; Franz, J. A. *Conf. Proc. - Int. Conf. Coal Sci., 7th* 1993, 1, 336-9.
- (5) Autrey, T.; Gleicher, G. J.; Camaioni, D. M.; Ferris, K. F.; Franz, J. A. *Prepr. Pap. - Am. Chem. Soc., Div. Fuel Chem.* 1991, 36, 521-8.
- (6) Autrey, T.; Franz, J. A. *Prepr. Pap. - Am. Chem. Soc., Div. Fuel Chem.* 1990, 35, 381-6.
- (7) Camaioni, D. M.; Autrey, S. T.; Franz, J. A. *J. Phys. Chem.* 1993, 97, 5791-2.
- (8) Camaioni, D. M.; Autrey, S. T.; Franz, J. A. *Prepr. - Am. Chem. Soc., Div. Pet.*

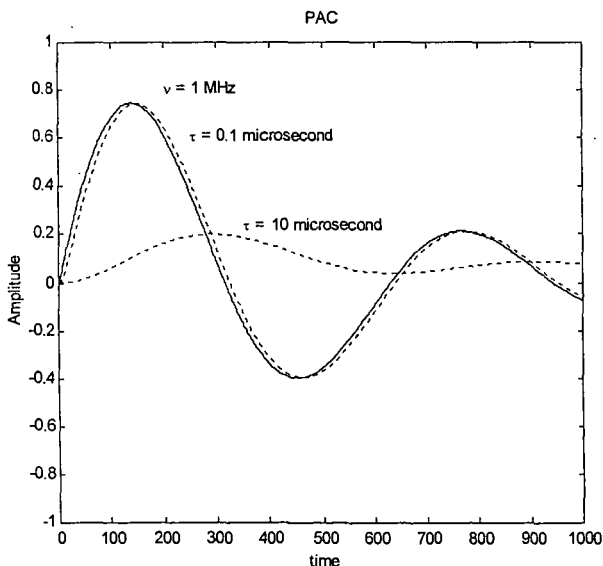
- Chem.* **1994**, *39*, 303-9.
- (9) Camaioni, D. M.; Autrey, S. T.; Salinas, T. B.; Franz, J. A. *J. Am. Chem. Soc.* **1996**, *118*, 2013-22.
 - (10) Savage, P. E. *Energy Fuels* **1995**, *9*, 590-8.
 - (11) McMillen, D. F.; Malhotra, R.; Tse, D. S. *Energy Fuels* **1991**, *5*, 179.
 - (12) McMillen, D. F.; Malhotra, R.; Chang, S.-J.; Fleming, R. H.; Ogier, W. C.; Nigenda, S. E. *Fuel* **1987**, *66*, 1611.
 - (13) Malhotra, R.; McMillen, D. F. *Energy Fuels* **1993**, *1993*, 227.
 - (14) Stein, S. E. *Acc. Chem. Res.* **1991**, *24*, 350.
 - (15) Autrey, T.; Linehan, J. C.; Steams, C. J.; Camaioni, D. M.; Kaune, L.; Franz, J. A. *Prepr. Pap. - Am. Chem. Soc., Div. Fuel Chem.* **1997**, *42*, 66-69.
 - (16) Autrey, T.; Linehan, J. C.; Camaioni, D. M.; Kaune, L. E.; Watrob, H. M.; Franz, J. A. *Catal. Today* **1996**, *31*, 105-111.
 - (17) Autrey, T.; Linehan, J.; Camaioni, D.; Powers, T.; Wartob, H.; Franz, J. *Prepr. Pap. -Am. Chem. Soc., Div., Fuel Chem.* **1995**, *40*, 973.
 - (18) Patel, C. K. N.; Tam, A. C. *Rev. Modern Phys.* **1981**, *53*, 517-549.
 - (19) Lai, H. M.; Young, K. *J. Acoust. Soc. Am.* **1982**, *72*, 2000-2006.
 - (20) Diebold, G. J. *J. Phys. Chem. B* **1998**, *102*, 5404-5408.
 - (21) Rudzki, J. E.; Goodman, J. L.; Peters, K. S. *J. Am. Chem. Soc.* **1985**, *107*, 7849-7854.
 - (22) Braslavsky, S. E.; Heihoff, K. *Photothermal Methods*; Scaiano, J. C., Ed.; CRC Press, 1989; Vol. 1, pp 327-355.
 - (23) Braslavsky, S. E.; Heibel, G. E. *Chemical Reviews* **1992**, *92*, 1381-1410.
 - (24) Melton, L. A.; Ni, T.; Qingzheng, L. *Rev. Sci. Instrum.* **1989**, *60*, 3217-3223.
 - (25) Arnaut, L. G.; Caldwell, R. A.; Elbert, J. E.; Melton, L. A. *Rev. Sci. Instrum.* **1992**, *63*, 5381-5389.
 - (26) Beck, K. M.; Gordon, R. J.; Tardy, D. C. *Adv. Chem. Kinetics and Dynamics* **1995**, *2B*, 299-332.
 - (27) Puchenkov, O. V.; Malkin, S. *Rev. Sci. Instrum.* **1996**, *67*, 672-680.
 - (28) Autrey, T.; Foster-Mills, N.; Klepzig, K. *Photochem. Photbio. A* **1999**. In press
 - (29) Autrey, T.; Foster, N. S.; Klepzig, K.; Amonette, J. E.; Daschbach, J. L. *Rev. Sci. Instrum.* **1998**, *69*, 2246-2258.
 - (30) Foster, N. S.; Amonette, J. E.; Autrey, T. *Applied Spectroscopy* **1999**, *53*(6), in press.
 - (31) Foster, N. S.; Autrey, T.; Amonette, J. E.; Small, J. R.; Small, E. W. *American Laboratory* **1999**, *31*(4), 96.

Table 1. Experimentally measured heats of reaction for hydrogen atom abstraction by t-butoxyl radical from a series of organic hydrogen donor solvents determined by time-resolved photoacoustic calorimetry in the layered prism cell. The calculated BDE's are compared to the literature values.

Donor	ϕ^a	Experimental		Literature BDE
		ΔH_{rxn} (kcal/mol)	BDE ^b	
MeOH	0.28	-9.2±.5	(>89.6) ^c	92-96
EtOH	0.24	-13±.7	(>90.4) ^c	>93
IPA	0.22	-13±1	(>90.7) ^c	>91
THF	0.29	-13.1±.5	(>89.1) ^c	92-95
Cyclohexane	0.31	-5.6±.8	98.6	98.2
Toluene	0.31	-16.6±.9	88.0	88.6

(a) fraction of heat released in hydrogen abstraction step. (b) calculated bond dissociation energy determined from photoacoustic measurement. (c) lower limit, see text.

Figure 1. Model of a photoacoustic signal obtained using a 1 MHz piezoelectric transducer. Comparison of the instrument response $S(t)$ with $M(t)$ with $\tau_A = 100$ ns, and $M(t)$ with $\tau_A = 10$ μ s.



VARIATIONAL TRANSITION STATE THEORY METHODS FOR CALCULATING REACTION RATE CONSTANTS IN GAS AND CONDENSED PHASES

Bruce C. Garrett
Environmental Molecular Sciences Laboratory,
Pacific Northwest National Laboratory,
P.O. Box 999, Richland, WA 99352

1. Introduction

Transition state theory (TST) in its thermodynamic formulation¹ is the most widely used tool for analyzing rate constants of chemical reactions (for example, see Benson²). The dynamical formulation of TST³ provides the best approach to examine the approximations in TST and the basis for systematically improving the conventional theory. Over the past two decades, significant progress has been made in developing methods for quantitative predictions of reaction rate constants based upon the dynamical formulation of TST (see reviews by Truhlar, Hase, and Hynes⁴ and Truhlar, Garrett, and Klippenstein⁵). As an example, quantized variational transition state theory (VTST) with multidimensional, semiclassical tunneling corrections⁶⁻⁸ are capable of accurate predictions of gas-phase rate constants.^{9,10} The accuracy of the potential energy surface is typically the major factor limiting the accuracy of the calculated rate constants. In this paper we briefly review VTST methods and their application to gas-phase reaction. We also briefly outline an approach to extend these methods to treat reactions in solution.

2. VTST for Gas-Phase Reactions

In the dynamical formulation of TST, the classical equilibrium rate constant is derived using a single approximation, the fundamental assumption of TST.^{3,11} A dividing surface is defined so that all reactive trajectories must pass through it. The fundamental dynamical assumption is then defined as follows: a reactive trajectory originating in reactants must cross the dividing surface only once and proceed to products. The TST expression for the rate constant can then be expressed using equilibrium statistical mechanics without the need to calculate classical trajectories. Classical trajectories that recross the dividing surface cause a breakdown of the fundamental assumption. All reactive classical trajectories must cross the dividing surface and these are correctly counted in TST. However, some nonreactive trajectories may also be counted as reactive so that TST provides an upper bound to the exact reactive flux of classical trajectories through the dividing surface. This is the basis of classical variational TST in which the definition of the dividing surface is optimized to minimize the rate constant.¹²⁻¹⁴

In VTST the dividing surface is viewed as a tentative dynamical bottleneck to flux in the product direction, and the best bottleneck (the dividing surface allowing the least flow of flux) is located variationally. A practical approach is to define the dividing surfaces to be orthogonal to the reaction path, where the reaction path is defined as the minimum energy path connecting the saddle point with both the reactant and product regions. The minimum energy path is located by following the path of steepest descents in both directions from the saddle point in a mass-weighted coordinate system such that each degree of freedom has the same effective mass in the kinetic energy expression. The generalized expression for the thermal rate constant for temperature T is given as a function of the location s of the dynamical bottleneck along the reaction coordinate

$$k^{GT}(T, s) = \sigma \frac{k_B T}{h} \frac{Q^{GT}(T, s)}{\Phi^R(T)} \exp(-V_{MEP}(s)/k_B T) \quad (1)$$

where σ is a symmetry factor, k_B is Boltzmann's constant, h is Planck's constant, $Q^{GT}(T, s)$ is the generalized partition function for the bound degrees of freedom orthogonal to the reaction path at s , $\Phi^R(T)$ is the reactant partition function, and $V_{MEP}(s)$ is the value of the potential along the reaction path at s . In conventional TST, the dividing surface is placed at the saddle point, defined by $s=0$

$$k^{TST}(T) = k^{GT}(T, s=0) \quad (2)$$

Conventional transition state theory requires information about the potential energy surface only in the saddle point and reactant regions. In particular, the value of the potential at the saddle point (relative to the reactant value) is required, and if the partition functions are computed using a harmonic approximation, then the matrix of second derivatives of the potential energy with respect to mass-weighted coordinates (Hessian matrix) suffices. In one version of variational transition state theory, the canonical variational theory (CVT),^{15,16} the rate constant expression in eq. (1) is minimized with respect to s

$$k^{CVT}(T) = \min_s k^{GT}(T, s) \quad (3)$$

The improved canonical variational theory (ICVT)¹⁷ also variationally optimizes the location of the transition state dividing surface for a given temperature, but provides an improved treatment of threshold energies by using an ensemble which removes energies below the ground-state adiabatic threshold. To compute the rate constant using either the canonical or improved canonical variational theory, more information about the potential energy surface is required than for a conventional transition state theory calculation; information about the potential in a region around the reaction path is also required. For a harmonic treatment of the partition functions, the Hessian matrix along the minimum energy path will suffice. In this case the potential information needed is the energy and its first and second derivatives along the minimum energy path.

For many reactions of practical interest, particularly those involving hydrogen atom transfer, quantitative accuracy in computed rate constants requires that quantum mechanical effects be included in the theory. However, the fundamental assumption is inherently a classical approximation since it requires knowledge of both the coordinate and momentum (or flux) at the dividing surface. Additional approximations are needed to include quantum mechanical effects into TST. The standard approach is a separable approximation^{1,18} that replaces classical partition functions by quantum mechanical ones and includes a correction factor for quantum mechanical motion along the reaction coordinate (e.g., tunneling). The failure of this approach has been attributed largely to nonseparable effects, particular on quantum mechanical tunneling.^{19,20} The development of multidimensional tunneling correction factors that are consistent with variational transition state theory was greatly facilitated by the realization that the adiabatic theory of reactions is equivalent to one form of variational TST (microcanonical VTST).^{15,16} In this approach, the partition functions in eq. (1) are evaluated quantum mechanically, and quantum mechanical effects on the reaction coordinate motion (e.g., quantum mechanical tunneling) are included by a multiplicative factor – the transmission coefficient.

In VTST, it is consistent to treat tunneling as occurring through the vibrationally-rotationally adiabatic potential

$$V_a(s, \alpha) = V_{\text{MEP}}(s) + \epsilon_{\alpha}^{\text{GT}}(s) \quad (4)$$

where α is a collective index of the quantum numbers for the bound modes and $\epsilon_{\alpha}^{\text{GT}}(s)$ is the bound energy level for state α at the generalized transition state located at s along the reaction path. For thermal rate constants the tunneling is approximated using only the ground-state adiabatic potential curve ($\alpha=0$). The adiabatic approximation is made in a curvilinear coordinate system, and although the potential term is simple, the kinetic energy term is complicated by factors dependent upon the curvature of the reaction path. For systems in which the curvature of the reaction path is not too severe, the small-curvature semiclassical adiabatic ground state method^{21,22} includes the effect of the reaction-path curvature to induce the tunneling path to 'cut the corner' and shorten the tunneling length. The small-curvature tunneling (SCT) probabilities $P^{\text{SCT}}(E)$ are computed for energies below the maximum in the ground-state adiabatic potential curve (denoted V^{AG}) where transmission occurs by tunneling and above V^{AG} where nonclassical reflection can diminish the transmission probability. The SCT transmission coefficient is given by the normalized Boltzmann average of $P^{\text{SCT}}(E)$

$$\kappa^{\text{SCT}}(T) = \beta \exp(\beta V^{\text{AG}}) \int_0^{\infty} dE P^{\text{SCT}}(E) \exp(-\beta E) \quad (5)$$

where $\beta=1/k_B T$. Combining the SCT transmission coefficient with the improved canonical variational theory rate constant yields

$$k^{\text{ICVT/SCT}}(T) = \kappa^{\text{SCT}}(T) k^{\text{ICVT}}(T) \quad (6)$$

To construct the adiabatic potential, the type of potential information required is identical to that needed for the variational transition state theory calculation. For the SCT calculation it is also necessary to know the curvature of the reaction path which can be obtained from second derivatives of the potential along the reaction path. Thus, to provide a consistent and accurate estimate of the tunneling, no new information about the potential energy surface is required.

Accurate quantum rate constants for nearly forty gas-phase bimolecular reactions provide benchmarks to test the accuracy of the VTST calculations. VTST calculations, which include multidimensional tunneling corrections, have been tested against accurate quantal results for about 30 atom-diatom reactions in a collinear world and nearly 10 reactions in three dimensions. Conventional TST was found to be accurate within a factor of 2 for only about 25% of these systems and had errors larger than of 5 in about 25% of the systems. The VTST calculations were generally within 50% of the accurate results with errors less than a factor of two in all cases.

3. VTST for Solution-Phase Reactions

The computational procedures described above to perform VTST calculations require identification of a saddle point and a reaction path connecting the saddle point with reactants and

products. For reactions in solution, there can be many saddle points that are close in energy and that differ significantly only in the configuration of the solvent. The multiple saddle points are a reflection of the large anharmonicity in the solvent that makes the quantum mechanical calculation of the partition functions impractical. Procedures are outlined elsewhere²³ that allow VTST calculations, which are based upon potential energy surfaces and include quantum effects, to be extended to solution-phase reactions. In this approach the system is separated into a cluster model that contains the part of the system undergoing reaction and the solvent that is treated in an approximate manner. The coordinates of the cluster model are treated explicitly, and the effects of the extended solvent are approximately included in an effective Hamiltonian. The constant proximity of solvent molecules around the solute changes the interaction potential within the solute. The resulting mean field potential for the solute is obtained from an equilibrium ensemble average over solvent configurations. Since this mean field potential is obtained from an equilibrium ensemble average at each solute configuration, the equilibrium solvation assumption implies that the solvent molecules instantaneously equilibrate to each new solute configuration. Effects of solvent fluctuation from their equilibrium values upon reaction dynamics are included using a reduced-dimensionality model that introduces a limited number of additional degrees of freedom in the effective Hamiltonian.

This approach for including solvation effects requires explicit treatment of only a limited number of degrees of freedom and information about the effective potential energy surface for these explicit coordinates is needed only in the region of a reaction valley. Explicitly treating only a limited number of coordinates obviates some of the difficulties inherent in quantum mechanical TST calculations on solution-phase reactions (e.g., the multiple saddle point problem) and also allows the quantum mechanical effects to be included by the standard gas-phase procedures outlined above. These procedures are computationally intensive, but given the recent advances in computational hardware and software, these calculations are possible.

Acknowledgments

This work was supported by the Division of Chemical Sciences, Office of Basic Energy Sciences, U.S. Department of Energy. Pacific Northwest National Laboratory is operated for the DOE by Battelle.

References

- (1) Glasstone, S.; Laidler, K. J.; Eyring, H. *The Theory of Rate Processes*; McGraw-Hill: New York, 1941.
- (2) Benson, S. W. *Thermochemical Kinetics*, second ed.; Wiley: New York, 1976.
- (3) Wigner, E. *Trans. Faraday Soc.* **1938**, *34*, 29.
- (4) Truhlar, D. G.; Hase, W. L.; Hynes, J. T. *J. Phys. Chem.* **1983**, *87*, 2664.
- (5) Truhlar, D. G.; Garrett, B. C.; Klippenstein, S. J. *J. Phys. Chem.* **1996**, *100*, 12771.
- (6) Truhlar, D. G.; Garrett, B. C. *Ann. Rev. Phys. Chem.* **1984**, *35*, 159.
- (7) Truhlar, D. G.; Isaacson, A. D.; Garrett, B. C. In *Theory of Chemical Reaction Dynamics*; Baer, M., Ed.; CRC Press: Boca Raton, FL, 1985; Vol. IV; pp 65.
- (8) Steckler, R.; Hu, W.-P.; Liu, Y.-P.; Lynch, G. C.; Garrett, B. C.; Isaacson, A. D.; Melissas, V. S.; Lu, D.-h.; Truong, T. N.; Rai, S. N.; Hancock, G. C.; Lauderdale, J. G.; Joseph, T.; Truhlar, D. G. *Comp. Phys. Comm.* **1995**, *88*, 341.
- (9) Garrett, B. C.; Truhlar, D. G. *J. Chem. Phys.* **1984**, *81*, 309.
- (10) Allison, T. C.; Truhlar, D. G. In *Modern Methods for Multidimensional Dynamics Computations in Chemistry*; Thompson, D. L., Ed.; World Scientific: Singapore, 1998; pp 618.
- (11) Miller, W. H. *J. Chem. Phys.* **1974**, *61*, 1823.
- (12) Wigner, E. *J. Chem. Phys.* **1937**, *5*, 720.
- (13) Horiuti, J. *Bull. Chem. Soc. Japan* **1938**, *13*, 210.
- (14) Keck, J. C. *J. Chem. Phys.* **1960**, *32*, 1035.
- (15) Garrett, B. C.; Truhlar, D. G. *J. Phys. Chem.* **1979**, *83*, 1052.
- (16) Garrett, B. C.; Truhlar, D. G. *J. Phys. Chem.* **1979**, *83*, 1079.
- (17) Garrett, B. C.; Truhlar, D. G.; Grev, R. S.; Magnuson, A. W. *J. Phys. Chem.* **1980**, *84*, 1730.
- (18) Eyring, H. *J. Chem. Phys.* **1935**, *3*, 107.
- (19) Truhlar, D. G.; Kuppermann, A. *Chem. Phys. Lett.* **1971**, *9*, 269.
- (20) Miller, W. H. *Acc. Chem. Res.* **1976**, *9*, 306.
- (21) Skodje, R. T.; Truhlar, D. G.; Garrett, B. C. *J. Phys. Chem.* **1981**, *85*, 3019.
- (22) Skodje, R. T.; Truhlar, D. G.; Garrett, B. C. *J. Chem. Phys.* **1982**, *77*, 5955.
- (23) Garrett, B. C.; Schenter, G. K. *Int. Rev. Phys. Chem.* **1994**, *13*, 263.

THERMOCHEMISTRY, SOLVATION, AND DYNAMICS

Donald G. Truhlar, Yao-Yuan (John) Chuang, E. Laura Coitiño, José C. Corchado, Christopher J. Cramer, Derek Dolney, Joachin Espinosa-Garcia, Patton L. Fast, Gregory D. Hawkins, Yongho Kim, Jiabo Li, Benjamin Lynch, Mala L. Radhakrishnan, Orlando Roberto-Neto, Jocelyn M. Rodgers, Maria Luz Sánchez, Jordi Villà, Paul Winget, and Tianhai (Tony) Zhu,

Department of Chemistry and Supercomputer Institute, University of Minnesota,
Minneapolis, MN 55455-0431

KEYWORDS: Multicoefficient correlation methods, solvation models, variational transition state theory with semiclassical multidimensional tunneling contributions

Abstract. This paper reviews recent advances in computational thermochemistry, solvation modeling, and the calculation of chemical reaction rates in the gas phase and in solution. Recent advances in computational thermochemistry include integrated molecular orbital methods, scaling correlation energy, extrapolation to infinite basis sets, and multi-coefficient correlation methods. Recent advances in solvation modeling include Charge Model 2 (a class IV charge model) and the SM5.42R and SM5.42 solvation models; the solvation models are based on semiempirical molecular orbital theory, the *ab initio* Hartree-Fock method, or density functional calculations in the presence of a reaction field and on atomic surface tensions representing first-solvation-shell effects of water or an organic solvent. Our reaction rate calculations are based on variational transition state theory with multidimensional semiclassical tunneling approximations; in liquid solution we may add either equilibrium or nonequilibrium solvation effects.

INTRODUCTION

Much of our recent work is directed to one or another of two complementary goals: (1) to develop improved practical methods for electronic structure calculations in the gas-phase and in liquid-phase solutions and (2) to develop improved methods for interfacing these electronic structure calculations with dynamical methods for the prediction of chemical reactions rates, especially in systems with hydrogenic motion in the reaction coordinate where it is necessary to take account of quantum effects on the nuclear motion. The present paper provides an overview of some areas where progress has been achieved.

GAS-PHASE ELECTRONIC STRUCTURE

Substituent effects on bond energies are very important for both thermochemistry and kinetics. We have recently shown that integrated molecular orbital methods may be used to calculate accurate substituent effects on bond energies by treating a small capped subsystem at a high level of quantum mechanical electronic structure and the rest of a large system at a much lower level.¹⁻³ We have also developed a method for geometry optimization with such a dual-level scheme^{4,5} In the same spirit one may use molecular mechanics for the low level on the entire system; we have recently applied this

technique to treat an enzyme reaction where the subsystem had 25 atoms and the entire system had 8888 atoms.⁶

Another type of dual-level or multi-level strategy involves applying two or more levels of electronic structure calculation to the entire system. One strategy we have used is to combine the results at the various levels linearly in order to extrapolate to the limit of full configuration interaction (FCI) or an infinite one-electron basis set (IB) or both (full configuration interaction for an infinite basis is denoted complete configuration interaction or CCI). We have developed several variations on this scheme:

SAC	scaling all correlation: combine an uncorrelated and a correlated calculation with a given basis to extrapolate to CCI ^{5,7}
MC-SAC	multicoefficient SAC: combine an uncorrelated and two or more correlated calculations with a single basis to extrapolate to CCI ⁸
IB	combine calculations with two basis sets to extrapolate to the infinite-basis-set limit for a given level of electron correlation ⁹⁻¹¹
MCCM	multicoefficient correlation method: simultaneous application of MC-SAC and IB to extrapolate to CCI. ⁸

We have organized our MC-CM calculations by the shape of a polygon enclosing the methods in the level-basis plane, and we have proposed Colorado, Utah, and New Mexico methods, where the polygons have the shapes of those states.⁸ In addition we have proposed multicoefficient Gaussian-2¹² and multicoefficient Gaussian-3¹³ methods that outperform the original Gaussian-2 and Gaussian-3 methods.

For dynamics calculations we sometimes use a bootstrap technique in which high-level electronic structure calculations are carried out at stationary points, and then the parameters of semi-empirical molecular orbital theory, for example, Austin Model 1 (AM1), are adjusted to reproduce these properties as well as possible; the adjusted parameters are called specific reaction parameters or specific range parameters (SRP), and the modified AM1 is called AM1-SRP.¹⁴⁻²⁰ The advantage is that now the AM1-SRP calculation provides a smooth interpolation of the original high-level calculations between the stationary points. We have also used specific reaction parameters in Becke's 3-parameter hybrid Hartree-Fock-density-functional theory that he derived by adiabatic connection; we call this adiabatic connection-SRP (AC-SRP).²¹

A more powerful version of the AM1-SRP approach is a dual-level scheme in which the energy is given by a linear combination of *ab initio* Hartree-Fock calculations and AM1-SRP calculations. This is called HF||AM1-SRP.²¹ We are currently working on another global interpolation scheme which we hope will accomplish many of the goals of SRP methods but in a more systematic way. The new method is called multiconfiguration molecular mechanics (MCMM), and it involves combining high-level *ab initio* calculations with the valence bond formalism and molecular mechanics calculations.

There are situations in which each of these many strategies may be the best way to achieve an objective. We believe that such multi-level strategies will become increasingly important in the coming years.

Many one-electron basis sets are available for electronic structure calculations, and in essentially all cases they have been developed on the basis of variational energy calculations. But this strategy ignores the fact that many times the molecular energy is not the goal of a calculation. For example, modest basis sets are often used to obtain molecular geometries or reaction paths, at which or along which higher-level calculations are often used to calculate energies. In other applications, modest-sized basis sets are used to calculate partial atomic charges for large molecules for use with

molecular mechanics calculations of the energy. In order to allow more accurate applications of this type, we developed the MIDI! basis set, which is a heteroatom-polarized split valence basis with polarization functions optimized entirely on the basis of geometries and balanced one-electron charge distributions.^{22,23}

Electronically excited states of very large molecules are of great interest but can typically be modeled only by semiempirical molecular orbital theory such as intermediate-neglect-of-differential-overlap for spectroscopy (INDO/S). We have reparameterized this theory for carbonyl compounds leading to a new version called INDO/S2.²⁴

Electronic structure calculations yield not only energies but also molecular properties. We have developed the concept of class IV charges,²⁵ which (like some of our methods for energies) are an attempt to transcend the limitations of truncated CI and finite basis sets at as low a cost as possible. Our second class IV charge model, called Charge Model 2²⁶ (CM2), has been parameterized for ground states with neglect-of-diatomic-differential-overlap (NDDO) semiempirical molecular theory,²⁶ INDO/S and INDO/S2 semiempirical molecular orbital theory,²⁴ *ab initio* Hartree-Fock (HF)^{26,27} theory, density functional theory (DFT),²⁶ and adiabatic-connection hybrid HF-DFT (AC).²⁶ It has been parameterized for electronically excited states with INDO/S and INDO/S2.²⁴ These parameterizations have been shown to yield accurate partial atomic charges. The combination of CM2 with HF/MIDI! is a particularly powerful combination.²⁶

LIQUID-PHASE ELECTRONIC STRUCTURE

Whereas a goal of gas-phase electronic structure calculations is to produce potential energies for atomic motions, the corresponding goal of liquid-phase electronic structure calculations is to produce free energies or potentials of mean force. These can be used to calculate free energies of solvation, partition coefficients, solvatochromic shifts, and solvation effects on reaction rates. We have developed Solvation Model 5 as a fifth-generation approach (following SM1, SM1a, SM2, and SM4—SM3 involved the same approach as SM2) to the calculation of electronic wave functions and free energies in liquids (neat and solutions). SM5 is actually a suite of models, each of which may have more than one parameterization. In general, SM5 models approximate the standard-state free energy of solvation as

$$\Delta G_s^0 = \Delta G_{\text{ENP}} + G_{\text{CDS}}$$

where ΔG_{ENP} is a bulk electrostatic term includes solute electronic (E) and nuclear (N) energies and solvent electric polarization (P) free energy, and G_{CDS} is a semiempirical first-solvation shell term including cavitation (C), dispersion (D), solvent structure (S), and the breakdown of the bulk electrostatic model in the first solvation shell. The models may be applied with gas-phase geometries (in which case we append R to the model name), or geometries may be optimized in liquid solution using analytic gradients (in which case the model name does not end in R). The SM5 models are:

SM5.0R ^{28,29}	SM5 model in which electrostatics are implicit
SM5.2R ³⁰	SM5 model in which electrostatics are based on class II charges
SM5.4 ³¹⁻³⁴	SM5 model in which electrostatics are based on class IV charges calculated by Charge Model 1
SM5.42R, SM5.42 ^{21,35-39}	SM5 models in which electrostatics are based on class IV charges calculated by CM2
SM5CR ⁴⁰	SM5 model in which electrostatics are treated by the Conductor-like Screening Model (COSMO).

All of these models have been parameterized for aqueous solution and for general organic solvents. The parameterizations are based on over 200 free energies of solvation in 91 solvents (and in some cases on additional free energies of transfer as well). The SM5.0R model is designed for use with molecular mechanics calculations. The SM5.2R model is parameterized for AM1, PM3, MNDO, and MNDO/d. The SM5.4 model is parameterized for AM1 and PM3. The SM5.42R model is parameterized for AM1, PM3, HF/MIDI!, HF/MIDI!6D, HF/6-31G*, HF/6-31+G*, HF/cc-pVDZ, BPW91/MIDI!, BPW91/MIDI!6D, BPW91/6-31G*, BPW91/DZVP, B3LYP/MIDI!, INDO/S, and INDO/S2. The SM5.42 model uses the same parameters as SM5.42R. The SM5CR model is parameterized for AM1, PM3, and MNDO/d. In addition to the original papers, some overviews discussing the SM5 models are available.⁴¹⁻⁴⁴

The SM5.42R/HF/6-31G*, SM5.42R/BPW91/MIDI!, and SM5.42R/AM1 all yield excellent results for the free energy of transfer of nucleic acid bases from water to chloroform.⁴⁵

GAS-PHASE DYNAMICS

Variational transition state theory with optimized multidimensional tunneling contributions (VTST/OMT) provides an accurate yet practical method for calculating chemical rate constants.⁴⁶⁻⁴⁸ The optimized multidimensional tunneling calculation allows for corner cutting tunneling paths of two kinds: small-curvature tunneling paths, which are localized in the zero-point-amplitude hypertube enclosing the reaction path, and large-curvature tunneling paths, which are straight lines in isoinertial coordinates. The calculations may be carried out in redundant curvilinear coordinates, which are more physical than rectilinear coordinates.^{49,50}

Our recent emphasis has been on devising algorithms for interfacing VTST/OMT calculations with electronic structure calculations in convenient and efficient ways, and we have especially concentrated on minimizing the amount of electronic structure data required because that would make it more affordable to calculate the required data at high levels.

For example, we have recently shown how the orientation of generalized transition state dividing surfaces may be optimized, and how such optimization allows one to increase the step size used to trace the reaction path or even to use local optimization at nonstationary points to obviate the need for a continuous reaction path. The resulting algorithms are called re-orientation of the dividing surface (RODS)⁵¹⁻⁵³ and variational reaction path (VRP).⁵⁴

Another way to increase the amount of electronic structure data needed is to use sophisticated interpolation schemes. We have developed a method called interpolated variational transition state theory by mapping (IVTST-M) that allows one to greatly reduce the number of energies, gradients, and Hessians required for VTST calculations with small-curvature tunneling contributions.⁵⁵ Another approach is to use two levels, including geometry optimization at both levels but reaction-path following only at the lower level; by interpolating the *difference* between the lower and higher levels one can greatly reduce the amount of data needed at the higher level. This approach, called variational transition state theory with interpolated corrections (VTST-IC), can be used for small-curvature, large-curvature, or optimized multidimensional tunneling contributions.^{5,14,17} We have shown that the VTST-IC method is much more accurate than simply adding single-point energy corrections at geometries optimized by the lower level.⁵⁶ The VTST-IC approach is particularly powerful when the high-level

calculations are used not only as corrections to the lower level but also to optimize SRP parameters for the lower level.

A recent set of applications⁵⁷⁻⁵⁹ of these techniques involved calculating the rate constant for $\text{H} + \text{C}_2\text{H}_4 \rightarrow \text{C}_2\text{H}_5$ and several isotopically substituted versions of these reactions. This reaction involves small-curvature tunneling, and we treated it using a dual-level scheme involving variable scaling of external correlation energy, the RODS algorithm, redundant curvilinear coordinates, and the IVTST-M algorithm. We obtained good agreement with experiment both for absolute rate constants and for kinetic isotope effects.

Other recent applications include $\text{H} + \text{N}_2\text{H}_2 \rightarrow \text{H}_2 + \text{N}_2\text{H}_3$,^{17,49} $\text{OH} + \text{C}_3\text{H}_8 \rightarrow \text{H}_2\text{O} + \text{C}_3\text{H}_7$,¹⁸ $\text{RhCl}(\text{PH}_3)_2(\eta^2\text{-CH}_4) \rightarrow \text{RhCl}(\text{PH}_3)_2(\text{CH}_3)\text{H}$,⁶⁰ $\text{O} + \text{HCl} \rightarrow \text{OH} + \text{Cl}$,⁶¹ $\text{Cl} + \text{CH}_4 \rightarrow \text{HCl} + \text{CH}_3$,¹⁹ $\text{O} + \text{CH}_4 \rightarrow \text{OH} + \text{CH}_3$,²⁰ and $\text{Cl} + \text{H}_2 \rightarrow \text{HCl} + \text{H}$.⁶²

SOLUTION-PHASE DYNAMICS

We have extended the gas-phase variational transition state theory formalism to treat reaction rates in solution, including curvilinear coordinates, small- and large-curvature tunneling, optimized multidimensional tunneling, and equilibrium and nonequilibrium solvation effects. The methods are designed to take full advantage of the advances discussed in all three sections above. We distinguish three general levels of liquid-phase dynamics calculations:

- SES separable equilibrium solvation⁶³
- ESP equilibrium solvation path^{21,63,64}
- NES nonequilibrium solvation^{65,66}

In SES calculations, one calculates stationary point geometries and/or reaction paths in the gas-phase and then adds the free energy of solvation to each point. In ESP calculations one first creates a potential of mean force surface by adding free energies of solvation to the gas-phase potential energy surface; then stationary point geometries and/or reaction paths are computed using the potential of mean force. Tunneling calculations involve a function of the potential mean force called the canonical mean shape potential, which reduces to the potential of mean force in zero order. Nonequilibrium effects may be incorporated via coupling of the solute to collective solvent coordinates.

We have recently demonstrated all three levels of theory for the reaction $\text{H} + \text{CH}_3\text{CH}_2\text{OH} \rightarrow \text{H}_2 + \text{CH}_3\text{CHOH}$ in aqueous solution.^{21,66}

ACKNOWLEDGMENTS

This research is supported by the National Science Foundation under grant no. CHE97-25965 (liquid-phase electronic structure and dynamics research and part of the gas-phase electronic structure research) and by the U.S. Department of Energy, Office of Basic Energy Sciences under grant no. DOE-DE-FG02-85ER13579 (gas-phase kinetics research and part of the gas-phase electronic structure research).

REFERENCES

1. Coitiño, E. L.; Truhlar, D. G.; Morokuma, K. *Chem. Phys. Lett.* **1996**, *259*, 159.
2. Noland, M.; Coitiño, E. L.; Truhlar, D. G. *J. Phys. Chem. A* **1997**, *101*, 1193.
3. Coitiño, E. L.; Truhlar, D. G. *J. Phys. Chem. A* **1997**, *101*, 4641.
4. Corchado, J. C.; Truhlar, D. G. *J. Phys. Chem. A* **1998**, *102*, 1895.
5. Corchado, J. C.; Truhlar, D. G. *ACS Symp. Ser.* **1998**, *712*, 106.

6. Alhambra, C.; Gao, J.; Corchado, J. C.; Villa, J.; Truhlar, D. G. *J. Amer. Chem. Soc.* **1999**, *121*, 2253.
7. Fast, P. L.; Corchado, J. C.; Sánchez, M. L.; Truhlar, D. G. *J. Phys. Chem. A* **1999**, *103*, 3139.
8. Fast, P. L.; Corchado, J. C.; Sánchez, M. L.; Truhlar, D. G. *J. Phys. Chem. A*, submitted.
9. Truhlar, D. G. *Chem. Phys. Lett.* **1998**, *294*, 45.
10. Chuang, Y.-Y.; Truhlar, D. G. *J. Phys. Chem. A* **1999**, *103*, 651.
11. Fast, P. L.; Sánchez, M. L.; Truhlar, D. G. *J. Chem. Phys.*, in press.
12. Fast, P. L.; Sánchez, M. L.; Corchado, J. C.; Truhlar, D. G. *J. Chem. Phys.*, in press.
13. Fast, P. L.; Sánchez, M. L.; Truhlar, D. G. *Chem. Phys. Lett.*, in press.
14. Hu, W.-P.; Liu, Y.-P.; Truhlar, D. G. *J. Chem. Soc. Faraday Trans.* **1994**, *90*, 1715.
15. Corchado, J. C.; Espinosa-Garcia, J.; Hu, W.-P.; Rossi, I.; Truhlar, D. G. *J. Phys. Chem.* **1995**, *99*, 687.
16. Rossi, I.; Truhlar, D. G. *Chem. Phys. Lett.* **1995**, *233*, 231.
17. Chuang, Y.-Y.; Truhlar, D. G. *J. Phys. Chem. A* **1997**, *101*, 3808. Erratum: **1997**, *101*, 8741 (1997).
18. Hu, W.-P.; Rossi, I.; Corchado, J. C.; Truhlar, D. G. *J. Phys. Chem. A* **1997**, *101*, 6911.
19. Roberto-Neto, O.; Coitiño, E. L.; Truhlar, D. G. *J. Phys. Chem. A* **1998**, *102*, 4568.
20. Corchado, J. C.; Espinosa-Garcia, J.; Roberto-Neto, O.; Chuang, Y.-Y.; Truhlar, D. G. *J. Phys. Chem. A* **1998**, *102*, 4899.
21. Chuang, Y.-Y.; Radhakrishnan, M. L.; Fast, P. L.; Cramer, C. J.; Truhlar, D. G. *J. Phys. Chem. A*, in press.
22. Easton, R. E.; Giesen, D. J.; Welch, A.; Cramer, C. J.; Truhlar, D. G. *Theor. Chim. Acta* **1996**, *93*, 281.
23. Li, J.; Cramer, C. J.; Truhlar, D. G. *Theor. Chem. Acc.* **1998**, *99*, 192.
24. Li, J.; Williams, B.; Cramer, C. J.; Truhlar, D. G. *J. Chem. Phys.* **1999**, *110*, 724.
25. Storer, J. W.; Giesen, D. J.; Cramer, C. J.; Truhlar, D. G. *J. Comput.-Aided Mol. Design* **1995**, *9*, 87.
26. Li, J.; Zhu, T.; Cramer, C. J.; Truhlar, D. G. *J. Phys. Chem. A* **1998**, *102*, 1820.
27. Li, J.; Xing, J.; Cramer, C. J.; Truhlar, D. G. *J. Chem. Phys.*, in press.
28. Hawkins, G. D.; Cramer, C. J.; Truhlar, D. G. *J. Phys. Chem. B* **1997**, *101*, 7147.
29. Hawkins, G. D.; Liotard, D. A.; Cramer, C. J.; Truhlar, D. G. *J. Org. Chem.* **1998**, *63*, 4305.
30. Hawkins, G. D.; Cramer, C. J.; Truhlar, D. G. *J. Phys. Chem. B* **1998**, *102*, 3257.
31. Chambers, C. C.; Hawkins, G. D.; Cramer, C. J.; Truhlar, D. G. *J. Phys. Chem.* **1996**, *100*, 16385.
32. Giesen, D. J.; Gu, M. Z.; Cramer, C. J.; Truhlar, D. G. *J. Org. Chem.* **1996**, *61*, 8720.
33. Giesen, D. J.; Chambers, C. C.; Cramer, C. J.; Truhlar, D. G. *J. Phys. Chem. B* **1997**, *101*, 2061.
34. Giesen, D. J.; Hawkins, G. D.; Liotard, D. A.; Cramer, C. J.; Truhlar, D. G. *Theor. Chem. Acc.* **1997**, *98*, 85. Erratum: **1999**, *101*, 309.
35. Zhu, T.; Li, J.; Hawkins, G. D.; Cramer, C. J.; Truhlar, D. G. *J. Chem. Phys.* **1998**, *109*, 9117.
36. Li, J.; Hawkins, G. D.; Cramer, C. J.; Truhlar, D. G. *Chem. Phys. Lett.* **1998**, *288*, 293.
37. Li, J.; Zhu, T.; Hawkins, G. D.; Winget, P.; Liotard, D. A.; Cramer, C. J.; Truhlar, D. G. *Theor. Chem. Acc.*, in press.
38. Li, J.; Cramer, C. J.; Truhlar, D. G. to be published.
39. Zhu, T.; Li, J.; Liotard, D. A.; Cramer, C. J.; Truhlar, D. G. *J. Chem. Phys.* **1999**, *110*, 5503.

40. Dolney, D.; Hawkins, G. D.; Liotard, D. A.; Cramer, C. J.; Truhlar, D. G. to be published.
41. Giesen, D. J.; Chambers, C. C.; Hawkins, G. D.; Cramer, C. J.; Truhlar, D. G. *ACS Symp. Ser.* **1998**, *677*, 285.
42. Chambers, C. C.; Giesen, D. J.; Hawkins, G. D.; Vaes, W. H. J.; Cramer, C. J.; Truhlar, D. G. *IMA Series Math. Its Applic.* **1999**, *108*, 51.
43. Hawkins, D. G.; Li, J.; Zhu, T.; Chambers, C. C.; Giesen, D. J.; Liotard, D. A.; Cramer, D. J.; Truhlar, D. G. *ACS Symp. Ser.*, in press.
44. Hawkins, G. D.; Zhu, T.; Li, J.; Chambers, C. C.; Giesen, D. J.; Liotard, D. A.; Cramer, C. J.; Truhlar, D. G. *ACS Symp. Ser.* **1999**, *712*, 201.
45. Li, J.; Cramer, C. J.; Truhlar, D. G. *Biophys. Chem.* **1999**, *78*, 147.
46. Truhlar, D. G.; Garrett, B. C.; Klippenstein, S. J. *J. Phys. Chem.* **1996**, *100*, 12771.
47. Garrett, B. C.; Truhlar, D. G. In *Encyclopedia of Computational Chemistry*; Schleyer, P. v. R.; Allinger, N. L.; Clark, T.; Gasteiger, J.; Kollman, P. A.; Schaefer, H. F. III, Eds.; Wiley: Chichester, UK, 1998; Vol. 5, p. 3094.
48. Allison, T. C.; Truhlar, D. G. In *Modern Methods for Multidimensional Dynamics Computations in Chemistry*; Thompson, D. L., Ed.; World Scientific: Singapore, 1998; p. 618.
49. Chuang, Y.-Y.; Truhlar, D. G. *J. Chem. Phys.* **1997**, *107*, 83.
50. Chuang, Y.-Y.; Truhlar, D. G. *J. Phys. Chem. A* **1998**, *102*, 242.
51. Villà, J.; Truhlar, D. G. *Theor. Chem. Acc.* **1997**, *97*, 317.
52. González-Lafont, A.; Villà, J.; Lluch, J. M.; Bertrán, J.; Steckler, R.; Truhlar, D. G. *J. Phys. Chem. A* **1998**, *102*, 3420.
53. Fast, P. L.; Corchado, J. C.; Truhlar, D. G. *J. Chem. Phys.* **1998**, *109*, 6237.
54. Fast, P. L.; Truhlar, D. G. *J. Chem. Phys.* **1998**, *109*, 3721.
55. Corchado, J. C.; Coitiño, E. L.; Chuang, Y.-Y.; Fast, P. L.; Truhlar, D. G. *J. Phys. Chem. A* **1998**, *102*, 2424.
56. Chuang, Y.-Y.; Corchado, J. C.; Truhlar, D. G. *J. Phys. Chem. A* **1999**, *103*, 1140.
57. Villà, J.; González-Lafont, A.; Lluch, J. M.; Truhlar, D. G. *J. Amer. Chem. Soc.* **1998**, *120*, 5559.
58. Villà, J.; Corchado, J. C.; González-Lafont, A.; Lluch, J. M.; Truhlar, D. G. *J. Amer. Chem. Soc.* **1998**, *120*, 12141.
59. Villà, J.; Corchado, J. C.; González-Lafont, A.; Lluch, J. M.; Truhlar, D. G. *J. Phys. Chem.*, submitted.
60. Espinosa-García, J.; Corchado, J. C.; Truhlar, D. G. *J. Amer. Chem. Soc.* **1997**, *119*, 9891.
61. Allison, T. C.; Ramachandran, B.; Senekowitsch, J.; Truhlar, D. G.; Wyatt, R. E. *J. Mol. Struct. Theochem.* **1998**, *454*, 307.
62. Srinivasan, J.; Allison, T. C.; Schwenke, D. W.; Truhlar, D. G. *J. Phys. Chem. A* **1999**, *103*, 1487.
63. Chuang, Y.-Y.; Cramer, C. J.; Truhlar, D. G. *Int. J. Quantum Chem.* **1998**, *70*, 887.
64. Truhlar, D. G.; Liu, Y.-P.; Schenter, G. K.; Garrett, B. C. *J. Phys. Chem.* **1994**, *98*, 8396.
65. Truhlar, D. G.; Schenter, G. K.; Garrett, B. C. *J. Chem. Phys.* **1993**, *98*, 5756.
66. Chuang, Y.-Y.; Truhlar, D. G., to be published.

A Combined Static and Dynamic Density Functional Theory Approach to Elementary Reaction Steps in Homogeneous Catalysis.

Peter Margl, Tom K. Woo, Rochus Schmid, Liqun Deng and Tom Ziegler*

Department of Chemistry, University of Calgary, 2500 University Drive, N.W., Calgary, Alberta, T2N 1N4, CANADA

email: ziegler@ucalgary.ca

Phone: (voice) 403 220-5368 (fax) 403 289-9488

KEYWORDS: molecular modeling, density functional theory, QM/MM, Brookhart catalyst, constrained geometry catalyst, *ab initio* molecular dynamics

ABSTRACT

We describe an approach in which first principle molecular dynamics calculations based on density functional theory (DFT) are used to locate reaction pathways and estimate free energies of activation whereas static DFT calculations were used to obtain stationary points and relative energies as well as reaction paths by the intrinsic reaction coordinate method. The approach has been applied to (a) copolymerization of polar and non-polar monomers by nickel and palladium based catalysts as well as (b) a comparison between rhodium and iridium based catalysts in Monsanto's acetic acid process (c) carbonylation of methane by a rhodium catalyst.

Introduction

Homogenous catalytic systems have often been used to model more complicated heterogeneous systems. However, even seemingly simple homogenous systems pose many challenges for computational chemists. Often times a first principle's calculation involves a stripped down model that only vaguely resembles the true system. If large, bulky ligand systems are involved they are most often neglected in high level calculations with the hope that they do not substantially influence the nature of the reaction mechanisms. Unfortunately, the surrounding ligand system or matrix can often play a crucial mechanistic role. In addressing this issue, the combined quantum mechanical/molecular mechanics (QM/MM) method¹ has recently received significant attention. In this hybrid method part of the molecule, such as the active site, is treated quantum mechanically while the remainder of the system is treated with a molecular mechanics force field. This allows extremely large systems which are out of the reach of pure QM calculations to be studied in an efficient and detailed manner. We have applied the QM/MM method to study the homogenous Brookhart diimine Ni olefin polymerization catalyst.² Since the QM/MM method was originally conceived to more adequately treat larger, more "real life" systems it naturally has applications in the area of heterogeneous catalysts.

Recently, our group has been utilizing Car-Parinello³ flavor *ab initio* molecular dynamics to explore potential energy surfaces and to obtain free energy barriers for catalytic processes. We have determined free energy barriers for several processes at the *ab initio* molecular dynamics level for the Ti mono-Cp constrained geometry olefin polymerization catalysts, (CpSiH₂NH)Ti-R⁺.⁴ The results compare well with similar free energy barriers determined from more traditional "static" electronic structure calculations. We will demonstrate that the *ab initio* molecular dynamics method (i) provides a general way of determining finite temperature free energy barriers which are in good agreement with static methods, (ii) can be used to efficiently explore complicated free energy surfaces and (iii) that the method can be effectively utilized in a synergistic fashion with traditional static methods.

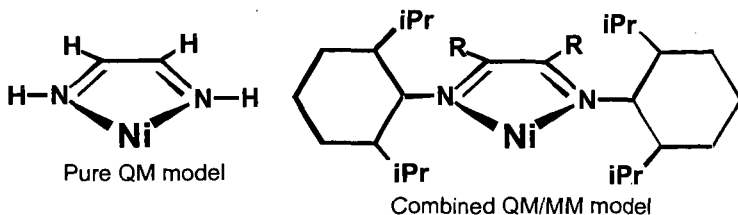
Computational Details

The reported "static" density functional calculations were all carried out by the ADF program system, developed by Baerends and others.⁵ Energy differences were calculated by including the local exchange-correlation potential by Vosko⁶ *et al.* with Becke's⁷ nonlocal exchange corrections and Perdew's⁸ nonlocal correlation correction. For the QM/MM calculations a version of the ADF program system as modified according to Morokuma and co-workers was utilized with the AMBER⁹ force field. For more details of the QM/MM work see reference¹⁰. All reported molecular dynamics simulations were carried out with the Car-Parinello Projector Augmented Wave (CP-PAW) code developed by Blöchl.¹¹ For more details of the molecular dynamics simulations and the constrained geometry work see references¹².

Results and Discussion

Combined QM/MM: Recently, Ni(II) and Pd(II) diimine based single-site catalysts have emerged as promising alternatives to newly developed metallocene catalysts for olefin polymerization.² Brookhart's group has shown that these catalyst are able to convert ethylene into high molecular mass polymers with a controlled level of polymer branching when bulky ligand systems are used.

We have investigated the chain propagation, chain termination and the chain branching processes with a truncated pure quantum mechanical model system where the bulky ligands are neglected and with a combined QM/MM model where the bulky ligands are included via a MM force field. Scheme 2 depicts the two model systems. The QM region of the QM/MM model is the same as the pure QM model.



Scheme 1

Experimentally, it has been determined that the relative magnitude of the barriers are in the order insertion > isomerization > termination. Table 1 shows that the pure QM model does not reproduce this trend. In fact, the results of the pure QM simulation suggest that the catalyst should not produce polymers at all but rather dimers or oligomers.

Table 1.

process	Reaction Barrier, ΔH^\ddagger (kJ/mol)	
	pure QM model	QM/MM model
propagation	71	49
branching	52	64
termination	42	77

However, when bulky ligands are not neglected but rather modeled by molecular mechanics force field, the barriers do follow the experimentally established trends. Moreover, the calculated propagation barrier is in remarkable agreement with the experimental estimate of 40-46 kJ/mol.¹³

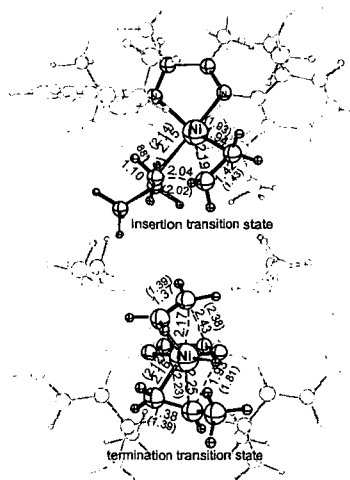


Figure 1. Combined QM/MM transition states for the propagation and termination processes. The parenthetical parameters are those of the equivalent pure QM transition states. The ghosted portions of the molecules represent the pure MM atoms.

Ab Initio Molecular Dynamics: We have examined several chain termination and long chain branching mechanisms with conventional "static" electronic structure calculations and with *ab initio* molecular dynamics in the density functional theory framework. Free energy barriers were computed by both methods and were found to be in excellent agreement with one another. Movies of all molecular dynamics simulations presented here can be found at our research group's world wide web home page <<http://www.chem.ucalgary.ca/groups/ziegler>>.

Table 2. Static and dynamic free energy barriers.

Process	Free Energy Barrier	
	ΔF^\ddagger	
	at 300 K (kJ/mol)	
	MD ^a	static
β -H transfer to monomer ^b	43 \pm 8	40.1
β -H transfer to metal ^c	57 \pm 3	53.9
olefin σ -bond metathesis ^b	87 \pm 5	91.7
alkyl σ -bond metathesis ^b	70 \pm 3	72.3

^a values are the average of the forward and reverse scans. Error bars are half the difference.

^b ethyl group and propyl group used to model growing chain in the static and dynamic simulations, respectively.

^c A propyl group used to model the growing chain.

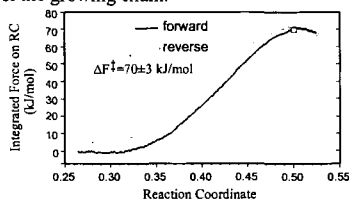


Figure 2. Free energy profile determined from the *ab initio* molecular dynamics simulation of the alkyl σ -bond metathesis process.

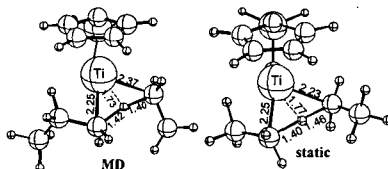


Figure 3. Transition state structures for the alkyl σ -bond metathesis process. The molecular dynamics (MD) structure is a snapshot geometry taken from the transition state region.

Although we have applied the Car-Parinello molecular dynamics method to study homogeneous catalytic reactions on a *ab initio* dynamics level, the method is as well suited to treating periodic systems. Hence the method shows promise for the computational modeling of heterogeneous catalytic processes such as those that take place in zeolite cavities.

Acknowledgment: This investigation was supported by NSERC of Canada, as well as by the donors of the Petroleum Research Fund, administered by the American Chemical Society (ACS-PRF No 31205-AC3).

REFERENCES

- Maseras, F.; Morokuma, K. *J. Comp. Chem.* **1995**, *16*, 1170.
- Johnson, L. K.; Killian, C. M.; Brookhart, M. *J. Am. Chem. Soc.* **1995**, *117*, 6414.
- Car, R.; Parrinello, M. *Phys. Rev. Lett.* **1985**, *55*, 2471.
- Chum, P. S.; Kao, C. I.; Knight, G. W. in *Plastics Engineering*, June 1995; pp. 21.
- Baerends, E. J.; Ellis, D. E.; Ros, P. *Chem. Phys.* **1973**, *2*, 41.
- Vosko, S. H.; Wilk, L.; Nusair, M. *Can. J. Phys.* **1980**, *58*, 1200.
- Becke, A. *Phys. Rev. A* **1988**, *38*, 3098.
- Perdew, J. P. *Phys. Rev. B* **1986**, *33*, 8822.
- Cornell, W. D.; Cieplak, P.; Bayly, C. I.; Gould, I. R., Jr., K. M. M.; Ferguson, D. M.; Spellmeyer, D. C.; Fox, T.; Caldwell, J. W.; Kollman, P. A. *J. Am. Chem. Soc.* **1995**, *117*, 5179.
- Deng, L.; Margl, P. M.; Ziegler, T. *J. Am. Chem. Soc.* **1997**, in press.
- Blöchl, P. E. *Phys. Rev. B* **1994**, *50*, 17953.
- (a) Woo, T. K.; Margl, P. M.; Blöchl, P. E.; Ziegler, T. **1997**, submitted. (b) Woo, T. K.; Margl, P. M.; Lohrenz, J. C. W.; Blöchl, P. E.; Ziegler, T. *J. Am. Chem. Soc.* **1996**, in press.
- Maurice Brookhart - a private communication.

Toward a New Generation of Hydrocarbon Reaction Models

John H. Shinn, Anil N. Patel.
Chevron Research and Technology
100 Chevron Way, Richmond, CA-USA 94802

ABSTRACT

Significant advances in several independent areas are enabling the development of new modeling tools well beyond those capable a short time ago. These significant advances include improvements in experimental kinetics, a priori prediction of molecular energetics and rates, instrumental approaches to the composition of complex mixtures, computational conversion of compositional information to molecular structure determination, and automated generation of reaction networks and modeling software. In this presentation, we will examine the state of development of these tools and their incorporation into online molecular optimization of conversion processes.

INTRODUCTION

The current business environment in the chemical process industry has resulted in an emphasis on improving performance of existing operations to maximize profitability of existing capital equipment. One strategy to achieve this objective is an increase in process monitoring, automation, control and optimization. For process equipment involved in chemical conversion, an essential step in reaching the on-line optimization objective is the creation of detailed reaction models capable of simulating a multitude of simultaneous reactions.

Much work has been done in moving chemical process models from the early linear programming correlative tools to a new generation of models based on actual reaction kinetics. Workers at Mobil introduced models based on molecular structural characteristics of the feed (Quann and Jaffe). This pioneering work demonstrated the practicality of construction of kinetic models for even the most complex feedstocks and processes.

Recent advances in many fields are enabling the construction of ever more detailed chemical reaction models. Although it is still not possible to identify and provide detailed kinetics of every reaction in a mixture as complex as a petroleum vacuum gas oil, significant improvements are now possible which will create a new generation of reaction models capable of controlling processes at the molecular level. This paper will discuss these advances and how they may be incorporated to improve the existing generation of modeling tools.

ADVANCES IN RELATED FIELDS

I. Analytical approaches - identifying the molecules

For years, gas chromatography has been the workhorse of detailed analysis. However, the use of gas chromatography for mixtures boiling above the light distillates range is greatly limited by the presence of a myriad of possible components at similar or equal retention times. Methods such as GCMS and separation-analysis approaches such as employed by Boduzsynski enable identification of some of the overlapping areas, but are too tedious or expensive to apply to online applications.

The use of simulated distillation methods and their extension to high boiling ranges, while not providing molecular detail, significantly expanded the range of chromatographic approaches. Petroleum-derived feeds boiling up to 1200 F and higher could be characterized in terms of the mass of materials boiling in very narrow boiling range fractions, with high precision. Workers began to develop additional methods to allow additional characterization of these narrow fractions, for instance by using chemiluminescence detectors (Chawla). Recent work employing Atomic Emissions Detection has made elemental determination practical for many elements including of carbon, hydrogen, nitrogen, sulfur, nickel, vanadium, and iron (Quimby et al). Use of additional detectors permit other molecular characteristics to be determined for the

narrow fractions such as mass distribution (GC-FIMS, Malhotra et al), and molecular type (using fragmentation MS detection). While still short of the objective of individual component determination, the capability exists for providing far greater detail than was previously available via methods that provided similar information across far wider boiling ranges.

The detailed information on composition of the narrow fractions must now be converted to an accurate quantitative representation of the distribution of molecular species in the sample. The work of Wilcox and Faulon have shown that this may be accomplished through optimization of selection of molecules from a library of possible species representing the possible components in a given boiling range. The development of the Signature algorithm by Faulon permits automated construction of molecular structures from analysis information. Application of Signature with expert knowledge of the molecular types present in petroleum fractions enables the construction of a library of possible molecular species for each boiling range fraction. The process of providing detailed molecular type distributions for a given feed then becomes an optimization problem of choosing the best possible match for the characteristics of each narrow fraction with the available library species. The analytical information is converted to a set of molecules representing in the greatest detail available the distribution of molecular types within the feed. Figure 1 provides an example application of this approach for the prediction of the molecular species in a light gas oil fraction. A high level of accuracy is obtained in comparison to detailed GCMS identification. The remaining degeneracy is between species with similar reaction performance (e.g. paraffin isomers).

II. Kinetics Advances – how do the molecules react?

With information on the distribution of molecular types in the feed, it is necessary to have kinetic information on their behavior in the mixture. Use of model compound reactions continues to be a key in defining the reaction pathways and rules that define the kinetics of specific reaction types (for example the work of Mochida and co-workers on desulfurization, Korre et al in aromatics hydrogenation, Souverijns et al in cycloparaffins isomerization). Additional information is required of the reactions of these species in complex mixtures as 'matrix effects' can cause variations in reactivity beyond those observed in pure feed studies. The analytical methods described above permit the examination of reactivities of individual species within complex mixtures. Recent revealing work by Shin and Mochida has shown the importance of these effects in HDN and HDS reactions.

III. Computation and Modeling advances – building the reaction models.

A central problem in construction of complex kinetic models is known as the 'explosion of species', that is the number of possible molecular species increases dramatically with carbon number. This fundamental problem makes it difficult to represent the possible reactions completely, and renders measurement of the detailed kinetics of each species impossible. One needs a way to reduce the number of species considered and to provide rate information and reaction network information to describe the process performance of the complex mixture. Research developments in computational chemistry and its use to model kinetics are enabling significant advances in this arena.

Approaches to limit the number of species utilize the molecular characteristics of the molecules to form groups that are presumed to behave similarly, a technique known as 'lumping'. Early lumped models grouped all molecules in a single boiling range as equivalent. The advances of Quann et al have moved this approach to the molecular characteristics level. The ultimate lumped model would group molecules on a reaction kinetic behavior basis. This possibility is enhanced by the presence of the advanced analytical information described above.

Another 'explosion' problem results due to the expansion in the possible reactions of species as carbon number increases. Early kinetic models used hand-written reaction networks to describe the essential reactions which connect feed and product species. Advances by Michael Klein and coworkers has created the prospect of computer-generated reaction networks, employing chemically specific reaction rules to limit the explosion of reaction types. Recently, Hou et al have shown that these approaches can be successful in representing the reaction behavior of catalytic hydroprocessing, while producing a model small enough to be solved on a personal-computer platform in solve times of under one minute. The Klein et al approach also employs computational approaches to write the necessary set of differential equations to integrate them to solve

the reaction model and predict the products from a given set of feed molecules and conditions.

Klein has also demonstrated approaches for lumping the reaction behavior of molecular species according to kinetic behavior. The work of Korre et al demonstrated the use of the relationship between linear free energy of formation and reaction rate for similar species to permit the calculation of the kinetics of many similar molecules without measuring the kinetics of each member. This approach has been demonstrated to be very effective even for complex reactions of molecular groups such as polynuclear aromatic hydrocarbons.

Advances in computational chemistry allow rate predictions for groups of molecules from first principles calculations. A first level approach allows computation of the free energies of reactants and intermediates to construct plausible reaction pathways and form the abscissa for the Linear Free Energy-Rate relationships developed by Klein. Perry and Goddard demonstrated the effectiveness of this approach even for catalytic systems by showing that the kinetic performance of catalytic reforming could be predicted using gas-phase molecular energetics with a very limited set of parameters to represent the interactions of various molecular types with the surface catalytic functions. More recent work involves the development of high-level group additivity relationships, based on detailed quantum mechanical calculations, to permit the rapid determination of the energetics of millions of molecules in a mixture. This information also facilitates the grouping of these molecules into species that have similar bonding energetics – a key to lumping based on reaction performance.

CONNECTING THE PIECES

The challenge for the modeler is to utilize the advances collectively to produce more accurate predictive tools based upon detailed reaction chemistry. Figure 2 provides a schematic representation of this approach. Analytical information is passed to the structure generator module providing detailed information on the composition of the feed (or products). The molecular information is passed to model, constructed on the basis of the process information using the automated reaction network generator, reaction-property information, and a model solver. QM calculations provide a basis for reaction rate information for similar molecules. The output molecules are then utilized with additional Quantitative Structure Property Relationship information (made possible by employing the detailed analysis approach on a broad range of products).

An additional critical step involves the use of database technology to sample the performance of pilot plant and commercial operations and determine the relationship between feed composition, controllable process parameters, and product composition. These commercial data sources are essential in validating and adjusting the model performance in a feedback loop that includes the kinetic model reconstruction (adjustments in reaction rules, molecular family kinetics, etc).

The ultimate use of these kinetic models comes in integration with the process itself. The analysis approaches described above are specifically developed for their capability to be utilized on-line. Computational network generation allows adjustment of the model itself as part of the validation process. Combination of the analysis information, 'living' kinetic models, and advanced monitoring and control information will permit a level of sophistication of process tuning we term 'molecular optimization'.

ACKNOWLEDGEMENTS

This work would not be possible without the ingenuity of leading research groups from around the world. Collaborations of this type are essential to create the prospects of significant advances in kinetic models – it is unlikely that any single research organization would have the combined capability to provide these advances. We are greatly indebted to and grateful for the work of Professor William A. Goddard of California Institute of Technology, Professor Michael T. Klein of Rutgers University, Professor Isao Mochida of Kyushu University, Dr. D. Duayne Whitehurst (consultant), Dr. Jason K. Perry of First Principles Inc., Dr. Jean Loup Faulon and R. Wilcox of Sandia National Laboratory, and Chevron colleagues Dr. David A. Grudowski, Dr. Ram Ramamoorthy, and Dr. Michael A. Shippey.

REFERENCES

- Boduszynski M. M.; *Energy & Fuels*, 1998, 2, 597-613
- Chawla B.; *Journal of Chromatographic Science*, 35, 97 - 104, 1997.
- Hou, G., T. I. Mizan and M. T. Klein, "Computer-Assisted Kinetic Modeling of Hydroprocessing," *ACS Div. Pet. Preprints*, 42, pp 670-673, 1997.
- Korre, S. C., M. T. Klein and R. J. Quann, "Hydrocracking of Polynuclear Aromatic Hydrocarbons. Development of Rate Laws Through Inhibition Studies," *I&EC Research*, 36, 2041-2050, 1997.
- Malhotra R., Coggiola M.J., Young S., Hsu C.S., Dechert G.J., Rahimi P.M., and Briker Y.; Symposium on Chemistry of Diesel Fuels, 216th meeting, ACS, Boston, MA, 1998
- Mochida I., Shin S., Sakanishi K., Grudoski D., and Shinn J.; *Hydrotreatment and Hydrocracking of Oil Fractions*, Unpublished
- Quann R. J., and Jaffe S. B.; *Ind. Eng. Chem. Res.* 31, 2483-2497, 1992
- Quimby B., Grudoski D., and Giarroccol V.; *Journal of Chromatographic Science*, 36, 1 - 9, 1998.
- Shin S. and Mochida I., Private communication, January 1999
- Souverijns W., Houvenaghel A., Feijen E.J.P., Martens J.A., Jacobs P.A.; *Journal of Catalysis*, 174, 201-209, 1998
- Whitehurst D.D., T. Isoda, Mochida I.; *Advances in Catalysis*, 42, 345-471, 1998
- Wilcox Robert, Grudoski D., Faulon J. L.; "Measurements to Molecules" Poster presentation at Gordon Research Conference, Ventura CA, January 1999

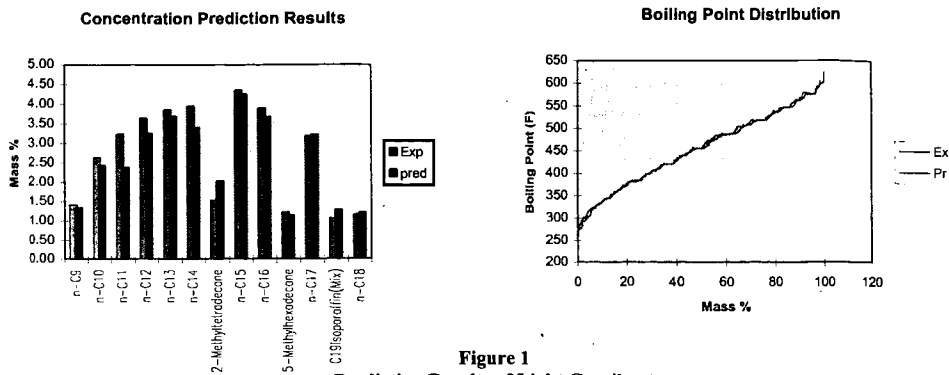


Figure 1
Prediction Results of Light Gasoil cut

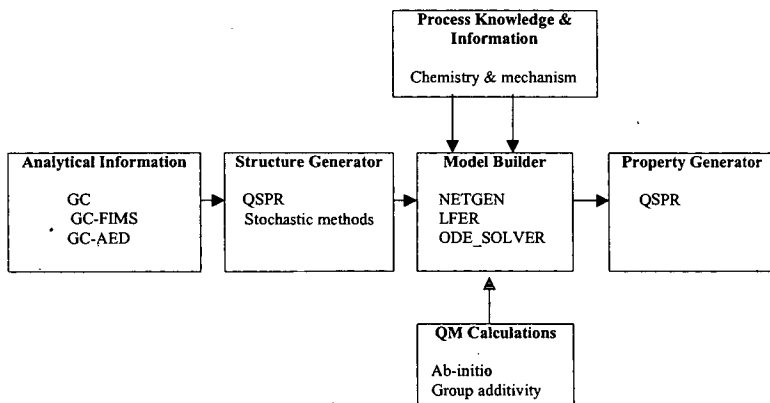


Figure 2
New Generation Models - Connecting the Pieces

Simulation of Chemical Mechanisms Using Computational Methods

Michael J. Manka, *Alchemy Software, Wesley Chapel, FL 33543-5759*

Keywords: Computer simulation, reaction modeling software, chemical mechanisms

Abstract

The use of computational methods for the simulation of chemical mechanisms is discussed. A computer program, *REACT for Windows*, is presented which implements the basic functions for simulating chemical mechanisms. Strategies for modeling experimental data and complex chemical mechanisms are discussed including methods for estimating kinetic rate data.

Introduction

With the proliferation and advancement of powerful desktop computers, the ability to simulate complex chemical mechanisms is readily available to even the most casual users of computational tools. An important factor in simulating chemical mechanisms is the availability of software which performs the necessary integration calculations and provides an easy to use interface for the entry of mechanistic and reaction time data, and contains the ability to present the calculated results in tables and plots for the user to view and print. Until recently software with these features has not been available in a single program running in a Microsoft Windows environment. A computer program, which provides all these features and many more, is now available. This program is called *REACT for Windows* and runs on desktop personal computers with any of the Microsoft Windows operating system. In this paper, I would like to review the important features involved in simulating chemical mechanisms and how they are implemented in a computer program such as *REACT for Windows*.

The three basic features of a functional program which performs computational simulations of chemical mechanisms are the input of mechanistic and reaction time data, the differential equation integration algorithm, and the output of the calculated results in useable formats. We will discuss each of these three areas and how they are implemented in the *REACT for Windows* program. Using specific mechanistic examples, we will also present results calculated using the *REACT* program. We will also suggest strategies for the modeling of experimental data based on a hypothetical mechanism and the simulation of a chemical mechanism where, perhaps, not all the reaction rate coefficients are known. While it may be straightforward to hypothesize individual reactions in a chemical mechanism, it can be a much more difficult matter to provide reasonable kinetic rate data for those reactions if none are available. Thus, methods for the estimation of kinetic rate coefficients will be discussed in some detail.

React for Windows Program

General Description. The *REACT for Windows* program evolved from previous programs^{1,2} developed at the National Institute of Standards and Technology (NIST) and used to solve chemical mechanisms by experimental chemical kineticists. Unlike its predecessors, *REACT* has been written to execute on personal computers (PC) running any of the popular Microsoft Window operating system environments, including Windows 3.1/3.11, Windows 95/98 and Windows NT. The program requires as a minimum an Intel 80486 microprocessor with math coprocessor and a clock speed of 66 MHz or its equivalent. The program also recommends a graphics accelerator card capable of supporting a monitor resolution of 1024 × 768 and 256 colors or better. The program was designed for a 17 inch monitor and this size monitor or larger is recommended for optimal use with the recommended monitor resolution. While a mouse is required, there is an equivalent keystroke combination for most mouse initiated actions. The program supports the printing of reports with tabulated results as well as printing plots of results. The program is composed of three integral parts: the chemical mechanism editor, differential equation integration algorithm, and calculated results tabulation and plotting function. Each of these three parts will now be discussed.

Chemical Mechanism Editor. The chemical mechanism editor facilitates the entry and editing of the mechanistic and reaction time data. This data includes the title of the mechanism and any ancillary information about the mechanism, the chemical reactions in the mechanism and their respective forward and reverse rate coefficients, the initial concentrations of each species involved in the mechanism, and the reaction times where the concentration data and its time derivative are reported for each species. The mechanism title identifies the mechanism under simulation and any additional information, such as the reaction temperature, can be entered as ancillary information and saved with the mechanistic data. The reaction equations are entered into the program with the limitation that each species name cannot exceed twelve characters. There is provision for including the charge of ions and the spectroscopic state of the species

within the species name. Like its predecessor programs, the *REACT* program does not permit the entry of reactions with orders higher than two. If higher order reactions, such as third-order reactions are involved in the mechanism, they can be simulated by using consecutive, second-order reactions. The program does allow the introduction and removal of species using zeroth-order reactions, as well as the more familiar first- and second-order reactions. If the rate coefficients are known, they can be entered directly after the entry of the reaction equation. If they are not known, but kinetic rate parameters for the reaction are available from the literature or a kinetic rate database like the NIST Chemical Kinetics Database⁵, a reaction rate calculator is provided to facilitate the calculation and entry of rate coefficient data. The mechanism editor provides the ability to add a reaction to the mechanism, insert a reaction into the mechanism, reposition a reaction within the mechanism, delete and hide a reaction from the mechanism, and edit a reaction within the mechanism. Once a reaction is added to the mechanism, it appears in the mechanism list of reactions where it can be accessed for editing or deletion. These features provide abundant flexibility in manipulating the reaction mechanism.

The mechanism editor monitors all entries for reasonableness and prevents illegal entries. It also automatically performs all the necessary bookkeeping regarding species in the mechanism as reactions are entered, deleted or edited. The species are arranged alphabetically by length of name in a list of components. Initial concentrations of species having non-zero values are easily entered using this list of components. The initial concentration of all newly added species are initialized to zero and may need to be changed prior to performing a calculation.

There is considerable flexibility available in selecting the reaction times. The reaction times can be any combination of as many as 1000 linearly or geometrically spaced values and any number of other specific values. Once all the pertinent mechanistic data has been entered, the integration algorithm can be called to perform the calculations. The mechanism can have no more than 85 species in the current version of the program, but the number of reactions allowed is quite large (>2000) and is mainly limited by the memory available in the computer. The program uses dynamic memory allocation to accommodate the array size requirements of the mechanism. Mechanistic data are easily saved to memory for future retrieval and use.

Integration Algorithm. The integration calculation simulates homogeneous reactions occurring in a fixed volume at a constant temperature. The differential equation integration algorithm is an implementation of an adaptive step size fifth-order implicit Runge-Kutta method with fourth-order error control^{2,4}. Similar differential equation integration algorithms have been presented previously⁵⁻¹⁰. To perform the integration in a reliable and efficient manner, the integration algorithm uses variable order, variable step methods of the linear multi-value type. This means that the integration algorithm adapts its integration step size, as well as the integration formula order, so as to progress from the initial end of the time range to the other with the least amount of work. The step size selection is completely automatic, including the initial step size. The relative integration error value, which is set by the user, controls the integration step size. A smaller value results in greater overall integration accuracy, at the expense of longer execution time. Solution values at the user's reaction time are rarely exact integration end points. Normally, integration proceeds beyond a reaction time value and then the solution is obtained by an appropriate backward interpolation. The integration method is implicit and requires the use of a Jacobian matrix, which is calculated exactly by the algorithm. The relative integration error value governs the error control mechanism, which in turn controls the step size strategy as previously mentioned. Errors are measured with each individual step. Thus, there is no guarantee that cumulative errors will not be significantly larger, but experience has shown that for stable systems this very rarely occurs. The integration process can be halted and its progress monitored. The integration algorithm automatically reports its status every 5000 integration steps if the final end point of the time range is not achieved or when an error occurs. The results of the integration process include not only concentration data but also the time derivative of the concentration data for each time point including zero time. The latter data are important in the simulation of photon emission in spectroscopic measurements.

Displaying Results. Once the integration has been successfully completed, the program displays the concentration results for all the species in a tabular format. The program provides considerable flexibility in the presentation and viewing of both the concentration data and time derivative of the concentration data of each species. The data for any number of species can be presented in any desired order for an enhanced focus and comparison of pertinent results. Any desired set of results can also be printed in a report format together with optional mechanistic information. Specific sets of data can be exported to an ASCII file for importing into other software applications such as Microsoft Excel for further analysis. Finally, any data set type, concentration or time derivative of concentration data, can be plotted for a graphical summary view of trends in the data for that species. In an effort to limit the complexity of an individual plot, no more than five such data sets can be plotted at one time. A printed copy of the plot can

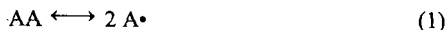
also be readily obtained using either laser or inkjet type printers. Customized plots intended for presentation or publication can be obtained using graphics programs and data exported as mentioned above. Reports containing calculated results can also be generated. Again, like the ability to display data, any combination of selected data can be included in the report. The amount of mechanistic information included in the report can be controlled as well.

Program Interface. As a Windows compatible program REACT has many features common to Windows programs. The menu bar contains menu items familiar to most users as well as menu items specific to REACT. It contains an extensive online Help function to aid the user in using the program efficiently and answering questions about the program. A tool bar is included to provide access to icons, which activate the most frequently used commands. A status bar at the bottom of the program window provides information about the status of the program and instructions about what to do next. The interface of the program is composed of four tabbed pages which can be selected using the mouse. The first page is titled, Mechanistic Data, and is used to enter and edit all the mechanistic data. The second page is the Reaction Times page and is used to enter and edit the reaction times and adjust the Relative Error Value for the integration process. The command button to begin the integration calculation is also located on this page as well as in the tool bar. The Tabulated Data page, which is used to present the calculated results in a tabular format, is automatically exposed after an integration calculation has been successfully completed. Once exposed, one can view the calculated results and access the display options for selecting data items for display. The Plot of Results page, which is used to display plots of selected results, also becomes accessible after an integration calculation has been successfully completed and is exposed to access the plot options for the selection of data items to be presented in a plot.

Modeling of Experimental Data

The modeling of experimental data provides a straightforward example of the application of the REACT program. Under ideal circumstances, experimental data is obtained under conditions where a single rate coefficient is determined from the rate of appearance or disappearance of a single reaction component. In this case a straightforward mathematical analysis of the data may be sufficient. However, modeling the complete mechanism may reveal insights into discrepancies in the fit of the data due to unanticipated reactions. The strategy used in making experimental measurements of kinetic rate parameters is to reduce the kinetic importance of all reactions except the one under investigation. This is usually done by judiciously adjusting the initial concentrations of the reactants and the reaction temperature. However, by modeling the mechanism in sufficient detail one can obtain a better appreciation for the influence each reaction may have on the one under investigation and anticipate difficulties in making kinetic rate measurements under various reaction conditions, i.e. as the initial component concentrations or reaction temperature are changed. Under simulation, any prior assumptions about reaction species, such as steady-state conditions, are not only not required but are totally unnecessary.

The recommended approach to modeling experimental data is as follows. First, it requires entering the chemical mechanism under investigation in as much detail as possible into the REACT or similar program. Consider the mechanism shown below which is operative for many mechanisms involving fuel-related reactions where radical chemistry is predominant. The mechanism includes thermally initiated bond homolysis, hydrogen transfer and radical recombination and disproportionation reactions. The available rate coefficients for the reactions at the temperature of interest and the initial species concentrations are also entered into the program. Reasonable estimates of the upper or lower limit for some of the rate coefficients may



Fuel-Related Thermal Mechanism

suffice if actual values are not available. The rate coefficient under investigation is then adjusted to provide the best fit with experimental results. Simulated results may be exported for use in a spreadsheet program like Microsoft Excel where statistical analyses of the experimentally measured results and the calculated results can be performed.

Dissociation Reaction. Let us first consider the modeling of experimental data from the measurement of the dissociation reaction of AA. Once the relevant mechanistic information, including available kinetic rate data, and initial species concentrations have been entered into the program, reaction times corresponding to experimental times are entered using the specific reaction times program feature. An initial choice for the value of k_1 can be made based on the first reliable experimental measurement of the disappearance of AA using the following equation.

$$k_1 = \frac{1}{t} \ln \frac{[AA]_0}{[AA]_t}$$

where t is the experimental time at which the measurement of the disappearance of AA was made. The simulation calculation is repeated, while adjusting the value of k_1 in the program mechanism, until an acceptable fit of the experimental data and the calculated results are obtained. Statistical analyses can be applied to obtain the goodness of fit using external programs. A typical plot of the result of modeling k_1 using the above mechanism is shown below in Figure 1. Alternatively, each experimental data point could be fit exactly under simulation and the resultant rate coefficient values would then be averaged. This method is effective when there are only a few data points. The ratio of the rate coefficients for the radical recombination and disproportionation reactions of D• radicals may also be obtained from experimental data if these reactions are operative in the above mechanism. The rate of hydrogen transfer may also be obtained, but more suitable initial reaction conditions will provide more reliable experimental data which we will address next.

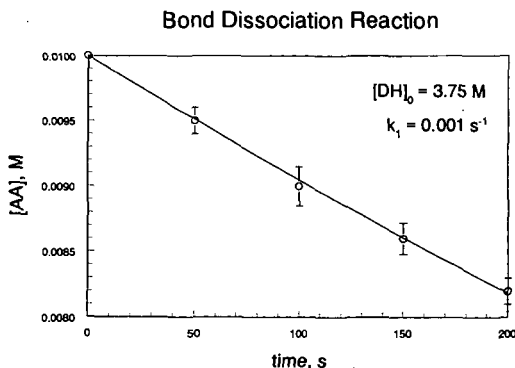


Figure 1. Plot of bond dissociation reaction experimental measurements and its reaction simulation results.

Hydrogen Transfer Reaction. The rate of hydrogen transfer from the hydrogen donor DH to the radical A• is governed by the rate coefficient k_2 in the above mechanism. This rate coefficient can be determined by again experimentally measuring the disappearance of AA and DH and the appearance of AH, but with the relative initial amounts of AA and DH changed. In this reaction the initial reactant concentrations of AA and DH are adjusted so that the rate of recombination of A• becomes competitive with its rate of hydrogen abstraction from DH. An initial choice for k_2 is given by the following equations¹¹.

$$k_2 = \frac{1}{t} \frac{[AH]}{[DH][A^{\bullet}]}$$

where

$$[\text{DH}] = [\text{DH}]_0 - [\text{DD}] - \frac{[\text{AD}]}{2}$$

and

$$[\text{A}^*] = \frac{\sqrt{k_1 [\text{AA}]^2}}{1 + 2 \frac{[\text{DD}]}{[\text{AD}]}}$$

The time average concentration of AA is given by

$$[\overline{\text{AA}}] = \sqrt{(1 - \xi_{\text{AA}}) [\text{AA}]_0^2}$$

where ξ_{AA} is the extent of reaction based on the disappearance of AA. The simulation calculation is repeated, while adjusting the value of k_2 in the program mechanism, until an acceptable fit of the experimental data and the calculated results is obtained. A typical plot of the result of modeling k_2 using the above mechanism is shown in Figure 2. Using additional experimental measurements of the concentrations of AA, DH and the various combination products, the rate coefficients for reactions affecting these species can also be adjusted to improve the overall fit of all the experimental data to the calculated results.

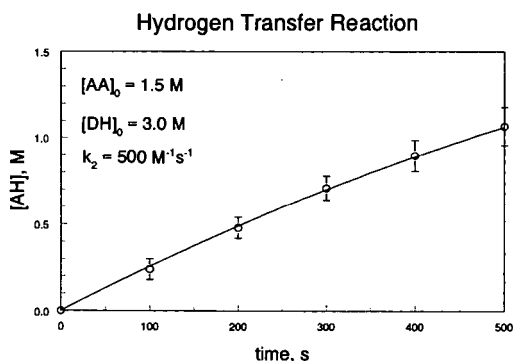


Figure 2. Plot of hydrogen transfer reaction experimental measurements and its reaction simulation results.

The strategy for adjusting any rate coefficient in a mechanism under simulation is to focus on the reactions having the most kinetic importance. This can be accomplished by determining the time derivative of each species concentration at initial reaction times where the reactant concentrations are known. Using estimated rate coefficients if necessary, a crude reaction analysis can be performed to provide an ordering of reaction importance. If the rate coefficient for a reaction is adequately known, it can be removed from the group of reactions with uncertain rate coefficients. If two reactions are contributing prominently to the change in the concentration of the species being measured, the only recourse may be to adjust the reactant concentrations of these reactions in order to discriminate their contributions. Once the final rate coefficients of interest are determined, the agreement between calculated results and experimental data should remain good for a wide range of initial species concentrations.

Simulation of Complex Chemical Mechanisms

The ability to simulate a complex chemical mechanism depends not only on providing a sufficiently complete reaction mechanism, but also requires providing rate coefficients for these reactions with adequate accuracy. As chemists, it should not be particularly difficult to hypothesize the important reactions in a mechanism, but the determination or estimation of

unknown rate coefficients can be quite challenging. The first step in the preparation for the simulation of any mechanism is to obtain as much information about it as possible from the literature. This information should provide the basic framework for developing a model of the mechanism. Once this information has been gathered, the task of assigning forward and reverse rate coefficients to each reaction begins. As information on the mechanism is researched in the literature, information on reaction rates should also be obtained. Kinetic rate parameters found in the literature can be used to calculate rate coefficients appropriate for the reaction temperature used in any simulation, even if the kinetic data must be extended to apply to the reaction conditions of interest. An excellent source for the compilation of gas phase rate data is the NIST Chemical Kinetics Database³ which is available for searching on personal computers. The NIST kinetics database primarily contains kinetic rate measurements of hydrocarbon reactions in the gas phase and provides kinetic rate parameters and references to the literature on these measurements. Some of the references provide critical evaluations of the available rate data for a reaction and these evaluations should be used as part of the evaluation of the kinetic rate parameters for the reactions in the mechanism being modeled. Often, however, an evaluation of the available kinetic rate data is left to the user. While this analysis may not be straightforward, it should provide a set of kinetic rate parameters which can be used to initially calculate rate coefficients. These initial values can be adjusted later to agree with whatever experimental data is available on the process. A similar compilation of gas phase reactions to consider is *Bimolecular and Termolecular Gas Reactions*¹², although these reactions should be included in the NIST database. Another excellent source of kinetic rate data is the *International Journal of Chemical Kinetics* where rate measurements for hydrocarbon reactions occurring in the liquid phase are also reported. *Chemical Abstracts* can also be searched to find additional literature references in other journals like the *Journal of Physical Chemistry* and engineering oriented journals on process chemistry. Despite the availability of these resources, it is often necessary to estimate the rate of a reaction where little or no data exists.

Estimation of Kinetic Rate Data

The ability to calculate kinetic rate data from first principles has made important progress. The calculation of energy barriers for hydrogen transfer reactions involving small hydrocarbon radicals and various hydrocarbons using *ab initio* methods and transition state theory has yielded results in good agreement with reliable experimental data¹³. But before we resort to this type of high-level calculation, let us explore simpler and more straightforward approaches to estimating rate parameters for a reaction. The relationship between kinetics and thermodynamics lies in the equilibrium constant. For a given reaction in the gas phase, the equilibrium constant for the reaction is given by the ratio of the forward and reverse rate coefficients as shown in the following equation.

$$K_{eq}(T) = \frac{k_f(T)}{k_r(T)} \quad (7)$$

where each variable is a function of the temperature T . But the equilibrium constant can be calculated directly from thermodynamic properties of the reactants and products involved in the reaction yielding the Gibbs energy of the reaction, $\Delta G(T)$. This relationship is represented by the following equation.

$$K_{eq}(T) = \exp\left(\frac{-\Delta G(T)}{RT}\right) \quad (8)$$

where R is the universal gas constant and

$$\Delta G(T) = \Delta H(T) - T\Delta S(T)$$

The enthalpy and entropy changes of a reaction, $\Delta H(T)$ and $\Delta S(T)$, respectively, are determined from the individual reactant and product enthalpies and entropies.

$$\Delta H(T) = \sum_{\text{products}} H_p(T) - \sum_{\text{reactants}} H_r(T)$$

and

$$\Delta S(T) = \sum_{\text{products}} S_p(T) - \sum_{\text{reactants}} S_r(T)$$

The problem is now reduced to determining the enthalpy and entropy change of the reaction over the temperature range of interest. This subject has been covered in detail in *Thermochemical Kinetics*¹⁴ by S. Benson. Benson eloquently discusses in his book how thermodynamic data are used to calculate kinetic rate parameters. However, the problem often arises that there are insufficient thermodynamic data to perform the calculation. Benson solves this problem in his book by introducing a group additivity method for calculating the enthalpy and entropy of a species based on group enthalpy and entropy values for molecular fragments of chemical species. Group values have been used to estimate thermodynamic properties of hydrocarbon molecules and radicals for over ten years^{15, 16} and new group values continue to be added although there does not seem to be a common compilation of currently accepted values.

Once the thermodynamic data is assembled and ΔH and ΔS are calculated, we can begin to address the problem of calculating the individual rate coefficients. If one of the rate coefficients is known, the other can be obtained directly using equations 7 and 8. If neither rate coefficient is known then one of them must be calculated. Benson addresses this calculation in his book as well for a number of common reaction types. He relates the above thermodynamic properties with the kinetic rate parameters, Arrhenius A factor and activation energy, E , for the forward and reverse reactions.

$$\frac{A_f}{A_r} = \exp\{T\Delta S\}$$

and

$$E_f - E_r = \Delta H$$

where the subscripts f and r refer to the forward and reverse reactions, respectively. In each of the equations above, one of the rate parameters for the forward or reverse reaction must be known in order to solve for the other parameter,

The rate coefficient for a reaction may also be obtained by analogy with a similar reaction whose rate coefficient is known or can be more easily estimated. Adjustment in the activation energy and A factor may be made to account for differences in the enthalpy and entropy change differences in the two reactions. Since the enthalpy change for a bond dissociation reaction can be equated with the bond dissociation energy, these values can be used directly as the activation energy when calculating these rate coefficients.

As an example, let us consider the initial stages of the pyrolysis mechanism of tetralin (1,2,3,4-tetrahydronaphthalene). Briefly, the mechanism initiation involves the bond homolysis reaction of a carbon-carbon bond in the saturated ring producing a diradical with benzylic and alkyl carbon-centered radicals. The alkyl carbon-centered radical portion in turn abstracts a hydrogen atom from other tetralin molecules forming a resonance stabilized radical, 1-tetralyl and reducing the diradical to a single resonance-stabilized carbon-centered radical, 3-propylbenzyl radical. Hydrogen transfer and structural rearrangements occur to form the major products, 1-methylindan, naphthalene and butylbenzene. The mechanism includes 20 reactions and 20 species. These reactions and their rate coefficients were obtained from the literature¹⁷⁻²⁸ or estimated for a reaction temperature of 478°C. Simulation calculations were performed in an effort to model experimental data. Comparisons of the calculated results and experimental data for the concentrations of tetralin and the major products are shown in Figures 3 and 4. The result of modeling this mechanism provides an affirmation of the important reactions involved and a framework by which evaluate extensions to this mechanism.

In conclusion, it can be stated that the simulation of chemical mechanisms is an important computational tool for understanding and modeling chemical reactions. Hypothetical mechanisms can be tested by comparison with experimental data and once verified predictive calculations can be performed with confidence. The simulation of chemical mechanisms is applicable to all areas of chemistry which involve chemical reactions and with the availability of

powerful desktop computers and suitable software, like *REACT for Windows*, its application is well within the capabilities of most researchers.

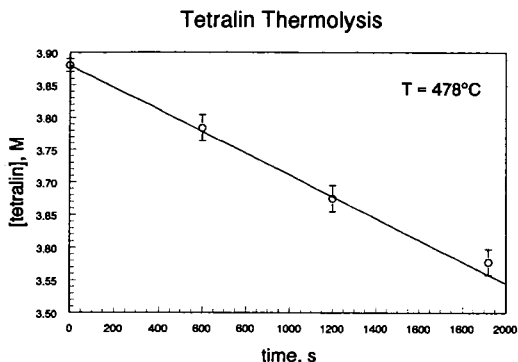


Figure 3. Simulation of tetralin concentration as a function of time during its thermolysis at a temperature of 478°C . Experimental data is indicated by the open circles and associated error bars.

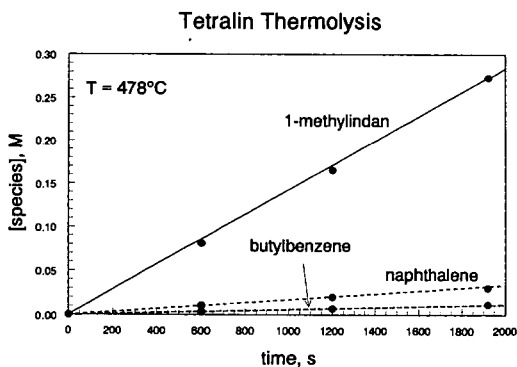


Figure 4. Simulation of species concentrations as a function of time during tetralin thermolysis at a temperature of 478°C . Experimental data is indicated by the closed circles.

References

1. Brown, R. L. *HICHM: A Fortran Code for Homogeneous Isothermal Chemical Kinetics Systems*, NBSIR 81-2281; National Bureau of Standards: Gaithersburg, MD, 1981.
2. Braun, W.; Herron, J. T.; Kahaner, D. K. *Int. J. Chem. Kinet.* **1988**, *20*, 51.
3. Mallard, W. G.; Westley, F.; Herron, J. T.; Hampson, R. F.; Frizzell, D. H. *NIST Chemical Kinetics Database: Version 5.0*; National Institute of Standards and Technology: Gaithersburg, MD, 1993.
4. Boisvert, R. F.; Howe, S. E.; Kahaner, D. K. *The Guide to Available Mathematical Software (GAMS)*, PB 84-17135; National Technical Information Service (NTIS): Springfield, VA 12161, 1984.
5. Gear, C. W. *Numerical Initial Value Problems in Ordinary Differential Equations*; Prentice Hall: Englewood Cliffs, NJ, 1971.
6. Vernier, J. H. *SIAM J. Numer. Anal.* **1978**, *15*.

7. Norris, A. C. *Computational Chemistry: An Introduction to Numerical Methods*; John Wiley & Sons: New York, 1981.
8. Cash, R.; Karp, A. H. *ACM Transactions on Mathematical Software* **1990**, *16*, 201.
9. Press, W. H.; Teulosky, S. A.; Vetterling, W. T.; Flannery, B. F. *Numerical Recipes in C*, 2nd ed.; Cambridge University: Cambridge, UK, 1992.
10. Conway, D. J. *Dr. Dobbs's J.* **1995**, *20*(12), 52.
11. Manka, M. J.; Brown, R. L.; Stein, S. E. *Int. J. Chem. Kinet.* **1987**, *19*, 943.
12. Kerr, J. A.; Moss, S. J. *Bimolecular and Termolecular Gas Reactions*, Vol. 1; CRC Press: Boca Raton, FL, 1981.
13. Litwinowicz, J. A.; Ewing, D. W.; Jurisevic, S.; Manka, M. J. *J. Phys. Chem.* **1995**, *99*, 9709.
14. Benson, S. W. *Thermochemical Kinetics*, 2nd ed.; John Wiley & Sons: New York, 1981.
15. O'Neil, H. E.; Benson, S. W. *Int. J. Chem. Kinet.* **1969**, *1*, 221.
16. McMillen, D. F.; Golden, D. M. *Annu. Rev. Phys. Chem.* **1988**, *33*, 493.
17. Hooper, R. J.; Battaerd, H. A. J.; Evans, D. G. *Fuel*, **1979**, *58*, 132.
18. Benjamin, B. M.; Hagaman, E. W.; Raaen, V. F.; Collins, C. J. *Fuel*, **1979**, *58*, 386.
19. Collins, C. J.; Raaen, V. F.; Benjamin, B. M.; Maupin, P. H.; Raork, W. H. *J. Am. Chem. Soc.* **1979**, *101*, 5009.
20. Franz, J. A.; Camaioni, D. M. *J. Org. Chem.* **1980**, *45*, 5247.
21. Franz, J. A.; Camaioni, D. M. *Fuel* **1980**, *59*, 803.
22. Pennington, J. M. L. *Int. J. Chem. Kinet.* **1982**, *14*, 761.
23. Brower, K. R.; Pajak, J. *J. Org. Chem.* **1984**, *49*, 3970.
24. Franz, J. A.; Barrows, R. D.; Camaioni, D. M. *J. Am. Chem. Soc.* **1984**, *106*, 3964.
25. McPherson, W. P.; Foster, N. R.; Hastings, D. W.; Kalman, J. r.; Gilbert, T. D. *Fuel* **1985**, *64*, 457.
26. King, H.; Stock, L. M. *Fuel* **1981**, *60*, 748.
27. Allen, D. T.; Gavalas, G. R. *Int. J. Chem. Kinet.* **1983**, *15*, 219.
28. Franz, J. A.; Camaioni, D. M.; Beishline, R. R.; Dalling, D. K. *J. Org. Chem.* **1984**, *49*, 3563.

APPLICATION OF COMPUTER GENERATION OF REACTION MECHANISMS USING QUANTITATIVE RATE INFORMATION TO HYDROCARBON PYROLYSIS

Matthew J. De Witt, David J. Dooling and Linda J. Broadbelt
Department of Chemical Engineering
2145 Sheridan Road, Northwestern University
Evanston, IL 60208

ABSTRACT

Novel modifications were made to the core components of the algorithms for rate-based generation of reaction mechanisms¹, including introducing thermodynamic constraints into the estimation of the controlling rate parameters and an alternative approach for determining the species included in the final mechanism. Once implemented, the adapted rate-based building criterion was successfully employed to construct a compact mechanistic model for low-pressure tetradecane pyrolysis. Though thousands of species and reactions were generated, only a small portion of these were deemed necessary and incorporated into the final model. Experimental data were used to determine frequency factors for a subset of the reaction families, while all other kinetic parameters were set based on the literature. The final optimized values for the frequency factors were consistent with literature, and the model was able to accurately fit experimental data from different reaction conditions. With no adjustment to the optimized frequency factors, the mechanistic model for tetradecane pyrolysis was able to accurately predict reactant conversions and product yields for varying reaction conditions. Both relative trends and the actual values were predicted correctly over a wide range of reactant conversions and initial reactant loadings.

I. INTRODUCTION

The advent of tools for computer generation of reaction mechanisms has dramatically reduced the time for the development of complex reaction models and increased the level of detail they may include. One of the challenges in building reaction mechanisms using algorithms for automated model construction, however, is to describe the essential chemistry and enable prediction of experimental data over wide ranges of reaction conditions while maintaining a manageable model size. For example, hydrocarbon pyrolysis is a chemistry in which molecular weight growth reactions may be important, and a mechanism generated automatically would therefore grow to infinite size without the application of external termination criteria. Implementation of a species rank criterion, which restricts those species capable of undergoing reaction based on the order in which they appear in the mechanism, overcame this obstacle¹. However, this criterion is usually not restrictive enough since insignificant species must also be included to capture the important ones.

This limitation motivated development of an alternative strategy for computer generation of reaction mechanisms that includes important reactions based on quantitative evaluation of reactivity¹. This approach exploits the capability to estimate rate constants as the mechanism is generated, allowing it to be solved at any point. The mechanism is built iteratively, as a growing reaction mechanism is alternatively generated and solved. Quantitative evaluation of the formation rates of all species during the mechanism building process determines the next set of species allowed to undergo reaction. The formation rates are compared to a characteristic rate of the current system, and a weighting factor, ϵ , is used to adjust the characteristic rate to allow more or fewer species to be included in the mechanism.

The work that will be described builds upon the previous work¹ but includes several important improvements. The first implementation of the rate-based approach used the disappearance rate of a single reactant to define a characteristic rate in the system to which all of the other rates were compared, and the conversion of this reactant was used as the marker of the completeness of the mechanism. If the reactant quickly equilibrated, the mechanism building process would not advance. In the new implementation, time is used as the independent variable, and the rates of all of the species in the system are used to determine the overall characteristic rate. Secondly, since the mechanism building process requires on-the-fly kinetic information, a lookup capability was implemented to allow experimental rate information to be incorporated. Finally, equilibrium information was obtained through on-the-fly calculation of heat capacity, enthalpy and entropy values. By marking reversible pairs of reactions, the rate constant for the reverse reaction could be calculated from the forward rate constant and the value of the equilibrium constant. This latter capability represents a substantial advance in our ability to generate complex reaction mechanisms via the computer.

II. PROCEDURE

A mechanism for low pressure tetradecane pyrolysis was generated to determine the effectiveness of the adapted rate-based generation algorithm. This reaction system serves as an adequate test for the rate-based generation criterion since thermolysis of a long chain paraffin can lead to thousands of intermediates and stable products. However, only a small fraction of these is actually kinetically significant. Furthermore, experimental information collected in our laboratory² was available to test the ability of the model generated to capture the reactant conversion and product selectivities over a wide range of reaction conditions. Low pressure batch pyrolysis reactions were conducted using initial loadings of tetradecane ranging from 0.01 to 0.045 M for times ranging from 10-150 minutes at temperatures of 420 and 450°C.

The reaction mechanism was built by implementing six reaction families deemed important for gas-phase hydrocarbon pyrolysis at moderate temperatures: bond fission, radical recombination, β -scission, radical addition, disproportionation and hydrogen abstraction (intermolecular and intramolecular through 1,4-, 1,5- and 1,6-hydrogen shift reactions). Estimates of the Arrhenius frequency factors and the parameters of an Evans-Polanyi relationship³, E_0 and α , for each reaction family were obtained from the literature. The model

was constructed using an initial tetradecane concentration of 0.0322 M and a reaction temperature of 420°C. The weighting factor, ϵ , was varied from 1.0 to 5×10^{-5} . The total number of species, the reactive species, the total number of reactions and the number of reactive reactions were tabulated as a function of the weighting factor. Each individual elementary step is specifically tallied; the numbers of reactions reported are not consolidated according to the known reaction path degeneracies nor are reverse and forward pairs lumped as a single reaction.

III. RESULTS

The model characteristics as a function of weighting factor are summarized in Table 1. As the weighting factor decreased, all quantities reported increased. However, the growth in the total number of species was more dramatic than the moderate growth observed for the number of reactive species. Thus, using rate-based building and the weighting factor as a "tuning" parameter, the size of the mechanism solved was easily controlled. The adequacy of the reaction mechanism was assessed by monitoring two key characteristics: whether all of the major products observed experimentally were included and if secondary reactions of olefins were described. For example, at a weighting factor of 1.0, only C_1 - C_7 alkane products were included in the model, while C_7 - C_{13} alkanes were detected experimentally. It was necessary to decrease the weighting factor to 5×10^{-5} before tridecane, the major product observed in the lowest yield, was included in the mechanism as a reactive species.

The mechanism generated employing a weighting factor of 5×10^{-5} was therefore used to capture the experimental behavior. Experimental data from 20 mg pyrolysis reactions of tetradecane conducted at 420°C and 450°C were used to determine controlling rate parameters. There were 27 parameters which could be varied, a frequency factor, an E_0 and an α value for each reaction family. However, only four parameters, $A_{\text{bond fission}}$, $A_{\beta\text{-scission}}$, $A_{\text{H-abstraction by R}}$, and $A_{1,5\text{-hydrogen shift}}$, were fit against the experimental data. All other parameters were set constant at values obtained from the literature. Note that only frequency factors were permitted to vary, while all intrinsic barriers and transfer coefficients were fixed.

A parity plot comparing the fitted model yields to the experimentally observed yields for major and minor products is shown in Figure 1. The model did an excellent job of fitting the experimental data from the pyrolysis reactions over several orders of magnitude. Reactant conversions for both temperatures were fit extremely well, even though no activation energies were used as fitting parameters. Gaseous hydrocarbons and liquid α -olefins were also fit very well.

The predictive capabilities of the model were then assessed by solving for the product yields and conversion at other reactant loadings with no further adjustment to any of the model parameters. A comparison of predicted and experimental yields of undecene as a function of reactant conversion and reactant loading is shown as a representative example of the predictive capability of the model in Figure 2. The model was able to predict accurately the trends in the data and the actual values over a wide range of conversions and reactant loadings. Similar predictive capabilities were observed for gaseous hydrocarbons and other long chain α -olefins.

ACKNOWLEDGMENT

The authors are grateful for the financial support from the Department of Energy (DE-FG22-96-PC96204).

REFERENCES

- (1) Susnow, R.G., Green, W.H., Dean, A., Peczak, P.K. and Broadbelt, L.J. "Rate-Based Construction of Kinetic Models for Complex Systems", *J. Phys. Chem. A*, 1997, 101, 3731-3740.
- (2) Broadbelt, L.J., Stark, S.M. and Klein, M.T., "Termination of Computer Generated Reaction Mechanisms: Species Rank-Based Convergence Criterion", *Ind. Eng. Chem. Res.*, 1995, 34(8), 2566-2573.
- (3) De Witt, M.J. and Broadbelt, L.J., "Binary Interactions Between Tetradecane and 4-(1-Naphthylmethyl) Bibenzyl During Low and High Pressure Pyrolysis", *submitted to Energy & Fuels*, 1999.
- (4) Evans, M.G. and Polanyi, M. "Inertia and Driving Force of Chemical Reactions", *Trans. Faraday Soc.*, 1938, 34, 11-29.

Table 1. Summary of model characteristics as a function of the weighting factor used to direct rate-based building.

Weighting factor	Number of total species	Number of reactive species	Number of reactions	Number of reactive reactions
1	1908	103	57116	15605
0.1	2401	107	65866	17633
0.01	3349	120	98286	26116
0.001	4676	130	132450	30436
0.0001	11158	236	319408	63004
0.00005	16269	302	477566	98240

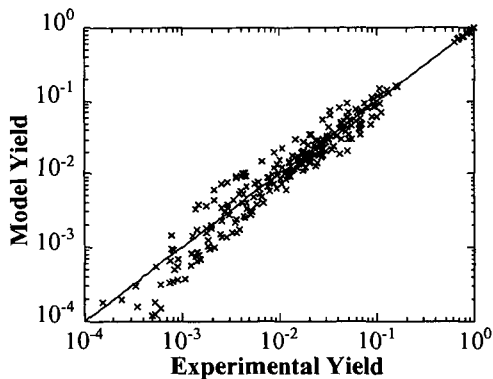


Figure 1. Comparison of fitted model yields and experimentally observed yields for major and minor products of tetradecane pyrolysis.

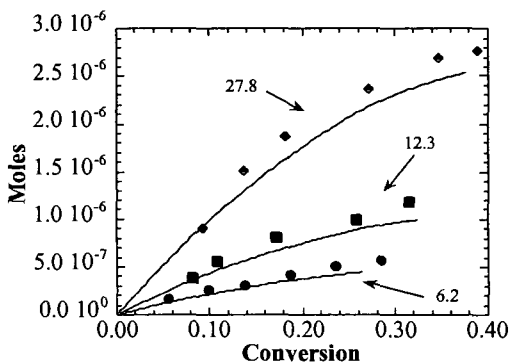


Figure 2. Comparison of the experimental (symbols) and predicted (lines) evolution of undecene for initial tetradecane loadings of 6.2, 12.3 and 27.8 mg.

FIRST PRINCIPLES STUDY OF POISONING BY SULFUR AND DEPOISONING BY CHLORINE OF PALLADIUM BASED HYDROGENATION CATALYSTS: FROM CLUSTERS TO SURFACES

Herve Toulhoat, Peter Gravil, and Gabriele Valerio
Institut Français du Pétrole
1 & 4 Avenue de Bois Preau
92852 Rueil-Malmaison, France

KEYWORDS

DFT Calculations, Thioresistant Catalysts, Palladium

ABSTRACT

From first-principles calculations we find evidence for a direct effect of co-adsorbed chlorine on the adsorption of dihydrogen and ethylene on sulfur-poisoned palladium. On the model (111) surface, chlorine restores molecular and atomic adsorption energies, and decreases the barrier to H₂ dissociation. By contrast, on Pd₄, one adsorbed sulfur increases, while one co-adsorbed chlorine decreases the adsorption energies compared to the clean cluster. We discuss the implications of such effects in the context of the preparation of noble metals based hydrogenation catalysts of improved thioresistance, needed by the refining industry.

I. INTRODUCTION

As specifications on sulfur and aromatics contents in diesel fuels become ever more severe, the development of more active as well as sulfur tolerant hydrogenation catalysts appears as an increasingly important issue for the refining industry. Halogens incorporated in the solid's formulation, or in the stream of reactants, are known to impart some degree of thioresistance to noble metals (Pt, Pd) based hydrogenation catalysts. Very little is known about the microscopic origin of this effect, although it could provide important guidelines for the preparation of new catalysts. A mechanism involving electrons attraction by halogens bound to the carrier and mediating an electron deficiency of supported metal particles, is usually invoked. However, such a long range effect on electronic structure may appear very unlikely. We have therefore undertaken systematic first-principles simulations aiming at probing the direct effect of adsorbed chlorine on the structural, electronic and adsorptive properties of the Pd (111) surface and Pd₄ clusters, poisoned by sulfur (2), (5), (7).

II. METHODS

The calculations were based on the density functional theory (DFT). For the clusters, we used the Gaussian 94 code (1) under the B3LYP option. Scalar relativistic effects for Pd were incorporated through the use of the LanL2DZ basis set, whereas the standard 6-311(d,p) basis set was chosen for the elements S, Cl, C and H. All geometries were fully relaxed. More details can be found in (2). The calculations on model surfaces were performed using the VASP code (3) using a plane-wave pseudopotential formalism. Exchange and correlation effects were included within the generalized gradient approximation (4) (GGA). We used a supercell geometry consisting of a palladium (or platinum) slab four layers thick with a 3x3 surface cell, and a vacuum gap of thickness equivalent to six layers. Adsorbates and adatoms were introduced on one side of the slab and allowed to fully relax, as well as the first two layers of metal atoms, the remaining two layers being fixed at bulk positions. Full details can be found elsewhere (5).

III. RESULTS AND DISCUSSION

The computed adsorption energies of sulfur and chlorine on palladium substrates are compared in Table 1. The magnitude of these energies correspond to strong chemisorptions. Both on the electron deficient clusters and on the full surfaces, sulfur binds more strongly than chlorine. The nature of these bonds has been demonstrated elsewhere (2), (5) : while the sulfur-palladium bond is essentially covalent, the chlorine-palladium bond has a significant ionic character, both on surfaces and clusters. The adatoms bind more strongly on the surface than on the cluster.

Bulk and surface metal-sulfur bond strengths are compared in Table 2 for Pd and Pt. For the bulk, we use either the cohesive energy per M-S bond as defined in (6), or the standard heat of formation of the isostructural sulfides which also includes the bulk metals cohesive energies. Albeit the surface bonds follow the same tendencies as the bulk bonds, their differences appear much less marked.

The competitive adsorption between sulfur and chlorine is analysed in Table 3: the strong repulsive interaction seen between co-adsorbates sharing two palladium atoms decreases rapidly as the S-Cl distance increases. On Pd₄, S and Cl can even mutually strengthen their adsorption when they share a single Pd atom. On the surface, the destabilization for S and Cl sitting in corner sharing or non adjacent three-fold hollows is quite comparable to that induced by increasing coverage with sulfur alone. Co-adsorption of S and Cl on palladium can therefore be taken as quite likely for systems where externally imposed chemical potentials of chlorine and sulfur are comparable (see (5) for a more detailed discussion).

The molecular chemisorption on ethylene is the first step of its heterogeneous catalytic hydrogenation. The computed adsorption energies of ethylene on our clean model substrates are reported in Table 4. The « top » π configuration is clearly preferred on the Pd₄ cluster, whereas the the di- σ bridging configuration is favoured on both the Pd(111) and Pt(111) surfaces, in accordance with other computational studies and experiment. Platinum binds ethylene a little more weakly than palladium.

As shown in Table 5, sulfur and chlorine co-adsorbed on the palladium surface or the Pd₄ cluster have contrasted effects on ethylene chemisorption. It is slightly enhanced by sulfur, and weakened by chlorine on the cluster. The cooperative effect of S and Cl leads to a significant poisoning of ethylene adsorption, obviously in a non-linear fashion. On the Pd(111) surface, a moderate poisoning is brought about by

0.22 ML sulfur, while chlorine has no effect at the same level of coverage. The mixed ad-layer behaves more like chlorine, which we take as an evidence of effective depoisoning.

We have shown elsewhere (5) the microscopic details of poisoning by sulfur of the dissociative chemisorption of molecular hydrogen on Pd(111), and the depoisoning effect of co-adsorbed chlorine: the latter involves a reduced barrier to dissociation, and restored stability of atomic H bound to the surface with respect to associative desorption. In the mixed ad-layer, the effect of chlorine is again dominant, indicative of another direct depoisoning effect.

IV. CONCLUSIONS

In summary, we have found that although sulfur binds more strongly than chlorine to palladium (or platinum) surface atoms, co-adsorption is likely to occur both on very small clusters and on extended metallic surfaces: in the latter case islands of chlorine may segregate because lateral repulsions between adsorbed sulfur atoms are stronger than between adsorbed chlorine atoms. Co-adsorption of chlorine and sulfur affects the molecular adsorption of ethylene differently on very small palladium clusters and on periodic surfaces, respectively weakening and strengthening the interaction. In both cases the effect is non-linear in the sense it is not the average of the effects of the separate adatoms.

We have demonstrated therefore the likeliness of a direct induction of thioresistance by co-adsorption of an halogen on the palladium surfaces. However, on very small palladium aggregates, chlorine could on the contrary amplify the poisoning by sulfur. For practical purposes, this would imply avoiding too high dispersions of the active metal in the supported catalyst.

Future studies should focus on the diffusion and segregation of adatoms at metal surfaces in presence of activated hydrogen, as well as the determination of energy profiles along reaction paths of hydrogenation reactions, in order to enable evaluations of kinetic data by Monte Carlo simulations (8).

ACKNOWLEDGMENTS

This work was partly performed within the Groupement de Recherche Européen « Dynamique Moléculaire Quantique Appliquée à la Catalyse et à l'Adsorption », supported by Institut Français du Pétrole, Centre National de la Recherche Scientifique, Total, and the University of Vienna.

REFERENCES

- (1) *Gaussian 94, Revision B.3; Gaussian Inc.; Pittsburgh, PA, 1995.*
- (2) Valerio, G.; Toulhoat, H. *J. Phys. Chem.*, **100**, 26, **1996**, 10827.
Valerio, G.; Toulhoat, H. *J. Phys. Chem. A*, **101**, 20, **1997**, 1969.
- (3) Kresse, G.; Hafner, J. *Phys. Rev. B*, **49**, **1994**, 14251; Kresse, G.; Furthmüller, J. *Comput. Mater. Sci.*, **6**, **1995**, 15; Kresse, G.; Furthmüller, J. *Phys. Rev. B*, **54**, **1996**, 11169.
- (4) Perdew, J.; Chevary, J.A.; Vosko, S.H.; Jackson, K.A.; Pederson, M.R.; Singh, D.J.; Fiolhais, C. *Phys. Rev. B*, **46**, **1992**, 6671.
- (5) Gravil, P.; Toulhoat, H. « *Hydrogen, Sulfur and Chlorine coadsorption on Pd(111): A Theoretical Study of Poisoning and Promotion* », Accepted by *Surface Science*, **1999**.
- (6) Toulhoat, H.; Raybaud, P.; Kasztelan, S.; Kresse, G.; Hafner, J. *Catalysis Today*, **50**, **1999**, 629.
- (7) Gravil, P.; Toulhoat, H. « *Ethylene, Sulfur and Chlorine coadsorption on Pd(111): A Theoretical Study of Poisoning and Promotion* », Accepted by *Surface Science*, **1999**.
- (8) Neurock, M.; Hansen, E.W. *Computers chem. Engng.*, **22**, **1998**, S1045.

Table 1. Adsorption energies of sulfur and chlorine on model metallic substrates (kCal.mol⁻¹)

Substrate	Sulfur	Chlorine	Ref.
Pd ₄	-85.3	-56.4	(2)
Pd ₆	-81.4	-65.2	(2)
Pd(111) ($\theta_s=0.33$)	-109.5	-71.1	(5)

Table 2. Comparison of computed bulk and surface metal-sulfur bond strengths (kCal.mol⁻¹)

System	E _{M,S}	ΔH°_f	Ref.
Bulk PdS	45	-16.9	(6)
S @ Pd(111) ($\theta_s=0.33$)	109.5	-	(5)
Bulk PtS	56.3	-19.5	(6)
S @ Pd(111) ($\theta_s=0.33$)	111.1	-	-

Table 3. Changes of the total adsorption energy of S+Cl as a function of S-Cl distance, relative to infinite separation (results from Ref. (5) for Pd(111)).

Substrate	S-Cl distance (nm)	Pd shared	E _{ads} (S+Cl) (kCal.mol ⁻¹)	Change (%)
Pd ₄	(i)	0	-141.7	0
Pd ₄	0.47(ii)	1	-142.9	+5.3
Pd ₄	0.47(iii)	2	-134.3	-5.2
Pd(111)	(iv)	0	-190.7	0
Pd(111)	0.187(v)	2	-16.6	-91.3
Pd(111)	0.323(vi)	1	-174.8	-8.3
Pd(111)	0.485 (vii)	0	-185.6	-2.7

(i): Adsorption of S and Cl on separate clusters, S stabilized in three-fold site (face of the tetrahedron), Cl in bridge site.

(ii): Adsorption of S on a three-fold site and Cl on a bridge site (non adjacent edge) of the same cluster

(iii): Adsorption of S on a three-fold site and Cl on a bridge site (adjacent edge) of the same cluster

(iv): Adsorption of S and Cl in separate cells at the low coverage limit ($\theta_s=0.11$)

(v): Adsorption of S and Cl in two edge-sharing adjacent three-fold hollow sites.

(vi): Adsorption of S and Cl in two corner-sharing opposite three-fold hollow sites.

(vii): Adsorption of S and Cl in two next to next neighbour three-fold hollow sites.

Table 4. Adsorption energies of ethylene on model metallic substrates (kCal.mol⁻¹)

Substrate	E _{ads}	Configuration	Ref.
Pd ₄	-18.5	π	-
Pd ₄	-9.4	di- σ	-
Pd(111)	-14.7	π	-
Pd(111)	-23.5	di- σ	(7)
Pt(111)	-10.6	π	-
Pt(111)	-20.2	di- σ	-

Table 5. Effect of sulfur and chlorine on the adsorption of ethylene on palladium (kCal.mol⁻¹)

Substrate	E _{ads} (C ₂ H ₄)	Configuration	Ref.
Pd ₄	-18.5	π	-
Pd ₄ S	-20.8	π	-
Pd ₄ Cl	-16.1	π	-
Pd ₄ SCl	-7.6	π	-
Pd(111)	-23.5	di- σ	(7)
Pd(111) + 0.22MLS	-19.3	di- σ	(7)
Pd(111) + 0.22MLCl	-23.5	di- σ	(7)
Pd(111) + 0.11MLS + 0.11 ML Cl	-22.3	di- σ	(7)

MOLECULAR MODELING OF GAS OIL HYDRODESULFURIZATION

Gang Hou[†] and Michael T. Klein^{*}

[†]Department of Chemical Engineering
University of Delaware
Newark, DE 19716
hou@che.udel.edu

^{*} Department of Chemical and Biochemical Engineering
Rutgers, The State University of New Jersey
Piscataway, NJ 08854
mtklein@jove.rutgers.edu

ABSTRACT

The hydrodesulfurization (HDS) process chemistry and reaction network have been modeled at the molecular level. The following sulfur compound types have been considered: mercaptans, sulfides, disulfides, thiophenes (T), benzothiophenes (BT), dibenzothiophenes (DBT), and their alkyl and hydrogenated derivatives. The steric and electronic effects of the alkyl side chain of thiophenic compounds (T, BT, and DBT) are taken into account. The dual-site mechanism - σ site for direct desulfurization and τ site for hydrogenation on catalyst surface - is incorporated; the corresponding dual-site LHHW formalism is constructed to describe the complex kinetics. A rigorous molecular model for gas oil HDS is thus developed fast and successfully by aid of the Kinetic Modeler's Toolbox (KMT). The model matches pilot plant data very well and can be used to optimize the HDS process.

KEYWORDS: Hydrodesulfurization (HDS), Molecular Modeling, Kinetic Modeling

INTRODUCTION

Hydrodesulfurization (HDS) has been one of the most important oil refining processes. The process chemistry has been studied extensively over the past two decades [1-3]. However, with more and more stringent environmental regulations, our interests in HDS process have been renewed. Low sulfur specifications caused the refiners to look at the hydrotreating options and thus more rigorous models are desired to better improve the process. In this paper, a practical molecular level modeling of HDS process is introduced and developed, which is part of a much wider effort aiming at automated molecule-based kinetic modeling of gas oil hydroprocessing [4].

MODEL DEVELOPMENT

Classification of Sulfur Compounds

The petroleum feedstock contains the following sulfur compound types: mercaptans, sulfides, disulfides, thiophenes (T), benzothiophenes (BT), dibenzothiophenes (DBT), and their alkyl and hydrogenated derivatives. HDS reactivity depends critically on the molecular size and structure of the sulfur compounds. The mercaptans, sulfides and disulfides have, generally, fast kinetics compared with the thiophenic compounds (T, BT, and DBT as shown in Figure 1). The substituent groups adjacent to the S atom on thiophenic compounds generally retard HDS. While methyl groups distant from the S atom generally increase HDS activity - an effect attributed to increased electron density on the S atom - those adjacent to the S atom decrease reactivity due to steric effect [2].

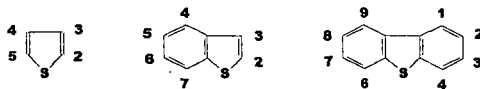


Figure 1. Thiophenes (T), Benzothiophenes (BT), and Dibenzothiophenes (DBT).

Those significant positions on T, BT, and DBT are identified as listed in Table 1. For example, it has been found that 4,6-dimethyldibenzothiophene (4,6-DMDBT) remains intact until the final stages of HDS of a light oil. The substituent groups on the significant and non-significant positions have different steric and electronic effects on HDS reactivities. As shown in Table 1, for example, we need at least two monomethyl, three dimethyl, and three trimethyl-substituted molecular structures to account for this position difference for alkyl-DBTs up to C3.

Table 1: The significant positions of thiophenic compounds.

Sulfur	Significant Position	Non-significant	Factor* (steric+electronic)	Representative Structures
T	2, 5	3, 4	$f_{1,T} \ll f_{2,T}$	2C1, 3C2, 2C3, 1C4
BT	2 (3, 7)	4, 5, 6	$f_{1,BT} \ll f_{2,BT}$	2C1, 2C2, 2C3, 2C4
DBT	4, 6	1, 2, 3, 7, 8, 9	$f_{1,DBT} \ll f_{2,DBT}$	2C1, 3C2, 3C3

* Subscript 1 denotes there is an alkyl chain at a significant position; 2 for non-significant position.

Reaction Pathways and Network

The following reaction pathways shown in Figure 2 are used to describe the HDS chemistry. The mercaptans, sulfides, and disulfides can be easily desulfurized. The T, BT, DBT and their alkyl

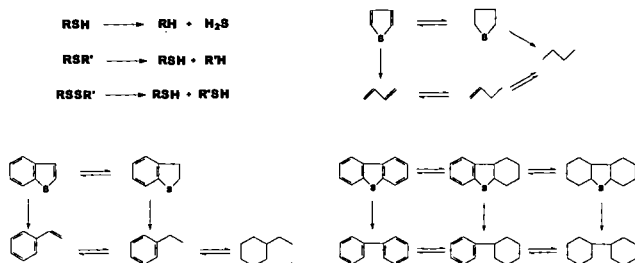


Figure 2. HDS reaction pathways and network.

derivatives can go through either the hydrogenation reaction at the τ site or the direct desulfurization reaction at the σ site on the catalyst surface [3].

Reaction Kinetics

Table 2 shows the rate laws used to model HDS kinetics. The classical dual-site mechanism - σ site for direct desulfurization and τ site for hydrogenation on catalyst surface in HDS process - is utilized to implement the corresponding dual-site LHHW formalism. This rate law is derived from the model compound studies by assuming the rate-determining surface reaction step between adsorbed reactants and two competitively adsorbed hydrogen atoms for both types of reaction [5].

Table 2: HDS rate law.

$$r = \frac{f_{\sigma} k K_{A,\sigma} K_{H_2,\sigma} [A] [H_2]}{(1 + \sum_i K_{i,\sigma} [I] + \sqrt{K_{H_2,\sigma} [H_2]})^n} + \frac{f_{\tau} k_{\tau} K_{A,\tau} K_{H_2,\tau} [A] [H_2] - [B] / K}{(1 + \sum_i K_{i,\tau} [I] + \sqrt{K_{H_2,\tau} [H_2]})^n}$$

Where r is reaction rate, $[I]$ is concentration of component, k is rate constant, K_i is adsorption constant of component, K is equilibrium constant and n is the exponent of inhibition term (3 for HDS).

The two global factors (f_{σ} and f_{τ}) are introduced to account for the total steric and electronic effects of substituents on thiophenic compounds at both σ and τ sites.

RESULTS AND DISCUSSION

A detailed molecular level kinetic model for HDS of light gas oil has been developed using the Kinetic Modeler's Toolbox (KMT) - a software package that automates the kinetic modeling of industrial complex processes [4]. The complete reaction model was built automatically in only 2 CPU seconds and solves very fast in less than 2 CPU seconds on an Intel Pentium II 333Mhz machine.

The current version of the model containing 243 species and 437 reactions was tuned to pilot plant data and the parity plot (Figure 3) shows the model matches the experimental data very well and can do a good job even in very low sulfur levels (<50ppm). The parity guarantees the model follows the right trends of the molecular conversions in the process stream and the developed model can certainly provide the quantitative insights to improve the HDS process.

CONCLUSIONS

The automated molecule-based kinetic modeling strategy was successfully extended to build rigorous HDS model as part of the effort to model gas oil hydroprocessing [4]. To rigorously model the HDS chemistry, it is necessary to incorporate at least all the representative molecular structures with substituents at both significant and non-significant positions. It is also very important to incorporate dual-site mechanism and implement the corresponding LHHW formalism to take into account the inhibitions of various compounds in the process stream (especially the H_2S inhibition at σ sites). The developed HDS Model matches the pilot-plant data very well and can be used to optimize the low sulfur hydrotreating process quantitatively.

REFERENCES

1. Girgis, M.J., and Gates, B.C., *Ind. Eng. Chem. Res.* **30**, 2021 (1991).
2. Topsøe, H., Clausen, B.S., and Massoth, F.E., in "Catalysis Science and Technology" (J.R. Anderson and M. Boudart, eds.), Vol.11. Springer-Verlag, New York, 1996.
3. Whitehurst, D.D., Isoda, T., and Mochida, I., *Advances in Catalysis*, **42**, 345 (1998).
4. Hou, G., Klein, M.T., 2nd International Conference on Refinery Processes Proceedings, AIChE, Houston, TX (1999)
5. Vanrysselberghe V., and Froment, G.F., *Ind. Eng. Chem. Res.* **35**, 3311 (1996).

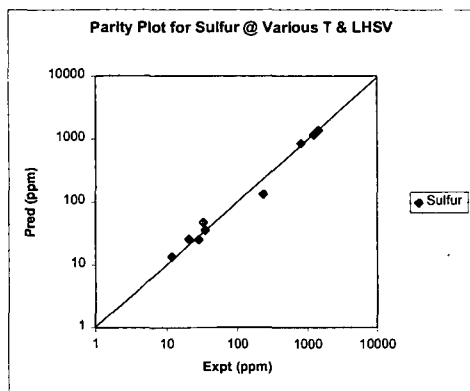


Figure 3. Parity plot of HDS model.

Molecule-Based Modeling of Gasoil Fluid Catalytic Cracking

Ankush Kumar
Department of Chemical Engineering
University of Delaware, Newark, DE 19716

Michael T. Klein
College of Engineering
Rutgers, The State University of New Jersey
Piscataway, New Jersey 08854-8058

INTRODUCTION

Fluid Catalytic Cracking (FCC) is a major refinery process designed to upgrade heavy and less valuable petroleum products to gasoline and lighter products. The feedstock for the FCC process ranges from light gas oils to heavy hydro-treated resids. The complexity of the feedstock, and the associated analytical chemistry and computational obstacles, helped shape early FCC modeling approaches (2,3,7). The traditional need for easily deployed reaction models led to the formulation of simple, lumped kinetic models. Lumped models often fail to capture the complex FCC chemistry and as a result are specific to the feedstock, the catalyst used and the operating conditions. Additionally, lumped models do not give the detailed product distribution required for process design and optimization.

The new paradigm is to track each molecule in the feed and product through the process and to move towards models having fundamental kinetic information. This has led to the modeling of the chemistry at the mechanistic level (5,6). These mechanistic models have a large number of gaseous and surface species and, hence, are very CPU intensive. Thus, on the one hand, the need for a detailed molecular representation and fundamental kinetic information make the use of mechanistic models attractive, but, on the other hand, the large solution time renders them of limited use in practice. This motivates the development of pathways-level models. Pathways-level models are not as large and complex as the mechanistic models because of the exclusion of reactive intermediaries, e.g., surface species. They also offer the advantage of being solved in a reasonable amount of time. They offer the opportunity to incorporate detailed kinetic information by the inclusion of all important observable molecules explicitly, and hence have the predictive capability lacking in the lumped models.

Developing such molecularly explicit models for gasoil fluid catalytic cracking is now possible because of two enabling advances. First, recent developments in analytical chemistry now allow a molecularly explicit stochastic description of gasoils. Second, the explosion in computational power makes possible the necessary bookkeeping to generate and solve reaction networks with a large number ($O(10^3)$) of molecules. The aim of this work is to develop an automated capability for building pathways-level FCC models for heavy hydrocarbons (e.g. gasoils). In the following sections, we will briefly discuss the methodology used for determining a molecular description of the feedstock and then also outline the strategy used for computer-generation of gasoil FCC pathways-level kinetic model.

FEEDSTOCK CHARACTERIZATION

The ability of a reaction model to describe the product distribution depends to a large extent on the initial conditions i.e., the structure and the mole fractions of the molecules in the feedstock. Such detailed characterization for the heavier feedstock, such as gasoils, is seldom available. Even modern analytical techniques reveal only structural attributes (i.e. the number of aromatic rings, number of saturated rings, number of sidechains, etc.) rather than the detailed individual molecular structures. The first challenge, then, is to determine a set of molecules and associated mole fractions characteristic of the feed from routinely available analytical data, such as true boiling point distribution, average molecular weight, elemental analysis, NMR data and GC/MS lumps. This can be done using the *MoleGen* technique (4).

In this technique, molecules are represented in terms of a collection of molecular attribute building blocks (e.g. number of aromatic rings, number of naphthenic rings, number and length of sidechains, etc.). Each attribute is represented by a probability density function. Monte Carlo sampling of the set of probability density functions provides a large ensemble of molecules ($O(10^3)$). The properties of this ensemble of molecules are compared to experimentally obtained analytical data to obtain an optimal set of probability density functions. These optimized probability density functions contain the statistical description of the feedstock and can be easily transformed into a set of molecular structures and their associated mole fractions.

MODEL BUILDING

Pathways models for complex feedstocks, such as gasoils, can have a large number of molecules and their reactions. It can be quite tedious and time-consuming to build such models by hand. This motivates the automation of the model building process.

To automate the process of reaction network building use is made of graph theoretic concepts. In this approach, a molecule is represented by a graph, the atoms being the nodes of the graph and the bonds being the edges of the graph. For all the reactions in FCC, the connectivities of only a few of the atoms in the involved molecules change. This means that a reaction can be represented by the change in the connectivity of only a few anodes in the graph. The connectivity matrices of the reactants are combined into an augmented reactant matrix, which, after permutation gives the reduced matrix for the reactants, containing the connectivities of only those atoms whose connectivity changes in the reaction process. The bond breaking and forming (i.e., the reaction) is then carried out by simple matrix addition operations (1).

The chemistry is represented through the implementation of reaction rules. These rules rely on theoretical and experience-based kinetic approximations and are useful tools in keeping the size of the model realistic without significantly effecting the product distribution. The reaction network is then converted to a set of differential equations using the *OdeGen* parsing code (1). Conceptually, the resulting mathematical model can then be solved with appropriate initial conditions and rate constants. However, during the developmental stage, the rate constants for most of the reactions are usually not known *a priori* and the model has to be solved within an optimization framework to determine the rate constants.

This requires that the number of rate parameters must be kept to a reasonable number to obtain true rate constant information from optimization to the experimental data. Even with the use of reaction rules for the complex FCC chemistry the detailed reaction model can have a large number of reactions and their associated rate constants ($O(10^3)$). Clearly, some organizational or "lumping" scheme that does not sacrifice the basic chemistry is in order. To this end, it is useful to realize that much of the complexity is statistical or combinatorial, and that the large number of reactions and rate parameters in the pathways-level model can be handled by lumping the reactions involving similar mechanistic steps into one reaction family. The kinetics of all the reactions within the same reaction family are described by a common set of parameters. Differences in the reactivity within the same reaction family can be traced to differences in the heat of the reaction.

RESULTS AND MODEL DIAGNOSTICS

These ideas of feedstock characterization and automated model building were applied to gasoil FCC reaction modeling. The analytical data available for gasoil included boiling point distribution, average molecular weight, Clay Gel analysis, MS lumps and average parameters from NMR analysis. These analytical data were used to determine a stochastic molecular representation of the feed using the *MolGen* technique. The feed was described in terms of 222 representative molecules and their mole fractions.

The feed was then grouped into a few compound classes (paraffins, iso-paraffins, naphthenes and aromatics), which, in turn, were allowed to react through a limited

number of reaction families (cracking, isomerization, dehydrogenation, hydrogenation, and aromatization). This allowed the division of all the reactions into a small number of reaction families with associated rate parameters. Table 1 shows the model diagnostics for the final model. The use of reaction family concept allowed the description of all the rate constants for 3293 reactions in terms of about 30 rate parameters.

Feed Molecules	222
Total number of molecules	823
Paraffin Cracking Reactions	574
Paraffin Isomerization Reactions	206
Olefin Cracking Reactions	131
Naphthenic Cracking Reactions	138
Aromatic Cracking Reactions	435
Hydrogenation Reactions	274
Dehydrogenation Reactions	221
Model Generation Time	433s
Model Solution Time	< 1 minute

Table 1. Gasoil Fluid Catalytic Cracking Model Diagnostics

To develop the optimal reaction network and to determine the rate constants the model predictions were constrained to match the pure components as well as gasoil experimental data. As an example of the quality of fit between model and experimental values Figure 1 shows the results for n-heptane cracking.

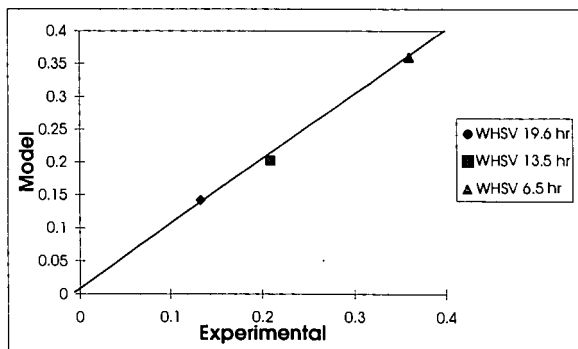


Figure 1a. Parity Plot for Heptane Conversion at different weight hourly space velocity (WHSV).

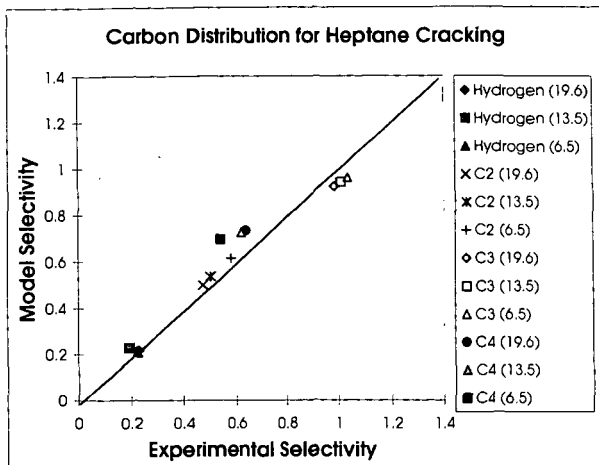


Figure 1b. Parity Plot of Selectivity by Carbon number for n-heptane cracking. Values in brackets are the WHSV.

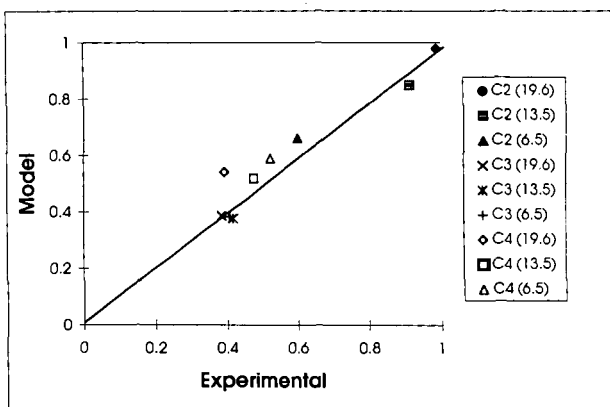


Figure 1c. Parity Plot of Paraffin / Olefin ratio for n-heptane cracking. Values in brackets are the WHSV.

CONCLUSIONS :

1. Graph theory was successfully used to generate a molecularly explicit gas oil FCC model containing 823 species and 3293 reactions.
2. The parity of the predicted results was reasonably good with the experiments. This suggests that the stochastic approach for generation of the feedstock and the reaction family concept for expressing the rate constants are very good tools for predicting the reactivity of a complex mixture.
3. This approach to automated pathways-level model building can be easily extended to other feedstocks and catalyst systems in order to obtain kinetics information.

REFERENCES

1. Broadbelt, L. J., Stark, S. M., Klein, M. T., "Computer Generated Pyrolysis Modeling: On-the-fly Generation of species, Reactions and Rates", *I. & E. C. Res.*, **33**, 790-799 (1994).
2. Jacob, S. M., Gross, B., Volts, S. E., and Weekman, V. W., "A Lumping and Reaction Scheme for Catalytic Cracking", *AIChE J.*, **22**, pp. 701-713 (1976).
3. John, T. M., and Wojciechowski, B. W., "On Identifying the Primary and Secondary Products of the Catalytic Cracking of Neutral Distillates", *J. Catal.*, **37**, pp. 348 (1975).
4. Kumar, A., Campbell, D., Klein, M. T., "Computer Assisted Kinetic Modeling: Interfacing Structure and Reaction Network Builders", *ACS Symposia Preprints*, v **42 (3)**, 662-665, (1997).
5. Watson, B. A., Klein, M. T., and Harding, R. H., "Mechanistic modeling of n-heptane cracking on HZSM-5", *Ind. Eng. Chem. Res.*, **35(5)**, pp. 1506-1516 (1996).
6. Watson, B. A., Klein, M. T., and Harding, R. H., "Catalytic Cracking of Alkylcyclohexanes: Modeling the Reaction Pathways and Mechanisms", *International Journal of Chemical Kinetics*, **29(7)**, pp. 545 (1997).
7. Weekman, V. W., and Nace D. M., "Kinetics of Catalytic Cracking Selectivity in Fixed, Moving, and Fluid Bed Reactors", *AIChE J.*, **16**, pp. 397-404 (1970).

KINETIC SOLVENT EFFECTS ON HYDROXYL HYDROGEN ATOM ABSTRACTIONS

Janusz Luszyk
 Steacie Institute for Molecular Sciences
 National Research Council of Canada
 100 Sussex Drive, Ottawa, Ontario
 Canada K1A 0R6

The rates of radical reactions are commonly assumed to be independent of the solvent. We have demonstrated that this assumption is fully justified for hydrogen atom abstraction from cyclohexane by cumyloxy radicals.¹ However, we have also demonstrated the occurrence of dramatic solvent effects on the rates of H-atom abstraction from phenol and *tert*-butyl hydroperoxide by the same radical.² These very large solvent effects were attributed to hydrogen bond formation between the substrate, XOH, and hydrogen bond accepting (HBA) solvents, S. The magnitude of this kinetic solvent effect (KSE) is therefore determined by the strength of the interaction between XOH, the hydrogen bond donor (HBD), and the HBA solvent. This led us to predict that the magnitude of a KSE (i.e., the rate constant ratio, k^A/k^B , measured in two solvents, A and B) would "depend on the Lewis acidity of XOH, (but would) generally be independent of the nature of the radical which abstracts the hydrogen atom".² That is, for the reaction



the ratio of the measured rate constants in solvents A and B will generally be independent of the structure of Y, i.e., $(k^A_{\text{XOH/Y}})/(k^B_{\text{XOH/Y}}) = \text{constant}$ (for the same XOH).

We have confirmed this prediction using phenol and α -tocopherol (vitamin E) as hydrogen atom donating reactants, XOH, and two Y[•] radicals having grossly different absolute reactivities in hydrogen atom abstraction.³ The highly reactive Y[•] radicals were alkoxyis, cumyloxy (CumO[•]) in the case of phenol and *tert*-butoxy (BO[•]) in the case of α -TOH. A single, relatively unreactive Y[•] radical was chosen, 2,2-diphenyl-1-picrylhydrazyl (DPPH), because of the ease with which its decay kinetics could be monitored in a conventional spectrophotometer via its strong visible absorption.

Dramatic kinetic solvent effects (KSEs) are shown by the kinetic data in Table 1. For example, the rate constants for abstraction of the phenolic hydrogen atom of α -TOH by DPPH[•] and by BO[•] decrease by factors of ~67 and ~60, respectively, on changing the solvent from *n*-pentane to γ -valerolactone. Similarly, the rate constants for hydrogen abstraction from phenol by DPPH[•] and CumO[•] decrease by factors of ~107 and ~136, respectively, on changing the solvent from *n*-octane to ethyl acetate.

These kinetic data in a dramatic fashion confirm our prediction that the magnitude of the KSE on XOH/Y[•] reactions would be essentially independent of the nature of Y[•]. Thus, a plot of $\log(k^S_{\text{TOH/BO}}/M^{-1} s^{-1})$ vs $\log(k^S_{\text{TOH/DPPH}}/M^{-1} s^{-1})$ has most of the points fall very close to the straight line with a slope = 1.0. It is truly astonishing considering that in the same solvent the absolute magnitudes of the two rate constants differ by a factor of over one million. That is, for almost any solvent:

$$k^S_{\text{TOH/BO}}/k^S_{\text{TOH/DPPH}} \approx 1.6 \times 10^6$$

Even more striking are the results with phenol. Once again, the plot of $\log(k^S_{\text{PhOH/CumO}}/M^{-1} s^{-1})$ vs $\log(k^S_{\text{PhOH/DPPH}}/M^{-1} s^{-1})$ has all but one of the points fall very close to the line drawn with a slope = 1.0. In this set of experiments the absolute magnitudes of the two rate constants in the same solvent differ by a factor of 10 000 000 000! That is,

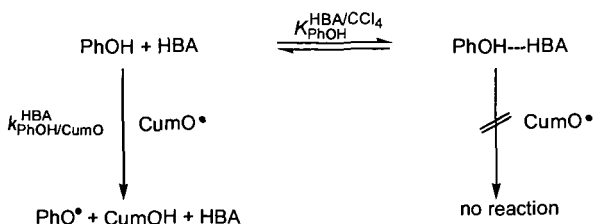
$$k^S_{\text{PhOH/CumO}}/k^S_{\text{PhOH/DPPH}} \approx 1.0 \times 10^{10}$$

Our findings were more recently additionally confirmed with peroxy^{4,5} and carbon-centered⁶ radicals, respectively.

Our studies on kinetic solvent effects (KSE) on free radical reactions have also serendipitously led to a completely new method for measuring equilibrium constants for hydrogen bonding from a variety of XOH to very many hydrogen-bond acceptors

(HBAs) in CCl_4 solvent, $K^{\text{HBA}/\text{CCl}_4}_{\text{XOH}}$. Since this method does not rely on infrared spectroscopy it can also be used to measure $K^{\text{HBA}/\text{CCl}_4}_{\text{XOH}}$ for HBAs containing hydroxylic groups provided only that the hydroxylic hydrogen atom in XOH can be abstracted by free radicals. We demonstrated the validity and simplicity of this new technique using phenol as XOH. Our kinetic measurements yielded $K^{\text{HBA}/\text{CCl}_4}_{\text{PhOH}}$ with HBA's which do not contain OH groups and which serve as a check for our method and $K^{\text{HBA}/\text{CCl}_4}_{\text{PhOH}}$ with HBA's which do contain OH groups, acetic acid, methanol, and *tert*-butyl alcohol.

We suggested a kinetic model² to explain the progressive reduction in the rate of hydrogen atom abstraction from phenol (and *tert*-butyl hydroperoxide) by cumyloxy radicals, CumO^\bullet , as the HBA abilities of the solvents increased. It invoked reactive non-hydrogen bonded XOH and non-reactive hydrogen-bonded XOH, e.g.,



Although we now recognize that this model is oversimplified³ it does yield a very simple and useful kinetic equation, viz.,²

$$k^{\text{CCl}_4}_{\text{PhOH}/\text{CumO}} = k^{\text{HBA}}_{\text{PhOH}/\text{CumO}} (1 + K^{\text{HBA}/\text{CCl}_4}_{\text{PhOH}} [\text{HBA}]) \quad (2)$$

which can be rearranged to

$$\frac{1}{k^{\text{HBA}}_{\text{PhOH}/\text{CumO}}} = \frac{1}{k^{\text{CCl}_4}_{\text{PhOH}/\text{CumO}}} + \frac{K^{\text{HBA}/\text{CCl}_4}_{\text{PhOH}} [\text{HBA}]}{k^{\text{CCl}_4}_{\text{PhOH}/\text{CumO}}} \quad (3)$$

Thus, for *dilute* phenol and HBA in CCl_4 (where their activity coefficients will be unity) a plot of the reciprocal of the rate constant (i.e., $1/k^{\text{HBA}/\text{CCl}_4}_{\text{PhOH}/\text{CumO}}$) measured at 25 °C against $[\text{HBA}]$, the concentration of the HBA in CCl_4 , should yield a straight line with an intercept equal to the reciprocal of the measured rate constant in CCl_4 and with a (slope) / (intercept) ratio equal to $K^{\text{HBA}/\text{CCl}_4}_{\text{PhOH}}$. The kinetically derived equilibrium constants for hydrogen bonding between phenol and HBAs are summarized in Table 2 and are compared therein with the ranges of equilibrium constants which have been obtained by the infrared (IR) method at 25 °C.

CONCLUSIONS

We have demonstrated that for hydroxyl hydrogen atom donors rate constants for hydrogen atom abstractions are strongly solvent dependent and independent of the nature of the abstracting radical species. Thus, provided rate constants have been measured for the reaction of one radical with a hydroxyl substrate in a range of solvents, then a measurement of the rate constant for reaction of the same substrate with some different radical need to be made in only one of these solvents for values in all the other solvents to be predicted accurately.

A simplified kinetic model advanced for hydrogen atom abstraction from hydroxyl hydrogen atom donors provides a new method for measuring equilibrium constants for hydrogen bonding from these donors to any hydrogen bond acceptors including alcohols.

REFERENCES

1. Avila, D. V.; Brown, C. E.; Ingold, K. U.; Luszyk, J. *J. Am. Chem. Soc.* **1993**, *115*, 466-470.
2. Avila, D. V.; Ingold, K. U.; Luszyk, J.; Green, W. H.; Procopio, D. R. *J. Am. Chem. Soc.* **1995**, *117*, 2929-2930.
3. Valgimigli, L.; Banks, J. T.; Ingold, K. U.; Luszyk, J. *J. Am. Chem. Soc.* **1995**, *117*, 9966-9971.
4. Valgimigli, L.; Banks, J. T.; Luszyk, J.; Ingold, K. U. *J. Org. Chem.* **1999**, *64*, 3381-3383.
5. Lucarini, M.; Pedulli, G. F.; Valgimigli, L. *J. Org. Chem.* **1998**, *63*, 4497-4499.
6. Franchi, P.; Lucarini, M.; Pedulli, G. F.; Valgimigli, L.; Lunelli, B. *J. Am. Chem. Soc.* **1999**, *121*, 507-514.

Table 1. Absolute Rate Constants for Abstraction of the Phenolic Hydrogen Atom from α -Tocopherol (TOH) in Various Solvents at 298 ± 2 K

solvent	10^{-8}	10^{-2}	10^{-7}	10^3
	$k_{\text{TOH/BO}}^{\text{S}}$ ($\text{M}^{-1} \text{s}^{-1}$)	$k_{\text{TOH/DPPH}}^{\text{S}}$ ($\text{M}^{-1} \text{s}^{-1}$)	$k_{\text{PhOH/CumO}}^{\text{S}}$ ($\text{M}^{-1} \text{s}^{-1}$)	$k_{\text{PhOH/DPPH}}^{\text{S}}$ ($\text{M}^{-1} \text{s}^{-1}$)
1 <i>n</i> -pentane	99	74		
2 <i>n</i> -octane	60	74	110 ^b	160
3 <i>n</i> -hexadecane	50	73		
4 carbon tetrachloride	42	36	86	93
5 chlorobenzene	36	27	48	59
6 benzene	31	18	28	31
7 anisole	20	14	5.6	7.2
8 acetonitrile	9.4	4.9		
9 acetic acid	7.7	6.2	1.8	3.1
10 methyl acetate	3.0	1.9		
11 ethyl acetate	2.9	1.6 ₅	0.8 ^b	1.5
12 γ -valerolactone	1.6 ₅	1.1		
13 <i>tert</i> -butyl alcohol	1.8	5.7	0.36	2.9

Table 2. Equilibrium Constants for Hydrogen Bond Formation at 25 °C between Phenol and Some Hydrogen Bond Acceptors Measured by the Kinetic Method (Comparison with 25 °C Equilibrium Constants Measured by Infrared Spectroscopy from the Literature)

HBA	[HBA] max (M) ^a	$k_{\text{PhOH}}^{\text{A/CCl}_4}$ (M^{-1})	
		kinetic	infrared (lit)
MeC(O)OH	1.2	1.4	no value
MeCN	0.6	3.5	4.6-6.5
MeC(O)OEt	1.5	6.6	8.8-12.3
MeOH	1.2	11	no value
<i>t</i> -BuOH	0.5	14	44
pyridine	0.3	30	41-53
Me ₂ NCHO	0.17	69	64-76

^aMaximum HBA concentration used to determine the equilibrium constant by the kinetic method.

THERMAL CONVERSIONS OF CONJUGATED CYCLIC POLYENES WITH ENDOCYCLIC *TRANS* CARBON CARBON DOUBLE BONDS

Dieter Hasselmann, Christoph Richter, Martin Hoppe, and Martin Glunz
Faculty of Chemistry, Organic Chemistry, Ruhr-University
Universitätsstrasse 150, D-44780 Bochum, Germany
e-mail: hasselmann@orch.ruhr-uni-bochum.de

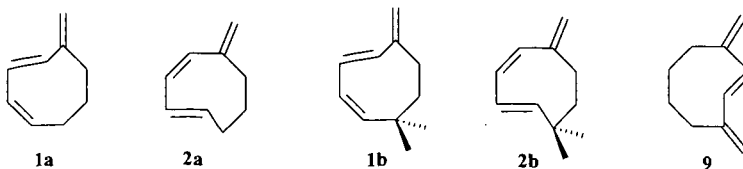
ABSTRACT

The strained monocyclic triene hydrocarbons (1*Z*, 3*E*)-5-methylene-1,3-cyclooctadiene (**1**) and (1*E*, 3*Z*)-5-methylene-1,3-cyclooctadiene (**2**) with endocyclic *trans* carbon carbon double bonds have been found to be key reactive intermediates in the complex thermal rearrangements of the *cis*-bridged bicyclic cyclobutene, 2-methylenebicyclo[4.2.0]oct-7-ene (**3**). Gasphase thermolysis (>160 °C) of **3** leads to three monocyclic trienes, **4**, **5** and **6**, and to two tricyclic alkenes, **7** and **8**. Indirect evidence for the involvement of **1** and **2** in the rearrangements of **3** follows from trapping intermediate **2** with furan and from their thermal generation by the cycloreversions of their independently synthesized *Diels-Alder* adducts with furan, respectively. Independent syntheses of the thermo-labile trienes **1** and **2** and of related hydrocarbons allows to directly investigate their thermal properties. Competing routes for stabilization of **1** - **3** to mono-, bi- and/or tricyclic products and their mechanistic implications are discussed. From experimental enthalpies of activation and molecular mechanics calculations energy profiles are modeled. Torquoselectivity as a function of ring size is discussed for *cis*-3,4-bridged cyclobutenes related to **3**.

I. INTRODUCTION

Thermal reorganizations of organic compounds often turn out to be highly stereoselective or even stereospecific. Frequently these reactions can be classified as concerted. These transformations usually demand only 'low' temperatures at which alternative reaction channels, e.g. those involving radical paths, are not accessible for energetic reasons. On the other side 'high' temperatures are required for reactions involving the thermal generation of radicals by breaking a carbon carbon bond. The cleavage of a simple C-C single bond necessitates an energy of about 80 - 90 kcal/mol, in crack processes of alkanes in many cases this is in accordance with temperatures up to 500 °C. However, temperatures for bond breaking can be lowered considerably by taking recourse to molecular strain and / or electronic stabilization of the carbon radical centers generated. This can be achieved to an extent that competition between concerted and multistep radical reactions has to be taken into account.

In this context monocyclic cyclobutenes easily undergo thermal cycloreversions to acyclic 1,3-butadienes in concerted reactions.¹⁻³ These archetypal electrocyclic reactions stereospecifically follow 'allowed' conrotation.^{1, 2} In simple cases the 'disallowed' disrotatory alternative is found to be energetically disfavored by about 10 kcal/mol.⁴ The profound electronic impact of substituents on the direction of conrotation observed in cyclobutene - butadiene reorganizations has found much attention, recently, from theory⁵ as well as from experiment.⁶⁻⁸ However, the stereochemical course of the cycloreversion of 3,4-bridged cyclobutenes which were structurally constrained proved to be considerably more complex. As a function of ring size of the annulated rings these compounds were found to thermally undergo 'allowed' conrotatory and / or 'forbidden' disrotatory ring openings to give *E/Z*-cyclohexadienes and / or *Z/Z*-stereoisomers.⁹⁻¹¹ The border-line case between both directions of cycloreversion, however, seems to rest with bicyclic cyclobutenes having attached a five or six membered ring.



Of special interest in this respect, therefore, is the thermal behavior of *cis*-3,4-bridged bicyclic cyclobutenes, e.g. 2-methylenebicyclo[4.2.0]oct-7-ene (3). The exocyclic methylene substituent in the 2-position of 3 should exert special effects on the mechanistic course and the energetics of the transformations of this hydrocarbon. Accessibility and thermal stability of the strained monocyclic conjugated triene hydrocarbons (1*Z*, 3*E*)-5-methylene-1,3-cyclooctadiene (1) and (1*E*, 3*Z*)-5-methylene-1,3-cyclooctadiene (2), expected to be central, although labile intermediates in the thermal rearrangements of 3, are of key importance. We now report on independent syntheses of 1 and 2. The thermal properties of these hydrocarbons have been determined as well as those of 3. The results provide insight into the competing pathways of stabilization, as for instance by electrocyclicization, by intramolecular cycloaddition, by direct geometric isomerization via diradicals, and / or by hydrogen migration. Suitably geminal methylated derivatives, 1b and 2b, and *E*-dimethylenecyclooctene 9, significant for the question of a direct geometric stereomutation, have been included in our investigations. Energy profiles for the thermal reorganizations involved are modeled from experimental enthalpies of activation and molecular mechanics calculations. Torquoselectivity⁵ as a function of ring size is discussed for *cis*-3,4-bridged cyclobutene 3 and related compounds.

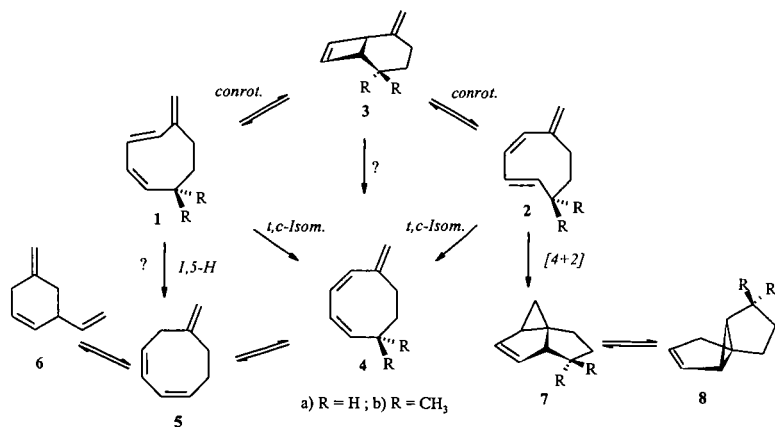
II. PROCEDURE

Thermolyses of 3 have been performed at low pressure (1-5 mbar) in the gasphase in a conditioned 20 l pyrex vessel. The flask was heated in an air-thermostat with a temperature constancy better than 0.1 °C and was connected to a high vacuum line with greaseless stopcocks. Kinetic measurements have been followed gaschromatographically. Rearrangements of the thermally labile hydrocarbons 1, 2 and 9 had to be carried out in solution. Toluene-*d*8 and cyclohexane-*d*12 were used as solvents to follow the reactions quantitatively by ¹H-NMR spectroscopy at 400 MHz.

Experimental details of the synthetic procedures for the relevant compounds will be reported elsewhere.

Molecular mechanics calculations have been performed with the programs MM2ERW¹² and MMEVBH¹³ developed by W. R. Roth¹⁴ and co-workers on the basis of Allinger's¹⁵ MM2 procedure. The MM2ERW¹² forcefield allows one to calculate conjugated π -systems with high accuracy without embarking on quantum-mechanical methods. The MMEVBH procedure has been developed^{13,14} to calculate heats of formation of hydrocarbons, conjugated and non conjugated polyenes as well as those of radicals and diradicals.

Scheme 1. Mechanistic Pathways for the Thermal Reorganizations of C₈H₁₂ Isomers 1 - 3, and Geminal Dimethyl Substituted Derivatives.



III. RESULTS

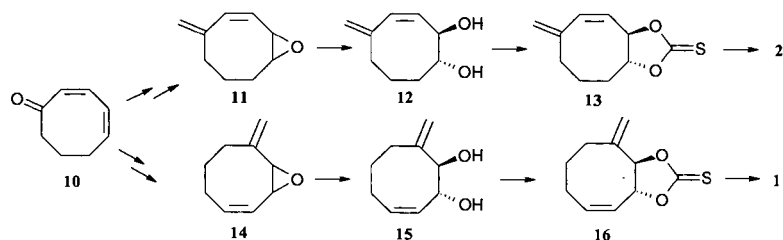
In the temperature range of about 165 to 215 °C gasphase thermolysis of the bridged bicyclic vinylcyclobutene 3 results in the formation of five new isomeric hydrocarbons. These can be grouped into two sets, on the one side into the three monocyclic trienes 4, 5, and 6, and on the

other side into two tricyclic alkenes **7** and **8**, with **4** and **7** constituting the main products.¹⁶ The kinetics of the decrease of **3** follows a first order reaction with $\log A = 13.27 \pm 0.06$ and $E_a = 36.13 \pm 0.12$ kcal/mol. However, not all of the products are primary ones. Under the reaction conditions conjugated triene **4** is in fast equilibrium with its 1,5-hydrogen shift product **5**. From this, secondarily the monocyclic unconjugated **6** is formed. The activation parameters for the mutual conversions $4 \leftrightarrow 5 \leftrightarrow 6$ have been determined independently at lower temperatures by starting with **5**.¹⁷ The tricyclic alkene **7** slowly undergoes a *vinylcyclopropane-cyclopentene* rearrangement to spiroalkene **8**. In view of our experimental findings and earlier results on *cis*-bicyclo[4.2.0]oct-7-ene¹⁸ the mechanistic pathways given in Scheme 1 have to be taken into account.

Central to product formation from **3** are the properties of the strained trienes **1** and **2** which could be formed by allowed conrotatory cycloreversion with inward and outward rotation of the exocyclic methylene substituent. However, these *trans*-cycloalkenes are unstable at the high temperatures necessary to convert **3**. Indirect evidence for the involvement of **1** and **2** is derived from our findings that **2**, but not **1**, can be trapped in the presence of furan as *trans*-[4+2] cycloaddition products and that thermal decomposition ($T > 155$ °C) of the four *Diels-Alder* adducts possible from **1** and **2** with furan, which all have been synthesized independently, results in the same product mixtures as that found from **3**.¹⁶ Mechanistically still unanswered are the questions if the observed *Z,Z*-product **4** is generated from **3** by direct disrotation, by direct cleavage of a double bond $1 \rightarrow 4$ or $2 \rightarrow 4$, respectively, or if a multistep sequence $3 \rightarrow 1 \rightarrow 5 \rightarrow 4$ is followed with a 1,5-hydrogen shift in **1** as the crucial step.

Substituting hydrogen by geminal methyl groups as in **3b** after electrocyclicization should lead to labile triene intermediates **1b** and **2b**. In **1b** stabilization by a concerted 1,5-hydrogen shift would be blocked and recyclization should dominate. Results of gasphase thermolyses at 175 - 220 °C with **3b** as an educt show, indeed, **7b** to be the main product followed by rearrangement to **8b**. The *Z,Z*-triene **4b** is formed only to a minor extent.¹⁹

Scheme 2. Synthetic Routes to Trienes (1*Z*, 3*E*)-5-methylene-1,3-cyclooctadiene (**1**) and (1*E*, 3*Z*)-5-methylene-1,3-cyclooctadiene (**2**).



Independent syntheses of the central intermediates **1** and **2** are accomplished for the first time by following a modified Corey/Winter²¹ protocol as shown in Scheme 2. Using such a sequence for the synthesis of strained trienes seems to be without precedent. Key steps are stereospecific ring openings of the vinyloxiranes **11** and **14** to give *trans*-diols **12** and **15**, respectively, after regioselective formation from dienone **10**, and desulfuration of the *trans*-thionocarbonates **13** and **16** at about room temperature and at low pressures to generate **1** and **2** with high isomeric purity.²⁰ The structures of both isomers have been characterized without doubt by NMR spectroscopy. Additionally, the *E*-configuration of the central carbon-carbon double bond in **1** has been secured by formation of the same *Diels-Alder* adducts with furan as those known from an independent route¹⁶ and by X-ray structure analysis of one of the adducts with diphenylisobenzofuran.²⁰ Synthesis of the geminal methylated isomers **1b** and **2b** proved to be more difficult and a modified route using β -hydroxyphosphinioxides as intermediates had to be taken.²² *E*-Dimethylenecyclooctene **9** is obtained by a multistep sequence to the *Z*-isomer followed by sensitized photoisomerization.

Slightly above room temperature triene **1** with a central *trans* double bond starts to cyclorevert to **3** and to isomerize to *Z,Z*-triene **4** in a 2 : 1 ratio, approximately. Not completely conjugated triene **5**, stable at the reaction conditions, is not observed. In toluene-d₈ and followed at temperatures of 30 - 70 °C reaction $1 \rightarrow 3$ shows $\log A/s^{-1} = 13.2 \pm 0.2$ and $E_a = 25.6 \pm 0.3$ kcal/mol. Trienes **2** and **2b** with the *trans* double bond in the end of the conjugated system prove

to be thermally more stable. At 60 -120 °C they predominantly undergo electrocyclization to 3 and 3b with $E_a = 26.7 \pm 0.3$ kcal/mol and $E_a = 26.9 \pm 0.9$ kcal/mol, respectively. The Z,Z-trienes 4 are formed, but to a smaller extent; from 2b traces of 7b are observed. However, thermolyses of 2 and 2b are complicated by some dimerization. At 50 - 95 °C E-cyclooctene 9 isomerizes to the Z-isomer with $E_a = 25.8$ kcal/mol, exclusively.²⁰

Schematic energy profiles of the reactions involved can be modeled by combining our experimentally determined activation parameters with enthalpies of formation calculated by the above forcefield programs for educts, products and the reactive intermediates participating. It is clearly shown that besides dominant electrocyclization in the first two cases the reactive trienes 1, 2 and 9 can be stabilized competitively by direct double bond cleavage to diradical transition structures followed by rotation and recombination to their thermally more stable Z-isomers, even at temperatures close to room temperature. Ring opening in 3 by disrotation and stabilization of *trans*-triene 1 by a 1,5-hydrogen shift does not take place. These findings are discussed with those of our earlier results on thermal rearrangements of hydrocarbons related to 3 which have contracted rings^{23, 24} and those of the relevant literature.

In addition, it is shown that by using substrates 3 stereospecifically substituted at the *exocyclic* methylene carbon the formations of the tricyclic products 7, formally intramolecular *Diels-Alder* reaction products, follow multistep routes via diradical intermediates.^{16, 19} Nevertheless, in some cases product formation with high stereoselectivity has been found.

IV. CONCLUSIONS

Highly strained monocyclic *trans*-trienes (1Z, 3E)-5-methylene-1,3-cyclooctadiene (1) and (1E, 3Z)-5-methylene-1,3-cyclooctadiene (2), obtained by direct syntheses for the first time, are established as key intermediates in the multiple thermal rearrangements of the 3,4-bridged vinylcyclobutene 2-methylenebicyclo[4.2.0]oct-7-ene (3). 1 and 2 stabilize competitively by electrocyclization to 3 and to their less strained Z-isomers 4 by direct double bond cleavage even at temperatures slightly above room temperature. The later also applies to the thermal stabilization of E-dimethylenecyclooctene 9. Ring opening in 3 by disrotation and by 1,5-hydrogen shift in 1 are not important.

Combining experimental enthalpies of activation and the results of forcefield calculations the energy profiles of these hydrocarbon reactions show that diradical transition structures are accessible and are of major importance. These findings are also of relevance to other hydrocarbon systems comprising 3,4-bridged cyclobutene structures.

ACKNOWLEDGMENTS

Financial support of this research by the Deutsche Forschungsgemeinschaft and the Fonds der Chemischen Industrie is gratefully acknowledged. The authors thank H.-J. Loch and A. Schaefer for valuable experimental contributions. We also thank N. Lehmann for skillful experimental assistance.

REFERENCES

- (1) Woodward, R. B.; Hoffmann, R. *The Conservation of Orbital Symmetry*; Academic Press: New York, 1970; *Angew. Chem., Int. Ed. Engl.* **1969**, *8*, 781-932.
- (2) Woodward, R. B.; Hoffmann, R. *J. Am. Chem. Soc.* **1965**, *87*, 395-396.
- (3) Houk, K. N.; Li, Y.; Evanseck, J. D. *Angew. Chem., Int. Ed. Engl.* **1992**, *31*, 682.
- (4) Roth, W. R.; Rekowski, V.; Börner, S.; Quast, M. *Liebigs Ann.* **1996**, 409-430.
- (5) Dolbier, W. R., Jr.; Koroniak, H.; Houk, K. N.; Sheu, C. *Acc. Chem. Res.* **1996**, *29*, 471-477.
- (6) Kirmse, W.; Rondan, N. G.; Houk, K. N. *J. Am. Chem. Soc.* **1984**, *106*, 7989-7991.
- (7) Dolbier, W. R., Jr.; Koroniak, H.; Burton, D. J.; Bailey, A. R.; Shaw, G. S.; Hansen, S. W. *J. Am. Chem. Soc.* **1984**, *106*, 1871-1872.
- (8) Curry, M. J.; Stevens, I. D. R. *J. Chem. Soc., Perkin Trans. 2* **1980**, 1391.
- (9) Branton, G. R.; Frey, H. M.; Skinner, R. F. *Trans. Faraday Soc.* **1966**, *62*, 1546.
- (10) Goldstein, M. J.; Leight, R. S.; Lipton, M. S. *J. Am. Chem. Soc.* **1976**, *98*, 5717-5718.
- (11) Branton, G. R.; Frey, H. M.; Montague, D. C.; Stevens, I. D. R. *Trans. Faraday Soc.* **1966**, *16*, 146-152.
- (12) Roth, W. R.; Adamczak, O.; Breuckmann, R.; Lennartz, H.-W.; Boese, R. *Chem. Ber.* **1991**, *124*, 2499-2521.
- (13) Roth, W. R.; Staemmler, V.; Neumann, M.; Schmuck, C. *Liebigs Ann.* **1995**, 1061-1118.

THE USE OF REACTION INTERMEDIATES TO PROBE SUPERCRITICAL FLUID SOLVENT EFFECTS

John E. Chateauneuf

Department of Chemistry Western Michigan University, Kalamazoo, MI 49008

Joan F. Brennecke

Department of Chemical Engineering, University of Notre Dame, Notre Dame, IN 46556

ABSTRACT

Reactions of free radicals and other reaction intermediates in supercritical fluids (SCFs) have proven to be excellent mechanistic probes of the influence of SCF solvation and SCF solvent effects on a variety of categories of chemical reactions in SCFs. This presentation will focus on mechanistic studies of reaction intermediates and, in particular, free radical reactions in SCFs and their relationship to our overall understanding of reaction chemistry under sub-critical and supercritical conditions. Three categories of reactivity that may be influenced in different fashions by SCF solvation and solvent effects will be described. The categories are: 1) diffusion-controlled reactions; 2) activated processes; and 3) reactions that may be influenced by solvent cage effects. The importance of solute-solute, solute-solvent and solute-cosolute interactions to these categories of reactivity will be addressed.

I. INTRODUCTION

Experimental, (1-9) theoretical (10-13) and simulation (7,14-24) investigations have now clearly documented that the local solvent density of SCFs about a dilute solute may be significantly greater than the bulk density of the fluid. This effect of enhanced solvent-solute interaction is often referred to as local density augmentation or SCF solvent clustering. Spectroscopic techniques and solvatochromic probes (1-9) have been particularly useful in the identification and quantification of local density enhancement about dilute solutes. Solvatochromic shifts and fluorescence intensity ratio measurements in a variety of SCFs have shown significant density dependent deviations in behavior from normal liquid solvents, and from behavior predicted from solution based theory. For example, *Kajimoto et al.* (5) have investigated the charge-transfer (CT) emission of (N,N,-dimethylamino)benzotrile in SC CHF₃. Bathochromic shifts of the CT emission are expected to vary linearly with solvent polarity, according to Onsager reaction field theory. (5) While *Kajimoto* found reasonable agreement with liquid data in high density SCF, large deviations from expected values occurred in the medium and low fluid density regimes. These deviations were attributed to solvent aggregation around the dilute solutes. Similar results have been observed for solvatochromic absorption probes where plots of the solvent polarity parameter, ET, versus density were also found to deviate from *McRae-Bayliss* theory at moderate to sub-critical densities. (4)

The physical and chemical properties of free radicals have also played an instrumental role in understanding local density enhancement about dilute solutes in SCFs. *Randolph* and coworkers (9,19-23) have demonstrated that electron paramagnetic resonance (EPR) spectroscopy of stable nitroxide free radicals may be used as an extremely versatile probe to simultaneously measure reaction kinetics and local solvent density augmentation. The nitrogen hyperfine splitting constants of nitroxides (AN) are known to be sensitive probes of solvent polarity and probe the cybotactic region of the solvent, i.e., probes the immediate volume around the nitroxide that has been

affected by the nitroxide radical. Therefore, AN values may be used to reflect degrees of solvation. The experimental data of Carlier and Randolph (9) for di-tert (9, 19-22) have clearly demonstrated that local density augmentation (solvent-solute clustering) does not generally correlate with kT . This indicates that local density enhancements are short-range effects and not related to long-range fluctuations that are responsible for the maximum in kT , and other phenomenon related to criticality, such as very large negative partial molar volumes of dilute solutes in SCFs. Therefore these results indicated that "supercritical fluid clustering" is not a long-range critical effect, but rather a result of short-range structural effect of solvation. This supports previous interpretations by Kajimoto, et al. in 1988, (5) and Knutson, et al. in 1992. (7) To date, several different methods of investigation of solvent-solute interactions have demonstrated that local density augmentation may be as much as two to three times the bulk solvent density and exhibits a maximum at fluid densities of one third to 0.8 of the critical density.

In addition to solvent-solute interactions in SCFs, it is also known that addition of small quantities (1-5 mol %) of cosolvent greatly enhances solubility of organic solutes in SCFs. This methodology is routinely used to enhance SC extraction and chromatography performances. Spectroscopic studies have indicated that this phenomenon is a result of enhanced solute-cosolvent interactions and may result in local composition enhancements in the cybotactic sphere as large as 8 to 10 times the bulk composition. (1-2, 7-8) Cosolvent enhancements are observed to increase from high to low mixture densities approaching the critical pressure in the compressible region of the SC solvent mixture. However, local compositions significantly greater than the bulk have been observed at temperatures and pressures well removed from the critical temperature. This indicates that changes in the local environment are not direct functions of the proximity of the critical point but, as with local density, are also controlled by short-range solvation interactions. Therefore, a second form of SCF "clustering" exists, local composition enhancement.

II. RESULTS

We have used several different types of reaction intermediates, including free radicals, electronically excited states, carbocations and radical anions to probe the influence of the above mentioned solvation effects on various categories of chemical reactions in supercritical fluids. (25-31) For example, we have examined the solvent density dependence of the non-geminate diffusion-controlled reactions of benzyl free radical and the triplet-triplet annihilation reaction of benzophenone (measured by second order kinetics). (25-26) In both cases these reactions were found to be influenced only by changes in the bulk physical property of change in diffusivity, and not by local solvent density enhancements. We have also found that this is true for diffusion-controlled reactions that are measured by pseudo-first-order kinetics. (27) However, for reaction that contain some activation, i.e., not fully diffusion-controlled, the influence of local composition "cosolvent enhancements" can appear as significantly enhancing absolute rate constants when bulk reactant concentrations are used in the kinetic analysis. (28-31)

III. CONCLUSIONS

Several examples of these types of reactions will be presented in order to demonstrate that factors that drive chemical reactions in supercritical fluids are often predictable and can be better understood when the specific reaction mechanisms under consideration are carefully examined.

ACKNOWLEDGMENTS

The authors would like to acknowledge support from the following agencies, foundations and institutions: the National Science Foundation, the Department of Energy, the Army Research Office, and the Western Michigan University Faculty Research and Creative Activities Support Fund. In addition, acknowledgment is made to the Donors of the Petroleum Research Fund, administered by the American Chemical Society, for partial support of this research.

REFERENCES

1. Yonker, C. R.; Frye, S. L.; Kalkwarf, D. R.; Smith, R. D. *J. Phys. Chem.* **1986**, *90*, 3022.
2. Kim, S.; Johnston, K. P. *AIChE J.* **1987**, *33*, 1603.
3. Kim, S.; Johnston, K. P. *Ind. Eng. Chem. Res.* **1987**, *26*, 1206.
4. Yonker, C. R.; Smith, R. D. *J. Phys. Chem.* **1988**, *92*, 2374.
5. Kajimoto, O.; Futakami, M.; Kobayashi, T.; Yamasaki, K. *J. Phys. Chem.* **1988**, *92*, 1347.
6. (a) Brennecke, J. F.; Tomasko, D. L.; Peshkin, J.; Eckert, C. A. *Ind. Eng. Chem. Res.* **1990**, *29*, 1682. (b) Zhang, J.; Lee, L. L.; Brennecke, J. F. *J. Phys. Chem.* **1995**, *99*, 9268.
7. Knutson, B. L.; Tomasko, D. L.; Eckert, C. A.; Debenedetti, P. G.; Chialvo, A. A. In *Supercritical Fluid Technology*, F. V. Bright and M. E. P. McNally, Eds., ACS Symposium Series 488, American Chemical Society: Washington, DC, **1992**; p. 60.
8. Eckert, C. A.; Knutson, B. L. *Fluid Phase Equil.* **1993**, *83*, 93.
9. Carlier, C.; Randolph, T. W. *AIChE J.* **1993**, *39*, 876.
10. Lee, L. L. *Molecular Thermodynamics of Nonideal Fluids*, Butterworths, Boston, **1988**.
11. Cochran, H. D.; Lee, L. L.; Pfund, D. M. *Proc. Int. Symp. on Supercritical Fluids*, M. Perrut, Ed., Nice, France, **1988**, p. 245.
12. Cochran, H. D.; Lee, L. L. in *Supercritical Fluid Science and Technology*, K. P. Johnston and J. M. L. Penninger, Eds., ACS Symposium Series 406, American Chemical Society: Washington, DC **1989**; p. 27.
13. Cochran, H. D.; Lee, L. L.; Pfund, D. M. in *Fluctuation Theory of Mixtures*, E. Matteoli, Ed., *Adv. in Thermo. Ser.*, Taylor and Francis, **1989**.
14. Petsche, I. B.; Debenedetti, P. G. *J. Chem. Phys.* **1989**, *91*, 7075.
15. Wu, R.-S.; Lee, L. L.; Cochran, H. D. *Ind. Eng. Chem. Res.* **1990**, *29*, 977.
16. McGuigan, D. B.; Monson, P. A. *Fluid Phase Equil.* **1990**, *57*, 227.
17. Chialvo, A. A.; Debenedetti, P. G. *Ind. Eng. Chem. Res.* **1992**, *31*, 1391.
18. Chialvo, A. A. *J. Phys. Chem.* **1993**, *97*, 2740.
19. O'Brien, J. A.; Randolph, T. W.; Carlier, C.; Ganapathy, S. *AIChE J.* **1993**, *39*, 1061.
20. Randolph, T. W.; O'Brien, J. A.; Ganapathy, S. *J. Phys. Chem.* **1994**, *98*, 4173.
21. Ganapathy, S.; O'Brien, J. A.; Randolph, T. W. *AIChE J.* **1995**, *41*, 346.
22. Ganapathy, S.; Randolph, T. W.; Carlier, C.; O'Brien, J. A. *Int. J. Thermophysics* **1996**, *17*, 471.
23. Ganapathy, S.; Carlier, C.; Randolph, T. W.; O'Brien, J. A. *Ind. Eng. Chem. Res.* **1996**, *35*, 19.
24. Liu, Q.; Wan, C.; Zewail, A. H. *J. Phys. Chem.* **1996**, *100*, 18666.
25. Roberts, C. B.; Zhang, J.; Brennecke, J. F.; Chateaufneuf, J. E. *J. Phys. Chem.* **1993**, *97*, 5618.
26. Roberts, C. B.; Zhang, J.; Chateaufneuf, J. E.; Brennecke, J. F. *J. Am. Chem. Soc.*, **1993**, *115*, 9576.
27. Zhang, J.; Roek, D. P.; Chateaufneuf, J. E.; Brennecke, J. F. *J. Am. Chem. Soc.* **1997**, *119*, 9980.

28. Chateauneuf, J. E.; Roberts, C. B.; Brennecke, J. F. in *Supercritical Fluid Technology*, F. V. Bright and M. E. P. McNally, Eds., ACS Symposium Series 488, American Chemical Society: Washington, DC, 1992; p. 106.
29. Roberts, C. B.; Chateauneuf, J. E.; Brennecke, J. F. *J. Am. Chem. Soc.* **1992**, *114*, 8455.
30. Roberts, C. B.; Brennecke, J. F.; Chateauneuf, J. E. *AIChE J.* **1995**, *41*, 1306.
31. Roberts, C. B.; Chateauneuf, J. E.; Brennecke, J. F. *J. Am. Chem. Soc.* **1992**, *114*, 8455.

THE SOLUTION PHASE CHEMISTRY OF ATOMIC HYDROGEN. REACTIONS WITH ORGANIC SUBSTRATES.

Dennis D. Tanner,¹ Pramod Kandanarachchi,^{1,2} Nema! C. Das,¹ and James A. Franz.²

Contribution from the Department of Chemistry, University of Alberta,

Edmonton, Alberta, Canada T6G 2G2¹ and

The Pacific Northwest National Laboratory, Richland, WA 99352 USA.²

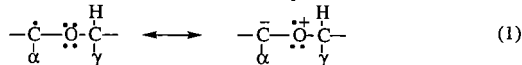
ABSTRACT

The solution-phase reaction of microwave-generated hydrogen atoms with terminal olefins is regioselective. Since addition is to the terminal end of the olefin, the reaction yields a secondary radical which undergoes either reaction with atomic hydrogen, disproportionation, combination, or addition to another olefin. At higher temperatures (23 °C) the olefin undergoes competitive allylic abstraction. The absolute rate constants for the addition of atomic hydrogen to mono- and trisubstituted olefins were determined and the data was used to extract the activation parameters for addition. Using competition kinetics the absolute rate constants for allylic abstraction were also determined. The stabilization of the carbon centered radical by an oxygen substituent was determined by the regioselective addition of a hydrogen atom to the terminal carbon of a vinyl ether or acetate. The same secondary radical can be formed by abstraction of an α -hydrogen from a dialkyl ether. The stereoelectronic enhancement or lack thereof of the rate constants for the reaction responsible for the formation of the radical intermediates will be discussed. The resonance effects due to oxygen were also investigated for addition to the five and six-membered rings of dihydrofuran and dihydropyran and for abstraction of the α -hydrogen from the saturated heterocycles.

I. INTRODUCTION

Recently, we reported a method for obtaining the absolute rate constants for the nonhomogeneous (gas-liquid) reaction of the addition of atomic hydrogen to an olefin.^{3b} The reaction of 1-octene was reported to be very close to diffusion controlled ($k_a^{25^\circ\text{C}} = 4.6 \times 10^9 \text{ M}^{-1} \text{ s}^{-1}$). The same kinetic method can be used to evaluate the stabilizing effect of a carbon centered radical having a geminal oxygen substituent. The addition of hydrogen to a terminal olefin was found to be regioselective, (i.e., only addition to give the most stable secondary, or tertiary radical)^{3a} The same regioselectivity was found for addition to the vinyl ether, a vinyl ester also underwent regioselective addition to give a radical center on carbon containing a geminal oxygen substituent.

The high reactivity and selectivity for a hydrogen atom on carbon α - to an oxygen substituent has been attributed to the resonance stabilization of the radical, eq. 1.⁴



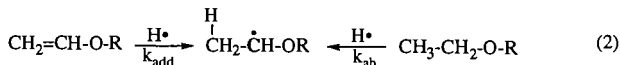
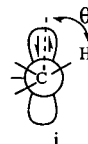
The importance of this resonance form has been substantiated by the observation that the EPR spectra of the radical shows a γ -hydrogen hyperfine coupling constant larger than that of the α -hydrogen (i.e., hyperconjugation).^{5,6}

The effect of this type of resonance stabilization predicts that a large solvent effect will stabilize or destabilize the contribution of a charge separated species. The reactions were carried out in both polar (acetone) and nonpolar (hexane) solvents.

Another approach to the question of reactivity and stability of the carbon radical α to an oxygen atom has been popularly termed stereoelectronic control.⁷

II. RESULTS & DISCUSSION

In order to probe the importance of this type of resonance stabilization the reactivity of an olefin which formed a radical α - to oxygen was looked at as a function of the dihedral angle formed between the reactive hydrogen and the doubly occupied orbitals on the oxygen lone pair, i . The secondary radical formed from addition to a vinyl ether can also be formed by abstraction of hydrogen from the α -position of the saturated ether, see eq. 2.



Using the same kinetic method developed for the reactions of atomic hydrogen with one octene,^{3a-c} after correcting the addition results for abstraction, disproportionation, combination, and addition of the α -radical to another molecule of vinyl ether the algorithm for the absolute rate constant for addition, eq. 3 was used to determine the value of k_a . The results of the addition and abstraction reactions for several ethers are listed in Table 1. An example of the entries used in the algorithm (eq. 3) for one of the determinations (-72 °C, acetone) is given in Table 2. A similar table was constructed for the other solvent.

$$k_a = f^{-1/2} \left[\frac{(\Delta P/\Delta t)_{\text{total}} (k_{\text{diff}}(\Delta P/\Delta t)_{\text{C,D}})^{1/2}}{[\text{olefin}][\Delta P/\Delta t]_{\text{RH}_2}} \right] \quad (3)$$

A plot of $\log (f^{1/2} k_a)$ vs the olefin concentration was used to calculate the value of k_a in both acetone (O) and hexane (●). When [olefin] is equal zero, $f = 1$, and the absolute rate constant for addition was determined, see Fig. 1.

[Fig. 1]

When the reactions were carried out at several temperatures an Arrhenius plot was used to calculate the activation parameters and the absolute rate constants of k_a for the reactions of ether in both solvents, see Fig. 2.

[Fig. 2]

The abstraction rate constant for the abstraction of the α -hydrogen from dibutyl ether was determined from the competition kinetics between the abstraction reaction and addition of $H\cdot$ to 1-octene. Since the value of k_a for 1-octene is known,^{3b} the value for k_{ab} from the ether could be calculated. The competition kinetics was carried out to diminished olefin concentration. Using the experimentally determined activation parameters for the addition and abstraction reactions listed in Table 1 and using the calculated and experimental ΔH_f of the reactants intermediates and products the free energy profile, Fig. 3 was constructed.

Stereoelectronic control for radical reactions has been proposed to have its maximum effect when the dihedral angle, θ , is 30° .^{7b} Model compounds claimed to have this geometry are cyclic ethers, tetrahydrofuran and tetrahydropyran. When $H\cdot$ was allowed to react with tetrahydrofuran or tetrahydropyran, at several temperatures (see Table 1) the abstraction reactions which form the radical at the 2-positions showed rate constants which were slower than the open chain ether. The rate constants determining for the formation of the radical by regioselective addition were the approximately same for the 6-membered ring, and only 5 x faster for the formation of the radical at the 2-position of furan, see Table 1.

The effect of multiple oxygen substitution α - to a radical center was investigated using as models, diethyl acetal and triethyl orthoformate. The relative rate of abstraction by $D\cdot$ of the tertiary hydrogen compared to the secondary hydrogen of the acetal, $CH_3CH(OCH_2CH_3)_2$ was estimated from the 2H -NMR of the reaction mixtures at several temperatures. A plot of the relative rates of deuterium incorporation vs. $1/T$ gave a value of $(k_{3^\circ}/k_{2^\circ}/H = 0.91 \pm 0.12)^{25^\circ C}$, while abstraction of the tertiary radical from the orthoformate, $(C_2H_5-O)_3C-H$ could not be detected although there was considerable $D\cdot$ incorporation from secondary H abstraction.

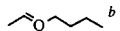
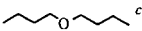
III. CONCLUSIONS

The absolute rate constants for the carbon centered radicals geminally substituted with oxygen can be compared to the value obtained from both addition to 1-octene or allylic abstraction from the terminal olefin.³ Both the addition and abstraction rate constants are within experimental error the same for the olefin and the vinyl ether. Only in the case of 2,3-dihydrofuran is the rate constant for addition more than one power of 10 faster, while abstraction from furan is slower than the open chain ether.

REFERENCES

1. (a) Department of Chemistry, University of Alberta. (b) Postdoctoral Fellow, University of Alberta, 1996.
2. Batelle Pacific Northwest Laboratories.
3. (a) Tanner, D.D.; Zhang, L. *J. Am. Chem. Soc.* **1994**, *116*, 6683. (b) Tanner, D.D.; Zhang, L.; Kandanarachchi, P. *J. Phys. Chem.* **1996**, *100*, 11319. (c) Tanner, D.D.; Zhang, L.; Kandanarachchi, P. *J. Phys. Chem. (A)*, **1997**, *101*, 9327.
4. Elad, D. *The Chemistry of the Ether Linkage*, Interscience Publisher, **1967**, Chapter 8, p. 355.
5. (a) Wertz, J.E.; Bolton, J.R. *Electron Spin Resonance*, Chapman and Hall, New York, **1986**, 112-114. (b) Dobbs, A.J.; Gilbert, B.C.; Norman, R.O.C. *J. Chem. Soc. (A)*, **1971**, 124.
6. Fisher, H. Z. *Naturforsch* **1965**, *20A*:428.
7. (a) Haydag, K.; McKelvey, R.D. *J. Org. Chem.* **1976**, *41*, 2222. (b) Malatesta, V.; Ingold, K.U. *J. Am. Chem. Soc.* **1981**, *103*, 609. (c) Beckwith, A.L.J.; Easton, C.J. *J. Am. Chem. Soc.* **1981**, *103*, 615. (d) Griller, D.; Howard, J.A.; Marriot, P.R.; Scaiano, J.C. *J. Am. Chem. Soc.* **1981**, *103*, 619.

Table 1. The Absolute Rate Constants for Addition and Abstraction Reactions by Atomic Hydrogen

Substrate	Solvent	($k_{rel}^{25^\circ C}$) ^a	$k^{25^\circ C} \times 10^9$ ($M^{-1}s^{-1}$)	$\Delta\Delta E_a$ (Kcal/mol)	ΔE_a (Kcal/mol)	log A
	Acetone	0.38±0.06	1.59	-0.49±0.05	4.8±2.9	13.2±4.2
	Hexane	1.14±0.40	4.79	-0.28±0.05	5.0±2.9	13.8±3.6
	Acetone	0.03±0.02	0.13	0.63±0.5	5.9±3.4	12.9±4.1
	Hexane	0.04±0.08	0.16	-0.1±1.0	5.2±3.9	12.5±4.9
	Acetone	0.20±0.10	0.84	-0.45±0.8	4.8±3.7	12.9±4.4
	Acetone	0.06±0.05	0.25	1.93±1.2	7.2±4.1	14.0±4.9
	Acetone	0.55±0.15	2.31	0.66±0.4	5.96±3.3	14.0±3.9
	Acetone	0.005±0.003	0.02	0.06±0.5	5.4±3.4	11.7±4.1

^a1-Octene was used as reference ($k_{rel} = k/k_{1-octene}$). ^bAddition reactions. ^cAbstraction reactions by atomic deuterium.

Table 2. Absolute Rate Constants ($f^{1/2}k_a$) for the Addition of Deuterium Atoms to Vinyl Butyl Ether at -72 °C in Acetone

[olefin]	$10^4(\Delta p/\Delta t)_{tot}^{bulk}$ ^a	$10^4(\Delta p/\Delta t)_{c,d}$ ^b	$10^7[R^*]$	$10^4(\Delta p/\Delta t)_{RD_2}$ ^c	$10^8[H^*]^c$	$10^{-3}f^{1/2}k_a^d$
mol L ⁻¹	mol L ⁻¹ s ⁻¹	mol L ⁻¹ s ⁻¹	mol L ⁻¹	mol L ⁻¹ s ⁻¹	mol L ⁻¹	M ⁻¹ s ⁻¹
1.12	6.19	5.37	7.84	0.82	11.9	4.09
0.45	7.36	5.60	8.43	1.13	15.2	11.20
0.09	1.90	1.33	3.90	0.34	9.92	30.57
0.045	1.01	0.81	3.05	0.19	6.42	40.83
0.034	0.58	0.19	1.47	0.16	2.69	63.47
0.022	0.52	-	-	-	(2.35)	126.7

^aExperimentally measured as the change in the concentration of vinyl butyl ether with time. ^bThe rate of the formation of combination and disproportionation products (see ref. 3b). ^cThe rate of the formation of radical-deuterium atom combination products (see ref. 3b). ^dCalculated by using eq. 3.

Table 3. Experimental and G2MP2 Enthalpies, 298K

Species	$\Delta H_{f,298}$ Kcal/mol, calcd, G2MP2	$\Delta H_{f,298}$ Kcal/mol, exptl	G2MP2 Enthalpy, 298K, hartrees
H	-	52.1 ^a	-0.497639
C(3P)	-	171.3 ^a	-37.781527
O(3P)	-	59.6 ^a	-74.976317
	-	-53.3 ^a	-
	-	-29.9 ^a	-
	-43.85	-44.0 ^a	-232.004551
	-18.28	-21.47 (Benson ^b)	-230.802457
CH ₃ OCH=CH ₂	-24.67	-24 ±2 ^a	-192.758133
CH ₃ OCH ₂ CH ₃	-52.3	-51.7 ^a	-193.963445
CH ₃ OC•HCH ₃	-9.05	-11.8 (bde 93)	-193.313900
	-0.9	-4.0, -2.9 (92.1 ^c or 93.2 ^d bde)	-231.355426
	-7.65	-12.4 (est., assumes 93 bde) ^e	-270.582035 -270.150798 ^f

^aLias, S.G.; Bartmess, J.E.; Liebman, J.F.; Holmes, J.L.; Levin, R.D.; Mallard, W.G. "Gas Phase Ion and Neutral Thermochemistry" *J. Phys. Chem. Ref. Data* **1988**, *17*, Supple. 1. ^bBenson, S.W. "Thermochemical Kinetics. Methods for the Estimation of Thermochemical Data and Rate Parameters", 2nd Ed. Wiley-Interscience, New York, N.Y. ^cLaarhoven, L.J.J.; Mulder, P. *J. Phys. Chem. B* **1977**, *101*, 73-77. ^dMuedas, C.A.; Ferguson, R.R.; Brown, S.H.; Crabtree, R.H. *J. Am. Chem. Soc.* **1991**, *113*, 2233. ^eThe heat of formation of tetrahydropyran is -53.3 Kcal/mol (ref. a above). Dihydropyran, -29.9. JMP2=FU/6-31G** enthalpy, 298K.

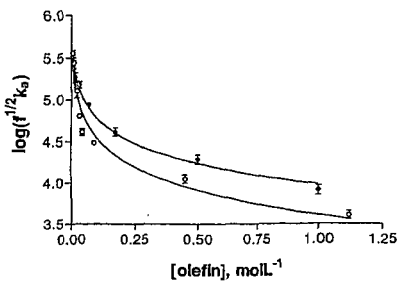


Fig. 1. The variation of the apparent rate constant $\log(f^{1/2}k_a)$ of vinyl butyl ether with the concentration of the olefin in (O) acetone and (●) hexane.

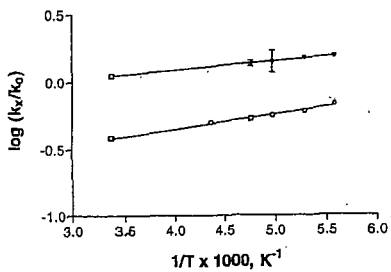


Fig. 2. An Arrhenius plot for the relative rates of addition to vinyl butyl ether in; (O) acetone, and (●) hexane.

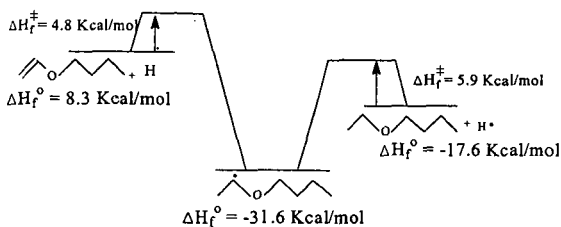


Fig 3. The free energy profile for the formation of methyl butoxy methyl free radical

REACTIONS OF ATOMIC HYDROGEN IN WATER: SOLVENT AND ISOTOPE EFFECTS

David Bartels
Chemistry Division,
Argonne National Laboratory
Argonne, IL 60439

I. INTRODUCTION

It has been known for many years that hydrogen atoms can be easily created and studied in water using radiolytic techniques [1]. The use of CW EPR detection coupled with electron radiolysis proved extremely useful in estimating many reaction rates, and revealed the interesting phenomenon of chemically induced dynamic electron polarization (CIDEP). [2] In recent years, we have made use of pulsed EPR detection to make precision reaction rate measurements which avoid the complications of CIDEP. [3] Activation energies and H/D isotope effects measured in these studies [4-14] will be described below.

An interesting aspect of the hydrogen atom reactions is the effect of hydrophobic solvation. EPR evidence -- an almost gas-phase hyperfine coupling and extremely narrow linewidth -- is quite convincing to show that the H atom is just a minimally perturbed gas phase atom inside a small "bubble". In several systems we have found that the hydrophobic free energy of solvation dominates the solvent effect on reaction rates.

II. PROCEDURE

The basic apparatus used in these measurements is illustrated in figure 1. Pulses of 3 MeV electrons are produced with a van de Graaff accelerator and strike the aqueous sample in an EPR cavity. The de-oxygenated solutions are recirculated through the cell at a high rate to allow signal averaging at 120Hz repetition frequency. In general acidic solutions (pH=2) are used to convert solvated electrons to hydrogen atoms on a nanosecond timescale and increase the signal amplitude. A small amount of methanol (ca. 10^{-2} M) is typically added as well to scavenge hydroxyl radicals. However, a major advantage of this technique is the ability to work in neutral and alkaline solution when necessary.

Some typical data from the experiment is plotted in figure 2. Immediately following the 12-50ns electron pulse, a 25ns x-band microwave pulse is applied to the cavity. After approximately 120ns, the sensitive detection electronics are switched in, and a free induction decay from the hydrogen atom is detected as in figure 2. In general the microwave frequency is set to about 10MHz above or below the Larmor frequency for the H atom low field transition. The effective damping time constant for the free induction decay is given by

$$1/T_2(\text{eff}) = 1/T_2^0 + k_s[S] + \sum_i k_{\text{ex}}^i [R_i] \quad (1)$$

where $1/T_2$ is the natural dephasing rate and $\sum k_{\text{ex}} [R_i]$ is the effect of second order reaction and spin exchange. This latter term is not negligible, but roughly constant over the five microsecond timescale of the experiment. A plot of the dephasing rate vs. scavenger concentration [S] gives the scavenging rate constant k_s as intercept.

III. RESULTS

Table 1 summarizes a large (but not exhaustive) number of hydrogen atom rate constant measurements in terms of Arrhenius activation energies and pre-exponential factors. Some of the greatest surprises were reactions of H with the nitrate [10] and hydrazinium [9] ions and with the per-iodic acid molecule [6], which have quite large activation energies, but enormous pre-exponential factors. These ion reactions involve large solvent (hydrogen bond) reorganization on the way to the transition state, and the large entropy increase dominates the activation free energy. In the case of per-iodic acid, the hydrated H_5IO_6 species must lose two water molecules and rearrange to IO_3^- and hydroxyl radical product. The rearrangements involved in the hydrazinium ion and nitrate ion reactions are not so obvious, and deserve further study.

The hydrophobic nature of the H atom solvation was demonstrated convincingly in the study of its addition to benzene [14]. The activation energy in solution is similar to that in the gas phase, but the rate constant is some forty times faster. Using the assumptions of transition state theory, the solvent effect (ratio of rates in gas phase to those in aqueous phase) can be reduced to an expression involving only the solvation free energies of reactants and transition state. Then, assuming that the transition state solvation free energy is very nearly the same as that of benzene itself or cyclohexadiene (both known from solubility measurements), the rate enhancement in water reduces simply to

$$k_{aq}/k_{gas} = \exp\{(\Delta G_{hyd}(H)/RT)\} = L^{-1} \quad (2)$$

and L is just the Ostwald solubility parameter for the hydrogen atom. The size and polarizability of the H atom are very similar to the H_2 molecule, and using the solubility of H_2 as a model in this equation produces essentially quantitative agreement with the benzene reaction rate data. The reaction is accelerated by the collapse of the hydrophobic solvation sphere of the H atom, resulting in a "hydrophobic attraction" of the H and benzene.

Other comparisons with gas phase reaction rate data are typically limited by the quality of the gas phase data available. In the case of methanol, the activation energy is found to be ca. 6kJ/mole higher in the aqueous phase, and one should expect an order of magnitude slower reaction rate. Instead, the reaction rate is roughly the same as the gas phase by virtue of a larger pre-exponential factor. We have suggested that this larger pre-exponential might represent a "hydrophobic acceleration" effect similar to that found in the benzene case [4,11].

No doubt the strangest reactions investigated in this work are the reactions of H and D with iodide and bromide ions (giving HI- and HBr- product) [15]. At 3×10^8 and $2 \times 10^6 \text{ M}^{-1} \text{ s}^{-1}$ for iodide and bromide respectively, the reactions have substantial free energy barriers, but the activation energies are zero or slightly negative! Measurements in H_2O/D_2O mixtures reveal a small isotope effect favoring D over H reaction. Other measurements have shown that the light Muonium atom (1/9 the mass of hydrogen) reacts about five times slower than H [7]. It is important to recall that our technique measures the rate of H atom dephasing, and so is not sensitive to any back reactions or equilibria which might occur: only the forward rate is measured. We have considered every alternative we can imagine, and conclude that the only barrier possible for these reactions consists of the water of the solvation shells. We postulate that the strongly hydrated small ions repel approach of the hydrophobic H atom. Molecular dynamics simulation of these systems has been initiated to explore the strange activation energy and isotope effects.

VII. CONCLUSIONS

The pulse radiolysis and EPR techniques described here have proven particularly useful for the study of hydrogen atom reactions in water. The hydrophobic hydrogen atom proves to be a unique probe for solvent and isotope effects in aqueous reactions.

ACKNOWLEDGMENTS

The author would like to express his thanks and appreciation for his coworkers in this research, who did most of the work: P. Han, E. Roduner, S. Mezyk, and A. Lossack.

Work at Argonne was supported by the U. S. Department of Energy under Contract No. W-31-109-ENG-38.

REFERENCES

- [1] G.V. Buxton, C.L. Greenstock, W.P. Helman, and A.B. Ross, *J. Phys. Chem. Ref. Dat.*, **17**, 513, (1988).
- [2] R.W. Fessenden and N.C. Verma, *Faraday Discuss. Chem. Soc.*, **63**, 104, (1977).
- [3] P. Han and D.M. Bartels, *Chem. Phys. Lett.*, **159**, 538, (1989).
- [4] Stephen P. Mezyk and David M. Bartels, *J. Phys. Chem.* **98**, 10578 (1994)
- [5] Stephen P. Mezyk and David M. Bartels, *Can. J. Chem.* **72**, 2516 (1994).
- [6] Stephen P. Mezyk, Roy MacFarlane and David M. Bartels, *J. Phys. Chem.* **98**, 12594 (1994)
- [7] David M. Bartels and Emil Roduner, *Chem. Phys.* **203**, 339-349 (1996)
- [8] Stephen P. Mezyk and David M. Bartels, *J. Chem. Soc. Faraday Trans.* **91**, 3127 (1995)

- [9] Stephen P. Mezyk, Miyoko Tateishi, Roy MacFarlane, and David M. Bartels, *J. Chem. Soc. Faraday Trans.* **92**, 2541 (1996).
- [10] S. P. Mezyk and D. M. Bartels, *J. Phys. Chem.*, **A101**, 6233 (1997).
- [11] S. P. Mezyk and D. M. Bartels, *J. Phys. Chem.*, **A101**, 1329, (1997).
- [12] S.P. Mezyk, A. Lossack, and D.M. Bartels, *Can. J. Chem.*, **75**, 1114, (1997).
- [13] A.M. Lossack, E. Roduner, and D.M. Bartels, *J. Phys. Chem.*, **A102**, 7462, (1998).
- [14] E.Roduner and D.M. Bartels, *Ber. Bunsenges. Phys. Chem.*, **96**, 1037, (1992).
- [15] S.P. Mezyk and D.M. Bartels, *J. Phys. Chem.*, **97**, 4101, (1993).

Table 1: Measured Arrhenius Parameters for H atom Reactions in Water

H reaction partner	$\log_{10}(A/M^{-1}s^{-1})$	E_a / (kJ/mole)
benzene:	12.34	19.1
alcohols:		
methanol	11.64	29.4
ethanol	11.53	24.1
ethanol-d ₅	12.03	31.9
2-propanol	11.86	22.0
2-propanol-d ₅	12.00	27.4
aldehydes:		
propionaldehyde	11.77	22.2
butyraldehyde	12.20	23.9
ketones:		
acetone	11.68	30.7
methyl ethyl ketone	11.25	22.3
diethyl ketone	11.30	21.0
methyl isopropyl ketone	10.96	17.2
methyl isobutyl ketone	11.24	21.2
cyclopentanone	11.15	19.7
iodo compounds:		
iodomethane	11.90	10.39
iodoethane	12.20	11.8
1-iodopropane	12.24	12.0
IO ₃ ⁻	11.96	27.46
HIO ₃	12.83	22.35
IO ₄ ⁻	13.30	36.55
H ₅ IO ₆	17.77	53.0
I ⁻	8.48	-1.0
peroxide and hydrazine:		
H ₂ O ₂	11.26	21.1
HO ₂ ⁻	13.65	25.6
D ₂ O ₂ (D atom reaction)	10.37	17.3
N ₂ H ₄	10.69	16.28
N ₂ H ₅ ⁺	16.95	61.38
nitrite and nitrate:		
NO ₂ ⁻	11.94	15.6
HNO ₂	12.36	21.5
NO ₃ ⁻	15.28	48.7

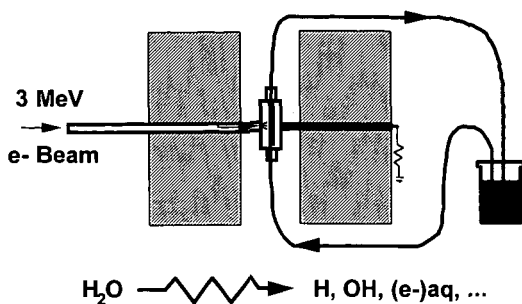


Figure 1. Typical experimental arrangement of the FID attenuation experiment. Temperature controlled aqueous sample is recirculated through a glass cell in the EPR cavity. H atoms are generated by in situ pulse radiolysis with 3 MeV electrons. Scavenger concentrations are changed by successive injections into the flow stream.

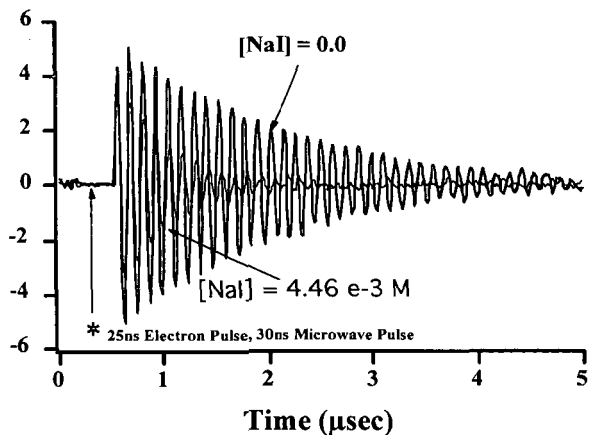


Figure 2. Free induction decay from the H atom low field EPR line. Addition of scavenger (in this example I-) shortens the damping time constant, and provides a pseudo-first order measurement of reaction rate.

THE CONSEQUENCES OF SURFACE CONFINEMENT ON FREE RADICAL CHEMISTRY

A. C. Buchanan, III and Phillip F. Britt

Chemical & Analytical Sciences Division
Oak Ridge National Laboratory
1 Bethel Valley Road
P.O. Box 2008, MS-6197
Oak Ridge, Tennessee 37831-6197

Keywords: Free radicals, pyrolysis, restricted diffusion

ABSTRACT

Mass transport limitations impact the thermochemical processing of fossil and renewable energy resources, which involves the breakdown of cross-linked, macromolecular networks. To investigate the molecular level details of the consequences of molecular confinement on high temperature (275-500°C) free-radical reaction pathways, we have been examining the pyrolysis of model compounds attached to the surface of non-porous silica nanoparticles through a thermally robust Si-O-C_{aryl} tether. Pyrolysis of silica-immobilized diphenylalkanes and related ethers have been studied in detail and compared with the corresponding behavior in fluid phases. The diffusional constraints can lead to reduced rates of radical termination on the surface, and enhancement of neophyl-like rearrangements, cyclization-dehydrogenation pathways, and *ipso*-aromatic substitutions. Furthermore, studies of two-component surfaces have revealed the importance of a radical relay mechanism involving rapid serial hydrogen transfer steps resulting from the molecular pre-organization on the low fractal dimension silica surface. Key findings are reviewed in this paper, and the implications of these results for fuel processing are described.

INTRODUCTION

Pyrolysis forms the basis for many current and envisioned technologically important processes for conversion of fossil and renewable resources into volatile fuels or chemicals. Since many of these resources are highly cross-linked, macromolecular organic materials, concerns over mass transport limitations are often well-founded. The effects of mass transport limitations have been documented in the pyrolysis of coal,⁽¹⁾ kerogen,⁽²⁾ cellulose,⁽³⁾ lignin,⁽⁴⁾ biomass,⁽⁵⁾ and polymers.⁽⁶⁾ Predictive models have been developed for pyrolysis of coal, lignin, and cellulose that explicitly include descriptions of mass transport mechanisms.^(1b-4) These mass transport limitations can impact pyrolysis rates, and govern the tar yields and molecular weight distributions.

Our knowledge of the effects of mass transport is primarily on a macro scale, e.g. lumped kinetic parameters and product classes. Pyrolysis studies on complex materials such as coal do not yield direct information about the *individual* chemical processes that control reaction rates, or about the actual molecules that are responsible for formation of particular products. An enhanced understanding of the effects of mass transport limitations on pyrolysis reactions *at a molecular level* has been a goal of our research. Hence, we have been exploring the pyrolysis chemistry of organic molecules that serve as models for constituents in biopolymers and geopolymers. Restricted mass transport conditions have been simulated by confining these molecules to the surface of nonporous silica nanoparticles through a covalent linkage. Many of the manifestations of mass transport limitations on high temperature organic reactions involving free-radical intermediates are now much better understood as a consequence of our extensive studies on these silica-immobilized model compounds. A brief overview of key findings from our studies of hydrocarbon pyrolysis will be presented, and a more detailed review of this work is in press.⁽⁷⁾

PREPARATION OF SILICA-IMMOBILIZED MODEL COMPOUNDS

In selection of a surface-immobilization technique for our investigations of the pyrolysis mechanisms, we were guided by several criteria. Both the support and linkage must be stable at the temperature regime of interest, up to ca. 450-500 °C. The support should have a moderately high surface area with enough accessible active sites for attaching significant quantities of the organic molecules of interest. Any unreacted sites should not be catalytically active, e.g. Brønsted or Lewis acid sites. The position of surface attachment within the organic moiety should be far enough removed from the normal position of thermal reactivity so as not to induce significant substituent effects. For flexibility, the organic functional group used in the attachment should be readily synthesized. Finally, a very important criterion arises from our desire to be able to identify and quantitate all pyrolysis products, both in the gas phase and those that remain attached to the surface

of the support. Namely, although the covalent link should be thermally stable, there must exist a facile chemical method for cleaving products from the surface for analysis. To meet all these requirements, we chose the reaction of substituted phenols with the silanols of a high purity, nonporous fumed silica (Cabosil M-5, 200 m² g⁻¹, ca. 4.5 SiOH nm⁻² or 1.5 mmol SiOH g⁻¹) as shown in Figure 1.⁽⁸⁻¹⁰⁾

Surface coverages can be varied (typical range of 0.06 - 0.6 mmol g⁻¹) by adjusting the initial phenol to surface hydroxyl ratio, and saturated surface coverages are obtained by using excess phenol. Unreacted phenol is removed either by sublimation under vacuum at ca. 270°C or by Soxhlet extraction with a solvent like benzene. The silicon-oxygen-aromatic carbon linkage, Si-O-C_{aryl}, has been found to be thermally robust up to at least 450°C.⁽⁸⁻¹¹⁾ However, the linkage is hydrolytically unstable under aqueous base conditions. This allows us to detach pyrolysis products from the silica surface as the corresponding phenols, as well as any unreacted starting material, for identification and quantitation. This important advantage for our pyrolysis studies also represents a potential limitation for this linkage if reaction studies in aqueous or nucleophilic solvents are of interest. Another limitation of this method is ambiguity in the point of attachment to the surface if a second active functional group (alcohol, thiol, etc.) is present in the molecule. Surfaces can also be prepared with two point attachment of the model compound (Figure 1),⁽¹²⁾ although high efficiencies for di-attachment (80-90%) occur only at rather low surface coverages (ca. 0.1 mmol g⁻¹). We have also found that a variety of two-component surfaces are easily prepared by co-attachment of the molecules to the silica in a single step.^(13,14)

PYROLYSIS STUDIES

The surface-attached diphenylalkanes, =C₆H₄(CH₂)_nC₆H₅ [n=0-4], have been prepared and used as models for aliphatic bridges between aromatic molecules in fossil fuels.^(8,12) The "=" notation is employed as an abbreviation to represent the Si-O-C_{aryl} linkage to the silica surface. In addition, analogs such as =C₆H₄XCH₂C₆H₅ [X = O,⁽¹⁵⁾ S⁽¹⁶⁾], =C₆H₄OCH₂CH₂C₆H₅^(17,18) and =C₆H₄CH₂CH₂OC₆H₅^(17,18) have been recently examined to explore the important effects of heteroatoms. The pyrolysis behavior of surface-immobilized compounds have been thoroughly examined as a function of reaction extent, temperature, surface coverage, and degree of cross linking,^(8,10,12) as well as the presence of a hydrogen atmosphere,^(14,19) a second co-attached molecule of variable structure,^(10,13,14) and a solid-state acid⁽²⁰⁾ or hydrogenation catalyst.⁽¹⁾ The reaction kinetics, mechanisms, and product selectivities have been compared with that of the corresponding molecules in fluid phases. Due to space limitations, only a few of the major findings will be surveyed below with an emphasis on free radical chemistry.

Vacuum pyrolysis reactions were typically performed in sealed T-shaped Pyrex tubes in a temperature controlled (± 1 °C) tube furnace. Volatile products were collected in the side arm trap cooled with liquid nitrogen, while surface-attached products were recovered as the corresponding phenols following basic digestion of the silica. The products were identified and quantitated principally by GC and GC-MS with the use of authentic reference materials and internal calibration standards.

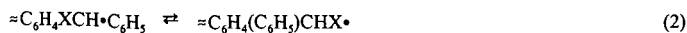
=C₆H₄(CH₂)_nC₆H₅ [n=0,1]. Biphenyl contains only strong bonds that are stable at 400°C. Likewise, we found that the surface-immobilized form, =Ph-Ph, was stable at 400°C for many hours.⁽⁶⁾ This indicates that the silica surface and residual silanol groups did not induce any new reaction pathways. Similarly, surface-immobilized diphenylmethane was also found to be stable at 375-400°C.⁽⁸⁾ This structure would be quite susceptible to acid-catalyzed cracking reactions,⁽²⁰⁾ and their absence is further testament to the inert nature of the fumed silica surface. At higher temperatures (425-450°C), we have recently observed a slow reaction involving a competing cyclization pathway and a previously undetected radical *ipso*-substitution pathway involving =C₆H₄CH•C₆H₅, as shown in Figure 2.⁽²¹⁾ The radical substitution path appears to be promoted by the diffusional constraints, and the selectivity for this path is currently being studied in more detail.

=C₆H₄XCH₂C₆H₅ [X = CH₂, O, S]. These model compounds represent structures containing weak bridges between aromatic rings that cleave at T < 400°C as shown in Eq. 1.



The rate constants and activation parameters measured for X = CH₂⁽⁸⁾ and O⁽¹⁵⁾ at high surface coverages are similar to those reported for fluid-phase analogs, indicating that the unimolecular homolysis steps are not affected by the surface attachment. However, we find that the product distributions are substantially impacted. This is illustrated in Figure 3 for the case of silica-attached 1,2-diphenylethane or bibenzyl. The formation of comparable amounts of surface-attached and gas-phase toluene products demonstrates a general finding that there is enough conformational freedom on the surface to permit oriented hydrogen transfers between surface-bound molecules and surface-bound free radicals. However, restricted diffusion retards the rates of radical termination on the surface through bimolecular coupling of intermediate radicals such as =C₆H₄XCH•C₆H₅. As shown in Figure 3 for the case of bibenzyl, this eliminates the formation of a major product (tetraphenylbutanes) found in fluid phases. As a consequence, new pathways emerge in significant

quantities such as cyclization-dehydrogenation (establishing the phenanthrene skeleton for $X = \text{CH}_2$, but not detected for $X = \text{O}, \text{S}$) and skeletal rearrangements. In particular, neophyl-like rearrangements involving 1,2-phenyl shifts have been found to be important for all cases (Eq. 2).^(8,15,16) The efficiency of the rearrangement path has been found to depend strongly on the



surrounding environment on the surface. Neighboring hydrogen sources are needed to trap the typically less stable rearranged radical. Hence, a low surface coverage of bibenzyl or the presence of neighboring aromatic spacer molecules (such as naphthalene) inhibits this rearrangement path.⁽²²⁾ Conversely, this path is prominent at high bibenzyl surface coverages or in the presence of neighboring molecules that can donate hydrogen (such as diphenylmethane). The resulting hydrogen transfer, radical relay path is important in overcoming some of the effects of diffusional constraints, and has been studied in detail in the pyrolysis of 1,3-diphenylpropane as discussed below. It is important to note that, for bibenzyl, this process is a retrograde pathway that generates a more refractive diphenylmethane linkage. For the benzyl phenyl ether analog, new reactive products (benzophenone and benzhydrol) are generated that were not previously reported in fluid phases. In the benzyl phenyl sulfide case, the rearranged product, $\approx \text{C}_6\text{H}_4(\text{C}_6\text{H}_5)\text{CHSH}$, is particularly unstable and reacts further to form surface-attached diphenylmethane.

Because of the significance of this rearrangement path under restricted mass transport conditions, the pyrolysis of immobilized bibenzyl has been investigated in several different environments. We recently found that a co-attached hydrogen donor, tetralin, is ineffective at retarding the rearrangement path.⁽²²⁾ The impact of hydrogen pressure on this pathway was also studied through pyrolysis of $\approx \text{BB}$ at 400°C in a high pressure reactor in the presence of a nitrogen or deuterium atmosphere (14 MPa).⁽¹⁹⁾ Pyrolysis under D_2 produced the expected higher yields of hydrocracked products such as $\approx \text{C}_6\text{H}_4\text{D}$ and $\text{C}_6\text{H}_4\text{CH}_2\text{CH}_2\text{D}$, as well as lower yields of alkene products, compared with pyrolysis under N_2 or vacuum. However, D_2 pressure was unable to prevent the retrogressive rearrangement pathway (or the cyclization pathway) from occurring under the diffusional constraints. A similar result was also obtained for a different type of silica-immobilized bibenzyl under D_2 , which was prepared by attachment of a carboxylic acid derivative to silica via a $\text{SiO} - \text{Ca}^{2+} - \text{O}_2\text{CPhCH}_2\text{CH}_2\text{Ph}$ ionic linkage.⁽²³⁾

$\approx \text{C}_6\text{H}_4\text{CH}_2\text{CH}_2\text{XC}_6\text{H}_5$ ($X = \text{CH}_2, \text{O}$). 1,3-Diphenylpropane (DPP) has been employed as a model for longer linkages between aromatic clusters in coal that decay at significant rates at 350-400°C by a free radical chain mechanism as shown in Figure 4. Our studies of silica-immobilized DPP showed that this type of linkage also decayed efficiently in this temperature regime under conditions of restricted mass transport, but pyrolysis rates were extremely sensitive to surface coverage and the structure of neighboring molecules on the surface.^(9,12,14) As shown in Table 1, the rate of decomposition of $\approx \text{DPP}$ decreased dramatically with decreases in surface coverage as the rate of the bimolecular hydrogen transfer steps decrease. In particular, hydrogen transfer between two surface bound species (Figure 4, Insert) would be particularly affected by increasing spatial separation on the surface. These effects were amplified when DPP was further restrained by having both ends of the molecule tethered to the surface.⁽¹²⁾ At a surface coverage of 0.1 mmol g^{-1} , the pyrolysis rate decreased by an additional factor of 4-7 for the two $\approx \text{DPP}$ isomers studied, for which about 80% of the molecules were di-attached with the remainder being mono-attached.

The rate of pyrolysis of $\approx \text{DPP}$ at 375°C spanned a remarkably wide range (830-fold), as shown in Table 1, and was very sensitive to the structure of neighboring spacer molecules on the surface. When compared at similar low surface coverages of $\approx \text{DPP}$ (ca. 0.10-0.14 mmol g^{-1}), aromatic spacer molecules such as biphenyl and naphthalene had little effect on the pyrolysis rate. However, spacer molecules containing benzylic C-H bonds, such as dimethylbenzene, diphenylmethane, tetralin, and fluorene, acted as catalysts to accelerate the decomposition of $\approx \text{DPP}$, and the decomposition rates correlated with reported relative rates for hydrogen donation of these molecules to benzylic radicals.^(14,24) This behavior is unique to the diffusional constrained system, since in fluid phases, these molecules behaved like other inert aromatic diluents. This unexpected behavior could be explained by a hydrogen transfer, radical relay mechanism on the surface as illustrated in Figure 5 for the diphenylmethane spacer. Rapid serial hydrogen transfer steps can occur on the surface since the reacting species are pre-organized for reaction in this reduced dimensional reaction space. The involvement of these hydrogen transfer steps for the diphenylmethane spacer were confirmed through isotopic labeling studies with $\approx \text{PhCD}_2\text{Ph}$ as spacer.⁽¹⁴⁾ As shown in Table 1, a full kinetic isotope effect of 2.8 was detected at 375°C for $\approx \text{DPP}$ pyrolysis, and deuterium was incorporated in both the vapor-phase and surface-attached toluene products. The significance of this omnipresent process is that radical centers can migrate by a non-diffusional pathway that overcomes some of the diffusional constraints and promotes the radical chain decomposition pathway. However, as noted earlier, retrogressive reactions for weak cross links as typified by $\approx \text{BB}$ are also limited by hydrogen transfer steps and are promoted by neighboring molecules that can participate in the radical relay mechanism.

Undoubtedly, the efficiency of this pathway also depends on the ability of molecules to become properly aligned for the oriented hydrogen transfer step on the surface, an area that needs

to be studied in more detail. Orientation effects can lead to regiospecificity in hydrogen transfer steps that impact product selectivities. This is illustrated in the pyrolysis of \approx DPP where hydrogen abstraction selectivities (Figure 1) varied modestly with changes in surface coverage, favoring abstraction from the benzylic methylene farthest from the surface at lower surface coverages. More dramatic effects on product selectivities were found during pyrolysis of surface-immobilized 1,4-diphenylbutane where radical chain decomposition products are formed from both benzylic and non-benzylic carbon-centered radicals as described previously.⁽¹⁰⁾ Once again, the presence of neighboring molecules that block or promote hydrogen transfer steps significantly alter product selectivities.

We have also been investigating ether analogs such as silica-attached phenethyl phenyl ether, \approx C₆H₄CH₂CH₂OC₆H₅ (\approx PPE), which are models for important structural elements in lignin.^(17,18) Pyrolysis at 375°C follows a similar course to that observed in fluid phases. Analogous to diphenylpropane, a radical chain pathway is observed that cycles through the benzylic radical, \approx C₆H₄CH•CH₂OC₆H₅, producing phenol and surface-attached styrene products. However, for \approx PPE, a second significant reaction pathway is detected that proceeds through the non-benzylic radical, \approx C₆H₄CH₂CH•OC₆H₅. As in the case of benzyl phenyl ether (see Eq. 2), this radical undergoes an oxygen to carbon phenyl shift resulting (following β -scission and H-abstraction) in the formation of benzaldehyde and surface-attached toluene.⁽¹⁷⁾ This pathway is significant for a number of substituted PPE's, but the selectivity is sensitive to substituent effects in a predictable manner. However, as opposed to fluid phases where dilution of PPE with biphenyl solvent had no effect of the selectivity of the two radical decay paths, the rearrangement path involving the O-C phenyl shift was recently found to be sensitive to the structure of neighboring spacer molecules on the silica surface.⁽¹⁷⁾ Aromatic spacer molecules such as biphenyl appear to hinder the O-C phenyl shift, presumably by steric interference. These spacer effects continue to be investigated.

SUMMARY

Restricted mass transport has been recognized as playing an important role in the pyrolysis of cross-linked, macromolecular systems. A molecular level understanding of the impact of diffusional constraints on pyrolysis mechanisms is crucial to bench marking results from analytical pyrolysis experiments, and could be important in developing more refined predictive models for the pyrolysis of fossil and renewable organic energy resources. Model systems that incorporate diffusional constraints such as polymers and covalently or ionically immobilized compounds can provide some of this needed information. Through our studies of silica-immobilized hydrocarbons, we have obtained comprehensive information on how pyrolysis rates and product distributions can be perturbed by restricted mass transport. In general, the rates of unimolecular homolyses are little perturbed by surface immobilization. However, termination reactions between diffusional constrained radicals are hindered, particularly coupling reactions. This often results in the emergence of competitive radical chain pathways involving unimolecular steps such as skeletal rearrangements and cyclizations. Furthermore, hydrogen transfer processes between diffusional constrained species can be particularly facile, although quite dependent on the distance between, and the orientation of, the participating species. Under optimum hydrogen transfer conditions, rapid serial hydrogen transfers can occur and provide a means for radical sites to be translocated in the matrix without the need for physical diffusion. Such a process promotes radical chain reactions that can produce smaller, more volatile products, as well as retrogressive reactions that produce more refractory products.

ACKNOWLEDGMENTS

This research was sponsored by the Division of Chemical Sciences, Office of Basic Energy Sciences, U.S. Department of Energy, under contract No. DE-AC05-96OR22464 with Oak Ridge National Laboratory, managed by Lockheed Martin Energy Research, Corp.

REFERENCES

1. (a) L. M. Stock, *Acc. Chem. Res.*, 22 (1989) 427; (b) P. R. Solomon, T. H. Fletcher, and R. J. Pugmire, *Fuel*, 72 (1993) 587; (c) M. A. Serio, D. G. Hamblen, J. R. Markham, and P. R. Solomon, *Energy & Fuels*, 1 (1987) 138; (d) P. R. Solomon, D. G. Hamblen, M. A. Serio, Z.-Z. Yu, and S. Charpenay, *Fuel*, 72 (1993) 469; (e) P. Gilot and B. R. Starnmore, *Energy & Fuels*, 9 (1995) 126; (f) E. M. Suuberg, in R. H. Schlosberg (Ed.), *Chemistry of Coal Conversion*, Plenum Press, New York, 1985, Chapter 4, p. 67; (g) G. R. Gavalas, *Coal Pyrolysis*, Elsevier, Amsterdam, 1982. (h) W. Wanzl, *Biomass and Bioenergy*, 7 (1994) 131.
2. A. K. Burnham, R. L. Braun, *Org. Geochem.*, 16 (1990) 27.
3. C. D. Blasi, *Biomass and Bioenergy*, 7 (1994) 87.
4. M. A. Serio, S. Charpenay, R. Bassilakis, and P. R. Solomon, *Biomass and Bioenergy*, 7 (1994) 107.
5. Y. Chen, S. Charpenay, A. Jensen, M. A. Serio, and M. A. Wójciewicz, *Prepr. Pap.-Am. Chem.*

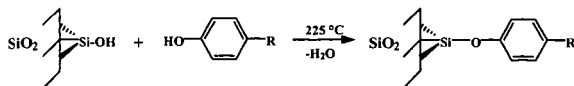
- Soc., Div. Fuel Chem., 42 (1997) 96.
- (a) C. C. Elam, R. J. Evans, and S. Czernik, Prepr. Pap.-Am. Chem. Soc., Div. Fuel Chem., 42 (1997) 993; (b) H. Bar and Z. Aizenshtat, J. Anal. Appl. Pyrolysis, 19 (1991) 265; (c) R. N. Hancox, G. D. Lamb, and R. S. Lehrle, J. Anal. Appl. Pyrolysis, 19 (1991) 333.
 - A. C. Buchanan, III and P. F. Britt, J. Anal. Appl. Pyrolysis, in press.
 - A. C. Buchanan, III, T. D. J. Dunstan, E. C. Douglas, and M. L. Poutsma, J. Am. Chem. Soc., 108 (1986) 7703.
 - A. C. Buchanan, III and C. A. Biggs, J. Org. Chem., 54 (1989) 517.
 - P. F. Britt and A. C. Buchanan, III, J. Org. Chem., 56 (1991) 6132.
 - S. C. Mitchell, C. J. Lafferty, R. Garcia, C. E. Snape, A. C. Buchanan, III, P. F. Britt, and E. Klavetter, Energy & Fuels, 7 (1993) 331.
 - P. F. Britt, A. C. Buchanan, III, E. A. Malcolms, and C. A. Biggs, J. Anal. Appl. Pyrolysis, 25 (1993) 407.
 - A. C. Buchanan, III, P. F. Britt, and C. A. Biggs, Energy & Fuels, 4 (1990) 415.
 - A. C. Buchanan, III, P. F. Britt, K. B. Thomas, and C. A. Biggs, J. Am. Chem. Soc., 118 (1996) 2182.
 - A. C. Buchanan, III, P. F. Britt, J. T. Skeen, J. A. Struss, and C. L. Elam, J. Org. Chem., 63 (1998) 9895.
 - K. Ismail, S. C. Mitchell, S. D. Brown, C. E. Snape, A. C. Buchanan, III, P. F. Britt, D. V. Franco, I. I. Maes, and J. Yperman, Energy & Fuels, 9 (1995) 707.
 - A. C. Buchanan, III and P. F. Britt, Prepr. Pap.-Am. Chem. Soc., Div. Fuel Chem., 44 (1999) 290.
 - P. F. Britt, A. C. Buchanan, III, K. B. Thomas, and S.-K. Lee, J. Anal. Appl. Pyrolysis, 33 (1995) 1.
 - R. D. Guthrie, S. Ramakrishnan, P. F. Britt, A. C. Buchanan, III, and B. H. Davis, Energy & Fuels, 9 (1995) 1097.
 - A. C. Buchanan, III, P. F. Britt, K. B. Thomas, and C. A. Biggs, Energy & Fuels, 7 (1993) 373.
 - A. C. Buchanan, III and P. F. Britt, Prepr. Pap.-Am. Chem. Soc., Div. Fuel Chem., 43 (1998) 630.
 - A. C. Buchanan, III, P. F. Britt, and K. B. Thomas, Energy & Fuels, 12 (1998) 649.
 - S. Ramakrishnan, R. D. Guthrie, P. F. Britt, A. C. Buchanan, III, and B. H. Davis, Prepr. Pap.-Am. Chem. Soc., Div. Fuel Chem., 40 (1995) 555.
 - J. A. Franz, M. S. Alnajjar, R. D. Barrows, D. L. Kasaki, D. M. Camaioni, and N. K. Suleman, J. Org. Chem., 51 (1986) 1446.
 - A. C. Buchanan, III, unpublished results.

Table 1. Pyrolysis of Silica-Immobilized Ph(CH₂)₃Ph at 375°C: Influence of Surface Composition on Pyrolysis Rate

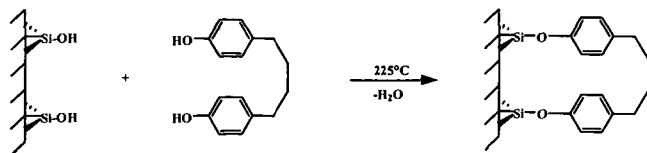
Surface Composition ^a	Coverage (mmol g ⁻¹)	Rate x 10 ⁻⁴ (% s ⁻¹) ^b	Ref.
=DPP	0.59	24	9
	0.14	1.1	9
	0.10	0.72	13
=DPP= (<i>p</i> -, <i>p</i> -)	0.10	0.17	12
=DPP= (<i>m</i> -, <i>p</i> -)	0.09	0.10	12
=DPP / =BP	0.13 / 0.51	2.2	14
=DPP / =NAP	0.12 / 0.44	1.9	14
=DPP / =DMB (3,4-)	0.12 / 0.25	8.5	14
=DPP / =DPM	0.14 / 0.41	37	14
=DPP / =DPM- <i>d</i> ₂	0.12 / 0.35	13	14
=DPP / =TET	0.11 / 0.45	47	25
=DPP / =FL	0.17 / 0.42	83	14

^a Abbreviations for surface-attached species are =DPP (1,3-diphenylpropane, mono-attached), =DPP= (DPP, 80 % di-attached, 20 % mono-attached), =BP (biphenyl), =NAP (naphthalene), =DMB (dimethylbenzene), =DPM (diphenylmethane), =DPM-*d*₂ (PhCD₂Ph), =TET (tetralin), =FL (fluorene). ^b Initial rates for total decomposition of =DPP based on 4-8 thermolyses. Standard deviations (1σ) in reported values are typically ≤ 15%.

Attachment Reaction



Di-attachment



Co-attachment

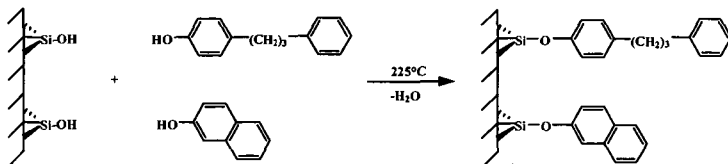


Figure 1. Preparation of silica-immobilized model compounds

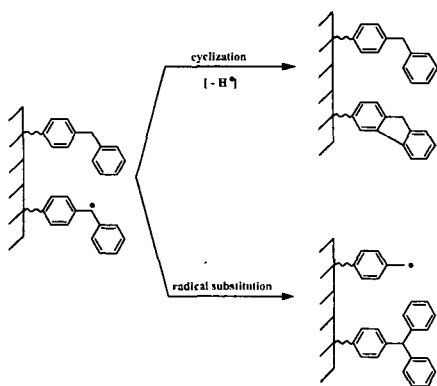
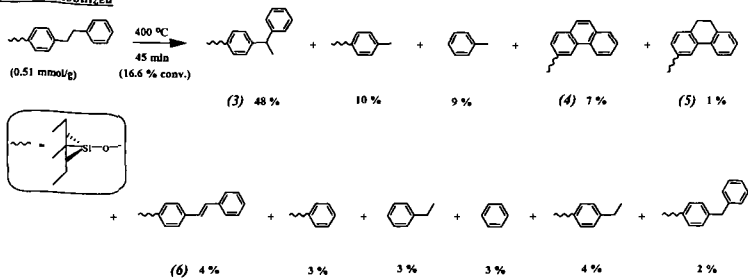


Figure 2. Competing cyclization and radical substitution pathways in pyrolysis of silica-immobilized diphenylmethane.

Silica Immobilized



Liquid Phase

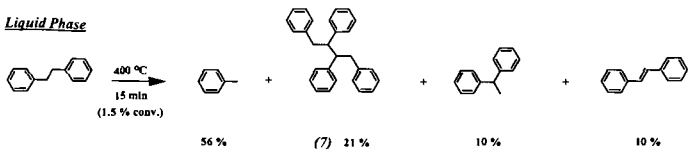
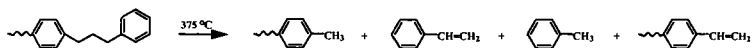


Figure 3. Comparison of pyrolysis products for silica-immobilized and liquid bibenzyl.



Radical Chain Mechanism:

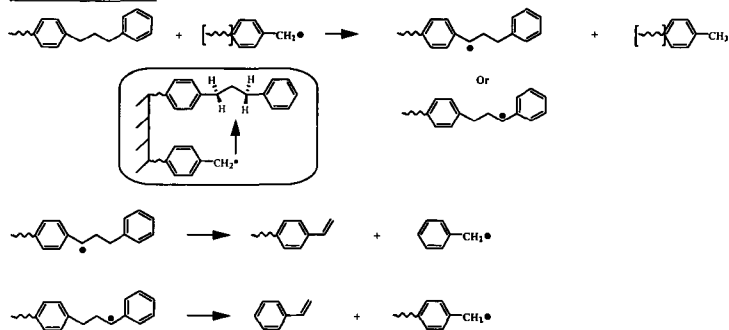


Figure 4. Radical chain propagation steps for the pyrolysis of silica-immobilized 1,3-diphenylpropane. Bracket notation denotes species exists in both gas-phase and surface-attached forms.

Hydrogen Transfer, Radical Relay Mechanism

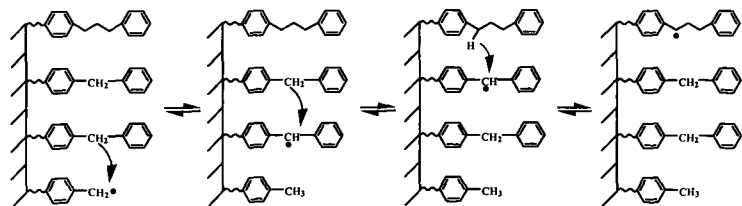


Figure 5. Radical relay mechanism in the pyrolysis of silica-attached 1,3-diphenylpropane.

SELECTIVE OXIDATION OF ALKANES PROMOTED BY COPPER IONS

Donald M. Camaioni, Michael A. Lilga, J. Timothy Bays, John C. Linehan,
Wendy J. Shaw, and Jerome C. Birnbaum

Pacific Northwest National Laboratory, Richland, WA, 99352

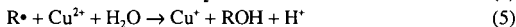
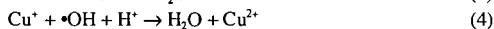
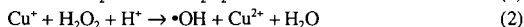
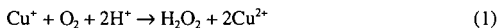
ABSTRACT

A system that uses the Cu(I)/Cu(II) couple and O₂ oxidizes alkanes, including methane, to alkyl ester in trifluoroacetic acid (TFA). Formation of an ester in large part protects the alkyl group from further oxidation, and the esters may then be hydrolyzed to the corresponding alcohol. We show that the system can be adapted to operate electrocatalytically with oxidation of alkane occurring in the cathodic compartment of an electrolysis cell due to the activation of O₂ by electrogenerated Cu(I) ions. The mechanism of the oxidation appears to involve alkyl radicals. Trapping by Cu(II) ions converts the alkyl radicals to the ester product. Alkyl radicals with 2 or more carbons may first convert to olefins which subsequently add TFA to give ester products. The results are compared with oxidation of alkanes in Cu(II)-H₂O₂-TFA.

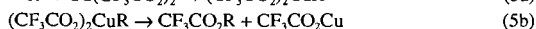
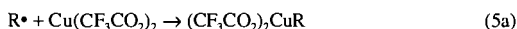
INTRODUCTION

Processes for directly and selectively oxidizing methane to methanol and alkanes to higher alcohols, instead of ketones and acids, could have enormous economic and environmental impacts. A major problem to be overcome is the high reactivity of alcohols toward oxidizing agents, relative to alkanes. Catalytica Advanced Technologies recently reported a significant conceptual advance: methane could be oxidized selectively to methyl sulfate using mercury or platinum catalysts in sulfuric acid.¹ This approach has been extended to other alkanes and ester-forming acids by other groups. Sen has reported extensively on the use of Pd(II) catalysis in TFA.² Also, Vargafik et al. observed Co(II)/Co(III) to be an effective oxidant in TFA.³ Simultaneously, Camaioni and Lilga developed a system based on the Cu(I)/Cu(II) couple and O₂.⁴ In all of these systems, formation of an ester in large part protects the alkyl group from further oxidation, and the esters may then be hydrolyzed to the corresponding alcohol.

The mechanisms of these oxidations are uncertain. The systems developed by Catalytica and by Sen are thought to involve non-radical electrophilic pathways in which metal ion oxidants directly activate the alkane C-H bond. In developing our Cu(I)/Cu(II)-O₂ oxidation system, we assumed free radical mechanisms operate analogous to Fenton-type reactions that operate in aqueous systems (Equations 1-5).

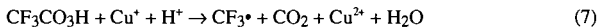
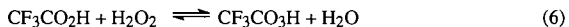


Rates of attack on functionalized substrates by strongly electrophilic radicals such as $\bullet\text{OH}$ and $\text{SO}_4^{\bullet-}$ show a pronounced dependence on the electronic character of the adjacent functional groups (see Table 1). Therefore, a viable system might involve electrophilic radicals abstracting H from alkanes to form organic radicals that subsequently convert to esters on oxidation by transition metal ions. The Cu(I)/Cu(II) couple is well suited for such a system in that O₂ rapidly oxidizes Cu(I) to Cu(II) and generates active oxidizing intermediates (Equation 1) and Cu(II) ions react non-selectively with alkyl radicals to form organocopper(III) intermediates that undergo reductive elimination to give esters or loss of a β -hydrogen to give an alkene (Equations 5a-c). Since TFA adds rapidly to alkenes (Equation 5d), esters are produced in either case.



In this paper, we present a study of alkane oxidation by the Cu(I)/Cu(II)-O₂-TFA system and by the complementary Cu(II)-H₂O₂-TFA system. The latter system was examined because H₂O₂

may be an intermediate in the former system. H_2O_2 reacts with TFA to make trifluoroperacetic acid (TFPA). TFPA oxidizes alkanes at room temperature without need for metal catalysis⁵ and the reactions are reported to occur without generation of alkyl radicals. Primary and methane C-Hs are relatively unreactive. However, Sen observed that addition of Pd(II) accelerated the rate and improved the yield methyl trifluoroacetate from methane.⁶ With respect to our system, reduction of TFPA by Cu(I) may result in decarboxylation (Equations 6 and 7) and initiation of free radical redox reactions.



PROCEDURES

Generally, experiments were performed in TFA solutions that contained the alkanes and other reagents as described below and in the Tables and Figures.

Oxidations promoted by reacting Cu(I) with O_2

In preliminary experiments, oxidations were promoted by reactive dissolution of Cu_2O and Cu metal in TFA solutions containing Cu(II) ions and alkane in contact with air or O_2 gas. Experiments were also performed by adding deoxygenated solutions of Cu(I) trifluoroacetate to solutions of alkane that were stirred under an O_2 atmosphere. See Table 2 for specific conditions and methods. To make the reactions catalytic in Cu ions, oxidations were run in an electrochemical cell that allowed for the generation of known amounts of Cu(I) at known rates without changing the total concentration of copper in the solution. Initial experiments simply used an open beaker with two platinum electrodes and a potentiostat operating in constant current mode. In subsequent experiments, we used a gas-tight, Teflon and glass cell (ca. 100 mL volume). Ports in the top of the cell admitted the electrodes and gas recirculation connections and allowed for gas/liquid sampling. The working electrode was a platinum mesh cylinder. The auxiliary electrode was a platinum mesh flag centered within the working electrode and separated from the working solution by a porous Vycor frit. The solution in the auxiliary electrode chamber was typically 1 M H_2SO_4 . A saturated calomel reference electrode was positioned next to the working electrode via a salt bridge with porous Vycor frit. The salt bridge contained 5 M KOC_2F_3 . Typically, the cell was operated at a potential of -0.1 V vs. SCE and a current of 50 mA. The cell was connected to a gas recirculation system that consisted of a MasterFlex pump with Teflon pump head and Teflon tubing and 5-L gas ballast that served to minimize changes in gas concentrations during experiments. Initial gas compositions were set with calibrated rotometers and verified by gas chromatography.

Oxidations using H_2O_2 -TFA

Solution experiments were conducted in 5 mL ampoules or in 8 mL screw-top sample vials with Teflon lined caps. Reaction mixtures were made by adding 200 μL of cyclohexane and 39.0 μL of 30% hydrogen peroxide to 2.00 mL of TFA or 2.00 mL of a TFA/Cu(II) stock solution. Anaerobic samples were degassed using three freeze-pump-thaw cycles, and the ampoules flame-sealed. For aerobic samples the head space was purged with oxygen after all components were added. Gas samples were taken using a Hamilton SampleLock™ syringe with a gas sampling needle. Gas analyses were performed by GC-MS and quantified by using an internal argon standard. 300 μL aliquots of each reaction solution were neutralized and the organic components extracted by adding the sample to a test tube containing approximately 0.7 g anhydrous sodium carbonate, 3 mL of dichloromethane and 10.00 μL of a decane in dichloromethane solution that served as an internal standard. After neutralizing the TFA, the dichloromethane layer was dried with magnesium sulfate and analyzed by gas chromatography.

Analyses

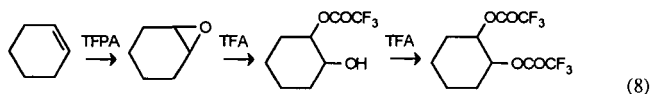
Gas chromatography was performed using an HP 5890 gas chromatograph with a 30-m HP-5MS capillary column (crosslinked 5% phenyl methyl silicone, 0.25 μm film thickness, 0.25 mm column i.d.). Chromatograms were recorded using an HP 5971 mass-selective detector. Gaseous components were quantified by using the mass-selective detector to extract ions unique to each component. All instrument responses were in the linear region of the respective calibration curves, and calibrations were verified periodically. ^1H NMR spectra were recorded at 300 MHz using a Varian VXR-300 spectrometer operating at 7.01 T with a standard 5 mm multinuclear broad band probe. ^1H NMR spectra in TFA were run unlocked, but were referenced

to cyclohexane and matched with spectra of mixtures prepared from authentic samples of cyclohexanol and 1,2-cyclohexanediol in TFA.

RESULTS

Several scoping experiments were performed to learn the potential of Cu promoted oxidations in TFA. Table 2 shows results for oxidations of methane and cyclohexane that were obtained under a variety of conditions. The results show that oxidations could be promoted by addition of Cu(I) solutions, Cu(I) oxides, or Cu(0) metal to solutions of Cu(II) and O₂. Consistent with a report by Vargaftik et al.,^{2a} no conversion was observed with O₂ and just Cu(II). In these experiments, the alkane was present in excess and Cu(I) was the limiting reagent. Therefore, the yields are calculated assuming a stoichiometry of 1 mole of product per 2 moles of Cu(I) ions. Addition of Cu(I) ions as solutions or solid Cu(I) oxides or Cu(0) metal causes the Cu(II) concentrations to increase and eventually precipitate. This situation can be circumvented by performing the oxidations in an electrolytic cell. The oxidations then become catalytic in Cu(I)/Cu(II) ions. The last entry in Table 2 shows a result obtained in a single compartment electrolytic cell. Here, Cu(II) is reduced to Cu(I) at the cathode and presumably water, present in solution, was oxidized at the anode. The 46% yield of cyclohexyl trifluoroacetate is based on the number of electrons discharged through the cell assuming that 2 electrons are required to produce 1 molecule of ester.

In addition to cyclohexyl trifluoroacetate, we observed lesser amounts of secondary oxidation products. Cyclohexanone was present in minor quantities, typically <2% of cyclohexyl trifluoroacetate. Of the possible disubstituted products, the mono and diester of *trans*-1,2-cyclohexanediol were dominant. The high regioselectivity for these secondary products probably is due to oxidation of cyclohexene. Epoxidation by TFPA is facile and subsequent reactions with TFA will give the monoester and diesters (Equation 8).



Electrocatalytic Oxidation of Cyclohexane in the Cu(II)-O₂-TFA System

We performed additional experiments in a divided electrolytic cell so that the cathodically-driven process could be studied, independent of processes occurring at the anode. The cell was closed from the atmosphere so that the gas composition could be controlled and analyzed as the oxidation proceeded. We were particularly interested in learning whether CO₂ was a byproduct. Its production would suggest a mechanism in which TFA is oxidized to CF₃• radicals. In which case, CF₃• or CF₃O₂• may attack alkane C-H bonds (e.g., Equations 9-11).



Figure 1 shows results obtained for cyclohexane oxidation that occurred in the cathodic compartment of the electrolytic cell. Moles of cyclohexyl trifluoroacetate and CO₂ are plotted against the moles of electrons discharged through the cell. CO₂ is a minor product relative to cyclohexyl trifluoroacetate. Therefore, Equations 9, 10 and 11 may contribute in a small way to the oxidation. Perhaps, having 10% water in the system and in situ generation of H₂O₂ favors reaction of Cu(I) with H₂O₂ rather than with CF₃CO₂H. The yield of cyclohexyl trifluoroacetate was found to be strongly dependent on the initial amount of O₂ in contact with the Cu(II) solution. Figure 2 shows the yields of monoester and diester for 3 cases: ~50 mL of air in the cathode compartment, cathode compartment recirculated with a 5-L volume of air, and cathode compartment recirculated with 5 L of O₂. The best yields were obtained with the smallest amount of O₂.

The Cu(II)-H₂O₂-TFA System

Reactions were run under aerobic and anaerobic conditions with and without Cu(II) ions present. Table 3 lists results for reactions run at 25 °C for 24 h. The first and second entries show results obtained with Cu(II) catalysis. The esters of cyclohexanol and *trans*-1,2-cyclohexanediol were the dominant cyclohexane products, and in contrast to the Cu(I)-O₂

system, yields of the diester exceeded yields of monoester. Anaerobic conditions and Cu(II) ions gave the highest yields and largest ratios of diester:monoester. Reactions run without Cu(II) ions gave predominantly monoester and showed little dependence on the presence or absence of O₂ (Table 3). Deno observed even greater preference for monoester using excess H₂O₂ (last entry of Table 3).⁵ NMR spectroscopy (¹H and ¹⁹F) of reaction mixtures showed that Cu(II) ions accelerated the oxidations. The NMR spectra also showed CF₃H was produced in significant quantities when reaction solutions were initially degassed. Gas chromatographic-mass spectral analyses of the gases above the reactions confirmed the identity of CF₃H and provided a measure of the amounts of CF₃H and CO₂ that were produced. The yields of CO₂ reported in Table 3 include dissolved CO₂, whereas yields of CF₃H in Table 3 represent only what was in the gas phase. Considering the solution NMR results, comparable amounts of CF₃H were in solution. The results show that yields of CF₃H were strongly dependent on O₂. Reactions that were run in the presence of O₂ generated little CF₃H, although yields of CO₂ were relatively unaffected when Cu(II) ions were present. Analysis of the results from Cu(II)-catalyzed reactions (Table 3) shows that reaction solutions that were initially degassed gave approximately 1 molecule of CO₂ per molecule of cyclohexane that converted. When O₂ was present initially, the stoichiometry was >1 (compare first and second entries of Table 3 and note that % yield of diester based on H₂O₂ is twice the % yield based on converted cyclohexane). When Cu(II) ions were absent and O₂ was present, the yield of CO₂ was very small. Finally, cyclohexane-d₁₂ was oxidized under anaerobic conditions to determine the fraction of CF₃H produced by Equation 9. In the absence of O₂, the ratio CF₃D/CF₃H was 20/1, both in the presence or absence of Cu(II) ions, showing that CF₃• radicals mainly had abstracted H from cyclohexane.

CONCLUSIONS

These experiments show that Cu ions are effective in promoting selective oxidation of alkanes to alkyl trifluoroacetate esters. Furthermore, it is possible to initiate oxidation in the cathodic compartment of an electrolysis cell making the oxidations catalytic in Cu and enabling continuous operation. The reactions appear to be Fenton-type systems in which oxidations of Cu(I) ion by O₂ and peroxide generate oxidizing species that abstract H to give organic radicals that react with Cu(II) converting to products and propagating a redox chain reaction (e.g., Equations 2-5). In the following discussion we reconcile observations and, in the end, comment on the mechanism of the uncatalyzed H₂O₂ system.

Distribution of Monoester and Diester from Cyclohexane

The distributions of mono and disubstituted products differ markedly for the Cu(I)-O₂-TFA and Cu(II)-H₂O₂-TFA systems. The former favors monoester and the latter favors diester. The former generates H₂O₂ in situ while the latter starts out with H₂O₂. These variations may be accommodated by a free radical redox chain reaction that involves Equations 1-3, 6, 7, 9-11, then 5a, and 5c followed by 5d and 8. Given that Equations 6 and 8 are facile, the different product distributions arise from how introduction of H₂O₂ affects the competing reactions. Presumably, in situ generation of H₂O₂ favors low steady-state concentrations of H₂O₂, such that Equation 6 is slow compared to Equation 2 and Equation 5d (with R(-H) = cyclohexene) is fast compared to Equation 8. Therefore, Equations 6-11 are not important in Cu(I)-O₂ oxidations. However, when starting with H₂O₂ as we do in the Cu(II)-H₂O₂-TFA system, TFA forms (Equation 6) in sufficient amounts such that Equation 8 competes effectively with Equation 5d.

Factors Affecting Yields

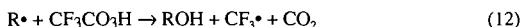
The yields of products have been calculated based on reducing equivalents used in the Cu(I)-O₂ system or H₂O₂ used in the Cu(II)-H₂O₂ system. These yields were generally less than 100% due to reactions that consume reagent without generating alkyl radicals. Equation 4 is an example of such a reaction. Liotta and Hoff observed that solutions of 30% H₂O₂/water in TFA decompose with generation of CF₃H.⁷ Apparently, the decomposition involves radical reactions that serve to initiate alkane oxidations when Cu(II) ions are present or O₂ is absent.

Effects of O₂

O₂ affects the reaction systems in various ways. First of all, it is required when peroxide is not a reagent. Even so, its effect in the electrocatalyzed system is curious in that yields of monoester vary inversely with the amount of available oxygen, i.e., the system is more efficient when starved for oxygen. Other products do not appear with increasing O₂. Therefore, we assume that reduction to water occurs. If so, then it may be that higher concentrations of O₂ allow direct reduction at the cathode and/or greater fractions of Equations 1 and 2 to occur near

the electrode surface where the $\bullet\text{OH}$ is reduced to water much faster than it is scavenged by alkane.

When peroxide is a reagent, the effects of O_2 are complex and not fully understood. In the absence of O_2 , CF_3H and CO_2 were produced in amounts that were comparable to the alkyl esters, and when cyclohexane- d_{12} was used, $\text{CF}_3\text{D}/\text{CF}_3\text{H}$ ratios of >20 were obtained. These observations are consistent with a radical chain decomposition in which propagation steps include: attack on RH by $\text{CF}_3\bullet$; and oxidation of $\text{R}\bullet$ by Cu(II) if present and by $\text{CF}_3\text{CO}_3\text{H}$ if Cu(II) is absent (Equation 12).⁸



When O_2 and Cu(II) ions are present, less CO_2 and little CF_3H were produced. Probably $\text{CF}_3\bullet$ radicals are scavenged by O_2 leaving the less reactive $\text{CF}_3\text{O}_2\bullet$ radical to propagate the reaction (Equation 11). The mechanism in the presence of O_2 and absence of Cu(II) is most uncertain. A dilemma that any radical mechanism must overcome is explaining how cyclohexanol⁸ and then ester are produced without making cyclohexanone and CO_2 . Perhaps, O_2 serves to inhibit the radical chain pathway and allow heterolytic pathways to operate.^{5,8}

ACKNOWLEDGEMENTS

This research was supported by the Advanced Energy Projects program of the U. S. Department of Energy. The Pacific Northwest National Laboratory is a multiprogram national laboratory operated by Battelle Memorial Institute under Contract No. DE-AC06-76RLO 1830.

REFERENCES

1. (a) Periana, R. A.; Evitt, E. R.; Taube, H. "Process for Converting Lower Alkanes to Esters" U.S. Patent No. 5,233,113, Aug. 3, 1993. (b) Periana, R. A.; Taube, D. J.; Evitt, E. R.; Loffler, D. G.; Wentreck, P. R.; Voss, G.; Masuda, T. *Science* **1993**, 259, 340-3. (c) Periana, R. A.; Taube, D. J.; Taube, H.; Evitt, E. R., *Catalytica*, "Catalytic Process for converting Lower Alkanes to Esters, Alcohols, and to Hydrocarbons" U.S. Patent No. 5,306,855, Apr. 26, 1994. (d) Periana, R. A.; Taube, D. J.; Gamble, S.; Taube, H.; Satoh, T.; Fuji, H. *Science* **1998**, 280, 560-4.
2. (a) Hogan, T.; Sen, A. *J. Am. Chem. Soc.* **1998**, 119, 2642-2646. (b) Sen, A. *Acc. Chem. Res.* **1998**, 31, 550-557. (c) Lin, M.; Hogan, T.; Sen, A. *J. Am. Chem. Soc.* **1997**, 119, 6048-6053.
3. (a) Vargaftik, M. N.; Stolarov, I. P.; Moiseev, I. I. *J. Chem. Soc., Chem. Commun.* **1990**, 1049-1050. (b) Gretz, E.; Oliver, T. F.; Sen, A. *J. Am. Chem. Soc.* **1987**, 109, 8109-11.
4. Camaioni, D. M.; Lilga, M. A. U.S. Patent No. 5,585,515, 1996; U.S. Patent No. 5,708,246, 1998; U.S. Patent No. 5,786,505, 1998.
5. Deno, N. C.; Jedziniak, E. J.; Messer, L. A.; Meyer, M. D.; Stroud, S. G.; Tomczesko, E. S. *Tetrahedron* **1977**, 33, 2503-8.
6. (a) Ref. 2a. (b) Sen, A. *Platinum Metals Rev.* **1991**, 35, 126. (c) Kao, L.-C.; Hutson, A. C.; Sen, A. *J. Am. Chem. Soc.* **1991**, 113, 700.
7. Liotta, R.; Hoff, W. S. *J. Org. Chem.* **1980**, 45, 2887-2890.
8. Deno reported cyclohexanol is initially produced (see Ref. 5). Using ^1H NMR, we too observed it to form and esterify in successive steps.

Table 1. Rate Constants^(a) for H-Abstraction from CH₃-X by HO• and SO₄^{-•}

X	HO•	SO ₄ ^{-•}
	<i>k</i> /10 ⁸ M ⁻¹ s ⁻¹	<i>k</i> /10 ⁶ M ⁻¹ s ⁻¹
-OH	9.6	10
-CH ₃ ^(b)	7	2.2
-OCOMe ^(c)	2.2	
-H	0.9	<0.8
-OSO ₃ ⁻	0.5	
-CO ₂ H	0.17	0.014

^(a)From Notre Dame Radiation Laboratory Radiation Chemistry Data Center (<http://www.rcdc.nd.edu/>). ^(b)Total rate constant divided by 2. ^(c)Attack on the acetoxy methyl group is neglected; see value for acetic acid.

Table 2. Yields of Alkyl Ester from Cu(I) Promoted Oxidation in Trifluoroacetic Acid^(a)

Alkane	% ^(b)	Method
Methane	5	Dissolution of Cu ₂ O under 1 atm. of 80/10/10 CH ₄ /O ₂ /N ₂
	9	Addition of CF ₃ CO ₂ Cu solution to 13 atm. 26/1 CH ₄ /O ₂
Cyclohexane ^(c)	17	Addition of CF ₃ CO ₂ Cu to solution stirred in air
	19	Dissolution of solid Cu ₂ O in air
	30	Comproportionation of Cu(0) and Cu(II) in air
	46	Electrolysis of Cu(II) solution in air

^(a)Solutions contained 10 vol% H₂O. ^(b)Based on Cu(I) added assuming 2 moles Cu(I) consumed per mole of ester formed. ^(c)Cyclohexane ~1 M.

Table 3. Oxidation of Cyclohexane in H₂O₂-TFA: Effects of Cu(II) and O₂

Cu(II) M	P _{O₂} Atm	% Yield ^(a)			
		Monoester	Diester	CO ₂	CF ₃ H
0.05	1	7	18	34	0.1
0.05	0	9	52	38	15
0	1	28	10	2	-0.1
0	0	32	10	34	20
0 ^(b)	0.2	66	5	nd ^(c)	nd

^(a)See note (a) in Table 3. ^(b)Deno, et al.,⁵ no Cu ions and [H₂O₂]/[C₆H₁₂] = 1.15.

^(c)not determined.

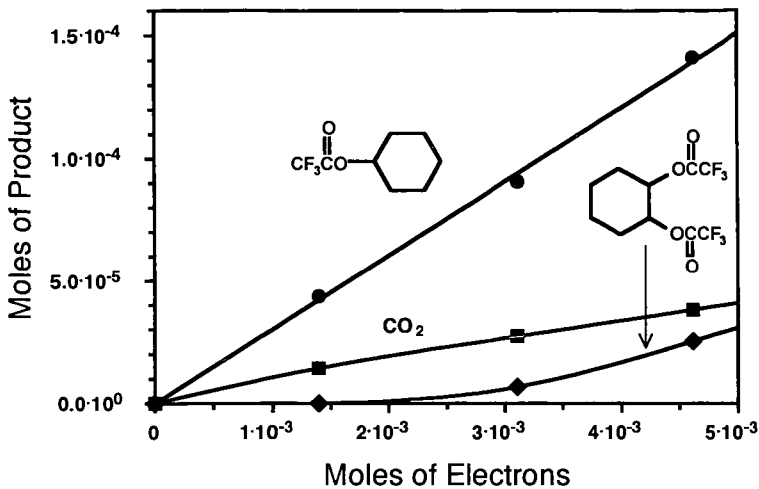


Figure 1. Cu(I)/Cu(II) promoted oxidation of cyclohexane to esters of cyclohexanol (●) and *trans*-1,2-cyclohexanediol (◆) and TFA to CO₂ (■) in the cathodic compartment of a closed, divided electrolysis cell. Conditions: 0.09 M cyclohexane, 0.08 M Cu(II), 10wt% H₂O/TFA, 2.2×10⁻³ moles O₂, E_{applied} = -0.1V vs. SCE.

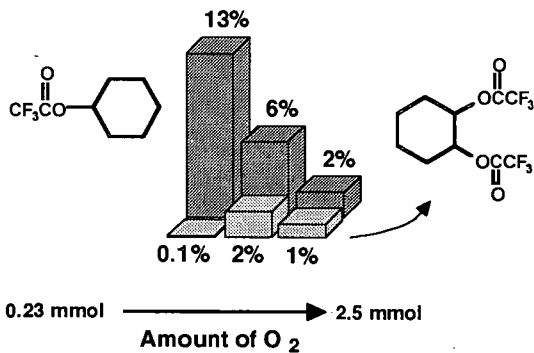


Figure 2. Effect of O₂ contacted with solution on ester yields (% moles product per mole e⁻ discharged). Conditions: 0.09 M cyclohexane, 0.08 M Cu(II), 10wt% H₂O/TFA, 6×10⁻³ moles e⁻ discharged at E_{applied} = -0.1V vs. SCE.

ESTIMATING THE HEATS OF FORMATION OF HYDROCARBON RADICALS BY A SEMIEMPIRICAL CALCULATION

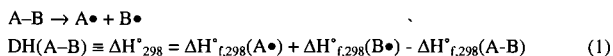
Xiaoliang Ma, and Harold H. Schobert
The Energy Institute, The Pennsylvania State University,
409 Academic Activities Building, University Park, PA 16802

KEYWORDS: hydrocarbon radical, heat of formation, molecular simulation

INTRODUCTION

Hydrocarbon free radicals play a very important role in many thermal-chemistry processes, including combustion, petroleum and coal coking, coal liquefaction and pyrolysis, oil shale retorting, thermal stability of fuels as well as free radical polymerization. To obtain heats of formation (ΔH_f°) of the radicals is very essential for the fundamental understanding of thermal chemistry and mechanism of the free radical process. Many experimental methods have been developed to determine ΔH_f° of free radicals, including halogenation kinetics, polyani relation, chemical activation, equilibrium study, electron-impact measurement, radical buffer, appearance energy, photoacoustic calorimetry, electrochemistry etc.[1-3]. However, the experimental determination of ΔH_f° of free radicals is complicated, difficult and expensive due to the instability of the radicals. In consequence, many approaches have been developed to estimate ΔH_f° of the radicals.

Three principal methods have been developed to estimate ΔH_f° of free radicals. The first method, and also the best characterized, is Benson's group additivity method [4], which estimates the ΔH_f° by summing the contributions of the heats of formation of the various groups, and correcting for various higher order interactions via "correction" terms. The second method is the bond-dissociation-energy (BDE) method that was reviewed in detail by McMillen and Golden in 1982 [5]. BDE is defined as:



According to equation (1), $\Delta H_{f,298}^\circ(A\cdot)$ can be calculated if $DH(A-B)$, $\Delta H_{f,298}^\circ(A-B)$ and $\Delta H_{f,298}^\circ(B\cdot)$ are known. For the estimation of prototypical primary, secondary and tertiary alkyl radicals, McMillen and Golden recommended 98, 95 and 92 kcal/mol for $DH(\text{primary C-H})$, $DH(\text{secondary C-H})$ and $DH(\text{tertiary C-H})$, respectively. For allyl or aryl radicals, a correction term, "resonance stabilization energy" (RSE), was used.

Although both of these empirical estimation methods for hydrocarbon radicals are very common in the chemical literature, the accuracy of the methods is unsatisfactory. Recently, molecular orbital methods have been developed and used to calculate ΔH_f° of compounds, including neutral molecules, ions and radicals. There are two main molecular orbital methods, *ab initio* and semiempirical methods. Of these, the *ab initio* method, having no need for empirically determined parameters, is the more theoretically "pure". However, *ab initio* methods are currently slow, and routine application at any reasonable degree of accuracy to systems of larger molecule and to the calculation of a large number of molecules is still not practical. The semiempirical methods are fast enough for routine application to quite large systems, and to a large number of molecules. With the heats of formation of systems related to those for which the semiempirical methods were parameterized, the accuracy of semiempirical methods is comparable with that of quite large basis set *ab initio* calculations [6].

In 1989, Stewart developed the MNDO-PM3 method for further optimizing parameters of semiempirical methods [7,8]. Stewart calculated the ΔH_f° of 7 hydrocarbon radicals by using this method. The average difference between the calculated and experimental values is 6.24 kcal/mol. In 1996, Camaioni et al. calculated ΔH_f° of 19 hydrocarbon free radicals by the MNDO-PM3 method, and correlated the calculated values with the experimental values [9]. They found that the errors are systematic for families of structurally related radicals.

In this study, we attempt to develop a new method for estimating the ΔH_f° of the prototypical hydrocarbon free radicals. The new estimation method, called PM3-systematic-correlation (PM3-SC) method, is based on both the MNDO-PM3 calculation and correlation between the calculated values and the experimental values from the literature. The errors in Benson's, DBE and MNDO-PM3 and PM3-SC methods are also compared and discussed in detail via statistical analysis.

COMPUTATIONAL METHODS

All quantum chemistry calculations in this study were performed by means of the semiempirical MNDO-PM3 method [7,8], using CAChe MOPAC, version 94. Geometry of the radicals was optimized by using EF method, and the corresponding ΔH_f° of hydrocarbon free radicals were calculated by using doublet multiplicity.

SOURCES OF EXPERIMENTAL DATA

The experimental data are from the available literature. As the experimental data from different sources are somewhat inconsistent with each other, we made the widest possible use of currently common and accepted ones [1-3,5,9-12]. Some of ΔH_f° of alkyl radicals were determined by the empirical BDE method using new BDE parameters reported by Seakins et al. [3] ($DH(\text{primary C-H})=101.05$, $DH(\text{secondary C-H})=98.26$, $DH(\text{tertiary C-H})=96.44$ kcal/mol).

RESULTS AND DISCUSSION

MNDO-PM3-calculated Results and Correlation with Experimental Data

The ΔH_f° values of 46 hydrocarbon free radicals, including primary alkyl, secondary alkyl, tertiary alkyl, alkenyl, aryl and cycloalkyl radicals, were calculated in this study by MNDO-PM3 method. Figure 1 plots the MNDO-PM3-calculated ΔH_f° vs. the experimental ΔH_f° for 46 hydrocarbon free radicals. As a whole, a considerable scatter exists with an R^2 value of 0.9535 and average errors of ± 10.57 kcal/mol. However, after examining the data, it is found that the structurally related radicals exhibit a very good linear correlation, as shown in Figure 1. According to the structural analogy of the radicals and the correlation, we can separate the 46 radicals into 5 groups. The first group consists of 15 primary alkyl radicals, including *n*-alkyl, *i*-alkyl, olefinic and phenylalkyl radicals with the experimental ΔH_f° values from 8 to 56 kcal/mol. A very good linear correlation between the experimental and calculated values was made by the least square fit with an R^2 value of 0.9982, although the calculated values are about 10 kcal/mol lower than the corresponding experimental values. The second group contains the secondary and tertiary radicals with an R^2 value of 0.9986. The MNDO-PM3-calculated values in this group are about 15-16 kcal/mol lower than the corresponding experimental values. The third group contains three cycloalkyl secondary radicals with an R^2 value of 0.9999. Alkenyl and aryl radicals together constitute the fourth group with an R^2 value of 0.9984, except for the 1-naphthylmethyl radical. The 1-naphthylmethyl radical deviates slightly from the regression line. Whether this deviation comes from the MNDO-PM3 calculation or from the experiment is still unclear. The last group consists of three cycloalkenyl radicals with an R^2 value of 0.9998.

The regression lines for alkyl radical groups, including the first, second and third groups, exhibit a similar slope, around 1.0, but with the corresponding intercepts different, being 11.71, 17.79 and 18.61 kcal/mol, respectively. The fourth group (alkenyl and aryl radicals), with intercept of 10.69 kcal/mol, shows the highest slope in all five groups, being 1.26. The group correlation reflects that the errors between MNDO-PM3-calculated and experimental values are systematic and dependent on the families of structurally related radicals. This finding allows one to be able to improve the accuracy of the estimates through scaling the calculated values. The linear regression equation for each group was obtained by a least squares fit. Using these regression parameters to scale the ΔH_f° calculated by the MNDO-PM3 method leads to a very significant reduction of the average error of the estimates, from ± 10.574 to ± 0.453 kcal/mol for the 45 hydrocarbon radicals.

Comparison of Different Estimation Methods Based on Statistical Analysis

In order to compare the errors from different estimation methods, the ΔH_f° values estimated by using Benson's, BDE and MNDO-PM3 methods, respectively, were also calculated. The calculation of ΔH_f° by Benson's method was performed according to reference [4]. The ΔH_f° values estimated by BDE method come from the review by McMillan and Coldren in 1982⁵. Statistical analysis of the errors for each methods was conducted. The experimental values vs. estimated values by Benson, BDE and MNDO-PM3 methods are plotted in Figure 2, 3 and 1, respectively.

With Benson's method, the expectation of errors is -2.901 kcal/mol, indicating the values estimated by this method are lower than the experimental values by about 3 kcal/mol as a whole. These errors can be attributed to that the experimental data used in specifying the group contribution to the ΔH_f° of the radicals in Benson's method are lower. For example, the experimental ΔH_f° values recommended in Benson's method were 26.5, 21.0, 17.6 and 8.4 kcal/mol for ethyl, *n*-propyl, *i*-propyl and *t*-butyl radicals, respectively, while recently, 28.9, 24.0,

21.5 and 12.2 kcal/mol were used instead [3]. The standard derivation of the errors in Benson's method is 1.909 kcal/mol, and thus, is scattered and unsatisfactory as Benson's method considers only the interaction between two linked atoms (short-range effect) and neglects the effect of interval atoms in the molecule (long-range effect).

The ΔH_f° values calculated by BDE method give an expectation of errors of -1.033 kcal/mol. It is still larger although being better than that for Benson's method. However, the standard derivation of the errors in this method is larger, being 2.497 kcal/mol. The errors in this empirical method are probably as the results of both using lower BDE values and using the BDE values derived from simple molecules to different and more complex molecules.

The ΔH_f° values estimated by MNDO-PM3 method exhibit larger errors. The expectation of errors is -8.108 kcal/mol, and the standard derivation is 8.908 kcal/mol, indicating that the ΔH_f° values calculated by the MNDO-PM3 method have to be scaled before use.

In all four methods discussed in this study, the PM3-SC method developed in this study gives the most accurate estimates, as shown in Figure 4. The expectation of errors is -0.001 kcal/mol, and the standard derivation is 0.575 kcal/mol. The statistical analysis indicates that we can use the PM3-SC method to estimate ΔH_f° of hydrocarbon radicals with a standard derivation below 0.60 kcal/mol. In other words, we can be 95 % confident that the difference between the estimated and experimental values is in the interval of ± 1.12 kcal/mol.

CONCLUSIONS

The families of structurally related radicals exhibit a very good linear correlation between the experimental and MNDO-PM3-calculated ΔH_f° values with the R^2 values higher than 0.998. On the basis of the MNDO-PM3 calculations, experimental data and statistical analysis, a new semi-empirical method, the PM3-SC method, has been developed to estimate ΔH_f° of hydrocarbon free radicals. The PM3-SC method can be used to estimate the ΔH_f° for almost all hydrocarbon radicals, including primary-alkyl, secondary-alkyl, tertiary-alkyl, alkenyl and aryl radicals. The PM3-SC method greatly improves the estimation accuracy and gives an average error of ± 0.453 kcal/mol only for the 46 hydrocarbon radicals, while the Benson's, BDE and MNDO-PM3 methods give the average error of ± 3.18 , ± 2.07 and ± 10.57 kcal/mol, respectively. The statistical analysis shows that with the PM3-SC method the difference between the experimental and estimated values is in the interval of ± 1.12 kcal/mol with 95 % confidence.

ACKNOWLEDGMENTS

This work was supported by the U.S. Department of Energy, Pittsburgh Energy Technology Center, and the Air Force Wright Laboratory/Aero Propulsion and Power Directorate, Wright-Patterson AFB. Funding was provided by the U.S. DOE under Contract DE-FG22-92104.

REFERENCES

1. Lias, S. G.; Bartmess, J. E.; Liebman, J. F.; Holmes, J. L.; Levin, R. D.; Mallard, W. G. *J. Phys. Chem. Ref. Data* **1988**, *17*.
2. Wayne, D. D. M.; Griller, D. *Free Radi. Thermochem.*; Tanner, D. D. Ed.; JAI Press Inc.: London, **1990**; Vol. 1, pp 159-192.
3. Seakins, P.; Pilling, M. J. *J. Phys. Chem.* **1992**, *96*, 9847-9855.
4. Benson, S. W. *Thermochemical Kinetics*; John Wiley & Sons: New York, London, Sydney, Toronto, 1976.
5. McMillen, D. F.; Golden, D. M. *Ann. Rev. Phys. Chem.* **1982**, *33*, 493-522.
6. Dewar, M. J. S.; Storch, D. M. *J. Am. Chem. Soc.* **1985**, *107*, 3898.
7. Stewart, J. J. P. *J. Comp. Chem.* **1989**, *10*, 209-220.
8. Stewart, J. J. P. *J. Comp. Chem.* **1989**, *10*, 221-264.
9. Camaioni, D. M.; Autrey, S. T.; Salinas, T. B.; Franz, J. A. *J. Am. Chem. Soc.* **1996**, *118*, 2013-2022.
10. Tsang, W. *J. Am. Chem. Soc.* **1985**, *107*, 2872-2880.
11. Freund, H. and Olmstead, W. N. *Intern. J. Chem. Kine.* **1989**, *21*, 561-574.
12. Tsang, W. *J. Phys. Chem.* **1986**, *90*, 1152-1155.

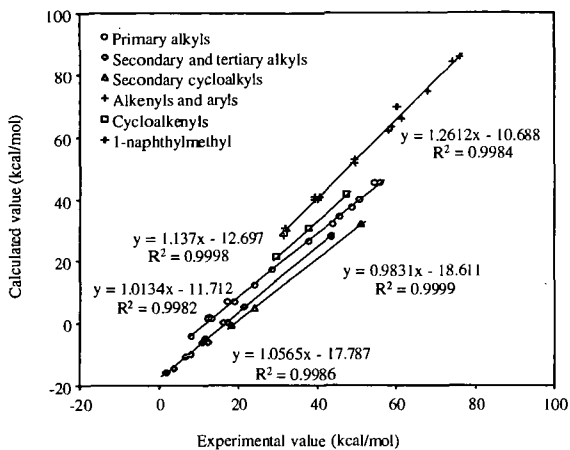


Figure 1 Correlation of MNDO-PM3-calculated ΔH_f° and experimental ΔH_f°

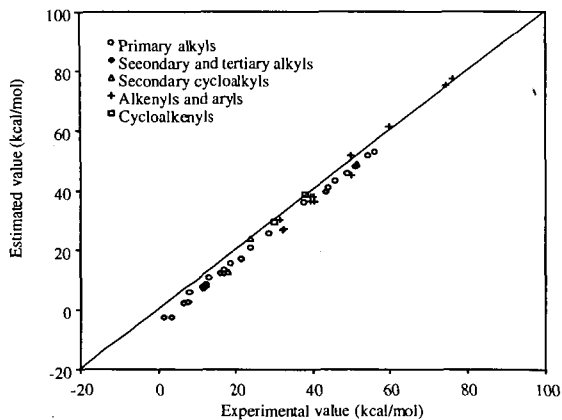


Figure 2 Benson-estimated ΔH_f° vs experimental ΔH_f° for hydrocarbon radicals

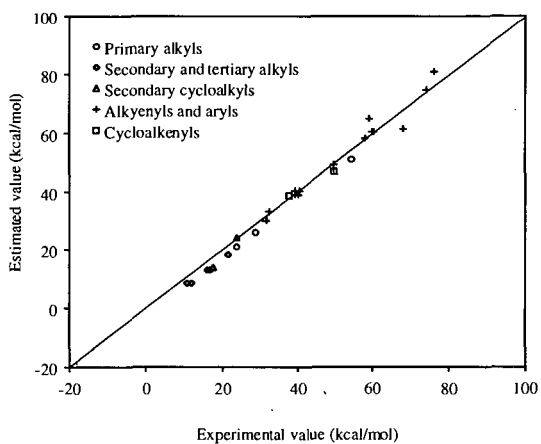


Figure 3 BDE-estimated ΔH°_f vs experimental ΔH°_f for hydrocarbon radicals

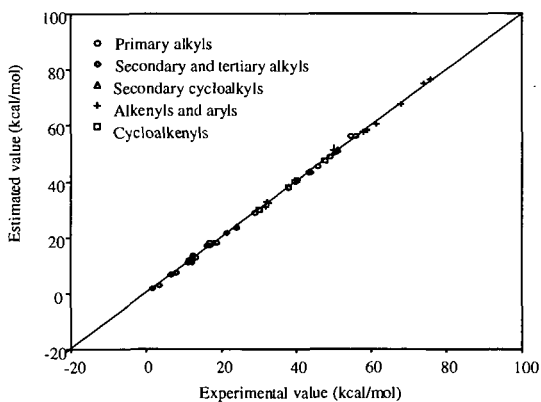


Figure 4 PM3-SC-estimated ΔH°_f vs experimental ΔH°_f for hydrocarbon radicals

ESTIMATING THE ACTIVATION ENERGY FOR HYDROGEN ABSTRACTION REACTIONS BY A SEMIEMPIRICAL CALCULATION

Xiaoliang Ma, and Harold H. Schobert
The Energy Institute, The Pennsylvania State University,
University Park, PA 16802

KEYWORDS: hydrogen abstraction, activation energy, molecular simulation

INTRODUCTION

Free radical processes play very important roles in thermal chemistry in combustion, petroleum and coal coking, coal liquefaction and pyrolysis, oil shale retorting, thermal stability of fuels as well as free radical polymerization. One of the most important elementary reactions in free radical processes is hydrogen abstraction, which involves hydrogen transfer from a hydrogen donor to a hydrogen acceptor (a radical). In a companion paper [1], we have reported our approach to estimating the heats of formation of hydrocarbon radicals. In this paper, we will report our approach to the kinetics of free radical reactions. This work is focused on the estimation of activation energy (E_a) for hydrogen abstraction reactions. To obtain the activation energy of hydrogen abstraction reactions is very essential for the fundamental understanding of hydrogen transfer mechanism, and for the evaluation of hydrogen-donation abilities of hydrogen donors and hydrogen-acceptation ability of radicals. However, experimental methods to determine the activation energy are complicate and difficult, as the radicals are very unstable. Molecular simulation approaches to the hydrogen abstraction reactions have been reported [2-5]. By using the MNDO-PM3 method, Camaioni et al. calculated the heats of formation of the transition states ($\Delta H_f^\circ(\text{TS})$) for 22 hydrogen abstraction reactions [6]. From the correlation of experimental and calculated $\Delta H_f^\circ(\text{TS})$ values, they obtained a linear regression equation:

$$\Delta H_{f,\text{calcd}}^\circ(\text{TS}) = 1.143\Delta H_{f,\text{exptl}}^\circ(\text{TS}) - 8.256 \text{ kcal/mol} \quad (1)$$

In the present study, our objective was to develop a new method for estimating the activation energy (E_a) of the hydrogen abstraction reactions between hydrocarbon radicals and hydrocarbon compounds on the basis of the MNDO-PM3 calculation, experimental data from the literature, transition-state theory and statistical analysis.

COMPUTATIONAL METHODS

All quantum chemistry calculations in this study were performed by using a semiempirical method, MNDO-PM3 method [7,8], in CAChe MOPAC, Version 94. Geometry of the radicals was optimized by using EF method, and the corresponding heats of formation (ΔH_f°) of hydrocarbon free radicals were estimated by the method reported in the other our paper [1]. Geometry of the transition states was located by using the Saddle Calculation method followed by the Minimize Gradient method, and the corresponding $\Delta H_f^\circ(\text{TS})$ was calculated. Calculation of the activation energy is based on the transition-state theory:

$$E_a = \Delta H^\ddagger + (1-\Delta\nu^\ddagger) RT \quad (2)$$

The standard activation enthalpy (ΔH^\ddagger) was calculated by the equation (3):

$$\Delta H^\ddagger = \Delta H_f^\circ(\text{TS}) - \sum \Delta H_f^\circ \text{reactant} \quad (3)$$

For the bimolecular reaction, the $\Delta\nu^\ddagger$ value is -1.

SOURCES OF EXPERIMENTAL DATA

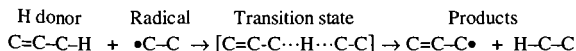
The experimental E_a values are from the available literature. As the data from different sources are somewhat inconsistent, we made the widest possible use of currently common and accepted experimental data. The main sources are from the reference 6 and 9. The experimental values of $\Delta H_f^\circ(\text{TS})$ were calculated by summing the activation enthalpy and ΔH_f° of the reactants:

$$\begin{aligned} \Delta H_{f,\text{exptl}}^\circ(\text{TS}) &= \Delta H^\ddagger + \sum \Delta H_f^\circ \text{reactant} \\ &= E_{a,\text{exptl}} - (1-\Delta\nu^\ddagger) RT + \sum \Delta H_f^\circ \text{reactant} \end{aligned} \quad (4)$$

RESULTS AND DISCUSSION

Hydrogen Abstraction Reaction

A representative hydrogen abstraction reaction of propene and ethyl radical is shown as follows:



In this reaction, ethyl radical (hydrogen acceptor) abstracts a hydrogen atom from propene (hydrogen donor). The corresponding configurations and spin densities for the reactants, transition state and products are shown in Figure 1. The TS structure has linear-centered C-H-C bonds with pyramidal C atoms intermediate between sp^2 and sp^3 with the bond length of 1.307 and 1.322 Å for $C_{\text{propene-H}}$ and $C_{\text{ethane-H}}$, respectively. The spin density indicates the location of the free radical (distribution of SOMO). In the TS structure, the radical is relocated on both C_{propene} and C_{ethane} atoms.

Heats of Formation of Transition States ($\Delta H^\ddagger(\text{TS})$)

The heats of formation of the transition states for 37 hydrogen abstraction reactions were calculated by the MNDO-PM3 method. The radicals involved in these reactions include alkyl, allyl and benzyl radicals.

As a whole, a considerable scatter exists, as shown in Figure 2 and 3, and the average error is ± 5.16 kcal/mol for the 37 transition states. However, we observed that the analogous reactions exhibit a very good linear correlation between experimental and calculated values. According to this observation, we can separate the 37 hydrogen abstraction reactions into 6 groups as follows:

Group	Radical	H donor
1	methyl	alkyl-H
2	methyl	alkenyl-H (or aryl-H)
3	ethyl (or propyl)	alkyl-H
4	ethyl (or propyl)	alkenyl-H (or aryl-H)
5	benzyl	alkyl-H or phenylalkyl-H
6	benzyl	partially hydrogenated polyaromatics

The least square fit was made for each group, with the R^2 values of 0.995, 0.999, 0.997, 0.995, 1.000 and 1.000, respectively. The group correlation reflects that the errors between PM3-calculated and experimental values are systematic and dependent on the reaction types. This finding allows one to be able to improve the accuracy of the estimates by scaling the $\Delta H^\ddagger(\text{TS})$ values calculated from MNDO-PM3 method. By using the regression parameters to scale the calculated $\Delta H^\ddagger(\text{TS})$, much accurate estimates are obtained with an average error of ± 0.33 kcal/mol for the 37 hydrogen abstraction reactions. We call this new method as PM3-systematical-correlation method (PM3-SC method).

Activation Energies for Hydrogen Abstraction Reactions

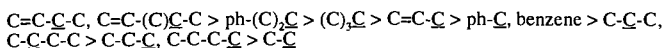
On the basis of the transition-state theory, the activation energies for the 37 hydrogen abstraction reactions have been estimated by the equation (2) using scaled $\Delta H^\ddagger(\text{TS})$ values. The estimated E_a in comparison with the experimental data from the literature are shown in Figure 4 for methyl, ethyl, propyl and benzyl as a hydrogen acceptor, respectively. In order to compare the errors from different estimation methods, the E_a values estimated by MNDO-PM3 method and Camaioni's method (using the linear regression (1) to scale the MNDO-PM3-calculated $\Delta H^\ddagger(\text{TS})$ values) are also shown in Figure 4. Statistical analysis of the errors for each method was conducted.

MNDO-PM3 method has an average error of ± 2.07 kcal/mol with the standard deviation of 2.71 kcal/mol. Camaioni's method shows lower average error than MNDO-PM3 method, being ± 1.69 kcal/mol with the standard deviation of 1.78 kcal/mol. In all three methods, our PM3-SC method gives the highest estimation accuracy with the average error of ± 0.24 kcal/mol and the standard deviation of 0.31 kcal/mol. In other words, with PM3-SC method, we can be 95 % confident that the difference between the estimated and experimental values is in the interval between -0.57 and $+0.63$ kcal/mol.

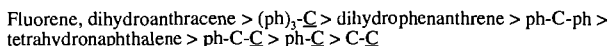
Evaluation of both Hydrogen-donation Ability of Hydrogen Donors and Hydrogen-acceptation Abilities of Radicals

The E_a value for hydrogen abstraction reactions is dependent on both the hydrogen-donation ability of hydrogen donors and the hydrogen-acceptation ability of the radicals. Using the same radical, the hydrogen-donation ability of the hydrogen donors is inversely proportional to the E_a ,

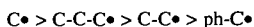
while using the same hydrogen donor, the hydrogen-accepting ability of the radical is inversely proportional to the E_a . Consequently, on the basis of analysis of the estimated E_a values for different hydrogen abstraction reactions, we can quantitatively evaluate both the hydrogen-donation ability of hydrogen donors and the hydrogen-accepting ability of radicals. By comparing the E_a values for hydrogen abstraction reactions with methyl radical as a hydrogen acceptor (the group 1 and 2), we can give the hydrogen-donation abilities of the hydrogen donors in the order as follows:



The underlined C atoms label the position of the donated hydrogen. By comparing the E_a values for hydrogen abstraction reactions with benzyl radical as a hydrogen acceptor (the group 5 and 6), we can give the hydrogen-donation abilities of other hydrogen donors in the order as follows:



On the other hand, by comparing the E_a values for hydrogen abstraction reactions using the same hydrogen donor (e.g. ethan) and different radicals, we can give the hydrogen-accepting abilities of the radicals in the order as follows:



Thus, we can use this method to expect quantitatively both the hydrogen-donation ability of other hydrogen donors and the hydrogen-accepting ability of other radicals.

CONCLUSIONS

After calculating $\Delta H^\ddagger(\text{TS})$ values for the 37 hydrogen abstraction reactions by MNDO-PM3 method and correlating them with the experimental data from the literature, it was found that the analogous reactions exhibit a very good linear correlation between experimental and calculated $\Delta H^\ddagger(\text{TS})$ values with the R^2 values higher than 0.994. On the basis of the MNDO-PM3 calculation, experimental data, transition state theory and statistical analysis, a new semiempirical method, PM3-SC method, has been developed to estimate the E_a for hydrogen abstraction reactions with an average error below ± 0.24 kcal/mol. The 95% confidence limits of the difference between the estimated and experimental E_a values is in the interval between -0.57 and +0.63 kcal/mol. The estimated E_a can be used to evaluate quantitatively the hydrogen-donation ability of hydrogen donors and the hydrogen-accepting ability of radicals.

ACKNOWLEDGMENTS

This work was supported by the U.S. Department of Energy, Pittsburgh Energy Technology Center, and the Air Force Wright Laboratory/Aero Propulsion and Power Directorate, Wright-Patterson AFB. Funding was provided by the U.S. DOE under Contract DE-FG22-921104.

REFERENCES

1. Ma, X. and Schobert, H. H. *Prep. Div. Fuel Chem., ACS* **1999**, in press
2. Yamataka, H., Nagase, S. *J. org. Chem.* **1988**, *53*, 3232-3238.
3. Chen, Y. and Tschuikow-Roux, E. *J. phys. Chem.* **1993**, *97*, 3742-3749.
4. Franz, J. A., Ferris, K. F., Camaioni, D. M. and Autrey, S. T. *Energy Fuels* **1994**, *8*, 1016-1019.
5. Logan, C. F. and Chen, P. *J. Am. Chem. Soc.* **1996**, *118*, 2113-2114.
6. Camaioni, D. M.; Autrey, S. T.; Franz, J. A. *J. Am. Chem. Soc.* **1996**, *118*, 2013-2022.
7. Stewart, J. J. P. *J. Comp. Chem.* **1989**, *10*, 209-220.
8. Stewart, J. J. P. *J. Comp. Chem.* **1989**, *10*, 221-264.
9. Allara, D. L. and Shaw, R. *J. Phys. Chem. Ref. Data* **1980**, *9*, 523

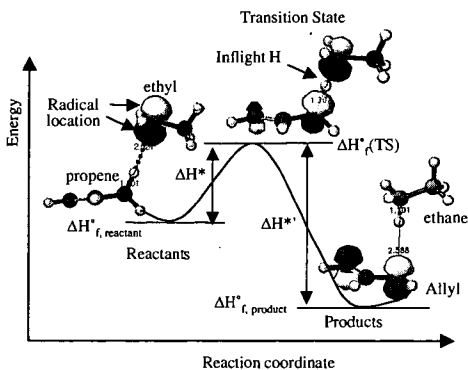


Figure 1 Configurations and spin densities for hydrogen abstraction reaction of propene and ethyl radical

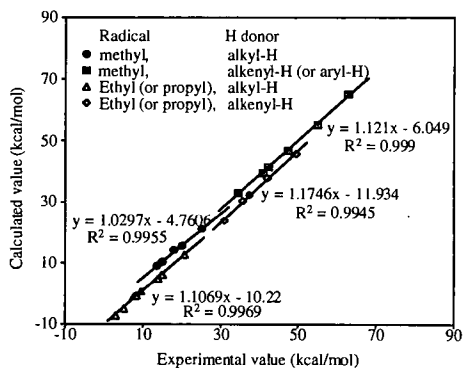


Figure 2 Systematic correlation of experimental and calculated $\Delta H^{\circ}_f(\text{TS})$ for H Abstraction with alkyl radicals as H acceptors

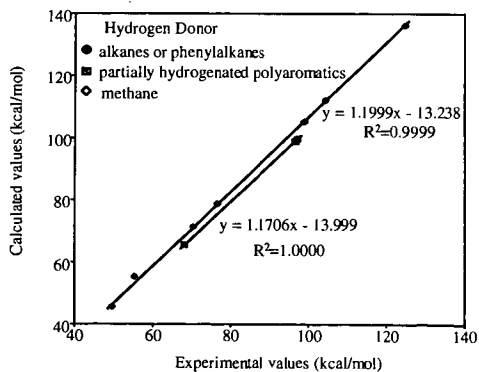


Figure 3 Systematic correlation of experimental and calculated $\Delta H^{\circ}_f(\text{TS})$ for H abstraction with phenyl radical as a H acceptor

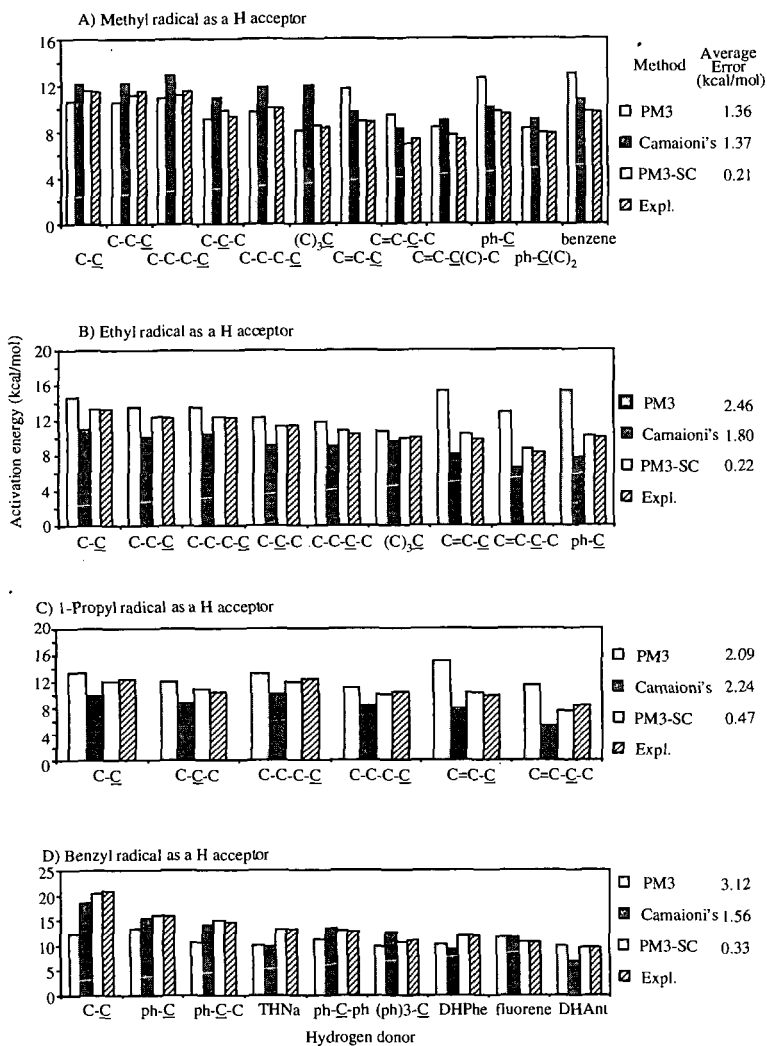


Figure 4 Experimental and estimated activation energies for H abstraction

MECHANISTIC INVESTIGATIONS INTO THE DECARBOXYLATION OF AROMATIC CARBOXYLIC ACIDS

Phillip F Britt,[†] A. C. Buchanan, III,[†] Thomas P. Eskay,[†] and William S. Mungall[‡]

[†]Chemical and Analytical Sciences Division, Oak Ridge National Laboratory,
MS 6197, P. O. Box 2008, Oak Ridge, Tennessee 37831 and

[‡]Department of Chemistry, Hope College, Holland, Michigan 49423

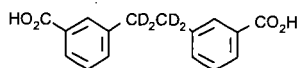
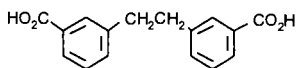
Keywords: Decarboxylation, Pyrolysis Mechanisms, Cross-Linking

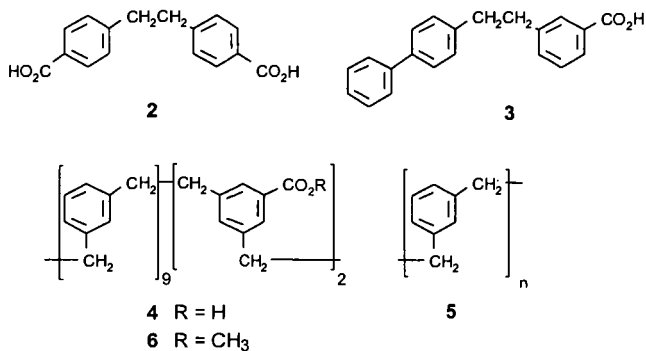
ABSTRACT

It has been proposed that carboxylic acids and carboxylates are major contributors to cross-linking reactions in low-rank coals and inhibit its thermochemical processing. Therefore, the thermolysis of aromatic carboxylic acids was investigated to determine the mechanisms of decarboxylation at temperatures relevant to coal processing, and to determine if decarboxylation leads to cross-linking (i.e., formation of more refractory products). From the thermolysis of simple and polymeric coal model compounds containing aromatic carboxylic acids at 250–425 °C, decarboxylation was found to occur primarily by an acid promoted ionic pathway. Carboxylate salts were found to enhance the decarboxylation rate, which is consistent with the proposed cationic mechanism. Thermolysis of the acid in an aromatic solvent, such as naphthalene, produced a small amount of arylated products (<5 mol%), which constitute a low-temperature cross-link. These arylated products were formed by the rapid decomposition of aromatic anhydrides, which are in equilibrium with the acid. These anhydrides decompose by a free radical induced decomposition pathway to form aryl radicals that can add to aromatic rings to form cross-links or abstract hydrogen. Large amounts of CO were formed in the thermolysis of the anhydrides which is consistent with the induced decomposition pathway. CO was also formed in the thermolysis of the carboxylic acids in aromatic solvents which is consistent with the formation and decomposition of the anhydride. The formation of anhydride linkages and cross-links was found to be very sensitive to the reactions conditions. Hydrogen donor solvents, such as tetralin, and water were found to decrease the formation of arylated products. Similar reaction pathways were also found in the thermolysis of a polymeric model that contained aromatic carboxylic acids. In this case, anhydride formation and decomposition produced an insoluble polymer, while the *O*-methylated polymer and the non-carboxylated polymer produced a soluble thermolysis product.

INTRODUCTION

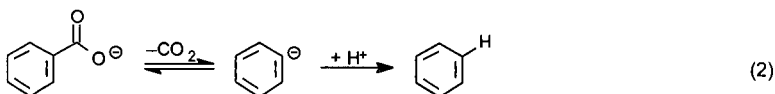
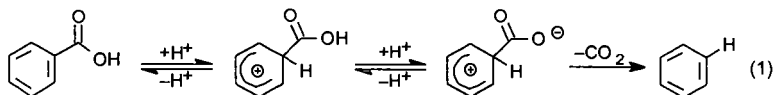
It has been proposed that carboxylic acids and carboxylates, which are prevalent in low-rank coals, are major contributors to retrograde reactions that inhibit efficient thermochemical processing of low-rank coals. In the pyrolysis and liquefaction of low-rank coals, low-temperature ($T < 400$ °C) cross-linking reactions have been correlated with the loss of carboxyl groups and the evolution of CO₂ and H₂O.^{1,2} Solomon et al. has modeled the pyrolytic loss of solvent swelling in coal by including one additional cross-link for every CO₂ evolved,^{2a,c} while Niksa has modeled the evolution rates and yields of oxygen bearing species by including char links when noncondensable gases (CO₂, H₂O, and CO) are expelled.^{2a} Pretreatments such as methylation or demineralization reduce cross-linking and CO₂ evolution in pyrolysis.^{2a,3,4} Exchange of Na⁺, K⁺, Ca⁺⁺, or Ba⁺⁺ into demineralized coals increase cross-linking and CO₂ evolution in pyrolysis and liquefaction.^{2,5} These results suggest that the reaction pathways that lead to decarboxylation may play an important role in the cross-linking of the coal polymer. However, the chemical pathways for decarboxylation of aromatic carboxylic acids are not understood at temperatures relevant to coal processing (300–450 °C).⁶ Therefore, to gain a better understanding of the role of decarboxylation in cross-linking reactions in low-rank coals, we have studied the liquid phase pyrolysis of simple (1–3) and polymeric (4–6) model compounds containing aromatic carboxylic acids from 250–425 °C (see below). These model compounds were chosen because aromatic carboxylic acids are known to exist in low-rank coals,⁷ their decarboxylation pathways can lead to cross-linking (see below), and homolysis of the weak bibenzylic bond provides a constant source of free-radicals that mimics some of the reactive intermediates found during the thermal processing of coal.⁸ Polymeric models were also investigated to study the impact of restricted mass transport on decarboxylation reaction pathways. A brief overview of the findings of these investigations will be presented as well as new data on pyrolysis of carboxylate salts.



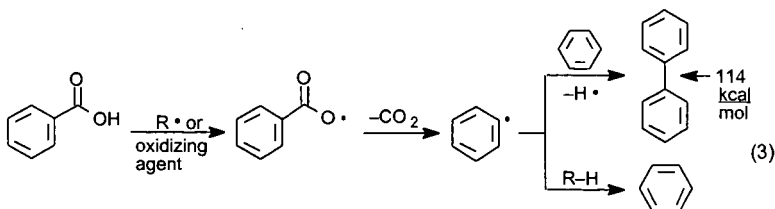


DECARBOXYLATION MECHANISMS

The reaction pathways for decarboxylation of aromatic carboxylic acids are surprisingly complex and dependent on the reaction conditions.⁹ The two major pathways for aromatic decarboxylation reactions are ionic and free radical. In aqueous solution, ionic decarboxylations can be catalyzed by acid or base. Acid-catalyzed decarboxylation reactions are the most common, and the reaction pathways are dependent on acid concentration, ionic strength, and substituents on the aromatic ring.⁹ In dilute acid, *ipso*-protonation of the aromatic ring is the rate-determining step (eq 1), while in highly acidic solutions, the rate determining step is decarboxylation of the aromatic cation. Electron donating substituents accelerate the acid-catalyzed decarboxylation reaction. In the absence of an acid-catalyst, decarboxylation of carboxylate salts or carboxylic acids with strongly electron withdrawing substituents, such as 2,4,6-trinitrobenzoic acid, occur by rate-determining unimolecular elimination of carbon dioxide from the anion (eq 2).



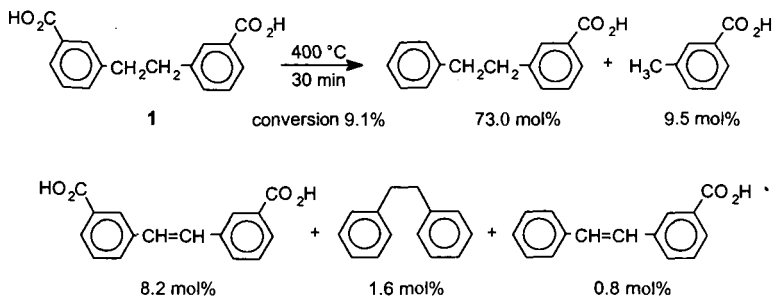
Decarboxylation of aromatic carboxylic acids can also occur by a free-radical pathway. Since free radicals are known to be formed as reactive intermediates in the thermolysis of coal, the free-radical decarboxylation pathway has been viewed as a possible route to cross-linking. Hydrogen abstraction or electron transfer to an acceptor¹⁰ can form the benzoyloxy radical (PhCO₂•) which will rapidly decarboxylate ($\log k \text{ (s}^{-1}\text{)} = 12.6 - 8.6 \text{ kcal mol}^{-1}/2.303RT$)¹¹ to form an aryl radical (eq 3). This highly reactive intermediate can abstract hydrogen or competitively add to an aromatic ring to form biaryls.¹² This aryl-aryl linkage is thermally stable at T = 400°C and would constitute a low-temperature cross-link.



PYROLYSIS OF THE ACID

The liquid phase thermolyses of 1,¹³ 2,¹³ 3,¹⁴ and substituted benzoic acids were conducted between 325-425 °C in sealed, degassed, Pyrex tubes. The reaction mixtures were silylated with *N,O*-bis(trimethylsilyl)trifluoroacetamide (since 1 and 2 were insoluble in most solvents) and quantitated by GC with FID. The products were identified by GC-MS and by comparison to authentic materials. Details of the experimental procedure can be found in references.^{13,14} For

all the compounds studied, decarboxylation was the major product from the thermolyses. Excellent mass balances were obtained in these thermolyses even at high conversion (for 1, 97% mass balance at 67% conversion) indicating that no significant amounts of high molecular weight products were undetected by the GC analysis. A typical product distribution from the thermolysis of 1 at 400 °C for 30 min (9.1% conversion) is shown below. Additional products



detected included 1,1-(3,3'-dicarboxyphenyl)ethane (4.6 mol%), 3-ethylbenzoic acid (1.3 mol%), 1-(3-carboxyphenyl)-1-phenylethane (0.3 mol%), and benzoic acid (0.1 mol%). The average conversion for a set of four 30 min thermolyses at 400 °C was $9 \pm 1\%$, and the average mass balance was $99 \pm 2\%$. At 400 °C, the apparent first-order rate constants for decarboxylation of 1, 2, and 3 at low conversion was $3.7 \pm 0.2 \times 10^{-5}$, $6.6 \pm 0.2 \times 10^{-5}$, and $2.8 \pm 0.7 \times 10^{-5} \text{ s}^{-1}$, respectively. The factor of two difference in the rate constant for decarboxylation of 2 relative to 1 and 3 indicates that the rate of decarboxylation is influenced by the position of the carboxyl group on the aryl ring (see below). The Arrhenius parameters for the apparent first-order rate constant for the decarboxylation of 1 to 1-(3-carboxyphenyl)-2-phenylethane was found to be $\log k (\text{s}^{-1}) = (9.4 \pm 0.4) - (43 \pm 1) \text{ kcal mol}^{-1}/2.303RT$. On the basis of the product distributions, mass balances, and decarboxylation rates, the decarboxylation of 1, 2, and 3 was proposed to proceed by an acid promoted, ionic pathway as shown in eq 1.

To provide additional evidence of the decarboxylation mechanism, the thermolysis of *p*-toluic acid and *p*-toluic acid-*d*₁ (*p*-CH₂C₆H₄CO₂D) were compared at 400 °C.¹⁵ The deuterium isotope effect $k_{\text{H}}/k_{\text{D}}$, determined from the average of four thermolyses on each substrate, was 2.1 ± 0.1 indicating that protonation of the aromatic ring is a rate-determining step (see below). The effect of electron donating substituents on the thermolysis of benzoic acid was also investigated at 400 °C in the liquid phase. As previously found, decarboxylation to the substituted benzene was the major product. A Hammett plot¹⁶ was constructed for the rate of decarboxylation (Figure 1), and a better linear correlation was obtained with σ^+ ($R = 0.999$) than with σ ($R = 0.950$). The slope (ρ) for the plot vs σ^+ was -5.2 indicating that a positive

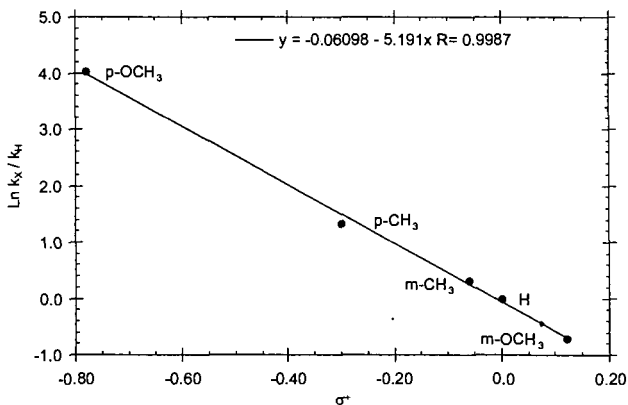
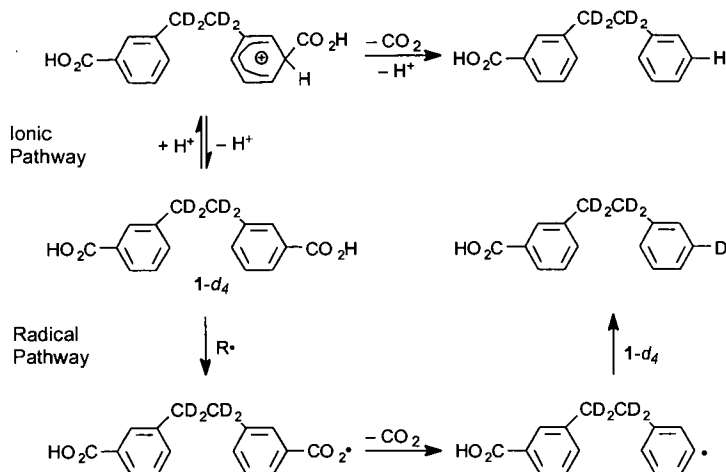


Figure 1. Hammett plot for the liquid phase thermolysis of substituted benzoic acids at 400 °C.

charge develops in the transition state in the decarboxylation, which supports the proposed cationic mechanism for decarboxylation. Since in low-rank coals all the aromatic rings are substituted with electron donating substituents, such as alkyl and oxygen functional groups,¹⁷ it is predicted that acid promoted decarboxylation reactions will be very rapid at 400 °C ($t_{1/2} < 30$ min).

To investigate the possibility that the free-radical pathway may also contribute to the decarboxylation reaction, the thermolysis of 1 containing deuterium in the ethylene bridge (1-*d*₄) was investigated.¹³ If decarboxylation proceeds by the acid-promoted ionic pathway, a *d*_r-monoacid will be produced, while a free-radical pathway would place a deuterium at the 3-position of the aromatic ring (from D abstraction by the aryl radical) to form a *d*_s-monoacid (Scheme 1).¹⁸ The thermolysis of 1-*d*₄ was performed at 325 °C and 400 °C, and the product distribution was similar to that reported for 1. At conversions ranging from 3-9%, GC-MS analysis of the 1-(3-carboxyphenyl)-2-phenylethane product showed no evidence of a *d*_s-species (<5%), based upon the comparison of the observed and calculated M⁺ and (M+1)⁺ peaks for the trimethylsilylated derivative of the *d*_r-monoacid. These data provide convincing evidence that decarboxylation of 1 is occurring predominantly by an ionic pathway in the neat liquid.

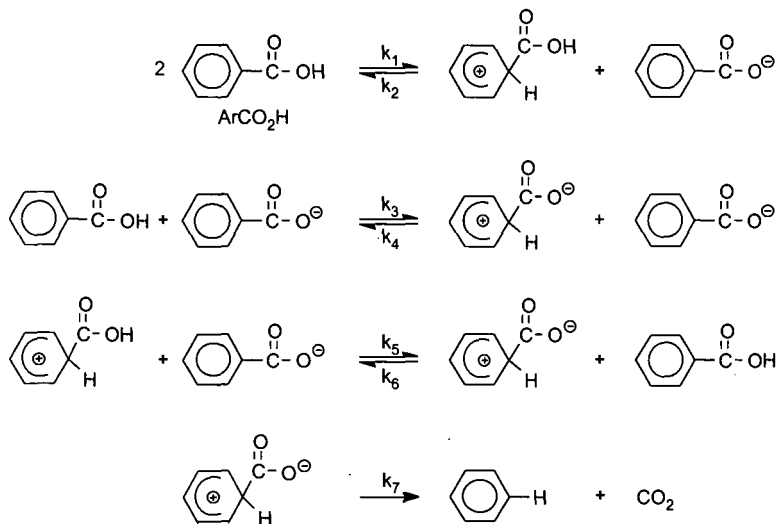


Scheme 1

PYROLYSIS OF CARBOXYLATE SALTS

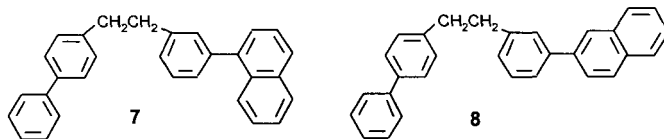
In coal, many of the carboxylic acids exist as carboxylate salts.¹⁹ Exchange of inorganic cations, such as Na⁺, K⁺, Ca⁺⁺, or Ba⁺⁺, into demineralized low-rank coals can significantly decrease liquefaction yields and increase cross-linking.^{2,5} For example, in the liquefaction of Zap lignite (400 °C, 30 min, tetralin, H₂), exchange of potassium cations into an acid demineralized coal decreased liquefaction yields 40% compared to the demineralized coal.^{3,4} Thermolysis of the dipotassium salt of 1 was investigated at 400 °C for 30 min neat, in tetralin, and in naphthalene.²⁰ No thermolysis products were detected and 1 was recovered unreacted (>99 mol%). Calcium benzoate was also found to be relatively stable at 400 °C (0.05% conversion to benzene in 1h). Addition of a small amount of water (1-3 equiv) to the reaction tubes did not significantly alter the conversions. However, if calcium benzoate was added to benzoic acid, the rate of decarboxylation increased. For example, the decarboxylation of benzoic acid increased by a factor of 7.7, 12.3 and 14.8 by the addition of 4.8, 11.1, and 15.1 mol% calcium benzoate, respectively. In the thermolysis of substituted benzoic acids, Manion et al. found that bases, such as pyridine, accelerated the decarboxylation of benzoic acid.¹⁰ It was proposed that decarboxylation occurred by the anionic mechanism (eq 2). However, the cationic mechanism is still consistent with these results (eq 1), and a new mechanistic pathway does not have to be invoked to rationalize these experimental results. In the decarboxylation of 4-aminobenzoic acids in dilute aqueous acid, it was concluded either *ipso*-protonation of the aromatic ring (k₁) or loss of the carboxyl proton (k₂) is wholly or partially rate controlling (Scheme 2).²¹ If the anion decarboxylates, protonation of the aromatic ring is rate controlling (k₃). Thus, if both *ipso*-protonation and proton loss from the carboxylic acid are rate controlling, the rate of decarboxylation would be accelerated for the carboxylate salt. This prediction was confirmed by Kaeding's study on the impact of benzoate salts on the decarboxylation of salicylic acid in benzoic acid at 200-230 °C.²² All the benzoate salts enhanced the decarboxylation rate, although the magnitude varied considerably with the metal. For example, the potassium, sodium, and calcium benzoate accelerated the decomposition of salicylic acid at 212 °C by a factor of 16.1, 10.7 and 6.3, respectively, and the decarboxylation rate was directly proportional to the concentration of the salt. Thus, decarboxylation of carboxylic acids and their salts can be described by the cationic mechanism shown in Scheme 2. In the presence of a weak base, carboxylate salts are formed and a similar series of reactions can be proposed. Moreover,

anilinium and pyridinium ions have been shown to catalyze the decarboxylation of salicylic acid.²³ Thus, a new mechanism does not have to be proposed for the base or salt catalyzed decarboxylation of aromatic carboxylic acids.



ANHYDRIDE FORMATION

The thermolysis of **3** was also studied in a non-hydrogen donor solvent, naphthalene, at 400 °C. In a 10-fold excess of naphthalene, the major products were the same as in the neat thermolysis except for the formation of two new minor products (<3 mol%) **7** and **8**, which constitute cross-linked products. Thermolysis of **1** and **2** in naphthalene also produced naphthylated products, but the yield of these products was ca. three times smaller than that for **3**.



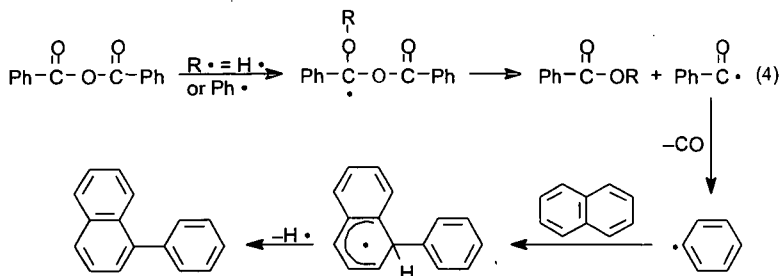
Arylated products were also found when biphenyl was used as the solvent, and 1- and 2-phenylnaphthalene were found in the thermolysis of benzoic acid in naphthalene. The formation of **7** and **8** were reduced by tetralin, a hydrogen donor solvent, indicating that the arylation reaction proceeded by a free radical pathway. The arylated products could also be reduced by small amounts of water (0.5-3 equiv).

The formation of small quantities of arylated products in the aromatic solvents was surprising on the basis of the liquid phase experiments. The yield of arylated products was found to be very sensitive to the reaction conditions and trace amounts of water, and at times, it was very difficult to obtain reproducible data. After the thermolysis of many model compounds had been investigated, it was concluded that the arylated products arise from formation and decomposition of aromatic anhydrides. In the thermolysis of benzoic acid in naphthalene (2.5 equiv) at 400 °C, a small amount of benzoic anhydride (ca. 1.4%) was observed in addition to benzene (1.2%), 1-phenylnaphthalene (0.06%), and 2-phenylnaphthalene (0.06%). When water (0.5 equiv) was added to the mixture of benzoic acid and naphthalene, benzoic anhydride was not observed. In the thermolysis of **3** in naphthalene, a small amount of the anhydride of **3**, (0.4%), was observed by HPLC and by LC-MS (by comparison with an authentic sample). These studies confirmed that anhydrides could be formed under the sealed tube reaction conditions used in this study and that small amounts of water minimize their formation.

Next, the thermolysis of the anhydrides were investigated since there was little literature information on the pyrolysis of aromatic anhydrides at moderate temperatures (<500 °C). It was discovered that the anhydrides decomposed very rapidly under the reaction conditions. The decomposition of benzoic anhydride (7.5% conversion) at 400 °C in naphthalene (10 equiv) was ca. 8 times faster than that for benzoic acid (0.97% conversion) under similar reaction

conditions. The major products from the thermolysis of benzoic anhydride in naphthalene were benzene (29.5 mol%), 1-phenylnaphthalene (40.4 mol%), 2-phenylnaphthalene (26.4 mol%) and phenyl benzoate (6.2 mol%). The anhydride of **3** also decomposed more rapidly than **3** (ca. 22-times faster) at 400 °C in naphthalene. The yield of arylated products was also shown to be sensitive to the nature of the aromatic acceptor (i.e., ease and reversibility of addition) and concentration of hydrogen donors.

The high conversions for the aromatic anhydrides were surprising. The C(=O)-O bond dissociation energy for benzoic anhydride was estimated as 84 kcal mol⁻¹.¹⁴ At 400 °C, C-O homolysis (to form the PhCO• and PhCO₂•) would not occur to any significant extent (<<1%). Therefore, it was proposed that the decomposition of the aromatic anhydride occurred by an induced homolysis reaction (eq 4), which has been observed in the decomposition of benzoyl



peroxide.²⁴ The induced decomposition is an addition-elimination reaction in which radicals add to the anhydride (most likely the C=O bond) and cleave to form a stable product, such as phenyl benzoate, and a new chain carrying radical, i.e., the benzoyl radical. The benzoyl radical will rapidly decarbonylate ($\log k \text{ (s}^{-1}\text{)} = 14.6 - 29.4 \text{ kcal mol}^{-1}/2.303RT$)²⁵ to form the phenyl radical. The phenyl radical can add to an aromatic ring to form an arylated product¹² and produce a hydrogen atom, which can continue the chain reaction.²⁶ The induced decomposition pathway also requires that more CO be formed than CO₂. In the thermolysis of benzoic anhydride and the anhydride of **3**, the ratio of CO:CO₂ was 3:1 and 25:1, respectively. The excess CO is consistent with the induced decomposition pathway and inconsistent with pure homolysis. In the thermolysis of acid **3** in naphthalene (10 equiv), the ratio of CO:CO₂ is 1:4. Thus, in the absence of water, small amounts of the aromatic anhydrides are in equilibrium with the parent carboxylic acid. Under free radical conditions, the anhydride undergoes a rapid free radical induced decomposition reaction, which produces aryl radicals that can lead to cross-linked products. Water and hydrogen donor solvents can reduce the yield of cross-linked products. However, can this sequence of reactions occur in the polymeric network structure of coal? To investigate this possibility, polymeric models of aromatic carboxylic in low-rank coals were prepared and their thermal chemistry investigated.

THERMOLYSIS OF POLYMER MODEL

The polymer model compound **4** was prepared with 2.3 acids per 100 carbons,²⁷ which is similar to the concentration of carboxylic acids in Beulah-Zap coal, 2.2 acids per 100 carbons.¹⁷ Overall, the TGA behavior of **4** is analogous to that reported for low-rank coals in which CO₂ evolution occurs prior to tar evolution and *O*-methylation reduces char yield (i.e., cross-linking).^{2,27} The carboxylated polymer **4**, forms ca. 2.4 times more char upon heating to 800 °C than the non-carboxylated polymer **5**. This indicates that the carboxylic acids are enhancing cross-linking in the polymer. Pyrolysis of **4** at 400 °C in a T-shaped tube, in which the volatile products are removed from the reaction, produced significant amounts of a THF insoluble residue (74 ± 2 wt%) independent of the thermolysis time (15-60 min). However, the thermolysis of **5** and **6** at 400 °C for 60 min produced a THF soluble residue. FTIR and solid-state ¹³C NMR analysis of the THF insoluble residue confirmed the presence of the aromatic anhydride linkage. Thermolysis of **4** in a sealed tube, in which the volatile products were not allowed to escape, produced a THF soluble product and no anhydride was observed by FTIR. Thus, aromatic anhydrides can form low-temperature cross-links that hold the polymer structure together. However, if the anhydride linkages were completely hydrolyzed (confirmed by FTIR), the polymer remained insoluble. It is proposed that the anhydride linkages in the polymer decompose by an induced decomposition reaction to form aryl cross-links as was observed for the simple model compounds. In support of this mechanism, CO evolution is observed in the TG-MS experiments before significant depolymerization of the polymer backbone occurs. Thus, the small amount of cross-linking observed in the simple model compounds is enhanced in the polymer models. However, the extent of anhydride formation and cross-linking is very sensitive to the experimental conditions and the presence of water. Can similar chemistry occur in the thermal processing of low-rank coal? To answer this question, additional characterization

studied are need on low-rank coals to determine if carboxylic acids form anhydrides during pyrolysis.

SUMMARY

The thermolysis of aromatic carboxylic acids was investigated to determine the mechanisms of decarboxylation at temperatures relevant to coal processing, and to determine if decarboxylation leads to cross-linking (i.e., formation of more refractory products). From the thermolysis of simple and polymeric coal model compounds containing aromatic carboxylic acids at 250-425 °C, decarboxylation was found to occur primarily by an acid promoted ionic pathway. Carboxylate salts were found to enhance the decarboxylation rate, which is consistent with the proposed cationic mechanism. Thermolysis of the acid in an aromatic solvent, such as naphthalene, produced a small amount of arylated products (<5 mol%), which constitute a low-temperature cross-link. These arylated products were formed by the rapid decomposition of aromatic anhydrides, which are in equilibrium with the acid. These anhydrides decompose by a free radical induced decomposition pathway to form aryl radicals that can add to aromatic rings to form cross-links or abstract hydrogen. Large amounts of CO were formed in the thermolysis of the anhydrides which is consistent with the induced decomposition pathway. CO was also formed in the thermolysis of the carboxylic acids in aromatic solvents which is consistent with the formation and decomposition of the anhydride. The formation of anhydride linkages and cross-links was found to be very sensitive to the reactions conditions. Hydrogen donor solvents, such as tetralin, and water were found to decrease the formation of arylated products. Similar reaction pathways were also found in the thermolysis of a polymeric model that contained aromatic carboxylic acids. In this case, anhydride formation and decomposition produced an insoluble polymer, while the *O*-methylated polymer and the non-carboxylated polymer produced a soluble thermolysis product.

ACKNOWLEDGMENT

This research was sponsored by the Division of Chemical Sciences, Office of Basic Energy Sciences, U.S. Department of Energy, under contract No. DE-AC05-96OR22464 with Oak Ridge National Laboratory, managed by Lockheed Martin Energy Research, Corp. T.P.E. was supported in part by an appointment to ORNL Postdoctoral Research Associates program administered jointly by Oak Ridge Institute for Science and Education and ORNL.

REFERENCES

- ¹ (a) Suuberg, E.M.; Lee, D.; Larsen, J.W. *Fuel* **1985**, *64*, 1668. (b) Suuberg, E.M.; Unger, P.E.; Larsen, J.W. *Energy and Fuels* **1987**, *1*, 305.
- ² (a) Solomon, P.R.; Serio, M.A.; Despande, G.V.; Kroo, E. *Energy and Fuels* **1990**, *4*, 42. (b) Ibarra, J.V.; Moliner, R.; Gavilan, M.P. *Fuel* **1991**, *70*, 408. (c) Solomon, P.R.; Best, P.E.; Yu, Z.Z.; Despande, G.V. *Prepr. Pap.-Am. Chem. Soc., Div. Fuel Chem.* **1989**, *34(3)*, 895. (d) Niksa, S. *Energy and Fuels* **1996**, *10*, 173.
- ³ Serio, M.A.; Kroo, E.; Charpenay, S.; Solomon, P.R. *Prepr. Pap.-Am. Chem. Soc., Div. Fuel Chem.* **1993**, *38(3)*, 1021.
- ⁴ Serio, M.A.; Kroo, E.; Teng, H.; Solomon, P.R. *Prepr. Pap.-Am. Chem. Soc., Div. Fuel Chem.* **1993**, *38(2)*, 577.
- ⁵ Joseph, J. T.; Forria, T. R. *Fuel* **1992**, *71*, 75.
- ⁶ Benzoic acid has been reported to decarboxylate by a unimolecular reaction (1,2-elimination) in the gas phase at 490 °C. Winter, K.; Barton, D. *Can. J. Chem.* **1970**, *48*, 3797.
- ⁷ Hagaman, E.W.; Lee, S.K. *Energy and Fuels* **1995**, *9*, 727.
- ⁸ The thermal chemistry of bibenzyl has been thoroughly studied, so the perturbation of the carboxyl substituent on the known reaction chemistry of bibenzyl can be determined. (a) Miller, R. E.; Stein, S. E. *J. Phys. Chem.* **1981**, *85*, 580. (b) Poutsuma, M. L. *Fuel* **1980**, *59*, 3357. (c) Stein, S. E.; Robaugh, D. A.; Alfieri, A. D.; Miller, R. E. *J. Am. Chem. Soc.* **1982**, *104*, 6567.
- ⁹ (a) Taylor, R. In *Comprehensive Chemical Kinetics* Bamford, C.H.; Tipper, C.F.H. Eds.; Elsevier Publishing Co; New York, 1972; Vol. 13, pp 303-316. (b) Longridge, J. C.; Long, F. A. *J. Am. Chem. Soc.* **1968**, *90*, 3092.
- ¹⁰ (a) Manion, J. A.; McMillen, D. F.; Malhotra, R. *Energy and Fuels* **1996**, *10*, 776. (b) Manion, J. A.; McMillen, D. F.; Malhotra, R. *Prepr. Pap.-Am. Chem. Soc., Div. Fuel Chem.* **1992**, *37(4)*, 1720.
- ¹¹ Chateaufeuf, J.; Luszyk, J.; Ingold, K. U. *J. Am. Chem. Soc.* **1988**, *110*, 2886.
- ¹² (a) Fahr, A.; Stein, S.E. *J. Phys. Chem.* **1988**, *92*, 4951. (b) Chen, R.H.; Kafafi, S.A.; Stein, S.E. *J. Am. Chem. Soc.* **1989**, *111*, 1418.
- ¹³ (a) Eskay, T. P.; Britt, P. F.; Buchanan, III, A. C. *Energy Fuels* **1996**, *10*, 1257. (b) Eskay, T. P.; Britt, P. F.; Buchanan, III, A. C. *Prepr. Pap.-Am. Chem. Soc., Div. Fuel Chem.* **1996**, *41(2)*, 739.

- ¹⁴ (a) Eskay, T. P.; Britt, P. F.; Buchanan, III, A. C. *Energy Fuels* **1997**, *11*, 1278. (b) Eskay, T. P.; Britt, P. F.; Buchanan, III, A. C. *Prepr. Pap.-Am. Chem. Soc., Div Fuel Chem.* **1997**, *42(1)*, 20.
- ¹⁵ Toluic acid-*d*₁ was prepared by the hydrolysis of toulic anhydride with D₂O using the procedure described for preparation of benzoic acid-*d*₁ in: *Organic Syntheses with Isotopes. Part II*; Murray, A., III; Williams, D. L., Eds.; Interscience Publishers: New York, 1958; p 1279.
- ¹⁶ Isaacs, N. *Physical Organic Chemistry*, 2nd ed.; Longman Group: London, 1995; pp 149-187.
- ¹⁷ Jung, B.; Stachel, S. J.; Calkins, W. H. *Prepr. Pap.-Am. Chem. Soc., Div. Fuel Chem.* **1991**, *36(3)*, 869.
- ¹⁸ Abstraction of a deuterium from the ethylene bridge is thermodynamically favored based on benzylic C-H, aryl C-H, and the carboxy O-H bond strengths of 85, 111, and 101 kcal/mol, respectively. (McMillen, D. F.; Golden, D. M. *Annu. Rev. Phys. Chem.* **1982**, *33*, 493.) Furthermore, Fahr and Stein have shown that in the reaction of phenyl radicals with toluene-*d*₁ at 450 °C, >90% of the hydrogen abstraction from toluene occurs at the methyl position rather than from the aromatic ring.¹²
- ¹⁹ Kuznetsov, P. N.; Kuznetsova, L. I.; Bimer, J.; Salbut, P.; Gruber, R.; Brodski, D. *Fuel* **1997**, *76*, 189. For example, the ratio of free carboxylic acids to carboxylate salts is ca. 1:1 for Kansk-Achinsk brown coal.
- ²⁰ Eskay, T. P.; Britt, P. F.; Buchanan, III, A. C. *Prepr. Pap.-Am. Chem. Soc., Div Fuel Chem.* **1996**, *41(2)*, 1084.
- ²¹ Los, J. M.; Rekker, R. F.; Tonsbeek, C. H. T. *Recueil* **1967**, *86*, 622.
- ²² Kaeding, W. W. *J. Org. Chem.* **1964**, *29*, 2556.
- ²³ Willi, A. V. *Trans. Faraday Soc.* **1959**, *55*, 433.
- ²⁴ Koenig, T. In *Free Radicals*; Kochi, J. K., Ed.; John Wiley and Sons: New York, 1973; Vol 1, Chapter 3, p 116-118. Studies on the thermal decomposition of benzoyl peroxide (PhCO₂)₂ found that the rate of decomposition varied considerably from solvent to solvent while radical scavengers reduced the rate. It was determined that a chain reaction occurred in certain solvents in which the phenyl radical, formed from O-O homolysis followed by decarboxylation of the benzoyloxyl radical, could abstract hydrogen from the solvent. The solvent radicals would add to the benzoyl peroxide to form the benzoyloxyl radical and an ester. For example, in diethyl ether, 1-ethoxyethyl benzoate was isolated in 95% yield.
- ²⁵ Solly, R. K.; Benson, S. W. *J. Am. Chem. Soc.* **1971**, *93*, 2127.
- ²⁶ It is not known if a free hydrogen atom is eliminated or whether a radical hydrogen transfer (RHT) reaction occurs. In the thermolysis of aromatic aldehydes in naphthalene at 400 °C,¹⁴ significant quantities of benzyl alcohol were formed (and no significant quantities of other products expected from hydrogen atom chemistry, such as biphenyl, ethyl benzene, or benzene) which implies a RHT pathway.
- ²⁷ (a) Britt, P. F.; Mungall, W. S.; Buchanan, III, A. C. *Energy Fuels* **1998**, *12*, 660. (b) Mungall, W. S.; Britt, P. F.; Buchanan, III, A. C. *Prepr. Pap.-Am. Chem. Soc., Div Fuel Chem.* **1997**, *42(1)*, 26.

PREDICTIONS OF ACTIVITY PATTERNS FOR METHANE REFORMING BASED ON COMBINATORIAL PATHWAY GENERATION AND ENERGETICS

Raúl E. Valdés-Pérez

Computer Science Department, Carnegie Mellon University, Pittsburgh, PA 15213, USA

Ilie Fishtik

Department of Chemical and Biochemical Engineering, The University of Iowa,
Iowa City, IA 52242, USA

Andrew V. Zeigarnik

Laboratory of Chemical Kinetics and Catalysis, Lomonosov Academy of Fine Chemical
Technology, Moscow, 117571 Russia

ABSTRACT

We have applied the method to carbon formation in CO₂ reforming of methane over eight transition metals, starting with a list of 164 elementary steps and published UBI-QEP calculations of their activation energies and using the MECHEM program for combinatorial pathway generation. The predicted coking pattern Fe > Ni > Ru > Rh, Ir, Pd > Cu, Pt is consistent with experimental results from the literature. Current work focuses on deriving an activity pattern for the production of CO+H₂ in methane reforming.

INTRODUCTION

During the past decades, physical chemistry and surface science have provided a basis for understanding catalytic processes at the molecular level.¹ However, the search for active, stable, and selective catalysts for any given chemical process still remains largely empirical and is performed in the face of great uncertainty about most aspects of the process.² For example, ideally the choice of catalysts should rely on knowledge of the reaction mechanism and kinetics and of the physical properties and structure of the catalyst, promoters, and support, among others. However, usually neither the mechanism nor kinetics of elementary steps is known.

Recent advances in computational methods have enabled searching comprehensively for hypothetical reaction pathways³ and bulk calculations of activation energies and enthalpies of candidate elementary steps.⁴ A combination of these techniques holds the promise of increasing the suite of systematic tools that can guide catalyst design.⁵

This article reports an initial attempt to combine combinatorial pathway generation with energetics for the purpose of catalyst design. The method adopts MECHEM^{2,6-8} – a computer aid for mechanism elucidation. To develop the approach, we focused on predicting the relative coking properties of metal single-crystal catalysts for carbon dioxide reforming of methane. This choice is motivated by the availability of published data and by the importance of coking control in the conversion of natural gas to syngas.⁹ The method enables finding a list of “best” coking pathway/catalyst pairs, which are then used to construct a qualitative ranking of metals in their activity toward coking. The advantage of basing a predicted activity pattern on the relative barriers of pathways rather than the relative barriers of presumed rate-determining steps is that it removes the need to postulate rate-determining steps, which ultimately only make sense in the context of a larger pathway.

Our starting data, taken entirely from Ref. 4, consist of 164 elementary steps and their activation energies for eight transition-metal catalysts. The single-crystal catalysts were Cu(111), Ni(111), Pd(111), Pt(111), Rh(111), Ru(001), Ir(111), and Fe(110). Activation energies were calculated by the UBI-QEP method.¹⁰ The accuracy of the calculated activation energies was claimed to be about 2 kcal/mol.⁴

METHODS

Background on Computational Methods. MECHEM^{2,6-8} is an ongoing, multi-year project whose goals are to provide high level assistance for the elucidation or exploration of chemical reaction mechanisms. Technical details can be found in specialized journals.¹¹ The basic approach is to comprehensively search the possible elementary reactions and pathways in a “first principles” spirit. The principle involved is that an elementary step involves a small (user-adjustable) number of changes in the bonding of the reactants. Since in mechanism elucidation the reaction starting materials are known, MECHEM builds elementary steps of the form *known reactants* → X + Y and then solves for all possible structures of the unknowns X and Y by using ad-hoc graph algorithms and assuming, say, at most three or four total changes (cleavage or formation) to the connectivity of all the molecular graphs, including X and Y. One could contrast this “logical” approach to generating elementary steps with an alternative empirical approach that, say, only generates steps that follow specific reaction schemata such as migratory insertion, reductive elimination, radical recombination, dissociative adsorption, and so on. An advantage of the “first principles” or logical approach is that there is an enhanced potential for finding reaction mechanisms that otherwise would escape notice. After X and Y become specific species, the program

considers all possible second steps in a similar way. The "space" of possible pathways is simply the set of possible lists of such elementary steps. The only unchangeable built-in assumption in MECHEM is that all elementary steps have at most two reactants and at most two products.

The program organizes its search in stages of simplicity, by first trying to find mechanisms that involve fewer species and steps. A chemist/user drives the process by supplying assumptions, based on experimental evidence and background knowledge. These assumptions are in the form of constraints whose templates (about 120) are implemented and available for use.

Pathway/catalyst generation. To explore coking pathways in conformity with our source energetics data,⁴ we formulated the starting materials as CH₄(ads) and CO₂(ads) and the sole target product as monoatomic carbon. These species and all intermediates or by-products below are actually surface species, although their notation will not indicate this fact.

We made use of the 82 elementary steps (forward and reverse, totaling 164) and their activation energies over eight single-crystal transition metal catalysts reported by the cited authors. MECHEM was constrained to reject any generated step or species that was not on this list. Thus, there were $8 \times 164 = 1312$ separate activation energies or step/catalyst pairs.

To simplify the task, we excluded any step/catalyst pair whose activation energy exceeded 30 kcal/mol; these would be much less likely to enable good coking pathways. Thus, a new constraint was added to MECHEM that rejects any complete (or partially-constructed) pathway whose steps cannot all take place on one metal and still remain below the energy ceiling. Thus, a sequence whose first step was within the energy ceiling only for metals Fe and Ni, and whose second step was within ceiling only for Pt and Pd, would be discarded because their intersection was empty. The alternative would be to run the program once for each catalyst under consideration; but considering them jointly turns out to be more convenient.

Pathway selection criteria. We chose four measures of the likelihood that a pathway will lead to substantial coking; in all four cases, smaller values are better: (1) the number of pathway species; (2) the number of pathway steps; (3) for a specific metal, the maximum activation energy appearing in the pathway; (4) the maximum possible stoichiometric yield of carbon obtainable through the pathway, expressed as the *cost* in moles of CH₄ and CO₂ required to form 1 mole of surface carbon.

For the task of catalyst ranking, the preference for more concise pathways (having fewer species or steps) is justified as follows. The fewer pathway species, the fewer the opportunities for side reactions that diverge from coking; given N species, there are N^2 formally possible bimolecular and N unimolecular steps. In this article we do not include an explicit measure of the potential for side reactions, but a preference for fewer pathway species can deal somewhat with this issue.

The preference for fewer steps is justified by the uncertainty in the calculated activation energies. The more steps, the greater the chances of an (undetected) inaccuracy that would render bad a seemingly good pathway. If mistakes in the calculated energies occur with probability p and are independent, then the probability of a mistake for a pathway of length L equals $1 - (1 - p)^L$ which approaches unity exponentially with pathway length.

Measures of the pathway energy barrier more elaborate than a simple *maximum* could be used, and we have experimented with several of them, but here we opt for the simplest choice. The use of maximum activation barriers to characterize pathways assumes that the pathway step with the highest barrier is the slowest. The principled choice of slowest steps should be based on knowledge of surface species concentrations and preexponential factors, but these data are not available.

Finally, we need a measure of *how much* coking can be achieved via a given pathway. Lacking data on reaction rates, we will use a heuristic measure of "selectivity" that is based only on the plain pathway: the maximum possible yield of surface carbon that can be obtained by freely varying the pathway stoichiometric numbers, but keeping them non-negative. The problem of finding the maximum possible yield can be formulated as a linear optimization problem and solved with the simplex algorithm.¹² The basic ideas are to require one mole of carbon after a time t_1 , to express the possible concentration changes in terms of the stoichiometries of the individual steps, and then to minimize the "cost" (i.e., the molar amounts) of starting materials at the prior time t_0 . A by-product of the optimization is a stoichiometric number for each pathway step.

However, there is a subtlety in the cost measure. Since some steps are below the energy ceiling of 30 kcal/mol in both directions, we score pathways in two ways: (1) keeping the original forward direction of steps, and (2) augmenting the pathway with all the reversed steps that are within the energy ceiling. In the latter case, the *maximum energy* measure is calculated over the step directions that correspond to the positive stoichiometric numbers as determined by the linear optimization. If a stoichiometric number is zero, we consider the energy only of the forward direction.*

* This tactic is not absolutely correct, since it is possible that a more limited use of backward steps will lead to the most advantageous combination of energy and cost, in the sense of enabling a pathway to survive the comparisons described in the next section. However, given the small sizes of our pathways, we believe that this omission is not important.

Combining measures. We know of no principled way to combine these four measures or objectives into a single optimizable objective. However, since the formulation is equivalent to a multi-objective optimization problem, we can use the standard concept of a Pareto optimum. A Pareto optimum is a solution which is not dominated by any other solution; one solution dominates another if it is better on one of the objectives and is no worse on all the other objectives.

Thus, we will find all the Pareto optima, that is, those pathway/catalyst pairs that are not dominated by any other pair in the sense of minimizing the four objectives of steps, species, energy, and cost. We will iterate this procedure several times: after finding the first set (depth 0) of Pareto-optimal pathway/catalyst pairs, we will delete these solutions and all supersets of any of these pathways that involve the same catalyst and do not improve the score along one of the measures; then we collect the (depth 1) Pareto optima among the remaining pathway/catalyst pairs. By carrying out this procedure several times to a depth of 1 or 2, combined with deleting a metal after its place in the ranking is determined, we will obtain a ranked list of good coking pathway/catalyst pairs, together with its justification in terms of explicit coking pathways.

Generating pathways of increasing complexity. MECHEM's task is to generate all the simplest (fewest species or steps) mechanisms that can form the declared products or intermediates from the starting materials, while respecting any user-specified constraints. (Here, the constraints are that (1) only steps from our list of 164 elementary steps are allowed, and (2) the activation energy of any directed step must be within 30 kcal/mol.) However, we need to generate not just the simplest mechanisms, but all mechanisms over some range of complexity.

One *reject-supersets* approach to this problem was used earlier:⁶ after finding N simplest mechanisms, an artificial constraint is activated which rejects any future mechanism that contains within itself any of the N previous mechanisms. At the next run the program will not stop after finding the same N mechanisms, but instead will search for more complex mechanisms that are guaranteed a degree of novelty with respect to the previous runs. The *reject-supersets* approach has a drawback, though. Consider the schematic pathway $A \rightarrow X + Y$, $2X \rightarrow T$, which has four species, two steps, some maximum activation energy, and a cost in the starting material of A equal to 2. No more complex pathway will be allowed to contain this two-step pathway, so the three-step pathway $A \rightarrow X + Y$, $2X \rightarrow T$, $Y \rightarrow X$ will never be considered, even though its cost would be reduced to 1 from the previous 2. (Of course, the steps are increased and the maximum activation energy could rise.) Thus, it is possible that we could miss a good pathway.

A second approach to the problem of generating more complex pathways is simply to reject any future mechanism that contains exactly S species and R steps, where S and R describe the last batch of pathways found. This *more-complex-pathways* approach avoids the cited drawback of the *reject-supersets* approach, but suffers from a potential combinatorial explosion in the number of pathways.

The entire procedure, while somewhat detailed, has been largely automated and is the same from one reaction to the next.

RESULTS

We generated coking pathways by repeatedly using the *more-complex-pathways* approach until a run generated over one thousand pathways; then we switched to the *reject-supersets* approach. We continued collecting pathways up to a limit of seven species not counting CH_4 , CO_2 , and C. The result was a total of 11678 pathways (all the computations were done in a few hours on a 300 MHz, 64Mb laptop computer).

Each pathway was evaluated according to the four measures *steps*, *species*, *energy*, and *cost* over each of the eight catalysts. As explained above, sometimes a pathway/catalyst pair gave rise to two sets of scores, depending on whether pathway steps were allowed to have positive stoichiometric numbers in the backwards direction. The total ensuing number of pathway/catalyst scores was 99267.

The first three sets of Pareto-minimal pathways are shown below. Each step is annotated with its activation energy, and following the listed metal are the scores: number of extra *species*, number of *steps*, maximum activation *energy* barrier, and the minimum *cost* in moles of starting material that is stoichiometrically obtainable via the pathway.

Depth 0

1. CO_2 -[4.5] \rightarrow O + CO
 2. $2(\text{CO})$ -[0.9] \rightarrow CO_2 + C
- Fe, species = 2, steps = 2, energy = 4.5, cost = 1

Depth 1

1. CO_2 -[6.7] \rightarrow O + CO
 2. $2(\text{CO})$ -[6.4] \rightarrow CO_2 + C
- Ni, species = 2, steps = 2, energy = 6.7, cost = 1

Depth 2

1. CH_4 + CO_2 -[8.1] \rightarrow HCOO + CH_3
2. HCOO -[3.2] \rightarrow OH + CO
3. CO_2 + OH -[3.5] \rightarrow HCOO + O

4. $2(\text{CO}) - [0.9] \rightarrow \text{CO}_2 + \text{C}$
Fe, species = 5, steps = 4, energy = 8.1, cost = 1

1. $\text{CH}_4 + \text{CO}_2 - [8.1] \rightarrow \text{HCOO} + \text{CH}_3$

2. $\text{HCOO} - [3.2] \rightarrow \text{OH} + \text{CO}$

3. $2(\text{CO}) - [0.9] \rightarrow \text{CO}_2 + \text{C}$

Fe, species = 4, steps = 3, energy = 8.1, cost = 3

1. $\text{CO}_2 - [12.7] \rightarrow \text{O} + \text{CO}$

2. $2(\text{CO}) - [3.9] \rightarrow \text{CO}_2 + \text{C}$

Ru, species = 2, steps = 2, energy = 12.7, cost = 1

We judged that Fe is the single best coking metal, because it possesses the best overall solution (at depth 0) and is backed up by two more pathways at depth 2 that, unlike the first solution, make use of interactions between CH_4 and CO_2 . The next step is to delete Fe from further consideration and consider the seven remaining metals.

After Fe, the best catalyst appears to be Ni, which is followed in turn by Ru. After repeated minimizations to some depth, followed by excluding from further consideration the metals which we judged to be the next best, we obtained the results summarized below.

Take all metals

Depth 0: 1 Fe pathway \Rightarrow Depth 1: 1 Ni pathway \Rightarrow Depth 2: 2 Fe and 1 Ru pathways

Conclude: Fe is best. Exclude Fe

Depth 0: 1 Ni pathway \Rightarrow Depth 1: 3 Ru and 1 Rh pathways \Rightarrow Depth 2: 18 pathway/catalyst pairs (5 Ni)

Conclude: Ni is best after Fe. Exclude Fe, Ni

Depth 0: 3 Ru and 1 Rh pathways

Conclude: Ru is best after Fe, Ni. Exclude Fe, Ni, Ru

Depth 0: 23 pathways (9 Ir, 8 Pd, 6 Rh)

Conclude: Ir, Pd, Rh are best after Fe, Ni, Ru. Exclude Fe, Ni, Ru, Ir, Pd, Rh

Depth 0: 10 pathways (8 Pt, 2 Cu)

Conclude: Pt, Cu are the two worst

Our overall ranking of metals based on this detailed analysis of coking pathways is: Fe > Ni > Ru > Rh ~ Ir ~ Pd > Cu ~ Pt. Thus, according to the available elementary steps and activation energies, Fe and Ni favor coke formation the most, and Cu and Pt the least.

DISCUSSION

Comparison of results with literature. Coke deposition on metals from both CH_4 and CO_2 or their mixtures is a very complex process.^{13,14} Catalyst resistance to coking strongly depends on the nature of the support^{15,16} and promoters,^{17,18} which is one reason why direct comparisons of coking for various transition metals have not been carried out. Another reason is that noble metals are expensive and industry prefers to use promoted nickel catalysts instead, which are the focus of most studies. So, there is scarce experimental precedence for comparing our predictions to empirical results.

The only reliable qualitative conclusion about carbon deposition in CO_2 reforming of methane that we are able to discern from numerous experimental investigations is that the noble metals (Pd, Rh, Ru, Ir, and Pt) are generally less susceptible to coke deposition than Fe, Co, and Ni.¹⁹ Our findings are in complete agreement with this pattern, as well as with the data that stability of carbides decreases from iron to nickel, with copper carbide unknown.²⁰

Interestingly, Trimm⁹ discusses an activity pattern Fe > Ni > noble metals for steam reforming that is consonant with our results and with the cited pattern of Arutyunov and Krylov.¹⁹ This consonance supports the Rostrup-Nielsen conjecture that the steps of both mechanisms are similar.²¹

Limitations. We have not considered coke removal, only its formation. The data on activation energies⁴ suggest that the coke-removal rate must be very high: the activation energies for the step $\text{CO}_2 + \text{C} \rightarrow \text{CO} + \text{CO}$ are zero for Cu, Ni, Pd, Pt, Rh, and Ir, 1.1 for Ru, and 6.1 kcal/mol for Fe. The Pareto-minimal pathways show that the highest energy barriers among coke formation steps are usually higher. Thus, the lowest (most competitive) energy barrier of the Pareto-minimal pathway at depth 0 is 4.5 kcal/mol. This suggests that coke formation is competitive with coke removal only on Fe (4.5 vs. 6.1 kcal/mol), whereas coke is removed faster than it is formed on the other metals. This obviously contradicts the common knowledge that on Ni, coke is formed faster than it is removed, which is why promoters are used in Ni-based catalysts. Assuming that relative activation energies are a satisfactory heuristic guide to the relative rates of steps, we conjecture that carbon polymerization on the surface and carbon-metal phase formation are faster processes than coke removal. Thus, the monoatomic carbon formed in our coking pathways is consumed by these fast, undesirable processes. So, the more that a pathway/catalyst pair favors coke formation, the more chances that the catalyst will be poisoned with coke.

We did not consider adsorption/desorption steps, which may slightly affect the result.

We are considering only the formation of monoatomic surface carbon, and not the solubility of carbon in the bulk of the metal. The available information on the solubility of carbon in metals somewhat correlates with our ranking of metals: Fe > Ni > noble metals¹⁹ and Rh > Pd > Ru > Ir > Pt (maximum solubility data)²⁰. Also, the data reported by Hei *et al.*⁴ were calculated at zero coverage and we inherit this limitation. A future step will be to re-calculate all the data at higher coverages and refine current data.

Of course, real catalysts are more complicated, due to nonzero surface coverage effects, formation of various carbon-metal phases, carbon dissolution in the bulk, diffusion processes, transformations of monoatomic carbon into polymeric carbon and vice versa, and so on. However, to the extent that some of these complicating effects can be captured in the formulation of elementary steps and their energetic barriers, our method will be able to accommodate them.

Finally, we also neglected preexponential factors and did not try to simulate the kinetics of any of these pathways. Further step will be to estimate preexponential factor using transition state theory.

CONCLUSIONS

We have proposed the combinatorial generation of pathway/catalyst pairs, screened for conciseness, energetics, and stoichiometry, as a computational method for ranking alternative catalysts with respect to a given target property, here, coking in CO₂ reforming of methane. The input to the method is a list of possible elementary steps and their energetics, and the output is a ranking of catalysts augmented with pathway-oriented justifications for the ranking. Rankings and pathways such as these can complement other approaches to catalyst design, e.g., those whose assumed starting point is a serviceable reaction mechanism.

We also started the work on the future use of this method for the ranking of metals in the main reaction: CO₂ + CH₄ → CO + H₂ and on improving the selectivity and activity criteria. One of these criteria is based on the calculation of the apparent activation energy as a function of the surface coverages for intermediate species. Preliminary results of this work show that Ir, Ru, and Rh are best among eight catalyst considered here. Cu, Pd, and Pt are worse than others. Fe and Ni hold an intermediate position.

Our findings on metal catalyst coking for CO₂ reforming are relevant to steam reforming since the list of steps is largely identical for both processes.²¹

REFERENCES

- (1) Somorjai, G. A.; Zaera, F. *J. Phys. Chem.* **1982**, *86*, 3070.
- (2) Cardenas-Galindo, M.; Aparicio, L. M.; Rudd, D. F.; Dumesic, J. A. In *Computer-Aided Design of Catalysts*; Becker, E.; Pereira, C., Eds.; Marcel Dekker: New York, 1993.
- (3) Zeigarnik, A. V.; Valdes-Perez, R. E.; Temkin, O. N. *Langmuir* **1998**, *14*, 4510.
- (4) Hei, M. J.; Chen, H. B.; Yi, J.; Lin, Y. J.; Lin, Y. Z.; Wei, G.; Liao, D. W. *Surf. Sci.* **1998**, *417*, 82.
- (5) Becker, E.; Pereira, C. In *Computer-Aided Design of Catalysts*; Becker, E.; Pereira, C., Eds.; Marcel Dekker: New York, 1993.
- (6) Zeigarnik, A. V.; Valdes-Perez, R. E.; Temkin, O. N.; Bruk, L. G.; Shalgunov, S. I. *Organometallics* **1997**, *16*, 3114.
- (7) Bruk, L. G.; Gorodskii, S. N.; Zeigarnik, A. V.; Valdes-Perez, R. E.; Temkin, O. N. *J. Mol. Catal. A: Chem.* **1998**, *130*, 29.
- (8) Zeigarnik, A. V.; Valdes-Perez, R. E.; White, B. S. *J. Chem. Educ.*, in press.
- (9) Trimm, D. L. *Design of Industrial Catalysts*; Elsevier: New York, N.Y., 1980.
- (10) Shustorovich, E.; Sellers, H. *Surf. Sci. Rep.* **1998**, *31*, 1.
- (11) (a) Valdes-Perez, R. E. *J. Comput. Chem.* **1992**, *13*, 1079; (b) Valdes-Perez, R. E. *J. Comput. Chem.* **1993**, *14*, 1454; (c) Valdes-Perez, R. E. *J. Comput. Chem.* **1994**, *15*, 1266.
- (12) Valdes-Perez, R. E. *J. Phys. Chem.* **1991**, *95*, 4918.
- (13) Rostrup-Nielsen, J. R. In *Catalysis - Science and Technology*, Vol. 5; Anderson, J.; Boudart, M., Eds.; Springer Verlag: Berlin, 1984.
- (14) Bradford, M. C. J.; Vannice, M. A. *Catal. Rev. - Sci. Eng.* **1999**, *41*, 1.
- (15) Bradford, M. C. J.; Vannice, M. A. *Appl. Catal. A: General* **1996**, *142*, 73.
- (16) Sodesawa, T.; Dobashi, A.; Nozaki, F. *React. Kinet. Catal. Lett.* **1979**, *12*, 107.
- (17) Trimm, D. L. *Catal. Today* **1999**, *49*, 3.
- (18) Haliche, D.; Bourab, R.; Cherifi, O.; Bettahar, M. M. *Catal. Today* **1996**, *29*, 373.
- (19) Arutyunov, V. S.; Krylov, O. V. *Oxidative Conversion of Methane*; Nauka: Moscow, 1998 (in Russian).
- (20) Joyner, R. W.; Darling, G. R.; Pendry, J. B. *Surf. Sci.* **1988**, *205*, 513.
- (21) Rostrup-Nielsen, J. R.; Bak Hansen, J. H. *J. Catal.* **1993**, *144*, 38.
- (22) Savitskii, E. M.; Polykova, V. P.; Gorina, N. B.; Roshan, N. R. *Physical Metallurgy of Platinum Metals*; Moscow: Metallurgiya, 1975 (in Russian).

MAGNETIC IMAGING OF FCC FEEDSTOCKS TO MODEL ASPECTS OF THEIR CRACKING KINETICS AND PRODUCT SLATES

P.S. Virk

Department of Chemical Engineering
M. I. T., Cambridge, MA 02139

KEYWORDS: Magnetic Resonance, Catalytic Cracking, Modelling.

INTRODUCTION

Motivation. This work reports on a system for the Magnetic Imaging of FCC Feedstocks, acronym MIFF, that is being devised to model the fundamental chemical aspects of their cracking kinetics and product slates. It is motivated by the need to engineer, and predict the performance of, fluidized cat crackers using modern catalysts to crack ever heavier feeds at ever increasing reaction severities and gasoline selectivities under ever closer environmental scrutiny. NMR imaging adds a unique dimension to FCC feed characterization because of its intimate relation to molecular topology. Thus acid catalysts can crack virtually all the C-C bonds in hydrocarbons except those either within or adjacent to aromatic rings and NMR can directly detect these uncrackable sp²-hybridized aromatic core carbons and their adjacent sp³ benzylic carbons, providing the asymptotic extent to which a feedstock can be cracked and proffering insights into the structures of the product fragments.

Background. Of the voluminous literature on NMR applied to hydrocarbon mixtures, the present work has most been influenced by the classic papers of Knight (1967), Shoolery and Budde (1976) and Deutsche, Jancke and Zeigan (1976), specific articles by Ladner and Snape ((1978), Gillet et al (1981), Netzel et al (1981), and especially Cookson and Smith (1985, 1987), and the texts by Stothers (1972), Breitmaier and Voelter (1987) and Croasmun and Carlson (1994). Earlier efforts relevant to FCC feeds include Bouquet and Bailleul (1986), who used the methods of Cookson and Smith (1985) to assay carbons by their attached protons; Mauleon et al (1987), who devised a coke factor from carbon aromaticity; and a recent note based on the present work (Kim et al 1998) which applied NMR to enhance conventional and mass spectrometric characterizations.

MIFF SYSTEM

Figure 1 schematically depicts the three facets of the MIFF system, sample preparation, NMR experiments, and data analysis. In sample preparation, internal standards are gravimetrically incorporated into the FCC feedstock oils, typically VGOs and ATBs, to enable precise analysis and interpretation of the NMR experiments. Three internal standards are used, namely, deuteriochloroform CDCl₃, as oil solvent and spectrometer lock; dioxane, C₄H₈O₂, abbr DIOX, to assist in spectral integrations; and tetramethylsilane, Si(CH₃)₄, abbr TMS, as a spectral frequency reference. The primary NMR experiments performed provide quantitative C13 and H1 spectra, the spectral regions and individual resonances observed therein being identified and interpreted by additional 1-D and 2-D procedures that include DEPT, COSY, HETCOR, and HMQC. Spectral data are analysed in two trains, according to either their integral regions, abbr IR, or their canonical groups, abbr CG. In the IR train, the observed spectra are parsed into more or less coarse regions, each comprising chemically similar sorts of atoms. The IR train accounts for 100% of feedstock atoms and provides useful overall parameters, such as the percent of feedstock atoms, either carbon or hydrogen, that are aromatic. In the CG train, certain groups of spectral peaks that arise from atoms belonging to particular molecular moieties are recognized, particularly those in n-alkane straight chains and in 2-, 3-, 4-, 5-, and interior-methyl alkane branched chains. The CG train thus provides high-level quantitative information about certain molecular species; however the sum of identified species is but a fraction of the total, typically amounting to ~ 40% of feedstock atoms. Outputs from the coarse but complete IR train and the fine but fractional CG train are shown in the bottom row of Figure 1. The IR train provides carbon and hydrogen aromaticities, as well as more detailed regional data, and thence hydrogen atom counts, and thermochemical information. The CG train detects n-alkane content and chain length, as well as the contents of a variety of methyl-alkane moieties. Both trains are combined to form a set of NMR groups that characterize the feedstock.

NMR EXPERIMENTS

13-C. Figure 2 shows the 13-C NMR spectrum of a VGO feedstock called V2 in Table 1 (infra). The position of a peak on the x-axis, its resonance frequency or chemical shift, c, in units of ppm relative to TMS, is indicative of C atom type, while peak height on the y-axis, its absorption intensity, i, with arbitrary units, is roughly proportional to the abundance of such C atoms in the sample. Precise carbon atom amounts are obtained from peak integration, these integrals being the five continuously increasing stepped segments in the figure, their c-domains and magnitudes being noted below the abscissa. The major spectral regions observed are:

Region	c (range)	C-atom type
TMS	0.0	methyl carbons in TMS
Cal	10 - 52	aliphatic carbons in feedstock, sp ³ hybridized
DIOX	~67	methylene carbons in DIOX
CDCl ₃	~78 triad	C in CDCl ₃ solvent
Car	112 - 150	aromatic carbons in feedstock, sp ² hybridized

The wide separation between the regions of aliphatic and of aromatic carbons is noteworthy, allowing unambiguous delineation of these two broad categories; the integrals corresponding to these regions provide the carbon aromaticity $Car = 16.8\%$. Further demarcations shown below the spectrum, called Cumulative Integral Regions, sort carbon atoms into categories with the following approximate chemical interpretations: Carqt is aromatic quaternary, which are inherently of two kinds, either fused ring junction or substituted, not distinguished here; Carpi and Carpo are both aromatic protonated, the *i* and *o* being subtle distinctions between them; the sum $Car(qt+pi+po) = Car$. Among aliphatic carbons, Calhs is aliphatic highly substituted, Calbr is aliphatic branched (single substitution, such as methyl), Calch is aliphatic chains, mainly CH₂, and Calme is aliphatic methyls, all CH₃. Many additional individual spectral regions can be distinguished in Figure 2, and these have been labelled beside their principal peaks as follows: Regions B, D, H, and G (two tall peaks at $c \sim 30$) respectively contain the carbon atoms C1, C2, C3, and (C4, C25) in linear n-alkane chains. Region C contains mainly methyl groups, pendant on a variety of alkane, cyclo-alkane and aromatic structures. Regions E and F contain carbon atoms in C5- and C6-cyclo-alkane rings, as well as C2 in 2-methyl-alkanes. Regions A, I, J and K contain carbon atoms from branched (iso-) alkanes. Peaks of the n-alkane moiety in regions B, D, H, and G, called a Canonical Group, reveal the present VGO to possess an n-alkane chain content of 17.1 C atoms per 100 C atoms of feedstock, with an average chain length $L = 7.8$, that is, for every set of terminal n-alkane atoms (C1, C2, C3), there are 4.8 interior n-alkane atoms (C4, C25).

1-H. Figure 3 shows the 1-H NMR spectrum of VGO feedstock V2. The x-axis is resonance frequency, or chemical shift, *h*, in units of ppm relative to TMS, indicative of hydrogen type, while the y-axis is absorption intensity, *i*, with arbitrary units, approximately proportional to the abundance of such hydrogen atoms in the sample. Accurate hydrogen amounts are obtained from integrals of peak intensities, seen as four continuous stepped lines in the figure, their h-domains and numerical magnitudes noted below the abscissa. The 1-H spectrum has the following regions:

Region(s)	<i>h</i> (range)	H-atom type
TMS	0.0	H in methyls of TMS
Hgam, Hbet, Hbzy	0.4 - 3.2	aliphatic H, attached to sp ³ hybridized C atoms
DIOX	~3.65	H in methylenes of DIOX
Har	6.5 - 9.2	aromatic H, attached to sp ² hybridized ring C atoms

The wide separation between the regions of aliphatic and of aromatic hydrogens is noteworthy, permitting their unambiguous delineation, and providing the hydrogen aromaticity $Har = 4.1\%$. The Cumulative Integral Regions, shown below the spectrum, have the following approximate chemical interpretations. The aromatic H region is subdivided into Hart, Hard, and Harm, with sum $Har(t+d+m) = Har$; of these, Harm contains H atoms from all aromatic rings; Hard contains H atoms from ≥ 2 - but not from 1-ring aromatics; and Hart contains H atoms from ≥ 3 - but not from ≤ 2 -ring aromatics. Next, Hbzy are benzylic H atoms, attached to aliphatic C atoms bonded to aromatic rings; Hbzy thus reflects the degree of aromatic ring substitution. Of the two broad benzylic peaks in the spectrum, $\alpha 1$ is mainly H atoms on methyls pendant on mono-aromatic rings, while $\alpha 2$ contains a host of other benzylic hydrogens. Hbet are H atoms attached to aliphatic C atoms bonded to other aliphatic C atoms; region Hbeta, with huge peak $\beta 1$, is primarily H atoms in the methylene CH₂ units of alkyl chains, while Hbetb includes H atoms on CH (methine) and CH₂ (methylene), the peaks $\beta 1$, $\beta 2$ including H atoms on alicyclic rings. Hgam, with large twin peaks γ , are H atoms in aliphatic methyls CH₃.

2-D HETCOR. Figure 4 is a 2-dimensional contour plot showing the islands in an H-C atom correlation spectrum of VGO feedstock V2. The HETCOR experiment, described by Gray (1994), is the equivalent of recording full 1-H spectra, such as shown in Figure 3, at each of a myriad slices of a 13-C spectrum, such as shown in Figure 2. A correlation island at chemical shift coordinates [*c*, *h*] represents a carbon of shift *c* connected to a hydrogen of shift *h*, with island cross-section (actually, its peak height and volume) crudely related to the abundance of the correlated atoms in the feedstock. In Figure 4, with abscissa (F2 axis) *c* and ordinate (F1 axis) *h*, the large lens-shaped island #3 at coordinates [*c*, *h*] = [14.2, 0.89] arises from the H and C atoms in the terminal methyl group of an n-alkane chain and is so labelled. Numerous other islands are also visible in the figure, with those that have been chemically identified being labelled in three rows respectively representing methyl CH₃, methylene CH₂, and methine CH carbons. Identified islands belong to the following Canonical Groups: n-alkane (C1, C2, C3, C4, C25), 2-methyl alkane (C1, C2, C3), 3-methyl alkane (C1, Me, C3), 4-methyl alkane (C1, C3), and interior-methyl alkane (Me, Cj(unction)). The present HETCOR spectrum had a dynamic range, that is, the ratio of tallest peak height/noise level, of 615, and the 30 islands in Figure 4 resulted from a contour threshold about 3 times higher than the noise level. Decreasing the threshold to 1.5 times noise resulted in 58 islands, of which 23 could be identified, revealing the additional moieties: 4-methyl alkane (C1, C2, C3, C4), 5-methyl alkane (C2, C4), interior-methyl alkane, including phytyl, (Me, Cj, Cj+1, Cj+2, Cj+3), alkyl-cyclo-C6-alkane (Me, Cr(ing)), and alkyl-benzene (C3).

RESULTS

Table 1 presents data from both conventional and MIFF characterizations of six representative FCC feeds, four VGOs V1 to V4 and two ATBs A1 and A2.

Conventional properties include gravity, Conradson carbon residue, and elemental assays of H, C, S, N, from which H elem, H atoms/100 C atoms, has been calculated.

MIFF data, from top to bottom, show results from the IR and CG trains; for samples run in duplicate, average values and an estimate of their experimental uncertainty are both quoted. Among IR train C13

data, the two rows labelled diox/oil are the ratios of carbon atoms in the dioxane internal standard to those in the oil; the gravimetric row was calculated from sample preparation and elemental assays while the spectral row is independently derived from the regional integrals of the experimental spectra. Agreement between these internal standard ratios is a stringent test of C13 NMR data fidelity. The next row, Car, and then the next seven rows, called CIRs for Cumulative Integral Regions, provide a breakdown of feedstock carbon atom types, as percentages. CIRs are so named because each is the accumulation of Detailed Integral Regions, DIRs, which represent the finest parsing of spectral integrals. The chemical significance of Car and the CIRs was earlier considered in connection with the 13-C NMR spectrum in Figure 2. The last row, H count, H / 100 C, is derived from the DIRs by summing the products of DIR amount times the number of H atoms per C atom of the type contained therein. Data from the IR train H1 are analogous to those from the IR train C13, with two diox/oil rows, gravimetric and spectral, followed by Har and then seven CIRs, whose chemical significance was earlier considered with the 1-H NMR spectrum in Figure 3. Finally, the first row of the CG Train C13 provides the average chain length of n-alkane moieties in the feedstock, Lna in C atoms. The second and third rows of the CG train respectively provides the percentages of C atoms in n-alkane moieties Cna, and in methyl-alkane moieties Cma, the latter comprising 2-, 3-, 4-, 5-, and interior-methyl substituted alkane chains. These are used, along with Car from the IR train, shown again in the fifth row, to form a final set of 4 NMR-derived canonical groups for each feedstock. The group Ccs in the fourth row, comprising cyclic and highly substituted aliphatic C atoms, is a (large) remnant obtained from $Ccs = 100 - Cna - Cma - Car$.

Dioxane/Oil Ratios. Figure 5 compares the internal standard ratios of dioxane to oil D/O,g from the gravimetric sample preparation procedure to those derived from spectral integration D/O,s. Data from C13 and H1 spectra are respectively differentiated by large solid and small hollow symbols in the plot and by suffixes c and h in the legend. Linear regression of these data, shown by the dashed line in the figure, yields:

$$(E1) \quad D/O,s = (0.00 \pm 0.01) + (1.08 \pm 0.06) D/O,g.$$

The present NMR integral measurements are accurate to within 8% absolute, with a precision of $\pm 6\%$ relative to one another. Such quantitative fidelity is a tribute to modern NMR spectrometers, which can evidently excite and detect diverse kinds of C and H atoms in the feedstock over wide frequency ranges on both sides of the C and H atoms in the dioxane internal standard.

MIFF Maps. MIFF data in Table 1 provide an aromaticity map, Car vs Har, and an n-alkane chain map, Cna vs Lna, of relevance to FCC performance as discussed in the next section. The aromaticity map showed Har ≈ 0.3 Car, from which, using feedstock H content ≈ 172 H/100 C, there are typically 51 aromatic H atoms/100 aromatic C atoms, that is, 51% of the aromatic carbons are protonated. The other 49% of the aromatic carbons must therefore be quaternary, and from the benzylic H atoms we estimate 19% of these to be substituted, so the remaining 30% are fused, at ring junctions. The n-alkane chain map showed that VGO and ATB feedstocks typically possess $[Cna, Lna] = [17 \pm 3, 9 \pm 1]$, with the highest observed content Cna = 40 and the longest L = 12.

Carbon Atom Groups. The upper panels of Figure 6 present NMR-derived carbon atom groups as pie charts for feedstocks A1 and V4. Each pie has four slices [Cna, Cma, Ccs, Car], respectively the percentages of n-alkane, methyl-alkane, alicyclic + highly substituted, and aromatic carbon atoms in the feedstock. The variations in pie slices between A1 and V4, the former containing more n-alkanes and possessing the lower aromaticity, anticipate differences between their performances in FCC units. By way of comparison, the lower panels of Figure 6 show mass spec-derived data for each of A1 and V4, using the high-resolution electron impact methods described by Fisher (1986, 1990). Mass spec data are compressed into four groups of decreasing Z-numbers [Wpar, Wcyp, Wmono, Wdih], respectively the weight percentages of paraffins, n- and iso- (Z = 2), cyclo-paraffins, mono-, di-, tri- and higher ($0 \geq Z \geq -4$), mono-aromatics (Z = -6), and di- and higher-aromatics (Z ≤ -8). The preceding characterizations differ fundamentally in that NMR distinguishes individual atoms by their bonding environment, without regard for the host molecules they inhabit, whereas mass spectrometry distinguishes whole molecules within homologous series of formula C_nH_{2n+Z} . By joint use of the MIFF and mass spec pies we can ascertain (Wmono + Wdih - Car), the aliphatic carbons associated with the aromatic core carbons, which respectively amount to 16% and 29% for A1 and V4, rather larger than Car itself. The methyl-alkane group Cma of MIFF has no analogue in mass spec data because the latter does not distinguish n- from iso-paraffins, both having the same Z = 2. Finally, it is curious that, despite their different chemical origins, the n-Alkane content Cna from MIFF and the paraffin content Wpar from the mass spec are numerically within $\pm 2\%$ of one another for each of A1 and V4, and this rough equality between Cna and Wpar also holds for all the other oils in Table 1.

MODELLING FCC PERFORMANCE

Theoretical Basis. Figure 7 depicts the possible relation of our NMR-derived characterizations of a feedstock to its FCC performance, comprising conversion kinetics and products, using data for oil V4. MIFF groups [Cna, Cma, Ccs, Car] = [19.7, 8.8, 54.2, 17.4] are shown in the uppermost ribbon, with segments proportional to their respective abundances. IR train H1 data were used to slightly elaborate Car and Ccs, with aromatic core C atoms classified by their ring sizes, mono-, di-, and tri-+higher, and the benzylic C atoms pendant upon such rings shown as a (small) subset of Ccs. The kinetics of cracking the MIFF groups under acid-catalysed conditions with carbenium ion intermediates are depicted in the

second ribbon from the top, based on the works of Nace (1969), Venuto & Habib (1979), and Pines (1981). N-alkane chains, comprising mainly secondary carbons, are amenable to acid cracking, but with modest kinetics that are further a function of chain length; methyl-alkanes and most of the alicyclic + substituted group crack rapidly, on account of reactive tertiary carbons within them; the entire aromatic core group and the benzylic portion of the Ccs group are not cracked at all. The third ribbon depicts potential products from complete conversion of the feedstock by acid-catalysed cracking only. Gas + gasoline products arise from n-alkanes, methyl-alkanes, alicyclic + substituted carbons excluding the benzylic di- and tri- segments, and mono-aromatics. Light cycle oil LCO is related to the di-aromatic group and to the benzylic carbons attached to di-aromatics, while decant oil + coke DO+C is associated with tri- and higher aromatics and their benzylic carbons. For the present feedstock V4, MIFF data provide potential product yields of $[GG^*, LCO^*, DO+C^*] = [85.4, 6.7, 7.9] C/100 C$. Actual product yields from FCC of V4 at commercial conditions are shown in the bottom ribbon, being $[Gas, Gasoline, LCO, DO, Coke] = [20.4, 43.7, 19.2, 11.6, 5.1] wt\%$. The actual yield of gas + gasoline = 64.1 is appreciably lower than the asymptotic maximum $GG^* = 85.4$ inferred from MIFF, with the actual yields of LCO and DO+Coke correspondingly higher than the asymptotic LCO^* and $DO+C^*$. These differences reflect both kinetic constraints on conversion as well as the operation of additional catalytic reaction paths, such as hydrogen transfer and polymerization, in parallel with the dominant acid cracking path.

Decant Oil + Coke Yields. As an example of how MIFF parameters might be employed to model the yields of FCC products, Figure 8 is a 3-dimensional plot of observed DO+Coke yields, wt%, on a MIFF aromaticity map of Har, H/100 H vs Car, C/100 C. The data can be seen to ascend from the origin at near lower left roughly along a diagonal toward the far upper right. A projection of the observed relationship on the x-z plane reveals that $DO+C \approx 0.9 Car$, about twice as large as the theoretically expected from the parameter $DO+C^*$ computed in Figure 7.

Overall Cracking Kinetics. The overall kinetics of feedstock conversion in the riser of an FCC unit have been considered by Weekman & Nace (1970) whose model, with Voorhies' (1945) expression for coke deposition on the catalyst, can be used to derive the overall cracking rate constant k_0 from operating conditions and observed conversions. The observed k_0 are then normalized to standard residence time τ and temperature T K to provide an apparent cracking rate constant ko^* characteristic of the feedstock. Figure 9 is a 3-D plot of ko^* on a MIFF n-alkane chain map of Lna, C atoms, vs $Cna, C/100 C$, for four FCC feeds, two each VGOs and ATBs, that possessed roughly the same specific gravities, $SG = 0.903 \pm 0.004$, and carbon aromaticities $Car = 15 \pm 1$. Three of these feeds, with chain lengths $8.6 \leq Lna \leq 10.1$ and n-alkane contents $18 \leq Cna \leq 40$, exhibit $ko^* \approx 0.15$, whereas the fourth, with $Lna = 10.6, Cna = 33$ has an appreciably lower $ko^* = 0.10$. These data imply that feedstock conversion kinetics may be retarded by n-alkane chains longer than a critical $Lna^* \approx 10.3$. More extensive data are needed to verify and define a critical (Lna^*, Cna^*, ko^*) surface for kinetic retardation, though it is interesting that Nace (1969) reported the cracking kinetics of pure n-alkanes to reach a maximum at $Lna = 8$ (hexadecane) and then decline for longer chains.

ACKNOWLEDGEMENTS: This work was initiated and supported by Larry Hallee, late of the Stone & Webster Engineering Corporation, Houston, TX. The author is indebted to Jeanne Owens of the MIT Spectrometry Laboratory, for help with NMR spectra, as well as Mike Silverman and Atulya Saraf of Stone & Webster, for discussions of Mass Spec and FCC.

REFERENCES

- Knight, S.A.: Chem. Ind., 1920-1923 (1967).
 Shooley, J.N.; Budde, W.L.: Anal. Chem., **48**, 1458-1461 (1976).
 Deutsch, K.; Jancke, H.; Zeigan, D.: J. Prakt. Chem. Ind., **318**, 177-184 (1976).
 Ladner, W.R.; Snape, C.E.: Fuel, **57**, 658-662 (1978).
 Gillet, S.; Rubini, P.; Delpuech, J.J.; Escalier, J.C.; Valentin, P.: Fuel, **60**, 221-225 (1981).
 Gillet, S.; Rubini, P.; Delpuech, J.J.; Escalier, J.C.; Valentin, P.: Fuel, **60**, 226-230 (1981).
 Netzel, D.A.; McKay, D.R.; Heppner, R.A.; Guffey, F.D.; Cooke, S.D.; Varie, D.L.; Linn, D.E.: Fuel, **60**, 307-320 (1981).
 Cookson, D.J.; Smith, B.E.: Anal. Chem., **57**, 864-871 (1985).
 Cookson, D.J.; Smith, B.E.: Energy & Fuels, **1**, 111-120 (1987).
 Stothers, J.B.: "Carbon-13 NMR Spectroscopy", Academic Press, New York, NY 1972.
 Breitmaier, E.; Voelter W.: "Carbon-13 NMR Spectroscopy: High-Resolution Methods and Applications", 3rd Ed., VCH Publishers, Weinheim, Germany, 1987, pp73-105.
 Croasmun, W.R.; Carlson, R.M.K.: "Two-Dimensional NMR Spectroscopy: Applications for Chemists and Biochemists", 2nd Ed., VCH Publishers, Weinheim, Germany, 1994.
 Bouquet, M.; Bailleul, A.: Fuel, **65**, 1240-1246 (1986).
 Mauleon, J.L.; Sigaud, J.B.; Biedermann, J.M.; Heinrich, G.: Proc. 12th World Petroleum Congress, Houston TX, [18], 1-7, Wiley, London (1987).
 Kim, H.N.; Verstraete, J.J.; Virk, P.S.; Fafet, A.: Oil & Gas J., **96** (37) 85-88 (1998).
 Gray, G.A., Ch 1, pp 46-49 in Croasmun, W.R.; Carlson, R.M.K.: "Two-Dimensional NMR Spectroscopy: Applications for Chemists and Biochemists", 2nd Ed., VCH Publishers, Weinheim, Germany (1994).
 Fisher, I.P.: Fuel, **65**, 473-479 (1986).

- Fisher, I.P.: Appl. Catalysis, **6**, 189-210 (1990).
 Nace, D.M.: Ind. Eng. Chem., Prod. Res. Dev., **8**, 31 (1969).
 Venuto, P.B.; Habib, E.T.: "Fluid Catalytic Cracking with Zeolite Catalysts", Marcel Dekker, Inc., New York, (1979).
 Pines, H.: pp1-122 in "The Chemistry of Catalytic Hydrocarbon Conversions", Academic Press, New York, (1981).
 Weekman, V.W.; Nace, D.M.: A.I.Ch.E. J., **16**, 397-404 (1970).
 Voorhies, A.: Ind. Eng. Chem., **37**, 318 (1945).

TABLE I. Conventional and MIFF Characterizations of Representative FCC Feedstocks.

Oil		V1	V2	A1	A2	V3	V4
CONV DATA							
API	deg	26.8	24.0	25.5	25.1	20.6	23.4
SG	15.6C	0.894	0.910	0.901	0.903	0.930	0.914
CCR	wt%	-	-	2.62	2.96	0.42	0.27
Elemental Assay							
H	wt%	12.91	12.50	12.94	12.54	12.14	12.47
C		86.63	86.28	86.60	87.08	85.52	86.65
S		0.44	1.03	0.50	0.28	2.22	0.98
N		-	0.19	0.20	-	0.20	0.11
H elem	H/100 C	177.6	172.6	178.0	171.6	169.1	171.5
MIFF DATA							
IR Train C13							
diox/oil	gravimetric	0.116	0.114	0.141 ± 0.000	0.141	0.024 * 0.143	0.094 ± 0.000
diox/oil	spectral	0.113	0.104	0.156 ± 0.000	0.151	0.027 * 0.163	0.104 ± 0.005
Car	C/100 C	12.5	16.8	14.8 ± 0.6	15.8	24.9 ± 0.7	17.4 ± 0.1
CIRs							
Carqt		5.4	7.5	6.6 ± 0.0	7.8	12.6 ± 0.9	8.2 ± 0.6
Carpi		1.8	2.3	1.9 ± 0.0	2.5	3.4 ± 0.1	2.4 ± 0.2
Carpo		5.3	7.0	6.3 ± 0.5	5.5	8.9 ± 0.3	6.8 ± 0.7
Calhs		7.5	7.5	2.9 ± 0.2	4.4	5.1 ± 0.0	6.8 ± 0.9
Calbr		18.9	17.9	13.2 ± 0.2	16.7	15.2 ± 0.5	18.4 ± 0.5
Calch		45.6	42.7	58.3 ± 0.2	51.5	38.7 ± 0.4	43.8 ± 1.2
Calme		15.6	15.1	10.8 ± 0.0	11.6	16.1 ± 0.3	13.7 ± 0.1
H count	H/100 C	182.1	173.6	178.9 ± 0.4	174.3	164.6 ± 1.1	171.7 ± 0.3
IR Train H1							
diox/oil	gravimetric	0.130	0.132	0.159 ± 0.000	0.164	0.028 * 0.169	0.110 ± 0.000
diox/oil	spectral	0.128	0.132	0.165 ± 0.003	0.163	0.029 * 0.197	0.120 ± 0.003
Har	H/100 H	4.3	6.7	3.5 ± 0.2	4.2	7.8 ± 1.0	5.8 ± 0.2
CIRs							
Hart		0.9	1.6	0.6 ± 0.2	0.7	1.5 ± 0.6	1.1 ± 0.2
Hard		1.4	2.2	1.2 ± 0.1	1.0	2.7 ± 0.3	2.0 ± 0.1
Harm		2.1	2.9	1.7 ± 0.0	2.5	3.6 ± 0.1	2.7 ± 0.0
Hbzy		3.4	3.6	3.4 ± 0.3	3.4	7.1 ± 1.3	4.0 ± 0.1
Hbetb		8.5	5.3	7.9 ± 0.6	8.6	9.6 ± 3.3	8.3 ± 0.3
Hbeta		55.1	53.9	64.8 ± 0.1	60.9	48.6 ± 1.1	53.3 ± 0.1
Hgam		28.6	30.5	20.5 ± 0.5	22.9	26.9 ± 2.5	28.7 ± 0.1
CG Train C13							
Lna	atoms	8.1	7.8	10.6 ± 0.0	10.0	8.2 ± 0.0	8.9 ± 0.0
Groups	C/100 C						
Cna	n-Alkane	18.2	17.1	32.6 ± 1.0	28.9	16.4 ± 0.1	19.7 ± 1.4
Cma	Me-Alkane	8.8	7.8	8.1 ± 0.9	11.2	8.2 ± 0.1	8.8 ± 0.1
Ccs	Cyc+Sub	60.6	58.3	44.5 ± 1.3	44.1	50.5 ± 0.9	54.2 ± 1.4
Car	Arom Core	12.5	16.8	14.8 ± 0.6	15.8	24.9 ± 0.7	17.4 ± 0.1
Sum		100.0	100.0	100.0	100.0	100.0	100.0

* Gravimetric dioxane/oil ratios were varied six-fold for samples of oil V3.

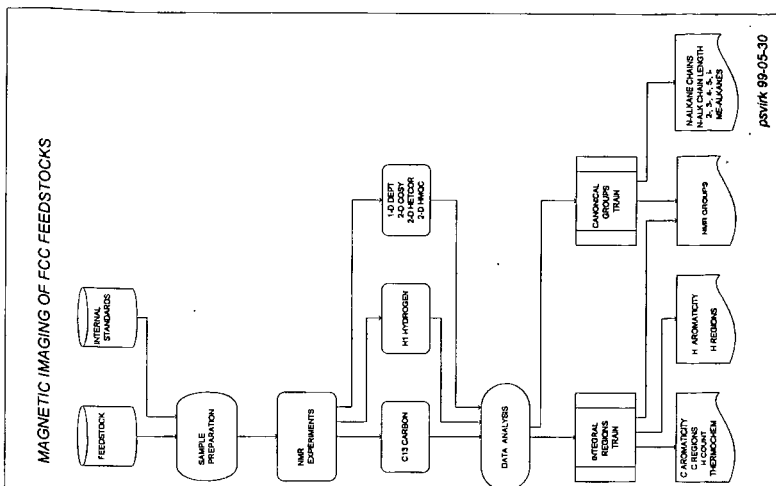


Fig. 1. Magnetic Imaging of FCC Feedstocks.

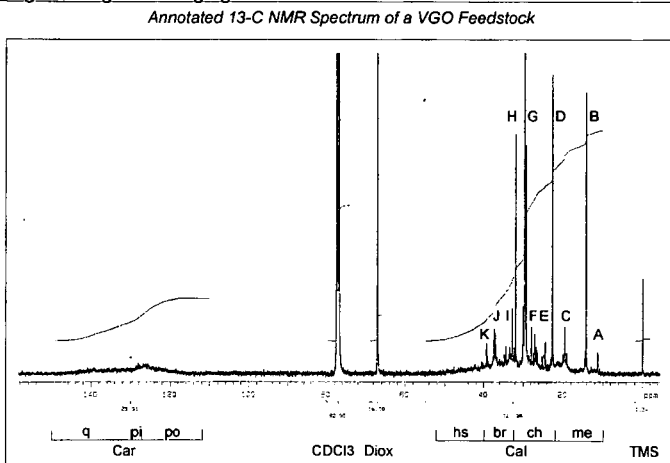


Fig. 2. Annotated 13-C NMR Spectrum of a VGO Feedstock.

psvirk 99-05-30

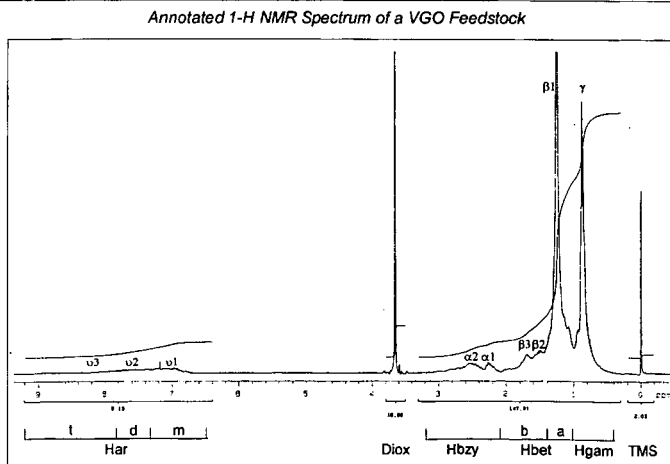


Fig. 3. Annotated 1-H NMR Spectrum of a VGO Feedstock.

psvirk 99-05-30

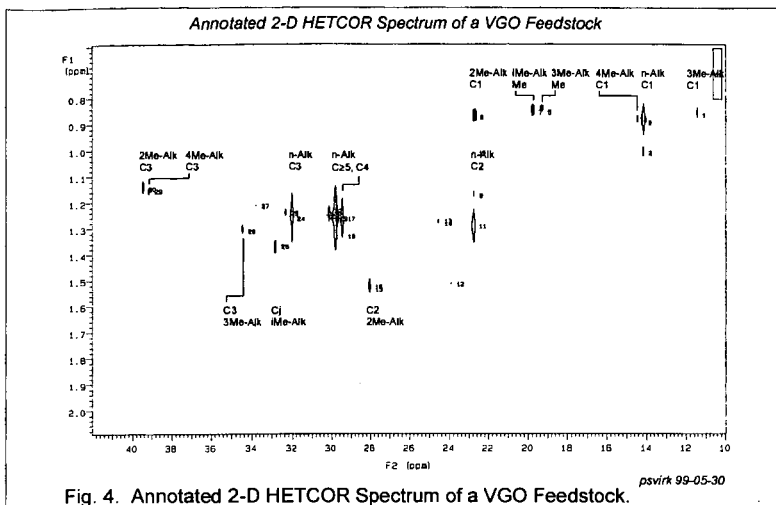


Fig. 4. Annotated 2-D HETCOR Spectrum of a VGO Feedstock.

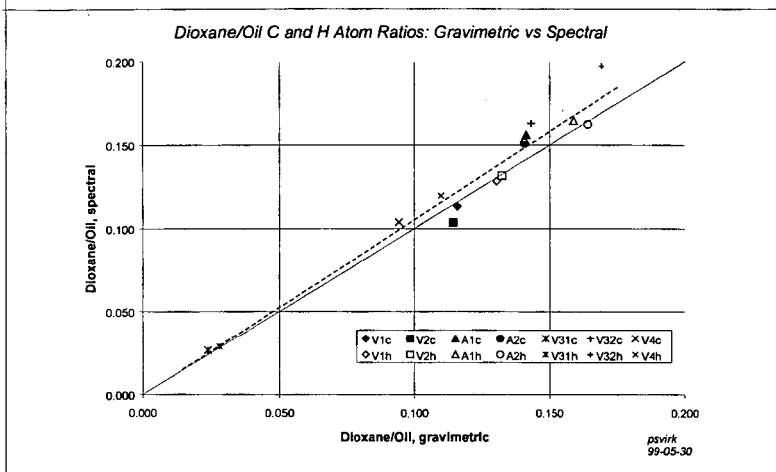


Fig. 5. Dioxane/Oil Ratios of C and H atoms: Gravimetric vs Spectral.

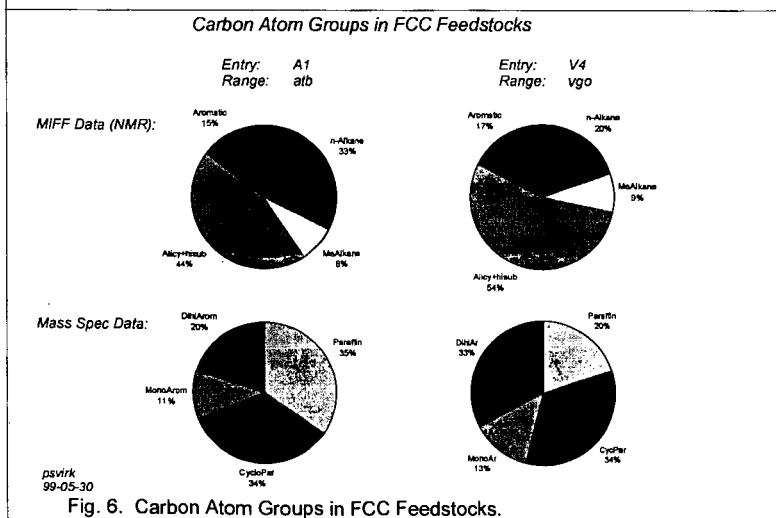
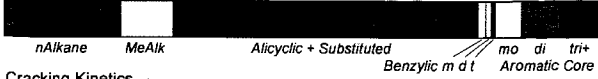


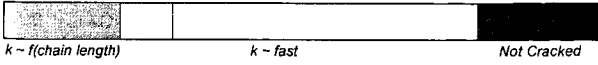
Fig. 6. Carbon Atom Groups in FCC Feedstocks.

Relation of NMR-Derived Feedstock Characterizations to FCC Performance.

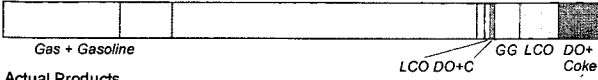
Advanced MIFF Groups



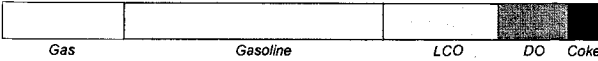
Cracking Kinetics



Potential Products



Actual Products

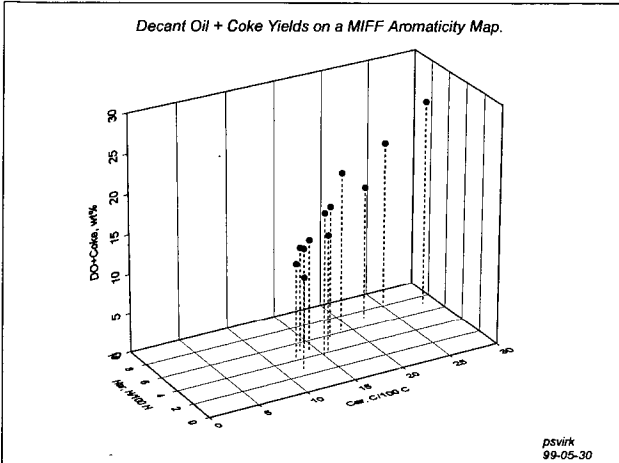


Sample: V4
Range: vgo

psvirk
99-05-30

Fig. 7. Relation of NMR-Derived Feedstock Characterizations to FCC Performance.

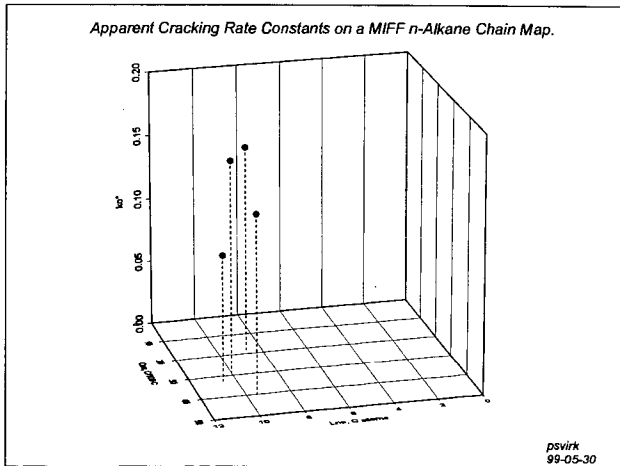
Decant Oil + Coke Yields on a MIFF Aromaticity Map.



psvirk
99-05-30

Fig. 8. Decant Oil + Coke Yields on a MIFF Aromaticity Map.

Apparent Cracking Rate Constants on a MIFF n-Alkane Chain Map.



psvirk
99-05-30

Fig. 9. Apparent Cracking Rate Constants on a MIFF n-Alkane Chain Map.

MODELING OF REACTIVITY OF LEWIS AND BRØNSTED SITES

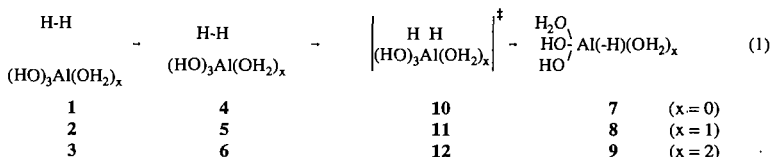
Dan Fărcașiu

Department of Chemical and Petroleum Engineering, University of Pittsburgh, 1249 Benedum Hall,
Pittsburgh, PA 15261

It is generally considered that the coordinatively unsaturated sites (cus) responsible for the catalytic properties of active aluminum oxide consists of tri- and pentacoordinated aluminum atoms. The remaining possibilities, hexa- and tetraordinated aluminum atoms, are considered coordinatively saturated and, therefore, unreactive. A careful NMR investigation has evidenced, however, only tetra-, penta-, and hexacoordinated aluminum atoms in alumina and in the intracavity material of steamed zeolites. No measurable amount of tricoordinated sites was found.¹ Even if vanishingly small concentrations of tricoordinated aluminum are present, it is difficult to assign all catalytic activity to them. An examination of the relative reactivity of various sites on alumina was, therefore, in order.

The isotope exchange between D₂ and the protons of the solid is a good model reaction for the reactivity of sites on alumina.² Theoretical modeling of the hydrogen chemisorption on alumina was attempted before by both semiempirical³ and ab initio calculations,⁴ at a rather low level of theory. One study considered only tricoordinated sites,^{4a} the other looked at pentacoordinated sites as well and concluded that they were inactive.^{4b} The aluminum sites were modeled by the simple clusters Al(OH)₃ and Al(OH)₅.⁴ It was not clear from the paper^{4b} whether the species considered was the dianion Al(OH)₅²⁻ or a dioxidized, electrically neutral, species of the same formula, but neither of them appears to us to be a good choice.

We considered the reactivity of electrically neutral single clusters, (HO)₃Al(OH₂)_x, containing tri- (1, x = 0), tetra- (2, x = 1), and pentacoordinated (3, x = 2) aluminum atoms. Thus, no unnatural, oxidized species was used. The full reaction profile for dissociative hydrogen chemisorption was studied (Eq. 1).



As the first step, the physisorbed complexes 4 (x = 0), 5 (x = 1) and 6 (x = 2) were examined. Their reaction to form the chemisorbed complexes, 7, 8, and 9, was mapped to determine the transition structures (10, 11, and 12) and the corresponding energies (E_{TS}), which measure the energy barriers for the exchange.

The ab initio calculations were conducted with the program Gaussian 94,⁵ in the manner described previously.⁶ All geometry optimizations were conducted with electron correlation with the MP2 method⁷ or with the DFT-B3LYP⁸ method. The 6-31G*, 6-31-G**, 6-31++G**, 6-311G** and 6-311++G** basis sets were used.

For the tricoordinated aluminum system (x = 0), the geometry of the starting cluster was obtained by the optimization of the species (HO)₃Al(OH₂) (2) and removal of the extra water molecule, on the idea that aluminum oxide surfaces are formed by calcination of hydrated forms. In one approach (A), the angles around the aluminum atom were then frozen as in the hydrated cluster and the other geometrical parameters of the dehydrated cluster were optimized. Alternatively (B), the rigidity of the solid was simulated by freezing the hydrogen atoms in their positions in the hydrated cluster and then optimizing the central part of the cluster (the Al-(O-)₃ group) after the removal of the extra water. The complexes with physisorbed and chemisorbed hydrogen were optimized in the same way. The reactions of tetra- and pentacoordinated aluminum clusters were studied without any constraints on the geometry.

The calculations predicted the hydrogen chemisorption to be endothermic in all cases, the order being $E(x=0) < E(x=1) < E(x=2)$. For $x=0$, the calculation by the approach B gave a much lower endothermicity for the chemisorption than the approach A. The energy barriers for chemisorption were similar, however, for the approaches A and B. Their variation with the coordination number of the aluminum atom was $E_{TS}(x=0) < E_{TS}(x=1) < E_{TS}(x=2)$. Reaction coordinate tracking indicated that chemisorption occurs through the interaction of H_2 with the Al atom, therefore it is a catalysis by a metal ion. A three-center bond involving the aluminum and the two hydrogens is formed, after which one of the hydrogens migrates to an adjacent oxygen atom. the transition state is located along this hydrogen shift.. B3LYP calculations give results in reasonable agreement with the MP2 calculations, attesting to the appropriateness of the DFT method for this type of structures.

The calculations indicate tetracoordinated aluminum sites to be catalytically active. As these sites are usually in higher concentration than the pentacoordinated sites and are intrinsically much more active, they should be considered *the* catalytic sites on active alumina.

The second type of acid sites on solid surfaces, the Brønsted sites, are most often characterized by neutralization with a probe base and examination of the product by spectroscopic methods or measurement of the thermal effect of this interaction.⁹ Pyridine (Py) and its derivatives have long been used as probe bases. Comparison of pyridine with 2,6-disubstituted pyridines was proposed to distinguish Lewis from Brønsted sites.¹⁰ The application of the highly crowded homolog, 2,6-di-*tert*-butylpyridine (DTBP) was proposed to distinguish between sites on the outer surface and sites inside cavities or channels.¹¹

It has been pointed out that all types of ionic reactions on solid surfaces must occur through the intermediacy of tight ion pairs.^{9a,12} Thus, the reaction of Py forms $PyH^+ \cdot A^-$ tight ion pairs, where A^- is the anion of the acid site. The direction of adsorption should be the one which maximizes the hydrogen bonding interaction, that is with the $N^+ - H$ perpendicular to the surface (sideways adsorption). A complete analysis of the thermodynamics of protonation in the gas phase and in water solution led to the conclusion that $DTBP^+$ also forms hydrogen bonds at nitrogen.¹³

The line-shape of the NMR signals of protons bonded to nitrogen in pyridinium (PyH^+) and di-*tert*-butylpyridinium ions ($DTBP^+$) in solution indicated a significant difference in their rates of longitudinal relaxation (R_1), the former ion relaxing the slowest. Computer modeling showed that the ratio of relaxation rates is 10-20. A significant difference between the relaxation times ($T_1 = 1/R_1$) for the carbon atoms in β and γ position (4.71 and 4.75sec for PyH^+ , 0.55 and 0.79 sec for $DTBP^+$) was observed as well. The different positions in the molecule of the N-H group and of those two carbon atoms indicate that the difference in longitudinal relaxation rates originates in a different rate of tumbling in solution, rather than a difference in the electrical field gradient. Calculations of the correlation times for the relaxation of molecules considered as ellipsoid-shape rotors in a medium of given viscosity indicate that the difference in size covers only a part of the difference in tumbling rates (lower τ_c for pyridine). The difference should come from specific interactions with the solvent, most likely in the form of electrical double layers which have to be disturbed during the rotation.

Differences between relaxation times for each individual ion in different acids were also observed. It was established that the differences are not solvent effects, but are brought about by the change in anion. Thus, in the same solvent PyH^+ relaxes slower, that is, tumbles faster, when the anion corresponds to a stronger acid. The reason for this behavior is that in the salt of the weaker acid the ions are ion-paired and the rotation, occurring around an axis perpendicular to the N-H⁺ bond, is hindered by this interaction.

The opposite effect is observed for the $DTBP^+$ cation: the salt of the *weaker* acid, which is present in solution as ion pairs, tumbles faster (relaxes more slowly). This behavior can be rationalized by the anion being situated in the ion pair along the axis around which the molecule rotates to produce the NMR relaxation, that means, at the top of the ring. Therefore, no hydrogen bond $N-H^+ \cdots A^-$ is formed for this cation, a finding which contradicts the assertions of previous authors.¹³

The same orientation should be encountered in chemisorption of DTBP on solid acids, that is with the ring facing the solid surface containing the acid site.

References

- (1) Coster, D.; Blumenfeld, A. L.; Fripiat, J. J. *J. Phys. Chem.* **1994**, *98*, 6201.
- (2) (a) Taylor, H. S.; Diamond, H. *J. Am. Chem. Soc.* **1935**, *57*, 1256. (b) Lee, J. K.; Weller, S. W. *Anal. Chem.* **1958**, *30*, 1057. (c) Hall, W.K.; Leftin, H. P.; Cheselske, F. J.; O'Reilly, D. E. *J. Catal.* **1963**, *2*, 506. (d) Hall, W.K.; Lutinski, F. E. *J. Catal.* **1963**, *2*, 518. (e) Carter, J.; Lucchesi, P.; Corneil, P.; Yates, D. J. C.; Sinfelt, J. H. *J. Phys. Chem.* **1965**, *69*, 3070.
- (3) Zelenovskii, V. M.; Zhidomirov, G. M.; Kazanskii, V. B. *Zh. Fiz. Khim.* **1984**, *58*, 1788.
- (4) (a) Senchenya, I. N.; Kazanskii, V. B. *Kinetika I Kataliz* **1988**, *29*, 1331. (b) Ioka, F.; Sakka, T.; Ogata, Y.; Iwasaki, M. *Can. J. Chem.* **1993**, *71*, 663.
- (5) Frisch, M. J.; Trucks, G. W.; Schlegel, H. B.; Gill, P. M. W.; Johnson, B. G.; Robb, M. A.; Cheeseman, J. R.; Keith, T.; Petersson, G. A.; Montgomery, J. A.; Raghavachari, K.; Al-Laham, M. A.; Zakrzewski, V. G.; Ortiz, J. V.; Foresman, J. B.; Cioslowski, J.; Stefanov, B. B.; Nanayakkara, A.; Challacombe, M.; Peng, C. Y.; Ayala, P. Y.; Chen, W.; Wong, M. W.; Andres, J. L.; Replogle, E. S.; Gomperts, R.; Martin, R. L.; Fox, D. J.; Binkley, J. S.; DeFrees, D. J.; Baker, J.; Stewart, J. P.; Head-Gordon, M.; Gonzalez, C.; Pople, J. A.; *Gaussian 94, Revision D.3*; Gaussian, Inc.: Pittsburgh PA, 1995.
- (6) Fărcașiu, D.; Lukinskas, P. *J. Phys. Chem. A*, **1998**, *102*, 10436.
- (7) (a) Pople, J. *Acc. Chem. Res.* **1970**, *3*, 217. (b) Pople, J. A. *Int. J. Mass Spectrom Ion Phys.* **1976**, *19*, 89. (c) Hehre, W. J.; Radom, L.; Schleyer, P. v. R.; Pople, J. A. *Ab initio Molecular Orbital Theory*; Wiley-Interscience: New York, NY, 1986.
- (8) (a) Hohenberg, P.; Kohn, W. *Phys. Rev.* **1964**, *136*, B864. (b) Kohn, W.; Sham, L. *Phys. Rev.* **1965**, *140*, A1133. (c) Parr, R.G.; Yang, W. *Density Functional Theory of Atoms and Molecules*, Oxford University Press: New York, 1989. (d) Becke, A. D. *J. Chem. Phys.* **1993**, *98*, 5648.
- (9) (a) Fărcașiu, D.; Ghenciu, A. *Progr. NMR Spectroscopy* **1996**, *29*, 129. (b) Cardona-Martinez, N.; Dumesic, J. A. *J. Catal.* **1990**, *125*, 427.
- (10) Murrell, L. L.; Dispenziere, N. C. *J. Catal.* **1989**, *117*, 275.
- (11) (a) Benesi, H. A.; *J. Catal.* **1973**, *28*, 176. (b) Corma, A.; Fornés, V.; Forni, L.; Martinez-Triguero, J.; Moschetti, D. *J. Catal.* **1998**, *179*, 451.
- (12) (a) Fărcașiu, D.; Ghenciu, A.; Li, J. Q. *J. Catal.*, **1996**, *158*, 116. (b) Ghenciu, A.; Fărcașiu, D. *J. Mol. Catal. A*, **1996**, *109*, 273.
- (13) H. P. Hopkins, Jr., D. V. Jahagirdar, P. S. Moulik, D. H. Aue, H. M. Webb, W. R. Davidson and M. D. Pedley, *J. Am. Chem. Soc.*, 1984, *106*, 4341.

SYNERGISTIC EFFECTS OF HYBRID HYDROGEN DONORS TOWARDS STABILIZATION OF PARAFFINIC JET FUELS IN THE PYROLYTIC REGIME

John M. Andrésen, James J. Strohm, Michael M. Coleman and Chunshan Song*
Applied Catalysis in Energy Laboratory, The Energy Institute
The Pennsylvania State University, University Park, PA 16802

KEYWORDS: Pyrolysis, thermal stability, aviation jet fuels.

ABSTRACT

The chemical interactions between n-tetradecane and the hybrid hydrogen donors of benzyl alcohol and 1,2,3,4-tetrahydro-1-naphthol, and benzyl alcohol and tetrahydronaphthalene have been studied. Compared to the use of a single hydrogen donor, the hybrids resulted in synergistic effects towards reducing the pyrolytic degradation of alkanes in jet fuels, resulting in an enhanced suppression of the formation of free radicals.

INTRODUCTION

Future high performance jet fuels are expected to be thermally stable at temperatures up to 900°F¹. Commercially available aviation fuels are high in paraffins, resulting in poor thermal performance due to their tendency to crack under these pyrolytic conditions². Hydrogen donors have been found to stabilize the fuels by terminating the propagation of free radicals from the cracking process^{3, 4}. The pyrolytic cracking of paraffins generates both primary and secondary free radicals, where a certain hydrogen donor may favor the interaction with only one type of free radical. This has been indicated previously, where the effects of hydrogen donors, such as benzyl alcohol (BA) and 1,2,3,4-tetrahydro-1-naphthol (THNol), on the product distribution of pyrolytic stressed tetradecane were studied⁵. Benzyl alcohol was found to reduce the amount of n-alkane cracking products, while THNol greatly reduced the 1-alkene. This was associated with the ability of BA to target primary radicals and, correspondingly, the targeting of THNol towards secondary radicals. Accordingly, this paper focuses on the potential of hybrid hydrogen donor for enhanced pyrolytic stabilization of paraffinic compounds typical for jet fuels. Hybrids of benzyl alcohol with tetrahydronaphthalene and 1,2,3,4-tetrahydronaphth-1-ol have been studied, and their synergistic effect upon tetradecane has been characterized.

EXPERIMENTAL

The compounds used were n-tetradecane (TD, Aldrich 99%), benzyl alcohol (BA, Aldrich 99.8%) tetrahydronaphthalene (THN, Aldrich 99%) and 1,2,3,4-tetrahydro-1-naphthol (THNol, Acros 97%). Stressing of TD alone or in different mixtures with one or two hydrogen donors, were performed for 30 minutes in a fluidized sandbath at 425, 450 and 475°C. A detailed description of the experimental setup and analytical determination of the product distribution using GC and GC/MS, has been reported elsewhere^{2, 5}.

RESULTS AND DISCUSSION

The thermal stability of tetradecane, TD, during the pyrolytic stressing can be expressed on the basis of the amount of TD remaining in the liquid over the amount in the original mixture weighed against the liquid yield of the experiment. This ratio is therefore normalized, and its enhancement when a hydrogen donor is added, compared to that of the TD alone, indicates that the hydrogen donor is indeed improving the thermal stability of the paraffinic compound. Figure 1 shows the remaining TD content over its initial concentration, stressed alone at 425, 450 and 475°C and its mixture with 0.5, 1, 3 and 5 mole% tetrahydronaphthalene (THN). With increasing stressing temperature, there is a dramatic decrease in the TD remaining content with no THN added, from around 85 mole% at 425°C to 27 mole% at 475°C. When THN is added at 425°C, there is a dramatic increase for the first mole% of hydrogen donor added up to 98% and it

stays stable at this level with further increase in the THN content. As the temperature is increased to 450°C, the TD remaining ratio for the TD stressed alone has been reduced to 56%. Again, there is a sharp increase up to 70% after only 0.5 mole% THN, and with further rise in the THN content, this ratio is slowly but steadily increasing to above 80% with 5 mole% THN addition. Increasing the temperature to 475°C, there is again a significant increase for the first half mole% THN added, as for the previous temperatures. A slower but steady rise is observed thereafter up to 5 mole% THN, reaching a TD remaining ratio of close to 50%. Similar behavior for the single addition of BA and THNol with TD has also been found⁵.

The GC traces of the liquid product distribution for TD alone and its mixture with 0.5 mole% THN, stressed at 475°C for 30 minutes, are plotted in Figure 2. As expected, the TD peak is the dominant peak, accounting for a major part of the total peak area. When no THN was added, as is the case for the top trace, a significant part of the total peak area is taken by the products from the thermal cracking of TD. To the left of the TD peak there are typical traces of linear alkanes and alkenes cracking products in the range of C4 to C13. The alkane and alkene with the same carbon number appear in pair, where the alkane is eluted at slightly lower retention times than the alkene, i.e. to the left. When the THN is added, the cracking products are greatly reduced as shown by the reduction in the peak heights and areas of the alkane and alkene derivatives in the bottom trace of Figure 2. The decrease in cracking products obtained by the addition of THN is therefore closely related to the reduced cracking of the TD. Further, the introduction of THN seems to especially reduce the 1-alkene peak in relation to the corresponding alkane peak, when compared to the TD stressed alone. Therefore, the THN seems to particular target the secondary radicals, similar to that found for THNol⁵. Figure 3 shows the ratio of the 1-alkene peak area over that of the corresponding n-alkane for TD alone and with 0.5 mole% THN and BA addition. There is a clear increase in the alkene/alkane ratio for the BA mixture, indicating that BA is indeed targeting the primary radicals. However, for the THN the ratios of the alkene over the alkane peaks are smaller than those observed for the TD alone, indicating that THN targets secondary radicals.

The observed effects on the thermal stabilization of TD by BA, THN and THNol are summarized in Scheme 1. The increased thermal stability of TD when hydrogen donors are added can be linked to the ability of the hydrogen donor to capture radicals formed during the stressing and therefore hinder the cracking. This results in an increased liquid product and enhances the TD remaining ratio, when compared to TD stressed alone. Scheme 1 presents in a simplified manner the role of the different hydrogen donors in the thermal stabilization of TD. A hydrogen is abstracted from the n-tetradecane due to the influence of heat into a secondary radical. The additive can then cap the radical at this stage, preventing the propagation of the reaction and leave the TD intact. THN and THNol have shown good ability to operate on secondary radicals as discussed above. However, if this radical is not stopped, it will undergo a β -scission, yielding a 1-alkene and a primary radical. These primary radicals are targeted by BA⁵. Accordingly, hybrids of BA and THN or BA and THNol should therefore produce synergetic effects at low concentrations towards enhanced thermal stabilization of TD.

Figure 4 compares the TD remaining ratio at 450°C for the TD mixed with a single hydrogen donor, BA, THN or THNol at 1 mole% addition, and that of TD added a hybrid of BA and THN or BA and THNol, at 0.5 mole% each. When added alone, both THN and THNol gave higher thermal stability than that of BA. However, the hybrid of 0.5 mole% BA and 0.5 mole% THN resulted in a clear enhanced thermal stability effect when compared to the 1 mole% single mixtures. This trend is further supported by the studies at 475°C, as shown in Figure 5. For the single hydrogen donor additions at 475°C, the TD remaining ratio increases from 27% for TD alone to around 35% after 1 mole% BA addition, and the use of THN has an even higher impact, where this ratio is around 46% (Figure 5). The hybrid of BA and THN would be expected to be in the range of 35 to 46%, but gave a result of 52% showing a clear synergistic effect between these two hydrogen donors. Correspondingly, the effect from the hybrid of BA and THNol would be expected to be in the range 35 to 39%, but showed an enhancement up to

46%. Although the BA/THN hybrid showed overall higher thermal stability effect at both 450 and 475°C, the synergistic effect from the BA/THNol hybrid was larger when taking into account the effect of the single hydrogen donors. These results are very promising for the development of additives that can work in both the autoxidative regime (150-250°C) and the pyrolytic regime, and further research will study the effect in both these regimes.

CONCLUSIONS

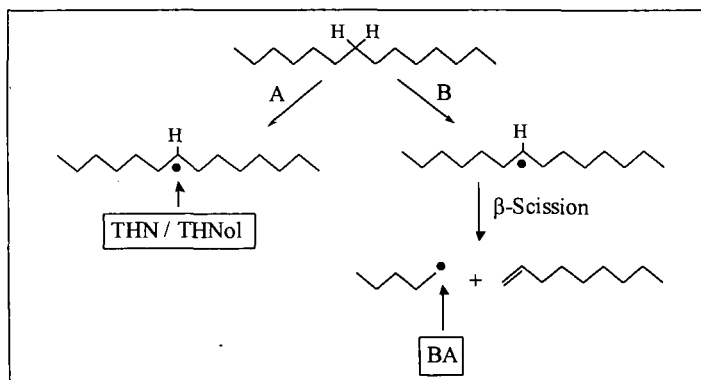
Hybrid hydrogen donors of (i) benzyl alcohol (BA) and tetrahydronaphthalene (THN), and (ii) benzyl alcohol (BA) and 1,2,3,4-tetrahydro-1-naphthol (THNol), have shown a synergistic effect on the thermal stabilization of tetradecane (TD) in the pyrolytic regime. The BA/THN hybrid showed the overall highest ability to stop the thermal decomposition of the paraffinic TD, but the BA/THNol hybrid showed the highest synergistic effect when compared to the BA and THNol alone.

ACKNOWLEDGMENTS

The authors wish to thank the U.S. Air Force Wright Laboratory, the U.S. DOE / Federal Energy Technology Center for their support. We also thank Prof. Harold H. Schobert for his support and helpful discussion.

REFERENCES

- (1) Edwards, T., *Prep. Am. Chem. Soc.- Div. Petro. Chem.*, **1996**, *41(2)*, 481.
- (2) Andrése, J.M., Strohm, J.J. and Song, C., *Prep. Am. Chem. Soc.- Div. Petro. Chem.*, **1998**, *43(3)*, 412.
- (3) Song, C., Lai, W.-C. and Schobert, H.H., *Ind. Eng. Chem. Res.*, **1994**, *33*, 548.
- (4) Coleman, M.M., Sobkowiak, M., Fearnley, S.P. and Song, C., *Prep. Am. Chem. Soc.- Div. Petro. Chem.*, **1998**, *43(3)*, 353.
- (5) Andrése, J.M., Strohm, J.J., Coleman, M.M. and Song, C., *Prep. Am. Chem. Soc.- Div. Fuel Chem.*, **1999**, *44(1)*, 194.



Scheme 1. Simplified role of the hydrogen donors, BA, THN and THNol on the thermal stabilization of TD in the pyrolytic regime.

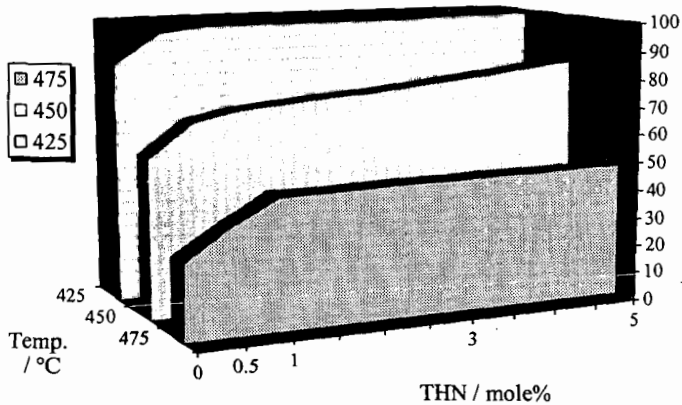


Figure 1. Comparison of remaining TD content over its initial concentration for different mixtures with tetrahydronaphthalene (THN) stressed at 425, 450 and 475°C for 30 minutes.

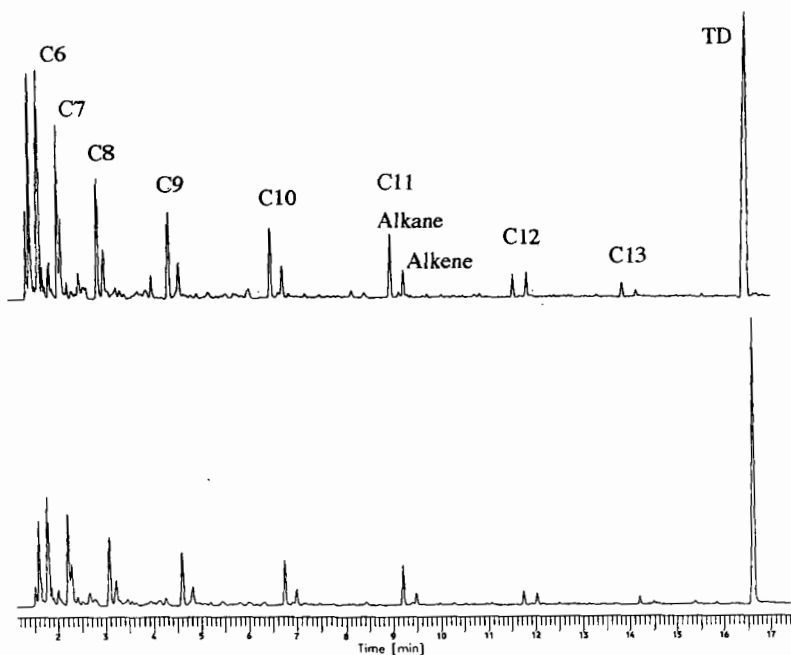


Figure 2. The GC traces of the liquid product distribution for TD alone (top) and its mixture with 0.5 mole% THN (bottom) stressed at 475°C for 30 minutes.

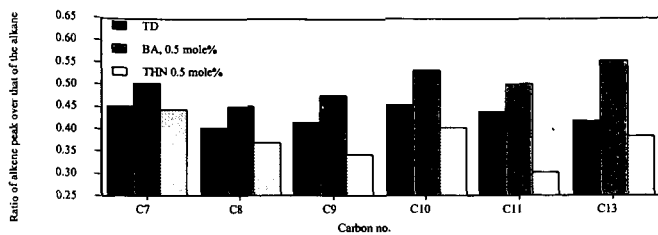


Figure 3. Ratio of the 1-alkene peak area over that of the corresponding alkane for TD alone and with 0.5 mole% THN and 0.5 mole% BA addition stressed at 475°C for 30 minutes.



Figure 4. Comparison of the ratio of TD remaining over that initial for TD mixed with 1 mole% of the single hydrogen donors BA, THN and THNoI, individually, and the effect of hybrids at 450°C.

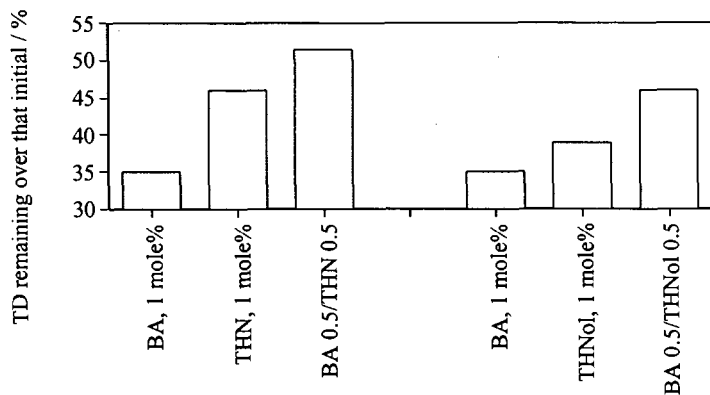


Figure 5. Comparison of the ratio of TD remaining over that initial for TD mixed with 1 mole% of the single hydrogen donors BA, THN and THNoI, individually, and the effect of hybrids at 475°C.

ALKYLATED INTERMEDIATE OF CYCLO-ALKANES FOR STABILIZATION OF PARAFFINIC JET FUELS UNDER PYROLYTIC CONDITIONS

John M. Andréseu, James J. Strohm and Chunshan Song*
Applied Catalysis in Energy Laboratory, The Energy Institute
The Pennsylvania State University, University Park, PA 16802

KEYWORDS: Pyrolysis, thermal stability, aviation jet fuels.

ABSTRACT

The thermal stability of linear alkanes, such as tetradecane, in the pyrolytic regime is enhanced by the addition of cyclo-alkanes, in particular decalin. Based on the product distribution from the thermal stressing of their mixtures, decalin was found to target primary radicals, particularly by a sharp reduction in the n-alkane products in relation to that of the 1-alkene. This thermal interaction has been further examined by GC/MS analysis, which revealed the formation of alkylated intermediates of decalin that stabilizes the paraffinic species in the pyrolytic regime.

I. INTRODUCTION

Jet fuels for high Mach applications are required to operate under severe thermal stressing, where exposures up to 900°F are expected¹. Liquids rich in cyclo-alkanes have been found to have superior stability at high temperatures compared to those high in paraffinic content². This has been associated with two factors. Firstly, cyclo-alkanes themselves have higher thermal stability than linear alkanes³. At 450°C after 1 hour, most of a linear alkane such as tetradecane has been pyrolyzed into different products, while trans-decalin mostly remains unconverted. This has been linked to the ability of the trans-decalin to form tertiary radicals after hydrogen abstraction. Further, hydrogen abstraction will transform the decalin into tetralin, which will act as a hydrogen donor⁴ and will strongly enhance the thermal stability of trans-decalin even at low concentrations. On the other hand, as tetradecane experiences hydrogen abstraction forming primary and secondary radicals, this leads to rapid decomposition due to propagation reactions. Secondly, previous studies have shown that decalin improves the thermal stability of tetradecane⁵. Again, this can be based on the buildup of tetralin from the pyrolytic H-abstraction from decalin, where the tetralin will strongly affect the propagation reaction in the mixtures. However, the thermal enhancement effect of decalin has been found at temperatures and concentrations, where the formation of tetralin from decalin can be neglected⁵. Therefore, there must exist additional routes in which the decalin quench the propagation reaction generated from the pyrolytic degradation of tetradecane. Accordingly, this work has studied the reactive intermediates involved during pyrolysis of mixtures with decalin and tetradecane at 450°C, stressed from 12 to 120 minutes. There was a clear thermal stability enhancement with the addition of decalin at all times. The reduction in the thermal cracking of tetradecane was found to derive from the capture of radicals by the decalin, forming alkylated derivatives. By increased thermal stressing, these were further dehydrogenated to form tetralins, which again act as a hydrogen source for stabilization.

II. EXPERIMENTAL

The compounds used were tetradecane (TD, Aldrich 99%) and decalin (DHN, Aldrich 98%, a mixture of 46 mole% cis- and 54 mole% trans-decalin). Stressing of TD alone or in 5 or 30 mole% mixtures with DHN were performed for 12, 30, 60 and 120 minutes in a fluidized sandbath at 450°C as reported elsewhere². The GC-MS was performed on a Hewlett-Packard 5890 Series II GC coupled with a HP 5971A MS detector and a J&W DB-17 column, which was heated from 40 to 290°C with a heating rate of 6°C min⁻¹.

III. RESULTS AND DISCUSSION

Figure 1 shows the remaining TD content over its initial concentration for TD alone and 5 and 30 mole% mixtures with DHN, stressed at 450°C for 30, 60 and 120 minutes. As the TD is stressed, its thermal stability can be expressed on the basis of the amount of TD remaining in the liquid over the amount in the original mixture weighted against the liquid yield of the experiment. This ratio is therefore normalized, and any enhancement in this ratio when DHN is added compared to that

of the TD alone indicates that the DHN is indeed improving the thermal stability of the linear alkane. With increasing stressing time, there is a dramatic decrease in the TD remaining content with no DHN added, from around 56 mole% at 30 minutes to 11 mole% at 120 minutes. When DHN is added there is a significant increase at all stressing times in the TD remaining content. A rapid increase in the thermal stability is achieved with only 5 mole% DHN addition, followed by a slower rise up to 30 mole% DHN mixture. The ratio of the TD remaining content for the 30 mole% DHN mixture over that of TD stressed alone gives an indication of the extent of interaction between the DHN and the TD. The effect of adding 30 mole% DHN is clearly dependent on the stressing time, where the extent of interaction is rising from 17% after 30 min stressing, to 24% at 60 min and is significantly increased to nearly 140 % at 120 min. Clearly, several reaction mechanisms are involved as discussed below.

Figure 2 compares the changes in the C4 to C10 product range from the thermal decomposition of TD with 30 mole% DHN addition at 450°C stressed for 12, 30, 60 and 120 minutes. The n-alkane and 1-alkene peaks appear in pairs, where the n-alkane has a slightly lower retention time than the 1-alkene. After 12 minutes stressing, the concentration of the cracking products is very low (5%), and the amount of 1-alkenes is slightly higher than that of the n-alkanes. At 30 minutes reaction time, the concentration of cracking products has increased to over 30%, and the relative distribution of the 1-alkene is now slightly lower than the n-alkane. As the stressing time is further risen to 60 minutes, the 1-alkene concentration is decreasing due to hydrogenation, alkylation or cyclization reactions⁶. The 1-alkenes are ultimately disappearing after 120 min exposure at 450°C. Compared with the stressing of TD alone at 450°C⁶, the relative concentration of 1-alkenes is higher at all times in the DHN mixture. The 1-alkene/n-alkane relative distributions found after 1 hour for the 30 mole% DHN mixture are comparable to those after only 30 minutes stressing for TD only. This indicates that the DHN is interacting with the thermal decomposition of the 1-alkanes by reducing their probability for hydrogen abstraction and capturing primary radicals, which promotes their alkylation. The ability of the DHN to affect the 1-alkane concentration through suppression of the n-alkanes is further illustrated in Figure 3, where the ratio of the 1-alkene peak area over that of the corresponding n-alkane for TD alone and with 30 mole% DHN addition after 30 minutes reaction time at 450°C is compared. This ratio is around 60% for TD stressed alone and there is a clear increase in the alkene/alkane ratio for the DHN mixture, giving values about 90%. This indicates that DHN indeed is targeting the primary radicals resulting in enhanced thermal stabilization of TD or other paraffinic liquids typical for jet fuels.

The route of preventing the thermal cracking of the linear alkanes by DHN is strongly connected to the ability of the cylo-alkane to become alkylated. Figure 4 compares the GC-MS trace for ethyl-DHN (166 a.m.u.) and dodecyl-DHN (306 a.m.u.) identified in the remaining liquid after stressing the 30 mole% DHN mixture at 450°C for 60 minutes. The main features are deriving from the DHN-ion, giving rise to the mass at 137 and below. The alkylated masses give rise to the parent ions, where the DHN-ion with a mass of 137 combined with either ethyl (mass of 29) or dodecyl (mass of 169) are deriving from the parent ions ethyl-DHN (166) and dodecyl-DHN (306), respectively. Other masses identified are 180, 194, 208, 222, 236, 250, 264, 278 and 292, indicating that alkyl substitution in the whole range C2 to C12 has taken place. However, no evidence of methyl, tridecyl or higher alkyl substitution was found. Neither was any DHN substituted with two alkyls identified. This strengthens the evidence that the thermal stability effect of DHN is initially associated with the capturing of primary alkyl radicals by substitution as illustrated in Scheme 1. The hydrogen abstraction of TD generally leads to a secondary radical. The secondary radical produces a 1-alkene and a primary radical through β -scission. If the primary radical is not captured, it will start a propagation reaction leading to further decomposition of the TD and rapid transformation of the 1-alkenes. The introduction of DHN captures primary radicals in two consecutive steps. First, the primary radical will abstract a hydrogen from the DHN, where the formation of a tertiary radical is favored. Second, the tertiary radical will recombine with a different primary radical. The above scheme will result in two overall effects. Firstly, the thermal decomposition of TD is halted and secondly, the product distribution will favor 1-alkenes. This alkylation process was further confirmed through studies on the stressing products from TD/DHN mixtures after only 30 minutes at 450°C. However, when increasing the stressing time to 120

minutes, the studies on the cracking products show that tetralin is the main product from the thermal decomposition of DHN. This confirms that dehydrogenation of decalin into tetralin is a further stabilizing factor, which becomes increasingly important at longer stressing times.

CONCLUSIONS

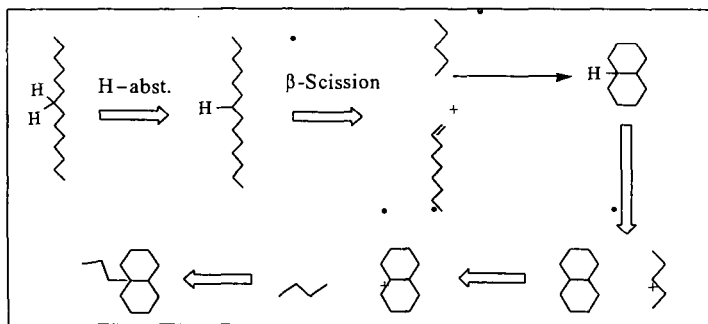
Tetradecane (TD) has been stressed alone and in mixtures with 5 and 30 mole% decalin (DHN) at 450°C, with stressing times ranging from 12 to 120 minutes. A significant increase in the amount of TD remaining was observed at all stressing times upon the addition of DHN. The improved thermal stability of the TD-DHN mixtures was mainly associated with the reduced cracking of the TD due to interactions with the DHN. Enhancements of up to 140% in the ratio of TD remaining over that initial for 30 mole% DHN addition compared to that of TD by itself, were observed. The suppression of the production of linear alkanes was found to derive from the capture of primary radicals by the DHN, forming alkylated derivatives. With increasing stressing times, these were further dehydrogenated to form tetralins, which again act as a hydrogen source for stabilization.

ACKNOWLEDGMENTS

The authors wish to thank the U.S. Air Force Wright Laboratory, the U.S. DOE / Federal Energy Technology Center for their support. We also thank Prof. Harold H. Schobert for his support and helpful discussion.

REFERENCES

- (1) Edwards, T., *Prep. Am. Chem. Soc.-Div. Petro. Chem.*, **1996**, 41(2), 481.
- (2) Andrése, J.M., Strohm, J.J. and Song, C, *Prep. Am. Chem. Soc.-Div. Petro. Chem.*, **1998**, 43(3), 412.
- (3) Song, C. and Lai, W.-C., *Prep. Am. Chem. Soc.-Div. Petro. Chem.*, **1998**, 43(3), 462.
- (4) Andrése, J.M., Strohm, J.J., Coleman, M.M. and Song, C, *Prep. Am. Chem. Soc.-Div. Fuel Chem.*, **1999**, 44(3-4), In press.
- (5) Andrése, J.M., Strohm, J.J. and Song, C, *Prep. Am. Chem. Soc.-Div. Fuel Chem.*, **1999**, 44(1), 199.
- (6) Song, C., Lai, W.-C. and Schobert, H.H., *I&EC Research*, **1994**, 33, 534.



Scheme 1. Simplistic view of the thermal stability effect of DHN associated with the capturing of alkyl radicals by substituting them to their structure.

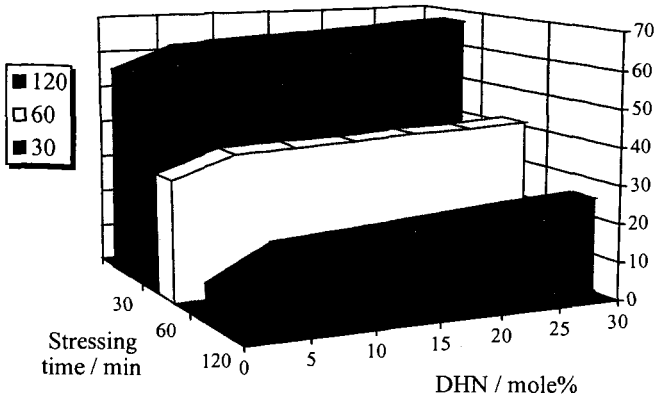


Figure 1. Comparison of remaining TD content over its initial concentration for different mixtures with DHN stressed at 450°C for 30, 60 and 120 minutes.

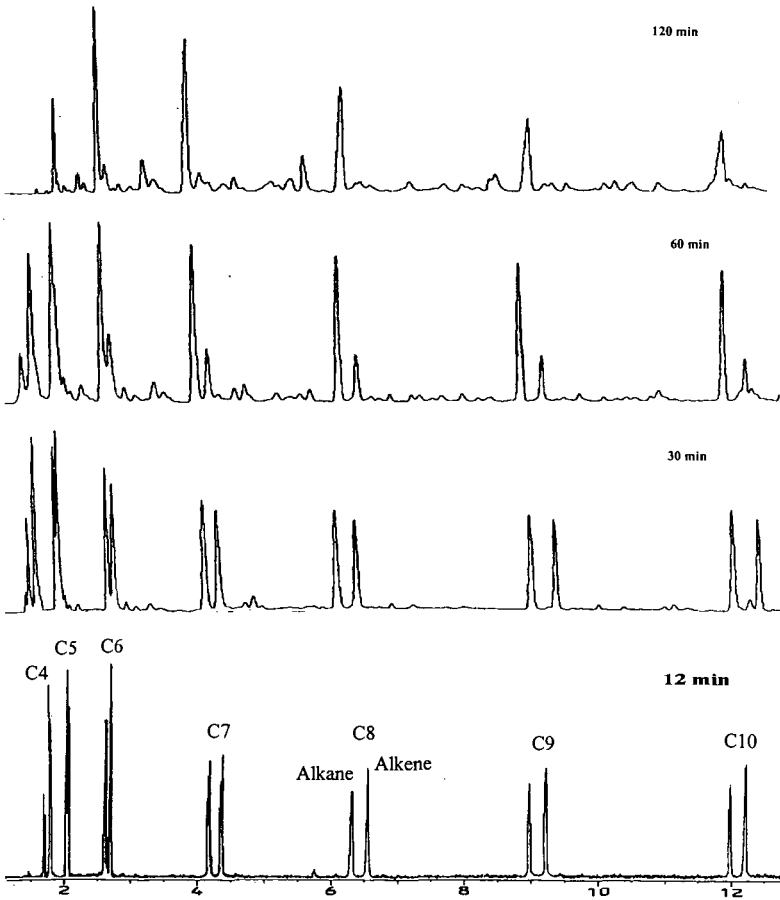


Figure 2. Changes in the TD pyrolysis products C4 to C10 after stressing the mixture of 70 mole% TD with 30 mole% DHN for 12, 30, 60 and 120 minutes at 450°C.

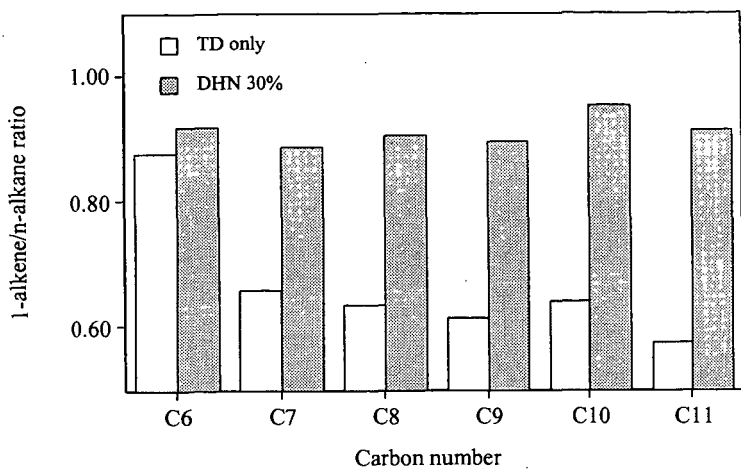


Figure 3. Ratio of the 1-alkene peak area over that of the corresponding alkane for TD alone and with 30 mole% DHN addition at 450°C stressed for 30 minutes.

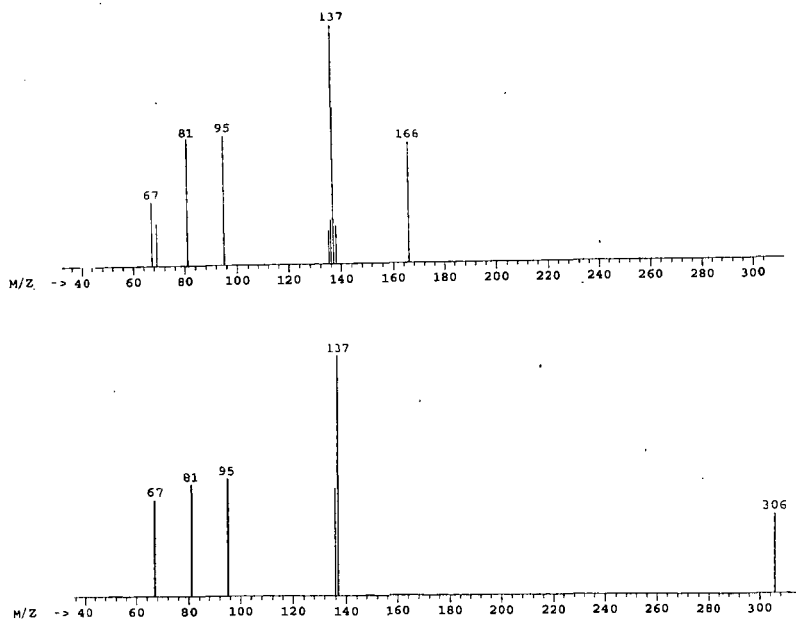


Figure 4. GC-MS traces for ethyl-DHN with parent mass 162 a.m.u. (top) and dodecyl-DHN (306 a.m.u., bottom).

STRUCTURAL DETERMINATIONS OF PENNSYLVANIA ANTHRACITES

Peter J. Pappano, Jonathan P. Mathews, Harold H. Schobert
The Energy Institute
The Pennsylvania State University
University Park, PA 16802

KEYWORDS: Anthracite, Molecular Modeling, Coal Structure

INTRODUCTION

Four Pennsylvania anthracites were selected for analysis, based on their availability from currently active mines and presumed geological differences. A battery of experiments was performed on these samples to determine their physical and chemical properties. The data collected from these experiments was used as input for modeling the structure of anthracite using Cerius², a Molecular Simulations Incorporated (MSI) software package. Visualization of anthracite structure is useful in visualizing the reactions necessary to produce advanced carbon materials, such as graphite, from anthracite.

EXPERIMENTAL

The anthracites come from the Harmony, Jeddo, LCNN, and Summit mines, all of which mine the Eastern Middle Field of Pennsylvania. LCNN and Jeddo mine the Mammoth vein; Harmony, the Lykens Valley #2; and Summit, the Tracey vein. No blending of coals is done at these plants, ensuring repeatability of data collected on the anthracites. Approximately 1000 lbs. of each anthracite were collected and a subset homogenized using techniques outlined by Glick and Davis of the Penn State Coal Sample Bank and Data Base [1]. The end products of this process were aliquots of -20 and -60 (U.S. Standard Sieve) mesh anthracite stored in foil laminate bags under an argon atmosphere [1]. Next, chemical and physical data were collected using X-ray diffraction, ¹³C NMR, proximate and ultimate analysis, maceral point counts, CO₂ surface area, and helium density. Values for aromaticity, H/C ratio, and interlayer spacing were used in generating possible anthracite structures using MSI software [2].

RESULTS

Ultimate and proximate analysis results are presented in Table 1 and Table 2, respectively. With increasing carbon content there is a decrease in the hydrogen content, as expected. This is indicative of ring condensation with concurrent loss of hydrogen. When normalized to 100 carbon atoms, Summit has the highest hydrogen content with 32 hydrogens per 100 carbon atoms while LCNN has the lowest with 19 hydrogen atoms per 100 carbon atoms. Table 2 shows relatively equal amounts of ash and volatile matter, except for the Summit anthracite, which has nearly twice the levels of ash in comparison to the other samples. High levels of mineral matter, as indicated by high levels of ash, are undesirable for graphite production [3]. The maceral compositions are shown in Table 3. The category "other inertinite" was used when the optical differences between fusinite and semi-fusinite could not be distinguished. Maceral composition is usually an important parameter as macerals are known to have different chemical structures which may lead to different levels graphitizability [4]. X-ray diffraction, diffractogram shown in Figure 1, was used to determine the distance between aromatic sheets in d-spacing. The XRD diffractogram of the Jeddo sample indicates d-spacings range from 12.91 to 2.57 nm in the identifiable peaks. ¹³C Single Pulse NMR, Figures 2, was used to determine the aromaticity of the samples. All the anthracites studied were found to be 100% aromatic.

DISCUSSION

Using the chemical data, a hypothetical structure for the Jeddo anthracite was generated and minimized using molecular mechanics (Drying force-field [5]), see Figure 3. The parameters utilized in generation of the model were %H, %N, %O, d-spacing, aromaticity, and number of rings in an aromatic, or pre-graphitic sheet. The atomic H/C ratio determined from the ultimate analysis (H/C=0.22) and calculated from the model (H/C=0.22) are in agreement. Unfortunately, the relative proportions of quarternary, pyrrolic, and pyridinic nitrogen have not been determined for anthracite. Therefore it was assumed the nitrogen was present primarily in the quarternary form (9 of the 11 nitrogens are quarternary in Figure 3), presumably from the condensation of smaller pyridinic containing sheets. Oxygen was assumed to be in open or closed ethers with perhaps some carbonyl. As there are only 18 heteroatoms per 1010 carbons in the proposed anthracite, any errors in their assignments will have a minimal impact on the gross structure of the model. However, their assignments and placements may well have a bearing on the reactivity of the structure.

Past research has shown graphitized anthracites have crystallite heights of <36.8 nm, therefore the raw anthracite modeled here was generated with heights significantly lower than 36.8 nm [6]. The anthracite model shown in Figure 3 is approximately 45 Å across (plan view) and approximately 15 Å high. Average d-spacings between the sheets fall within the acceptable experimentally determined range, approximately 4 Å. However, the structure shown has not been subjected to molecular dynamics (thus may be trapped in a local minimum) nor does the force-field used contain an implicit $\pi - \pi$ interaction term. Furthermore, the model was minimized in a vacuum and has not experienced high pressures or interactions with neighboring sheets, which may be important in the overall structural alignment. Hence the structural representation is a product of less accurate modeling methods (due to model size restrictions on quantum mechanics and computational expense).

Ring condensation in anthracite is believed to be between >10 and 100 (rings per sheet) [7], so the number of rings in a polycyclic sheets shown in Figure 3 is a maximum of 91 and minimum of 47 rings. Combining the chemical data with stated assumptions resulted in a simplistic structure for the Jeddo anthracite, Figure 3. The model contains five pre-graphitic planes with an average of 81 rings comprising a sheet. The beginnings of graphitic stacking are apparent, Figure 3. The aromaticity of the model is 99%, while the experimentally determined aromaticity is 100%. Recall that the model is in agreement with the elemental composition. Hence the model is in close agreement with the chemical data determined to date. Incorporation of physical data, such as helium density, and additional chemical data will further refine the structure [8].

CONCLUSIONS

The coals selected for this research are all in the anthracite range, yet exhibit varied chemical properties (mostly hydrogen content, maceral composition and degree of crystallinity) presumably as a result of different geological histories. It may be assumed that the graphitizability of these samples will vary with their constitution. These differences can be better presented through visualization of the anthracite's structure and its changes upon carbonization. A model structure for Jeddo anthracite is presented. Incorporation of additional physical and chemical data will further refine the proposed model.

REFERENCES

1. Glick, D.C. and Davis, A., Operation and composition of the Penn State Coal Sample Bank and Data Base. *Organic Geochemistry* 1991;17(4):421-430
2. MSI, Molecular Simulations Incorporated. Cerius² Version 3.5, San Diego CA 1998
3. Zeng, S. M., Rusinko, F, Schobert, H. H., Producing High-quality Carbon and/or Graphite Materials from Anthracite by Catalytic Graphitization, PEDAs, 9303-4019, 1996
4. Taylor, G. H., Teichmuller, M., Davis, A., Diessel, C. F. K, Littke, R., Robert, P., *Organic Petrology*. Berlin Germany: Gebruder Borntraeger. 1998: 112
5. Mayo, S. L., Olafson W.L., Goddard W.A., Drieding: A generic force-field for molecular simulations. *J. Phys. Chem.* 1990;94:8897-8909
6. Atria, J., Novel Approach To The Production Of Graphite From Anthracite, The Pennsylvania State University, MS thesis, 1994
7. Schobert H.H. *The Chemistry of Hydrocarbon Fuels*. London UK: Butterworths. 1990:112
8. Faulon J.L., et al. Correlation between micropore and fractal dimension of bituminous coal based on computer generated models. *Energy & Fuels* 1994;8(2):408-415

Table 1. Ultimate Analysis Of Anthracite Samples*

Anthracite	% C	% H	% N	% S	% O (by diff.)
LCNN	95.7	1.5	1.2	0.5	1.0
Jeddo	95.2	1.8	1.1	0.6	1.3
Harmony	94.0	2.2	1.0	0.5	2.3
Summit	93.2	2.5	1.6	0.6	2.2

*dry ash-free basis

Table 2. Proximate Analysis Of Anthracite Samples

Anthracite	% Moisture	% Volatiles	% Ash	Fixed Carbon
LCNN	3.3	4.5	6.7	88.3
Jeddo	4.7	6.1	8.1	85.9
Harmony	4.6	7.5	6.6	86.2
Summit	2.6	11.1	17.6	71.2

Table 3. Maceral Percentages (from point counts)

Anthracite	Vitrinite	Fusinite	Semi-fusinite	Other Inertinite	Liptinite
LCNN	80	10	7	2	1
Jeddo	86	6	5	2	1
Harmony	60	24	14	1	1
Summit	80	15	4	0.5	0.5

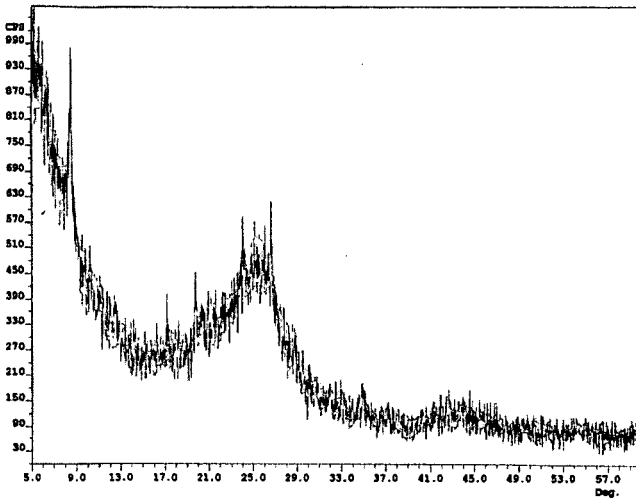


Figure 1. XRD Diffractogram Of Jeddo Anthracite

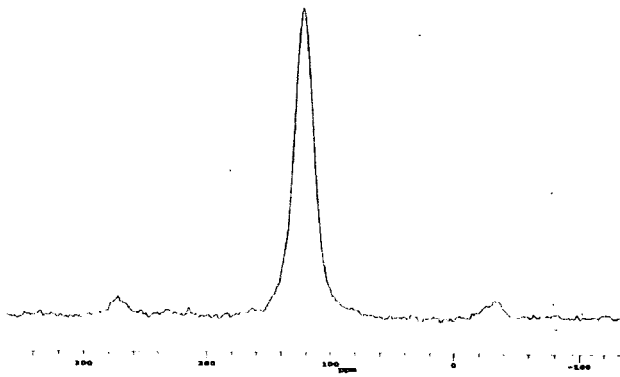


Figure 2. ¹³C CPMAS Spectra Of Jeddo Anthracite

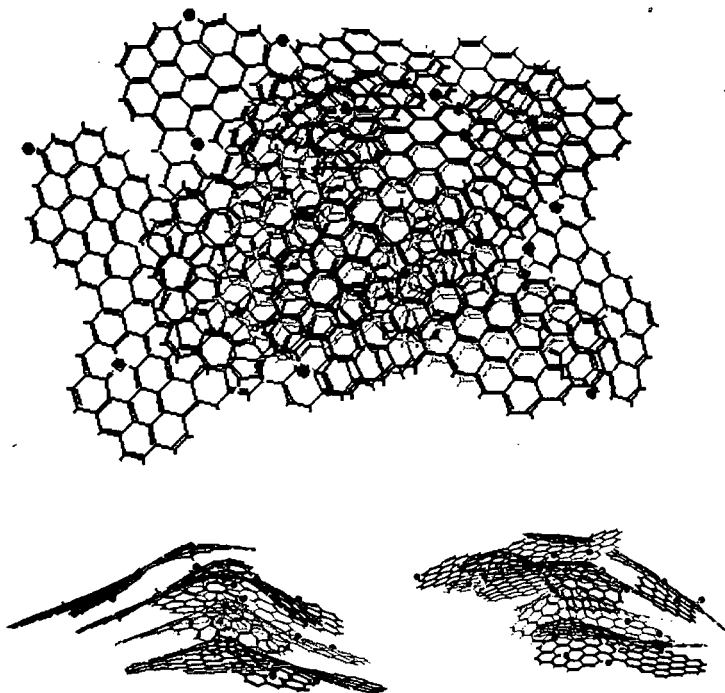


Figure 3. Plan And Side Views Of A Simplistic Model Of Jeddo Anthracite. $C_{1016}H_{2223}O_9N_9$
Heteroatoms shown as spheres.

VERIFICATION OF THE AIDA'S CHEMICAL DETERMINATION METHOD FOR OXYGEN-FUNCTIONALITY IN COAL AND COAL PRODUCT

Tetsuo Aida, Aiko Nishisu, and Issei Yamanishi
Department of Industrial Chemistry, Faculty of Engineering in Kyushu, Kinki University
11-6 Kayanomori, Iizuka, Fukuoka 820, JAPAN

Keywords: Coal, carboxylic acid functionality, phenolic hydroxyl functionality, non-aqueous titration

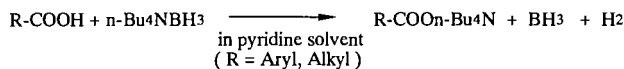
INTRODUCTION

Coal contains various type of chemical functionality. It is believed that the oxygen-containing functionality in coal plays very important role to control its physical and chemical properties. Particularly, since a carboxylic acid and phenolic hydroxyl functionality have a relatively strong acidic characteristic comparing with other functionality such as alcoholic hydroxyl functionality, they can induce strong cohesive forces like a hydrogen bonding, which seems to be responsible to determine many characteristics of coal based on the macromolecular network structure. Thus, it is critical to have the quantitative information about such functionality as carboxylic acid and phenolic hydroxyl functionality in coal or coal product in order to develop the efficient chemical transformation processes of coal such as a liquisfaction, gasification, chemical desulfurization, etc..

It has long been a common sense in the coal science community that the hydrogen bonding contribution by carboxylic acid functionality to the chemical and physical property of coal could be almost negligible toward the high ranked coals like a bituminous coal, simply because of the very small amount of the functionality, which used to be determined by the chemical method developed by Blom et al.[1] about 40 years ago.

Although the recent development of sophisticated instrumentation such as FT-IR, ¹³C-NMR, XPS, etc., has made it possible to provide quite reliable information about such hetero-atom-functionality as sulfur-, nitrogen- and oxygen-containing functionality, they still seem to fall into a common problem, that is, the low accuracy to determine a small amount of the functionality.

Recently, we had developed a chemical method [2], using following chemical reactions.



This method has several advantages compared to the conventional one mentioned above.

First of all, this reaction proceeds quantitatively with a single step in pyridine solution generating a gaseous product, H₂, which, gives us much better accessibility of the chemical reagent to the carboxylic acid functionality buried into macromolecular network structure of coal than in aqueous solution reaction(cf. Blom's method) based on the swelling behavior, and also a reasonable accuracy due to the volumetric determination of the gaseous product (H₂).

Secondly, this reaction exhibits a significant difference of the reaction rate depending upon the acidity of functionality, which makes easy to distinguish other functional groups such as phenolic and alcoholic hydroxyl functionality by using more reactive chemical reagents. Figure 1 demonstrates one of the examples of our experiment [3], which were carried out by using n-Bu₄NBH₄, LiBH₄ and LiAlH₄ as reactants, and determined the distribution of oxygen functionality in the pyridine extract of coal. Although we have not enough data concerning the difference of functionality between coal and pyridine extract at present moment, 8.0fold difference between our data and previous one [4] seems to be too much and quite interesting.

Most striking experimental result came out from the -COOH determination for various kind of coals, as shown in Figure 2, which demonstrates the coal rank dependency of the -COOH content, comparing the data previously reported[5]. Very interestingly, there is a quite large discrepancy in the range of high rank coal. This fact convinced us that our approach to develop more reliable chemical determination method could be right, because the coal swelling in water used to be dramatically decreased over higher rank region than sub-bituminous coal.

As Niksa pointed out in his recent personal communication and paper [6], it was well-known contradiction that the most of the CO₂ released during the pyrolysis of sub-

bituminous and bituminous coals could not be rationalized with the uni-molecular decomposition chemistry of carboxylic acid functionality in coals. Because the amount of carboxylic acid functionality reported in the raw coal was too small to handle it.

In order to verify the analytical data obtained by our new methodology, we have conducted a non-aqueous titration as an alternative method. In this paper, we like to report the experimental results

EXPERIMENTAL

The chemical reagents were commercial products (Aldrich's gold label grade) which were used without further purification. Pyridine for the chemical determination of carboxylic acid functionality was dried over calcium hydride and distilled before use.

Coals from the Argonne National Laboratory (premium) and the Ames Coal Library were ground, seized, and dried with a silica-gel at room temperature under vacuum for three days, and stored under a dry nitrogen atmosphere. The pyridine extract of coal was prepared by means of the ultrasonic irradiation method [7].

A typical procedure of the non-aqueous titration of carboxylic acid and phenolic hydroxyl functionality in coal extract was as follows: 100mg of coal extract was dissolved in 5.0ml of dried pyridine, and placed into a Pyrex cell under N₂-atmosphere which has an Pt-electrode and magnetic stirrer. The solution was potentiometrically titrated with a pyridine solution of n-Bu₄NOH (0.1mol/l).

RESULTS AND DISCUSSION

1. Non-aqueous titration of model compounds

Benzoic acid and 2-naphthol were used as model compounds for carboxylic acid and phenolic hydroxyl functionality, respectively. The non-aqueous titration of each functionality was carried out in pyridine solution by using n-Bu₄NOH (0.1mol/l) pyridine solution as a titrant. The reaction is considered to proceed with following chemical equations.

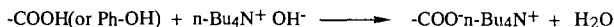


Figure 3 shows the dependence of a potential difference on the titrant volume observed in the determination of individual model compounds, benzoic acid and 2-naphthol, and that of these mixture is shown in Figure 4. Obviously, there are two inflection points on the titration curves of mixture, and it was confirmed that they were appearing at exactly right volume of the titrant corresponding to the concentration of carboxylic acid (the first inflection point) and the sum of both compounds (the second inflection point), respectively.

2. Non-aqueous titration of pyridine extract of coal

Based on the results obtained from the model compound experiment described above, the determination of carboxylic acid and phenolic hydroxyl functionality in the pyridine extract of Pittsburgh No.8 coal has been performed by using the same procedure. The results demonstrated in Figure 5 and 6

Comparing with model compounds experiments mentioned above, a characteristic feature seems to be the difficulty to judge one of the two inflection points, which is thought to be due to the carboxylic acid functionality in coal extract. Although the reason of this phenomenon is not clear at this moment, the indistinct pK_a distribution due to heterogeneous carboxylic acid functionality in coal may be responsible for that.

Anyway, the concentration of carboxylic acid and phenolic hydroxyl functionality in the pyridine extract of Illinois No.6 coal was determined by the same manor as shown in Figure 6, and they are compared in Table 1 with those obtained from our chemical method (Aida's method) previously reported[2].

It is quite interesting that the values calculated from the two inflection points seems to be reasonably matched with those of the chemical determination. Particularly, we have convinced the matching between the sum of carboxylic acid and phenolic hydroxyl functionality determined by the chemical method (LiBH₄) and the value obtained from the second inflection point, which used to be clear and have no difficulty to find out.

3. Non-aqueous titration of pyridine extract of coal with internal standard

In order to verify the data obtained by the non-aqueous titration, we may be able to use an internal standard compound. Namely, the addition of a standard compound, such as phthalic acid into the coal extract solution will force to shift the two inflection points with the titrant volume corresponding to the amount of the standard compound, if the identification of two inflection points was correct.

In Figure 7, the experimental results obtained were shown. Expectedly, the inflection points were shifted with exact amount of the titrant volume corresponded to phthalic acid.

CONCLUSION

A chemical determination method (Aida's method) for the oxygen containing functionality in coal and coal product has been verified by using an alternative analytical technique, "non-aqueous titration".

It seems to be a very serious mischief concerning the content of the carboxylic acid functionality in higher rank coals than sub-bituminous coal in previous literatures, which used to be reported as a almost negligible amount. In according with our chemical determinations the content of carboxylic acid functionality in Illinois No.6 coal reach up to 5times more than previous data.

ACKNOWLEDGEMENTS

A part of this research was supported by the grant from The Japanese Ministry of Education through The 148th Committee on Coal Utilization in The Japan Society of Promotion of Science (JSPS).

REFERENCES

- (1) Blom, L., Edelhausen, L., and van Krevelen, D.W., *Fuel*, **36**, 135(1957)
- (2) Aida, T, et al., *Prepr. Am. Chem. Soc. Div. Fuel Chem.*, **41**(2), 744(1996)
- (3) Yoneda, M., Yamanishi, I., Aida, T., *Prepr., Sekitan Kagaku Kaigi (Japanese)*, 97(1998)
- (4) For instance, the content in the Shinn's model, *Fuel*, **63**, 1187(1984)
- (5) Jung, B., Stachel, S.J., and Aalkins, W.H., *Pap. Am. Chem. Soc., Div. Fuel Chem.*, 36 869(1991)
- (6) Niksa, Stephen, *Energy & Fuels*, **10**, 173(1996); Solomon, P. R., et al., *Energy & Fuels*, **4**, 319(1990)
- (7) After irradiation with ultrasonic wave for 3hours at room temperature, the suspension of powdered coal and excess amount of piridine was filtrated by using the Memblem Filter (5 μ m) under pressure.

Table 1. Functionality analyses of pyridine extract of Illinois No.6 coal

Functionality	Aida's method		Non-aqueous titration	
	(mmol / g)			
-COOH	0.83	(n-Bu ₄ NBH ₄)	0.88	(1st inflection point)
Ph-OH + -COOH	2.90	(LiBH ₄)	2.76	(2nd inflection point)

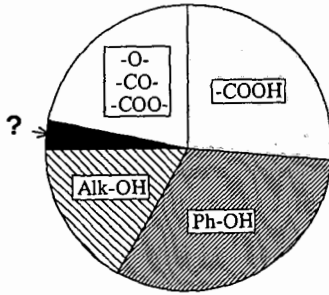


Figure 1. Distribution of oxygen functionality in pyridine extract of Illinois No.6 based on total oxygen

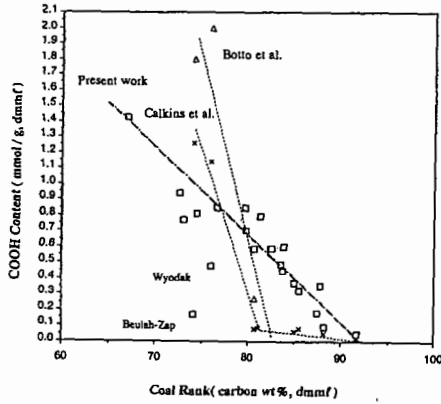


Figure 2. Correlation between content of carboxylic acid functionality and coal rank

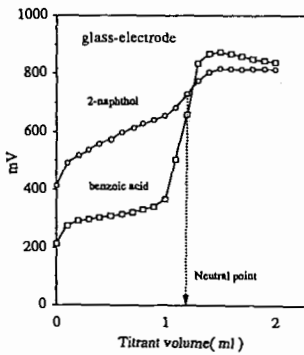


Figure 3. Non-aqueous titration of model compound

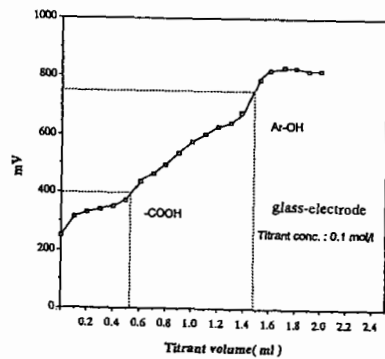


Figure 4. Non-aqueous titration of model compound mixture

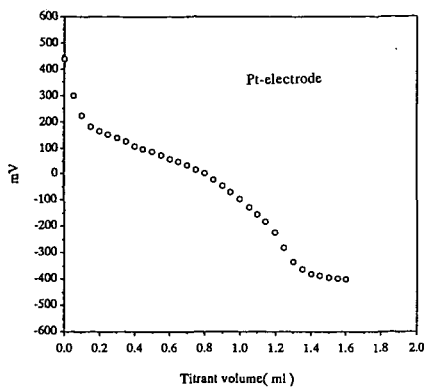


Figure 5. Non-aqueous titration of pyridine extract of Pittsburgh No.8

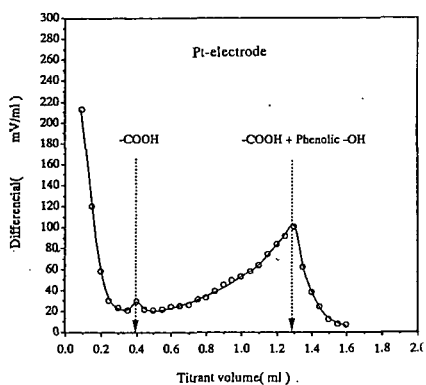


Figure 6. Non-aqueous titration of pyridine extract of Pittsburgh No.8

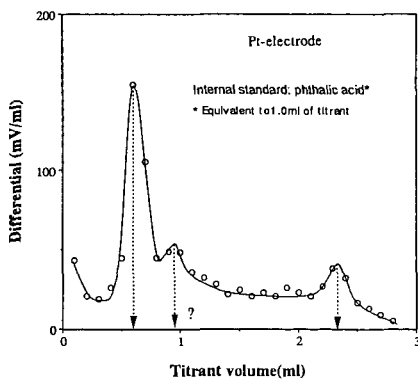


Figure 7. Non-aqueous titration of pyridine extract of Pittsburgh No.8 with internal standard

TIME RESOLVED SMALL ANGLE X-RAY SCATTERING REACTIVITY STUDIES ON COALS, ASPHALTENES, AND POLYMERS

R. E. Winans, S. Seifert, and P. Thiyagarajan[†]
Chemistry Division and [†]Intense Pulsed Neutron Source Division
Argonne National Laboratory, Argonne, IL 60439

Keywords: Argonne Premium Coals, pyrolysis small angle X-ray scattering

ABSTRACT

The objective of this study is to examine changes in the structures of coals, asphaltenes, and polymers in situ with small angle X-ray scattering (SAXS) during thermal treatments. We have built a SAXS instrument at the Basic Energy Sciences Synchrotron Radiation Center at the Advanced Photon Source that allows us to obtain scattering data on very small samples and in the millisecond time domain. The Argonne Premium Coal samples, petroleum derived asphaltenes, and polymers with functionality to model fossil fuels were used in this study. The information that can be derived from these experiments includes: changes in fractal dimensionality, surface topology, and size and type of porosity. The information is correlated with other methods on the same samples.

INTRODUCTION

Small angle scattering is a good method to observe features such as porosity and surface properties of disordered systems over broad length scales. This non-destructive technique is useful for in situ analysis and with the advent of third general light sources with high photon flux, rapid data acquisition is possible. The nature of the porosity of a suite of 15 coals has been studied by SAXS and the results compared to adsorption techniques.¹ Coal pyrolysis followed by gasification has been followed by SAXS. They found that upon pyrolysis there was an increase in micro and meso pores.² SAXS investigation of pore sizes of Canadian coals and their chars showed that reactive chars from low rank coals have greater pore volumes compared to the coals, while the opposite effect is seen for less reactive chars from higher rank coals.³ The fractal pore structure of raw and heated brown coals was studied by SAXS.⁴ All of these were done with lab instruments. Synchrotron sources allowed faster data acquisition such that in situ experiment are facilitated such as the dynamics of solvent swelling.⁵ The Argonne coals have been looked at by a number of temperature programmed techniques such as TGA-FTIR,⁶ TGA-MS,⁷ Py-FIMS,⁸ Py HRMS,⁹ PMRTA,¹⁰ and IGC.¹¹ These results will be used to help interpret data from temperature programmed (TP) SAXS of the Argonne Coals, resids, and polymers.

EXPERIMENTAL

The eight Argonne Premium Coal Samples were used without modification in this study.¹² The ethylene [I] and oxymethylene [II] linked polymers have been used as possible models.^{13,14} More recent studies have looked at ethylene linked benzene with [III] and without carboxylic acid groups [IV].^{15,16} The purpose of this later study was to examine the possible role of carboxylic acids to form crosslinks in low rank coal pyrolysis. The SAXS instrument was constructed at ANL and used on the Basic Energy Sciences Synchrotron Radiation Center CAT undulator beamline ID-12 at the Advanced Photon Source (<http://www.bessrc.aps.anl.gov>).

Quartz capillaries (1 mm) were used to sample 5 mg of -100 mesh coal or polymer. Scattering patterns were obtained as the sample is heated from 25-600 °C. Monochromatic X-rays (8.5 - 23.0 keV) are scattered off the sample and collected on a 19 x 19 cm² position sensitive two-dimensional gas detector. More recent data are taken using a 9-element mosaic CCD detector (15 x 15 cm) with maximum of 3000 x 3000 pixel resolution. An advantage of this new detector is that unlike the wire detector, the full beam from the undulator can be used which gives a factor of 1000 increase in intensity. The scattered intensity has been corrected for absorption, the empty capillary scattering, and instrument background. The differential scattering cross section has been expressed as a function of the scattering vector Q, which is defined as $Q = (4\pi/\lambda) \sin \theta$, where λ is the wavelength of the X-rays and θ is the scattering half angle. The value of Q is proportional to the inverse of the length scale (\AA^{-1}). The instrument was operated with two different sample-to-detector distances, 68.5 cm to obtain data at $0.04 < Q < 0.7 \text{\AA}^{-1}$ and 3740 cm to measure at $0.006 < Q < 0.1 \text{\AA}^{-1}$.

Small Angle X-ray Scattering

A typical plot of the time temperature-resolved data for the pyrolysis of the Illinois No. 6 bituminous coal (APCS 3) is shown in Figure 1. These curves can be analyzed to determine size of features,

topology, and changes in total scattering. Power law slope from the data, such as is shown in Figure 1, are used to describe the topology of the system. Finally, the invariant Q_0 is calculated and is proportional to the fluctuation of the electron density in the system. Changes in the invariant are useful in monitoring topological changes in the sample, $Q_0 = \int_0^\infty I(Q) Q^2 dQ$. For example, the invariant goes to zero for a homogeneous system that does not have any concentration fluctuation.

RESULTS AND DISCUSSION

The results from the TP SAXS are initially best understood by comparing them to results from other techniques and by looking at the various trends observed between the different rank premium coals. An example of the scattering curves as a function of Q is shown in Figure 1 for the Illinois bituminous coal (APCS 3). To avoid confusion, a few selected curves are drawn to represent the changes seen as the sample heats up. An obvious feature that is seen for the low rank coals but is most pronounced with the Illinois coal is the increase in scattering over an intermediate temperature range. This result is best observed in the changes of the invariant with temperature which is shown in Figure 2. There is a rapid increase in the Q_0 at $\sim 130^\circ\text{C}$ where most likely water is being driven off. This could result from structural reorganization of the macromolecules in coal. These structural changes are common with the coals of $< 80\%$ carbon, but are not seen in the higher rank coals. However, the role of water release is not the only factor since the lignite and subbituminous coals have a greater water content and yet the effect is much less. The structure change is more than just a physical swelling of the structure since the free swelling index of this coal (4.8) is much less than, for example, the Upper Freeport (APCS 1), which has a FSI of 8.5.¹²

With the Upper Freeport, the increase in Q_0 is not observed, but instead shows the transitions at the softening and fluidity points. Normally the approaches used to look at these transitions are plasticity or fluidity measurements and inverse gas chromatography (IGC). A comparison of the SAXS and ICC data are shown in Figure 3. One expects the IGC transition to occur at a lower temperature since the heating rate was in hours compared to the total heating time of 10 min. for the SAXS data. However, note that the slope is the same (dashed line). In IGC, this slope is used to calculate the enthalpy of adsorption which for APCS 1 is 12.5 kcal/mole.¹¹ These values increase with rank of the coal in the bituminous range. The trend in Q_0 is also similar and is indicative of the increase in homogeneity of the system at these temperatures as the coals are becoming fluid. The low rank coals which do not become fluid show much different trends in Q_0 at these higher temperatures.

The changes in the power law slope can be correlated with TGA results under the same heating rates. For bituminous coals, such as the Illinois No. 6 and Pocahontas, there is a reasonable correlation as shown in Figure 4. However, for the low rank coals, the changes in d_f is much different and actually may have increased instead of decreasing with temperature as seen in the higher rank coals. One possible explanation for this is the fact that these coals are still early in the coalification process and what may be occurring is an accelerated coalification process. Part of this process may be the establishment of increased crosslinks instead of decreasing crosslinks, which normally occurs in the pyrolysis of bituminous coals. This has been suggested in other studies.¹⁵ Recently, model polymers with carboxylic acid functionality have been studied to try to understand this crosslinking phenomena. Later, we will discuss the results of TP SAXS on the polymer.

In Utah coals (APCS 6), the d_f decreased at a much lower temperature than the other bituminous coals. This has also been observed for this coal by proton magnetic resonance thermal analysis (PMRTA). It has been suggested that the increased mobility observed is due to the liptinite macerals in this coal (which is rich with resinates, 75%) at lower temperatures. Our SAXS data would confirm this conclusion. The volatile release of the coal is not unusual but the increase in extractability with heating is much greater than other bituminous coals of similar rank. The resinite must have a synergistic effect on overall thermal degradation of the macromolecular matrix.

To better understand TP SAXS results for the coal samples, four polymers which represent various potential structures and functionality in coals have been examined under the same conditions as the coal pyrolysis. For both the naphthalene based polymers [I] and [II], the structure changes at much lower temperatures than coals. However, as expected, the oxymethylene linked polymer [III] is the most reactive. In both polymers, a broad feature between $Q = 0.1$ to 0.3 emerges at high temperature which would be the formation of larger polycyclic aromatics. The PyHRMS has shown that these polymers, especially [II] undergo secondary reactions to form strong Ar-Ar links which can lead to larger polycondensed aromatics.

The polymers from ORNL behaved much differently. For [III] with carboxylic acid functionality, the Q_0 did decrease but not nearly as much as seen in [I] and [II]. The structure seen by SAXS for

the hydrocarbon polymer [IV] appeared to be very stable over the temperature range studied even though it is known that the solubility increased with increasing temperature.¹⁵ However, up to about 475 °C these polymers showed no weight loss in TG analysis. The most direct comparison is between I and IV, which have the same linkages but differ in the aromatic ring, where the naphthalene [I] appears to be much more reactive.

CONCLUSIONS

Structural changes upon pyrolysis are observed in the SAXS data for coals and polymers. These changes can be correlated and contrasted with a number of other thermal analytical methods on the same coal and polymer samples. The results are very rank dependent with the lower rank coals showing variations over the entire temperature range. The naphthalene based polymers are much more reactive than the benzene-ethylene linked polymers and appear to give more secondary transformations.

ACKNOWLEDGMENTS

This work was performed under the auspices of the Office of Basic Energy Sciences, Division of Chemical Sciences and Division of Materials Sciences, U.S. Department of Energy, under contract number W-31-109-ENG-38. The support of the BESSRC staff is appreciated, especially Jennifer Linton and Mark Beno.

REFERENCES

1. Kalliat, M.; Kwak, C. Y.; Schmidt, P. W. In *New Approaches in Coal Chemistry*; Blaustein, B. D., Bockrath, B. C., Friedman, S., Eds.; ACS Symposium Series 169; American Chemical Society: Washington, D.C., 1981; pp. 3-22.
2. Foster, M. D.; Jensen, K. F. *Fuel* **1990**, *69*, 88-96.
3. Xu, Yingnian; Koga, Yoshikata; Watkinson, A. Paul. *Fuel* **1994**, *73*, 1797-801.
4. Johnston, P. R.; McMahon, P.; Reich, M. H.; Snook, I. K.; Wagenfield, H. K. *J. Colloid Interface Sci.* **1993**, *155*, 146-51.
5. Winans, R. E.; Seifert, S.; Thiyagarajan, P. *Prepr. Pap. - Am. Chem. Soc., Div. Fuel Chem.* **1999**, *44*, 149-152.
6. Solomon, P. R.; Serio, M. A.; Carangelo, R. M.; Bassilakis, R.; Gravel, D.; Baillargeon, M.; Baudais, F.; Vail, G. *Energy Fuels* **1990**, *4*, 319-33.
7. Yun, Y.; Meuzelaar, H. L. C.; Simmleit, N.; Schulten, H.-F. *Energy Fuels* **1991**, *5*, 22-29.
8. Simmleit, N.; Schulten, H.-R.; Yun, Y.; Meuzelaar, H. L. C. In *Advances in Coal Spectroscopy*; Meuzelaar, H. L. C., Ed.; Plenum Press: New York, 1992; pp. 295-339.
9. Winans, R. E. In *Advances in Coal Spectroscopy*; Meuzelaar, H. L. C., Ed.; Plenum Press: New York, 1992; pp. 255-274.
10. Sakurovs, R.; Lynch, L. J.; Barton, W. A. In *Magnetic Resonance of Carbonaceous Solids*; Botto, R. E., Sanada, Y., Eds.; Adv. Chem. Series 229; American Chemical Society: Washington, D.C.; 1993; pp. 229-251.
11. Neill, P. H.; Winans, R. E. In *Inverse Gas Chromatography: Characterization of Polymers and Other Materials*; Lloyd, D. R., Ward, T. C., Schreiber, H. P., Eds.; ACS Symposium Series 391; American Chemical Society: Washington, D.C., 1989; pp. 290-305.
12. Vorres, K. S. *Energy Fuels* **1990**, *4*, 420-426.
13. Winans, R. E.; Hayatsu, R.; Squires, T. G.; Carrado, K. A.; Botto, R.E. *Prepr. Pap. - Am. Chem. Soc., Div. Fuel Chem.* **1990**, *35*, 423-429.
14. Squire, K. R.; Solomon, P. R.; Carangelo, R. M.; DiTaranto, M. B. *Fuel* **1986**, *65*, 833-43.
15. Mungall, W. S.; Britt, P. F.; Buchanan, A. C., III. *Prepr. Pap. - Am. Chem. Soc., Div. Fuel Chem.* **1997**, *42*, 26-30.
16. Britt, P. F.; Mungall, W. S.; Buchanan, A. C. III. *Energy Fuels* **1998**, *12*, 660-661.

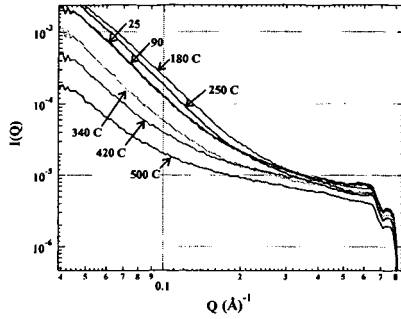


Figure 1. SAXS data from Illinois 6 pyrolysis at selected temperatures.

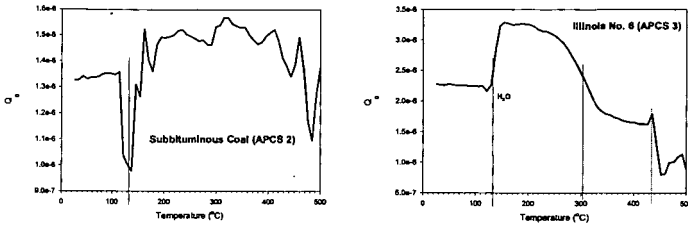


Figure 2. Invariant changes with pyrolysis.

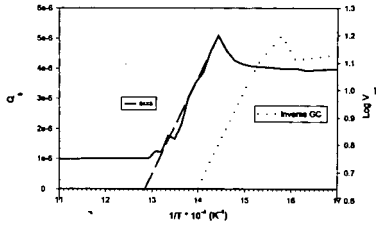


Figure 3. Comparison of SAXS with IGC data for the Upper Freeport coal (APCS 1).

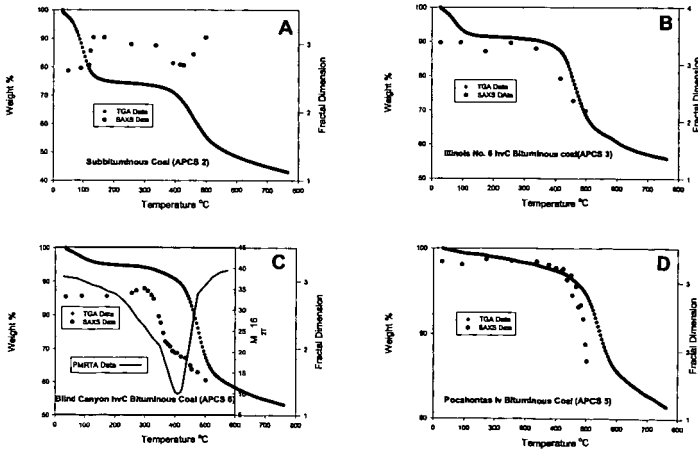


Figure 4. Comparison of TGA data with the d_v from SAXS.

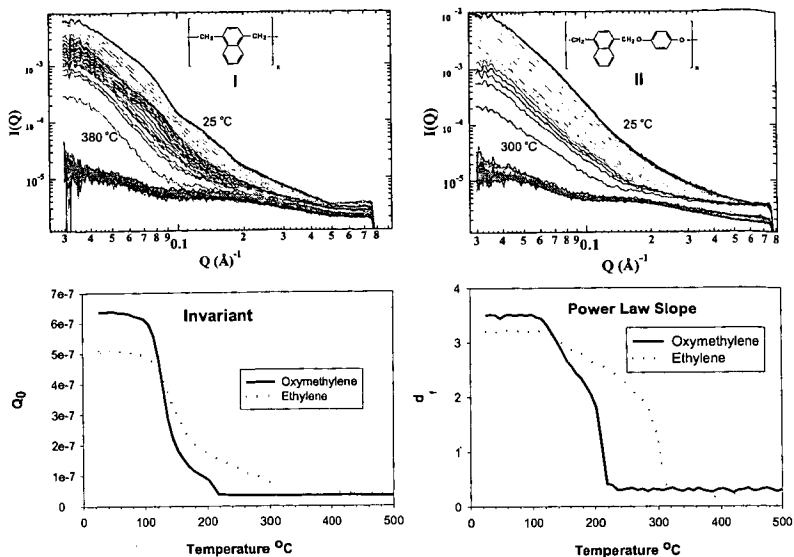


Figure 5. SAXS data for naphthalene polymers I and II with a comparison of invariants and power law slopes.

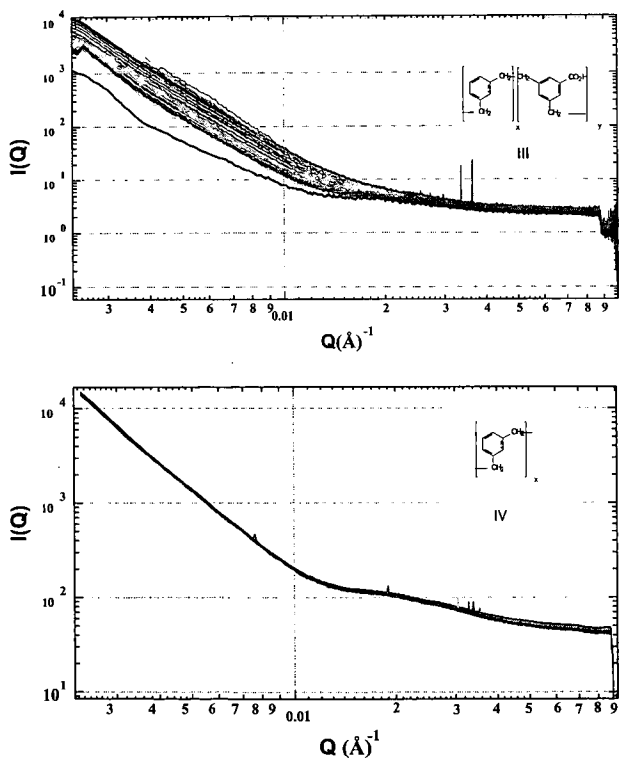


Figure 6. SAXS data for benzene polymers III and IV.

USE OF INTRA- AND INTER-MOLECULAR MODELS TO SIMULATE THE WIDE ANGLE X-RAY SCATTERING OF COALS. David L. Wertz, Department of Chemistry & Biochemistry, University of Southern Mississippi, Hattiesburg, MS 39406, USA.

INTRODUCTION. Hirsch et al.,¹ using the terminology of diffraction where $d = \lambda/2 \times \sin\theta$ for first order reflections in the x-ray experiments, assigned this peak to the average distance between layers which were proposed to contain the poly-cyclic units at the molecular level in coals. Using copper K_{α} Xrays, they found this peak (quite broad) to occur at $2\theta \approx 25^\circ$, corresponding to $\langle d \rangle \approx 3.5 \text{ \AA}$. Their proposal of layering, at the molecular level in coals, has been verified, both by molecular modeling² and x-ray analysis using more modern equipment and several of the Argonne Premium Coals,³ but their the use of ideal diffraction concepts to define structuring in coals is troubling because coals are not crystalline.

An alternative method for relating the measured x-ray intensities, which now may be accurately obtained using modern quantum counting equipment and computer-controlled data acquisition and processing method, has been utilized by our group.^{4,5} This method correlates the measured intensity, which is a series of broad maxima and minima, with the average short-range structural unit in the coal and has been illustrated in the scattering studies of liquids, solutions, and amorphous solids. The Debye relationship correlates the structure of any molecular-level species, averaged of time and space, with the simulated wide angle phase interference curve caused by that species by:

$$j(q) = (\sum \sum q \times r_{ab})^{-1} \times \sum n_{ab} \times \sin(q \times r_{ab});$$

where n_{ab} is the number of a-b atom pairs which occur at the distance r_{ab} in the structure, $f_a(q)$ and $f_b(q)$ are the scattering powers of atoms a and b, respectively, and $q = [4 \times \pi / \lambda] \times \sin \theta$.⁶ For several of the Argonne Premium Coals, the average intra-molecular structural unit, (i.e., the average PC and its attachments) have been reasonably well identified;^{7,8} so the n_{ab} 's and the r_{ab} 's for the average intra-molecular structural unit may be determined using three-dimensional geometry and then used to calculate the simulated phase interference curve for that coal using the Debye equation. This has been accomplished for several coals.⁴

The actual phase interference curve, $i(q)$, may be obtained from the wide angle x-ray scattering (WAXRS) experiment. The comparison of $j(q)$ to $i(q)$ allows a judgement in the validity of the structural model used to calculate $j(q)$, i.e., the array of n_{ab} 's and the r_{ab} 's that define that model. The comparison may be quantified by:

$$\tau^2 = \sum \{i(q) - j(q)\}^2 / \sum i(q)^2.$$

The lower the value of τ , the better the agreement between the experimentally measured phase interference curve and the phase interference curve calculated from the model.

Solum et al propose that the average poly-cyclic unit in Pittsburgh #8 (PIT) coal is *ca.* C_{15} with four attachments.⁷ Shown in Figure 1 is the simulated phase interference curve calculated for the C_{15} unit. Also shown in Figure 1 are the experimentally measured $i(q)$'s using both Mo K_{α} and Cu K_{α} Xrays.³ As previously noted, the agreement between the experimentally determined $i(q)$ and the $j(q)$ calculated from the intra-molecular model based on C_{15} agree well at $q > 3 \text{ \AA}^{-1}$. The $j(q)$ curve calculated from the C_{15} structural model is featureless in from 1.0 - 3.0 \AA^{-1} ; but the experimentally measured $i(q)$ has a large maximum, centered at *ca.* 1.6 \AA^{-1} with minima preceding and following this maximum. Similar results have been obtained for other coals.^{3,4} Thus, it may be concluded that the dominant maximum in the measured x-ray intensity curves for coals, located at *ca.* 1.7 - 1.9 \AA^{-1} , is not due to structuring within the average PC unit.

Recently, an improved explanation of the measured x-ray intensities, expanding on the layering concept, has been proposed as the result of an x-ray scattering study of Beulah Zap lignite.⁹ This procedure incorporates the concept of molecular-level layering in coals by calculating the distances between atoms in adjacent layers within the average short-range structural domain for that coal and correlating these distances with the structure curve calculated for each coal from wide angle x-ray scattering (WAXRS) experiments.

The objective of this study is to simulate the dominant peak in each experimentally determined $i(q)$ using simplified structural models which approximate the average PC unit in the coal as a disc whose radius may be estimated from the NMR information available in the literature.

RESULTS. Shown in Figure 2 are several crude models of layering in the short-range domains in coals. The models differ, of course, in the number of layers in the average domain. To relate each of the models to coals, it has been assumed that the radius of the average PC unit (rad) is ca. 2.5 Å and average distance between the layers (<d>) is ca. 3.8 Å which is similar to the average inter-layer distance reported for a number of the Argonne Premium Coals.³ Shown in Figure 3 are the relative frequencies of the atom-pair distances (i.e., the structure curve) calculated from each model by:

$$F(r) = \sum \{rad^2 + [n \times \langle d \rangle]^2\}^{3/2};$$

where n describes the relationships between the layers in the model, and r is the distance between the atom in the various layers.

Using the Debye eq., each frequency function has been transformed into reciprocal space to produce its corresponding j(q). The simulated phase interference curve for each layer model is presented in Figure 4. Although the inter-layer structural models differ in the number of layers contained within each, their resulting phase interference curves are similar, with each featuring a maximum in the q = 1.8 Å⁻¹ region. Minima precede and follow this maximum. The sharpness of the maximum is related to the number of layers in the short-range structural domain.

In the three layer model, C-C atom-pair distances are expected to be centered at ca. 4.5 Å and at ca. 8.0 Å with a relative peak intensity of 2/1. The j(q) calculated for the three layer model is similar to the experimentally determined i(q) obtained for PIT. Shown in Figure 5 is the j(q) calculated from the three layer model compared to the i(q) measured for Pittsburgh #8 coal. For this comparison, τ = 0.021 when <d> = 3.92 Å and rad = 2.6 Å. This very low structure correlation factor verifies the excellent agreement between i(q) and the J(q) calculated from the 3-layer model. The average interlayer distance determined by this method is similar to the average interlayer spacing distance reported by the earlier non-ideal diffraction interpretation of the secondary x-ray intensity reported for PIT.

The inter-molecular structure curve has been obtained by Fourier transform of the inter-molecular portion of the experimentally determined phase interference curve for PIT. This inter-molecular structure curve contains two maxima with relative intensities of 2/1. In Figure 6, this inter-molecular structure curve is compared to the atom-distance/frequency function calculated for the three layer model. The good agreement between these two functions indicates that the average short-range structural domain in PIT contains three layer units.

CONCLUSIONS. A simplified inter-layer model of the layering of the PC units in coals is consistent with both the phase interference curve obtained for Pittsburgh #8 coal by wide angle x-ray scattering. This model also predicts an atom-pair frequency curve which is consistent with the inter-molecular structure curve obtained for PIT.

REFERENCES

1. Hirsch, P. B., *Nature (London)*, 1956, 177, 500-513 and numerous other publications.
2. Nakamura, K., Nakanoshashi, T., Iono, M., Sato, M., Yokoyama, S., and Sanada, Y., *Energy Fuels*, 1995, 9, 1003-1010.
3. Wertz, D. L. and Bissell, M., *Energy Fuels*, 1994, 8, 613-617.
4. Wertz, D. L., *Fuel*, 1995, 74, 1431-35; 1998, 77, 43-53.
5. Wertz, D. L., and Bissell, M., *Adv. X-Ray Anal.*, 1994, 37, 491 - 497.
6. Kruh, R. F., *Chem. Rev.*, 1962, 62, 319 - 346.
7. Solum, M. S., Pugmire, R. J., and Grant, D. M., *Energy Fuels*, 1989, 3, 187-193.
8. Munteen, J. V. and Stock, L. S., *Energy Fuels*, 1991, 5, 768 - 769.
9. Wertz, D. L. and Quin, J. L., *Energy Fuels*, 1998, 12, 697-703; 1999, 13, 513-517.

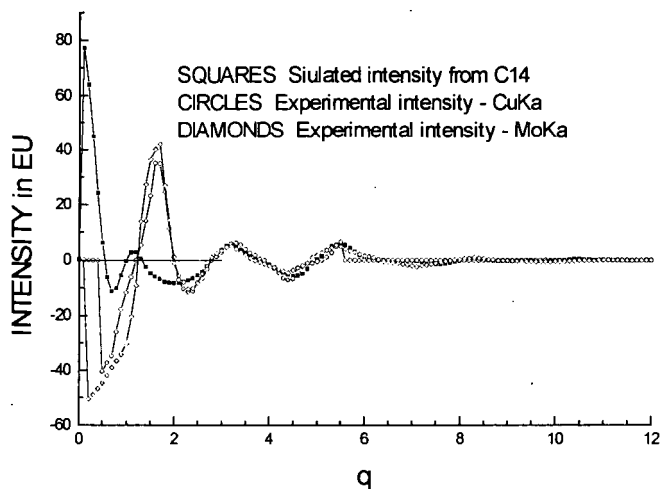


Figure 1. Comparison of the experimental phase interference curves for PIT with the simulated phase interference calculated for the C_{13} poly-cyclic unit.

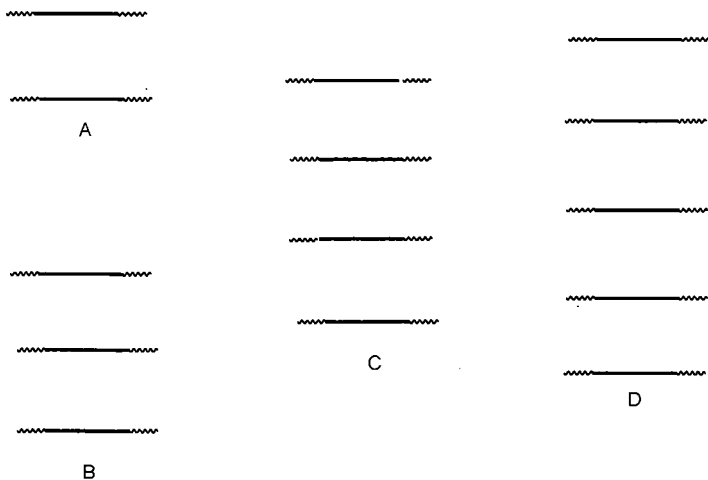


Figure 2. Models of molecular-level layering. Two layers (A), three layers (B), four layers (C), and five layers (D).

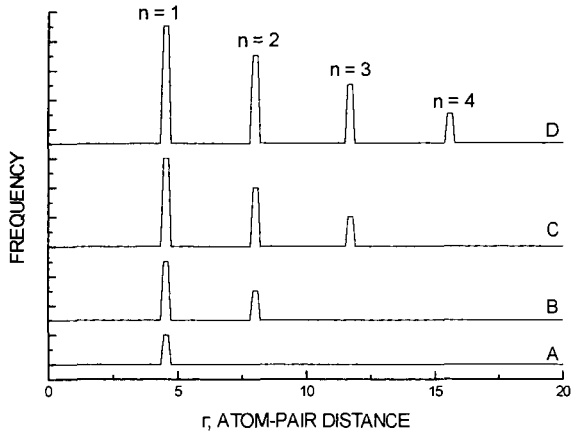


Figure 3. Frequency vs. atom-pair distance for the two-layer model (A), three-layer model (B), four-layer model (C), and the five-layer model (D).

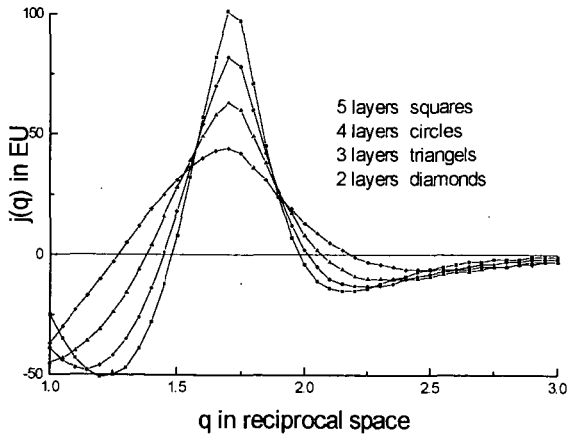


Figure 4. Simulated phase interference curves for the four inter-layer models.

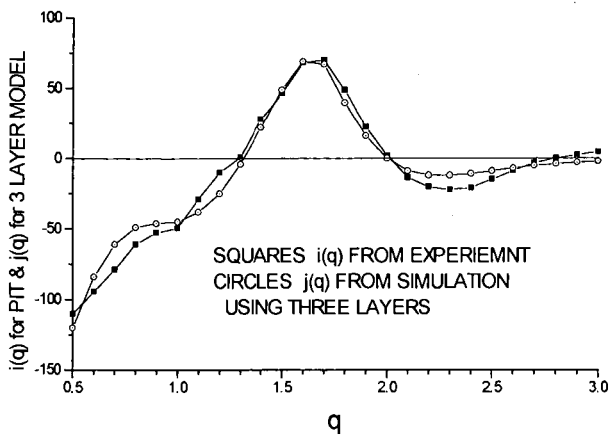


Figure 5. The $i(q)$ for PIT compared to the optimized $j(q)$ for the three-layer model.

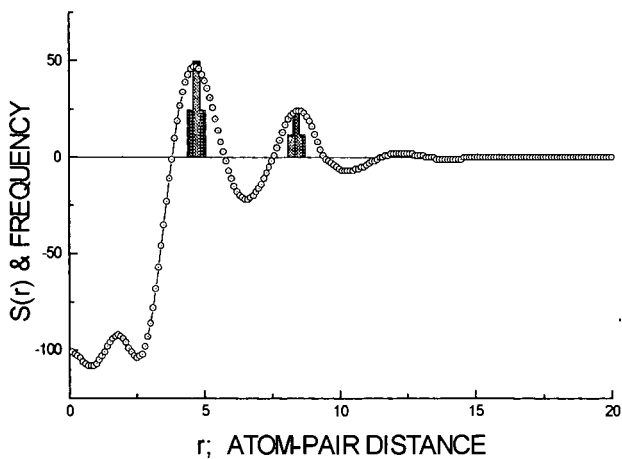


Figure 6. Inter-molecular structure curve for PIT compared to the frequency vs. atom-pair distance graph for the three-layer model.

STRUCTURAL PARAMETERS OF COALS FROM 002 LATTICE FRINGE IMAGES USING HRTEM

Atul Sharma, Takashi Kyotani and Akira Tomita

Institute for Chemical Reaction Science, Tohoku University,
Sendai, JAPAN.

Key words: Coal structure, Lattice image, HRTEM.

INTRODUCTION

Over the years several studies have been done using different techniques to get the insight into the coal structure. All these studies converge on one understanding that coal is heterogeneous in nature and made up of very small aromatic layers more or less randomly orientated. The layer size and stacking number increases with the rank of coal. Direct evidence about the arrangement of these aromatic layers, obtained by the electron microscope lattice imaging, is obviously an attractive complementary technique. Not much literature have been available on TEM observation of coals as such and most of the studies report about the heat treated coals. McCartney and Ergun [1] used electron microscopy to determine crystalline dimensions of meta-anthracite coal. Another attempt was made by Evans et al. [2] who observed anthracite coal and heat-treated coals. They found the coal samples to be completely amorphous and no evidence of any ordered layers. Millward [3] also reported that when coals were observed by electron microscope, no fringes which could be evidence of layered molecules was found. He highlighted the problems associated with instrument and irradiation damages which make it difficult to observe raw coals. Oberlin [4] developed dark field image technique to observe the coal structure. The electron microscope operation and theoretical consideration of image formation are now fully understood. With recent advances in electron microscope instrument like anti-contamination device which successfully preserve the specimen from irradiation damages during high-resolution observation, it is possible to image even the highly electron beam-sensitive materials like coals.

In this article we are presenting the structure of three different coals as observed by HRTEM. We also attempted to obtain stack distribution using image analysis technique developed by us and described elsewhere [5].

EXPERIMENTAL

Argonne Premium Coal Samples, Pocahontas no. 3 (POC), Illinois no. 6 (IL) and Beulah-Zap (BZ), were selected for the investigation. The coal samples, ground in ethanol and sprayed on a copper microgrid, were observed under a TEM (JEOL-2010) operating at 200 kV for high resolution images. The transmission electron microscope was equipped with computerized imaging system and EDS for elemental analysis. To get a general view of the coal samples, nearly 7 to 8

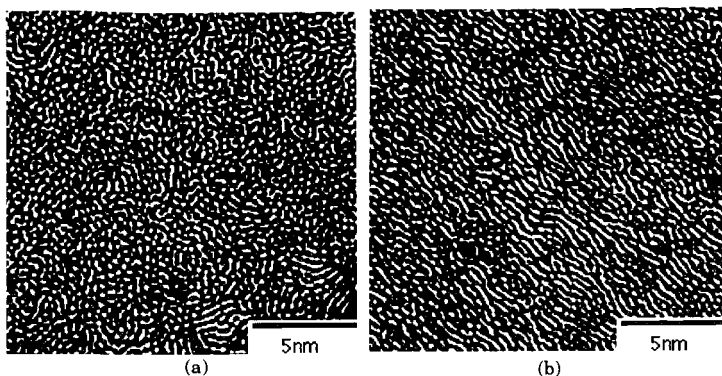


Figure 1 HRTEM images of Beulah-Zap coal: (a) amorphous structure and (b) ordered structure.

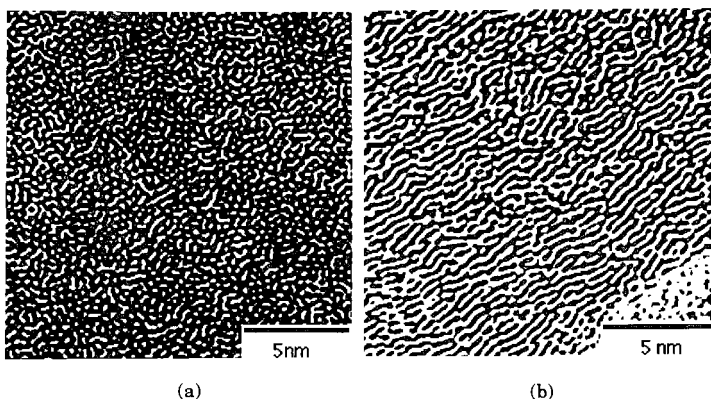


Figure 2 HRTEM images of Illinois no. 6 coal: (a) amorphous structure and (b) ordered structure.

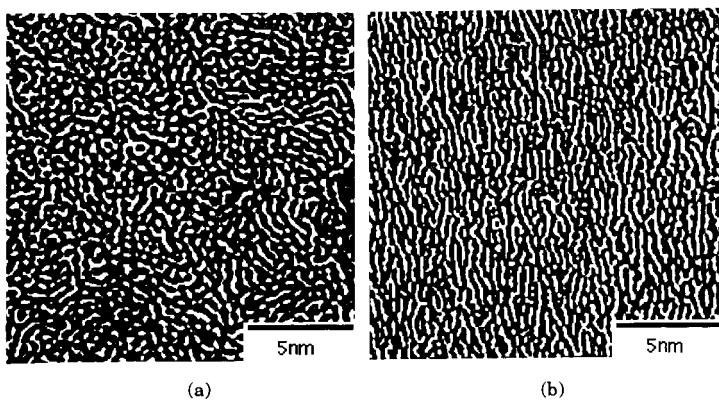


Figure 3 HRTEM images of Pocahontas no. 3 coal: (a) amorphous structure and (b) ordered structure.

different spots were observed. A quantitative analysis was done to evaluate stack distribution using our newly developed image analysis technique [5].

OBSERVATION OF COALS USING HRTEM

It is necessary first to ascertain that the TEM micrographs presented here are those of coals. In all cases, first a sub-micron size particle was selected for observation at a very low magnification and its diffraction pattern was taken and elemental analysis was carried out. The elemental analysis showed signatures of all the elements present in the coals as mineral matter which was also confirmed by the sharp spots observed in the SAD patterns. After confirming that this sub-micron size particle is coal, very thin edges of this particle were observed at a high magnification ($\times 500k$). To prevent the sample from irradiation damages, the current density on the screen was kept at less than 1 pa/cm^2 . At this illumination almost nothing can be observed on the fluorescent screen. However, the structure can be observed on the TV screen by increasing the aperture and sensitivity of the camera. By this approach we considerably reduced the number of electrons hitting the sample.

RESULTS AND DISCUSSION

In Figures 1 to 3, the HRTEM images from two different spots for BZ, IL and POC coals are shown. All three coals show the presence of both amorphous and ordered structure. Even in ordered structures, layers are not plane and show lack of mutual orientation. It is known that coals contain small condensed aromatic units. These units show a parallel stacking but lack orientation and planarity because of the presence of hetero-atoms or hydroaromatic portions. These fringes or layers observed from HRTEM images are in accordance with the above understanding, and hence these layers are not graphite-like layers. Figure 4 shows a typical example of extracted images from HRTEM images using the filtration technique [5] for quantitative analysis. The extracted images from five different spots were subjected to image analysis algorithm [5] to evaluate stack distribution and the results are shown in Figure 5. The distributions show that the fraction of single layers or amorphous part is higher in BZ coal than in POC coal and the fraction of highly stacked group is relatively large with POC. However, the number of photographs taken in this study are too less to discuss further on the difference among the three coals. Figures 6a-c show the presence of mineral matter in the three coals. BZ and IL show very clear lattice fringes from the mineral matter. To make the fringes more clear, we separated these from the organic part by drawing a white line. In Figure 6a, these are enclosed by the white line while in Figure 6b, these are towards left of the white line. In POC coal, mineral matter is present as nearly circular dark spots. Figure 6d shows an onion-like structure similar to fullerene as suggested by Fang et al [6]. This was observed only in POC coal and only in one spot.

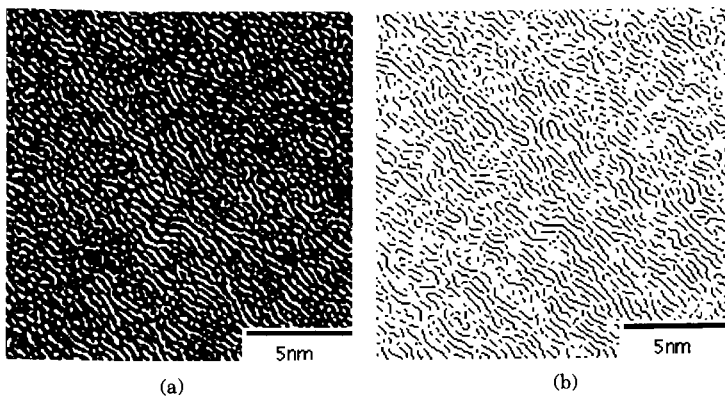


Figure 4: (a) HRTEM image and (b) corresponding extracted image.

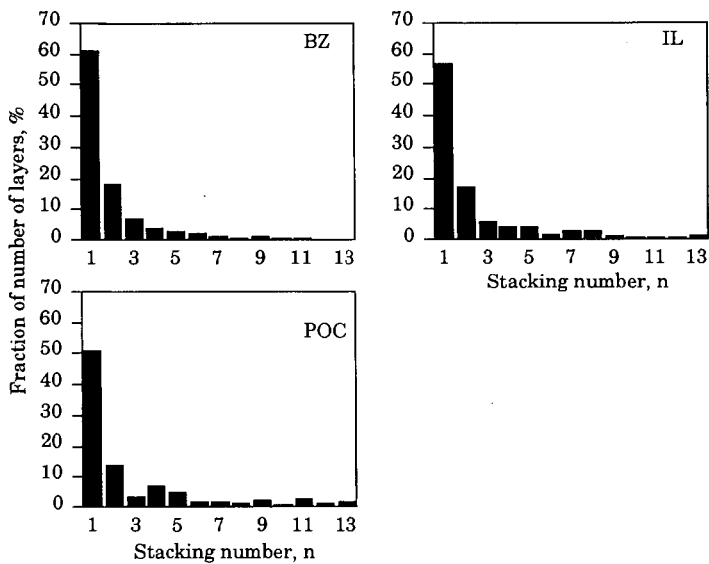


Figure 5 Fraction of number of layers occurring in n layers.

CONCLUSIONS

The HRTEM technique is a powerful tool for extracting microstructure information of coals. Both amorphous and ordered structures were observed. Direct evidence of lattice fringes which can be ascribed to layers was found.

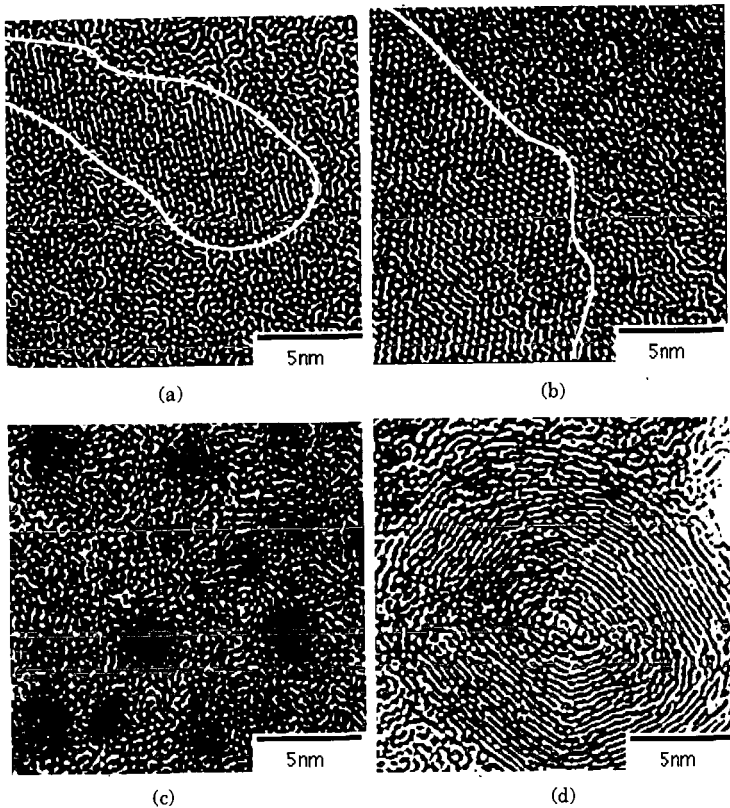


Figure 6 HRTEM images of: (a) mineral matter in Beulah-Zap coal, (b) mineral matter in Illinois no.6 coal, (c) mineral matter in Pocahontas no. 6 coal, and (d) onion-like structure in Pocahontas no. 3.

ACKNOWLEDGMENT

This study was part of "Research for the Future Program- Molecular Engineering of Coal" which was supported by the Japan Society for the Promotion of Science.

REFERENCES

1. McCartney, J.T., Ergun, S. *Nature*, 1965, 205, 962-964.
2. Evans, E.L., Jenkins, J.L., Thomas, J.M. *Carbon*, 1972, 10, 637-642.
3. Millward, G.R. In *Coal and modern coal processing: An introduction*, Pitt, G.J., Millward, G.R., eds., Academic press, 1979, pp. 94.
4. Oberlin, A. *Carbon*, 1979, 17, 7-20.
5. Sharma, A., Kyotani, T., Tomita, A. A new quantitative approach for microstructural analysis of coal char using HRTEM images. *Fuel*, in press.
6. Fang, P.H., Wong, R. *Mat. Res. Innovat.*, 1997, 1, 130-132.

MICROHETEROGENEITY OF SOLVENT-SWOLLEN COAL PROBED BY PROTON SPIN DIFFUSION

Koyo NORINAGA ^{*†}, Jun-ichiro HAYASHI, Tadatashi CHIBA, and Masashi IINO [†]
Center for Advanced Research of Energy Technology (CARET), Hokkaido University
N13, W8, Kita-ku, Sapporo 060-8628, Japan

[†]*Institute for Chemical Reaction Science, Tohoku University*
Katahira, Aoba-ku, Sendai, 980-8577, Japan

KEYWORDS: Coal, Swelling, Microphase separation

ABSTRACT

Phase separated structure of solvent swollen coal was characterized through its property of proton flip-flop spin diffusion. It is shown that the fashion of coal swelling is non-uniform on a segmental scale and a microscopic phase separation does take place on a scale from several to 20 nm even in good solvents like pyridine.

INTRODUCTION

The most convincing model of coal structure is that of a cross-linked macromolecular network. All attempts to relate the macromolecular network parameters such as the molecular weight between cross-link points to the degree of swelling in a good solvent have taken the Flory-Rehner theory ¹ as a starting point for the swelling of macromolecular networks. The theory involves the assumption that the deformation is affine, i.e., that the primitive chain is deformed in the same way as the macroscopic deformation (swelling) of the sample. Accordingly, the premise is required that the swollen coal is uniform in the segmental scale when we relate the macroscopic swelling to the molecular characteristics such as cross-link density. Based on the ¹H NMR transverse relaxation characteristics, however, it was found that the hydrogens in pyridine-swollen coals could be divided into two groups: those whose relaxation was characteristic of solids and those whose relaxation was characteristic of liquids. Barton et al. ² reported that the ¹H NMR transverse relaxation signals measured at ambient temperature for bituminous coals swollen by deuterated pyridine, show that up to ~60% of the coal molecular structures can be sufficiently destabilized to become mobile. Therefore, at least 40% of the coal hydrogen remains in rigid molecular structures and is characterized by an NMR signal component that is similar to the signal for the corresponding dry coal. This result demonstrates that the swollen coal can be recognized to have a phase separated structure involving solvent rich phase and apparently solvent impervious phase. However the scale of heterogeneity in the swollen coals is presently not fully understood.

In spite of its indirect character, measurements of ¹H spin diffusion by pulsed NMR have proven to be a useful technique for evaluating the compatibility of polymer blends ³⁻⁶ and the microdomain structure of multiphase polymers. ⁷⁻¹¹ When a nuclear system is disarranged from equilibrium in an NMR experiment, the excess spin energy acquired by the resonant nuclei can remain in the spin system for a long time compared to transverse relaxation time, T_2 , before being transferred to the lattice. This follows directly from the fact that longitudinal relaxation time, T_1 , is much larger than T_2 in solid materials. ¹² During this time the spin energy can disperse between neighboring nuclei by energy-conserving "flip-flop" spin transitions. This process is termed spin diffusion and may provide observable energy transport over distances of several tens of nanometers. For the coal swollen by the saturation of deuterated pyridine, there exists at least two distinct morphological regions in the NMR sense. In such a case, owing to their state of motion, certain regions or sites responsible for the mobile phase provide exceptionally efficient transfer of energy to the lattice, while the rigid component weakly coupled to the lattice, can exhibit molecular motions that disfavor relaxation. It is possible, through the mechanism of spin diffusion, for the component that is tightly coupled to the lattice to relax other resonant nuclei in the spin system either totally or partially. By analyzing the spin diffusion process under an appropriate initial and boundary conditions, we can estimate the diffusive path length, and then get an information about the domain size of each phase.

In this study, the phase separated structure of solvent swollen coal is characterized through its property of proton flip-flop spin diffusion. Six coals of different rank swollen by the saturation of deuterated pyridine were subjected to ¹H NMR relaxation measurements. The NMR experiments provide transverse relaxation time, T_2 , longitudinal relaxation time, T_1 , and that in the rotating frame $T_{1\rho}$. The time dependency of the spin diffusion is also monitored by Goldman-Shen pulse sequence. The dimension of a heterogeneity of the swollen coal is evaluated by analyzing the spin diffusion process.

EXPERIMENTAL

Samples. Four Argonne Premium Coal Sample Program (PCSP) coals ¹³ and a brown coal were used as coal samples. Their particle sizes were finer than 150 μm . They were dried under a pressure of less than 1 Pa at 333 K for 48 h, which is long enough to attain a constant weight. The elemental composition, ash and water contents, and swelling ratios of the coal samples in pyridine or pyridine/CS₂ mixed solvent are listed in Table 1. The coal sample was weighed and transferred to an NMR tube with a 10 mm o.d. The mass of the sample was 0.3 g. A 0.5 g of fully deuterated pyridine, Py-d₅, (Aldrich, 99.99% atom D) was

then added to the sample and the tube was sealed under pressure of less than 2 Pa while frozen with liquid nitrogen. A mixture of Py- d_6 and CS₂ (1:1 by volume) was also used as a solvent for UF coal. The coal-solvent mixtures were stored at 303 K for at least 4 months before the NMR measurement. Styrene/divinylbenzene copolymers (St/DVB, crosslink density, 2, 4, and 8%) swollen in benzene- d_6 were also prepared.

¹H NMR. NMR measurements were carried out at 303 K using JEOL Mu-25 NMR spectrometer equipped with spin locking unit operating at a proton resonance frequency of 25 MHz. The solid-echo pulse sequence, 90°_x-τ-90°_x (90° phase shift) provided an approximation to the complete free induction decay (FID). Typical values for the pulse width, pulse spacing, repetition time and number of scans were 2.0 μs, 8.0 μs, 6 s and 32, respectively. The saturation recovery pulse sequence, 90°_x-t-90°_x was used to monitor the recovery of the magnetization with the pulse separation time, *t* and provided *T*₁. *T*_{1ρ} was measured by the so-called spin-locking pulse sequence, that is 90°_x pulse is followed by a reduced amplitude pulse, sustained for a time *t* and phase shifted 90°. The magnetization remaining at time *t* is monitored by observation of the free induction signal. Rotating frame measurements were made at radiofrequency field of 6 G. Spin diffusion was monitored by the Goldman-Shen pulse sequence.¹⁴ The original pulse sequence was modified as 90°_x-t_ρ-90°_x-t-90°_x-τ-90°_y, according to Tanaka and Nishi¹¹ in order to avoid the dead-time effect after the pulse.

RESULTS AND DISCUSSION

Transverse relaxation characteristics. The natural logarithm of the FID curves for the dried and swollen YL coal are drawn as a function of decay time in Figure 1(a). Although the solvent swelling enhance the fraction of slowly decaying components, a portion of coal hydrogen remains rigid. The observed FID was assumed to be expressed by the following equations and numerically analyzed by nonlinear least squares methods.

$$I(t) = I_G(0) \exp[-t^2/2T_{2G}^2] + I_{L1}(0) \exp[-t/T_{2L1}] + I_{L2}(0) \exp[-t/T_{2L2}] \quad (1)$$

where *I*(*t*) and *I_i*(*t*) are the observed intensity at time *t*, and that attributed to component *i*, respectively, and *T*_{2*i*} is the transverse relaxation time of the *i*th component. The fraction of hydrogen producing exponential decays, *H_m*, are listed in Table 2. *H_m* for the swollen coal samples range from 0.2 to 0.6, and *T*_{2*G*} value is similar to that for the corresponding dry coal. In contrast, when exposed to benzene- d_6 , hydrogens in St/DVB crosslinked copolymer are entirely converted to mobile hydrogens producing exponential decays, regardless of cross link densities of St/DVB as illustrating in Figure 1(b). This indicates that solvent penetrates thoroughly into St/DVB and it is likely to be deformed in a more or less uniform fashion. For the swollen coal samples, it is clear that there are domains which do not swell and are not penetrated by solvent as shown schematically in Figure 2. The phase structures of the swollen coal are separated into at least two phase, i.e., solvent rich (SR) and solvent impervious phase (SI). Brenner¹⁵ studied the changes in optical anisotropy of dry and solvent-swollen thin section samples of a bituminous coal. He found that the natural optical anisotropy was completely relaxed by immersion of the coal in pyridine. These different experimental techniques, i.e., ¹H NMR and optical microscopy, produce different conclusion on the phase structure in the solvent-swollen coal. This contradiction seems to be responsible for the difference in the spatial resolution between these experimental techniques. The optical microscopy technique can hardly detect heterogeneities whose spatial dimensions are less than the optical wavelength (400–700 nm). Therefore, the dimension of heterogeneities of the swollen coal must be smaller than ~700 nm.

Longitudinal relaxation characteristics and spin diffusion. To examine whether the spin diffusion process is active or not in the swollen coal samples, proton longitudinal relaxation was measured both in the laboratory and rotating frame. Figure 3 (a) shows the result of *T*₁ measurement for the swollen UF coal. *T*₁ is almost composed of one component while *T*_{1ρ} can be analyzed by the sum of two exponential functions as shown in Figure 3 (b). From these results, one can clearly understand the effect of spin diffusion. *T*₂ signals are composed of three components without the effect of spin diffusion while *T*_{1ρ} and *T*₁ measurements are affected strongly by spin diffusion and the number of the components decreases from *T*_{1ρ} to *T*₁. The existence of at least two time constants for a rotating frame longitudinal relaxation process i.e., *T*_{1ρ}, in a system means that spin-diffusion processes cannot effectively average the different dynamical properties of protons in different spatial domains on the relevant time scale of the specific relaxation process. On the other hand, in the time scale of *T*₁ measurements, the distinctly separated spin systems were sufficiently averaged by the spin diffusion. The scale of spatial heterogeneities of the swollen coals can be estimated by evaluating the diffusive path length, *L*, i.e., the maximum linear scale over which diffusion is effective. The approximate expression is

$$L = (2dDt)^{1/2} \quad (2)$$

where *d* is spatial dimension, i.e., the degree of freedom of diffusion, *D* is diffusion coefficient, and *t* is characteristic time for diffusion. *d* is one, two, and three corresponds to the domain shape of lamella, cylinder and sphere, respectively. It has been shown that in a regular lattice with lattice constant *a*, the spin diffusion coefficient due to dipolar spin flip is given

by⁸

$$D = 0.13 a^2 \sqrt{M_2} \quad (3)$$

where M_2 is the second moment of the NMR line shape. For both Gaussian and Lorentzian line shapes, $\sqrt{M_2} = T_2^{-1}$. For a regular lattice, D can be principally calculated from eq 3, but since the lattice constant is an ill-defined quantity for disordered materials like coals, a theoretical value can only be estimated by

$$D = 0.13 \bar{a}^2 / T_{20} \quad (4)$$

where \bar{a}^2 is the average of the square of distances between adjacent protons in the solvent impervious domain. Because of the lack of information on the molecular structure of coal, it is impossible to accurately determine \bar{a}^2 . However, \bar{a}^2 of the coal samples can be estimated semiquantitatively from the data of true densities evaluated by helium pycnometry¹⁶ and hydrogen contents of the corresponding dry coal¹³ by assuming a cubic lattice of hydrogens. In Table 2, the estimated values of D are listed. D range from 5.1×10^{-12} to 6.2×10^{-12} cm²/s and have the same order in many organic polymer systems. The observed longitudinal relaxation time corresponds to the characteristic time t . By assuming d is 3, we can estimate L as 40 nm from eq 2 for UF/Py- d_5 . Therefore the linear dimension of the structural heterogeneity in UF/Py- d_5 is certainly less than 40 nm on the basis of T_1 data. Following the same procedure for the $T_{1\rho}$ data the lower limits of the heterogeneity can be estimated to be 1 nm from the short $T_{1\rho}$. For UF/(Py- d_5 + CS₂), the limiting size in heterogeneity can be estimated as 1 - 20 nm. Recently, Xiong and Maciel¹⁷ studied the proton longitudinal relaxation characteristics in dry coal using a solid state high resolution NMR technique. They found two $T_{1\rho}$ values for the three kind of bituminous coals, which indicates the existence of structural heterogeneity in the coals on a spatial scale of at least of 5 nm. While these estimates are crude they nevertheless provide some information of the maximum diffusive path lengths probed by the NMR experiment when spin diffusion is operative. The Goldman-Shen pulse sequence was thus employed to monitor the spin diffusion process. The advantage of the Goldman-Shen experiment is that the time for spin diffusion can be arbitrarily varied, and if this time is much less than T_1 , the analysis is straightforward.

Goldman-Shen experiment. The Goldman-Shen experiment is a technique to put the separate spin systems at different spin temperatures and then sample them as a function of time so that their approach to equilibrium can be followed. The modified Goldman-Shen pulse sequence used in this experiment is shown in Figure 4. During time τ_0 , the magnetization in the SI phase has decayed to zero, while there is still sufficient magnetization in the SR phase. During the pulse interval t , spin diffusion through the magnetic dipolar coupling occurs from the SR phase to the SI one. The third 90° pulse rotates the magnetization into the transverse plane for observation and the final 90° pulse creates the solid echo. The typical decaying signals after the Goldman-Shen pulse sequence observed in IL/Py- d_5 for various values of the pulse interval t are shown in Figure 5. The recovery of the fast decaying component is observed. The recovery factor, $R(t)$, of the magnetization of SI phase can be defined as

$$R(t) = \frac{M(t) - M(t \rightarrow 0)}{M(t \rightarrow \infty) - M(t \rightarrow 0)} \quad (5)$$

In Figure 6, $R(t)$ is plotted versus $\tau^{1/2}$ for the solvent-swollen BZ and PT coal. The time evolution of $R(t)$ is analyzed by the diffusion equation solved by Cheung and Gerstain⁸ to get information on the domain size. The transfer of the magnetization in solids via dipolar spin flip interaction may be described by the spin diffusion equation

$$\frac{\partial}{\partial t} m(r, t) = D \nabla^2 m(r, t) \quad (6)$$

where $m(r, t)$ is the local magnetization density at site r and time t . The differential equation is then solved according to the appropriate boundary and initial conditions. The analytical solution of eq 6 due to Cheung and Gerstain⁸ is

$$R(t) = 1 - \varphi_x(t) \varphi_y(t) \varphi_z(t) \\ \varphi_a(t) = \exp(Dt / \bar{b}^2 a) \operatorname{erfc}(Dt / \bar{b}^2 a)^{1/2} \text{ for } a = x, y, z \quad (7)$$

where \bar{b} is the mean width of domains in SR phase. The quantity $(D / \bar{b}^2 a)^{1/2}$ was considered as an adjustable parameter. The solid curves in Figure 6 represent the nonlinear least squares fits to the data by using eq 7. The results for the analytical fits are listed in Table 2. These calculations indicate that the SR phase domain in the swollen coals have sizes ranging from several to 20 nm. The size seems to become smaller with decreasing coal

rank. The information on the morphologies of the domains is necessary to estimate the domain size adequately. However there is presently little information available on the shape of domains in the swollen coal. \bar{b} is the mean width of domains in SR phase and would corresponds to the distance between the domains in SI phase. Cody and Thiagarajan¹⁸ estimated the interdomain spacing of a pyridine-swollen bituminous coal to be approximately 15 nm by the small angle neutron scattering technique. This value agrees well \bar{b} of the swollen bituminous coals, i.e., IL, PT, and UF coals, which were evaluated under the assumptions that the domain shapes are cylinder or sphere.

ACKNOWLEDGMENT. The authors are grateful to Drs. Tadashi Yoshida and Masahide Sasaki of the Hokkaido National Industrial Research Institute for their useful advice on the NMR measurements. This work was supported in part by a "Research for the Future Project" grant from the Japan Society for the Promotion of Science (JSPS), through the 148th Committee on Coal Utilization Technology.

REFERENCES

- (1) Flory, P. J. *Principles of Polymer Chemistry*; Cornell University Press: Ithaca, NY 1953.
- (2) Barton, W. A.; Lynch, L. J.; Webster, D. S. *Fuel* **1984**, *63*, 1262.
- (3) Kwei, T. K.; Nishi, T.; Roberts, R. F. *Macromolecules* **1974**, *7*, 667.
- (4) Nishi, T.; Wang, T. T.; Kwei, T. K. *Macromolecules* **1975**, *8*, 227.
- (5) Douglass, D. C.; McBrierty, V. J. *Macromolecules* **1978**, *11*, 766.
- (6) McBrierty, V. J.; Douglass, D. C.; Kwei, T. K. *Macromolecules* **1978**, *11*, 1265.
- (7) Assink, R. A. *Macromolecules* **1978**, *11*, 1233.
- (8) Cheung, T. T. P.; Gerstain, B. C. *J. Appl. Phys.* **1981**, *52*(9), 5517.
- (9) Cheung, T. T. P. *Phys. Rev. B* **1981**, *23*, 1404.
- (10) Cheung, T. T. P. *J. Chem. Phys.* **1982**, *76*, 1248.
- (11) Tanaka, H.; Nishi, T. *Phys. Rev. B* **1986**, *33*, 32.
- (12) Bloembergen, N. *Nuclear Magnetic Relaxation*, Benjamin, New York 1961.
- (13) Vorres, K. S. *User's Handbook for the Argonne Premium Coal Sample Program*; Argonne National Laboratory, IL, 1993.
- (14) Goldman, M.; Shen, L. *Phys. Rev.* **1966**, *144*, 321.
- (15) Brenner, D. *Nature* **1983**, *306*, 772.
- (16) Huang, H.; Wang, K.; Bodily, D. M.; Hucka, V. J. *Energy Fuels* **1995**, *9*, 20.
- (17) Xiong, J.; Maciel, G. E. *Energy Fuels* **1997**, *11*, 866.
- (18) Cody, G. D.; Thiagarajan, P. *Proceedings of Adv. Energy. Thech.*, Sapporo, Japan 1998, p 31.

Table 1 Properties of Coal Samples.

Coal	(Symbol)	C	H	N	S	O ^a	ash	Swelling ratio ^d	
								[wt% daf ^b coal]	[wt% mf ^c coal]
Yallourn	(YL)	65.0	4.6	0.6	0.2	29.6	57.5	2.7	
Beulah Zap	(BZ)	72.9	4.8	1.2	0.7	20.3	32.2	2.2	2.0
Illinois#6	(IL)	77.7	5.0	1.4	2.4	13.5	8.0	2.8	
Pittsburgh	(PT)	83.2	5.3	1.6	0.9	8.8	9.3	2.4	
Upper Freeport	(UF)	85.5	4.7	1.6	0.7	7.5	13.2	1.0	1.9

^a by difference. ^b dry-ash-free. ^c moisture-free. ^d determined by the method proposed by Green et al.

Table 2 Domain Size of Solvent Rich Phase.

Sample	Solvent	S/C ^a	H _m ^b [-]	D[10 ⁻¹² cm ² /s]	\bar{b} [nm]		
					1-D	2-D	3-D
YL	py	1.75	0.56	-	-	-	-
YL	py	3.50	0.60	5.7	2	5	8
BZ	py	1.75	0.44	6.2	2	5	8
BZ	py/CS ₂	1.81	0.34	-	-	-	-
IL	py	1.75	0.55	5.6	5	12	19
PT	py	1.75	0.51	5.5	5	12	21
UF	py	1.75	0.20	-	-	-	-
UF	py/CS ₂	1.81	0.45	5.1	5	10	16
St/2%DVB	benz	4.75	1.00	-	-	-	-
St/4%DVB	benz	2.31	1.00	-	-	-	-
St/8%DVB	benz	2.31	1.00	-	-	-	-

^a Mass ratio of solvent to coal or polymer. ^b Fraction of mobile hydrogen producing exponential decays.

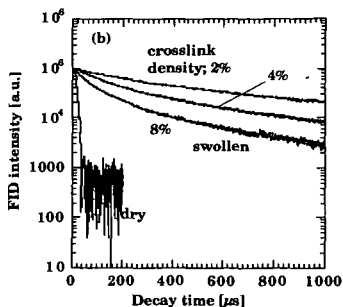
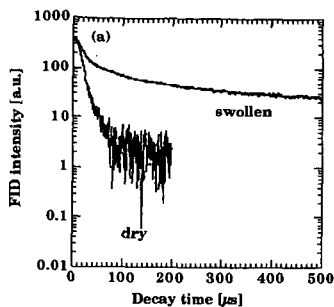


Figure 1 $^1\text{H-NMR}$ transverse relaxation signals. (a) dried and swollen YL. (pyridine- d_5 , $S/C=1.75$), (b) dried and swollen St/DVB. (benzene- d_6 , $S/C=2.31$ for 4% and 8% crosslink densities, $S/C=4.75$ for 2%)

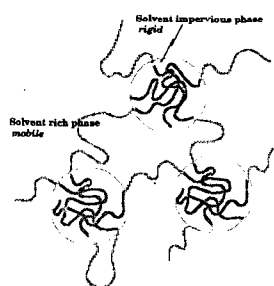


Figure 2 Conceptual model for microdomain structure of solvent-swollen coal.

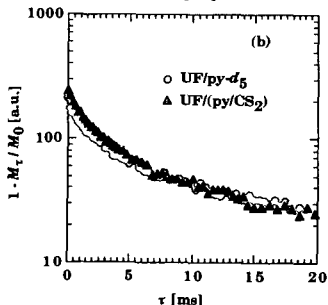
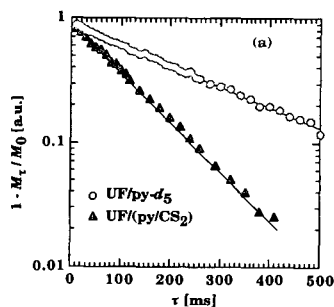


Figure 3 T_1 and $T_{1\rho}$ plots for solvent-swollen UF. (a) T_1 , (b) $T_{1\rho}$

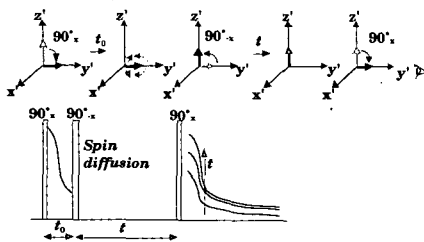


Figure 4 Schematic figure of the Goldman-Shen pulse sequence.

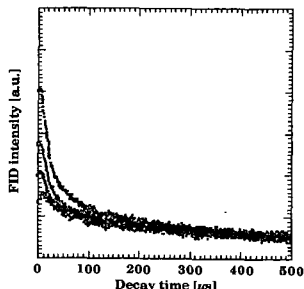


Figure 5 Solid-echo signals of swollen YL (pyridine- d_5 , $S/C=1.75$) after the modified Goldman-Shen pulse sequence for various value of t . t is equal to 1, 25, 64 and 225 ms from the bottom

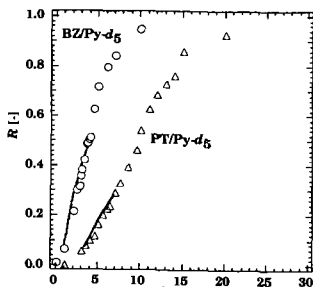


Figure 6 Recovery of proton magnetization in SI phase as a function of $t^{1/2}$ for the solvent-swollen BZ and PT coal. Solid lines represent the best fit to the data by using eq 7.

PHENOLIC RESINS AS MODELS FOR THE STRUCTURE OF COAL

Paul Painter, Pakorn Opaprakasit,
Maria Sobkowiak and Alan Scaroni
Energy Institute
Penn State University
University Park, PA 16802

KEYWORDS: Models for the macromolecular structure of coal: phenolic resins

INTRODUCTION

For many years the "standard model" for coal structure has essentially considered most coals to consist of covalently cross-linked networks with a cross-link density and sol fraction that varies systematically with rank (this model excludes arthracites and other high rank coals that are more graphitic in their structure). It has also been proposed that certain types of secondary forces, such as hydrogen bonds or charge-transfer complexes, can act as cross-links, although with respect to hydrogen bonds we disagree with this viewpoint (1). There is also an alternative model, proposed a few years ago, that places even more weight on the role of non-covalent interactions, proposing that most coals are associated structures held together by these secondary interactions acting in some undefined co-operative manner (2-6). These different views of coal structure remain to be resolved.

One of the problems with characterizing coal, particularly the nature of its network structure, is that crucial parameters such as the cross-link density can only be measured indirectly by techniques such as swelling and by recourse to a theoretical model. The most widely used model has been that originally proposed by Flory and Rehner, modified in various ways by different workers over the years to account for the specific character of coal (a high cross-link density, hence "short" chains between cross-linked points, and the presence of strong specific interactions such as hydrogen bonds, see reference 7 and citations therein). What is clearly needed is a model, highly cross-linked system where the cross-link density is known or can be measured directly, thus allowing an experimental test of the validity of various approaches. Here we will propose the use of phenolic resins and present preliminary results that demonstrates the close resemblance of the properties of these materials to coal.

RESULTS

The nature of phenolic resins

Ordinary phenol/formaldehyde resins were the first true synthetic polymers produced commercially (as opposed to chemically modified natural polymers) and were called Bakelite. Depending upon reaction conditions either novolak or resol resins can be produced, the former essentially consists of branched oligomers of phenol units, linked by methylene bridges at their ortho and meta (to the hydroxyl group) positions, as illustrated in figure 1. These materials are not cross-linked, in the sense of forming a densely interconnected network of units through covalent linkages. Resols, on the other hand, form methylol (CH_2OH) groups and their synthesis does lead to a densely cross-linked network, as illustrated in figure 2.

At least superficially one recognizes an immediate correspondence to the "standard model" structure of coal; aromatic clusters linked by methylene and some ether units. Coal, of course is far more heterogeneous, containing larger aromatic units, many of which are heterocyclic, and these are presumably linked

by a broader range of "bridge types" (e.g. ethylene). This is reflected in the infrared spectrum, as can be seen in figure 3, where the spectrum of a simple phenol formaldehyde resol is compared to that of a randomly chosen coal. The bands present in the coal spectrum are generally broader, the aromatic "ring-breathing" mode in the resol near 1600 cm^{-1} is much weaker, as is the aliphatic stretching modes near 2900 cm^{-1} . Methylene bridges between aromatic units clearly absorb very weakly (but it is well known that the absorption coefficient for CH_2 stretching increases as CH_2 units are linked to form longer aliphatic chains). However, the situation becomes much more interesting if we increase the level of complexity of the system just slightly.

Figure 4 compares the spectrum of a phenol/dihydroxynaphthalene/formaldehyde copolymer (50:50, meaning 50% phenol and 50% dihydroxynaphthalene) to that of a coal. Because of the multiplicity of linkage sites on the naphthalene ring, we produce an apparently densely cross-linked network even under conditions used to synthesize novolaks based on phenol alone. The infrared spectrum of this resin is now strikingly similar to that of the coal, the principal differences being in the aliphatic CH stretching region (the bands in the synthetic resin are much weaker) and the C-O stretching region ($1200\text{-}1300\text{ cm}^{-1}$) where the resin absorbs more strongly than coal because of its higher OH content. The spectra can be made even more similar by chemical "tinkering". For example, if we copolymerize with p-cresol instead of phenol, bands in the CH stretching region become more prominent, and so on. However, space does not permit us to explore this here. Next we will briefly describe our synthetic procedure, which we used to produce a range of copolymers, then briefly summarize the results of solvent swelling and extraction experiments, which again bear a striking resemblance to those obtained from coal.

Synthesis

Appropriate quantities of phenol, 1,5-dihydroxynaphthalene and oxalic acid were first dissolved in water. The mixture was then stirred and preheated at 65°C for 30 minutes. Formaldehyde was then added and the mixture was refluxed at 100°C for 2-3 hours. As the polymerization proceeded the solution or suspension gradually changed color. Finally, water was then removed by heating under vacuum at a temperature of 200°C . The resulting resin is a black solid copolymer, only partially soluble in solvents such as pyridine, THF and NMP.

The samples were characterized by ^{13}C nmr, FTIR and pyrolysis GC/MS. The latter results were particularly interesting because we have always been concerned that reactions leading to larger aromatic clusters could occur when this technique is applied to coal. We had no evidence for this in our studies of the synthetic resins. The details of this characterization work will be presented in a separate publication.

Extraction and Swelling Experiments

Extraction and swelling experiments were performed on the resins using the usual techniques applied to coal. In these initial experiments the solvent used was pyridine. Swelling experiments (measured on ground particles placed in a graduated cylinder) were performed on the extracted material. The results are presented in Table I.

It can be seen that an ordinary resol has 32% pyridine soluble material and swells to approximately twice its original dimensions in pyridine, very similar to results obtained with coals like Illinois #6. Copolymers synthesized with dihydroxynaphthalene units behave similarly at low concentrations of this co-

Substituting p-cresol, which can only polymerize in a linear, non-branched fashion, for phenol, restores much of the extractability.

CONCLUSIONS AND RAMIFICATIONS

We have synthesized resins that mimic the spectroscopic, swelling and solubility characteristics of coal. The crucial point is that we start with a knowledge of the structure of these materials and whether or not they are covalently cross-linked. We are comparing the behavior of these materials in various solvents as a means to determine the role that association through secondary forces plays in swelling and solubility. Although the cross-link density of these resols is not known (but could possibly be estimated by the pattern of linkages revealed by the aromatic CH out-of-plane bending modes in the IR spectrum), it is a relatively easy task to chemically cross-link initially oligomeric novolaks with labeled compound and measure this parameter directly. We believe this approach will prove valuable in sorting out various models of coal structure and the role of secondary interactions such as hydrogen bonds.

ACKNOWLEDGMENT

The authors gratefully acknowledge the support of the Office of Chemical Sciences, U.S. Department of Energy, under grant No. DE-F602-86ER1353.

REFERENCES

1. Painter, P.C. *Energy and Fuels*, 1996, **10**, 1273.
2. Nishioka, M., Gebhard, L.A. and Silbernagel, B.G. *Fuel*, 1991, **70**, 341.
3. Nishioka, M. *Fuel*, 1991, **70**, 1413.
4. Nishioka, M. *Fuel*, 1992, **71**, 941.
5. Nishioka, M. *Energy and Fuels*, 1991, **5**, 487.
6. Takanohashi, T., Iino, M. and Nishioka, M. *Energy and Fuels*, 1995, **9**, 788.
7. Veytsman, B. and Painter, P.C. *Energy and Fuels*, 1997, **11**, 1250.

Table 1

Sample	Extraction Yield in Pyridine %	Swelling Ratio
Resol (phenol formaldehyde)	32%	2.06
PDHNF20	42%	2.01
PDHNF30	12%	
PDHNF40	6%	
PDHNF50	6%	1.74
PCDHNF50	35%	
PDHNFx	= Phenol-co-dihydroxynaphthalene/formaldehyde copolymer with x wt% of dihydroxynaphthalene.	
PCDHNFx	= p-cresol-co-dihydroxynaphthalene/formaldehyde copolymer	

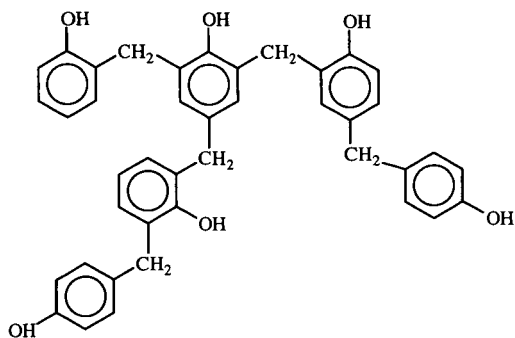


Figure 1. Typical oligomeric structure found in a novolac resin.

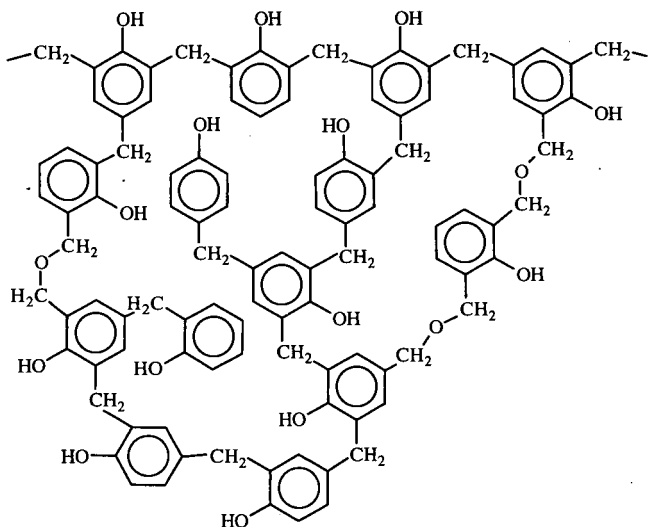


Figure 2. Schematic representation of part of the structure of a cured phenolic resin.

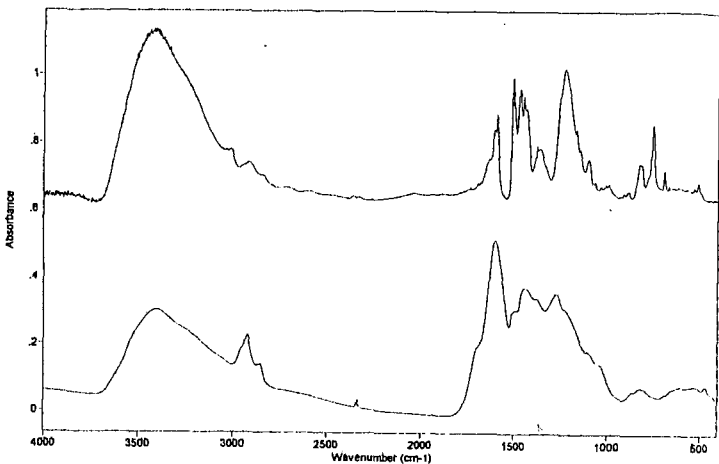


Figure 3. Comparison of the infrared spectrum of a cured resol (phenol-formaldehyde to a coal (PSOC 1423 P, 70% C)

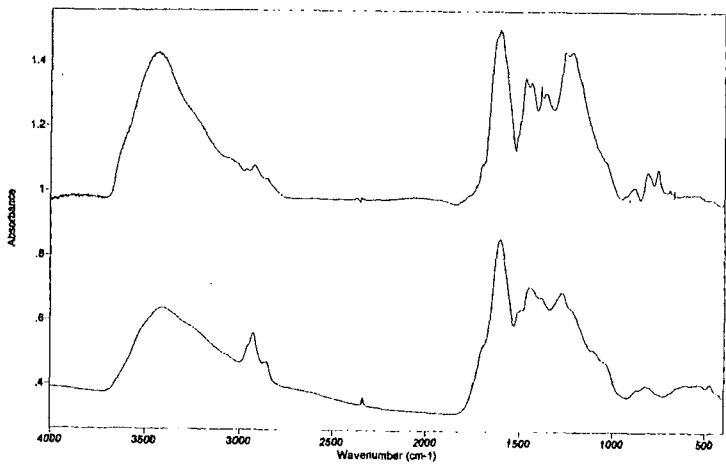


Figure 4. Comparison of the infrared spectrum of a cured phenol-co-dihydroxynaphthalene (50%) formaldehyde copolymer to that of a coal (PSOC 1423 P, 70% C)

EFFECT OF VARIOUS ADDITIVES ON SOLVENT EXTRACTION OF COALS

Masashi Iino¹, Toshimasa Takanohashi², E. Sultan Vayisoglu Giray¹, Chong Chen¹,
Yoshihiro Masui¹, and Kazuhiro Takahashi¹

¹Institute for Chemical Reaction Science, Tohoku University,
Katahira, Aoba-ku, Sendai 980-8577, JAPAN

²Energy Resources Department, National Institute for Resources and Environment,
Onokawa, Tsukuba 305-8569, JAPAN

KEYWORDS: Coal extraction, additive, carbon disulfide / *N*-methyl-2-pyrrolidinone mixed solvent

INTRODUCTION

The extraction of bituminous coals with carbon disulfide / *N*-methyl-2-pyrrolidinone (CS₂ / NMP) mixed solvent (1:1 by volume) was found to give very high extraction yields at room temperature (1). We have also found that the addition of a small amount of various additives such as tetracyanoethylene (TCNE) and *p*-Phenylenediamine(*p*-PDA) to the mixed solvent increases the extraction yields greatly(2,3). For example, the yield of the room temperature extraction of Upper Freeport coal with the 1:1 CS₂ / NMP mixed solvent increases from 59 wt% (daf) to 85 wt% (daf) by adding only 5% (based on coal) of TCNE to the mixed solvent(2). Recently inorganic salts of chloride and fluoride are found to be also effective for the increase of the extraction yields.

We have also found (4) that when the extracts obtained with the CS₂/NMP mixed solvent were fractionated with pyridine to yield pyridine-insoluble (PI) and -soluble (PS) fractions, part of PI became insoluble in the mixed solvent, though it is a part of the extracts with the mixed solvent. By the addition of a small amount of the additives such as TCNE, tetracyanoquinodimethane (TCNQ) or *p*-phenylenediamine to the mixed solvent, PI became soluble in the mixed solvent.

While, swelling and viscoelasticity behaviors of coal show that coal has a kind of macromolecular network structure. The changes of reactivity and product selectivity of coal by heat or solvent treatment were often explained by the changes of this network structure. But the nature of the macromolecular network structure are still unknown. Although covalently connected crosslinking structures are often assumed, the evidences for them are not enough. Recent works, including our results, suggest that for some bituminous coals, large associates of coal molecules i.e., non-covalent (physical) network are a better network model than the covalent one. Coal extracts and coal derived liquids are known to readily associate between themselves to form complex associates (5-8).

Solubility limit of coals, i.e., how high extraction yields can be obtained without the breaking of covalent bonds is one of the key points to clarify a kind of network bonds, i.e., covalent or non-covalent (physical) networks. If coal consists of highly developed covalent networks and low molecular weight substances occluded in them, coal extractability is low, as observed in the extractions with conventional solvents such as pyridine. However, 85wt% of the extraction yield obtained for CS₂ / NMP / TCNE solvent system described above suggests that Upper Freeport coal has little covalent networks.

In this presentation the effect of various additives on extraction yield of coal, and solubility of the extract component (PI) in the mixed solvent was reviewed including recent results. Mechanisms for the enhancement of the extraction yield and the solubility by the additives are discussed.

EXPERIMENTAL

Extraction of coals with CS₂ / NMP mixed solvent

The coals used in this study are shown in Table I. A coal was extracted with CS₂ / NMP mixed solvent (1:1, volume ratio) under ultrasonic irradiation repeatedly at room temperature (1) with or without an additive. The extract obtained was fractionated with acetone and pyridine, respectively, to give acetone-soluble(AS), pyridine-soluble and acetone-insoluble(AI/PS), and pyridine-insoluble(PI) fractions. Solubility of PI in the mixed solvent was examined at room temperature under ultrasonic irradiation with or without an additive.

RESULTS AND DISCUSSION

Effect of Additives on Extraction Yields of Coals

Tables 2 - 4 show the yields of the extractions of Upper Freeport coal with the CS₂/NMP mixed solvent with electron acceptors, donors (aromatic amines), and halogenide salts, respectively. Table 2 shows the effect of an electron acceptors, together with their electron affinity, which is a measure of the electron acceptability of electron acceptor. Table 2 shows that only TCNE and TCNQ gave high extraction yields as expected from their high electron affinities. However, other electron acceptors used here do not show the extraction yield enhancements. Table 3 also shows that the effectiveness of electron donors is not an order of their electron donatability, since *N,N,N',N'*-tetramethyl-*p*-phenylenediamine (TMPDA), which is the strongest electron donor, gave much lower yield than other donors. The results for halogenide salts in Table 4 indicate that a kind of halogenide anions affects the extraction yields, i.e., the yields increased in the order; F>Cl>Br>I, and little change between Li and tetrabutylammonium cations.

Table 5 shows the effect of the addition of tetrabutylammonium fluoride (TBAF) on the extraction of various coals. Upper Freeport, Lower Kittanning, and Stigler coals increased their extraction yields with the CS₂ / NMP mixed solvent by the addition of TBAF, but for Pittsburgh No.8, Illinois No.6 coals the yields did not increase. For the addition of TCNE the same tendency of the extraction yields were obtained for the five coals above (2).

Effect of Additives on Fraction Distribution of Extracts

Table 6 shows the fraction distribution of the extracts obtained from the extraction of Upper Freeport coal with TCNE, *p*-PDA, and TBAF. Table 6 indicates that the increase in the extraction yields is mainly due to the increase of the heaviest extract fraction, i.e., P1, and little increase in the lighter fractions of AS and Al/PS.

Effect of Additives on Solubility of Extract Fraction

Tables 7 and 8 show the effect of electron acceptors and donors (aromatic amines) on the solubility of P1 in the CS₂ / NMP mixed solvent, respectively. Table 7 shows a similar tendency as the effect of electron acceptors on the extraction yields (Table 2), i.e., only TCNE and TCNQ are effective for the increase in the solubility of P1. Table 8 shows that aniline and *p*-PDA increased the solubility of P1 greatly, and especially *p*-PDA is as effective as TCNE and 25mg (0.23mmol)/g-P1 increased about 40% of the solubility.

Mechanisms for the enhancement of the extraction yield and the solubility by the additives

The solubility increase of P1 by TCNE addition, and also the increase in the extraction yield are considered to be caused by the breaking of noncovalent bonds in aggregates among coal molecules(8), since the effect of TCNE addition is reversible, i.e., P1', which is considered to be free of TCNE by washing the TCNE-solubilized P1 by pyridine, is again partly insoluble in the mixed solvent, and it becomes almost completely soluble by the re-addition of TCNE. From similar behaviors of the other additives toward a kind of coals and fraction distribution of the extracts as TCNE they also solubilize coal by the same mechanism as TCNE.

The 1:1 CS₂-NMP mixed solvent can break the weak non-covalent bonds which are not broken conventional solvents such as pyridine. The additive such as TCNE and *p*-PDA in the mixed solvent, which has strong interaction with coal molecules, can break even the strong noncovalent bonds. A kind of interactions between the additives and coal molecules are not clear, but the results here suggest that charge-transfer (donor-acceptor) interaction may not be a main interaction.

The additives such as TCNE, *p*-PDA, and TBAF is very efficient for the extraction yield enhancement of Upper Freeport coal. For example, the addition of TCNE more than 0.05g to 1g of the coal reached an almost constant extraction yield of about 85 wt% (daf). Using the structural parameters of fa and degree of aromatic ring condensation for Upper Freeport coal reported by Solum et al.(9), 0.05g of TCNE per 1g of coal is calculated to correspond to 1 molecule of TCNE per about 8 aromatic clusters of the coal. The reasons why these additives are so effective, and the effectiveness is depend on a kind of coals are not clear, though all the coals which increase their solubility remarkably by the additives contain much of the heaviest extract fraction, P1.

These results obtained strongly suggest that at least some bituminous coals, which gave very high

extraction yields with the CS₂/NMP/additive solvent, have chemical structure consisting of complex mixture of the aggregates among coal molecules, and having no giant covalently bound cross-linked network.

CONCLUSIONS

The effects of various additives on the extraction yield of coals and the solubility of extract fraction were investigated. The additives such as TCNE, *p*-PDA, and lithium and ammonium salts of fulfurate and chloride are found to be very effective for the increase in the extraction yield and the solubility of the extract fraction. A mechanism that noncovalent bonds in the aggregates among coal molecules are broken by the additives is proposed.

ACKNOWLEDGMENT

This work was supported by "Research for the Future" project of Japan Society for the Promotion of Science.

REFERENCES

1. Iino, M., Takanohashi, T., Osuga, H. and Toda, K., *Fuel*, **1988**, *67*, 1639-1647.
2. Liu, H., Ishizuka, T., Takanohashi, T. and Iino, M., *Energy Fuels*, **1993**, *7*, 1108-1111.
3. Ishizuka, T., Takanohashi, T., Ito, O. and Iino, M. *Fuel*, **1993**, *72*, 579-580.
4. Sanokawa, Y., Takanohashi, T. and Iino, M., *Fuel*, **1990**, *69*, 1577-1578.
5. Sternberg, H. W., Raymond, R. and Schweighardt, F. K., *Science*, **1975**, *188*, 49-51.
6. Stenberg, V. I., Baltisberger, R. J., Patel, K. M. et al., *Coal Science* (ed Gorbarty, M. L., Larsen, J. W., Wender, I.), Academic Press, New York, **1983**, pp 125-171.
7. Nakamura, K., Takanohashi, T., Iino, M. et al., *Energy Fuels*, **1995**, *9*, 1003-1010.
8. Iino, M., Liu, H., Hosaka, N., Kurose, H. and Takanohashi, T., *Prepr. Pap. Am. Chem. Soc., Div. Fuel Chem.* **1997**, *42*(1), 248-252.
9. Solum, M. S., Pugmire, R. J., Grant, D. M., *Energy Fuels*, **1989**, *3*, 187-192.

Table 1. Analysis of coals

Coal	Ultimate analysis(wt%,daf)				Ash(wt%,db)
	C	H	N	O+S ^a	
Sewell'B'	88.4	5.3	1.4	4.9	4.6
Upper Freeport	86.2	5.1	1.9	6.8	13.1
Lower Kittanning	84.0	5.6	1.7	8.7	9.0
Lewiston Stockton	82.9	5.4	2.0	9.7	19.6
Pittsburgh No.8	82.6	5.5	2.1	9.8	8.7
Stigler	77.8	4.8	1.5	15.9	11.7
Illinois No.6	76.9	5.5	1.9	15.7	15.0

^a By difference

Table 2. Effect of the addition of electron acceptors on extraction yields^a of Upper Freeport coal together with their electron affinity

additive ^b	Extraction yield (wt%)	Electron affinity (eV)
None	64.6	-
TCNE ^c	85.0	2.2
TCNQ ^d	80.0	1.7
DDQ ^e	49.8	1.95
1,2,4,5-Tetracyanobenzene	44.4	0.4
<i>p</i> -Benzoquinone	39.3	0.77
2,6-Dichloro- <i>p</i> -benzoquinone	49.7	1.2
<i>p</i> -Chloranil	45.5	1.37

^a CS₂/NMP mixed solvent (1:1 by volume), room temperature

^b 0.2mmol/g-PI of an election acceptor, ^c Tetracyanoethylene

^d 7,7,8,8-Tetracyanoquinodimethane, ^e 2,3-Dichloro-5,6-dicyano-*p*-benzoquinone

Table 3. Effect of the addition of electron donors (aromatic amines) on extraction yields^a of Upper Freeport coal together with their ionization potential

Additive ^b	Extraction yield (wt%,daf)	Ionization potential (eV)
None	51.4	
aniline	72.3	7.7
<i>p</i> -PDA ^c	81.3	6.87
TMPDA ^d	61.4	6.5
melamine	61.8	-

^a CS₂/NMP mixed solvent (1:1 by volume), room temperature

^b 25 mg/g-coal of an electron donor

^c *p*-phenylenediamine, ^d N,N,N',N'-tetramethyl-*p*-phenylenediamine

Table 4. Effect of the addition of halogenide salts on extraction yields^a of Upper Freeport coal

Additive (mmol/g-coal)	Extraction yield (wt%,daf)	Additive (mmol/g-coal)	Extraction yield (wt%,daf)
None	56.4, 59.8	(<i>n</i> -butyl) ₄ NH ₄ F (0.25)	83.9
LiCl (0.24)	81.7	(<i>n</i> -butyl) ₄ NH ₄ Cl (0.25)	78.8
LiBr (1.0)	68.7	(<i>n</i> -butyl) ₄ NH ₄ Br (0.25)	61.8
LiI (1.9)	60.9	(<i>n</i> -butyl) ₄ NH ₄ I (0.25)	59.3

^a CS₂/NMP mixed solvent (1:1 by volume), room temperature

Table 5. Effect of the addition of TBAF on the extraction yields^a of various coals and fraction distributions of the extracts

Coal	TBAF	Extraction yield (wt%,daf)	Fraction distribution (wt%,daf)		
			AS	PS	PI
Upper Freeport	None	60.1	8.2	25.0	26.9
	0.25mmol/g-coal	82.4	11.5	12.7	58.2
Lower Kittanning	None	38.7	6.3	27.1	5.3
	0.25mmol/g-coal	63.7	9.4	17.9	36.4
Pittsburgh No.8	None	43.5	12.3	30.0	1.2
	0.25mmol/g-coal	39.9	11.8	23.4	4.7
Stigler	None	21.2	6.1	14.5	0.6
	0.25mmol/g-coal	62.4	6.4	17.2	38.8
Illinois No.6	None	27.9	7.8	19.1	1.0
	0.25mmol/g-coal	27.4	10.0	16.8	0.6

^a CS₂/NMP mixed solvent (1:1 by volume), room temperature

Table 6. Fraction distribution of the extracts obtained from the extraction^a of Upper Freeport coal with the additives

Additive	extraction yield (wt%,daf)	fraction distribution of the extract (wt%,daf)		
		AS	AI/PS	PI
none	60.1	8.2	25.0	26.9
TCNE	85.0	10.5	28.5	47.0
<i>p</i> -PDA	81.3	9.8	23.1	48.4
LiCl	83.6	10.2	16.1	57.3
TBAF	82.4	11.5	12.7	58.2

^a CS₂/NMP mixed solvent(1:1 by volume), room temperature

Table 7. Effect of the addition of electron acceptors on solubility^a of pyridine-insoluble extract (PI)

Additive ^b	Solubility of PI (wt%)		Electron affinity (eV)
	PI from Upper Freeport Coal	PI from Zao Zhuang Coal	
None	66.4	51.0	-
TCNE ^c	99.5	99.5	2.2
TCNQ ^d	94.3	81.0	1.7
DDQ ^e	88.8	53.8	1.95
1,2,4,5-Tetracyanobenzene	71.2	47.7	0.4
<i>p</i> -Benzoquinone	76.1	44.1	0.77
2,6-Dichloro- <i>p</i> -benzoquinone	67.4	37.0	1.2
<i>p</i> -Chloranil	51.8	34.8	1.37

^a CS₂/NMP mixed solvent (1:1 by volume), room temperature

^b 0.2mmol/g-PI of an electron acceptor, ^c Tetracyanoethylene

^d 7,7,8,8-Tetracyanoquinodimethane, ^e 2,3-Dichloro-5,6-dicyano-*p*-benzoquinone

Figure 8. Effect of the addition of electron donors (aromatic amine) on solubility^a of pyridine-insoluble extract fraction (PI) from Upper Freeport

Additive ^b	Solubility of PI (wt%)	Ionization potential (eV)
None	55.1	-
aniline	85.4	7.7
<i>o</i> -PDA	91.8	7.2
<i>m</i> -PDA	85.1	7.1
<i>p</i> -PDA	96.5	6.9

^a In CS₂/NMP mixed solvent(1:1 by volume), room temperature

^b 25mg/g-PI of an additive

ROLE OF SOLVENT IN THE INTERACTION OF TCNE/TCNQ WITH COAL

Chong Chen and Masashi Iino
 Institute for Chemical Reaction Science
 Tohoku University
 Katahira 2-1-1, Aoba-ku, Sendai 980-8577, Japan

Keywords: additive, coal, solubility

INTRODUCTION

After N-methyl-2-pyrrolidinone(NMP)-CS₂(1:1, v/v) mixed solvent was found having the magic ability to dissolve coal up to about 60wt% based on *daf* coal¹, the seeking for higher solubility of coal has never stopped. Enhancement of the coal solubility by adding additives is our way. Up till now, more than 10 additives including electron acceptors and donors were examined²⁻⁵. Electron acceptors, Tetracyanoethylene(TCNE) and 7,7,8,8-Tetracyanoquinodimethane(TCNQ) were found to be two powerful additives. However, the mechanism is still not clear. Previous studies on the mechanism have been concentrated on the charge-transfer complex formation between additives and coal leaving the role of the solvents out of focus^{2,9-10}. However, the attempt to correlate the solubility of coal and the electron acceptor-ability was not successful. Therefore, other mechanism must be involved. In this work, solvent was found strongly related to the mechanism of TCNE/TCNQ to increase the coal solubility.

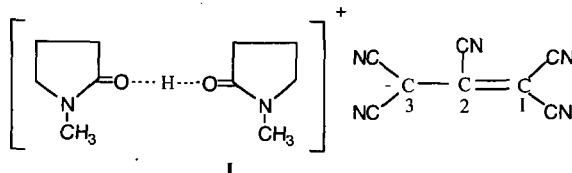
The conclusion of charge-transfer complex formation between coal and TCNE/TCNQ was drawn from the IR shift of ν_{CN} in TCNE/TCNQ when they were mixed with coal in solvent. We have reported that the coal containing TCNE deposited from NMP-CS₂(1:1, v/v) mixed solvents had a pair of IR band at 2200cm⁻¹ and 1500cm⁻¹. Initially, the band at 2200cm⁻¹ had been proposed arising from charge-transfer complex between TCNE and coal⁶. However, further investigation found that the two IR bands arisen from the reaction product of TCNE and NMP, i.e., NMP 1,1,2,3,3-pentacyanopropene salt(NPCNP). TCNE does not exist as a neutral molecule in NMP, instead, an anion derivative of TCNE was formed, which may be the key component to enhance the coal solubility. Addition of NPCNP was found also effective for the coal solubility increase.

In the case of TCNQ, the interaction of TCNQ with coal aromatics seems to be related to the solvent used. TCNQ radical anion generated in NMP may be an intermediate of TCNQ interaction with coal aromatics. The extent of TCNQ interaction with coal aromatics depends on the structure of aromatics.

EXPERIMENTAL

UV spectral properties of TCNE/TCNQ in various solvents were measured on HITACHI U2000 UV spectrometer with 1 cm quartz cell. FTIR spectra were recorded on JASCO FT/IR-8300 spectrometer using KRS-5 or KCl cell(thickness of 0.1mm), 16 scans at resolution of 4cm⁻¹. NMR measurement was carried out on JEOL JNM-LA400 spectrometer. CDCl₃ was used as solvent. All the solvents used for spectral analysis are spectrophotometric grade. "Anhydrous" NMP was dehydrated by 4 Å molecular sieves overnight.

The procedure of the reaction of TCNE with NMP in the presence of water referred to that of TCNE reaction with pyridine in the presence of water⁸, but it was carried out at room temperature. 30mL acetone containing 6.3g TCNE was added into 100ml NMP containing 10% water under N₂ protection. After the reaction, acetone and NMP were removed via a rotary evaporator at 40°C and large volume of diethyl ether was decanted into reactor. A yellow solid was obtained(yield, 58wt%, based on raw product). Recrystallization of a portion of the solid from diethyl ether gave a yellow crystal of I, mp 51-52°C: UV-visible(NMP) λ_{max} nm(log ϵ) 400(4.41), 418(4.40); FTIR(thin film, cm⁻¹) 1519(ν_{C-C}), 2203($\nu_{C\equiv N}$); (liquid film) 2199(in NMP, $\nu_{C\equiv N}$); ¹H-NMR(CDCl₃) δ 3.70, 3.06, 2.77, 2.24ppm, a broad and weak peak at 7.5-11ppm downfield shift as the increase of concentration of I; ¹³C-NMR(CDCl₃) δ 178.32, 135.60, 116.70, 114.06, 113.78, 57.91, 51.95, 31.26, 30.46, 17.38ppm. Anal. Calcd for NMP-1,1,2,3,3-Pentacyanopropene salt(I, C₁₈H₂₀N₇O₂): C, 59.02%; H, 5.29%; N, 26.75%; O, 8.78%. Found: C, 59.18%; H, 5.46%; N, 26.78%; O, 8.74%.



RESULTS AND DISCUSSION

Spectra properties of TCNE-NMP system.

The shift of stretching frequency of $C\equiv N(\nu_{CN})$ of TCNE in some solvents indicates that TCNE may react or interact with solvents (Table 1). In acetone and THF, almost no shift was observed. The small shift in toluene is attributed to the formation of charge-transfer complex of TCNE with toluene. However, the large shift of ν_{CN} in NMP indicates that TCNE does not exist as a neutral molecule in this solvent. Instead, a new substance may be generated by the reaction of TCNE with NMP. In dehydrated NMP, ν_{CN} shifts to 2338cm^{-1} arose from complex of TCNE-NMP, while in commercial NMP (used for extraction) containing very small amount of water (estimated from the hydroxyl band), the ν_{CN} band appears at 2199cm^{-1} , which indicates the presence of PCNP anion.

Figure 1 shows the change of UV spectra of TCNE in NMP of different water content. In dehydrated NMP, PCNP anion absorptions at 400 and 418nm are very weak. However, they are increasing but the peak of TCNE-NMP complex at 298nm decreasing as the increase of water content in NMP, indicating that PCNP anion is generated from the reaction of TCNE with NMP in the presence of water.

The reaction of TCNE with pyridine⁸ or pyridone¹¹⁻¹² to generate PCNP anion was known 30 years ago, but the reaction of TCNE with NMP to generate the same anion is found first time.

Although this reaction needs water, commercial grade NMP used for extraction usually contains small amount of water. Based on our experimental procedure, 1 gram coal or PI was added 0.2mmol TCNE in 60 mL NMP-CS, mixed solvent (1:1, v/v), 0.012wt% water in NMP is enough for 0.2mmol TCNE to generate PCNP anion. Although we have not measured the water content of the NMP, it is quite possible that 97% commercial grade NMP used for extraction contains enough water for the reaction. Moreover, NMP is very easy to absorb water. It is very difficult to remove all the water from NMP. Even dehydrated NMP was used, PCNP anion band at 400 and 418nm is still observable (Figure 1) in TCNE-NMP system. This is probably due to incomplete dehydration by molecular sieves or re-absorption of water during the operation. It was also found that in commercial NMP, ν_{CN} of TCNE in NMP always shifts to 2199cm^{-1} . These results demonstrate that TCNE exists as PCNP anion in NMP but not neutral TCNE molecule.

Effect of 1,1,2,3,3-pentacyanopropene(PCNP) anion to increase the solubility of PI

Based on the spectral study, TCNE does not exist as a neutral molecule in NMP as well as in the NMP-CS, mixed solvent. Instead, NPCNP is formed. The solubility of PI and its parent coal(UF) in the NMP-CS, mixed solvent was examined by adding small amount of NPCNP. Figure 2 shows that the addition of only 0.04mmol/g-PI NPCNP is enough to increase the solubility of PI from 54% to 96%; more NPCNP, 0.2mmole/g-PI, results in 99.9% solubilization of PI. The addition of 0.2mmol/g-coal NPCNP increases the UF coal solubility from 64.6% to 71.5%, which is closed to the increment by adding the same amount of TCNE³. Another PCNP anion contained compound, Pyridinium 1,1,2,3,3-pentacyanopropenide, which was synthesized from pyridine and TCNE in the presence of water⁸, was also found effective to enhance the solubility of PI. The two experiments indicate that PCNP anion is the key component to enhance the solubility of coal.

The mechanism of PCNP anion to enhance coal solubility is believed to be attributed to breaking hydrogen bonding. NMR study confirms the possibility of this anion being able to break the hydrogen bonding formed between pyridine and phenol. The details will be reported in a paper submitted to Energy Fuels.

Spectral property of TCNQ in various solvents

The UV-visible spectra property of TCNQ depends on solvent, as shown in Figure 3. It is quite different in NMP and pyridine than in THF and chloroform. The peaks around 800nm, i.e., 752, 771 and 833, 854nm, were assigned to the TCNQ radical anion¹³⁻¹⁴. Figure 3 illustrates that TCNQ generates TCNQ radical anion in NMP and pyridine but not in THF and chloroform.

In the room temperature, the addition of aromatics into the NMP solution containing TCNQ results in the change of its UV-visible spectrum. As shown in the Figure 4, the absorption of TCNQ radical anion around 800nm disappeared as accompanied by appearing a new absorption at 490nm, which may be arisen from the complex formed between TCNQ and aromatics. However, when the aromatics were added into the mixture of TCNQ and chloroform, chlorobenzene or THF, no such change occurs. The spectra are just a summation of the TCNQ-solvent and aromatics. Accordingly, we can not deny the possibility that TCNQ reacts with aromatics by the TCNQ radical anion as an intermediate.

The extent of TCNQ reaction with the aromatics depends on the structure of aromatics. Phenanthrene reacts with TCNQ radical anion quickly, the peaks around 800nm disappeared in several minutes after it was added into the mixture of TCNQ-NMP and a new peak at 490nm appeared. However, anthracene, the isomer of phenanthrene, is hard to react with TCNQ radical at room temperature. The spectrum has no change even after 180min. The larger size

aromatics, pyrene, can react with the TCNQ radical anion, but it takes longer time than phenanthrene needed. The different distribution of π electrons on the aromatic ring may cause the difference. Coal from different source and rank contains aromatics of different ring size and structure, which may cause the selective effect of TCNQ for certain coal, e.g., TCNQ is effective for some coals but not effective for others.

When pyridine insoluble fraction(PI) from Upper Freeport coal extracts(extraction with CS₂-NMP mixed solvent, 1:1 by volume) was used instead of pure aromatics to repeat the experiment mentioned above, similar spectra changes were observed. As the reaction time increases, the absorption of TCNQ radical anion around 800nm decreased but the absorption at 490nm increased(see Figure 5). Based on the results of pure aromatics, aromatics in PI reacts with TCNQ radical anion to generate a new complex(around 490nm) is concluded.

CONCLUSIONS

The importance of solvent was noted in examination the mechanism of TCNE/TCNQ to enhance the coal solubility. TCNE was found not to be existed as a neutral molecule in NMP. Instead, it reacts with NMP in the presence moisture to generate 1,1,2,3,3-pentacyanopropene (PCNP) anion, which is considered a key component to enhance the coal solubility by breaking coal-coal interaction, e.g., hydrogen bonding. TCNQ generates TCNQ radical anion in NMP and pyridine, which is an intermediate of TCNQ interaction with coal aromatics.

ACKNOWLEDGMENTS

This work was supported by "Research for the Future" project of Japan Society for the Promotion of Science(JSPS). We are greatly grateful to Prof. John Larsen of Lehigh University for his valuable discussion and comments on this work.

REFERENCES

1. Iino, M.; Takanohashi, T.; Ohsuga, H.; Toda, K. *Fuel* **1988**, *67*, 1639-1647
2. Iino, M.; Kurose, H.; Giray, E. S.; Takanohashi, T. *Prepr.Pap. Am. Chem. Soc., Div. Fuel Chem.* **1998**, *43(3)*, 712-716
3. Liu, H-T; Ishizuka, T.; Takanohashi, T.; Iino, M. *Energy Fuels* **1993**, *7*, 1108
4. Ishizuka, T.; Takanohashi, T.; Ito, O.; Iino, M. *Fuel* **1993**, *72*, 579-580
5. Sanokawa, Y.; Takanohashi, T.; Iino, M. *Fuel* **1990**, *69*, 1577-1578
6. Schwager, I.; Kwan, J. T.; Miller, J. G.; and Yen, T. F. *Prepr.Pap. Am. Chem. Soc., Div. Fuel Chem.* **1978**, *23*, 284-289
7. Thompson, R. L.; Rothenberger, K. S.; Retcofsky, H. L. *Energy Fuels* **1997**, *11*, 739-746
8. Middleton, W. J.; Little, E. L.; Coffman, D.D.; Engelhardt, V. A. *J. Am. Chem. Soc.*, **1958**, *80*, 2795-2806
9. Flowers, R.A.; Gebhand, L.; Larsen, J. W.; Sananda, Y; Sasaki, M.; Silbernagel, B. *Energy Fuels* **1994**, *8*, 1524-1525
10. Iino, M.; Liu, H-T; Hosaka, N.; Kurose, H.; Takanohashi, T. *Prepr. Pap. Am. Chem. Soc. Div. Fuel Chem.* **1997**, *42*, 248-252
11. Thyagarajan, B. S.; Rajagopalan, K.; Gopalakrishnan, P. V. *Chem. Ind.* **1996**, *5*, 1887-1888
12. Thyagarajan, B. S.; Rajagopalan, K.; Gopalakrishnan, P. V. *J. Chem. Soc.(B)* **1968**, 300-303
13. Melby, L. R.; Harder, R. J.; Hertler, W. R.; Mahler, W.; Bensin, R. E. and Mochel, W. E., *J. Am. Chem. Soc.*, **1962**, *84*, 3374.
14. Shin, D-M.; Choi, K-H. and Park, J. S., et al., *Thin Solid Films*, **1996**, *523*, 284.

Table I. List of TCNE in various solvent

solvent	$\nu_{CN}(cm^{-1})$
blank	2260
acetone	2257
THF	2257
toluene	2252
NMP ^a	2338
NMP ^b	2199

^adehydrated by 4 Å molecular sieves;
^bcommercial one(NMP content 97%)
 containing small amount water(estimated from the weak hydroxyl band in the spectrum).

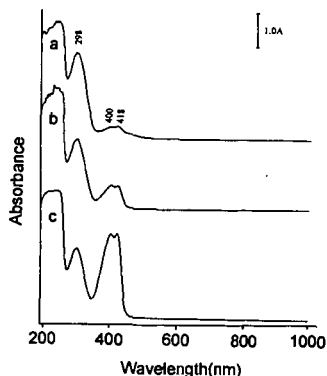


Fig. 1. UV-visible spectra of TCNE in NMP containing water(mg/mL). a, 0; b, 15; c, 50

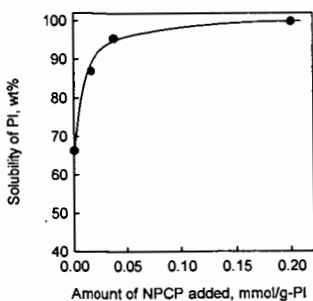


Fig. 2. Increase of the solubility of PI(pyridine insoluble fraction) from Upper Freeport coal in the NMP-CS₂ mixed solvent by adding NPCNP

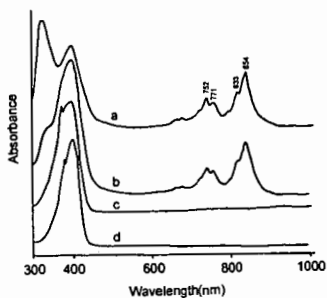


Fig. 3. UV-visible spectra of TCNQ in various solvents.

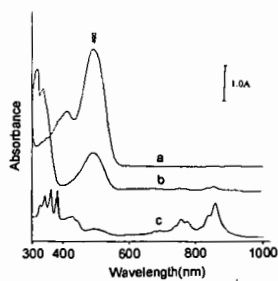


Fig. 4. UV-visible spectra of aromatics(1×10^{-3} mole L⁻¹) in 5×10^{-3} mole L⁻¹ TCNQ NMP solution.
a, phenanthrene(reaction for 3 min); b, pyrene(40 min); c, anthracene(180 min)

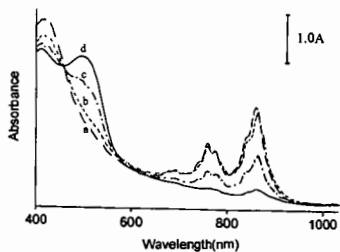


Fig. 5. UV-visible spectra of PI-TCNQ-NMP-CS₂(1:1, v/v) system.
a, 0 min; b, 30 min; c, 60 min; d, 90 min

Molecular Size and Structure in Pyridine Extracts of Upper Freeport Coal as Separated by M41S Sieving

Jerry E. Hunt, Randall E. Winans, Mike Ahrens, and Langqiu Xu
Chemistry Division
Argonne National Laboratory
9700 South Cass Ave.
Argonne, IL 60439

KEYWORDS: coal, extracts, sieving, separation, mass spectrometry

INTRODUCTION

The determination of the structure of coal has long been of interest due to its crucial importance in research on reactivity and processing. However, the chemically and physically heterogeneous nature of coals makes determination of the chemical nature of even the building blocks complicated, since the molecular structure and molecular weight distribution are not dependent on a single molecule or repeat unit as in technical polymers or biopolymers, but on a complex mixture of molecules and potential connections between them which may vary among coals.

Coal extracts have long been used to obtain coal material in solution form that can readily be characterized. However, what part of the total coal structure these extracts represent is not completely known. Pyridine has been a particularly good solvent for coal; for example, the extractability of Upper Freeport has been shown to be as high 30%. Although pyridine extracts of coal have been referred to as solutions, there is good evidence that they are not truly solvated, but are dispersions which are polydisperse in particle size.¹ The particle sizes may span the size range from clusters of small molecules (a few Å) to extended clusters of large particles (a few hundred Å), not unlike micelles, where the functional groups of molecules which interact favorably with the pyridine solvent lie at the surface of particles.

Mesoporous silicates are attractive candidates for separations due to their high surface areas and porous nature. MCM-41 is one member of a new family of highly uniform mesoporous silicate materials introduced by Mobil, whose pore size can be accurately controlled in the range 1.5 Å-10 nm.^{2,3} This recently discovered M41S class of zeolites should be useful to effect size separation, due to their large pore sizes and thus their potential for the separation of larger compounds or clusters. True molecular sieving on the size range of molecular and cluster types found in coal solutions should be possible with M41S materials by tuning the pore size.

We have synthesized a mesoporous silicate material with a surface area of approximately 1100 m²/g and pore sizes of approximately 25 Å and 33 Å. The results of a study on the ability of this mesoporous materials (M41S) to be used as stationary phases for separations of coal complexes in pyridine is the subject of this paper.

EXPERIMENTAL

The coal used in this study is the mv bituminous Upper Freeport coal (APCS 1) of the Argonne Premium Coal Samples series.⁴ We have used a new room temperature extractor, the Gregar extractor and traditional refluxing in pyridine to extract the coal. Approximately 10 g of coal was extracted in the Gregar extractor for one week. The extract was filtered and stirred with the M41S material for one week. This was then filtered and the zeolite-containing coal was extracted with methylene chloride. The extraction removed the coal material from the zeolite quantitatively.

A similar quantity of coal (10 g) was extracted by pyridine reflux for one week. The extract was divided and stirred for one week in 33 Å and 25 Å M41S material. After filtering, the zeolite material containing the coal was extracted with methylene chloride. Approximately 25% of the coal material was recovered from each zeolite by methylene chloride extraction. Further extraction with chlorobenzene resulted in only a few additional percent of coal.

Synthesis of MCM-41 was an approach combining the advantages of several literature works^{2,3,5}. Different chain length of surfactants, ranging from dodecyltrimethylammonium to octadecyltrimethylammonium bromide, were used as template to construct a periodic mesophase. The silica source used was tetramethyl orthosilicate. The synthesis was carried out at room temperature in the

solution of methanol and sodium hydroxide mixture. Pure silica versions of these zeolites were prepared to alleviate irreversible absorption by aluminum sites.

Mass spectra were recorded on a Kratos Maldi III instrument for laser desorption (LD) and a Kratos MS-50TA for low voltage high resolution mass spectrometry (LVHRMS). For the LD spectra, the laser intensity for the N₂ laser (337 nm) was kept at ion appearance threshold for all samples. The LVHRMS was recorded using low energy electron ionization (18eV) to maximize ionization of high mass compounds with minimal fragmentation. TGA-DTA (thermal gravimetric analysis and differential thermal analysis) measurements were obtained on a SDT 2960 from TA Instruments. For these samples, measured against an alumina standard in a 100 mL/min O₂ flow with a temperature ramp of 10°C/min to 800°C. The TGA data is also represented in its first-derivative or differential thermal gravimetry (DTG) format. Total organic loss were calculated by measuring the weight loss over the approximate temperature range of 200-600 °C. XRD analyses were carried out on a Rigaku Miniflex+ instrument using CuK α radiation, a NaI detector, a 0.05° step size, and a 0.50°, 2/min scan rate. XRD and SAXS showed pore sizes of 25 Å and 33 Å for the two M41S-class zeolites.

RESULTS AND DISCUSSION

The Gregar extractor extracted only 7.45% of the Upper Freeport coal into pyridine. The LD mass spectrum of the coal-zeolite extract showed only minimal ion intensity. The LVHRMS of this sample was used to estimate the number of aromatic rings present in the extracts. The results show that the largest mole % of hydrocarbon containing material was zero rings (5.5%), one ring (2.5%), two ring (0.8%) species. There is a small amount of material that can be attributed to multiple ring systems above three rings (2.87%). The reason for the low extractability using this technique may be a result of room temperature pyridine extraction as opposed to refluxing pyridine for the traditional technique. Although the amount of material is less, it is interesting that the majority of this is essentially aliphatic with very little aromatic character.

The refluxing pyridine extracted 29.6% of APCS 1, which is consistent with published results of extractabilities of this coal.

We used TGA to determine the weight loss as a function of temperature. From this data we can determine the total amount of organic material in the mesoporous zeolite. The TGA data shown in Fig 1 indicates that the 33 Å pore size material contains a larger amount of coal extract from the pyridine solution than the 25Å M41S mesoporous material. This is shown as the weight loss per cent of the total sample weight of 22.6% for the 33Å material versus 15.6% for the 25Å material (Fig. 1 & 2).

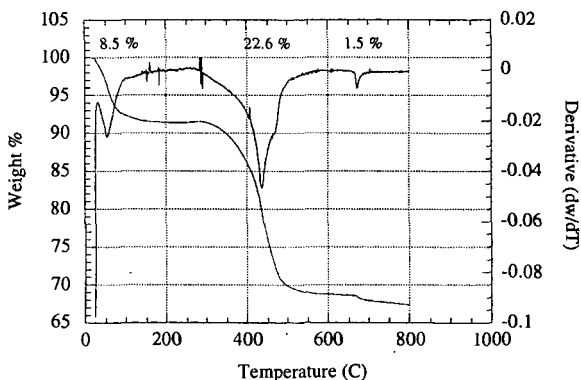


Fig. 1. The TGA of 33Å M41 S material with pyridine extract of Upper Freeport coals

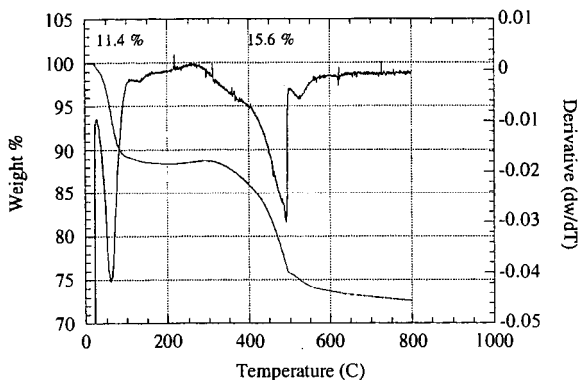


Fig. 2. The TGA of 25Å M41 S material with pyridine extract of Upper Freeport coals

Certainly, very polar material will bind to the silica. In the case of both M41S mesoporous materials only 25 % can be removed from the zeolite. The more nonpolar will be extracted in the washes of coal-infused M41S material. The TGA indicates that very low molecular weight material is evolved at about 60°C, which we assign to occluded pyridine. The major part of the organic material begins to come off at roughly 300°C and peaks at 440°C for the 33Å material and at 500 for the 25Å material. In addition, there is a distinct shoulder at 460 in the 33Å and at 520 in the 25Å which may indicate different organic compounds or clusters of compounds. The peak at 675 in the 33Å material is only 1.5% of the total weight, but may be related to very tightly bound (very polar) organic material on the silica.

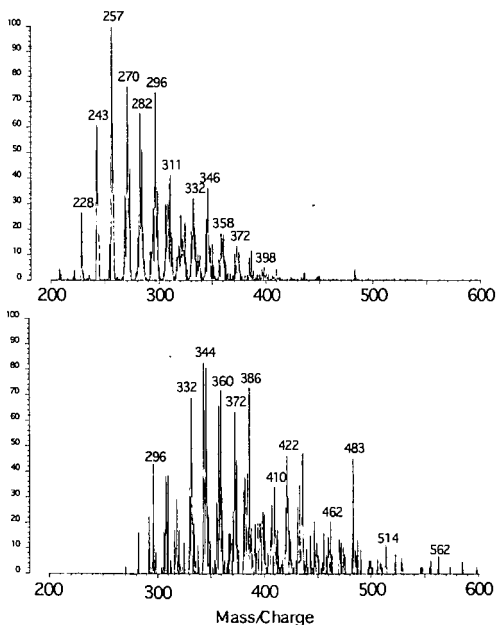


Fig. 3 The laser desorption mass spectrum of methylene chloride extract of APCS 1 imbibed M41S zeolite. 25 Å pore diameter (upper panel) 33 Å pore diameter (lower panel)

The laser desorption mass spectra of the extracts from the coal-containing mesoporous zeolites is shown in figure 3. Here there is a clear distinction in mass between the 25 Å and the 33 Å sieves. The average mass of the 33 Å extract is higher than that of the 25 Å extract by roughly 44 mass units. This would correspond to an additional ring system. Since LD chiefly accesses the aromatic content of a sample, we believe that this difference can be attributed to one additional ring in the 33 Å over the 25 Å extract. That is, the separation of the extract using mesoporous sieving by M41S-class zeolites is effectively differentiating small ring sizes. This suggests that one additional ring is responsible for the separation difference between 25 and 33 Å. Clearly, the average molecular size of an aromatic molecule of molecular weight 300 is much smaller than either pore size. This suggests that the separation takes place on larger clusters of molecules of similar ring sizes. We suggest that molecular clusters which are manifested in the LD spectra as relatively small aromatic molecular ions are separated as large clusters of molecules. Evidence from small angle neutron scattering of pyridine coal systems shows a high polydispersity in cluster size. We may be accessing one portion of that range in the 20-30 Å size range. Further experiments with larger pore size mesoporous M41S materials are underway.

The LVHRMS results comparing the 25 Å and 33 Å is shown in Figure 4. The average aromatic ring size is an estimate based on the number of double bond equivalents calculated from the high resolution data. The 33 Å shows an increased aromatic ring size over the 25 Å.

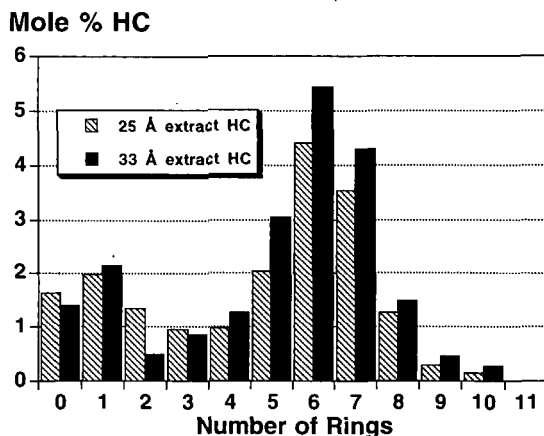


Fig 4. Comparison of aromatic ring size from HRLVMS of methylene chloride extracts of 25Å and 33Å M41S sieves loaded with pyridine extracts of Upper Freeport coal (APCS 1).

ACKNOWLEDGMENT

This work was supported by the Division of Chemical Sciences, Office of Basic Energy Sciences, U. S. Department of Energy, under contract W-31-109-ENG-38.

REFERENCES

1. Cody, G.D., Thiyagarajan, P., Botto, R. E., Hunt, J. E., Winans, R. E., *Energy Fuels*, 1994, 8(6): p. 1370-8.
2. Beck, J. S., U.S. Pat., No. 5,057,296, 1991
3. Beck, J. S.; Vartuli, J. C.; Roth, W. J.; Leonowicz, M. E.; Kresge, C. T.; Schmitt, K. D.; Chu, C. T.-W.; Olson, D. H.; Sheppard, E. W.; McCullen, J. B.; Higgins, J. B.; Schlenker, J. L., *J. Am. Chem. Soc.*, 1992, 114, 10834-43
4. Vorres, K., *Energy & Fuels* 4, 420-426 (1990)
5. Pinnavaia, T. J.; Thorpe, M. F., *Access in Nanoporous Materials*, Plenum Press: New York, 1995.

CONSTRUCTION OF MODEL STRUCTURES OF UPPER FREEPORT COAL EXTRACTS USING SOLID-STATE ^{13}C NMR CHEMICAL SHIFT CALCULATION

Hiroyuki Kawashima and Toshimasa Takanohashi
National Institute for Resources and Environment
16-3, Onogawa, Tsukuba, Ibaraki, 305-8569, Japan

KEYWORDS: Coal model structure, Solvent extraction, Solid-state ^{13}C NMR

INTRODUCTION

Many analytical techniques have been used for coal research and the analytical data have enabled the construction of model chemical structures of coal. The construction of model structure of coal is important in improving our understanding of the relationships between coal structure and its properties; this knowledge can lead to more effective and economical methods of coal conversion. Iino et al. investigated the extract fractions obtained from the extraction of Upper Freeport coal with a carbon disulfide/*N*-methyl-2-pyrrolidinone mixed solvent at room temperature and the fractionation with acetone and pyridine by using ^1H NMR, elementary analysis, SEC and hydroxyl group estimation.¹ Based on the structural parameters obtained, i.e., f_a (aromaticity), σ (the degree of substitution on aromatic rings) and $H_{a,r,u}/C_{a,r}$ (the degree of condensation of the aromatic rings), Takanohashi et al. constructed the model structures of the extract fractions, as shown in Fig. 1.² Recently, for calculating the NMR chemical shifts of known molecular structures, several programs have been developed. We modified the chemical structure of Upper Freeport coal extracts constructed by Takanohashi et al. using the ^{13}C NMR chemical shift calculations. The purpose of the present work is to improve the model structures by comparison of actual and calculated solid-state ^{13}C NMR spectra.

EXPERIMENTAL

Sample: The extract (60 wt% on raw coal basis) from a carbon disulfide/*N*-methyl-2-pyrrolidinone mixed solvent extraction at room temperature for Upper Freeport coal was fractionated with acetone and pyridine into three fractions, i.e., acetone-soluble (AS), acetone-insoluble/pyridine-soluble (PS), and pyridine-insoluble (PI) fractions. These extract fractions of Upper Freeport coal were used as samples. Data on structural analysis of the extracts are summarized in Table I.

NMR measurements: Solid-state ^{13}C NMR measurements were made by the SPE/MAS method using a Chemmagetics CMX-300 NMR spectrometer. About 100 mg of sample were packed in the sample rotor. The measuring conditions were as follows: the 90° ^1H pulse width was $4\ \mu\text{s}$; ^{13}C frequency, 75.46 MHz; spinning rate of MAS, 10 kHz; number of scans, 2000; and pulse repetition time, 60 s. Chemical shifts were calibrated with respect to tetramethylsilane using the hexamethylbenzene's methyl group peak at 17.4 ppm as the external standard.

Chemical shift simulations: Chemical shift calculations were carried out using ACD Laboratory CNMR predictor software. Thomas et al. calculated ^{13}C chemical shifts for some substituted pyridines using several NMR prediction programs and showed that the CNMR predictor gave the best results in their work.³ Kohnert et al. evaluated and tested for prediction of NMR spectra of photosynthetic metabolites using the CNMR predictor.⁴ The software allows treatment of molecules containing up to 256 carbon atoms. The software calculates chemical shifts by searching for similar sub-structural fragment with the corresponding experimental shift value in the internal database and evaluating the chemical shift value taking into account intramolecular interactions. Using the software, we calculated the chemical shifts of all carbons of each model structure constructed by Takanohashi et al.² Next, the calculated ^{13}C NMR spectra were obtained by considering an adequate line width to each peak and summing, supposing that all peaks were Gaussian peaks. (This process was performed by Spinsight ver.3.5.2 software.) The line width fitted to the actual spectra was adopted. For AS, PS and PI, the line width for aromatic carbon was 814 Hz, 1203 Hz and 1344 Hz, respectively, and the line width for aliphatic carbon was 354 Hz, 460 Hz and 601 Hz, respectively. As the fraction became lighter, the line width of each peak became narrower, with narrower lines for aliphatic than for aromatic carbon. Although, all aromatic or

aliphatic carbons may not have the same line width, it is time consuming to derive a line width for each carbon, so each one line width was used for aromatic or aliphatic carbon of the each extract fractions. By comparison with actual spectra, the model structures were modified. The chemical shifts were calculated again for the revised structures. By repeating this process, the best fitting structures were determined.

RESULTS AND DISCUSSION

Fig 2 shows the experimental NMR spectra of the extract fractions and the calculated NMR spectra for model structures of each fraction. For AS, with regard to the actual spectra, the model structure had high fractions for non-protonated aromatic carbon (125~140 ppm) and CH₂ carbon(15~25 ppm), and low fractions for protonated aromatic carbon(100~120 ppm), CH₂ carbon(30~45 ppm) and methyl carbon(0~15 ppm). We added methyl carbon to the model structure of AS and reduced the substituted aromatic carbon and β CH₂ carbon. The resulting structure of AS is shown in Fig. 3(a) and the calculated NMR spectrum for the revised model structure is shown in Fig.4(a) with the measured spectrum. For PS and PI, the model structures had high fractions for non-protonated aromatic carbon (125~140 ppm) and CH₂ carbon(35~50 ppm), and low fractions for methyl carbon(0~20 ppm). We added methyl carbon to the model structures of PS and PI and reduced the substituted aromatic carbon. Figs. 3(b) and (c) show the resulting structures of PS and PI that best fitted the actual spectra. Fig. 4(b) and 4(c) show the calculated NMR spectra of the revised model structures with the measured spectra. We modified all structures of extract fractions mainly by adding methyl and ethyl groups and reducing naphthenic ring structures. This indicates that the all initial structures lacked methyl and ethyl groups and were rich in naphthenic ring structures, which we could not distinguish by the previous analytical data. By these techniques, the correction of the model structures for the extract fractions could be made.

The chemical shift at 60 ~ 80 ppm corresponds to the aliphatic carbon connected with oxygen such as -CH₂-O-, which is thought to be important for the crosslink of coal. For the calculated spectra for PS and PI, the peaks appeared in this chemical shift range. Considering the crosslinks in coal, such oxygen containing methylene bonds possibly exist in coal, but the actual spectra showed no peak in this chemical shift range between aromatic and aliphatic carbon peak, and we cannot confirm the peaks. The amounts of the aliphatic carbon connected with oxygen may or can not be so large compared with the other forms of carbon, and the peaks may be overlapped, so in the actual spectra the peaks might not appeared.

Table 2 shows structural parameters of the revised model chemical structures. The values of f_a and H_m/C_m were almost similar between the initial and the revised model structures, but the values of σ and H/C were different. The values of σ were higher for the initial structures and the values of H/C were higher for the revised structures. This was because, in the modification process, we added some methyl and ethyl groups and reduced some naphthenic ring structures in order to fit the actual spectra. In this regard, further examination is required to coincide these data. However, relatively good agreement was obtained between the actual spectra and calculated ones by the new models.

CONCLUSION

The solid-state ¹³C NMR spectra of the model structures for the three extract fractions were estimated using the NMR chemical shift calculation method. By comparison of the estimated spectra with the observed ones, some corrections were made to the chemical structure of models to fit their spectra, and we proposed the modified model structures based on NMR chemical shift calculations. The energy-minimum conformation will be calculated by the molecular mechanics and molecular dynamics

ACKNOWLEDGMENT

This work was supported by the Japan Society for the Promotion of Science("Research for the Future" Project).

REFERENCES

- 1.M.iino, T.Takanohashi, S.Obara, H.Tsuta and Y.Sanokawa, Fuel, 68, 1588(1989)
- 2.T.Takanohashi, M.iino and K.Nakamura, Energy Fuels, 12, 1168(1998)
- 3.St.Thomas, I.Bruhl, D.Heilman and E.Kleinpeter, J.Chem.Inf.Comput.Sci., 37, 726(1997)
- 4.R. L. Kohnert, B. Arbogast and L. S. Daley, Biotechnology Software and Internet Journal, June 1996, p. 17

Table 1. Structural parameters of extracts of Upper Freeport coal²

Sample	Ultimate analysis (wt%) ^a					Structural parameters						molecular formula
	C	H	N	S	O ^b	M _n	f _s	H _m /C _m	σ	H/C		
Original coal	86.2	5.1	1.9	2.2	4.6					0.71		
AS	88.5	6.7	1.1	0.5	3.2	520	0.71	0.69	0.39	0.91	C ₃₈ H ₃₄ NO	
PS	86.6	5.8	2.0	1.8	4.5	1270	0.78	0.72	0.51	0.75	C ₉₂ H ₆₈ N ₂ O ₅	
PI	85.8	5.0	2.1	1.1	6.0	2210	0.79	0.71	0.48	0.70	C ₁₅₈ H ₁₁₀ N ₃ SO ₈	

a) dry ash free

b) calculated as the difference

Table 2. Structural parameters of the revised model chemical structures

Sample	Structural parameters				molecular formula
	f _s	H _m /C _m	σ	H/C	
AS	0.71	0.71	0.30	1.03	C ₃₈ H ₃₉ NO
PS	0.79	0.69	0.44	0.81	C ₉₁ H ₇₄ N ₂ O ₅
PI	0.80	0.67	0.40	0.77	C ₁₅₇ H ₁₂₁ N ₃ SO ₈

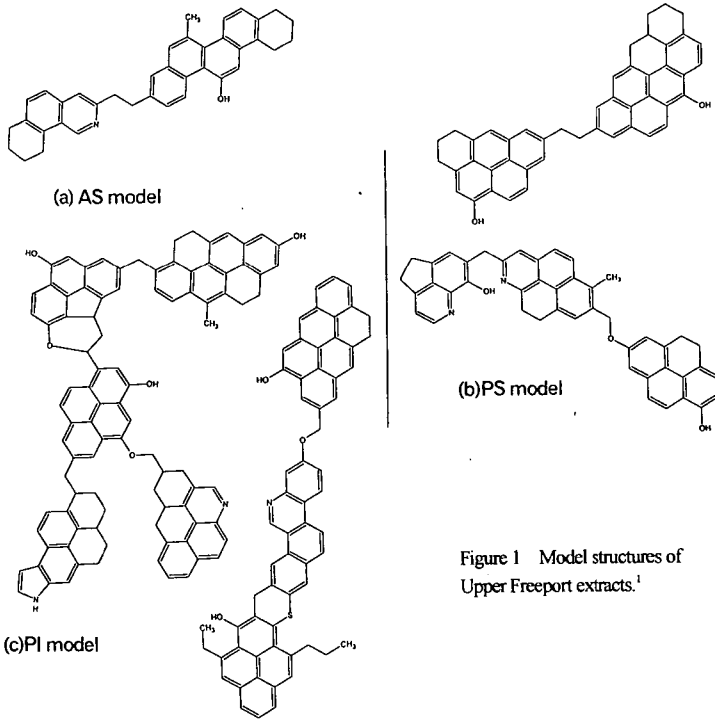


Figure 1 Model structures of Upper Freeport extracts.¹

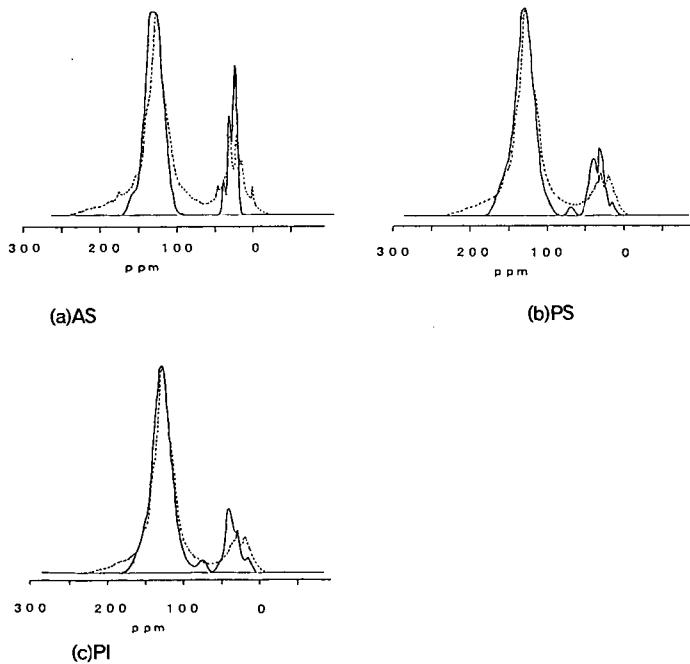


Figure 2 Measured SPE/MAS ^{13}C NMR spectra of solvent extracts(-----) and calculated NMR spectra of model chemical structures(—).

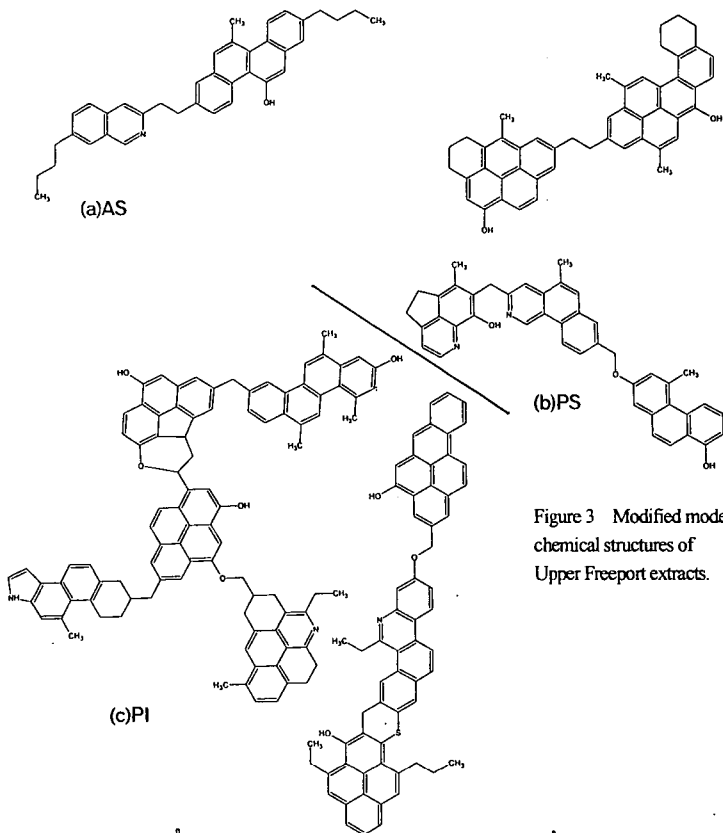


Figure 3 Modified model chemical structures of Upper Freeport extracts.

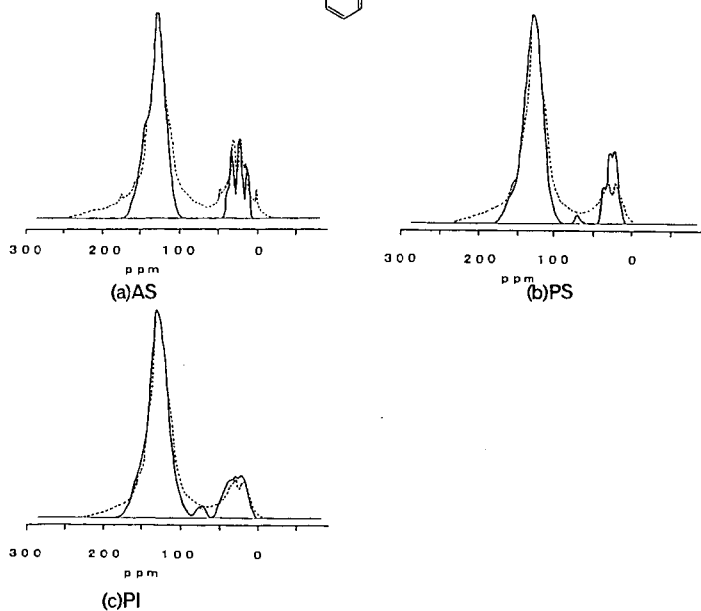


Figure 4 Measured SPE/MAS ^{13}C NMR spectra of solvent extracts(-----) and calculated NMR spectra of modified model chemical structures(—).

ADSORPTION AND DIFFUSION OF ALCOHOL VAPORS FOR ARGONNE PREMIUM COALS

Toshimasa Takanohashi
Energy Resources Department, National Institute for Resources and Environment,
Tsukuba 305-8569, JAPAN

Yuki Terao and Masashi Iino
Institute for Chemical Reaction Science, Tohoku University,
Sendai 980-8577, JAPAN

KEYWORDS: coal, sorption isotherm; sorption model

INTRODUCTION

Green and Selby reported [1] that pyridine sorption isotherms can be explained by a dual-mode sorption model that has been widely applied to the sorption of glassy polymers. This model is represented by two phenomena, adsorption on the surface described by a Langmuir isotherm, predominant at the initial portion of the plot of sorption isotherm, and diffusion (absorption) into the bulk structure described by Henry's law, the linear portion with relative pressures. Shimizu et al. [2] carried out research on organic vapor sorption using various ranks of coals and found that sorption data for Illinois No. 6 coal could be treated by the Langmuir-Henry equation regardless of a kind of the organic vapors (methanol, benzene, pyridine, and cyclohexane) used. Takanohashi et al. [3] reported that methanol sorption in the residues from coals with the high extraction yields greatly increased compared to the corresponding raw coals, suggesting that more microporosity has been developed by the extraction. In contrast, for coals with low extraction yields, sorption behavior of residues was similar to that of the raw coals, regardless of coal rank.

The steric effects on the kinetics of solvent swelling of coals have been reported.[4,5] Solvent swelling of coal involves diffusion of solvent molecules into the macromolecular structure of coals. Larsen et al. [4] reported the steric effects of various alkyl-substituted pyridines and anilines on equilibrium swelling ratio of coals. Aida et al. [5] determined the initial swelling rates in addition to the equilibrium swelling values of Illinois No.6 coal in various solvents, and showed that the rate retardation of diffusion of alkyl-substituted amines can be increased by almost a thousandfold by changing from *n*-butylamine to *tert*-butylamine. However, the swelling of coal in liquid phase also causes other structural changes such as extraction and relaxation of macromolecular structure, which can influence the swelling behavior.

To investigate the steric effect on alcohol vapor sorption for coals, the sorption isotherms of alcohols with different size of alkyl groups were measured for four Argonne premium coal samples. Data were analyzed using the Langmuir-Henry dual-mode sorption equation. Based on the adsorption and diffusion parameters from the model equation, micropore and cross-linking structures of the coals are discussed.

EXPERIMENTAL

Sample Preparation

Four Argonne premium coal samples (Pocahontas No.3, Upper Freeport, Illinois No.6, and Beulah-Zap coals) were obtained in ampoules (5 g of $\sim 150 \mu\text{m}$). Because water and gases adsorbed on the coals prevent the measurement of sorption, samples were dried at 80 °C for 12 h *in vacuo*, just before the sorption measurements. Various alkyl-substituted alcohols were used without further purification as the sorbate.

Upper Freeport coal was extracted exhaustively with a carbon disulfide / *N*-methyl-2-pyrrolidinone (CS₂ / NMP) mixed solvent at room temperature.[6] The residue was washed with acetone and dried in a vacuum oven at 80 °C for 12 hr. The extraction yield was 60 wt% on the dry-ash free basis. The extraction residue was also used as the sorbent.

Sorption Experiments

Sorption isotherms were measured with an automatic vapor adsorption apparatus (BELSORP18, BEL JAPAN, INC) at 30 °C. Approximately 200 mg of sample was placed in the sample tube and weighed. The deaeration treatment of methanol in the solvent tank was carried out with liquid

nitrogen three times through freeze-thaw cycles. Samples were pretreated under vacuum ($< 10^{-4}$ Torr) at 80°C for 12 h. The sorption isotherm was measured at the relative vapor pressures of $0.01 < p < 1$ at 30°C by using the constant-volume gas adsorption method. Each sorption was measured when the change in the amount of sorption remained constant within 5% for 10 min.

RESULTS AND DISCUSSION

Sorption Behavior.

Sorption isotherms of methanol, ethanol, *n*-propanol and *n*-butanol (only for Upper Freeport coal) are shown in Figures 1. The amount of sorption is represented on the basis of each sample (g). Generally, the sorption increased exponentially at low vapor pressures and then increased linearly with pressure in the intermediate pressure range, although the total sorption was different among the coals used. The sorption by Upper Freeport raw coal was the smallest for all alcohols used. As the size of alkyl group increased, the total sorption became smaller for all coals, showing that alkyl groups prevent the alcohols from being sorbed by the coals. For lower rank coals, Beulah-Zap and Illinois No.6 coals, the sorption behaviors of methanol and ethanol were similar at vapor pressures more than 0.2, i.e., the slope of isotherm was almost the same. While, for high rank coals, Upper Freeport and Pocahontas No.3 coals, the slope of isotherms in the cases of *n*-propanol and *n*-butanol was relatively small, indicating that they would hardly be sorbed.

Sorption Analysis Using the Dual-Mode Sorption Model

The results of curve fitting from the Langmuir-Henry dual mode equation (1) are also shown in Figure 1.

$$C = C_H + C_D = C'_H b p / (1 + b p) + k_D p \quad (1)$$

where C is the total sorption (mmol/g-sample), C'_H is adsorption on the surface, C_D is the amount of diffusion (absorption) into the bulk, C'_H is the pore saturation constant, b is the pore affinity constant, p is the relative vapor pressure (P/P_0), and k_D is the Henry's dissolution constant.

For all the cases except for Beulah-Zap-ethanol and *n*-propanol systems, data were fit by the Langmuir-Henry equation, suggesting that alcohol sorption can be explained by adsorption on the surface that occurred at low relative pressures and diffusion into the bulk that increased linearly with pressure. Since coals have many interacting sites such as functional groups on their surface, adsorption preferentially occurs at low vapor pressure. A steep increase of sorption observed for all coals at low vapor pressures, especially for low rank coals, can be due to the adsorption on oxygen functional groups of the surface, although in the case of *n*-propanol the rate of the sorption increase at low vapor pressures was small.

Constants of the Langmuir-Henry equation obtained by the fitting are listed in Table 1. The values for Beulah-Zap-ethanol and *n*-propanol systems were obtained by a different fitting method, i.e., the adsorption parameter was obtained by fitting in the low vapor pressure range less than 0.2 and the diffusion parameter by fitting in the intermediate pressure range more than 0.4, because a discontinuity point exists at around vapor pressure of 0.2. The C'_H (mmol/g-sample) for Upper Freeport coal was the smallest for all alcohols, showing that Upper Freeport coal has fewer pores on the surface than other coals. As the size of alkyl group increased, i.e., methyl, ethyl and propyl, the C'_H decreased, especially for high rank coals the rate of decrease was large. The result suggests that high rank coals have smaller micropore sizes. The b which is related to the ratio of the adsorption rate to the desorption rate, showed a tendency to decrease in the cases of *n*-propanol and *n*-butanol. The steric effect of alkyl group of alcohols may accelerate their desorption.

The Henry's dissolution constant k_D (mmol/g-sample), which represents the degree of diffusion into the bulk, was also the smallest for Upper Freeport coal in all cases. For low rank coals, the k_D values of methanol and ethanol were similar, while the value of *n*-propanol was small. In contrast, for high rank coals k_D greatly decreased in the order of methanol, ethanol and propanol, suggesting that the difference in the size of alkyl group on alcohols might greatly influence their diffusion into the bulk.

Effect of Extraction

Figure 2 shows the isotherms for Upper Freeport residue, with the Langmuir-Henry fitting curves. Constants of the Langmuir-Henry equation obtained by the fitting are also listed in Table 1. The C'_H of each alcohol for the raw coal and its extraction residue was almost similar in magnitude, although the value of methanol for the residue was smaller than that for the raw coal. The values of b increased by the extraction for all alcohols. In contrast, the k_D for the residue was quite larger than that for the raw coal in all cases. Even for bulky alkyl-substituted alcohols such as *n*-propanol

and *n*-butanol, high the k_b values were obtained, 1.6 for both. These results suggest that the adsorption sites on the surface did not change so much by the extraction, while a considerable amount of large void was formed in the bulk. Since the oxygen content of the Upper Freeport residue, 6.3 wt%, is much lower than those for Illinois No.6 and Beulah-Zap raw coals, the increase in the k_b for the residue may be due to increased physical diffusion into the formed voids.

CONCLUSIONS

Almost all sorption isotherms of various alcohols could be explained by the Langmuir-Henry dual-mode sorption equation, and adsorption and diffusion parameters could be estimated. Both pore saturation and dissolution constants were the smallest for Upper Freeport coal of all coals used. As the size of alkyl group increased, their constants decreased for all coals. Especially for high rank coals, Pocahontas and Upper Freeport coals, the dissolution constant greatly dropped. In contrast, the dissolution constant for the extraction residue from Upper Freeport coal was quite large for all alcohols, compared to those of the raw coal, although the pore saturation constant did not change so much. A considerable amount of micropores with relatively large sizes formed by the extraction may be responsible for the increased diffusion.

ACKNOWLEDGMENT

This work has been carried out as one of "Research for the Future" projects of the Japan Society for the Promotion of Science (JSPS) through the 148th committee on coal utilization technology of JSPS.

REFERENCES

- Green, T.K. and Selby, T.D., *Energy Fuels*, **8**, 213 (1994).
- Shimizu, K., Takanohashi, T. and Iino, M., *Energy Fuels*, **12**, 891 (1998).
- Takanohashi, T., Terao, Y. and Iino, M., *Fuel*, in press.
- Larsen, J.W. and Lee, D.Y., *Fuel*, **64**, 981 (1985).
- Aida, T., Fuku, K., Fujii, M., Yoshihara, M., Maeshima, T. and Squires, T.G., *Energy Fuels*, **5**, 79 (1991).
- Iino, M., Takanohashi, T., Ohsuga, H. and Toda, K., *Fuel*, **67**, 1639 (1988).

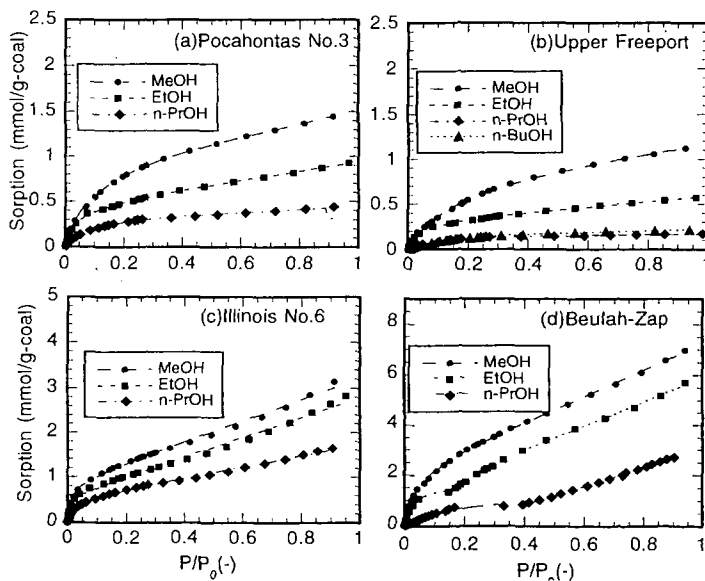


Figure 1 Sorption isotherms of various alcohols at 30 °C for Pocahontas No.3 (a), Upper Freeport (b), Illinois No.6 (c) and Beulah-Zap (d) coals, with the fitted lines with the Langmuir-Henry dual mode equation.

Table 1 The adsorption and diffusion parameters by Langmuir–Henry dual-mode sorption equation for the raw coal – alcohol systems and Upper Freeport extraction residue

coal	sorbate	C'_H^a (mmol/g-coal)	b^b (-)	k_D^c (mmol/g-coal)
Pocahontas No.3 raw	methanol	0.98	10	0.61
	ethanol	0.46	26	0.49
Upper Freeport raw	<i>n</i> -propanol	0.35	12	0.12
	methanol	0.81	35	0.79
	ethanol	0.30	30	0.29
	<i>n</i> -propanol	0.18	9	0.01
Upper Freeport residue	<i>n</i> -butanol	0.20	7	0.05
	methanol	0.58	55	3.1
	ethanol	0.33	69	2.3
	<i>n</i> -propanol	0.35	35	1.6
Illinois No.6 raw	<i>n</i> -butanol	0.37	13	1.6
	methanol	0.97	58	2.9
	ethanol	0.66	108	1.9
	<i>n</i> -propanol	0.58	32	1.1
Beulah-Zap raw	methanol	2.3	29	5.0
	ethanol	1.7	39	4.8
	<i>n</i> -propanol	1.3	6	3.7

^a Pore saturation constant. ^b Pore affinity constant. ^c Dissolution constant.

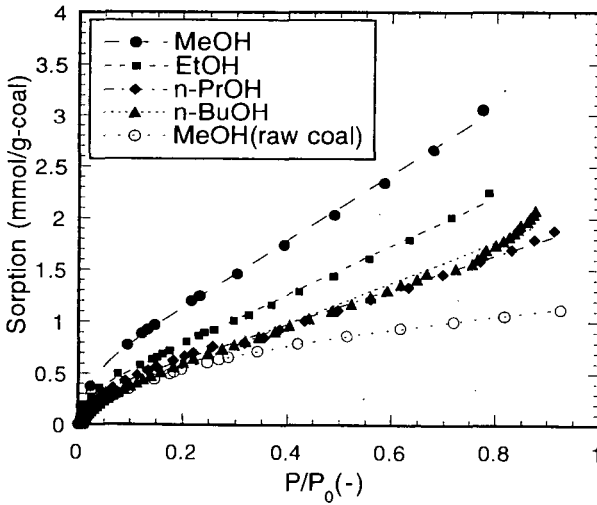


Figure 2 Sorption isotherms of various alcohols at 30 °C for Upper Freeport residue, with the fitted lines with the Langmuir–Henry dual-mode equation.

SYNERGISTIC EFFECT ON SOLVENT SWELLING OF COAL

Tetsuo Aida, Eisaku Suzuki, issei yamanishi, and Masaki Sakai
Department of Industrial Chemistry, Faculty of Engineering at Kyushu
Kinki University, 11-6 Kayanomori, Iizuka, Fukuoka 820, JAPAN

Keywords: coal, solvent swelling, synergistic effect

INTRODUCTION

It has long been curious question why the coal swelling exhibited a synergistic effect in a certain binary solvent system. In 1986, Hombach[1] observed a significant synergistic effect on the solvent swelling of coal in the mixed solvent such as amine and methanol, and tried to rationalize with a hypothesis which the change of the solubility parameter of the mixed solvent was responsible for that phenomena.

In the meantime, Iino et al.[2] also found a quite interesting binary solvent system on the coal extraction, that is, the mixture of CS₂ and N-methyl pyrrolidinone(NMP) gave a maximum extraction yield at their 50:50(vol-%) mixing conditions. This solvent system is well-known as a "Magic" solvent for the coal extraction, of which detailed mechanism has not yet been clarified.

In the course of our studies on the coal swelling, we have learned that the coal has an significant steric requirement[3] toward the penetrating solvent molecules due to the cross-linking macromolecular network structure. Also, the maximum swelling ratio of coal swelling was very much depending on the donorability of the swelling solvent, as previously pointed out by Marzec[4], probably because of the specific interaction between the solvent molecule and the cross-linking network structure formed by the relatively weak bonding interactions, such as hydrogen bonding, charge transfer bonding, π - π bonding and even the van der Waals bonding interactions. These findings are now extending to our new sight of the coal chemistry, the elucidation of synergistic effects on coal swelling and the empirical determination of a "Coal Affinity Parameter".[5] Eventually, we could categorize the synergistic effects on the solvent swelling into the three types of the mixed solvent systems.

In this paper, we present our recent experimental results concerning the mechanism of synergistic effect appeared on the solvent swelling of coal, especially focusing on Type-I and Type-II.

EXPERIMENTAL

The chemical reagents were commercial products (Gold label grade) which were used without further purification. Solvents used in this study were dried over appropriate drying agents and distilled before use. Coals from the Ames Coal Library and Argonne National Laboratory were ground, seized in N₂ atmosphere, dried at 110°C under vacuum overnight, and stored under a dry nitrogen atmosphere.

The measurement of the solvent swelling of coal was carried out by means of our hand-made instrument, and the experimental procedures were same as previously reported.[6]

RESULTS AND DISCUSSION

1. Synergistic effects on coal swelling in mixed solvent

As reported by Hombach, a coal swelling in a mixture of methanol and tertiary amine, such as dimethylaniline, trimethylamine, or trimethylamine affords a significant synergistic effect on its equilibrium swelling values(Q).

Figure 1 shows the typical example obtained our swelling measurements which is exhibiting the relationship between Q-value and the swelling rates (V-value) vs. concentration of methanol on the Illinois No.6 coal swelling in triethylamine/methanol mixed solvent.

It is quite interesting that in spite of the large synergistic effect on the Q-value there was almost no effect on the V-value (swelling rates). This fact strongly suggests that the synergistic phenomena appearing on this solvent system will not very much depend on the specific molecular interaction between tri-methylamine and methanol. We like to categorize this type of swelling system, as "Type-I".

Meanwhile, it has long been well-known phenomenon in the coal chemistry that the benzene-methanol mixed solvent enhanced its coal extractability. Actually, as far as our swelling measurements, both individual solvent can not give us a large amount of Q-

value, but the mixed solvent system has demonstrated completely different figures on their swelling parameters (Q & V) as shown in Figure 2. In this case, not only the Q-value, but also the V-value exhibited large synergistic effects on the solvent composition.

Obviously, there are several interesting features on this swelling behavior, suggesting the different swelling mechanism from the Type-I synergistic effect described above. Namely, in this case, both the Q-value and the V-value showed large synergistic effects on the solvent compositions. This means that some specific interactions will exist between each solvent molecule toward the macromolecular network structure of coal. We can categorize this type of swelling, as "Type-II".

Almost ten years ago, Iino et al.[2] reported so-called "magic solvent system" on a coal extraction. Since then, any detailed information concerning the extraction mechanism did not come out in the literatures. We have initiated a study on the rationalization of the mechanism of the *Magic solvent extraction* by means of the solvent swelling technique.

In Figure 3, a solvent swelling phenomena of Illinois No.6 coal in CS₂-NMP system measured by our instrument was demonstrated.

As expectedly, the significant synergistic effect was observed on both the Q-value and the V-value like a Type-II swelling system described above. As far as the swelling data shown in Figure 2, and 3, it seems to be quite difficult to rationalize the difference on the swelling mechanism between them. However, there are quite interesting data suggesting different type of a specific molecular interaction between both solvents like a kind of an electron donor-acceptor complex formation, of which detailed discussions will appear in our next paper.

Anyway, we like to categorize this type of synergistic effect as "Type-III".

2. "Type-I" synergistic effects on coal swelling

Some years ago, we had revealed the steric requirement of coal towards penetrating solvent molecules.[3] Coal exhibits a significant steric restriction to the penetrating molecules probably because of their cross-linking network structure like a "molecular sieve". For example, the initial swelling rates of Illinois No.6 coal in n-, sec-, iso- and tert-butylamine were 3.7×10^{-1} , 6.8×10^{-2} , 3.1×10^{-2} , and $6.2 \times 10^{-3}(\text{min}^{-1})$, respectively. This means that the swelling rate (V-value) of Illinois No.6 coal in a sterically bulky t-butyl amine was 600 times slower than that of a less sterically hindered n-butylamine.[3] Therefore it is quite difficult to evaluate the accurate equilibrium swelling value (Q) in the bulky molecule solvent system, because of the very slow swelling rate, i.e., in the case of t-butyl amine its swelling was still continuing even after 10 days.

Meanwhile, as shown in Figure 4, we have found that this steric requirement of coal could be dramatically relieved in a mixed solvent system such as a methanol solution. Namely, in this solvent system, the equilibrium swelling value (Q) of the sterically hindered molecule seems to be increased by the addition of a small amount of methanol, and the further increase of the methanol concentration results the exactly same Q-values of the less hindered molecule.

In order to confirm this speculation, we had conducted a dynamic swelling measurements of Illinois No.6 coal in the 20%-MeOH / Et₃N solution. The result is demonstrated in the Figure 5 comparing with the one in CS₂/NMP mixed solvent.

In the case of MeOH/Et₃N solvent system, a strange behavior was observed at the initial stage of the coal swelling. Namely, a rapid penetration of solvent molecules into the coal matrix was induced within a minute after the mixing of coal and solvent, and then a slow but steady swelling was followed it.

It will be quite interesting to examine the solvent composition change at the initial stage of such coal swelling as shown above, because we can assume what kind of solvent molecule predominantly penetrated into the coal matrix. For this experiment we had carefully arranged the experimental condition as follows: The ratio of the coal and solvent was determined by a calculation from their ratio at the equilibrium swelling, which will make us easy to determine a small change of the solvent compositions in the supernatant by means of gas-chromatography. The initial contact between coal and solvent was performed by the introduction of the mixed solvent into the previously evacuated test tube in which the coal sample was placed. The results obtained are shown in Figure 6.

Very interestingly, the MeOH-concentration in the mixed solvent significantly decreased at early stage of swelling, which seemed to be comparable to the change of swelling volume of coal.

All of these experimental data strongly suggest that the coal swelling in the binary

solvent system composed by a sterically hindered molecule and a less hindered molecule will result an initial coal/solvent-gel formation induced by the predominant penetration of the less hindered solvent molecule. Actually, in according with our previous swelling measurement in the neat solvent system, Illinois No.6 coal swelled in methanol 60times faster than in t-butyl amine.[3] Thus in the binary solvent swelling system a methanol molecule has to predominantly penetrate into the coal, inducing a significant relaxation of a steric requirement due to the cross-linking network structure of coal, which will make the sterically hindered molecule like a triethylamine easy to penetrate into the coal matrix. We would like to call this type of steric relaxation as "Wedge Effect" of the mixed solvent demonstrating in Figure 7.

Actually, the solvent swelling was always involved with a sterically hindered molecules as a counter part of methanol, like a trimethylamine or dimethyl aniline.

In order to verify our speculation discussed above, we took another advantage to use a cross-linked synthetic polymer (styrene-divinylbenzene co-polymer: Bio-bead SX, BIO-Rad Ltd.), which had the known covalent cross-linking density and chemical structures.

Figure 8 shows our experimental data, which was obtained by using a hexamethyl phosphoramide (HMPA) as a sterically hindered component and a dimethylformamide (DMF) as a less bulky component. Obviously, there is a dramatic increase of the Q-value of HMPA by the addition of small amount of DMF.

All of these experimental data discussed above seems to be consistent with that the Type-I synergistic effect will be induced by the relaxation of the steric requirement of coal resulted by the initial formation of the coal-gel due to the predominant penetration of the less hindered solvent molecule.

3. "Type-II" synergistic effects on coal swelling

Just recently, we had developed a reliable chemical determination of the oxygen functionality in coal,[7] and learned that there were significant amount of carboxylic acid functionality, phenolic hydroxyl and alcoholic functionality in even bituminous coal like Illinois No.6 coal. Based on our preliminary analysis of coals by means of this new technique, the content of these acidic hydroxyl functionality in Illinois No.6 coal (pyridine-extract) reached up to 1.5, 12, and 10units over 100carbon atoms, respectively.[8] This means that the density of the functionality in the macromolecular network structure of coal is approximately one unit per 16 carbon skeleton. This is just an amazing fact, because the most of these oxygen functionality in coal are potentially capable to form a hydrogen bonding which is thought to play a major role for inducing the apparent cross-linking, as illustrating in Figure 9.

This modeling is our standpoint to understand the mechanism of the "Type-II" synergistic effect on coal swelling.

There may be at least two key factors for distinguishing Type-II from Type-I synergistic effects. Namely, the Type-II can be observed even in the mixed solvent composed of less hindered molecules, and also exhibits a significant synergistic effect on the swelling rate (V-value in Figure 2).

If the coal had such polar hydroxyl functionality as mentioned above, a benzene molecule must have a big trouble in its initial stage of the penetration, because of the blocking by the polar cross-linking like a hydrogen bonding, even if there were some comfortable spaces inside of the macromolecular network structure. In this case, very naturally, the coexistence of a polar and small sized molecules like a methanol in the solvent will induce a destruction of an apparent cross-linking structure constructed by a hydrogen bonding with same manor as Type I synergistic effect discussed above.

It will be also true that the polar solvent like a methanol could be in trouble to penetrate into the macromolecular network structure, because of the apparent cross-linking due to π - π interactions between aromatic rings. In this case, the coexistence of benzene in the solvent must help its penetration by breaking such non-polar bonding interactions in macromolecular network structures.

This speculation, "Co-operative Swelling" can be verified by the same treatments as applied to the Type-I synergistic effect shown in Figure 6. The solvent compositions during the coal swelling in a benzene/MeOH mixed solvent were analyzed by using the same technique as described in Type-I synergistic effect. The results obtained are summarized in Figure 10.

It is obvious that there is an interesting difference between the Type-I and Type-II synergistic effects on the solvent composition change during a coal swelling, that is, in the case of the Type-II synergistic effect, both solvent systems, 20vol%-benzene/MeOH and 20vol%-MeOH/benzene, exhibited the predominant penetration of benzene and MeOH

molecule into the macromolecular net work structure of coal, respectively. These phenomena can result in a synergistic effect because of their cooperative destruction toward apparent cross-linking structure formed by polar and non-polar bonding interactions in the coal matrix.

Actually, we often experience a curious solvent dependency of the solubility of the condensed aromatic compounds, for example, benzene can dissolve anthracene very nicely, but a methanol, even DMF can not dissolve it. This phenomenon is suggesting that the aromatic-aromatic interaction in coal may be far larger than our imagination.

Anyway, in this solvent system, the major role of the methanol molecule is thought to be the relaxation of the apparent cross-linking structure caused by destruction of the hydrogen bonding. If so, the combination with a molecule which has more stronger hydrogen bonding ability than methanol, like trifluoroacetic acid ($pK_a=2.5$) must induce a more larger synergistic effect. The same idea will be applicable to the swelling experiment, in which a strong base like a tetra-butylammonium hydroxide ($n\text{-Bu}_4\text{NOH}$) is used as a destruction agent of a hydrogen-bonding cross-linking in the macromolecular network structure of coal.

These facts can be rationalized with the decreasing cross-linking due to hydrogen bonding in the macromolecular network structure of coal. Under these circumstances the equilibrium swelling value (Q) and the swelling rate (V -value) of the coal swelling must be increased by their cooperative destruction of the apparent cross-linking structure of coal.

CONCLUSION

The synergistic effect observed on the coal swelling in binary solvent were categorized three types, Type-I, Type-II, and Type-III. The Type-I can be rationalized by the relaxation of the steric requirement of coal induced by the initial formation of coal-gel. The Type-II synergistic effect consistent with the cooperative destruction of the apparent cross-linking structure, such as hydrogen bonding or a π - π bonding interaction.

ACKNOWLEDGEMENT

A part of this research was supported by the grant from The Japanese Ministry of Education through The 148th Committee on Coal Utilization in The Japan Society of Promotion of Science (JSPS).

REFERENCES

- (1) Hombach, H.P., *Fuel* **59**, 465(1980)
- (2) Iino, M., Matsuda, M., *Fuel*, **62**, 744(1983)
- (3) Aida, T., Fuku, K., Fujii, M., Yoshihara, M., Maeshima, T., *Energy & Fuels*, **5**, 79(1991)
- (4) Szeliga, J., Marzec, A., *Fuel*, **62**, 1229(1983)
- (5) Aida, T., Yamanishi, I., *Prepr. Sekitan Kagaku Kaigi*(Japanese), 169(1998)
- (6) Aida, T., Squires, T.G., *Prepr. Pap.-Am. Chem. Soc., Div. Fuel Chem*, **30**, 95(1985)
- (7) Aida, T., Yoshinaga, T., Yamanishi, I., Tsutsumi, Y., *Proceedings of 9th International Conf. on Coal Science, Essen*(Germany), 179(1997); Aida, T., Hiram, N., Tsutsumi, Y., *Prepr., Pap.-Am. Chem. Soc., Div. Fuel Chem*, **42**, 218(1997); Yoneda, M., Yamanishi, I., Aida, T., *Prepr., Sekitan Kagaku Kaigi*(Japanese), 97(1998)
- (8) Aida, T., unpublished results

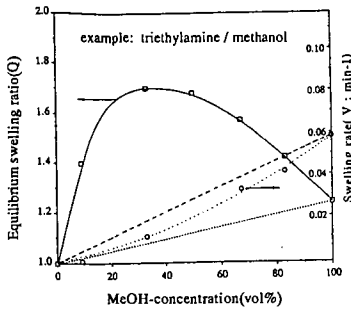


Figure 1. Swelling of Illinois No.6 in binary solvent (Et₃N/MeOH)

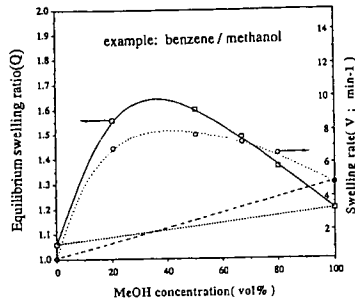


Figure 2. Swelling of Illinois No.6 in binary solvent (benzene/MeOH)

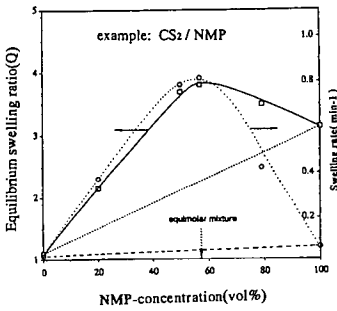


Figure 3. Swelling of Illinois No.6 in binary solvent (CS₂/NMP)

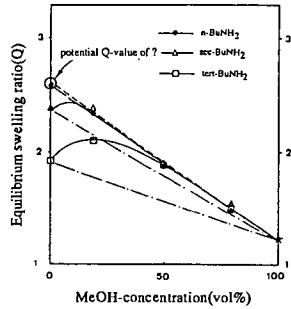


Figure 4. Swelling of Illinois No.6 in binary solvent (BuNH₂/MeOH)

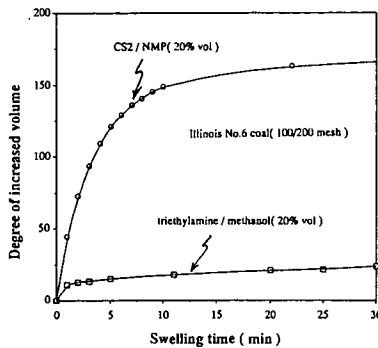


Figure 5. Swelling behavior of Illinois No.6 in binary solvent

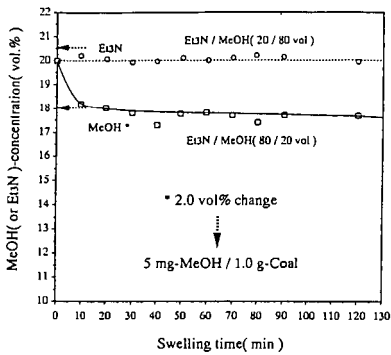


Figure 6. Composition change in binary solvent during coal swelling

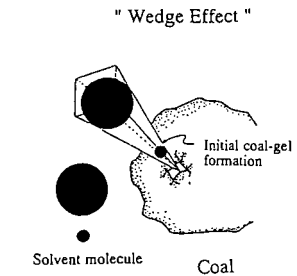


Figure 7. Penetration model of mixed solvent into macromolecular network structure of coal

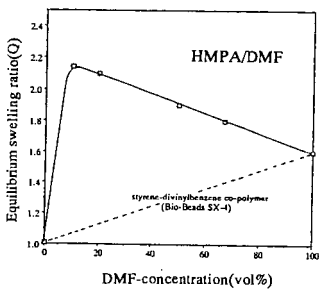


Figure 8. Solvent swelling of cross-linked synthetic polymer in HMPA/DMF mixed solvent

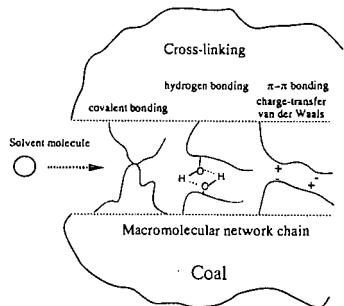


Figure 9. Penetration model of solvent molecule into macromolecular network structure of coal

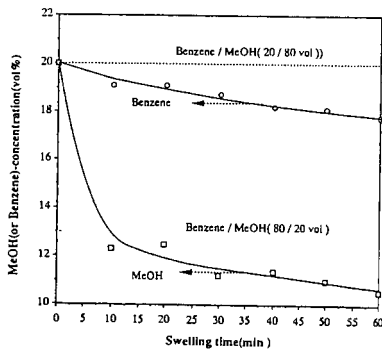


Figure 10. Composition change in binary solvent during coal swelling

STRUCTURE OF COALS REVEALED BY SLOW STEP SCAN XRD AT THEIR SWELLING

Kinya Sakanishi, Izumi Watanabe, and Isao Mochida

Institute of Advanced Material Study, Kyushu University,
Kasuga, Fukuoka 816-8580, Japan

Keywords: Argonne coal samples, step scan XRD, solvent swelling

ABSTRACT

Argonne coal samples were treated in dilute acetic acid aq. or polar solvents such as DMF and pyridine, and analyzed by high resolution slow step scan XRD to clarify the effects of such pretreatments on the secondary aggregate structure in the coals caused by non-covalent bonds interactions. Solvent swelling ratios of the lower ranked Beulah-Zap and Wyodak coals with pyridine and DMF increased significantly by the mild acid treatment, suggesting that the coal aggregate structure may be rearranged to more mobile and weaker forms through the removal of ion-exchangeable cations. The slow step scan XRD profiles of the coals showed that the peaks for the organic components can be classified into two parts; one is ascribed to the aromatic plane stacking interactions (around 26°), the other is probably due to the interactions among aliphatic side chains (around 20° , that is called γ -band). The solvent-swollen coals with polar solvents such as pyridine or DMF intensified the peaks for the γ -band even after the removal of the solvent by washing with methanol. The solvent-impregnated coal gel (solvent/coal weight ratio of unity) also showed the intensified γ -band, suggesting that the solvent itself may contribute to the rearrangement of the ordered packing in the coal aggregate structure probably due to the aliphatic side chain entanglement and hydrogen bond.

INTRODUCTION

Coals consist of primary macromolecular structure and its secondary network, latter of which is caused by aromatic ring stacking, aliphatic side chain entanglement, and hydrogen bonds, cation bridges, charge transfer interactions through oxygen functional groups.¹⁻⁵

Coal pretreatments have been developed to modify the coals for their easier transportation, grinding, drying, storage and the following conversion processes such as pyrolysis, liquefaction, and gasification.^{6,9} Flotation and washing treatments with water, acid or basic solution are one of the conventional procedures for the removal of mineral matters and contaminants by a simple gravimetric separation and filtration, respectively. The former process can be performed to the demineralization of coals by the aid of oil agglomeration or air-bubble flotation. The selected solvents for the latter procedure can dissolve a part of water-soluble mineral matters and ion-exchangeable cations during the storage, transportation or grinding procedures.

Solvent swelling and impregnation treatments of the coals have been the one of the most classical methods for the modification of the coal macromolecular structure induced by the non-covalent bonds interactions such as hydrogen bond, electrostatic interactions, and aromatic plane stacking.^{10,15} Selection of solvent and its amount required for the swelling or impregnation should be carefully optimized for the design of the most efficient and adequate solvation of the coals. Polar solvents such as pyridine, THF, and DMF have been reputed to be quite effective for the liberation of the non-covalent bonds interactions in the coal macromolecular network. It was reported that the impregnation of a small amount of pyridine enhanced the coal fusibility and the following carbonization reactivity even after the extraction of the soluble fraction, because pyridine played an important role in the liberation of hydrogen bond and the favorable rearrangement of the coal aggregate structure during the heat treatment and carbonization.¹⁶

X-ray diffraction (XRD) have been applied to the characterization of carbonaceous materials including coals for the better understanding of their molecular-level structuring and ordered packing extent of their unit structure.^{17,21} Slow step scan XRD analyses have been reputed to give the higher resolution of the diffractograms, classifying the carbon-related peak around $20 - 26^\circ$ into two parts; one is derived from aromatic ring stacking around 26° , and the other is derived from aliphatic chain entanglement around 20° . The ratio of the two peaks depends on the coal rank, and hence the secondary macromolecular network in coals is influenced by their ratio.

In the present study, four coals in the Argonne Premium Coal Bank were treated in diluted acetic acid or polar solvents such as DMF and pyridine for the modification of the secondary aggregate structure of the coals. A preliminary measurement of the slow step scan XRD indicated that the XRD patterns of the coals may change by the mild acid treatment and/or solvent swelling treatment.²²

EXPERIMENTAL

Coals

Four coals (100 mesh under) of Beulah-Zap(BZ), Wyodak(WY), Illinois No.6(IL), and Upper Freeport (UF) in the Argonne Premium Coal Bank were used in the present study.

Acid Pretreatment

1.5 g of the coal was treated in aqueous 1.6 mol acetic acid or methoxyethoxy-acetic acid with 10wt% ethanol at room temperature under atmospheric nitrogen flow for 26 - 46 h. After the filtration, the acid-treated coals were dried overnight at 60 °C under vacuum. The filtrates were analyzed by Inductively Coupled Plasma(ICP; SP1500, Seiko Electronics) to quantify the eluted metal cations by the acid treatment. The degrees of the demineralization were calculated based on the difference in the elemental compositions between original and treated coals. The removal ratio of respective metal was calculated based on the ash analysis data supplied from Argonne Premium Coal Bank.

Solvent Swelling and Impregnation

0.4 g of the coal was mixed with a prescribed amount of solvent in a graduated test tube, and settled at 40 °C under nitrogen flow for a few days to measure the swelling ratio by some solvents. Pyridine, DMF, methanol and benzene were used as solvents for the swelling of coal. The swelling ratio (Q) was calculated as follows;

$$Q = h/h_0$$

h: height of swollen coal layer in the tube

h₀: height of coal particle layer without solvent

The solvent impregnation treatment of the coals with pyridine, DMF, or THF was performed by mixing the coal powder with solvent at the weight ratio of unity at 40 °C. The solvent-swollen coal was washed with methanol to remove the solvent.

XRD Measurements

The slow step scanning XRD (Rigaku Geigerflex) of coals before and after the acid pretreatments was measured by the scanning speed of 0.4 sec/0.01° at room temperature. The solvent-coals were analyzed by the step scan XRD with or without the removal of solvent.

RESULTS AND DISCUSSION.

Change of Coal Aggregate Structure by the Acid Pretreatment

Figure 1 illustrates slow step scan XRD patterns obtained for coals before and after the acid treatment. In all coals, a broad diffraction profile was obtained around 20°. The acid treatment intensifies the diffraction in lower-ranked coals of BZ and WY coal. In contrast, a higher-ranked coal of IL did not change its diffraction patterns before and after the acid treatment. It is suggested that ordered packing in the lower ranking coals can be rearranged by the liberation of aggregate structure due to the removal of cation bridge.

Solvent Swelling Behaviors of the Coals

Figure 2 illustrates the swelling ratio in coals of different ranks by four solvents. The extent of swelling of original coal was in the order of pyridine > DMF > methanol > benzene. The acid treatment significantly increased the swelling ratio of the lower rank coals of BZ and WY, while the swelling ratio of IL coal did not change so much by the acid treatment.

Non-treated lower-ranking coals are very refractory against the swelling by the polar solvents such as pyridine and DMF probably due to the strong cation-bridging through the oxygen functional groups. The aggregate structure of a higher-ranked coal IL, is essentially not changed by the acid treatment because of its lower contents of both ion-exchangeable cations and oxygen functional groups, resulting in the insensitivity to the swelling with polar solvents. Less and non-polar solvents showed much smaller swelling of which extent appears rather independent on their ranks.

Figure 3 shows the XRD profiles of BZ coal before and after the solvent swelling treatment with DMF or pyridine followed by washing with methanol. The peak around 20° was intensified by the solvent treatment even after the washing with methanol, indicating that solvent swelling treatment with polar solvents

may rearrange the aggregate structure caused by aliphatic chain entanglement to more oriented form. It is noted that such effect with DMF is more significant than that with pyridine.

Figure 4 illustrates the XRD profiles of DMF-treated BZ coal before and after the acid treatment. The acid treatment slightly intensified the peak around 26°, indicating that the aromatic ring stacking may be rearranged to a small extent by the removal of bridging cations. In other words, the solvent treatment of BZ coal with DMF may contribute to the aliphatic chain entanglement, while the acid treatment may be more sensitive to the aromatic ring stacking caused by newly formed hydrogen bonds.

Figure 5 shows the XRD patterns of Beulah-Zap and Wyodak coals before and after the solvent-swelling treatments with and without the removal of DMF. The solvent-swollen coals with polar solvents such as pyridine and DMF intensified the peaks for the γ -band even after the removal of the solvent by washing with methanol. It is noted that the solvent-impregnated coal gel (solvent/coal weight ratio of unity) also showed the intensified γ -band peak without the removal of solvent, suggesting some contribution of the solvent itself to the rearrangement of the coal aggregate structure. It is also suggested that the interaction of polar solvent with coal macromolecules through the oxygen functional groups may survive and influence the secondary aggregate structure in the lower ranked coals even after the removal of solvent.

Figure 6 shows the XRD profiles of IL and UF coals before and after the impregnation treatment with DMF. The DMF-impregnated coals of the higher rank gave a intensified peak around 20°, although the extent was much smaller than that with the lower ranked coals of BZ and WY. It is suggested that DMF may interact more weakly with the higher ranked coals which have less oxygen functional groups but with more and larger aromatic rings.

Based on the above results, the interactions between coal and solvent can be controlled by changing the combinations of coals of different rank with solvents of different polarity. The slow step scan XRD measurements is effective for the detection of the change in coal aggregate structure caused by the non-covalent bonds interactions such as aliphatic chain entanglement, aromatic ring stacking, charge transfer, and/or hydrogen bonds.

ACKNOWLEDGMENT

This work has been carried out as one of the "Research for the Future" projects of the Japan Society for the Promotion of Science (JSPS) through the 148 committee on coal utilization technology of JSPS.

REFERENCES

1. Solum, M.S.; Pugmire, R.J.; Grant, D.M. *Energy Fuels* **1989**, *3*, 187.
2. Cody, G.D.; Davis, A.; Hatcher, P.G. *Energy Fuels* **1993**, *7*, 455.
3. Carlson, G.A. *Energy Fuels* **1992**, *6*, 771.
4. Nakamura, K.; Takanohashi, T.; Iino, M.; Kumagai, H.; Sato, M.; Yokoyama, S.; Samada, Y. *Energy Fuels* **1995**, *9*, 1003.
5. Larsen, J.W.; Gurevich, I. *Energy Fuels* **1996**, *10*, 1269.
6. Evans, D.G. *Fuel* **1973**, *52*, 185.
7. Miura, K.; Mae, K.; Morozumi, F. *Prep. ACS Div. Fuel Chem.* **1997**, *42*, 209.
8. Mochida, I.; Sakanishi, K.; Sakata, R.; Honda, K.; Umezawa, T. *Energy Fuels* **1994**, *8*, 25.
9. Mochida, I.; Sakanishi, K. *Advances in Catalysis (Academic Press, Inc.)* **1994**, vol.40, 39.
10. Suuberg, E.M.; Otake, Y.; Yun, Y.; Deevi, S.G. *Energy Fuels* **1993**, *7*, 384.
11. Otake, Y.; Suuberg, E.M. *Fuel* **1998**, *77*, 901.
12. Otake, Y.; Suuberg, E.M. *Energy Fuels* **1997**, *11*, 1155.
13. Hall, P.J.; Larsen, J.W. *Energy Fuels* **1993**, *7*, 47.
14. Cody, G.D.; Eser, S.; Hatcher, P.; Davis, A.; Sobkowiak, M.; Shenoy, S.; Painter, P.C. *Energy Fuels* **1992**, *6*, 716.
15. Aida, T.; Nawa, Y.; Shiotani, Y.; Yoshihara, M.; Yonezawa, T. *Proc. Int. Conf. Coal Sci.*, **1993**, pp.445.
16. Korai, Y.; Torinari, Y.; Mochida, I. *Cokes Circular, Jpn.* **1992**, *41*, 232.
17. Cartz, L.; Diamond, R.; Hirsch, P.B. *Nature* **1956**, *177*, 500.
18. Shiraishi, M.; Kobayashi, K. *Bull. Chem. Soc. Jpn.* **1973**, *46*, 2575.
19. Wertz, D.L.; Bissell, M. *Energy Fuels* **1994**, *8*, 613.
20. Wertz, D.L.; Quin, J.L. *Energy Fuels* **1998**, *12*, 697.
21. Wertz, D.L. *Energy Fuels* **1999**, *13*, 513.
22. Mochida, I.; Sakanishi, K. *Fuel* in submission.

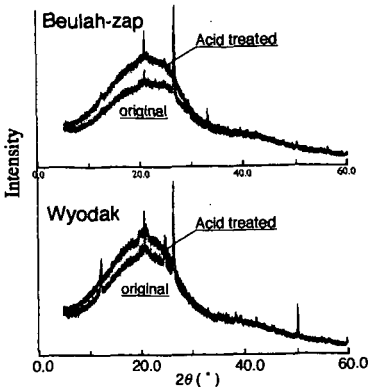


Figure 1 Effect of acid treatment on XRD patterns of BZ and WY coals

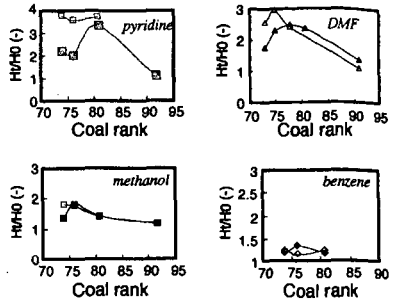


Figure 2 Swelling behavior of coals with various solvents

Opened symbol is acid treated coal
Closed symbol is original coal

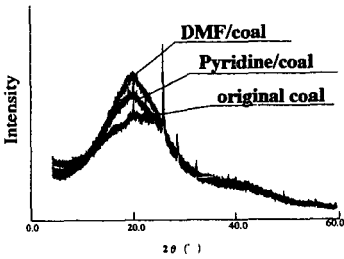


Figure 3 Effects of swelling by DMF and pyridine on XRD patterns of BZ coal with MeOH washing

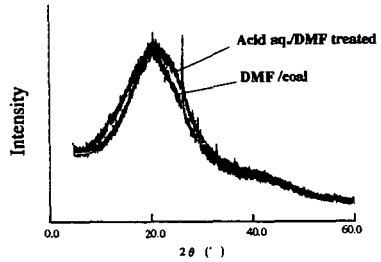


Figure 4 Effect of acid treatment on XRD of DMF-treated BZ-coal with MeOH washing

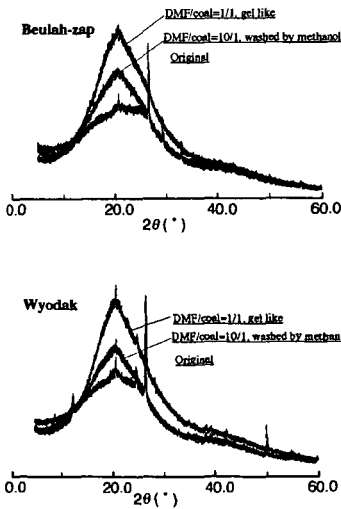


Figure 5 XRD patterns of BZ and WY coals before and after treatment with DMF

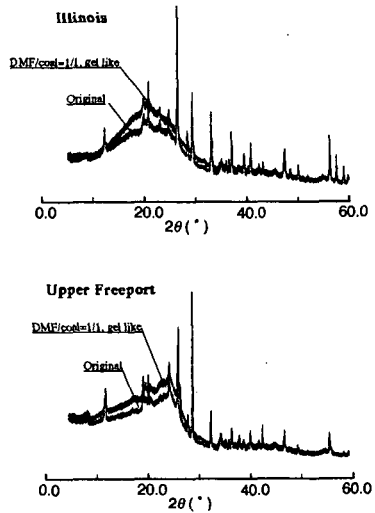


Figure 6 Effect of swelling with DMF on XRD patterns of IL and UF coals

CHANGE IN PHYSICAL AND CHEMICAL CHARACTERISTICS OF BROWN COAL ALONG WITH A PROGRESS OF MOISTURE RELEASE

Haruo Kumagai¹, Tadatoshi Chiba¹, Kazuo Nakamura²

¹Center for Advanced Research of Energy Technology, Hokkaido University,
Sapporo 060-8628, Japan

²Fundamental Research Laboratories, Osaka Gas Co., Ltd.,
Osaka 554, Japan

Keywords : moisture release, macromolecular structure, CAMD

INTRODUCTION

Low rank coals, such as lignite and brown coal, have high residual moisture contents in the range of 30-70wt% [1]. Due to such a high moisture content of the coal, moisture removal is the first and essential step in almost any process for upgrading or utilizing them. Since the moisture removal is known to have a significant effect on the physical and chemical properties of dried coal, fundamental understanding of moisture removal is of some consequence. It would be easy to imagine that the effects are brought about by the change in macromolecular structure of coal along with moisture release [2]. Although it is considerable that the physical change of coal during drying process is caused by the change in macromolecular structure of the coal, the natures of macromolecular structure of coal have not been fully understood. Recently, computer-aided molecular design (CAMD) technique has applied to the area of fuel chemistry to obtain insight into the structure, properties and interactions of macromolecules. Carlson has determined three-dimensional minimum-energy conformation of four bituminous coal models, and indicated that nonbonding interactions, in particular, van der Waals and hydrogen bonding interactions, are strong driving forces to form and stabilize the three-dimensional structure of the coal models [3]. Takanohashi and co-workers determined the minimum-energy conformation of bituminous coal by CAMD and reported that the bituminous coal has a possibility to have associated structure of coal molecules which have a continuous distribution of molecular weight [4,5]. In the present study, the conformational change in macromolecular structure of an Australian brown coal with its moisture removal process was simulated by means of a CAMD method.

EXPERIMENTAL

CAMD calculation method

The CAMD study was carried out using PolyGraf software. The software allows treatment of relatively large molecules containing up to 20 000 atoms and is capable of calculating the most stable structures with the minimum conformational energies using AMBER, MM2 and DREIDING force fields. In this study, the DREIDING force field was used. The energy for model molecule was evaluated from forces of bonded interactions (bond; E_b , angle; E_a , torsion; E_t , inversion; E_i), and forces of non-bonded interactions (van der Waals; E_{vdw} , electrostatic; E_{el} , hydrogen bond; E_{hb}), as follow:

$$E = (E_b + E_a + E_t + E_i) + (E_{vdw} + E_{el} + E_{hb})$$

The structure of Yallourn brown coal (YL) was modeled by two oligomers, namely a tetramer (Mw=1540) and a pentamer (Mw=1924), of unit structure. The unit structure which was constructed on the basis of the data from elemental analysis and ¹³C-NMR spectroscopy of the coal is shown in figure 1. Each oligomer was specially arranged so as to have no interaction with others. Simulations of moisture removal process were initiated by generating 360 water molecules (65.25wt%, wet basis) surrounding the model molecule and the minimum energy conformation (MEC) for the model with water molecules was calculated based on molecular mechanics and molecular dynamics methods. After MEC was obtained, the potential energies and volume were calculated individually for the model molecule with water and model molecule alone. The volume was defined as the void volume using water as a probe molecule. The

calculation was repeated decreasing the number of water molecules step by step to 0, and finally MINEC for model molecule with 0 water, i.e., completely dried coal was obtained. Re-adsorption of water onto the completely dried coal was also simulated in the same manner by generating 360 water molecules surrounding the model molecule with 0 water.

Coal Sample

Yallourn brown coal (YL, Moisture;60.0wt% wet basis, ash; 1.1wt% dry basis, C;62.6wt%, H;4.6wt%, N;0.7wt%, S;0.3wt%, O;31.6wt% diff.) was selected and used as a sample. The moisture content of the sample coal was controlled by varying the relative humidity in a vessel from 0 to 84% at 303K using conc. H_2SO_4 and aqueous solutions saturated by selected salts.

Volumetric Change Measurements

For coal drying process, partially and completely dried brown coal samples were placed in constant diameter tubes (8 mm i.d.), then centrifuged for 5 min at 4 500 rpm. After which the height of the coal particle bed was measured by caliper. For volumetric recovery measurement, water was added in the tube containing completely dried sample, then the contents were vigorously stirred. The tube was sealed and placed in an oven kept at 303K for 7 days. The tube was centrifuged again for 5 min at 4 500 rpm, then the height of coal bed was measured. The volumetric shrinkage of sample during moisture release process was determined by referring to the initial volume of as received sample. The volumetric recovery of dried sample was determined by referring to the initial volume of as received sample.

RESULTS AND DISCUSSIONS

The volumetric change of the YL during moisture release process was determined. The results are shown in figure 2 as a function of the extent of moisture removal. During moisture release process, the volume decreases monotonously with moisture removal, and reaches nearly a half of initial volume at the final stage. The volumetric recovery for completely dried brown coal was also determined. The volume of the completely dried sample is not recoverable with moisture re-adsorption. These results reveal that the volumetric change of YL is irreversible when the moisture is removed completely from the coal and imply that the irreversibility is caused by conformational change in the macromolecular structure of the coal during moisture release process. In order to elucidate the conformational change, CAMD technique has been applied for simplified brown coal model molecule.

Volumetric change in MEC of YL model molecule during moisture release process obtained with CAMD calculation is shown in figure 3. The MEC were extracted after 100 pico-second molecular dynamics calculation. The calculated volume for MEC of YL model molecule with water molecules, here after defined as *COAL/WATER*, shows monotonous decrease with moisture removal. The volumetric changes of *COAL/WATER* well corresponded to the experimentally observed volumetric changes of YL. The conformation for MEC of YL model molecule alone, defined as *COAL*, showed an extensive shrinkage of the size from the initial expanded to the contracted as well as deformation of the shape with a decrease in the number of water molecules. The volume for *COAL* remains constant with the extent of moisture removal up to 60%. A significant decrease in *COAL* volume is observed with the extents higher than 80%, resulting in a completely dried *COAL* with a volume being 80% of the initial one. For re-adsorption of water molecules onto the completely dried coal, *COAL/WATER* recover its volume by 85% of the initial one. The volume of *COAL*, however, is not affected by moisture re-adsorption. These CAMD calculation results indicate that removal of water molecules is responsible for the volumetric change of *COAL/WATER* with progress of moisture release, and change in the conformation of *COAL* proceeds in the final stage of moisture release. Also, the conformational change is irreversible and re-adsorption of water molecules causes an increase in coal volume without affecting the coal conformation.

The total potential energies for *COAL/WATER* ($E_{C/W}$) can be assumed as a sum of three potential energies, i.e. *COAL* (E_C), water molecules (E_w) and interaction between brown coal model

molecule and water molecules (E_{NT}), as follow;

$$E_{\text{C/W}} = E_{\text{C}} + E_{\text{W}} + E_{\text{NT}}$$

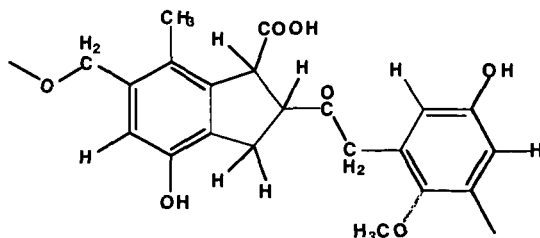
Figure 4 shows the change in $E_{\text{C/W}}$ and E_{C} as a function of moisture removal. Monotonous increase in $E_{\text{C/W}}$ clearly indicates the marked contribution of water molecules on the stabilization of *COAL/WATER*. The stabilization could be attributed to the non-covalent interactions among water molecules and between YL model molecule and water molecules. E_{C} decreased drastically for the extent of moisture removal of 80% and the change corresponded well to the volumetric change of *COAL*. The decrease of E_{C} suggests the stabilization of *COAL*, whereas the increase of $E_{\text{C/W}}$ means that *COAL/WATER* becomes unstable along with moisture release process. For moisture re-adsorption, E_{C} shows incomplete recover, since $E_{\text{C/W}}$ reverts completely to its initial value. This means that the YL model molecule has most stable conformation at completely dried state. While the effects of moisture release on the conversion reactivity thought to be due to a physical change, such as collapse of pores, the stabilization of the macromolecular structure also makes contributions to the conversion reactivity. In summary, the change in conformation for YL model molecule with its moisture release process could be successfully simulated by using the CAMD method. Although the coal model molecule employed in this study is rather simple, the results appear to represent the characteristics of the brown coal, at least volumetric change with moisture release process.

CONCLUSIONS

1. Change in conformation of Yallourn coal model simulated by CAMD method well correspond to the observed volumetric changes of the coal
2. Removal of water molecules results in a drastic conformational change in the final stage of moisture removal.
3. Re-adsorption of water molecules causes increase in coal volume without affecting the coal conformation.

REFERENCE

1. Allardice, D. J. In *The Science of Victorian Brown Coal*; Durie, R. A., Eds., Butterworth-Heinemann: Oxford, 1991; Chapter 3, pp 104-150.
2. Vorres, K. S.; Kolman, R.; Griswold, T. *Prepr. Pap. Am. Chem. Soc., Div. Fuel Chem.* 1988, 33 (2), 333.
3. Carlson, G.A. *Energy Fuels* 1992, 6, 771.
4. Takanohashi, T.; Iino, M.; Nakamura, K. *Energy Fuels* 1994, 8, 395.
5. Nakamura, K.; Takanohashi, T.; Iino, M.; Kumagai, H.; Sato, M.; Yokoyama, S.; Sanada, Y. *Energy Fuels* 1995, 9, 1003.



C:65.6, H:5.2, O:29.2 wt%

Mw:384.37

H-bond acceptor:7, H-bond donor:3

Figure 1 Unit structure assumed for YL model molecule.

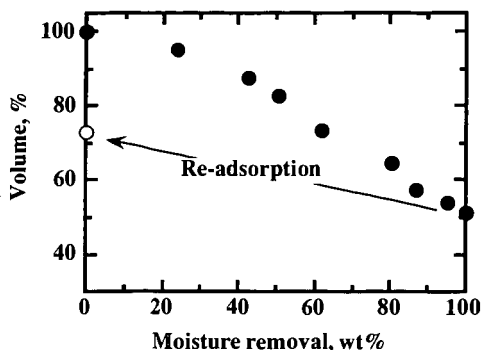


Figure 2 Volumetric change of YL during moisture release and re-adsorption process.

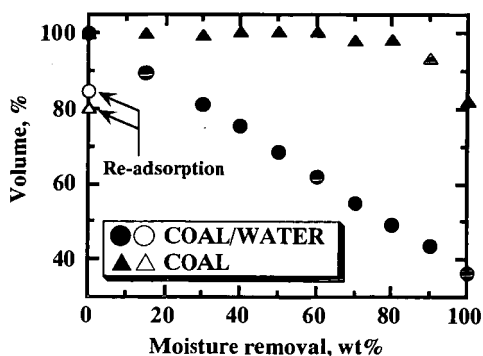


Figure 3 Volumetric change in YL model molecule with (COAL/WATER) and without (COAL) water molecules obtained with CAMD calculation.

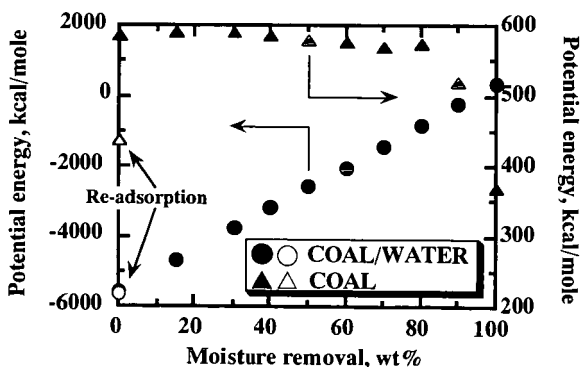


Figure 4 Variation in potential energies for YL model molecule with (COAL/WATER) and without (COAL) water molecules as a function of moisture removal.

ELECTRIC CHARGE REDISTRIBUTION INDUCED BY HYDROGEN BONDING IN LOW RANK COALS

Erik Kroo

Hydrocarbons Group, Advanced Fuel Research Inc.
87 Church Street, East-Hartford, CT 06108-3742

Keywords: hydrogen bonds, IR absorbance, apparent density

ABSTRACT

The nature of hydrogen bonds is predominantly electrostatic and strongly coupled to the environment in such a way, that formation or breaking of hydrogen bonds is accompanied by redistribution of electric charge among the participants. The intensity of infrared absorptions is related to charge separations along a particular bond. Therefore Fourier-Transform Infrared (FT-IR) spectroscopy is a promising tool to study the question whether charge separation in hydrogen bonding is important in coal. The objective of this study is to observe trends in infrared absorption intensities of hydrogen bonds, and in addition free OH and aliphatic deformation modes, as a function of moisture content in low rank coals, where hydrogen bonding is significant. FT-IR spectra of Zap lignite with varying moisture (0-22%) content were collected using the KBr pellet technique, and the spectra were curveresolved in the 3700-1900 cm^{-1} spectral region. The Mie theory of scattering was used for baseline correction and to calculate apparent density of coal particles. The data suggest that, in this particular lignite, charge redistribution as a result of hydrogen bonding is significant. It was observed that all of the measured quantities, i.e. the intensities of free OH, weak, medium and strong hydrogen bonds, aliphatic deformation modes as well as apparent density are influenced by the water monolayer buildup below 10% moisture, and that the direction of this influence reverses after saturation of the monolayer. A qualitative explanation of the charge redistribution mechanism involving polarization by hydrogen bond is given.

INTRODUCTION

Model calculations concerning quantitative aspects of hydrogen bonding in coal require that other noncovalent interactions, such as van der Waals forces, ionic and charge transfer type interactions, be more or less separable from hydrogen bonding. However, considering the nature of hydrogen bonds, this might not be true for coal. It is widely accepted that the nature of hydrogen bond is strongly electrostatic [1,2]. Consequently, the formation or breaking of hydrogen bonds is accompanied by redistribution of charge among the participants. Hydrogen bonds are also strongly coupled to the environment. For example, it was shown that in polypeptide chains hydrogen bonding and π - π stacking reinforce each other [3]. Quantum mechanical calculations reveal that a small change in the interaction potential originating from the vicinity of the hydrogen bond may lead to large-scale change in the bonding [4,5]. This interaction may be enhanced by the cooperative behavior of certain electric charges in coal. As a result this charge redistribution may well be extended beyond the participating coal molecules. Perhaps a good example of this is that coal can sustain and stabilize free electrons by delocalization along a larger condensed aromatic segment. Moreover, Flowers and coworkers [6] reported that the electron transfer to coal was a bulk property. If secondary effects of hydrogen bonding in coal are significant, it concerns important aspects of volumetric swelling theories like the separation of physical intermolecular interactions from hydrogen bonding interactions [7,8], and also dynamic properties of hydrogen bonding [8]. Another question is whether coal swelling can properly differentiate between free and hydrogen bonded OH functionalities [9] and/or inter and intramolecular hydrogen bonds. Since the intensity of infrared absorptions are related to charge separations along a particular bond, infrared spectroscopy seems to be a suitable tool to study this question. As a bonus to this approach, the apparent density of the coal particles can be calculated by applying Mie theory of scattering on the infrared spectra [10]. Water is natural to the coal structure and it was assumed that its presence in varying concentrations would invoke gradual changes in hydrogen bonding. A low rank coal (Zap lignite, Argonne Premium Coal Bank) was chosen in this work to study this question because of its capability to absorb significant amounts (up to about 26%) of moisture.

EXPERIMENTAL

The Zap lignite was dried in vacuum oven for 24 hours at 107 $^{\circ}\text{C}$ to decrease the moisture content to about 1.5%. The residual moisture was estimated by the TG-FT-IR technique [11]. The samples with varying moisture content were prepared by mixing wet (26%) and dried (1.5%) samples, and equilibrating them in sealed vials for one month. Fourier Transform Infrared (FT-IR) spectra were collected using the KBr pellet technique [12]. It was found that the

moisture equilibration between the coal particles and KBr at room temperature was very slow. However, at 107 °C in vacuum the moisture content of the coal particles in the KBr pellet could be decreased below 1.5%. A typical coal spectrum is shown in Fig.1. The sloping baseline is the result of light scattered by coal particles, and it can be corrected using the Mie theory [10] where the adjustable parameters are n (index of refraction), D (average particle size, μm) and d (particle density, g/cc). There are two regions with only scattering (above 3700 cm^{-1} and between $1800 - 1900\text{ cm}^{-1}$) to occur and scattering vanishes below $\approx 800\text{ cm}^{-1}$. Therefore the values of the d , n , and D could be determined iteratively through minimizing the integral functions

$$\int (I_{\text{Mie}}(d, n, D) - I_{\text{Spectr.}}) d(d, n, D) \quad 1.$$

All three adjustable parameters are known [10] to fall between $1 \leq d, n, D \leq 2$, I is the sum of adsorbances in the $3700\text{--}4500$ and $1800\text{--}1900\text{ cm}^{-1}$ region for the calculated (Mie) and measured (Spectr.) spectra with $I_{\text{Mie}} = 0$ below 800 cm^{-1} . The errors of the adjustable parameters, Δd , Δn and ΔD , were obtained through setting $\Delta d = 0.05$, and then estimating the corresponding errors of n and D ($\Delta n = 0.01$ and $\Delta D = 0.01$). This approach is valid, because the fit with the d , n , D parameters is excellent. n and D was constant within the error bar for all samples with $n=1.64$ and $D=1.50$.

The baseline-corrected spectrum of the 1.5% moisture sample is shown in Fig.1. It is also seen from this figure, that the pellet drying of this sample resulted in decreased hydrogen bond band intensities ($3600\text{--}3000\text{ cm}^{-1}$ region) but significantly increased the scattering. The additional scattering occurred on microcracks in the KBr pellet as a result of pellet drying. Therefore the Mie theory is not applicable to dried pellet samples without proper modifications. A rectilinear baseline correction [12] approximation was used in this particular case.

The conventional spectral deconvolution techniques usually fail if applied to spectra with highly overlapping bands [13,14]. An alternative approach used in this work is to choose available literature band assignments as the input parameters for the active IR bands in the $3700\text{--}1900\text{ cm}^{-1}$ spectral envelope. The input band positions were: free OH (3618 cm^{-1}) [15], weak (3560 ; 3495 cm^{-1}), medium (3450 ; 3409 ; 3300 ; 3204 ; 3122 cm^{-1}) [14-19] and strong hydrogen bonds (2741 ; 2555 ; 2372 ; 2215 ; 2043 ; 1902 cm^{-1}) [20], aromatic stretching vibrations (3040 cm^{-1}) [20] and aliphatic stretching and deformations (2960 ; 2935 ; 2900 ; 2870 ; 2840 cm^{-1}) [20,21]. The aromatic and strong hydrogen bond bands were broadband (bandwidths in the 100 cm^{-1} order) contributions, and the band shapes were Voigt functions [21]. The final band positions and shapes can be optimized by the curve-resolving routine (Spectra Calc., Galactic Ind.), but curve-resolving does not work well if narrow and broad bands overlap, which is the case for the aliphatic modes as seen in Fig.1. (between 3000 cm^{-1} and 2800 cm^{-1}). Therefore, the aliphatic absorptions were stripped off from the spectra and the two spectral fragments were curve-resolved separately.

RESULTS AND DISCUSSION.

Infrared intensity data. The total line intensity of a given $i \rightarrow j$ vibrational transition can simply be given as

$$I_{i,j} = \frac{h\nu}{3c} [(\mu_x^{(i)})^2 + (\mu_y^{(i)})^2 + (\mu_z^{(i)})^2] \quad 2.$$

where N is the Avogadro number, c is the speed of light and $\mu_{x,y,z}^{(i)}$ are the coefficients of the normal coordinate Q_k in the expansion of the electric moment

$$\mu_x = \mu_x^0 + \sum_{k=1}^{3N-6} \mu_x^{(k)} Q_k + \text{higher terms} \quad 3.$$

where the higher terms are thought to be small. The same can be written for the y and z components. The x component of the electric moment possessed by the molecule in its equilibrium position, μ_x^0 , is practically equal to the x component of the permanent electric moment and only vibrations that cause change in the electric moment are IR active. Since almost every molecule possesses sufficient symmetry, practically only one of the x, y, z components is different from zero. IR absorption of an intermolecular bond of the type $A - A$ may vanish because no dipole is generated by the vibration, but the IR absorptions in intramolecular hydrogen bonds may also vanish in molecules possessing sufficient conjugation in the vicinity of the hydrogen bond [22]. The same reduction occurs in stretching intensities of CH_3 , CH_2 and CH groups adjacent to double bonds [23]. Thus, the weakness of the IR intensity of a particular band is not necessarily connected with symmetry. Rather, charge transfer or conjugation compensates dipoles induced by the vibration. For this reason, trends in hydrogen bond and aliphatic stretching mode intensity changes can reflect charge redistribution in highly unsaturated materials like coal. On the contrary, free (non hydrogen-bonded) OH intensity is fairly proportional to the free OH concentration and is less effected by conjugation. It was found, that in lignites with increasing moisture content first a water monolayer is formed which is saturated at around 10% water [24,25]. Then a simple scenario for the coal macromolecule can be

described as follows. If water is added, the specific sites of the molecule will form hydrogen bonds with water, and the sites may be either hydrogen donor or acceptors depending on the electronegativity difference between water and the macromolecule. After the monolayer is filled up, hydrogen bonding between the second and first layer of water decreases the actual donor or acceptor character of the first layer, thereby changing the trend of charge transfer between water and coal as further water molecules are added. However, in heterogeneous complex aggregates like coal, these trends might be scrambled. The results are summarized in Table 1, and it is seen that samples with around 10% moisture are indeed distinct.

The free OH concentration is very low below 1.5% and it is maximum at 1.5% moisture. As a result of hydrogen bond formation with water, the free OH gradually decreases with filling up the water monolayer. Glass and Larsen [26] also observed the reaction of free OH with a number of organic bases. Free OH in coal can be stabilized sterically if there is no reacting partner in the immediate vicinity to form a hydrogen bond, or an existing hydrogen bond can be destabilized to form free OH through polarization by neighbors [5]. If the diminishing IR intensities below 1.5% water (see Table 1) were caused by partial decomposition of OH groups or other functionalities, it would not decrease significantly the free OH concentration, because the remaining OH groups will have an increased chance to remain free from interacting neighbors. A more suitable mechanism is intramolecular hydrogen bond formation coupled with increased conjugation. This supports a coal swelling model proposed by Painter and coworkers [27,28]. According to the model, the swelling of coal is associated with topological reorganization of the network rather than changing chain dimensions. Favoring intramolecular hydrogen bonding requires special folding of the macromolecules of which plenty of examples, especially among helical structures, exists in nature.

The change of aliphatic intensities (see Table 1.) as a function of water content is a proof, that the charge transfer as a result of hydrogen bond formation with water extends to, at least, a larger section of the coal molecule being involved in the hydrogen bonding. An intensity minimum was observed at around the monolayer saturation. The aliphatic stretching intensities decrease with electron transfer towards the aliphatic functionalities. With hydrogen bond formation the electron density increases at the donor site. Therefore a qualitative explanation is that the coal is the donor in the hydrogen bond with water.

The reduction, rather than the increase, of hydrogen bond intensities with the water monolayer buildup can also be related to the water monolayer buildup. As additional hydrogen bonds are formed, the donor strength of coal is decreased reducing the electronegativity difference between coal and water and increasing the symmetry of the hydrogen bonds.

Apparent density data. Fig. 2 shows the calculated apparent (or particle) densities as a function of moisture. Using the linear relationship established by Suuberg and coworkers [29] for the swelling of Zap lignite with water, the proportional decrease of apparent density with moisture content can be predicted. The same trend is expected from comparing the true (He) density (1.55 g/cc) [30] with water density (1.31 gr/cc, measured in our lab). Note, that the "water density" which is the true density of coal saturated with water (in place of He), is an approximation of the apparent density of water saturated coal. The apparent "swelling" densities in Fig.2 were calculated from the linear relationship (Suuberg) by normalizing the actual value at 1.5% moisture to 1.09, which is the average "Mie" density between 1.5 and 10% water. It is seen that, while the apparent "Mie" density is identical with the "swelling density at 1.5 and 21.8% water content, the change with water is not gradual, but rather abrupt at the monolayer saturation point. It is possible, that this is due to the particle size difference between the two type of experiment. The size of coal particles in the KBr pellets was 1.5 μm , therefore the presence of macropores larger than about half of that ($\approx 0.6 \mu\text{m}$) could be excluded. If the ratio of larger than $\approx 0.6 \mu\text{m}$ pores abruptly changes after the monolayer fill-up, this would explain the discrepancy between the scattering and macroscopic measurement techniques.

CONCLUSIONS

Infrared absorption intensities in the 3700-1900 cm^{-1} spectral region have been measured as a function of moisture in Zap lignite. The trends in absorption intensity changes as a function of moisture content can be related to water monolayer and subsequent secondary layer buildup. The polarization of hydrogen bonds changes direction at the monolayer saturation ($\approx 10\%$ water). These data suggest that the electric charge redistribution resulting from hydrogen bond formation and/or breaking in low rank coals is significant.

ACKNOWLEDGMENTS

The author is thankful to E.M. Suuberg and M. Serio for helpful criticism. The help of S. Charpenay in providing the Mie scattering software is gratefully acknowledged. The FT-IR spectra utilized in this work were collected under the U.S. Department of Energy contracts DE-AC22-88C88814 and DE-FG05-93-ER81593.

REFERENCES

- Baur, W.H. *Acta Cryst.* **1965**, 19, 909.
- Yamabe, S.; Morokuma, K. *J. Am. Chem. Soc.* **1975**, 97, 4458.
- Schall, O.F.; Gokel, G.W. *J. Org. Chem.* **1996**, 61, 1449.
- Hall, G.G. *Theor. Chim. Acta* **1985**, 67, 439.
- Schmidt, P.P. *J. Phys. Chem.* **1993**, 97, 4249.
- Flowers, I.I., R.A.; Gebhard, L.; Larsen, J.W.; Sanada, Y.; Sasaki, M.; Silbernagel, B. *Energ. Fuels* **1994**, 8, 1524.
- Panauiotou, C.; Sanchez, I.C. *J. Chem. Phys.* **1991**, 95, 10090.
- Painter, P.C. *Energ. Fuels* **1996**, 10, 1273.
- Larsen, J.W.; Gurevich, I. *Energ. Fuels* **1996**, 10, 1269.
- Solomon, P.R.; Carangelo, R.M.; Best, P.E.; Markham, J.R.; Hamblen, D.G. *Fuel* **1987**, 8, 897.
- Carangelo, R.M.; Solomon, P.R.; Gerson, D.J. *Fuel* **1987**, 66, 960.
- Solomon, P.R.; Carangelo, R.M.; *Fuel* **1982**, 61, 663 and **1987**, 67, 949
- Jackson, R.S.; Griffiths, P.R. *Anal. Chem.* **1991**, 63, 2557.
- Pierce, J.A.; Jackson, R.S.; Van Every, K.W.; Griffiths, P.R. *Anal. Chem.* **1990**, 62, 447.
- Painter, P.C.; Sobkowiak, M.; Youtcheff, J. *Fuel* **1987**, 66, 973.
- Solomon, P.R.; Hamblen, D.G.; Carangelo, R.M. *ACS Symp. Ser.* 205 **1982**, 4, 77.
- Gethner, J.S. *Fuel* **1982**, 61, 1273.
- Malhotra, V.M.; Jasty, S.; Mu, R. *Appl. Spectr.* **1989**, 43, 638.
- Karsen, J.W.; Baskar, A.J. *Energ. Fuels* **1987**, 2, 232.
- Solomon, P.R.; Hamblen, D.G.; Carangelo, R.M. in *Fuel Science ACS Symp. Ser.* **1982**, 205, 77.
- Friesen, W.I.; Michaelian, K.H. *Appl. Spectr.* **1991**, 45, 50.
- Detoni, S.; Hadzy, D.; Juranji, M. *Spectrochim. Acta* **1974**, 30A, 249.
- Bellamy, L.J. *The Infrared Spectra of Complex Molecules*. Chapman and Hall, London, **1975**, pg.20.
- Suuberg, E.M.; Otake, Y.; Deevi, S.C.; Yun, Y. *Int. Conf. on Coal Sci. Proc.* Butterworth-Heinemann Ltd. **1991**, pg.36.
- Lynch, L.J.; Barton, W.A.; Webster, D.S. *Int. Conf. on Coal Sci. Proc.* Butterworth-Heinemann Ltd. **1991**, pg.8.
- Glass, A.S.; Larsen, J.W. *Energ. Fuels* **1994**, 8, 629.
- Painter, P.C.; Graf, J.; Coleman, M.M. *Energ. Fuels* **1990**, 4, 393.
- Painter, P.C.; Shenoy, S.L. *Energ. Fuels* **1995**, 9, 364.
- Suuberg, E.M.; Otake, Y.; Langner, M.J.; Leung, K.T.; Milosavljevic, I. *Energ. Fuels* **1994**, 8, 1247.
- Smith, K.L.; Fletcher, T.H.; Pugmire, R.J. *The Structure and Reaction Processes of Coal*. Plenum Press, New York, **1994**, pg.164.

Table 1. Infrared intensities. Peak areas, arbitrary units.

wt% water	Partial sum of hydrogen bonds				Aliphatic		
	Free OH*	Weak**	Medium**	Strong**	CH ₃ *	CH ₂ *	CH*
< 1.5	0	7.1	55.0	46.1	1.5	4.3	2.1
1.5	11.8	36.8	133.7	66.0	1.6	4.9	1.9
4.3	10.2	45.7	131.1	148.4	1.8	4.8	1.9
8.9	9.2	44.9	125.5	62.9	0.7	3.8	1.2
10.3	5.2	20.3	93.3	63.8	1.4	3.5	1.7
16.2	5.8	31.8	95.9	53.1	1.7	4.6	2.0
21.8	2.2	11.3	85.9	12.2	2.3	5.1	2.6

* Dry coal basis

** Wet coal basis

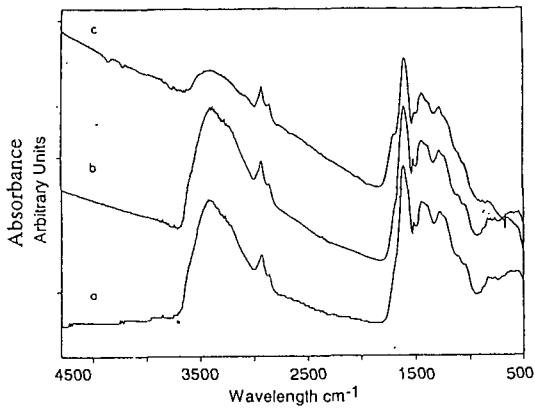


Figure 1. FT-IR spectra of Zap (1.5% moisture) a) after baseline correction; b) before pellet drying; and c) after pellet drying.

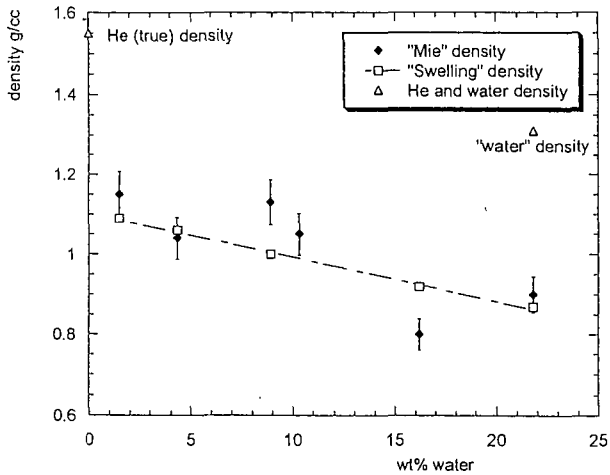


Figure 2. Comparison of calculated apparent densities. The "swelling" densities were derived from literature swelling data (Suuberg et.al. [29]) and normalized to 1.09 at 1.5% moisture, while the "Mie" density was calculated from FT-IR scattering data using the Mie theory of scattering and the KBr pellet technique. In addition the true (He) density [30] (dry coal) together with the water density (wet coal) is also shown.

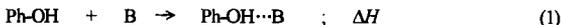
***In Situ* F.T.I.R. MEASUREMENT OF THE CHANGE IN HYDROGEN BONDING OF COAL THROUGH HEAT TREATMENT**

Kouichi Miura*, Kazuhiro Mae, Li Wen, Takumi Kusakawa and Akiko Kumano
Department of Chemical Engineering, Kyoto University, Kyoto 606-8501, Japan

INTRODUCTION

It is well known that hydrogen bonding plays an important role to keep the macromolecular structure of coal.¹⁻⁵ Several attempts have been made to estimate the amount and the strength of hydrogen bonding in coal. However, no definite methods have been presented for the estimation. One of the difficulties encountered for the estimation is the distribution of hydrogen bonding, and another problems associated with the estimation is the effect of adsorbed water. F.T.i.r. is believed to be a most powerful and convenient method to estimate the hydrogen bonding.⁶⁻¹¹ The water problem can not be completely overcome when the KBr pellet method was used, although the method is said to be suitable to quantitative studies.⁹ Fuller and Smyrn¹⁰ showed that the *in-situ* diffuse reflectance i.r. Fourier transform (DRIFT) technique with neat, undiluted, coal samples can be well utilized to trace the *in-situ* reactions such as oxidation, dehydration, etc. Painter *et al.*⁷ clarified the attribution of hydrogen bonded absorption bands ranging from 2800 to 3600 cm⁻¹. It is known that the absorption wave number of hydrogen bonded OH stretching vibration shifts from that of free OH by Δν_{OH}, and that the Δν_{OH} value increases with the increase of the strength of hydrogen bonding.

In liquid phase hydrogen-bonded adduct formation reactions between phenolic OH groups and various bases (B) have been examined in detail.¹²⁻¹⁵



where ΔH (< 0) is the enthalpy change of the reaction, and -ΔH is regarded as the strength of hydrogen bonding in general. Δν_{OH} (>0) for this reaction is the wave number difference between the free OH in Ph-OH and the hydrogen bonded OH in Ph-OH⋯B. Through separate measurements of ΔH [kJ/mol] and Δν_{OH} [cm⁻¹] for many phenol-base combinations a linear relationship was found to hold between them by many investigators. The relationship obtained by Drago *et al.*¹³, for example, is given by

$$-\Delta H = 0.067\Delta\nu_{\text{OH}} + 2.64 \quad (2)$$

For solid-gas interactions, Kiselev¹⁶ found that a linear relationship between the heat of adsorption, ΔQ_a [kJ/mol], and the Δν_{OH} [cm⁻¹] for a hydroxylated silica surface and various vapors including steam. It was represented by

$$\Delta Q_a = 0.064\Delta\nu_{\text{OH}} - 1.16 \quad (3)$$

These works clarified that the OH wave number shift caused by the formation of hydrogen bonding is well related to the enthalpy change of the hydrogen bonding formation. However, neither the distribution nor the amount of hydrogen bonding were not taken into account in these works.

Recently Miura and his co-workers¹⁷ have presented a method to estimate the strength distribution of hydrogen bonding (HBD) in coal by use of F.T.i.r. and DSC. The method was developed by combining and extending the works of Drago *et al.*, Painter *et al.*, and Kiselev. They found the following -ΔH vs. Δν_{OH} relationship for water free coals:

$$-\Delta H = 0.069\Delta\nu_{\text{OH}} \quad (4)$$

In their analysis, however, F.T.i.r. measurements were performed using the KBr pellet technique, and hence the water effect might not be completely eliminated. Furthermore, the absorption coefficients for different hydrogen bonded OH were assumed to be same as the first approximation. The latter assumption affects the amount of hydrogen bonding but does not affect the -ΔH vs. Δν_{OH} relationship given by eq 4.

To overcome these weak points in the former analysis, an *in-situ* diffuse reflectance F.T.i.r. (DRIFT) technique was employed for the measurement of spectra, and the change in absorption coefficients was taken into account in this paper. The improved method was applied to estimate the change of hydrogen bonding during the heating of the Argonne premium coals from 30 to 290 °C.

ANALYSIS METHOD

The method to obtain the HBD was originally presented in a previous work.¹⁷ The method was improved in this paper by taking into account the change in absorption coefficients for different hydrogen bonded OH groups. The procedure to obtain the HBD by the improved method is summarized as follows:

1. Divide F.T.i.r. spectrum ranging from 2200 to 3700 cm⁻¹ into several hydrogen bonded peaks by a curve fitting method as schematically given in Fig. 1(a). The Gaussian distribution was assumed for each absorption band in this work. Three peaks associated with aromatic and aliphatic CH stretch vibrations are easily eliminated from the spectrum.
2. Estimate the amount of OH for the j-th peak, (n_{OH})_j, by the Beer law as follows:

$$(n_{\text{OH}})_j = \alpha_j A_j \quad (5)$$

where A_j and α_j are respectively the integral intensity and the absorption coefficient of the j-th peak. In this analysis α_j was assumed to be represented by the equation presented by Detoni *et al.*¹⁸ for the hydrogen bonded NH groups

$$\alpha_j = \frac{\alpha_0}{1 + 0.0141(\Delta\nu_{\text{OH}})_j} \quad (6)$$

where α_0 is the absorption coefficient of the stretch vibration of the free OH. Then the amount of the OH corresponding to the j -th peak, $(n_{OH})_j$, is given by

$$(n_{OH})_j = \frac{\alpha_0}{1 + 0.014(\Delta \nu_{OH})_j} A_j \quad (7)$$

3. Calculate the strength of j -th hydrogen bonding, $(-\Delta H)_j$ by eq. 3 as

$$(-\Delta H)_j = 0.069 (\Delta \nu_{OH})_j \quad (8)$$

4. $(n_{OH})_j$ vs. $(-\Delta H)_j$ relationship gives the distribution of the strength of hydrogen bonding as shown schematically in Fig. 1(c).

Table 1. Ultimate analyses and oxygen distribution of 8 Argonne premium coals used [wt%]

Coal (abbrev.)	Ultimate analysis [d.a.f.]				Oxygen content [d.a.f.]			
	C	H	N	O(diff)	as COOH	as OH	as C=O	as Ether
Beulah-Zap (ND)	72.9	4.8	1.2	20.1	3.81	9.16	1.96	2.28
Wyodak (WY)	75.0	5.4	1.1	21.0	3.33	7.68	0.74	2.56
Illinois #6 (IL)	77.7	5.0	1.4	13.5	0.23	5.86	0.93	0.57
Blind Canyon (UT)	80.7	5.8	1.4	13.5	0.23	5.22	0.63	3.68
Lewinston-Stockton (ST)	82.6	5.3	1.6	9.8	0.20	2.70	0.18	2.67
Pittsburg#8 (PITT)	83.2	5.3	1.6	8.8	0.16	4.32	0.18	2.08
UpperFreeport (UF)	85.5	4.7	1.6	7.5	0.14	1.96	0.44	0.36
Pocahontas (POC)	91.1	4.4	1.3	2.5	0.05	0.98	0.32	0.24

EXPERIMENTAL

Coals samples. Eight Argonne premium coals were used as samples. The ultimate analyses and the amount of OH and COOH oxygen¹⁹ are given in Table 1. Coal samples -200 mesh were further ground for 1 minute in a mortar just before measurement.

Apparatus and procedure. All the IR spectra were measured at 4 cm^{-1} resolution on a JEOL JIR-WINSPEC50 F.T.i.r. spectrometer with a microscope stage. A Mettler 84HPT hot stage, shown schematically in Fig. 2, was attached to the microscope stage for the *in-situ* measurement. A mirror, which is believed not to absorb water, was used as a background. About 0.5 mg of neat coal samples were leveled and pressed on the mirror by hand using a spatula. It is essential to make a flat surface for obtaining good and reproducible spectra. The coal samples were equilibrated at 30 °C in a flowing nitrogen stream. Then they were heated at the rate of 5 K/min up to 300 °C during which nitrogen was continually supplied at the rate of 100 cc/min to prevent any possible leakage of air into the chamber and to keep the stability of the temperature. A BaF₂ disc was put on the pin hole from where the light passes through. The light source was a heated Ni-Cr wire and the detector was MCT (mercury cadmium-tellurium). F.T.i.r. spectrum was collected by acquisition of 100 scans at every 20 °C of interval.

RESULTS AND DISCUSSION

Change of spectra with heating. Figure 3 shows the *in-situ* F.T.i.r. spectra ranging from 2200 to 3650 cm^{-1} for four coals measured at every 20 °C. One of the problems encountered by many investigators in using *in-situ* F.T.i.r. was the spectra quality at high temperatures due to change in refractive index. Very beautiful and reproducible spectra could be obtained by use of the proposed measurement technique for all the coals in this work. Very flat base lines were obtained at all the temperatures, and the spectra for POC were almost same above 70 °C. This suggested that the spectra were not affected by the heating. Separate experiments were performed using kaolinite to check the change of spectra with increasing temperature up to 350 °C. The mirror backgrounds at 30 °C and at corresponding temperatures were used respectively to get the F.T.i.r. spectra. The spectra do not change with the background at different temperatures. Then all the spectra shown in this work were obtained using the background at 30 °C. This made the *in-situ* measurement convenient, fast and reliable.

To get accurate information of hydrogen bonded OH groups, it is essential to ensure that the artifact does not exist during experiments and/or during the data processing after experiments. It is easily checked by tracing the change in the aliphatic and aromatic C-H bands. Because the C-H bond is hard to decompose or to form below 300 °C, we can easily know whether some artifact exists or not from the variation of the 2890 and 2930 cm^{-1} bands (the absorption of aliphatic C-H bond), and 3050 cm^{-1} band (the absorption of aromatic C-H bond). It was found that these intensities were not affected by the temperature up to 300 °C. Therefore, all the changes in the OH spectra were really what happened in coal during the heating. Now, significant changes in the OH spectra were judged to occur for ND and WY coals, whereas very little change was judged to occur for PITT and POC coals during the heating for the four coals given in Fig. 2.

Change in strength distribution of OH associated with hydrogen bondings. All the spectra measured for the eight coals were analyzed by the procedure given above to estimate the change in HBD through the heating. Figure 4 shows the result of peak division and the HBD distributions obtained for ND as an example. The spectra ranging from 2200 to 3650 cm^{-1} were divided into 9 peaks by a curve-fitting method. The peak assignments were determined as follows by referring to the work of Painter *et al.*⁷: six hydrogen bonded bands (HB1 at 3516 cm^{-1} ; OH- π , HB2 at 3400 cm^{-1} ; OH-OH, HB3 at 3280 cm^{-1} ; OH-ether, HB4 at 3150 cm^{-1} ; cyclic OH-OH, HB5 at 2940 cm^{-1} ; OH-N, and HB6 at 2650 cm^{-1} ; COOH-COOH) and three C-H bands (3050, 2993, and 2920 cm^{-1}). No free OH band was detected for all the coals. In actual peak

division the peak positions were slightly changed, depending on the sample by referring to the second derivative of each spectrum. The bands for the C-H bonds did not change during the heating, then they were easily separated from the hydrogen bonded bands. The amount of OH and the strength of each hydrogen bonding were calculated from each peak intensity, A_j , and the OH wavenumber shift, $\Delta\nu_{\text{OH}}$, with the aid of eqs 7 and 8, where the total OH value given in Table 1 was used as the value at 150 °C to estimate α_0 in eq 7. The strength distributions of hydrogen bonding thus estimated, $(n_{\text{OH}})_j$, vs. $(-\Delta H)_j$ relationships, for ND are shown in the right of Fig. 4. It is clearly shown that the amount of weakly hydrogen bonded OH preferentially decreases with the increase of temperature.

Quantitative analysis of change in hydrogen bonding during the heating. The changes of the amounts of the six hydrogen bonded OH with increasing temperature are shown for four coals in Fig. 5. As is expected from the spectra shown in Fig. 4, the amounts of HB1 to HB4 decrease significantly with increasing temperature for ND and WY, whereas all the hydrogen bondings do not change with increasing temperature for POC. The decrease in the total amount of OH with increasing temperature is related to the formation of H_2O . It is noteworthy that only the distribution changes without affecting the total amount of OH for PITT above 230 °C. This means that stronger hydrogen bonding, HB5, shifted to weaker hydrogen bondings, HB1 and HB2, above 230 °C.

To examine the change in the hydrogen bonding in more detail, total enthalpy for the formation of all OH associated hydrogen bondings, $(-\Delta H)_{\text{total}} (< 0)$, at each temperature was calculated by

$$(-\Delta H)_{\text{total}} = \sum_j (n_{\text{OH}})_j (-\Delta H)_j \quad [\text{kJ/kg}] \quad (9)$$

Utilizing $(-\Delta H)_{\text{total}}$ and the total amount of OH groups, $(n_{\text{OH}})_{\text{total}}$, the average strength of hydrogen bonding, $(-\Delta H)_{\text{av}}$, can also be calculated by

$$(-\Delta H)_{\text{av}} = \frac{(-\Delta H)_{\text{total}}}{(n_{\text{OH}})_{\text{total}}} = \frac{\sum_j (n_{\text{OH}})_j (-\Delta H)_j}{\sum_j (n_{\text{OH}})_j} \quad (10)$$

The $(-\Delta H)_{\text{total}}$ values and the $(-\Delta H)_{\text{av}}$ values are shown in Fig. 5 and Fig. 6, respectively. $(-\Delta H)_{\text{total}}$ decreases with the increase of temperature due to the changes in the hydrogen bondings. When the number of total OH groups does not change, the decrease in $(-\Delta H)_{\text{total}}$ is due to the rearrangement of hydrogen bondings. When H_2O is produced during the heat treatment, the number of OH groups decreases by the two mechanisms, and consequently $(-\Delta H)_{\text{total}}$ decreases. The first mechanism is the desorption of adsorbed water and the other is the formation of H_2O by the decomposition of two OH groups. For ND and WY, both $(-\Delta H)_{\text{total}}$ and $(n_{\text{OH}})_{\text{total}}$ decreased with increasing temperature, indicating that the change in $(-\Delta H)_{\text{total}}$ is brought about by the formation of water. On the other hand, for PITT above 230 °C, only the $(-\Delta H)_{\text{total}}$ value decreased without affecting the value of $(n_{\text{OH}})_{\text{total}}$. This indicates that the rearrangement of hydrogen bondings occurred at above 230 °C as stated above. This rearrangement may be associated with the glass transition as detected by DSC by several investigators.^{20,21}

The changes in the average hydrogen bonding strength, $(-\Delta H)_{\text{av}}$, in Fig. 6 are also informative. The $(-\Delta H)_{\text{av}}$ values are around 20 to 24 kJ/mol-OH and kept almost constant during the heating for ND, WY, UT and IL. The $(-\Delta H)_{\text{av}}$ value for PITT is around 23 kJ/mol-OH below 230 °C, but it decreases to 20 kJ/mol-OH above 230 °C, indicating that the glass transition occurred between 230 to 270 °C. For high rank coals of UF and POC, the $(-\Delta H)_{\text{av}}$ values are 28 to 30 kJ/mol-OH, which are larger than for the other coals by 4 to 8 kJ/mol-OH. The $(-\Delta H)_{\text{av}}$ value for UF also decreased to 23.7 kJ/mol-OH above 230 °C, again indicating the occurrence of the glass transition. The $(-\Delta H)_{\text{av}}$ values estimated here are rather close to the values reported as the strength of hydrogen bonding in the literature.¹⁻³ A little bit larger $(-\Delta H)_{\text{av}}$ values for UF and POC are associated with the relative abundance of OH-N hydrogen bonding in these coals. It was clearly shown that the glass transition behavior can be detected from the change in $(-\Delta H)_{\text{av}}$ value for higher rank coals.

What we would like to stress here is that the value of α_0 is not required to calculate $(-\Delta H)_{\text{av}}$, as can be found from eqs 7, 8, and 10, which means that only F.T.i.r. spectra measurements are enough to obtain $(-\Delta H)_{\text{av}}$. This is a great merit of the proposed analysis method. Then the accuracy of the $(-\Delta H)_{\text{av}}$ values are well expected.

Differentiation between adsorbed water and decomposed water. It has been rather difficult to distinguish the chemisorbed water and the water formed by decomposition reaction, which made it difficult to define the dried state of coal. In this analysis we could estimate the changes in the amount of OH, $(n_{\text{OH}})_{\text{total}}$, and the enthalpy related to hydrogen bonding, $(-\Delta H)_{\text{total}}$, as shown in Fig. 5. Then we can estimate the change in the enthalpy related to hydrogen bonding with the formation of water by using the values of $(-\Delta H)_{\text{total}}$ and $(n_{\text{OH}})_{\text{total}}$ as

$$(\Delta H)_{\text{H}_2\text{O}} = 2 \frac{d(-\Delta H)_{\text{total}}}{d(n_{\text{OH}})_{\text{total}}} \quad [\text{kJ/mol-H}_2\text{O}] \quad (11)$$

where 2 in the r.h.s. was included to account for the fact that one H_2O molecule contains two OH groups. The magnitude of $(\Delta H)_{\text{H}_2\text{O}}$ thus estimated is well expected to be dependent on the mechanism of water

formation. Then the $(\Delta H)_{\text{H}_2\text{O}}$ values calculated by eq 11 with the aid of eqs. 7, 8, and 9 are shown against temperature in Fig. 7. The values obtained for an Australian brown coal (Morwell; MW) and a lignin are also included in the figure for comparison. The $(\Delta H)_{\text{H}_2\text{O}}$ vs. temperature relationships were so close each other, and there was a distinct jump at about 140 °C: the $(\Delta H)_{\text{H}_2\text{O}}$ values below 140 °C were close to or slightly smaller than the heat of vaporization of water, ΔH_{vap} , whereas the $(\Delta H)_{\text{H}_2\text{O}}$ values above 140 °C were significantly larger than ΔH_{vap} . These results suggest that the water detected below 140 °C is the chemisorbed water and that formed above 140 °C is the water formed by some decomposition reaction. Thus the HBD estimated by the proposed method is found to be utilized to distinguish the type of water formed. Finally we would like to stress that the value of α_0 or the value of $(n_{\text{OH}})_{\text{total}}$ is not required to obtain $(\Delta H)_{\text{H}_2\text{O}}$ as was the case to calculate $(-\Delta H)_{\text{H}_2\text{O}}$. Only F.T.i.r. spectra measurements are enough to obtain $(\Delta H)_{\text{H}_2\text{O}}$. This is a great merit of the proposed method and it simplifies the procedure to obtain $(\Delta H)_{\text{H}_2\text{O}}$.

CONCLUSION

In situ F.T.i.r. measurements were performed for the Argonne premium coals to estimate the change in hydrogen bonding through heat treatment. Neat, undiluted, coal samples were placed in a specially designed cell and they were heated from room temperature up to 300 °C in an inert atmosphere. F.T.i.r. spectra were collected in every 20 °C using the diffuse reflectance infrared Fourier transform (DRIFT) technique and the spectra ranging from 2200 to 3650 cm^{-1} were divided into 6 hydrogen bonded OH peaks and other peaks. The strength distribution of hydrogen bonding (HBD) at each temperature was well estimated through the analysis of the divided peaks by the proposed method. By utilizing the HBD the changes in enthalpies associated with the desorption of water, the glass transition, and the decomposition of OH groups were well estimated. Only F.T.i.r. spectra measurements were found to be enough to obtain such enthalpies. This greatly simplified the calculation procedure and increased the accuracy of the enthalpies. The validity of the proposed *in situ* F.T.i.r. measurement method and the analysis method for obtaining HBD was well clarified.

ACKNOWLEDGEMENT

This work was supported by "Research for the Future" project of the Japan Society for the Promotion of Science (JSPS) through the 148 committee on coal utilization technology of JSPS.

REFERENCES

- Larsen, J. W.; Green, T. K.; Kovac, J., *J. Org. Chem.*, **1985**, *50*, 4729-4735.
- Glass, A. S.; Larsen, J. W., *Energy & Fuels*, **1987**, *1*, 230-232.
- Larsen, J. W.; Baskar, A. J., *Energy & Fuels*, **1994**, *8*, 284-285.
- Arnett, E.M.; Tamweir, A., *Fuel*, **1993**, *72*, 1169-1176.
- Miura, K.; Mae, K.; Takabe, S.; Wakiyasu, H.; Hashimoto, K., *Energy & Fuels*, **1994**, *8*, 874-880.
- Solomon, P. R.; Carangelo, R.M., *Fuel*, **1982**, *61*, 663-669.
- Painter, P.C.; Sobkobiak, M.; Youtcheff, J., *Fuel*, **1987**, *66*, 973-978.
- Mu, R.; Malhotra, V. M., *Fuel*, **1991**, *70*, 1233-1234.
- Sobkobiak, M.; Painter, P.C., *Energy & Fuels*, **1995**, *9*, 359-363.
- Fuller, E.L. Jr.; Smyrl, N., *Fuel*, **1984**, *64*, 1143-1150.
- Chen, C.; Gao, J.; Yan, Y., *Energy & Fuels*, **1998**, *12*, 446-449.
- Purocell, K.F.; Drago, R.S., *JACS*, **1967**, *89*, 2874-2879.
- Drago, R.S.; Epley, T. F., *JACS*, **1969**, *91*, 2883-2890.
- Arnett, E. M.; Mitchell, E. J.; Murty, T. S. S. R.; Gornie, T. M.; Schleyer, P. V. R., *JACS*, **1970**, *92*, 2365-2377.
- Arnett, E. M.; Mitchell, E. J.; Murty, T. S. S. R., *JACS*, **1974**, *96*, 3875-3891.
- Kiselev, A. V., *Surface Science*, **1965**, *3*, 292-293.
- Miura, K.; Mae, K.; Morozumi, F., *Am. Chem. Soc., Div. Fuel Chem.*, **1997**, *42*(1), 869-876.
- Detoni, S.; Hadzi, D.; Smerkolj, R., *J. Chem. Soc. (A)*, **1970**, 2851-2859.
- Jung, B.; Sachel, S.; Calkins, W. H., Preprint, *Am. Chem. Soc., Div. Fuel Chem.*, **1991**, *36*(3), 869-876.
- Lucht, L.M.; Larson, J.M.; Peppas, N.A., *Energy & Fuels*, **1987**, *1*, 6-58.
- Yun, Y.; Sunberg, E. M., *Fuel*, **1993**, *72*, 1245-1254.

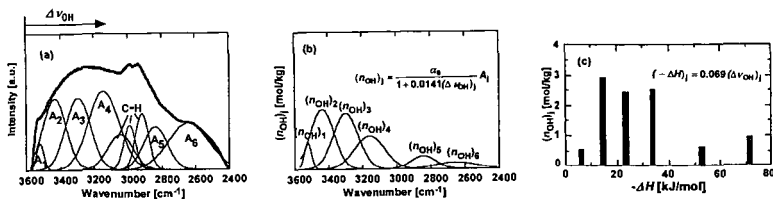


Figure 1 Procedure to obtain HBD from the spectra ranging from 2200 to 3650 cm^{-1} .

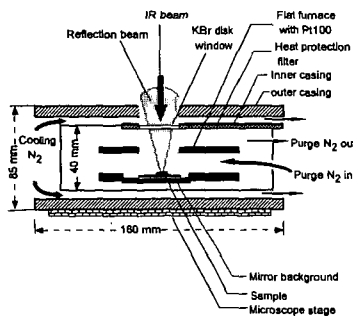


Figure 2 Schematic of a modified Mettler 84HPT hot stage used for *in-situ* FTIR measurements.

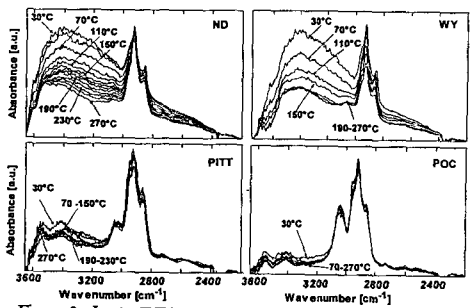


Figure 3 *In-situ* FTIR spectra measured at every 20 °C for four Argonne premium coals.

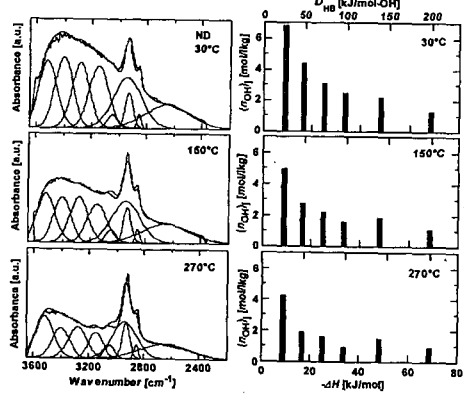


Figure 4 Typical examples of peak division of spectra and the HBDs estimated (ND coal).

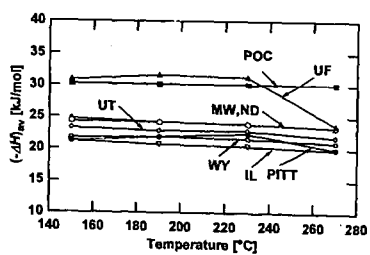


Figure 6 Change of $(-\Delta H)_{av}$ with increasing temperature for seven Argonne premium coals.

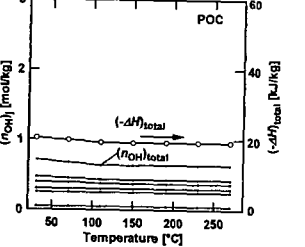
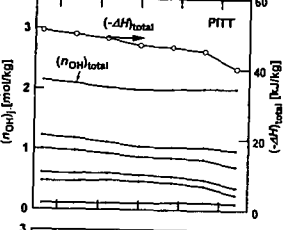
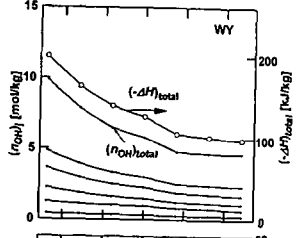
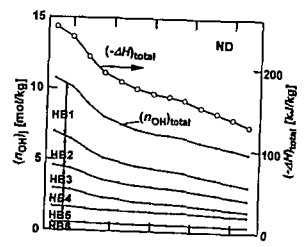


Figure 5 Change of (n_{OH}) , $(n_{OH})_{total}$ and $(-\Delta H)_{total}$ with increasing temperature for four Argonne premium coals

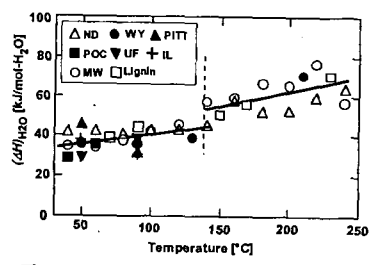


Figure 7 Change of $(\Delta H)_{T20}$ with increasing temperature for Argonne premium coals, MW coal and a lignin.

QUANTITATIVE DESCRIPTION OF OXIDATIVE DEGRADATION OF BROWN COAL IN AQUEOUS PHASE BASED ON LATTICE STATISTICS

Jun-ichiro Hayashi and Tadatoshi Chiba

Center for Advanced Research of Energy Technology, Hokkaido University
N13-W8, Kita-ku, Sapporo 060-8628, Japan

Keywords: Bethe lattice, O₂ oxidation, degradation

INTRODUCTION

Some recently developed pyrolysis models^{1,3} reasonably combine the kinetics of bridge breaking/formation with the Bethe lattice statistics^{4,5} that recognizes aromatic clusters and bridges as *sites and bonds*, respectively. The assumption of coal as a lattice can be examined by analyzing the characteristics of its degradation, which provides the measurable structural changes of coal, namely, the decrease in the bridge concentration and corresponding increase in the fraction of low-molecular-mass components released from the network. The relationship between these changes may be quantitatively described by assuming coal as a lattice having a particular chain configuration. The authors^{6,7} found that an O₂ oxidation in weakly alkaline aqueous phase solubilizes low rank coals to considerable extent. The oxidation increased the mass fraction of solvent-extractable material in a brown coal from 0.15 to 0.97. Analyses of the products revealed that aromatic carbon was selectively oxidized into carboxyls in the residual solid as oxidized coal, water-soluble non-aromatic acids and carbon dioxide, while aliphatic carbon was minimally involved in the reaction. Considering that the coal consists of aromatic clusters and inter-cluster bridges, they proposed a reaction mechanism that the oxidation converted aromatic carbons bonded to bridges into peripheral carboxyl groups on the neighboring clusters, and did the other aromatic carbons into non-aromatic acids or carbon dioxide. According to this mechanism as illustrated in Figure 1, the oxidation decomposes the macromolecular network of the coal by eliminating clusters as *sites* and converting bridges as *bonds* into peripherals. If the mechanism is valid, the extent of the degradation can be quantified by determining the amounts of lost bridges and clusters from those of formed carboxyls and oxidized aromatic carbon, respectively. In addition, the number of carboxyls formed as peripherals is expected to be equal to that of bridges which were bonded to eliminated clusters. The present paper examines the validity of the above-described mechanism of the oxidation and the applicability of general lattice statistics to the analysis of the degradation characteristics.

EXPERIMENTAL

Acid washed Morwell brown coal was oxidized at 85 °C for 1 – 12 h in an aqueous solution of Na₂CO₃, into which atmospheric oxygen gas was continuously bubbled. Details of the experimental procedure were described elsewhere⁷. The oxidized coal obtained through the oxidation for X h is hereafter referred to as SX. The oxidized coals were analyzed by a CP/MAS ¹³C-NMR, and the carbon type distributions of the individual samples were determined. Details of the measurements, peak assignment and curve resolution of spectra were reported previously⁷. The concentrations of carbonylic, carboxylic and phenolic groups were measured by means of oximation, ion exchange and acetylation, respectively. The samples were also subjected to exhaustive extraction with various single and mixed solvents at ambient temperature under ultrasonic irradiation. For the all samples, the mass fraction of solvent-extractable material was defined as that of material extracted with DMF that gave the greatest fractions among the solvents employed⁷. Molecular mass distribution of the extracts was measured by a laser desorption-ionization spectrometry (LD/MS) on a spectrometer (Japan Perseptive, model Voyager™ RP-DE). The spectra were observed in a linear mode under the following conditions: accelerating voltage; 25 kV, mass range; 50 – 100000, pressure; 1 – 2·10⁻⁷ torr. Pulses of a nitrogen laser operating at 337 nm was used for the laser desorption.

RESULTS AND DISCUSSION

The structural analyses determined the fractions of different types of carbon found in the oxidized coals: f_{CO} (carbonylic carbon), f_{COOH} (carboxylic carbon), f_{OH} (phenolic carbon), f_{a-e} (aromatic C bonded to ether), f_{a-c} (aromatic C bonded to carbon), f_{a-H} (protonated aromatic C), f_{a-o} (aliphatic C bonded to O other than methoxy carbon), f_{al-OCH_3} (methoxy), f_{al-CH_2} (methylene or methin at α position to aromatic C), f_{al-CH_2} (methylene at β position), f_{al-CH_3} (methyl at α position) and f_{al-CCH_3} (methyl at remote position). These fractions are indicated in the unit of mol-C per 100-mol C in S0. The fractions of total aromatic and aliphatic carbons, referred to as f_a and f_{al} , respectively, are defined as

$$f_a = f_{a-e} + f_{a-OH} + f_{a-c} + f_{a-H}$$

$$f_{al} = f_{al-O} + f_{al-OCH_3} + f_{al-CH_2} + f_{al-CH_2} + f_{al-CH_3} + f_{al-CH_3} + f_{al-acids}$$

$f_{al-acids}$ is the fraction of aliphatic carbon contained in non-aromatic acids. f_{a-e} was calculated by the difference between the fraction of oxygen-bonded aromatic carbon that was determined by the NMR and f_{a-OH} . Figure 2 shows f_a , f_{al} and f_{COOH} as a function of oxidation time. f_a decreases monotonously with time while f_{al} remains unchanged. It is also seen that f_{COOH} increases as the oxidation progresses. Here, the differences of f_a and f_{COOH} from those of S0 are defined as Δf_a and Δf_{COOH} , respectively. The figure also shows the change in the fraction of aromatic carbon bonded to bridges, f_{a-b} , which was calculated according to Solum et al.⁸.

$$f_{a-b} = f_{a-c} + f_{a-e} - (f_{cCOOH} + f_{a-OCH3} + f_{a-CH3} + f_{a-aCH3})$$

The decrease in $f_{a,b}$ with time indicates the loss of bridges by the oxidation. The total amount of bridges is calculated from a simple stoichiometry.

$$N_b = f_{a-b}/2$$

The loss of bridges, ΔN_b , is here defined as

$$\Delta N_b = N_b \text{ (for S0)} - N_b \text{ (for SX)}$$

When aromatic clusters are eliminated by the oxidation of aromatic carbon involved in them, the amount of eliminated clusters (ΔN_c) is expected to have a linear relationship with the loss of aromatic carbon leading to the elimination, defined as Δf_a^* . ΔN_c and Δf_a^* are expressed in the units of mol-cluster/100 mol-C in S0 and mol-C/100 mol-C in S0, respectively. They are related as

$$\Delta N_c = \Delta f_a^* / n_a$$

where Δf_a^* is the loss of aromatic carbon accompanied with the loss of an aromatic ring, and is a little smaller than the observed loss, Δf_a , due to the formation of a small amount of quinones that never contributes to the elimination of clusters. The calculation of Δf_a^* was described in our previous report⁷. n_a is the average number of aromatic carbon atoms per cluster. The number can be estimated from the abundance of bridgehead carbon relative to total aromatic carbon⁸. As reported previously, for S0 - S12, f_{b-a} was found to account for at most 4 % of f_a . Such appreciably small values of f_{b-a} indicate that the assumption of monoaromatic rings, in other words, n_a is 6 mol-C/mol-cluster, is reasonable for the all samples.

Figure 3 shows ΔN_b and Δf_{cCOOH} as a function of ΔN_c . ΔN_b is seen to be in good agreement with Δf_{cCOOH} as expected by the proposed mechanism of the oxidation, although some deviations are seen. Also, ΔN_b and Δf_{cCOOH} can be related linearly with ΔN_c at a slope of about 2.2. This means that 2.2 bridges are lost when an aromatic cluster is eliminated by the oxidation, and hence that each of the lost clusters was bonded to the same number of bridges in average. Moreover, the linear relationship itself should be noted when the mechanism of the oxidation is considered. As illustrated in Figure 1, the elimination of a cluster accompanies the formation of carboxyl groups at the chain ends of the neighboring clusters. As we described in the previous paper⁷, aromatic rings carrying carboxyls generally have oxidation reactivities orders-of-magnitude smaller than do those without carboxyls. Therefore the neighboring clusters may behave as inert ones after carboxyls are formed, while they also lose bridges initially connected to them. Thus, the elimination of clusters would occur non-randomly, producing deactivated clusters that accumulate as the oxidation progresses. Here, let us consider the degradation of a macromolecular network or lattice consisting of clusters and bridges, of which initial concentration of inter-cluster bridges is $n_{b,0}$ ($= 2 \cdot N_{b,0} / N_{c,0}$). The degradation is supposed to be caused by the elimination of clusters (or sites). In the case of a degradation involving deactivation processes as described above, the average number of bridges bonded to a remaining 'reactive' cluster is independent of $N_c / N_{c,0}$, and equals to the initial bridge concentration, namely $n_{b,0}$. Then, when a cluster is eliminated, $n_{b,0}$ bridges are always lost, and the following relationship holds.

$$n_b = 2N_b / N_c = 2 \{ N_{b,0} - n_{b,0} (N_{c,0} - N_c) \} / N_c = n_{b,0} \{ 2(N_c / N_{c,0}) - 1 \} / (N_c / N_{c,0}) \quad (1)$$

where $N_c / N_{c,0}$ is the fraction of remaining clusters to that before degradation and is a measure of the extent of cluster elimination. Figure 4 shows the observed n_b as a function of $N_c / N_{c,0}$ together with lines drawn on the basis of Eq.(1) assuming $n_{b,0} = 2.23$. The observed change of n_b is seen to be well explained by the equation, i.e., the non-random degradation. Eq.(1) can apply to any lattices having different dimensions, coordination numbers and bridge densities. Thus, the results shown in Figures 2-4 reveal that the changes in f_{cCOOH} , N_c and N_b are reasonably explained on the basis of the proposed oxidation mechanism, and are also quantitatively described by the assumption that the coal is a lattice with $n_{b,0}$ of 2.2, while other parameters such as the coordination number are so far unknown.

The above explanation of the change in n_b by Eq.(1) not only provides the initial bridge concentration but also allows us to analyze other characteristics of the degradation assuming that the coal is a lattice. Bethe pseudo lattices are statistical lattices, each of which has infinite number of sites and is defined by the coordination number (Z) and site occupation probability (p , $0 \leq p \leq 1$) that is the number fraction of occupied sites to the total number of sites. When two sites neighboring to each other are both occupied, they are recognized to be linked by a bridge. Another characteristic of Bethe lattices is that no loops are allowed in them. The absence of loops provides analytical solutions of states of the lattices by only giving the parameters, Z and p , and this is the reason why the coal is assumed to be a Bethe lattice in the models described below. For a Bethe lattice with Z and p , n_b is expressed as

$$n_b = Z \times p$$

When the degradation of the lattice occurs with a random site-elimination mechanism, a given probability p^* and corresponding bridge concentration n_b^* are related as follows.

$$n_b^* / n_{b,0} = p^* / p_0 \quad (2)$$

where p_0 is the site-occupation probability of the initial lattice with $n_{b,0} = Z \times p_0$. The lattice statistics can also provide the distribution of degree of polymerization. The possibility of that an occupied site belongs to m -mers, each of which consists of m sites and $(m-1)$ bridges, is given as

$$F_m(p^*) = m b_m p^{(m-1)} (1-p^*)^{m(2-2)+2}$$

where mb_m is the total number of configurations possible for m -mers. $F_m(p^*)$ is essentially the same as the fraction of m -mer with regard to the occupied-sites. Figure 5 shows the fractions of finite-sized m -mers as a function of p^* for the Bethe lattice with $Z = 3$. $F_{i,j}(p^*)$ seen in the figure is defined as

$$F_{i,j}(p^*) = \sum_{m=i}^{m=j} F_m(p^*)$$

Further details of the Bethe lattice statistics are well described in literature^{4,5}, and are therefore not done here. Eq.(2) that gives the relationship between the changes in n_b^* and p^* is applicable to the description of Bethe lattice degradation only when the elimination of sites occurs randomly (Case-I). In another case (Case-II) that the elimination of a site accompanies the deactivation of the neighboring sites as seen in the present oxidation, the elimination of a site results in the loss of $n_{b,0}$ bridges. Then, n_b at a site occupation probability, p , is expressed as

$$n_b/n_{b,0} = \{1 - 2(p_0 - p)/p_0\} / \{p/p_0\} \quad (3)$$

Eq.(3) is directly derived from Eq.(2), since $p/p_0 = N_c/N_{c,0}$. As shown in Figure 6, n_b in Case-II is smaller than n_b^* in Case-I when $p = p^*$. Essentially, degradation of lattice/network is brought about by the elimination of bridges, and in this sense, the extent of degradation could be evaluated on the basis of the decrease in the bridge concentration, i.e., n_b . Considering the above, p can be converted into another probability, p^{**} , that gives n_b equivalent to n_b^* . p^{**} is then calculated as

$$p^{**} = p_0 \{1 - 2(p_0 - p)/p_0\} / \{p/p_0\}$$

Thus, if the chemical network of the coal can be assumed to be a Bethe lattice, its degradation caused by the oxidation would be approximately described by a random degradation using p^{**} .

Here, a structural model of the coal are proposed and examined on the applicability to quantitative explanation of changes in the fraction of extractable material caused by the oxidation and molecular mass distribution of the material. The first model assumes the followings:

1. S0 consists of solvent extractable material and a fully developed network. The extractable material comprises of m -mers with m ranging from 1 - 40, while the network is described as a Bethe lattice with $p_0 = 1$ and thus $n_{b,0} = Z$.
2. The fractions of the network and extractable material in S0 are 0.85 and 0.15, respectively, which is based on the observed Y_{DMF} for S0, 0.15.
3. The concentration of bridges for the extractable material (referred to as $n_{b,0}^*$) is 1.8, which was determined by analyzing a CP/MAS ¹³C-NMR spectrum of DMF extract from S0.
4. When a site is eliminated, the probability of that the site belongs to the network is 0.85. This is based on the assumption that the network and extractable material have equivalent reactivity to the oxidation.
5. The solvent extractable material, given as DMF extract, consists of molecules whose degree of polymerization ranges from 1 to 40. The basis of this assumption is mentioned below.

In addition to the above, the second assumption for the model A is also considered in the model B. Figure 7 compares calculated $F_{1-40}(p)$ as a function of p^{**}/p_0 with Y_{DMF} . It should be noted that $F_{1-40}(p)$ strongly depends on Z and also agrees well with Y_{DMF} at $Z = 2.18$. In the model B, the bridge concentration of S0, namely $n_{b,0}$ is given as

$$n_{b,0} = 0.85Z + 0.15n_{b,0}^*$$

and then $n_{b,0}$ is calculated as 2.1 using $Z = 2.2$. This value of $n_{b,0}$ is in good agreement with that determined from the results shown in Figure 5, i.e., 2.2. This is, however, not enough to demonstrate the validity of the model B. The predicted distribution of molecular mass or degree of polymerization of the solvent extractable material should also be in agreement with that observed. Figure 8 illustrates LD/MS spectra of DMF extracts from S0, S3, S6, S9 and S12. The spectra reveal that the features common among the extracts from different oxidized coals; that the molecular mass distributes widely over the range from 100 up to 8,000 and that compounds with molecular mass of around 300 are the most abundant. Moreover, the distribution seems not to vary significantly with the extent of the oxidation. The distribution of molecular mass could be converted into that of degree of polymerization, by giving the average molecular mass of the monomeric unit. The average molecular mass, M_m , was calculated as about 200 by considering the carbon content, n_b and f_c . The value of M_m means that the degree of polymerization of the extracts ranges from 1 to approximately 40. This is the basis of that $F_{1-40}(p)$ is considered in the above-described models. Figure 9 shows the molecular mass distribution predicted by the model B assuming $M_m = 200$. The calculated distribution is little sensitive to the probability p^{**} as seen for the mass spectra of DMF extracts. It should also be noted that the distribution agrees well with that observed, although the quantitative comparison of them is difficult at present, due to that the molecular mass per monomeric unit itself should more or less distribute due to variety of chemical structure of peripherals and bridges.

CONCLUSIONS

The oxidation depolymerizes the coal by eliminating aromatic clusters. When a cluster is eliminated, the bridges that have been connected to the cluster are converted into peripheral chains of the neighboring clusters, and carboxyl groups are formed at the ends of the peripherals. The elimination of the cluster also accompanies the deactivation of the neighboring clusters due to the formed carboxyls. The mechanism of the oxidation allows us to describe the following relationships;

$$\Delta f_{\text{COOH}} = \Delta N_b \text{ and } \Delta f_{\text{COOH}} / \Delta N_c = \Delta N_b / \Delta N_c = n_{b,D} = 2.2$$

The model B, which assumes that coal is a mixture of a fully developed Bethe lattice with $Z = 2.2$ and $p_0 = 1$, and solvent extractable material with $n_{b,0} = 1.8$, reasonably predicts the observed increase in the fraction of DMF extractable material. The model can also predict the extract's molecular mass distribution semi-quantitatively as a function of p^{**} , the corrected.

ACKNOWLEDGMENT

This work was supported by a "Research for the Future Project" (Coordinator; Prof. M. Iino, Tohoku University) grant from The Japan Society for the Promotion of Science (JSPS), through The 148th Committee on Coal Utilization Technology.

REFERENCES

1. Niksa, S.; Kerstein, A.R. *Fuel* 1987, **66**, 1389.
2. Grant, D.M.; Pugmire, R.J.; Fletcher, T.H.; Kerstein, A.R. *Energy Fuels* 1989, **3**, 175.
3. Fletcher, T.H.; Kerstein, A.R.; Pugmire, R.J.; Solum, M.S.; Grant, D.M. *Energy Fuels* 1992, **6**, 414.
4. Stauffer, D. "Introduction to Percolation Theory" 1985, Taylor & Francis, London.
5. Stockmayer, W.H. *J. Chem. Phys.* 1943, **11**, 45
6. Hayashi, J.-i.; Matsuo, Y.; Kusakabe, K.; Morooka, S. *Energy Fuels* 1997, **11**, 284.
7. J.-i. Hayashi, Aizawa, S.; Kumagai, H.; Chiba, T.; Yoshida, T.; Morooka, S. *Energy Fuels* 1999, **13**, 69.
8. Solum, M.S.; Pugmire, R.J.; Grant, D.M. *Energy Fuels* 1989, **3**, 187.

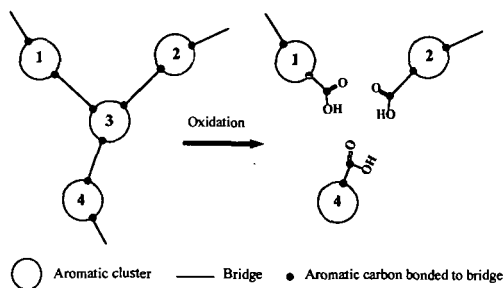


Figure 1. Elimination of aromatic cluster and conversion of inter-cluster bridge into carboxyl group by oxidation.

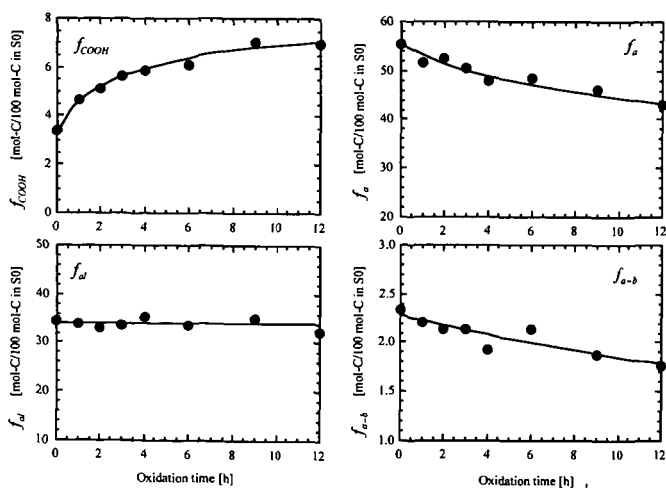


Figure 2. Fraction of different types of carbon, f_a , f_b , f_{COOH} and f_{a-b} , as a function of oxidation time.

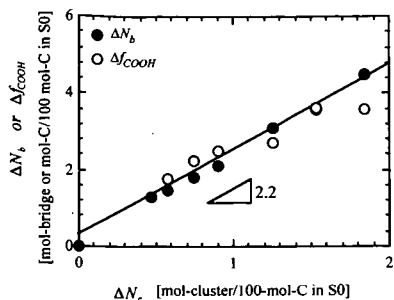


Figure 3. Δf_{COOH} and ΔN_b as a function of loss of aromatic clusters, ΔN_c .

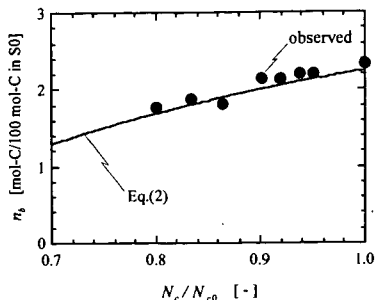


Figure 4. Observed and calculated n_b as a function of $N_c/N_{c,0}$.

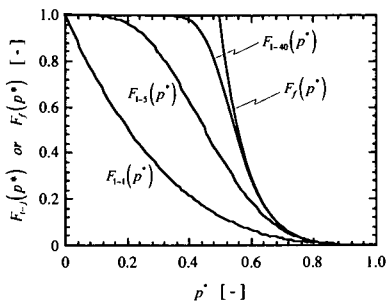


Figure 5. Fraction of site belonging to n -mers as a function of site-occupation probability, p^* .

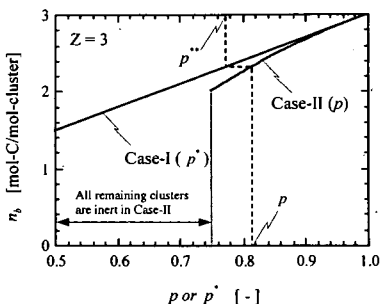


Figure 6. n_b^* as a function of p^* in random degradation (Case I), n_b as a function of p in non-random degradation (Case II) and p^{**} calculated from relationship between n_b^* and n_b .

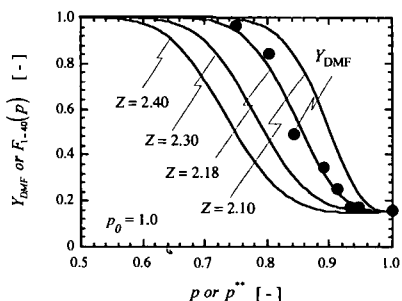


Figure 7. Fraction of DMF-extractable material, Y_{DMF} , as a function of normalized probability p^{**}/p_0 and its comparison with $F_{1-4}(p)$ predicted by model-B assuming different values of Z .

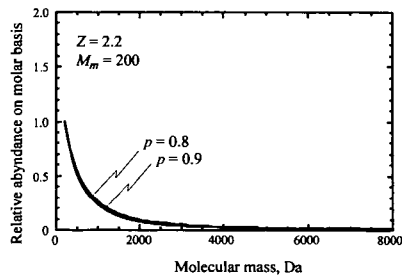


Figure 9. Molecular mass distribution predicted by model assuming $M_m = 200$.

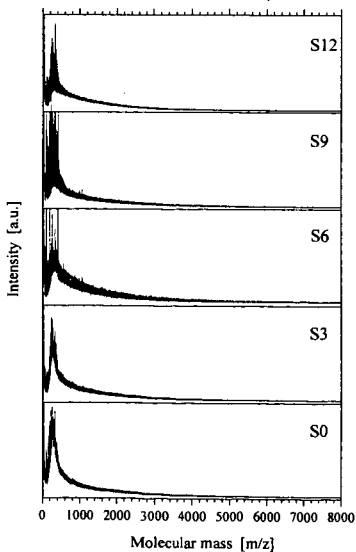


Figure 8. MALDI spectra of DMF extracts.

COAL DEGRADATION THROUGH EXTRACTION AND DEPOLYMERIZATION IN A FLOWING SOLVENT UNDER PRESSURE

Kouichi Miura*, Kazuhiro Mae, Hwang Yoo Seock, Ryuichi Ashida, and Masato Morimoto
Department of Chemical Engineering, Kyoto University, Kyoto 606-8501

INTRODUCTION

Solubilization and/or depolymerization are the initial steps of coal liquefaction, coking, or pyrolysis. Most of the solubilization/depolymerization experiments performed at rather high temperature in relation to coal liquefaction utilized a batch reactor, the so-called autoclave, where the interaction between the solubilized small molecules and the insoluble macromolecules can not be neglected. Furthermore, it is almost impossible to know the actual extraction yield at a high temperature using autoclave, because we can not separate the fraction which is soluble at the high temperature but is precipitated at room temperature from the residue. The solid recovered at room temperature after experiments is the mixture of the residue and the precipitated solid. Blessing and Ross¹ used a specially designed autoclave which is equipped with a basket assembly. Solvent can penetrate the basket through the glass frits fitted at the top and the bottom of the basket. Coal samples were placed in the basket assembly, and the extract was expected to come out from the basket through the glass frits. Unfortunately this trial was unsuccessful, because the diffusion rate of the deposit through the frit was very small. Flow reactors have been used by several investigators for examining the solubilization/depolymerization behavior of coal at a rather high temperature. Aida et al.² tried to extract coal in a flowing stream of solvent with an UV spectrometer as a detector. This enabled them to monitor the products continuously, but detailed analysis of the products has not been performed because of the experimental difficulty. Kandiyoti et al.^{3,6} have heated coal up to 450 °C in a flowing stream of solvent to avoid the secondary reaction. They have examined the effect of operating conditions in detail. Their interest was, however, the hydrogenation reaction above 400 °C, because their main research target was to examine the coal liquefaction mechanism.

We have recently found that some bituminous coals can be extracted up to 75 % in a flowing non-polar solvent at 350 °C without appreciable decomposition.⁷ At room temperature about a half of the extract were still soluble in the solvent and the rest half precipitated as solid. Both the soluble fraction and the precipitated solid were almost free from mineral matters, suggesting the possibility of preparing clean fuel from coal in high yield.

In this paper the solubilization/depolymerization experiments of eight Argonne premium coals were performed at 350 °C in a flow type reactor, where coal samples were heated in a flowing stream of tetralin. The purposes of this work were to examine the coal structure through detailed analyses of the extract and the residue, and to examine the possibility of preparing clean fuels and/or raw materials for the subsequent conversion. The possibility to decompose further the soluble, the precipitated solid and the residue recovered from Pittsburgh #8 coal was also examined.

EXPERIMENTAL

Coal Samples. Eight coals of the Argonne premium coals were used in this work. The analyses of these coal samples are given in Table 1.

Experimental Procedure for extraction/depolymerization. Figure 1 shows a schematic diagram of the apparatus used for extraction and/or depolymerization. 100 to 200 mg of coal samples were placed between two filters (11.2 mm OD and 0.5 mm opening) in a reactor made of Swagelok. Tetralin was supplied continuously using a high pressure pump at the flow rate of 1 ml/min. The pressure was regulated using a pressure regulating valve (TESCOM) at 10 MPa. The reactor was heated at the rate of 5 K/min to 350 °C where it was kept for 0 to 90 min, then it was cooled immediately by a sufficient amount of water to terminate the solubilization and/or depolymerization. The coal fraction extracted and/or depolymerized at the reactor temperature became soluble in the solvent and came out from the reactor with the flowing solvent, but a part of the solubilized components precipitated as solids when the solvent flow was cooled to room temperature. The solid thus precipitated, called "deposit" in this paper, was collected by 3 filters (20, 10, and 2 μ m openings) placed in series just before the pressure regulating valve. The deposit which passed these filters were collected in a separation trap with the soluble components at room temperature. The components soluble at room temperature are called "soluble" here. Product gas was collected in a gas bag, and analyzed using a gas chromatograph for the components smaller than C₆ hydrocarbons in molecular weight. Thus each coal sample was separated into the residue that is not extracted or depolymerized, the deposit, the soluble, and gaseous components. The weights of the residue and the deposit were directly measured after drying them in vacuo at 70 °C. The weight of gaseous components was calculated from the analysis using the gas chromatograph. The rest of the product was regarded as the soluble.

Decomposition of soluble and deposit. The deposit prepared from PITT was served to the flash hydro-pyrolysis and the pyrolysis in a liquid tetralin to examine the possibility to decompose the deposit further. The flash hydro-pyrolysis was performed using a small scale of batch reactor at 700, 800, and 900 °C at the residence time of 60 s. The decomposition of the soluble, the deposit and the residue in liquid tetralin was performed using a small batch reactor (6 ml in volume). About 50 mg of sample was placed with 5 ml of tetralin in the batch reactor. The whole reactor was immersed in a sand bath regulated at a temperatures between 380 to 450 °C, and kept there for 60 min. The products were separated into hexane-soluble fraction (HS), hexane-insoluble and tetralin soluble fraction (Tets-HI), residue and gas components by a similar procedure presented above.

Analyses of the products. The soluble, the deposit and the residue were characterized through various analyses. Ultimate analysis and SPE/MAS ^{13}C solid NMR analysis⁸ of the deposit and the residue were performed using a CHN coder (Yanaco, CHN-500) and a NMR spectrometer (Chemagnetics, CMX-300), respectively. The gel permeation chromatography (GPC) was used to estimate the molecular weight distribution of the deposit, because the more than 95 % of deposit could be solubilized in dimethylformamide (DMF). The packed column used is a Shim-pack GPC-8025 (Shimadzu), and an eluent DMF was supplied at the flow rate of 0.5 ml/min. The matrix-assisted laser desorption/ionization time-of-flight mass spectrometry (MALDI-TOFMS; Shimadzu/Kratos KOMPACT-MALDI-II) was used to estimate the molecular weight distributions of the soluble, the deposit, the residue, and the raw coal.

RESULTS AND DISCUSSION

Changes in yields of soluble and deposit with increasing temperature and extraction time. Figure 2 shows the changes in the yields of the soluble, the deposit, and the residue with increasing temperature and extraction time for IL coal. The soluble yield increased with the increase of temperature, reached 25% at 350 °C, and finally reached more than 30 % at the holding time (t_p) of 30 min at 350°C. On the other hand, the deposit yield was very small up to 350 °C while temperature is increased, but it increased gradually with the increase of holding time at 350°C and finally reached about 40% at $t_p = 60$ min or so. The increase of the soluble yield is judged to be brought about through the relaxation of coal structure upon heating in solvent, because most of the soluble was produced below 300 °C, in other words, the soluble was not produced through decomposition reaction. By keeping the coal for extended time at 350°C relatively large molecule components that are soluble in tetralin at 350 °C gradually came out from the coal particles. It would be because the intraparticle diffusion rate of the deposit is not so fast.

Figure 3 compares the ultimate product yields at 350 °C, which were arbitrarily defined as the yields at $t_p = 60$ min, for eight Argonne premium coals. The yields of soluble and deposit for bituminous coals, IL, PITT, and UF coals, were very large. The extract yields for these coals are as follows: 80 % (soluble: 41 %, deposit: 39 %) for UF, 67 % (soluble: 29 %, deposit: 38 %) for PITT, and 63 % (soluble: 27 %, deposit: 36 %) for IL. Surprisingly, 80 % of UF coal were extracted at 350 °C. For the lowest rank coal, ND, the deposit yield was very small and appreciable amount of gaseous components were produced. Both the soluble and the deposit yields were small for the highest rank coal, POC. These results indicate that decomposition reaction occurred for the lowest rank coal ND, but little decomposition reaction occurred for the other higher rank coals. Therefore, most of the soluble and the deposit for the higher rank coals are judged to be relatively small molecule components existent in the original coal. The small molecules could come out because the macromolecular network of coal was relaxed through the heat treatment in the solvent.

These results suggest that the structure of the bituminous coals used in this work is rather close to the model B of Nishioka (physically associated model).^{9,10} The soluble and the deposit are assumed to be physically associated each other and/or with the residue in the raw coal.

Ultimate analysis and ^{13}C NMR analysis. The above discussion clarified that 50 to 80 % of coal can be extracted with little decomposition by tetralin at 350 °C for bituminous coals. Then the solid products, the deposit and the residue, were characterized by various analyses to examine the change accompanying the extraction. Table 2 compares the ultimate analysis and ash content of the raw coal, the residue, and the deposit prepared at $t_p = 60$ min at 350°C for PITT and IL coals. Since the soluble concentration was very small and hence could not be subjected to the analyses, the numbers for the soluble in Table 2 were calculated by the proportional allotment from the data for the raw coal, the residue and the deposit using their yields given in Fig. 3. Although the ultimate analyses were not significantly different among the raw coal, the deposit, and the residue, the hydrogen content and the atomic H/C ratio of the residue were appreciably smaller than those of the raw coal and the deposit. As a result of this difference, the atomic H/C ratio of the soluble was the highest. This indicates that the soluble is richer in hydrogen than the other fractions. The most distinguishing result is that the soluble and the deposit contain little ash, which means most of ash remains in the residue. This presents the possibility to prepare clean fuel or clean raw materials in a high yield from bituminous coals by simple extraction.

Figure 4 compares the ^{13}C NMR spectra among the raw coal, the residue, and the deposit prepared at $t_p = 60$ min at 350°C for PITT. The carbon distributions estimated from these spectra are given in Table 3. Again the carbon distribution for the soluble was calculated by the proportional allotment from the distributions for the raw coal, the residue, and the deposit by assuming that no decomposition reaction occurred during the extraction. Although the distributions for the raw coal, the residue, and the deposit are rather close, the proportions of methyl groups ($-\text{CH}_3$) and methylene bridge ($-\text{CH}_2-$) are smaller and the proportions of the bridgehead carbon (Bridgehead) are larger in the deposit and the residue than in the raw coal. These differences reflected on the difference in the values of the aromaticity index, f_a , of the raw coal, the residue, and the deposit: they are 0.733, 0.785 and 0.782, respectively. The calculated carbon distribution for the soluble shows that the soluble is rich in methyl groups and methylene bridge and the proportions of the bridgehead carbon is small, resulting in the small f_a value of 0.650. These results are consistent with the ultimate analyses shown in Table 2.

Above results suggest that soluble is the fraction consisting of small and more aliphatic molecules in the original coal, and that the average chemical structure of the raw coal, the residue, and the deposit are very close. This circumstantially supports the above discussion concluding that bituminous coals were extracted with little

decomposition below 350 °C. Then the detailed analyses of the soluble, the deposit, and the residue will give us a more realistic picture of bituminous coals.

Molecular weight distribution of soluble, deposit and residue. We have clarified that the molecular weight distribution (MWD) can be well estimated by the MALSI-TOFMS method for molecules less than 5000 in molecular weight by comparing the MALDI and the GPC measurements for a deposit solubilized in dimethylformamide (DMF).⁷ Then Figure 5 compares the MWDS measured by the MALSI-TOFMS method for the soluble, the deposit and the residue prepared from PITT at $t_f = 60$ min at 350 °C with the MWD of the raw PITT coal. The MWDS for the raw coal, the residue and the deposit are all bimodal having peaks at $M_w = \text{ca. } 300$ and $\text{ca. } 2200$. The M_w of the peak position for the larger molecules in the deposit seems to be slightly smaller than that in the residue. On the other hand, the soluble consists of only small molecules of less than 600 in M_w , and the peak position almost coincides with the peaks of smaller M_w in the raw coal, the residue and the deposit. These results again support the model B of Nishioka for the structure of PITT. The deposit and the residue still contain the small molecule components which could not be dissociated at 350 °C.

Decomposition of soluble, deposit and residue in tetralin. The soluble, the deposit and the residue prepared from PITT were heated in tetralin at 380 to 450 °C in the batch reactor to decompose them further. Figure 6 shows the product distribution through the decomposition for the deposit. The yields of oil (HS) and TeS-HI fraction increased with increasing temperature up to 420 °C monotonously and the sum of the two yields reached 78 wt %. By further increasing the temperature up to 450 °C a part of the TeS-HI fraction were decomposed into oil fraction, and the yields of oil and TeS-HI reached 56 wt % and 22wt%, respectively. Figure 7 compares the MWDs of the products at 450 °C, which were measured by the MALDI-TOFMS method. Comparing with the MWDs of the soluble and the deposit, the oil fraction consists of the components smaller than these in the soluble, the components in TeS-HI fraction are similar to those in the soluble, and the TeI fraction consists of the components smaller than those in the deposit. These results show that the deposit can be further decomposed into small molecule compounds just by heating it in tetralin at 450 °C. Figure 8 enlarges the MWD of the oil fraction so as to identify the components more easily involved. Most of the oil fraction consists of the components of $M_w = 250$ to 350. These components were judged to be dimers of two aromatic ring components from the ¹³C NMR analysis.

Figure 9 compares the product distributions through the decomposition of the soluble, the deposit and the residue at 450 °C. Since 72 wt % of the soluble consisted of oil, the oil yield increased by only 9 % for the soluble through the decomposition. A small amount of gaseous components (CH₄ and CO are main components) were simultaneously produced. This indicates that the soluble fraction is hardly decomposed at 450 °C. The residue was converted into 32 wt % of oil, 1 wt% of gaseous components and 67wt % of TeI and residue. Figure 11 shows that more than 52 wt % of PITT coal (d.a.f. basis) are converted into oil fraction through the combination of extraction at 350 °C and the decomposition at 450 °C in tetralin. This is very attractive as a coal conversion process, since this conversion process does not require expensive gaseous hydrogen. These results with the detailed analyses of the soluble, the deposit, and the residue given above clearly show that the unit components composing the soluble, the deposit, and the residue are similar.

Flash hydrolysis of deposit. The above results and discussion showed that the unit structures of the deposit produced from PITT coal are two aromatic ring components. Then the flash hydrolysis of the deposit was performed to examine the possibility to convert most of the deposit into two aromatic ring components such as naphthalene, methylnaphthalenes, etc. Figure 10 shows the effect of temperature on the product yields for the flash hydrolysis of the deposit. Main products were, unexpectedly, CH₄ and benzene, and the total conversion to volatiles was less than 50 % even at 900 °C. Flash hydrolysis over 700 °C seems to be too severe to preferentially obtain two aromatic ring components. We are now examining the possibility of milder hydrolysis conditions for this purpose.

CONCLUSION

Eight Argonne premium coals were extracted in a flowing stream of tetralin under 10 MPa at 350 °C. Bituminous coals, Illinois #6, Pittsburgh #8, and Upper Freeport, were extracted by 65 to 80% at 350°C, and the extract was divided into about 30 to 40 % of soluble (soluble) at room temperature and 25 to 40% of precipitated solid (deposit) at room temperature. The contribution of the decomposition reaction on the extraction yield is judged to be neglected for these coals. The extraction yields of lower rank coals, Beulah-Zap was not so large as those for the bituminous coals. At 350°C appreciable gas formation was observed, indicating that the decomposition reaction as well as the extraction proceed for these coals. The extraction yield of the highest rank coal, Pocahontas, was also small reflecting its structure. Since both the soluble and the deposit were almost ash free, they will be well utilized as a starting material of subsequent upgrading processes such as liquefaction, pyrolysis, and coking.

The treatment of the extraction products prepared from PITT coal were performed in tetralin at 380 to 450 °C to examine the possibility to decompose the fractions under mild conditions. Through the extraction and the heat treatment at 450 °C Pittsburgh #8 coal was converted into 52 wt % of oil (hexane soluble). This is very attractive as a coal conversion process, since this conversion process does not require expensive gaseous hydrogen. The detailed analyses of the extraction and the decomposition products clearly showed the structure of PITT coal is represented by the model B of Nishioka (physically associated model).

ACKNOWLEDGEMENT

This work was supported by "Research for the Future" project of the Japan Society for the Promotion of Science (JSPS) through the 148 committee on coal utilization technology of JSPS. The authors thank to Prof.

REFERENCES

- Blessing, J.E.; Ross, D.S., *Organic Chemistry of Coal, ACS Symposium Series 71*, Larsen, J., Ed., 1978, pp 171-185.
- Aida, T.; Slomka, B.; Squires, T.G. *Proc. the 25th Conf. Coal. Sci. (Japanese)*, 175-178, 1988 (Tokyo).
- Gibbins, J. R.; Kandiyoti, R., *Fuel* **1991**, *70*, 909-915.
- Zhang, S.-F.; Xu, B.; Moore, S.A.; Herod, A.A.; Kandiyoti, R., *Fuel* **1996**, *75*, 597-605.
- Zhang, S.-F.; Xu, B.; Moore, S.A.; Herod, A.A.; Kimber, G.M.; Dugwell, D.R.; Kandiyoti, R., *Fuel* **1996**, *75*, 1557-1567.
- Zhang, S.-F.; Xu, B.; Moore, S.A.; Herod, A.A.; Kandiyoti, R., *Energy Fuels* **1996**, *10*, 733-742.
- Miura, K.; Shimada, M.; Mae, K., *1998 International Pittsburgh Coal Conf.*, Paper No. 30-1.
- Artok, L.; Schobert, H. H.; Nomura, M.; Erbatun, O.; Kiden, K., *Energy Fuels* **1998**, *12*, 1200-1211
- Nishioka, M., *Fuel* **1992**, *71*, 941-948.
- Nishioka, M., *Fuel* **1993**, *71*, 1719-1724

Table 1. Ultimate and proximate analyses of coals used [wt%]

Coal	Ultimate analysis [da.f]				Prox. analysis [db.]		
	C	H	N	O(dff)	FC	VM	Ash
Boublik-Zap (ND)	72.9	4.8	1.2	20.1	45.3	44.9	9.7
Wyosick (WY)	73.0	5.4	1.1	18.5	46.5	44.7	8.8
Illinois#6 (IL)	77.6	5.0	1.4	16.0	44.4	40.0	15.4
Blind Canyon (UT)	80.7	5.8	1.6	11.9	49.5	45.8	4.7
Levinston-Stockton (ST)	82.5	5.3	1.6	10.6	49.9	30.1	19.8
Pittsburgh#1 (PITT)	83.2	5.3	1.6	9.9	52.9	37.8	9.3
Upper Freeport (UF)	85.5	4.7	1.6	8.2	59.3	27.4	13.1
Pocahontas (POC)	91.0	4.4	1.3	3.3	76.6	18.6	4.8

Table 2. Analyses of the deposit and the residue produced from PITT.

	Ultimate analysis [wt%, da.f]				Ash	toracic ratio [-]	
	C	H	N	O(dff)		H/C	O/C
PITT							
Raw	80.6	5.4	1.8	12.2	7.3	0.81	0.11
Residue	80.8	4.8	2.0	12.4	21.3	0.71	0.12
Deposit	81.4	5.4	2.2	11.0	0.8	0.80	0.10
Soluble	79.8	5.9	1.3	12.4	=0	0.89	0.12
(Calculated)							
IL							
Raw	77.6	5.0	1.4	16.0	15.5	0.77	0.15
Residue	77.4	4.6	1.5	16.6	32.1	0.71	0.16
Deposit	79.2	5.3	1.8	13.7	0.1	0.80	0.10
Soluble	75.7	5.1	0.7	18.2	0.3	0.81	0.18
(Calculated)							

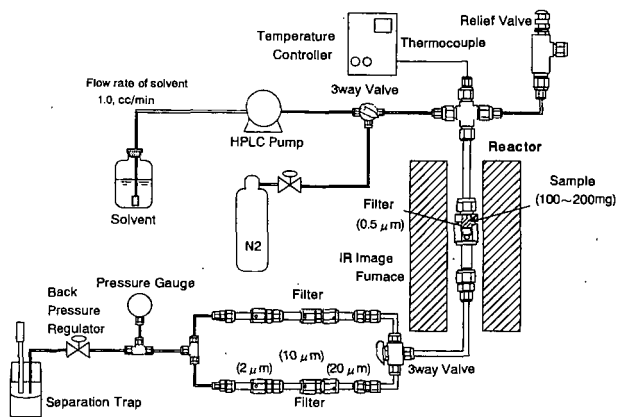


Figure 1. Schematic of experimental apparatus used for extraction/depolymerization in a flowing solvent.

Table 3. Carbon distribution in the raw coal, the residue, and the deposit prepared at 350 °C ($t_f = 60$ min) for PITT.

Carbon type	Raw Coal	Residue	Deposit	Soluble (Calculated)
Aliphatic carbon				
-CH ₃	0.069	0.047	0.049	0.103
-CH ₂	0.168	0.154	0.158	0.188
-OCH ₃	0.013	0.008	0.010	0.020
-CO-C, R-OH	0.017	0.006	0.001	0.039
Aromatic carbon				
A-H	0.328	0.336	0.323	0.325
Bridgehead	0.299	0.336	0.337	0.238
A-OH, -OCH	0.092	0.105	0.120	0.054
-COOH	0.014	0.008	0.002	0.028
Aromaticity index, f_a	0.733	0.785	0.782	0.650

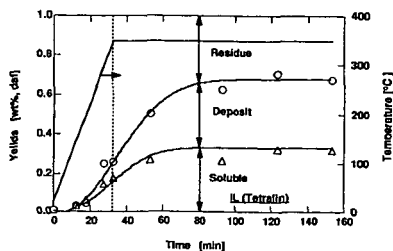


Figure 2. Change in the yields of soluble, deposit and residue with the increase of the holding time at 350 °C for IL.

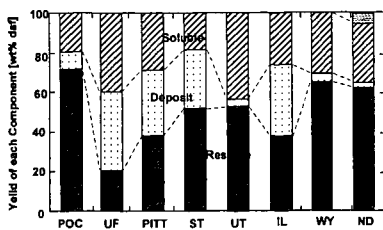


Figure 3. Yields of soluble, deposit and residue for Argonne premium coals (350 °C, $t_f=60$ min).

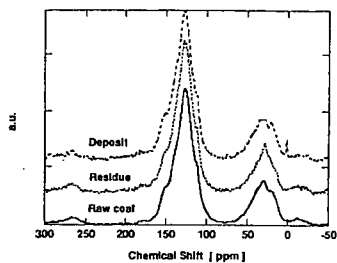


Figure 4. ^{13}C NMR spectra for the raw coal, and the deposit and the residue prepared at $t_f=60$ min at 350 °C for PITT.

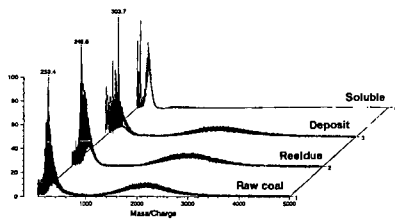


Figure 5. MWDs of the raw coal, and the residue and the deposit prepared at $t_f=60$ min at 350 °C for PITT (MALDI-TOFMS).

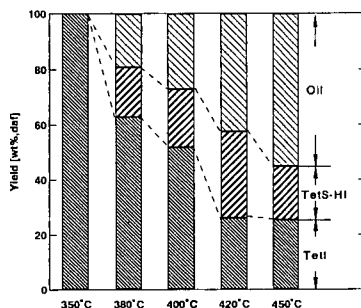


Figure 6. Product distributions through the decomposition of the deposit at different temperatures (PITT).

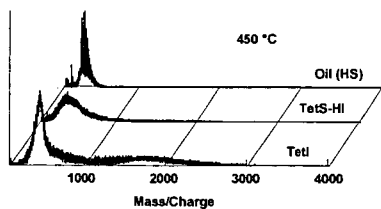


Figure 7. Comparison of the MWDs of the decomposition products from the deposit at 450 °C (PITT).

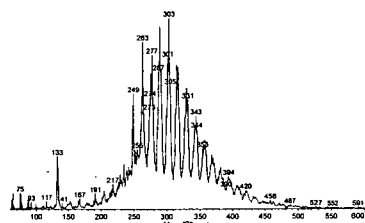


Figure 8. MWD of the oil fraction produced by the decomposition of the deposit at 450 °C (PITT).

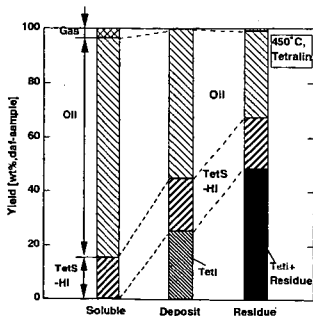


Figure 9. Product distributions through the decomposition of the soluble, the deposit and the residue at 450 °C (PITT).

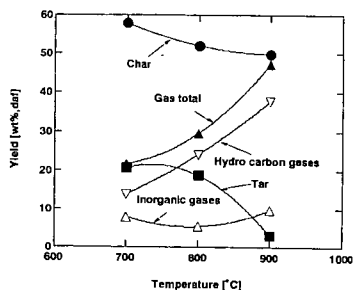


Figure 10. Effect of temperature on the product yields for the flash pyrolysis of the deposit (PITT).

HYDROGEN TRANSFER BETWEEN COAL AND TRITIATED ORGANIC SOLVENT

Atsushi Ishihara, I Putu Sutrisna, Masaru Saito, Weihua Qian and Toshiaki Kabe
Department of Applied Chemistry, Tokyo University of Agriculture and Technology, 2-24-16
Nakacho, Koganei, Tokyo 184-0012, JAPAN.

Keywords: hydrogen transfer, coal, tritiated tetralin

INTRODUCTION

To develop coal conversion techniques into useful fuels and chemicals by thermolysis and hydrogenation, it is important to elucidate the coal structure.^{1,2)} Although coal has a complex structure which includes various aromatics and functional groups, it can be considered that the reactivities of hydrogen in coal could reflect the coal structure since each hydrogen in aromatics, aliphatics, functional groups with heteroatoms etc. has the different reactivities. Therefore, the determination of reactivities of hydrogen in coal will provide significant information for coal structure.

Useful methods to measure hydrogen in coal are to utilize isotopes such as deuterium and tritium tracers.³⁻¹¹⁾ A deuterium tracer was effective to trace reactive sites in coal and coal model compounds, however, there were few examples which enable quantitative analysis of the hydrogen mobility in coal because of the poor solubility of coal products and the difficulty of quantification of the deuterium tracer.³⁻⁷⁾ In contrast, we have reported that tritium tracer techniques were effective to trace quantitatively hydrogen in the coal liquefaction.⁸⁻¹¹⁾ In these works, it was shown that the quantitative analysis of hydrogen transfer in coal could be given through the hydrogen exchange reactions among coal, gas phase and solvent as well as hydrogen addition. However, the method under coal liquefaction conditions includes destruction of the original structure of coal. In the course of our study, we were interested in the direct non-destructive determination of hydrogen in coal with its original form. Recently, we have reported that the tritium tracer methods are effective to determine the amount of hydrogen in the functional group of coal and examine the reactivities of hydrogen in coal through the reaction of coal with tritiated water and gaseous hydrogen in a pulse flow reactor or a batch reactor.¹²⁻¹⁴⁾

In this study, we investigate the hydrogen transfer between coal and tritiated organic solvent to estimate the reactivity of hydrogen in coal. A hydrogen donor solvent tetralin was tritiated with tritiated water. To avoid significant destruction of the coal structure, reaction was performed in the range 200-300 °C below usual coal liquefaction conditions. After the reaction of coal with tritiated tetralin, the reaction of the tritiated coal and water was carried out to remove tritium in functional groups and to obtain the information for the position of hydrogen exchanged in coal.

EXPERIMENTAL

Reaction of Coal with Tritiated Tetralin

Four kinds of Argonne Premium Coal Samples (Beulah-Zap (ND), Illinois No. 6 (IL), Upper Freeport (UF), and Pocahontas #3 (POC)) were obtained in 5 g of ampules (< 100 mesh). The samples of Wandoan coal (WA) were ground to -150 mesh particles. Coal samples were dried for 2 h at 110 °C under 10^{-1} Torr. The analytical data of coals are shown in Table 1. Coal rank increases in the order ND < WA < IL < UF < POC and the oxygen content decreases in the same order. Tritiated tetralin was prepared by modifying the reported method.¹⁵⁾ Tritiated water ($2\text{g}, 10^8\text{ dpm/g}$), tetralin (1.2g), and sodium carbonate (0.005g) were added into a stainless tube reactor. After argon purge, the reactor was kept for 1 h at 420 °C under supercritical condition of water. After separation of tritiated water, tritiated tetralin was diluted to about 10^6 dpm/g of water (0.5 g) and tritiated tetralin ($0.5\text{ g}, 10^6\text{ dpm/g}$) was packed into a stainless tube reactor (6 mL). After the reactor was purged with argon, the reactions were performed under the conditions, 200-300 °C and 5-360 min. After the reaction, coal and tetralin were separated under vacuum at 200 °C for 2 h and the tritiated coal was washed with n-hexane, dried and oxidized by an automatic sample combustion system (Aloka ADS-113R) into tritiated water to measure its radioactivity. Every tetralin sample was dissolved into a scintillator solvent (Instafluor, Packard Japan Co. Ltd.) and measured with a liquid scintillation counter (Beckman LS 6500). The tetralin sample was also analyzed by gas chromatography equipped with FID

Procedure of Hydrogen Exchange Reaction between Tritiated Coal and Water.

In order to predict locations of exchangeable hydrogen in coal, the hydrogen exchange reactions of coal that reacted with tritiated tetralin, i.e., tritiated coal, with water were performed. The tritiated coal and water were added into a glass reactor. The reactor was immersed into an oil bath with stirring. The reaction was performed at 100 °C for 24 h. After the reaction, suction filtration was performed and tritiated coal was washed with hot water. Further, the separated coal was dried under vacuum ($< 10^{-1}$ Torr) at 120 °C for 1 h. After the coal was dried, it was oxidized by a method similar to the above using the combustion of coal.

Calculation of Hydrogen Transfer Ratio.

Hydrogen transfer includes both hydrogen addition and hydrogen exchange. The Hydrogen Transfer Ratio (HTR) estimated in this paper means the ratio of the amount of hydrogen transferred into coal (H_{tr}) to the total amount of hydrogen in an original coal (H_{coal}). HTR between coal and tetralin was calculated on the basis of eq 1:

$$HTR = H_{tr} / H_{coal} \quad (1)$$

H_{coal} was calculated with the analytical data presented in Table 1. The amount of hydrogen transferred from tetralin into coal (H_{tr}) was calculated on the basis of eq 2:

$$R_{coal} / H_{tr} = R_{tet} / H_{tet}; \quad H_{tr} = H_{tet} \cdot R_{coal} / R_{tet} \quad (2)$$

H_{tet} is the amount of hydrogen contained in tetralin and R_{tet} is the radioactivity of tritium contained in tetralin after the reaction. In eq 2, it was assumed that the hydrogen transfer reaction between tetralin and coal is at equilibrium. Thus after the reaction, the ratio of the radioactivity in coal to the amount of the hydrogen transferred in coal (R_{coal} / H_{tr}) is equal to the ratio of the radioactivity in tetralin to the amount of hydrogen in tetralin after the reaction.

RESULTS AND DISCUSSION

Figure 1 shows the change in hydrogen transfer ratio (HTR) of coal with reaction time at 300 °C. Total HTR increased with reaction time and reached constant value at 180 min. At this time, it can be considered that hydrogen transfer reaction has reached the equilibrium state. After hydrogen transfer reaction, the hydrogen exchange between the tritiated coal sample and water was performed to remove tritium in the functional group of coal and know the extent of hydrogen exchange of functional group in the reaction of coal with tritiated tetralin. As shown in Figure 1, HTR corresponding to the hydrogen exchange between hydrogen in functional group of coal and tetralin increased with reaction time similarly and reached the constant value at 180 min.

Figure 2 shows the change in HTR of coal with reaction temperature at 180 min. Although HTR was observed for each coal at 200 or 250 °C, this may be due to the sorption of tetralin molecule into coal as well as the hydrogen exchange. HTR remarkably increased in most of coals with increasing temperature from 250 °C to 300 °C, while HTR for POC coal increased only slightly. Total HTRs for all coals and HTRs corresponding to hydrogen exchange of hydrogen of functional group in coal with tritiated tetralin are listed in Table 2. The result shows that at lower temperature, 200 and 250 °C, hydrogen exchanges between hydrogen in functional group and tetralin were very low. These results were significantly different from those for the reaction of coal with tritiated gaseous hydrogen, where most of hydrogen in functional groups exchanged with tritiated gaseous hydrogen at the same lower temperature in the presence of catalyst.¹⁴⁾ However, HTR for functional group of coal with tritiated tetralin also remarkably increased with a rise from 250 °C to 300 °C.

Figure 3 shows the change in tetralin conversion to naphthalene with temperature at 180 min. The trend of increase in tetralin conversion with temperature was similar to that in HTR. In the cases of lower rank coals, ND and WA, tetralin conversion increased with increasing temperature from 200 to 300 °C. In the cases of higher rank coals, IL, UF and POC, tetralin conversions were very low at temperatures 200 and 250 °C. However, those remarkably increased with a rise in temperature from 250 to 300 °C. The result suggests that, since lower rank coals, ND and WA, generated larger amount of radical species even at lower temperature, tetralin conversion

to naphthalene, that is hydrogen addition into coal was enhanced. For higher rank coals, however, it seems that a large amount of radicals were generated at 300 °C. Tetralin conversion for IL coal was highest at 300 °C and this may be due to the catalysis by a larger amount of pyrite included in IL coal.

In Figure 4, total HTR of coal with tritiated tetralin and HTR corresponding to hydrogen exchange for functional group in the reaction with tritiated tetralin at 300 °C and 360 min were compared with HTR corresponding to hydrogen exchange between coal and tritiated water at 100 °C which was previously reported. Except for ND coal, HTR corresponding to hydrogen exchange for functional group of coal in the reaction with tetralin was very similar to HTR of functional group between coal and tritiated water. The results shows that at 300 °C most of hydrogen in functional group of coal exchanged with tritiated tetralin. In the reaction of coal with tritiated tetralin, HTR decreased in the order IL>UF>WA>ND>POC which was different from that of the reaction of coal with tritiated water where HTR decreased with increasing coal rank.¹⁴ There might be the decomposition of coal structure in lower rank coals at 300 °C which seems to affect the hydrogen transfer.

CONCLUSIONS

Hydrogen transfer reaction between coal and tritiated tetralin significantly proceeded at 300 °C and the amount of hydrogen transferred increased in the order POC<ND<WA<UF<IL. The trend for temperature dependence of hydrogen transfer between coal and tetralin was very similar to that of tetralin conversion to naphthalene. Except for ND coal, most of hydrogen of functional group in coal exchanged with hydrogen in tetralin at 300 °C. In contrast, at lower temperatures, 200 and 250 °C, hydrogen transfer from tetralin to coal was very low for each coal and hydrogen in functional group only slightly exchanged.

ACKNOWLEDGMENT

This study was supported by the Research for the Future Project of the Japan Society for the Promotion of Science (the 148 Committee on Coal Utilization Technology) under Contract JSPS-RFTF96R14801.

REFERENCES

- 1) Solomon, P. R., Hamblen, D. G., Yu Z., and Serio, M. A., *Fuel*, **1991**, *70*, 754.
- 2) Kelemem, S. R., George S. N., and Gorbaty, M. L., *Fuel*, **1990**, *69*, 939.
- 3) Franz, J. A. and Camaioni, D. M., *Am. Chem. Soc. Div Fuel Chem. Prepr.*, **1981**, *26*, 106.
- 4) Cronauer, D. C., Mcneil, R. I., Young, D. C., and Ruberto, R. G., *Fuel*, **1982**, *61*, 610.
- 5) Wilson, M. A., Vassalo, A. M., and Collin, P. J., *Fuel Processing Technology*, **1984**, *8*, 213.
- 6) Collin, P. J. and Wilson, M. A. *Fuel*, **1983**, *62*, 1243.
- 7) Skowronski, R. P., Ratto, J. J., Goldberg, I. B., and Heredy, L. A., *Fuel*, **1984**, *63*, 440.
- 8) Kabe, T., Kimura, K., Kameyama, H., Ishihara, A., and Yamamoto, K., *Energy & Fuels*, **1990**, *4*, 201.
- 9) Kabe, T., Horimatsu, T., Ishihara, A., Kameyama, H., and Yamamoto, K., *Energy & Fuels*, **1991**, *5*, 459.
- 10) Kabe, T., Ishihara, A., and Daita, Y., *Ind. & Eng. Chem. Res.*, **1991**, *30*, 1755.
- 11) Ishihara, A., Morita, S., and Kabe, T., *Fuel*, **1995**, *74*, 63.
- 12) Ishihara, A., Takaoka, H., Nakajima, E., Imai, Y., and Kabe, T., *Energy & Fuels*, **1993**, *7*, 362.
- 13) Qian, W., Ishihara, A., Fujimura, H., Saito, M., Godo M., and Kabe, T., *Energy & Fuels*, **1997**, *11*, 1288.
- 14) Kabe, T., Saito, M., Qian, W., and Ishihara, A., *Fuel*, **1999** in press.
- 15) Yao, J. and Evilia, R. F., *J. Am. Chem. Soc.*, **1994**, *116*, 11229.

Table 1 Ultimate analysis of coals used (% daf)^{a)}

Coal	C	H	N	S	O	
ND	72.94	4.83	1.15	0.70	20.38	(L)
WA	76.9	6.7	1.1	0.3	15.0	(SB)
IL	77.67	5.00	1.37	2.38	13.58	(HVB)
UF	85.50	4.70	1.55	0.74	7.51	(MVB)
POC	91.05	4.44	1.33	0.50	2.68	(LVB)

a) Abbreviations: ND: Beulah-Zap, WA: Wandoan, IL: Illinois No.6, UF: Upper Freeport, POC: Pocahontas No.3; L: lignite, SB: subbituminous coal, HVB: high-volatile bituminous coal, MVB: medium-volatile bituminous coal, LVB: low-volatile bituminous coal. Except for WA, samples are coals of the Argonne Premium Coal Sample Program.

Table 2 HTRs of coals with tritiated tetralin

Coal	200 °C		250 °C		300 °C	
	Total HTR	HTR of OH ^{a)}	Total HTR	HTR of OH ^{a)}	Total HTR	HTR of OH ^{a)}
ND	4.4	1.7	4.6	-	8.1	3.8
WA	2.5	0.3	3.3	1.0	9.0	4.6
IL	4.5	1.6	5.7	0.9	14.4	6.2
UF	2.8	1.4	3.5	-	11.7	2.0
POC	2.3	0.1	2.9	-	4.2	0.5

a) Hydrogen transfer ratio of functional groups such as hydroxyl group which was determined by the reaction of tritiated coal with water at 100 °C.

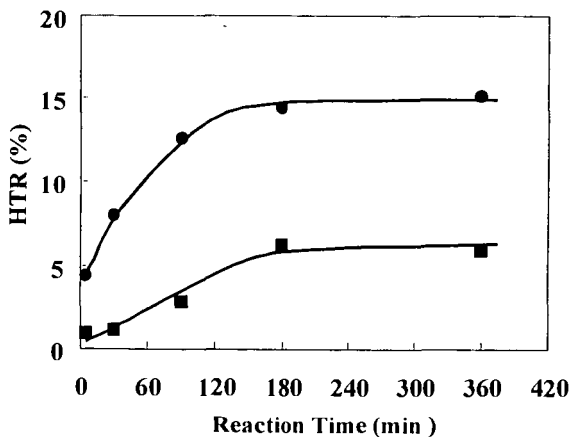


Figure 1. HTRs of Illinois No. 6 with [³H]tetralin at 300 °C
 ●: Total HTR; ■: HTR for functional group in coal

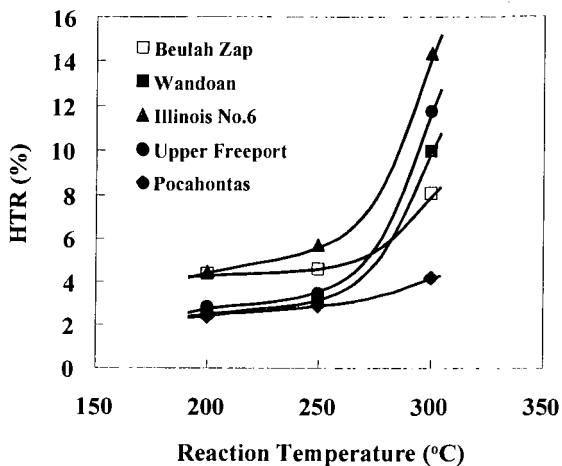


Figure 2. Effect of temperature on HTR of coal with $[^3\text{H}]$ tetralin for 3 h.

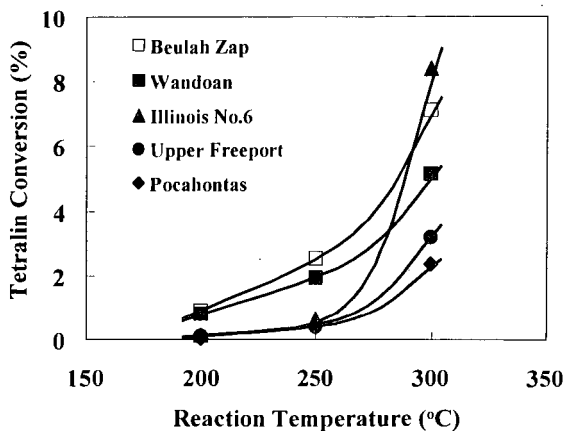


Figure 3. Effect of temperature on tetralin conversion in the reaction of coal with tetralin (3h).

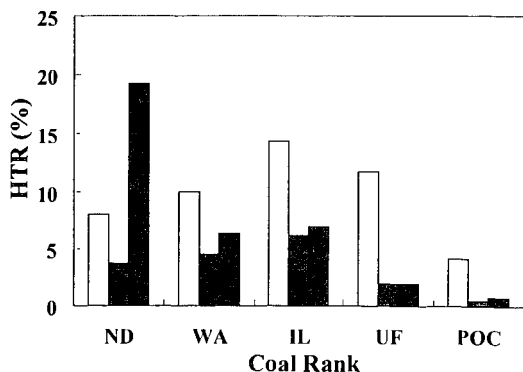


Figure 4. Comparison of HTRs of coals
 □: Total HTR of coal with $[^3\text{H}]$ Tetralin at 300 °C for 3 h
 ◻: HTR of functional group in coal with $[^3\text{H}]$ Tetralin at 300 °C for 3 h
 ■: Total HTR of functional group in coal with $[^3\text{H}]$ H₂O at 100 °C for 6 h

EVALUATION OF COAL TAR PITCH FRACTIONS AS FEEDSTOCKS FOR THERMALLY STABLE JET FUEL

Suchada Butnark, Mark W. Badger, Harold H. Schobert
The Energy Institute
The Pennsylvania State University, University Park, PA 16802

Keywords: Coal tar pitch, hydrogenation, thermal stability, jet fuel, tetralin.

INTRODUCTION

Coal tar pitch, a by-product from the metallurgical coke industry, is made up of the volatile compounds evolved during coal carbonization. The inherent cyclic structure content indicates its ability to be upgraded into hydroaromatic and cycloalkane compounds that have been shown to contribute towards high fuel stability at elevated temperature [1,2,3]. Since 1960s coal tar pitch fractions have been successfully demonstrated to be a suitable feedstock for the production of jet fuels for high Mach aircraft [1,4], and have also been included in full-scale demonstrations in French fighter aircraft [5].

For the future development of high-performance jet aircraft flying at high Mach speeds, the fuel specifications have to be increased significantly due to the extreme operating conditions the fuel must experience. The fuel may potentially be used as a heat sink in some parts of the aircraft and operated at temperature as high as 900°F. Under these conditions the fuel is stressed to temperatures above its thermal stability, which in turn leads to fuel degradation and coke formation [6,7]. It has been found that high thermal stability hydroaromatic and cycloalkane compounds are desirable components for advanced jet fuels [1,2,3]. As a result, coal tar pitch distillates, which can be converted to those structures under hydrotreatment process, are chosen again for jet fuel production. However, current evaluations on coal tar production have shown that the production of raw coal tar in the US has declined significantly over the past 30 years due to the environmental issues. But, by incorporating with suitable petroleum refinery streams, the feasibility and desirability of coal tar blending as a viable route for the production of thermally stable jet fuel would increase. Thus, we would need to protect and extend the lifetime of coal tar as a resource for advanced thermally stable jet fuel production.

The blends of various coal tar pitch distillates and suitable refinery streams have undergone laboratory-scale catalytic hydrotreatment. Coal tar pitch streams – high quinoline insolubles and low quinoline insolubles, carbon black oil, creosote oil, naphthalene still residue (NSR) and refined chemical oil (RCO) – and refinery streams – kerosene and light cycle oils (LCO) – were selected. The majority of these were eliminated early on in the study because of poor processing ability. Difficulties arising from asphaltene and pre-asphaltene precipitation from the heavy fraction were the main cause. The problems included a loss in catalytic activity and a decrease in hetero-atom removal. However, RCO proved to be an excellent feedstock. RCO is a very narrow boiling fraction, which contains over 50 % naphthalene. The hydrogenated products from the blends of RCO and LCO have produced good jet fuel fraction yields and high tetralin production – tetralin has been shown to have high thermal stability. Variations in reaction condition, pressure and temperature, as well as catalyst used have been performed to maximize the jet fuel fraction yield and tetralin conversion.

EXPERIMENTAL

Analysis Performed. Ultimate analysis of carbon, hydrogen and nitrogen compositions are obtained from a LECO CHN-600 analyzer and a LECO SC-132 sulfur determination analyzer. The feedstocks and products were analyzed by high temperature simulated distillation (HT-SimDis) GC analysis using a Hewlett-Packard 5890 series II plus fitted with a Restek MXT-500 SimDis column. The boiling point distribution and the cut point of 200-260°C fraction, jet fuel range, were observed. Quantitative analysis and chemical specification were performed on the feeds and samples using a Hewlett Packard 5890 GC fitted with a 5971 mass selective detector (MSD) fitted with a J+W DB17 capillary column. The analysis of feedstocks is shown in Table 1.

Catalyst Preparation. NiMo/Al₂O₃ and NiMoP/Al₂O₃ catalysts from Criterion have been employed for this work. The catalysts were presulfided following the method used by Ueda and co-workers [8].

Sample Used. Refined chemical oil (RCO) was obtained from Koppers Industries Company. British Petroleum (BP) supplied light cycle oils (LCO): LCO^a light cycle oil feed, LCO^b hydrogenated light cycle oil and LCO^c deeply hydrogenated light cycle oil.

Methods for Hydrogenation. Hydrogenation experiments were performed in 25 ml microautoclave reactors following the methods used by Reddy *et al* [9]. The conditions for hydrogenation experiments included pressures between 500-1300 psig H₂ and temperatures between 325-375°C. Variations in the feedstock blending composition (LCO: RCO = 3:1, 1:1, 1:3 and 0:1) were assessed as well as the effect of the two catalysts, NiMo/Al₂O₃ and NiMoP/Al₂O₃. After collecting a small part of the reaction products from the reactor, the remainder was recovered with THF followed by filtration.

RESULTS AND DISCUSSION

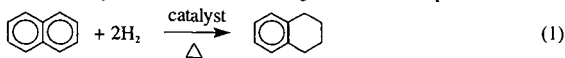
First, we compared the basic blends between different LCOs (LCO^a, LCO^b and LCO^c) and RCO at varying compositions and catalysts, and under the baseline conditions. Figure 1 shows that the blend of different LCO with RCO gave different jet fuel yields. LCO^c blends gave the outstanding jet fuel yield whereas those of LCO^a and LCO^b were in the same low-range yield. This is mainly due to the presence of hydroaromatic compounds in the LCO^c that contribute to the higher conversion of the RCO through hydrogen donation and shuttling reactions.

The blending compositions of LCO^c: RCO also affected the jet fuel yield (see Figure 1). By increasing the RCO concentration and using the NiMoP/Al₂O₃ catalyst, we see an increase in the proportion of the sample boiling in the jet fuel fraction (200-260 °C). This is due in part to the increase in tetralin in the products, through the composition of high boiling material and subsequent hydrogenation. Tetralin conversion, during RCO hydrogenation using NiMoP/Al₂O₃ catalyst (see Table 1) was lower than those of 1:1 blends under baseline condition in Table 2. Therefore, there was some synergistic effect promoted by the blend of LCO^c and RCO. This again was probably due the hydrogen donation reactions.

Figures 2-3 show chromatograms of blends of LCO^c and RCO before and after hydrogenation. The conversion of a significant portion of the naphthalene to tetralin can be seen along with the formation of other products. For an indication of the tetralin conversion, the calculated value was based on saturation of naphthalene ring only. Therefore, the actual value would be higher due to the contribution of the tetralin from the decomposition and hydrogenation of the high boiling point compounds. Furthermore, other cyclic structures in jet yield fraction of LCO^c also play an important role in the production of potentially thermally stable compounds. Therefore, to optimize jet fuel yield, tetralin production and other thermal stable components, we need to blend RCO with LCO^c with RCO loadings greater than 50%.

In addition, the hydrogenation conditions have formed products that have shown great increases in the H/C ratio and effective removal of sulfur and nitrogen. Table 2 shows the analyses of hydrogenated products by varying pressure, temperature and catalyst used. The H/C ratio of hydrogenated products has been increased and their colors become lighter as the increase of temperature. Sulfur and nitrogen content were decreased more than 80% and 70% respectively. This result shows that the catalysts, especially NiMoP/Al₂O₃, have worked well in both desulfurization and denitrogenation reactions.

Figure 4-5 shows the effects of pressure and temperature on tetralin conversion and jet fuel yield with the use of NiMo/Al₂O₃. Increases in temperature greatly affected both tetralin production and jet yield. The effect of pressure shows that conversion to tetralin and the fraction boiling in the jet fuel range goes through a maximum around the baseline conditions of 1000 psig. For the reactions at high temperatures, cracking of heteroatoms and large aromatic compounds and the



saturation of naphthalene molecules are more likely to occur. But at low-pressure condition, the reaction tends to shift chemical equilibrium to the right (Equation 1). This is why tetralin conversion is less likely to occur.

High-pressure condition also hindered the tetralin production as well as jet yield. Thus, it can be summarized that 1000 psig H₂ and 350-375 °C is the most suitable condition for hydrogenation of LCO^c: RCO blends.

CONCLUSIONS

The blend of LCO^c and RCO under appropriate catalytic hydrogenation reaction can produce high quantities of tetralin, which indicates the potential high thermal stability, and an increase of sample boiling in the jet fuel fraction. The balance between jet fuel fraction yield, tetralin conversion and the production of other potentially thermally stable cyclic structures and can be controlled by blending composition and reaction conditions. The catalyst used plays an important role in tetralin conversion, desulfurization and denitrogenation processes.

ACKNOWLEDGEMENTS

The authors would like to express their gratitude to the Department of Defense and Air Force Wright-Patterson Laboratory for the support of this project under contract F33615-98-D2802 delivery order 3. Samples from Kopper Industries and BP Corporation are also gratefully appreciated.

REFERENCES

1. Letort, M. "Now-Make Jet Fuels from Coal", *Hydrocarbon Processing and Petroleum Refiner*, **41**(7), 1962.
2. Waiwright, H. W. "Coal's Place in Space Rocket Fuels from Tars", *Missiles and Rockets*, 43-48, October 1958.
3. Donath, E.E. and Hess, M. "Thermally Stable Hydrocarbon Fuels" *Chemical Engineering Progress*, **56**(4), 68-71, 1960.
4. Schlesinger, M.D. and Hiteshue, R.W. "Synthetic Fuel from Coal for Supersonic Aircraft", *US Bureau of Mines Report of Investigations No. 5902*, 1961.
5. Arnold, J. and Paul F.M. "Aviation Fuels from Coal", *Journal of the Institute of Energy*, 55-62, 1980.
6. Song, C., Eser, S., Schobert, H.H. and Hatcher, P.G. "Pyrolytic Degradation Studies of a Coal-Derived and a Petroleum-Derived Aviation Jet Fuel", *Energy and Fuels*, **7**(2), 234-243, 1993.
7. Heneghan, S.P., Zabarnick, S., Ballal, D.R. and Harrison III, W.E. "JP-8+100: The Development of High-Thermal-Stability Jet Fuel", *Journal of Energy Resources Technology*, **118**, 170-179, 1996.
8. Ueda, K, Matsui, H., Song, C. and Xu, W., "Catalytic Hydrocracking of Phenanthrene over NiMo/Al₂O₃, CoMo/ Catalysts and Metal-loaded Y-Zeolites", *Journal of the Japan Petroleum Institute*, **33**(6), 413-417, 1990.
9. Reddy, K.M., Wei, B. and Song, C., "Mesoporous Molecular Sieve MCM-41 Supported Co-Mo Catalysts for Hydrodesulfurization of Petroleum Resids", *Catalysis Today*, **1303**, 1-12, 1998.

Table 1: Ultimate analyses of LCO (a-c) and RCO.

Feed	% C	% H	% N	% S	H/C ratio	Jet range (200-260 °C)
LCO ^a	90.0	10.8	0.14	<0.05	1.44	18.5
LCO ^b	88.8	11.3	0.12	<0.05	1.53	28.8
LCO ^c	83.8	14.0	0.36	<0.05	2.00	32.5
RCO	91.7	6.5	0.43	0.42	0.84	52.1

Table 2: Analyses of hydrogenated products from refined chemical oil (RCO) and deeply hydrotreated light cycle oil (LCO) under varying conditions.

Reaction condition	NiMo				NiMoP			
	H/C ratio	%N	%S	%Tetralin Conversion	H/C ratio	%N	%S	%Tetralin Conversion
LCO: RCO = 1:1 at 1000 psig H₂								
325°C	1.50	0.12	0.042	57.0	1.50	0.13	0.053	63.1
350°C (baseline)	1.51	0.09	0.041	67.7	1.61	0.07	0.034	73.8
375°C	1.56	0.12	0.040	80.8	1.69	0.03	0.021	81.7
LCO: RCO = 1:1 at 350°C								
500 psig	1.47	0.13	0.011	63.9	1.54	0.08	0.017	74.6
1000 psig (baseline)	1.51	0.09	0.041	67.7	1.61	0.07	0.034	73.8
1300 psig	1.67	0.13	0.069	56.3	1.56	0.12	0.061	57.6

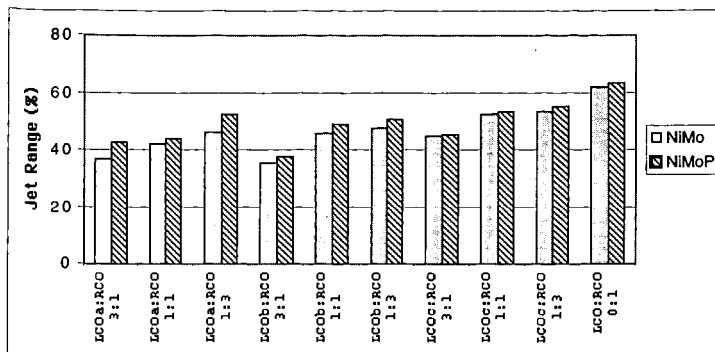


Figure 1: The effects of variation of blending types and composition on jet fuel yield.

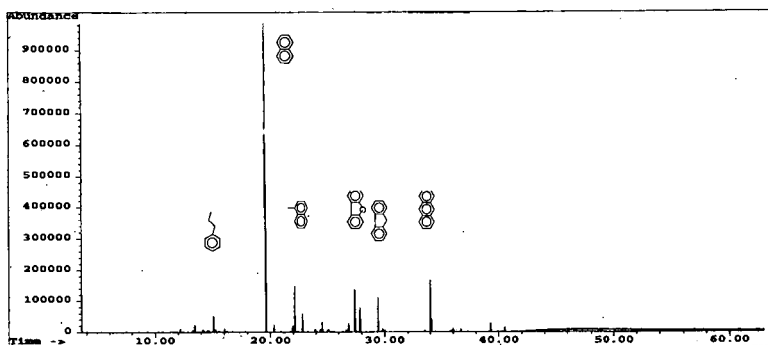


Figure 2: GC trace of the blend of LCO^c and RCO before hydrogenation reaction.

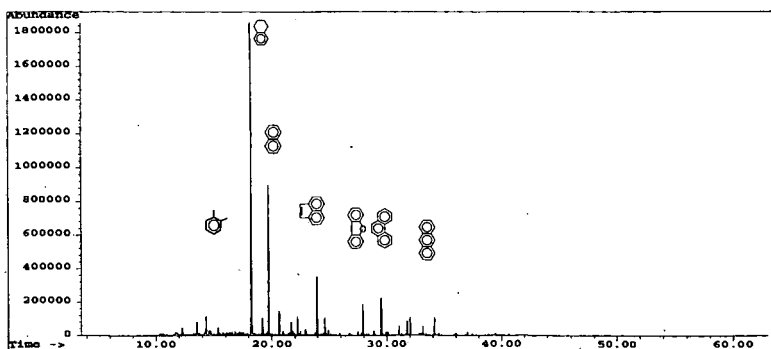


Figure 3: GC trace of hydrogenated product from the blend of LCO^c and RCO after hydrogenation at 50°C, 1000 psig H₂ by using NiMo/Al₂O₃.

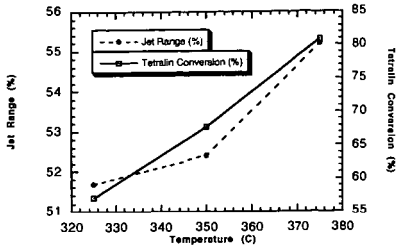


Figure 4: Temperature effects on jet fuel yield and tetralin conversion.

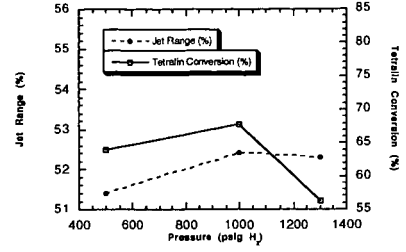


Figure 5: Pressure effects on jet fuel yield and tetralin conversion.

CARBON-CARBON BOND FISSION DURING HEAT TREATMENT OF COAL IN THE PRESENCE OF POLYCYCLIC AROMATIC COMPOUNDS

Satoru Murata, Koh Kidena, Nobuo Bandoh, Motoki Kouchi, and Masakatsu Nomura*

Department of Applied Chemistry, Faculty of Engineering, Osaka University,
2-1 Yamada-oka, Suita, Osaka 565, Japan

Keywords : Coal, Polycyclic aromatic compounds, C-C bond fission

INTRODUCTION

Coal liquefaction is believed to be one of the most important processes among coal utilization technologies in near future, which can convert solid coal to liquid fuel. In Japan, two coal liquefaction processes, brown coal liquefaction process (so called, NBCL process) and bituminous coal liquefaction process (NEDOL process), have been developed under financial support provided by NEDO. Many studies were conducted concerning the effects of the reaction temperature, residence time, the structures of recycle solvents, properties of iron catalysts, etc on the yield of liquid products.

Coal liquefaction had been thought to proceed via thermal cleavage of relatively weak bonds followed by stabilization of the resulting radicals by hydrogen donatable solvents, these mechanisms being described in the paper published in early 80's. In 1987, Malhotra *et al.* proposed another mechanism including radical hydrogen transfer (RHT) instead of thermal cleavage, with which they explained the experimental results of coal liquefaction and coprocessing of coal with heavy oil.¹⁾ On the other hand, Franz *et al.*²⁾ and Savage *et al.*³⁾ proposed reverse radical disproportionation (RRD). The radical formed from RHT or RRD reaction, released alkyl radicals via β -cleavage, which will be stabilized by hydrogen donatable solvents. In this paper, we have investigated methyl groups generated from C-C bond fission of coal during heating in the presence of polycyclic aromatic compounds.

EXPERIMENTAL

Reagents and Coal Samples.

In the present study, about forty kinds of coal samples with carbon contents ranging from 67 % to 91 % (wt%, daf) were employed, which were provided by Nippon Steel Chemical Ltd., Center of Coal Utilization, Japan (CCUJ), the Iron and Steel Institute of Japan (ISIJ), and Nippon Brown Coal Liquefaction Co. Ltd. (NBCL). These coals were ground under 100 mesh and dried at 40 °C for a night before use. 9-Methyl-, 9-ethyl-, and 9-methoxyanthracenes were prepared by the method reported previously. The other reagents employed in this study were commercially available and purified by conventional recrystallization or distillation prior to use.

Reaction of Coal Samples with Aromatic Compounds.

Details of reaction of coal samples with polycyclic aromatic compounds were described elsewhere.⁴⁾ Typical procedure was as follows: A mixture of 100 mg of a sample coal and 100 mg of anthracene was put in a pyrex tube (ϕ 6 mm x 100 mm long), then the tube being sealed. The resulting tube was put into an electric furnace preheated at 420 °C and kept for 5 min. After the reaction was quenched by removing the tube from the furnace, the products were recovered by washing the inside of the tube with methylene chloride and submitted to GC and GC-MS analyses.

MO Calculations.

All MO calculations were carried out on an Apple Macintosh computer by using a semiempirical molecular orbital calculation program, CAChe (Computer Aided Chemistry) MOPAC.94, which was purchased from CAChe Scientific Inc. The values of heat of formation for the polycyclic aromatic hydrocarbons were determined by solving the Schrödinger equations using the AM1 semiempirical Hamiltonians.

Solid State NMR Spectroscopy.

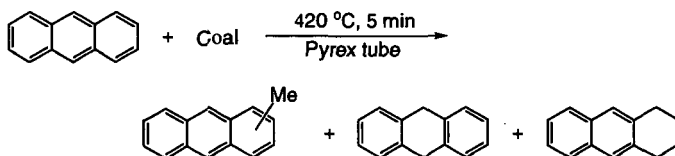
SPE/MAS ¹³C NMR spectra were recorded on a Chemagnetics CMX-300 spectrometer under the following conditions; resonance frequency for ¹³C 75.5 MHz; pulse width 45°; proton decoupling frequency 83 kHz (90° pulse width=3.0ms); scan number 1000; pulse delay 100 s; and MAS

frequency 10.5 kHz. Curve fitting was conducted on an Apple Macintosh computer with a data processing software, MacFID (TechMag Inc., Ver. 5.4). The classification of carbon types was as follows: carbonyl and carboxyl (the deconvoluted peak centered at 187 and 178 ppm), aromatic carbons attached to oxygen (167 and 153 ppm), aromatic carbons attached to carbon or hydrogen (140, 126 and 113 ppm), methoxy (56 ppm), methylene (40 and 31 ppm), α -methyl to aromatic ring and branched methyl (20 ppm) and terminal methyl in side chains (13 ppm).

RESULTS AND DISCUSSION

The Reaction of Coal Samples with Aromatic Compounds.

More than forty kinds of coal samples ranging from brown to semi-anthracite were employed in this study. The reaction of the coal samples (100 mg) with anthracene (100 mg) was conducted at 420 °C for 5 min in a pyrex tube. The main products containing anthracene skeleton were 9,10-dihydroanthracene (DHA), 1,2,3,4-tetrahydroanthracene (THA), and methylanthracene isomers (MA, mainly consisted of 9-methyl isomer along with minor amount of 1- and 2-methyl ones).



Although dimethylanthracenes and methyl-dihydroanthracenes were also detected, their yields were very small. In almost all runs, the recovery of anthracene derivatives was more than 90 mol%, which seems to be a reliable value for the following discussion. The results are summarized in Figure 1. DHA and THA were produced *via* hydrogen abstraction by anthracene from hydrogen donatable parts in the coal samples, while the formation of MA suggests that anthracene could capture the methyl radicals produced by C-C bond fission. Yields of DHA and THA became the highest from the reaction of the coal with *ca.* 86% of carbon (Figure 1a), while yield of MA showed different tendency, *i.e.*, the lower the coal rank was, the higher the MA yield was (Figure 1b). With elongation of reaction duration from 5 min to 30 min, MA yield increased monotonously.

We also conducted the reaction of the coal samples with pyrene and acridine, radical acceptability of which is known to be different from that of anthracene. Therefore, we would like to investigate correlation between radical acceptability and methylarene yields. The results are shown in Figure 2. In the every coals employed, yield of methylarenes obeyed the following sequence; pyrene < anthracene < acridine. We evaluated radical acceptability of these arenes according to the following equation using MO calculation program package (MOPAC 94):

$$\Delta\Delta H_f = \Delta H_f(\text{ArHMe}\cdot) - \Delta H_f(\text{ArH}) - \Delta H_f(\text{Me}\cdot)$$

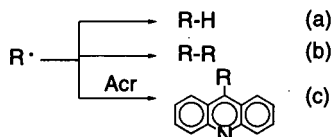
where ΔH_f means standard heat of formation. The values of $\Delta\Delta H_f$ for pyrene, anthracene, and acridine were calculated to be +1.1, -4.8, and -28.6 kcal/mol, respectively. This indicates that using the arenes with higher radical acceptability, methyl radical migrates to the arenes more easily.

It is known that various kinds of carbon or methyl group are present in coal. The methyl migration reaction observed in this study should be caused by a certain type of methyl group. In order to get an information concerning the source of the methyl groups migrated, we measured solid state ^{13}C NMR spectra for the sample coals, the resulting spectra being divided into twelve curves and the carbon distribution was estimated as shown in experimental section. Figure 3 shows the plots of MA yield (wt%, from the reaction at 420 °C for 5 min) against concentration of methyl groups (methoxy, α -methyl, terminal methyl and their total) in the coals (mol%) estimated from the ^{13}C NMR spectra. The concentration of methoxy, terminal methyl and total methyl groups seemed to correlate weakly. Since the errors in the NMR measurements and estimation of carbon types were not so small, we could not determine what the origin of methyl groups migrated is. Only what we can say is larger amount of methyl gave higher yields of methylanthracenes in the reaction of coal with anthracene.

Migration of Methyl Groups from Methyl-Containing Compounds to Polycyclic Aromatics.

To discuss about the mechanism of methyl groups-migration reaction, we conducted the reaction of model compounds. We selected 9-methyl-, 9-ethyl-, and 9-methoxyanthracenes (abbreviated as 9-MA, 9-EA, and 9-MeOA, respectively). This reaction requires a hydrogen donatable solvent and a radical accepting compound, for which 9,10-dihydroanthracene (DHA) and acridine (Acr) were employed, respectively. The reaction was conducted at 420 °C for 5 min in a pyrex tube, the results being summarized in Table 1. The order of reactivity (judging from the conversion) of the anthracenes obeyed the following sequence; 9-MA \approx 9-EA < 9-MeOA. The reaction of 9-MA afforded methylacridines (M-Acr), dimethylanthracenes (DMA), and methane in 18, 2.4, and 1.1 % yield, respectively, as the major methyl group-containing products. In the case of 9-EA, main products were ethylacridines (E-Acr, 15 %), diethylacridines (DE-Acr, 2.7 %), and ethane (3.9 %) along with small amount of methylacridines (2.2 %). In the reaction of 9-MeOA, the main products were M-Acr (44 %), methane (36 %), and anthrone (42 %).

Formation of light hydrocarbon gases and alkylacridines indicate that alkyl radicals participate this reaction and there are three possibilities for the fate of the radicals formed (Scheme 1), i.e., a) hydrogen abstraction to form alkanes, b) dimerization to alkanes, and c) capture with aromatics to form alkylarenes.



Contribution of these pathways a,b,c seemed to be varied depending on the functionality of methyl groups. Now, we are investigating the factors affecting the products distribution.

REFERENCES

- 1) McMillen, D. F.; Malhotra, R., Chang, S.-J.; Ogier, W. C.; Nigenda, S. E.; Fleming, R. H. *Fuel* **1987**, *66*, 1611; Malhotra, R.; McMillen, D. F. *Energy Fuels* **1990**, *4*, 184; McMillen, D. F.; Malhotra, R. *Energy Fuels*, **1991**, *5*, 179; Malhotra, R.; McMillen, D. F. *Energy Fuels* **1993**, *7*, 227; McMillen, D. F.; Malhotra, R.; Hum, G.P.; Chang, S. J. *Energy Fuels* **1987**, *1*, 193.
- 2) Autrey, T.; Alborn, E. A.; Franz, J. A.; Camioni, D. M. *Energy Fuels* **1995**, *9*, 420
- 3) Savage, P. E. *Energy Fuels* **1995**, *9*, 590
- 4) Kidena, K.; Murata, S.; Nomura, M. *Energy Fuels* **1998**, *12*, 782.

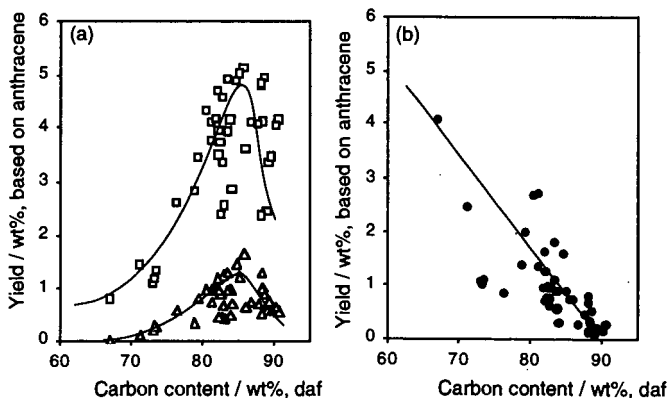


Figure 1 Plots of the yield of DHA (\square), THA (\triangle), and MA (\bullet) from the reaction of coal with anthracene at 420 °C for 5 min against carbon content of the coals

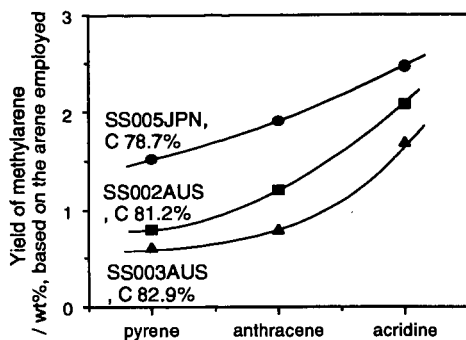


Figure 2. Yield of methylarenes from the reaction of coal with polycyclic aromatics (at 420 °C, for 5 min, in a pyrex tube)

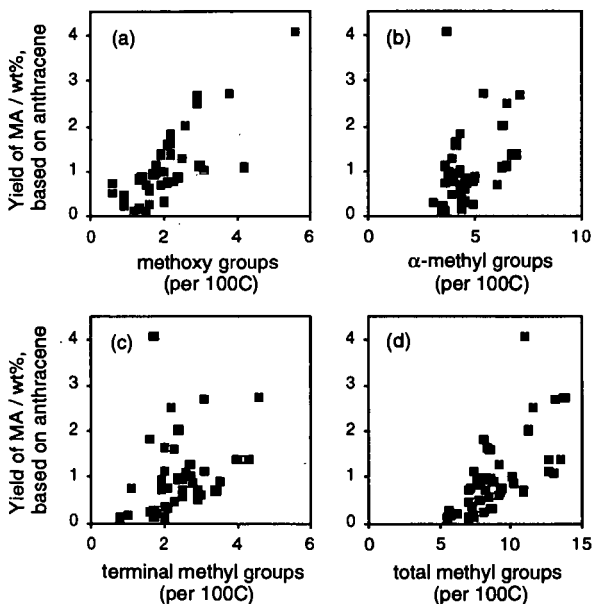


Figure 3. Plots of the yields of methylanthracene (MA) against concentration of each type of methyl group in the coal samples

Table 1. The reaction of methyl group-containing anthracene with acridine in the presence of DHA^{a)}

Substrate	Conv. of Subst. (mol%)	Yield (mol%)			Yield of gas (mol%)			
		DMA	M-Acr	E-Acr	DE-Acr	H ₂	CH ₄	C ₂ H ₆
9-MA	28	2.4	18	-	-	0.41	1.1	-
9-EA	28	-	2.2	15	2.6	0.37	-	3.9
9-MeOA	87	5.3	44	-	-	0.35	36	0.6

a) A mixture of substrate (0.25 mmol), Acr (0.25 mmol), and DHA (0.0625 mmol) was heated at 420 °C for 5 min in a pyrex tube.

Effects of Superacid Depolymerization and Catalytic Hydrogenation on Pyrolysis Reactivity of Illinois #6 Coal

Hideyuki TAKAGI, Takaaki ISODA, Katsuki KUSAKABE
and Shigeharu MOROOKA

Department of Materials Physics and Chemistry,
Graduate School of Engineering, Kyushu University,
Fukuoka 812-8581, Japan

KEY WORDS: coal, structural change, pyrolysis

INTRODUCTION

Pretreatments under mild conditions do not substantially alter the structure of coal and increase its extractability with organic solvents [1,2]. Up to 80 wt% of Yalloom coal, which had been oxidized at 60°C with aqueous H₂O₂ in the presence of 1-propanol, was solubilized in ethanol [1]. The ethanol soluble fraction was further hydrogenated using a Ru/Al₂O₃ catalyst in a mixed solvent of ethanol and acetic acid at 120°C for 12-72 h at a hydrogen pressure of 10 MPa [2], to give a yellowish white solid (hydrogenated white coal). This catalytic hydrogenation altered the aromatic structure of the coal, in part, and increased its reactivity with respect to pyrolysis. However, the H₂O₂ oxidation was not effective in increasing the extractability of bituminous coals.

Shimizu et al. [3,4] depolymerized a subbituminous coal using a superacid at 150°C. This was a unique process which greatly increased the solubility of coal. In the present study, Illinois #6 coal was depolymerized using the superacid, trifluoromethanesulfonic acid (CF₃SO₃H, hereafter, referred to TFMS), in the presence of solvents at 120°C, and the treated coal was then extracted with tetrahydrofuran (THF). The THF solubilized coal was then hydrogenated over a Ru catalyst at 120°C for 48 h under a hydrogen pressure of 10 MPa. Changes in coal structure and pyrolysis reactivity by the combination of superacid treatment and catalytic hydrogenation were then examined.

EXPERIMENTAL

Depolymerization via Treatment with Superacid Followed by THF Extraction: Figure 1 shows the procedure for superacid treatment and THF extraction of Illinois #6 coal. 1 g of the coal, which was pulverized to 74-125 μm in size, 3-5 mL of TFMS, and 13 mL of a solvent were mixed in an autoclave of 25 mL. Toluene, methylcyclopentane or isopentane were used as the solvent, and the suspension was stirred at 120°C for 3 h [3]. After the depolymerization, the product was neutralized with an aqueous solution (5 wt%) of Na₂CO₃. The precipitate was washed with water and extracted with THF under ultrasonic irradiation at room temperature. The mixture was then separated into THF-soluble (TS_d) and THF-insoluble (TI) fractions by centrifugation. The TS_d fraction was then subjected to hydrogenation. The raw coal was also

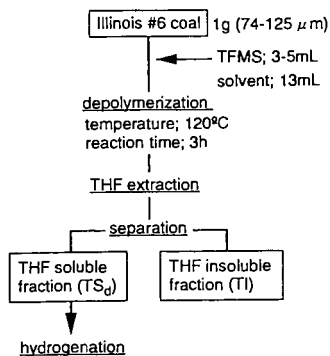


Figure 1. Depolymerization and fractionation procedure.

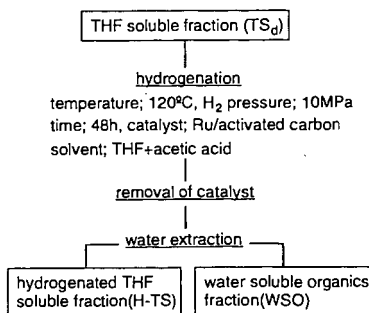


Figure 2. Hydrogenation and fractionation procedure.

extracted with THF, and the THF soluble fraction was subjected to further characterization. The TS fraction of the raw coal is hereafter referred to as the TS_d fraction.

Hydrogenation of THF Extract: Figure 2 illustrates the procedure used for the hydrogenation of the TS_d fraction. A ruthenium-supported activated carbon catalyst (metal content = 5 wt%, Wako Chemical) was used for the hydrogenation. 1 g of the TS_d fraction was dissolved in a mixture of 8 mL of acetic acid and 6 mL of THF in a 25 mL autoclave equipped with a magnetic stirrer, and hydrogenated using 1.5 g of the catalyst at 120°C for 48 h under a hydrogen pressure of 10 MPa. After the removal of the catalyst by filtration, the solvent was evaporated. The product was then extracted with water under ultrasonic irradiation, leading to a hydrogenated, THF-soluble (H-TS) fraction and a water-soluble organic (WSO) fraction. Each fraction was dried at 70°C for 6 h under vacuum, and the yields were determined gravimetrically.

Structural Analysis and Flash Pyrolysis of Products: The H/C atomic ratio of the coals was evaluated by elemental analysis, and the molecular weight was determined by GPC analysis described previously [2]. The hydrogen distribution and aromaticity (f_a) were estimated by H-NMR spectroscopy and elemental analysis using the Brown-Lander equation [5]. The thermal reactivity of the coals was evaluated by flash pyrolysis at 764°C under an inert atmosphere using a Curie-point pyrolyzer (CPP, Japan Analytical Industry, JHP-22). Inorganic gases (IOG; CO, CO₂, H₂O and H₂) and hydrocarbon gases (HCG; C₁-C₅) were analyzed using gas chromatographs (GC) equipped with TCD and FID detectors. The tar fraction was analyzed using a CPP connected to a GC interfaced with a mass spectrometer (GC/MS, Shimadzu, QP-5000) [6].

RESULTS

The TS_d and TS_d fractions were recovered as solids after the removal of the solvent, while the H-TS fraction was a viscous black liquid. Figure 3 shows the yields of the TS_d, TS_d and TI fractions. The yields are expressed in wt% of the mass of the dry raw coal. The TS_d yield, which was 14

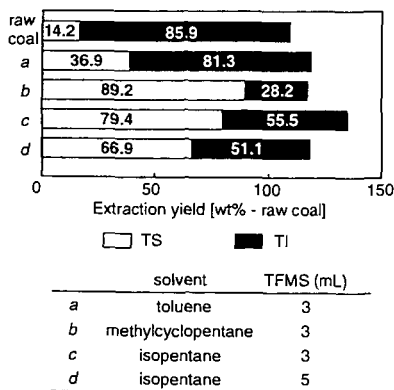


Figure 3. Yields of TS and TI fractions by depolymerization using TFMS.

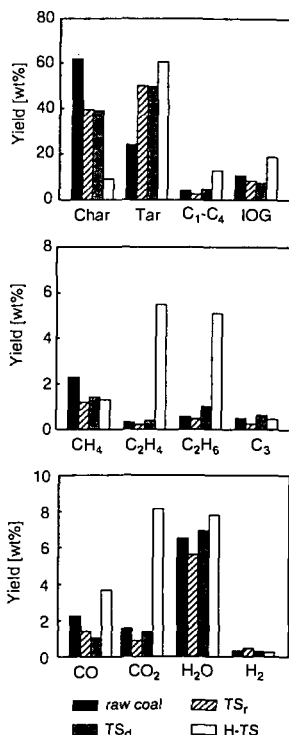


Figure 4. Product distributions of flash pyrolysis.

wt% for the raw coal, was increased by the depolymerization to 89 wt% for the case of methylcyclopentane, and 79 wt% for isopentane. Figure 4 shows the product distributions of the flash pyrolysis for the raw coal, the TS_r and TS_d fractions, and the H-TS fraction. The yields are expressed based on the initial mass of each sample used for pyrolysis. The char yield was 62 wt% for the raw coal, 40 and 38 wt% for the TS_r and TS_d fractions, respectively, and 5 wt% for the H-TS fraction. The tar yield was increased from 24 wt% for the raw coal to 61 wt% for the H-TS. The total yield of hydrocarbon gases, which were rich in ethylene and ethane, was increased as a result of the hydrogenation. The yields of CO, CO₂ and H₂O were increased, while the yield of H₂ remained unchanged by the hydrogenation.

Table 1 shows the elemental analysis of the raw coal and the TS_r, TS_d and H-TS fractions, as well as the molecular weight of the TS_r, TS_d and H-TS fractions. The H/C atomic ratio was increased from 0.89 for the raw coal to 1.52 for the H-TS fraction. The molecular weight of the H-TS fraction at the peak of the elution curve was approximately 1000. Table 2 shows the hydrogen distribution, as well as the aromaticity, of the TS_r, TS_d and H-TS fractions, as determined by H-NMR spectroscopy. The depolymerization resulted in an increase in the H_β and H_γ of the TS_r fraction. The hydrogenation of the TS_d fraction resulted in a decrease in the H_{ar}, H_a and f_a, and an increase in the H_β. The H_γ remained unchanged by the hydrogenation.

The tar component, obtained by the pyrolysis of the H-TS fraction at 764°C, contained approximately 40 components. The unit structures of 6 major components were analyzed by GC/MS, elemental analysis, molecular weight and hydrogen distribution. As shown in Figure 5, these species were composed of 1-3 rings, suggesting a partial hydrogenation of the coal structure. The yield of these species was 14 wt% for (A), 13 wt% for (B), 11 wt% for (C), 7 wt% for (D), 8 wt% for (E) and 4 wt% for (F) with respect to the initial mass of the H-TS.

DISCUSSION

The Illinois #6 coal, which was depolymerized using TFMS in the presence of methylcyclopentane, was solubilized in THF at a yield of 89 wt%. As shown in Table 2, the increase in the H_β and H_γ after superacid treatment suggests that alkyl groups, derived from the solvent, are introduced into the coal structure [3]. The decreases in H_{ar}, H_a and f_a indicate that the aromatic rings in the coal structure are hydrogenated over the Ru catalyst. The increase in H_β, which is assigned to methylene and alicyclic hydrogens, is also indicative of the hydrogenation of the aromatic structure of the coal. The H_γ, which is assigned to methyl hydrogens of the TS_d, remains unchanged by the hydrogenation, suggesting that side chains are not greatly decomposed during the hydrogenation.

No differences in pyrolysis reactivity were observed between TS_r and TS_d. The HCG yield is increased by only 2 wt% by depolymerization. Thus the superacid treatment leads to an increase in the amount of extracts without altering the pyrolysis reactivity of the TS_r fraction. The yield of volatile matters is increased by the hydrogenation from 62 wt% for the TS_d fraction to 95 wt% for the H-TS fraction. Assuming that the decrease in the f_a is caused by the hydrogenation of aromatic rings, 21 mol% of the aromatic carbons in the coal are converted to alicyclic carbons.

CONCLUSIONS

THF-solubilized coal was depolymerized with TFMS and then hydrogenated over a Ru catalyst in a mixed solvent of THF and acetic acid at 120°C. The pyrolysis reactivity of the THF-

Table 1. Elemental Analysis and Molecular Weight of the Raw Coal, TS_r, TS_d and H-TS Fractions

sample	C H N (O+S) diff				H/C	O/C	Mw ^a
	[wt% - d.a.f.]						
raw coal	74.5	5.5	1.5	18.5	0.89	0.19	
TS _r	75.3	5.5	1.4	17.8	0.88	0.18	3000
TS _d	77.2	6.3	0.9	15.6	0.98	0.15	1500~2000
H-TS	68.7	8.7	0.1	22.5	1.52	0.25	1000

^a molecular weight

Table 2. Hydrogen Distribution and Aromaticity of TS_r, TS_d and H-TS Fractions

sample	mol/100 mol of hydrogen				f _a
	H _{ar}	H _α	H _β	H _γ	
TS _r	25.3	29.4	34.0	4.9	0.61
TS _d	19.9	22.5	39.8	11.2	0.60
H-TS	10.1	13.3	53.2	12.0	0.39

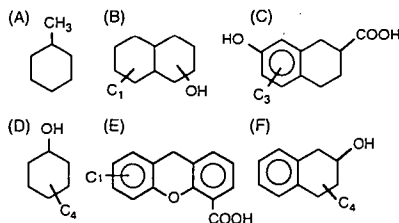


Figure 5. Unit structures of major compounds formed by pyrolysis of the hydrogenated TS fraction.

solubilized coal was increased by catalytic hydrogenation, which clearly altered the aromatic structure of the coal.

ACKNOWLEDGMENTS

This research was supported by Japan Society for the Promotion of Science (JSPS), Organization of New Energy and Industrial Technology Development Organization (NEDO), and Center for Clean Coal Utilization, Japan (CCUJ). The support by Research for the Future Projects (Coordinator; Prof. M. Iino, Tohoku Univ.) and International Joint Research Program (Coordinator; Prof. M. Nomura, Osaka Univ.) is especially acknowledged.

REFERENCES

- [1] Isoda, T.; Tomita, H.; Kusakabe, K.; Morooka, S.; Hayashi, J.-i. *Proc. of Intern. Conference on Coal Science* **1997**, *2*, 581.
- [2] Isoda, T.; Takagi, H.; Kusakabe, K.; Morooka, S. *Energy Fuels* **1998**, *12*, 503.
- [3] Shimizu, K.; Karamatsu, H.; Inaba, A.; Suganuma, A.; Saitou, I. *Fuel* **1995**, *74*, 853.
- [4] Olah, G. A.; Bruce, M. R.; Edelson, E. H.; Husain, A. *Fuel* **1984**, *63*, 1130.
- [5] Brown, J. K.; Lander, W. R. *Fuel* **1960**, *39*, 87.
- [6] Hama, H.; Matsubayashi, K.; Murata, S.; Nomura, M. *J. Jpn. Inst. Energy* **1993**, *72*, 467.

DETERMINATION OF STRUCTURAL VARIATIONS FOR A SERIES OF STEAM ACTIVATED ANTHRACITES

M. Mercedes Maroto-Valer, John M. Andrésen and Harold H. Schobert

The Energy Institute, The Pennsylvania State University,
405 Academic Activities Bldg, University Park, PA-16802, USA

Keywords: Activated carbon, anthracite, structural variations, porosity.

Although significant research has been conducted on the characterization of porosity, significantly less attention has been paid to the structural variations occurring during the activation process. Accordingly, this paper presents the structural characterization of a series of activated carbons using several analytical techniques. For this study, a Pennsylvania anthracite was steam activated in a vertical tube furnace for different periods of time. Solid yields below 60% enhanced the formation of mesopores. With increasing activation time, the atomic H/C ratios decrease and there is a significant rise in the condensation of the aromatic structures, regardless of the type of porosity developed.

INTRODUCTION

There is a continuous worldwide growing demand for the production of activated carbons, due to the increasing number of applications of these materials, especially those related to environmental protection [1]. The main reason for this expanding market is the ubiquitous use of activated carbons as adsorbent materials in a broad range of increasing applications, including both gas-phase and liquid-phase adsorption. In the US, the demand for activated carbon is forecast to increase 5-6% annually, and it is expected to reach 440 million pounds in the year 2002. The adsorptive properties of activated carbons are known to depend on both their porous and chemical structures. Although significant research has been conducted on the characterization of porosity, significantly less attention has been paid to the structural variations occurring during the activation process. Accordingly, this paper presents the structural characterization of a series of activated carbons by using several analytical techniques. For this study, anthracites were selected as precursors for the production of activated carbons. Their inherent fine pore structure makes them excellent raw materials for producing adsorbent carbons with molecular sieve properties for gas separation in pollution control technologies [2]. A Pennsylvania anthracite was steam activated in a vertical tube furnace for different periods of time. The chemical structures of the resultant series of activated samples were extensively characterized using elemental, solid state ^{13}C NMR and X-ray analyses. The structural variations determined by the above techniques were related to the adsorptive properties of the resultant activated carbons.

EXPERIMENTAL PROCEDURE

The Pennsylvania anthracite selected (Lehigh Coal & Navigation) contains ~ 6.8 % ash (db) and the atomic H/C ratio is 0.21. For this study, the anthracite was ground and sieved to generate particle size fractions of 150-250 μm and 1-3 mm. The activation set-up used consists of a vertical tube furnace, where a stainless steel tube reactor, containing around 5 g of sample, is placed. A thermocouple inserted in the reactor monitors the sample temperature. When the sample reaches the activation temperature (850°C), a flow of steam is introduced by pumping water into the reactor at low flow rates (~1.2 g/min). The porosity of

the samples was characterized conducting N_2 adsorption isotherms at 77K using a Quantachrome adsorption apparatus, Autosorb-1 Model ASIT, as previously described [3]. The elemental analyses were carried out on a Leco CHN analyzer. The solid state ^{13}C NMR measurements were conducted on a Chemagnetics M-100 instrument with a field of 2.4 T and a spinning speed of 3.5 kHz. For the quantitative single pulse excitation experiments (SPE) about 8000-14000 scans were acquired with recycle delays ranging from 60-100 seconds. As in earlier work [4], tetrakis(trimethylsilyl)silane (TKS) was used as an internal standard to determine the proportion of carbon observed by SPE. The dipolar dephasing (DD) SPE experiments were conducted using dephasing times between 1-400 μs .

RESULTS AND DISCUSSION

Development of porosity Table 1 lists the solid yields, BET surface area (SA), total pore volume (V_{TOT}) and micro- (V_{micro}) and mesopore (V_{meso}) volume for the activated anthracites. For the particle size fraction 150-250 μm , the solid yield decreases as the activation time increases, going from 59% to 33% after 60 and 90 minutes' activation, respectively. As expected, the larger particle size fraction presents a much higher solid yield, 79% for the 1-3 mm fraction at 90 minutes activation, compared to that of 33% for the 150-250 μm fraction. Thus, the solid yield is strongly dependent on the particle size of the precursor, with higher yields for the bigger particle size fractions. The anthracite fraction 150-250 μm activated for 90 minutes presents the highest SA and V_{TOT} (1037 m^2/g and 0.46 cc/g , respectively), while the fraction 1-3 mm activated for 90 minutes presents the lowest SA and V_{TOT} (284 m^2/g and 0.13 cc/g , respectively). These differences are strongly related to the solid yields [5]. A very good correlation has previously been obtained between the solid yields and the surface area and total pore volume, regardless of the particle size of the precursor [5].

The adsorption isotherms of the raw anthracite and the activated samples are Type I, corresponding to microporous systems. Table 1 also lists the micro- and mesopore volumes of the activated anthracites and Figure 1 shows the evolution of the micro- and mesopore volume with solid yield. For all the activated anthracites, the micropore volume is significantly larger than the mesopore volume. However, extensive gasification (solid yields < 60%) seems to promote the formation of mesopores, as illustrated by the rapid change of slope of the mesopore volume evolution (Figure 1). For instance, the mesopore volume accounts for only ~8% of the total pore volume at 59% solid yield (fraction 150-250 μm activated for 60 minutes), while the mesopore volume comprises ~19% of the total pore volume at 33% solid yield (fraction 150-1250 μm activated for 90 minutes). Previous studies have shown that the increasing formation of mesopores with decreasing solid yields are due to the removal of some pore walls and enlargement of some micropores [2].

Structural changes Table 2 lists the atomic H/C ratios for the parent anthracite and activated samples. As expected, the atomic H/C ratios decrease with activation, going from 0.21 for the parent anthracite to 0.07 for the sample activated for 90 minutes (150-1250 μm). Solid state ^{13}C NMR experiments were conducted in all the samples, using the quantitative Single Pulse Excitation (SPE) method [4]. Figure 2 shows the ^{13}C SPE spectrum for the anthracite (150-1250 μm) activated for 90 minutes. The internal standard (TKS) used for the quantitative SPE experiments gives a resonance at 3.2 ppm, while the aromatic carbon band is centered at ~122 ppm. The spectrum is dominated by the aromatic peak accounting for >99% of the total carbon. This is also the case for all the samples investigated, where the carbon aromaticity (f_a) is ~1 (Table 2). The higher concentrations of paramagnetic centers expected in the activated samples did not affect the amount of carbon observed by SPE. For instance, for the anthracite (150-1250 μm) activated for 90 minutes, that is presumably the sample with the highest concentration of free radicals, over 90% of the carbon was observed by the SPE technique.

Additional structural information can be obtained by conducting NMR dipolar dephasing (DD) experiments to determine the proportions of non-protonated aromatic carbons (f_{non-prot}) and further calculation of bridgehead aromatic carbon [4]. Figure 3 shows the ¹³C SPE-DD spectra for the parent anthracite, with dephasing times of 1, 40, 150 and 300 μs. The signal from protonated carbon has decayed after 40 μs, and the remaining signal is from the non-protonated aromatic carbon. The ratio of non-protonated to total aromatic carbon can be found by deconvoluting the decay of the NMR signal, as illustrated for the parent anthracite in Figure 4. The initial decay of the signal intensity is dominated by the dephasing of the protonated aromatic carbons and can be described with a Gaussian lineshape, while the longer decay is attributed to non-protonated aromatic carbon and is Lorentzian distributed. Table 2 lists the f_{non-prot} for all the samples investigated. With increasing activation time, there is a significant rise in the f_{non-prot} indicating an increase in the degree of condensation of the aromatic structures. The ¹³C NMR structural data for all the activated anthracites will be correlated with X-ray data and the atomic H/C ratios.

CONCLUSIONS

Anthracites can easily be converted into activated carbons by steam activation. The particle size of the precursor strongly affects the solid yields of the resultant activated samples, with higher yields for bigger particle size fractions. For all the activated anthracites, the micropore volume is significantly larger than the mesopore volume. However, solid yields below 60% enhance the formation of mesopores. The SPE ¹³C NMR experiments conducted show that with increasing activation time, there is a significant rise in the condensation of the aromatic structures, regardless of the type of porosity developed. Mechanisms that correlate the evolution of the porous structure with the chemical structure will be reported.

ACKNOWLEDGMENTS

The authors wish to thank the Consortium for Premium Carbon Products from Coal (CPCPC) at the Pennsylvania State University and the Research Council of the Basque Government for financial support. We also want to thank Lehigh Coal & Navigation Company for providing the anthracite sample.

LITERATURE CITED

1. Song, C.S. and Schobert, H.H., 1995, *Fuel*, **75**, 724.
2. Gergova, K., Eser, S. and Schobert, H.H., 1993, *Energy & Fuels*, **7**, 661.
3. Maroto-Valer, M.M., Taulbee D.N., and Schobert H.H., 1998, *Prepr. Am. Chem. Soc. Fuel Division*, **44**, 101.
4. Maroto-Valer, M.M., Andréseñ, J.M., Rocha, D.C. and Snape, C.E., 1996, *Fuel*, **75**, 1721.
5. Maroto-Valer, M.M., Andréseñ, J.M., and Schobert, H.H., 1999, *24th Biennial Carbon Conference*, In Press.

Table 1: Yield, BET-surface areas, and total, micro- and mesopore volume for the activated anthracites¹.

	Activ. time	Yield	SA	V _{TOT}	V _{micro}	V _{meso}
	min	%	m ² /g	cc/g	cc/g	cc/g
150-250 μm	60	59	613	0.32	0.30	0.02
150-250 μm	90	33	1037	0.46	0.37	0.09
1-3 mm	60	79	284	0.13	0.12	0.01

¹ The solid yields and surface areas are expressed in ash free basis.

Table 2: Atomic H/C ratios, carbon aromaticities (fa) and proportion of non-protonated aromatic carbon (fnon-prot) for the parent and activated anthracites.

	Activ. time / min	Atomic H/C	fa	fnon-prot
Parent	--	0.21	0.99	0.76
150-250 μm	60	n.d.	1.00	0.86
150-250 μm	90	0.07	1.00	0.93

n.d.: Not determined

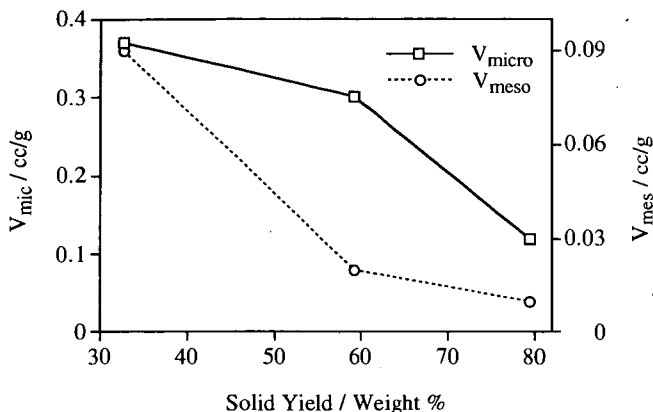


Figure 1 Evolution of the micro- and mesopore volume for the activated samples as a function of the solid yield.

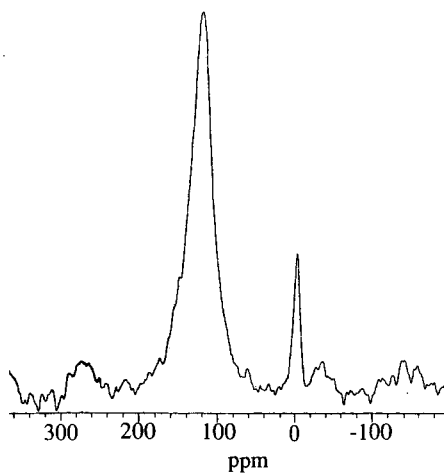


Figure 2 Solid state ^{13}C NMR spectrum for the anthracite (150-1250 μm) activated for 90 minutes using the quantitative SPE method.

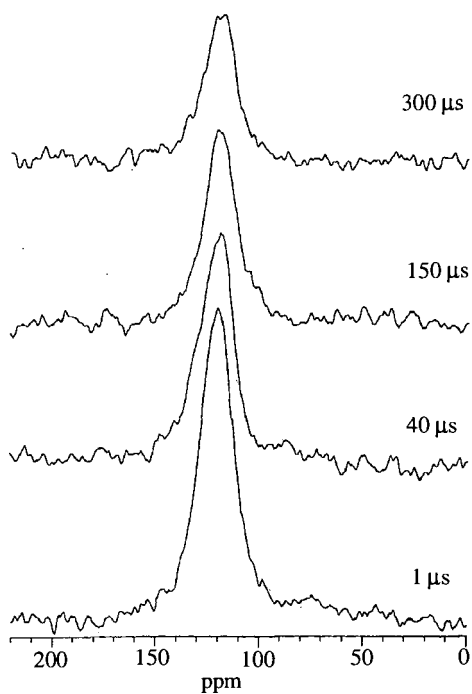


Figure 3 Spectra from SPE-DD ^{13}C NMR spectra for the parent anthracite (150-250 μm), with a dephasing time of 1, 40, 150 and 300 μs .

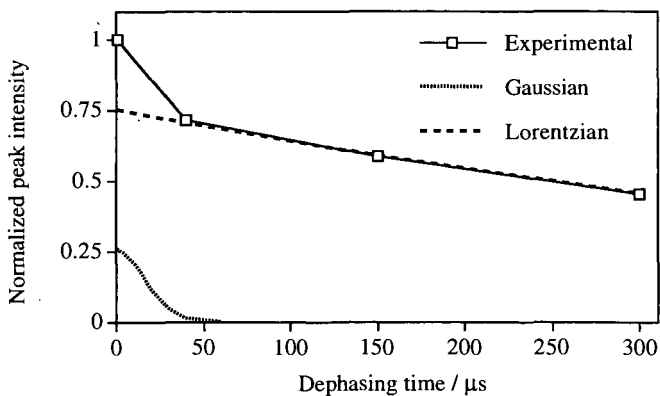


Figure 4 Plot of aromatic carbon peak intensity from the SPE dipolar dephasing experiments for the parent anthracite.

THE INVESTIGATION OF THE STRUCTURAL FACTORS FOR THE APPEARANCE OF COAL PLASTICITY

Koh Kidena^a, Masataka Hiro^a, Tsukasa Chikada^b, Satoru Murata^a,
and Masakatsu Nomura^a

^a Department of Molecular Chemistry, Graduate School of Engineering,
Osaka University, 2-1 Yamada-oka, Suita, Osaka, 565-0871, JAPAN

^b Sumitomo Metal Industry, Kashima, Ibaragi 314-0255, JAPAN

Keywords: Coking coal, Coal plasticity, Heat-treatment

INTRODUCTION

Even now, about a half of coal consumption in Japan corresponds to coke production for steel making. Therefore, carbonization process is very important among coal utilization techniques. Much effort has been paid to the development of effective carbonization process and/or replacement of the present coking processes by new concept such as the direct iron ore smelting process because our country has been imported almost all the coking coals and worried about a precious resource exhausting problem. Therefore, a deep understanding of plastic phenomena of coal was desired earnestly. We have been studying the phenomena of fusibility of coals by the estimation of amounts of transferable hydrogen, the measurement of their solid-state ¹³C NMR spectra and their thermogravimetric analyses (TGA)[1,2]. In those investigations, we found the relationship between R_{max}/WL (obtained from TGA) and Gieseler fluidity and also that solid state ¹³C NMR can evaluate the amount of transferable hydrogen. We referred to the schematic illustration of the structural change during heating which was proposed by Spiro[3] in considering the mechanism of coal plasticity. Although Spiro's illustration was based on the chemical structure of coal of 1980's, the structural analyses of coal and the detailed analyses of structural change during heating should be examined again in order to understand fusibility chemistry of coal at the level of molecule. Snape et al.[4] reported the characterization of partially carbonized coals based on solid-state ¹³C NMR and optical microscopy: the change of aromatic cluster size with the heat-treatment was discussed. In the present study, we employed a typical coking and a non-coking coals, Goonyella and Witbank. Ruthenium ion catalyzed oxidation (RICO) reaction of two coals was performed to get information concerning aliphatic portion of these coals. At the same time, the sample coals were heat-treated in the electric furnace in order to observe the structural changes during heat-treatment at the level of molecule, and the resulting char fraction and the devolatilized tar fraction were analyzed by solid-state ¹³C NMR and FT-IR spectroscopy, respectively.

EXPERIMENTAL SECTION

Samples.

The coal samples used in this study were Goonyella coal (GNY; C 88.1%, H 5.1%, N 1.9%, daf.) from Australia and Witbank coal (WIT; C 82.7%, H 4.5%, N 2.2%, daf.) from South Africa. WIT is called as non-coking coal in the field of coke industry, however, this coal shows a little degree of plasticity. The sample coals were provided by the Iron and Steel Institute of Japan, these being pulverized (-100 mesh) and dried at 60°C under vacuum for a night prior to use.

Ruthenium ion catalyzed oxidation (RICO) reaction of coal.

Coal sample (1 g), Na₂O₄ (20 g) and RuCl₃·*n*H₂O (40 mg) were put into a glass flask and stirred in the presence of mixed-solvent, H₂O (30 ml), CH₃CN (20 ml) and CCl₄ (20 ml), under the nitrogen flow at 40°C for 48 h. The resulting carbon dioxide was purged with N₂ flow through CaCl₂ and ascarite, and the yield of CO₂ was determined by the weight increase of ascarite. The details of the products workup and analysis were indicated elsewhere[5]. We could analyze the fractions containing lower carboxylic acids, higher carboxylic acids, aliphatic polyacids, and aromatic polyacids.

Heat-treatment of coal and analysis of the products.

Heat-treatment of coal was conducted by using a tubular electric furnace (Isuzu DKRO-14K with a temperature controller EPP-14) under 50 ml/min of nitrogen stream. One gram of coal sample was placed at the center of the quartz tube, and heated up to a determined temperature at a heating rate of 3 K/min. Final temperatures of heat-treatment were softening, maximum fluidity and resolidification temperatures of each coal (these were determined by Gieseler plastometry; 397, 456 and 498°C for GNY and 412, 432 and 446°C for WIT, respectively). The resulting char and tar fractions were recovered and weighed to obtain their yields. Tar fractions were analyzed by FT-IR spectroscopy (Shimadzu FTIR-8100M), and char fraction by ¹³C NMR spectroscopy (Chemagnetics CMX-300).

RESULTS AND DISCUSSION

RICO reaction of two sample coals

In order to observe the structural differences between GNY and WIT at the level of molecule, we performed RICO reaction of these two coals. After the reaction, we recovered carbon dioxide, lower carboxylic acids, acids in organic layer and water layer, and residue with less solubility and high molecular weight materials. The yields of carbon dioxide reached around 50% of the whole product because of the high aromaticity of these coals, however, the carbon recovery of this reaction was excellent; 96% for GNY and ~100% for WIT. We determined the amount of a series of mono- and dicarboxylic acids from the analyses of lower acids fraction and organic layer. Figure 1 shows the distribution of mono- and dicarboxylic acids. Monoacids correspond to the side chains in coal, while diacids indicate the presence of bridge bonds between two aromatic moieties. From Figure 1a, we can recognize ~3 mol/100molC of acetic acid derived from methyl group in coal, and the amount of other acids derived from longer side chains decreased monotonously with the number of carbon. Diacids also showed similar tendency. As to the comparison of GNY and WIT, several differences were found: longer side chains and bridges were detected in larger amount for WIT than for GNY, and the longest side chains and bridges were found for WIT. As the other products derived from RICO reaction of coal, we obtained aliphatic polycarboxylic acids and aromatic polycarboxylic acids. The precursors of these acids were considered to be alicyclic structure attached to aromatic cluster and highly condensed aromatic cluster, respectively. However, the apparent differences of the amounts of these acids between two coals could not be observed. The results obtained by ^{13}C and ^1H NMR of two coals indicated that GNY had slightly larger aromatic cluster than WIT.

Structural changes during heat-treatment

We performed the heat-treatment of GNY and WIT in the electric furnace in order to investigate the structural changes during heating. The devolatilization started at about 300°C, and the deposition of tar fraction appeared around 400°C in the heat-treatment of coals. We recovered char and tar fractions after the end of heat-treatment. Other products were gases such as CH_4 and CO_2 , and lighter hydrocarbons such as benzene. The yields of char and tar fractions obtained by the heat-treatment of coals at above three different temperatures were shown in Table 1. The weight loss (100% - char yield) at each heat-treatment temperature was similar to the data obtained from TGA, however, they were not exactly same because of the limitation for temperature control in the furnace during heat-treatment using an electric furnace. Atomic hydrogen/carbon ratio of char fraction decreased as the heat-treatment temperature increased. The decrease of H/C for a series of char samples may be due to the structural change during heating or the devolatilization of light fraction. In order to obtain more detailed information about the structural changes during the heat-treatment, we measured solid-state ^{13}C NMR spectra of the char samples. The spectra were shown in Figure 1 together with carbon aromaticity, f_a , evaluated from the ^{13}C NMR spectra for each sample. Although f_a of raw coal was different (0.83 and 0.79 for GNY and WIT, respectively), f_a values of the heat-treated samples became similar. Then, the ^{13}C NMR spectra were divided into 16 Gaussian peaks by referring to the assignment of carbon types in several model compounds, and we estimated the carbon distribution for each sample. We evaluated the change of amounts of each type of carbon based on the carbon distribution of char samples, their elemental analysis data and char yields. The data indicated the remarkable disappearances of the region of CH_2 , CH_3 and oxygen or carbon substituted aromatic carbon. On the other hand, amounts of other type of aromatic carbon did not change. These results supported that elimination of alkyl side chains underwent during the heat-treatment at the temperature of coal plastic range but other structural changes such as the increase of aromatic cluster size did not occur. Furthermore, release of CH_4 was observed at temperature range of 400 - 600°C by TG-GC[2], and the decrease of H/C during heating could be explained by the release of aliphatic rich volatile fraction.

In the previous paper[2], we reported that the amount of volatile materials from coal at the temperature between maximum fluidity temperature and resolidification temperature was important for the appearance of coal plasticity. Furthermore, we analyzed the tar fractions from TG furnace by field desorption-mass spectroscopy to observe molecular weight distribution and aromaticity of the fractions, and indicated that the different rank coals provided volatile components with different composition. In this viewpoint, we analyzed tar fraction obtained from the heat-treatment of two kinds of coals by FT-IR and gas chromatography. For the materials which can be detected by gas chromatograph, a series of aliphatic hydrocarbons and complicated mixture of hydrocarbons were observed for WIT and GNY. The aliphaticity (evaluated from the ratio of peak intensity of 3040 cm^{-1} to that of 2956 cm^{-1}) of tar fractions for these coals seemed to be high in the FT-IR spectra (Figure 2). However, as the heat-treatment temperature increased, the aliphaticity of tar fraction evaluated from FT-IR spectra dropped. Therefore, the volatile materials in the plastic stage had higher aromaticity than those before softening. We can calculate apparent H/C ratio of the volatilized fraction (including lighter fraction than tar) based on the yield of char and elemental analysis data of raw coal and the char. It was higher for GNY than for WIT. FTIR results did not agree with them,

but we can explain this by the fact that GNY coal released more amount of CH_4 during the heat-treatment as reported previously[2].

SUMMARY

We obtained the information concerning about aliphatic portion of two sample coals by using RICO reaction, which oxidize aromatic carbon in coal, and we observed the structural changes during heat-treatment of two coals. As to the structural features of original coal, RICO reaction implied that longer aliphatic chains or bridges were existed in WIT than in GNY, and the size of aromatic cluster for GNY was evaluated to be somewhat larger than that for WIT according to the ^{13}C NMR data. The structural changes during heat-treatment were also observed. The increase of f_a and the decrease of H/C were observed in the char fraction, while the tar fraction has aliphatic carbons richly. The differences of structural feature and pyrolytic behavior between coking and non-coking coals were not so large, therefore, it is interesting to pay attention to the detailed analyses of both volatile fractions before softening and in the plastic range.

ACKNOWLEDGMENT

This work was partially supported by a Grant-in-aid provided by the Iron and Steel Institute of Japan.

REFERENCES

1. Kidena, K.; Murata, S.; Nomura, M., *Energy Fuels* **1996**, *10*, 672.
2. Kidena, K.; Murata, S.; Nomura, M., *Energy Fuels* **1998**, *12*, 782.
3. Spiro, C. L., *Fuel*, **1981**, *61*, 1121.
4. Maroto-Valer, M. M.; Atkinson, C. J.; Willmers, R. R.; Snape, C. E., *Energy Fuels* **1998**, *12*, 833.
5. Artok, L.; Murata, S.; Nomura, M.; Satoh, T. *Energy Fuels*, **1998**, *12*, 391.

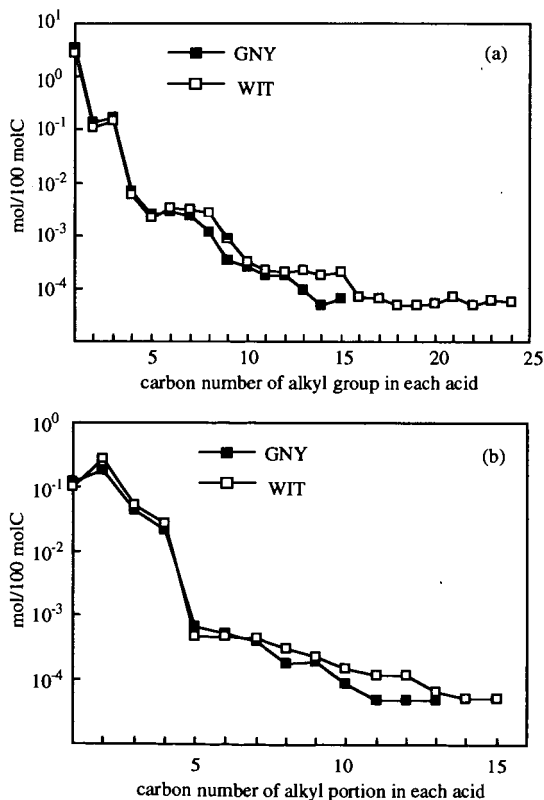


Figure 1. The yields of (a) monocarboxylic acids and (b) dicarboxylic acids from RICO reaction of GNY and WIT.

Table 1. The yields of char and tar after heat-treatment of coals and atomic H/C of char

Coal	Heat-treatment temperature (°C)	Yields (wt%, db.)		Atomic H/C ratio of char
		Char	Tar	
GNY	raw coal	-	-	0.69
GNY	397	97.5	1.4	0.68
GNY	456	89.2	7.5	0.59
GNY	498	86.9	11.0	0.56
WIT	raw coal	-	-	0.65
WIT	412	90.0	4.8	0.63
WIT	432	87.0	6.9	0.60
WIT	446	85.6	6.4	0.59

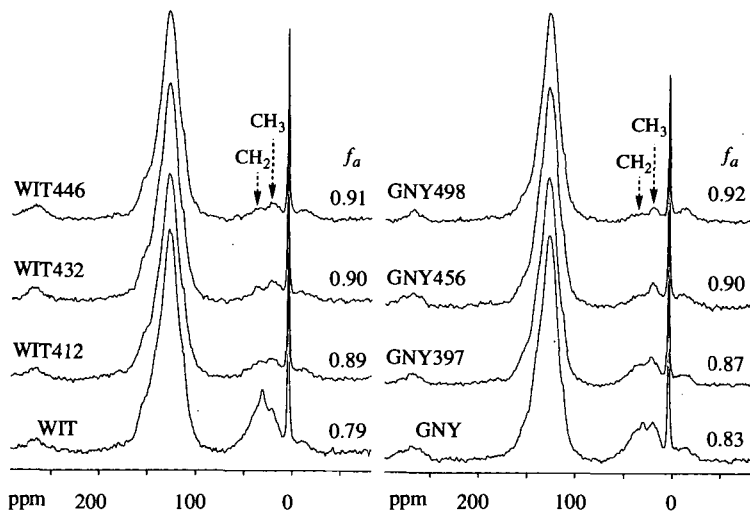


Figure 2. ^{13}C NMR spectra and their carbon aromaticity (f_a) of original coals and char samples after heat-treatment.

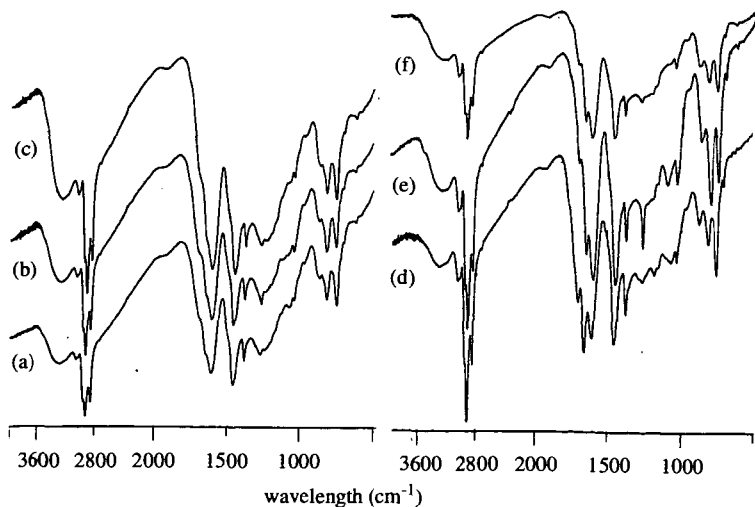


Figure 3. FT-IR spectra of the tar fraction obtained from the heat-treatment of WIT coal at (a)412, (b)432 and (c) 446 °C and GNY coal at (d)397, (e)456 and (f)498 °C.

THE CHARACTERIZATION OF PRODUCTS FROM COAL/RESID CO-COKING

Anne E. Fickinger, Mark W. Badger, Gareth D. Mitchell and Harold H. Schobert
The Energy Institute
Coal Utilization Laboratory
The Pennsylvania State University, University Park, PA. 16802

Keywords: Coal/resid co-coking, coal-derived jet fuels, coke formation.

Introduction

Co-coking is a novel process that incorporates the fundamentals of coal liquefaction and coal pyrolysis. The main motivation behind this novel process was to obtain coal-derived liquid products and carbon-rich solid products, by introducing coal and petroleum resid into a delayed coking operation and simultaneously upgrading them. The liquid products obtained would contain coal-derived material that is desirable because it would include cyclic structures, which when hydrotreated would produce a product that may have higher thermal stability than petroleum-based fuels in advanced aircraft applications. This is important since the next generation of aviation fuel may use the fuel as a heat sink, requiring the fuels to withstand the higher operating temperatures of high Mach aircraft.

In the past direct coal liquefaction processes satisfied the need for producing a feedstock for coal-derived jet fuel, that was a high yield of low-boiling aromatic hydrocarbons, which can be upgraded to hydroaromatic and cycloalkane compounds [1]. Coal liquefaction at present is not an economically viable solution. Coal pyrolysis is also a process that yields these coal-derived products using mild operating conditions. However, the main products obtained from coal pyrolysis are water, carbon oxides and light hydrocarbon gases while the desired coal-derived liquids are produced in low quantities [2]. In our approach to this study we wanted to see how we could adapt a well known and extensively used process for the production of coal-derived feedstocks for advanced jet fuel production. To this end we chose to study how we could utilize the delayed coking process.

Delayed coking is a process used commercially to obtain quality coke and light hydrocarbon fractions from low value petroleum resids and decant oil. This process typically operates in the temperature range of 450-500 °C [3]. Martin and co-workers researched the effects of simulating delayed coking conditions with the co-processing of resid and coal, on the overall products formed [4].

The work presented here represents a continuation of previous studies of co-coking [4,5,6], while focusing in on the characterization of the coal-derived products from this novel co-coking process.

Experimental

Three coals were selected from the Penn State Coal Sample Bank and Database based on their high fluidity, high volatile content and relatively low ash values. Two of the coals were high volatile bituminous coals from Virginia, while the third was a high volatile bituminous coal from the Pittsburgh seam. Table 1, displays the main characteristics of the three coals selected for co-coking. The samples were ground to a -60 mesh and vacuum dried at 110 °C for 2 hours prior to each of the experiments to remove excess moisture. The petroleum vacuum resid used was a coker feed supplied by BP America and was used as received.

Table 1. Properties of the coals used in this study

RANK	POWELLTON	EAGLE	PITTSBURGH #8
	hVAb	hVAb	hVAb
MOISTURE	6.5	6.8	2.4
ASH	5.0	5.5	10.0
%C	87.6	87.3	83.3
%H	5.8	5.6	5.7
%N	1.6	1.6	1.4
%S	0.9	-	1.3
%O	3.9	-	8.4
TEMP. MAX FLUIDITY (C)	448.0	437.0	438.0
FLUIDITY (DDPM)	30000+	30000+	20002

The reactions were carried out in vertical 25 ml microautoclave sealed reactors with *ca* 6 grams of coker feed and 3 grams of coal (resid/coal ratio of 2:1 by weight) at four temperatures (450, 465, 475, and 500 °C). The reaction length was 2 hours. The reactors were purged with nitrogen to remove any air within the reactors and left at ambient pressure. Once the reaction was complete, the reactors were cooled and the gases that evolved were vented. Any pourable liquid was collected through the stem and later included in the oils (hexane soluble fraction). The products were then removed from the reactor and subjected to a Soxhlet extraction using hexane to remove the oils, toluene to remove the asphaltenes, and finally THF to remove the preasphaltenes. The THF insolubles were then dried in a vacuum oven for 2 hours at 30 °C to remove any excess solvent so the coke product yield could be recorded on a dry weight basis.

The hexane-soluble fractions were subject to analysis using GC-MS and SimDis GC. Semi-quantitative analysis was performed using a Shimadzu GC 17A linked to a QP5000 MS and fitted with a Restek XTI-5 30 meter column. Boiling point distributions were measured using an HP 5890 II plus instrument with and FID and fitted with a 6 meter Restek MXT-500 SimDis column. Ultimate analysis was performed on the coke products using a LECO 600 CHN analyzer and a LECO MAC 400 was used for proximate analysis. Optical microscopy was also performed to determine how the coal and the resids interacted in the coke products.

Results and Discussion

Table 2 shows the overall distribution of the liquid and solid products obtained from co-coking experiments at temperatures of 450, 465, 475 and 500 °C respectively. From these results we can conclude the general trend that as the temperature increases the coke yield increases while the liquid products decreases. Similar conclusions were shown in the work carried out by Hossain and co-workers [7], in that the higher the internal pressures in the tubing bomb reactor the higher the solid carbon yield. In our system the higher temperatures promotes greater decomposition of the liquid phase to gaseous products, which in turn leads to higher internal pressure, and thus higher coke yields.

Table 2: Percent yields for the solvent fractions from co-coking experiments using Eagle, Powellton, and Pittsburgh coal plus coker feed at 450, 465, 475, and 500 °C

PERCENT YIELDS						
TEMP (°C)	FEED	GAS	OILS	ASPHALTENES	PREASPHALTENES	COKE
450	CO-EAGLE	14.0	24.7	3.5	2.5	42.1
	CO-POWELLTON	12.1	32.2	17.2	4.0	37.1
	CO-PITTSBURGH	12.2	19.5	4.3	3.9	44.5
	COKER ONLY	16.9	52.5	5.0	1.6	21.2
	POWELLTON ONLY	19.2	2.3	1.1	20.0	86.2
465	CO-EAGLE	22.3	13.2	2.7	4.7	50.4
	CO-POWELLTON	22.5	7.1	0.3	0.8	25.91
	CO-PITTSBURGH	18.0	16.9	1.8	1.1	49.1
	COKER	16.1	47.7	7.9	1.9	14.5
475	CO-EAGLE	18.3	6.5	8.0	2.3	47.6
	CO-POWELLTON	9.1	7.7	0.6	2.4	36.5
	CO-PITTSBURGH	24.9	12.5	1.4	4.5	51.2
	COKER	37.2	28.2	1.6	6.9	25.9
500	CO-EAGLE	17.0	5.4	0.3	4.4	48.5
	CO-POWELLTON	28.3	6.7	0.3	2.2	50.6
	CO-PITTSBURGH	28.6	6.3	0.5	2.7	50.9
	COKER	47.1	16.9	0.4	6.0	35.3

Reactions preceded by a Co- indicates co-coking experiments.

GC-MS was performed on the hexane soluble fractions to obtain the specific compound distribution of the products from these experiments. The major peaks and volume percents were identified and based on the total area under the peaks. From Table 3, we can see that as the temperature of the reaction is increased, the presence of aromatic compounds increased. This would indicate that the coal conversion and the inclusion of coal derived material in the products was increasing. The coker feed on the other hand consisted of mainly saturated alkanes, which we see contributed to the high content of alkanes for the co-coking reactions at lower temperatures. It is also worth noting that the different coals produced coal-derived compounds at similar reaction temperatures. For example, co-coking experiments performed at 465 °C with Eagle produced high quantities of naphthenes, Pittsburgh produced high quantities of pyrenes, and Powellton had compounds that averaged out across the range of those identified. In addition we can see that in the identified products from co-coking, with the exception of Eagle at 465 °C, that no phenols have been identified. This suggests that their numbers have been sufficiently reduced under the reaction conditions, possibly due to their inclusion in the propagation reactions that lead to coke formation, and thus, their removal from liquid products. These compound distributions obtained from co-coking experiments showed similarities with the products derived from flash pyrolysis experiments by Nip *et al* [7].

Tables 4 shows the percentage yields of methyl substituted compounds that were identified in the oil fraction from co-coking experiments. C1, C2, C3, etc. correspond to mono, di, and tri substituted compound, respectively. It is clear to see that heat-treated coker feed does not contribute any significant quantities of substituted aromatic compounds to the oil fraction (see Table 3). Therefore all the aromatics identified come from coal-derived material.

Once again it can be seen that the different coals produced compounds with differing levels of substitution. Thus indicating the differences in the molecular composition of the coals, even though they are of the same rank classification. The most likely reason for this would be in the subtle structural differences in the reactive macerals, although this is difficult to prove. The increases in temperature are exemplified in the series of tests performed on Powellton coal between

450-500 °C. The general trend shown is that with an increase in temperature, there is a decrease in the amount of substitution in the compounds after the reaction is complete. This is due to the increased cleavage of the methyl groups from the ring at elevated temperatures, with formation of gaseous products. Although not reported, this does also contribute to a reduction in the H/C ratio in the products at higher temperature.

Ultimate analysis and optical microscopy was performed on the THF-insoluble to give an indication of the quality of the coke products being formed. Figure 1 shows that the H/C ratio for the products from co-coking have a lower value than the individual heat-treated feeds. If we calculated the H/C ratios for the products from co-coking from the results of the feeds coked individually, the estimated value is higher than the actual result from the co-coking experiments. This suggests that in co-coking we are enhancing coke formation and the formation of a more carbon-rich product. This is different from what other researchers, such as Tanabe and Gray [8], have seen. In their study the presence of fine particles such as clays, inhibited coke formation during the heat-treatment of vacuum resid.

The optical microscopy results indicated that the coal was contributing more to the mass of the coke product than the petroleum resid. The optical microscopy results also concluded that good mixing was occurring in the reactor between the resid and coal. Which was also a conclusion we gained from fluidity studies which were performed on the feeds and mixtures, that showed both the coals and coker feed were fluid over the same temperature range, and underwent devolatilization at the same rate. In addition optical microscopy gave a good indication of the fine mosaic structures formed during the co-coking conditions. Although there was little evidence to support the homogenizing of the two phases – coal and resid – the analyses showed interesting features. Amongst them were the influences of coal particle size on the degree mesophase formation and the elongated fluid structures from the coal, which were produced during the reactions.

Simulation distillation GC was performed on the hexane soluble fractions produced, to obtain boiling point distributions. For this research, the primary temperature range that was desired for the hexane soluble fraction to fall within was the jet fuel range. The jet fuel range is defined as liquids falling within the 200-260 °C temperature ranges. Figure 2, shows the boiling range for the three different coals with the coker feed, as well as the coker feed and heat-treated coals only, reacted at 465 °C. We can see the effect of combining both the coker feed and the coal lowers the yield of the jet fuels fraction by about half. It seems that the coal is acting as a catalyst for decomposition. When coal is present there is both an increase in gas and coke yields. Couple this with a decrease in liquids yields, we can assume the extra coke and gas come from the decomposition of the coker feed. One reason for this decomposition may be due to the presence of relatively high quantities of phenols being produced from the coal under the reaction conditions. Phenols are known to be good sources of radicals, which in turn can initiate retrogressive polymerization reactions, and the increased yield of coke.

Conclusions

From the work performed so far in the sealed batch reactor systems, we believe that 465 °C is the best temperature to produce the best quality oil fraction and carbon-rich product at reasonable yields. Further study will include feed ratio studies, alternative feeds and the effects of reaction length on yields. Future investigation of product characterization from this co-coking process will include the use of a vented reactor to increase the yield of liquid products at the optimum operating temperature of 465 °C, while still maintaining a relatively high yield of carbon-rich coke.

Acknowledgements

The authors would like to express their gratitude to the Department of Defense and Air Force Wright-Patterson Laboratory for the support of this project under contract F33615-98-D2802 delivery order 3.

References

1. Elliot, M.A.(Ed.), in "Chemistry of Coal Utilization Secondary Supplementary Volume", Wiley-Interscience Publication, New York, (1981).
2. Kural, O.(Ed.), in "Coal: Resources, Properties, Utilization, Pollution", Orhan Kural, Turkey, (1994).
3. Speight, J.G.(Ed.) in "The Chemistry and Technology of Petroleum. 2nd Edition", Marcel Dekker Inc., New York, (1991).
4. Martin, S.C., Tomic, J. and Schobert, H.H., ACS Div. Fuel Chem. **42**, 3, 121, (1997).
5. Badger, M.W., Fickinger, A.E., Martin, S.C., Mitchell, G.D., Schobert, H.H., AIE 8th Australian Coal Science Conference Preprints p. 245, December 1998
6. Fickinger, A.E., Badger, M.W., Mitchell, G.D., and Schobert, H.H, ACS Div. Fuel Chem. **44**, 1, 106, 1999.
7. Nip, M., de Leeuw, J.M., Crelling, J.C. Energy and Fuels **6**, 1, 125, (1992).
8. Tanabe, K. and Gray, M.R., Energy and Fuels, **11**, 5, 1040, (1997).

Table 3. Compound Distribution Yield in the Hexane Soluble Fraction

Feed	Oil Yield	Benzenes	Phenols	Alkanes	Naphthenes	Fluorenes	Anthracenes/ Phenanthrenes	Pyrenes
Eagle 450	4.4	-	0.30	0.31	0.53	-	0.17	-
Pow 450	2.3	0.20	0.13	0.27	0.02	0.11	-	-
Coker 465	47.7	-	-	18.28	0.97	-	-	-
CoEagle 465	13.2	0.19	0.16	1.30	2.99	0.19	0.75	0.08
CoPitts 465	16.9	-	-	2.06	1.89	-	0.35	4.63
CoPow 450	32.2	-	-	11.34	-	-	-	-
CoPow 465	14.1	0.13	-	0.47	2.62	0.11	0.97	0.18
CoPow 475	7.7	0.32	-	-	1.84	0.11	0.77	0.13
CoPow 500	6.7	-	-	-	1.52	0.11	0.91	0.29

Table 4. Yield of substituted compounds in hexane soluble fractions from co-coking studies.

REACTION	Benzene			Phenols			Naphthenes			Fluorene	Anthracene/ Phenanthrene		Pyrene
	C1	C3	C4	C1	C2	C3	C1	C2	C3	C1	C1	C2	C1
Pow 450	-	-	-	0.07	0.09	0.04	0.08	0.14	0.06	0.02	0.09	-	-
Eagle 450	-	-	-	-	0.21	0.09	0.21	0.25	-	-	0.11	-	-
CoEagle 465	-	-	0.15	0.05	0.11	-	0.76	1.21	0.88	0.19	0.53	0.09	0.04
CoPitts 465	-	-	-	-	-	-	0.56	0.98	0.35	-	0.20	-	-
CoPow 450	-	-	-	-	-	-	-	-	-	-	-	-	-
CoPow 465	0.11	-	-	-	-	-	0.78	1.17	0.48	0.11	0.49	0.30	-
CoPow 475	-	0.04	0.27	-	-	-	0.61	0.74	0.29	0.11	0.45	0.15	0.05
CoPow 500	-	-	-	-	-	-	0.59	0.60	0.15	0.05	0.50	0.12	0.08

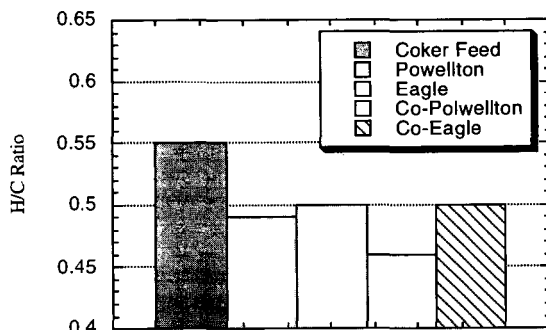


Figure 1. H/C ratios of THF insoluble products from coking experiments performed at 450 °C.

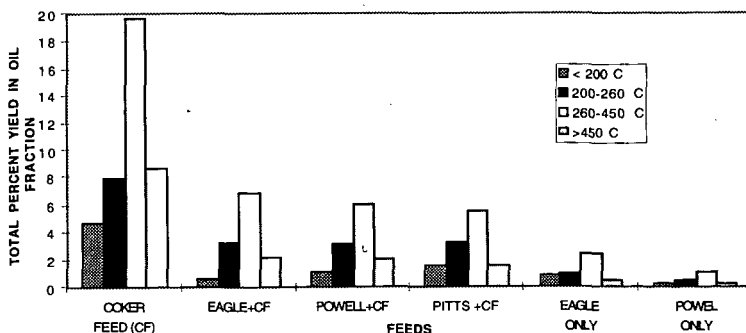


Figure 2. Boiling point distribution analysis of hexane soluble fraction from select co-coking experiments at 465 °C.

CHANGING MARKETS AND NEEDS LEAD THE DOE TO REFOCUS AND EXPAND THE INTEGRATED GASIFICATION COMBINED CYCLE TECHNOLOGIES PROGRAM

Gary J. Stiegel

U. S. DOE, Federal Energy Technology Center
P. O. Box 10940, Pittsburgh, PA 15236
Tel: 412-892-4499
Fax: 412-892-4822
E-Mail: stiegel@fetc.doe.gov

Russell C. Maxwell

Burns and Roe Services Corporation
P. O. Box 18288, Pittsburgh, PA 15236
Tel: 412-892-6247
Fax: 412-892-4604
E-Mail: maxwell@fetc.doe.gov

Keywords: Integrated Gasification Combined Cycle (IGCC); Gasification; Federal Energy Technology Center (FETC)

ABSTRACT

Changing market conditions, brought about by utility deregulation and increased environmental regulations, have encouraged the Department of Energy/Federal Energy Technology Center (DOE/FETC) to restructure its Integrated Gasification Combined Cycle (IGCC) program. The program emphasis, which had focused on baseload electricity production from coal, is now expanded to more broadly address the production of a suite of energy and chemical products. The near-term market barrier for baseload power applications for conventional IGCC systems has combined with increasing opportunities to process a range of low- and negative-value opportunity feedstocks to provide incentives for the refocused and expanded IGCC program. The new program is developing a broader range of technology options that will increase the versatility and the technology base for commercialization of gasification-based technologies. This new strategy supports gasification in niche markets where, due to its ability to coproduce a wide variety of commodity and premium products to meet market requirements, it is an attractive alternative. By obtaining operating experience in industrial coproduction applications today, gasification system modules can be refined and improved leading to commercial guarantees and acceptance of gasification technology as a cost-effective technology for baseload power generation and coproduction as these markets begin to open.

INTRODUCTION

Integrated Gasification Combined Cycle (IGCC) combines gasification with gas cleaning, synthesis gas conversion, and turbine power technologies to produce clean and affordable energy. The combination of combustion turbine and steam turbine is highly efficient in generating electricity. The synthesis gas can be converted to fuels for clean efficient fuel cell generation of power and conversion to high quality liquid fuels. Different variations of the combinations can offer to industry the capability to use low-cost and readily available carbonaceous energy resources and wastes in highly efficient energy conversion options. These options can be selected to meet any of a whole host of market applications as may be suitable for the particular business opportunity. Compared with today's commercial and advanced technologies, IGCC is one of the most efficient and environmentally friendly technologies for the production of low-cost electricity and synthesis gas and can be readily adapted for concentrating and sequestering CO₂. IGCC is the only advanced power generation technology that is capable of coproducing a wide variety of commodity and premium products to meet future market requirements. Through specific selections of the gasification-based technologies, an IGCC configuration can be built to convert virtually any carbon-based feedstock into such varied products as electric power, steam, hydrogen, high-value liquid fuels, and value-added chemicals.

The basic IGCC process for the production of electricity (see Figure 1) initially converts the carbonaceous feedstock in a gasifier into a synthesis gas, a mixture of carbon monoxide and hydrogen. The synthesis gas is cleaned of particulates, sulfur, and other contaminants and is then combusted in a high efficiency gas turbine/generator. The heat from the turbine exhaust gas is extracted to produce steam to drive a steam turbine/generator. The Brayton cycle gas turbine operating in conjunction with the traditional Rankine cycle steam turbine make up this combined cycle. Gasifier technology and combined cycle integrated in this way offers high system efficiencies and ultra-low pollution levels, ultimately reaching efficiencies of 60%, near-zero pollution, and closing the carbon cycle.

In addition to steam and power, the clean synthesis gas can be catalytically converted into hydrogen, environmentally superior transportation fuels, and a variety of chemicals in the coproduction mode. The high quality steam can also be exported for applications other than the production of electricity.

WHY SHOULD INDUSTRY BE INTERESTED?

IGCC has inherent characteristics which will enable major energy industries -- electric power generation, petroleum refineries, chemicals, fuels, and energy users -- to remold their technology and business structure to meet future market needs and take advantage of new opportunities. Deregulation, restructuring, and new types of cost competition are emerging with increased environmental pressures. As a result, the boundaries of these industries and the business structures will be changing significantly. The inevitable result will be opportunities for lower cost, more efficient, and less polluting energy conversion technologies that complement and contribute to the structural changes in both the technology base and business interests of the major energy industries. The unique advantages of IGCC systems have created a significant market for gasification technologies in industrial market applications. Gasification is the only technology that offers both upstream (feedstock flexibility) and downstream (product flexibility) advantages.

Worldwide energy consumption is expected to grow 75 percent between 1995 and 2020, according to the Energy Information Administration (International Energy Outlook 1998). Almost half of the world's future increase (or increment) in energy demand will occur in developing Asia. China alone expects to more than double its current electric generating capacity by 2015. This nation of 1.8 billion people will be considering new technology as a way to reduce environmental and health challenges from increasing energy consumption while, at the same time, using its abundant coal resources. The United States and the rest of the world will also increase its energy consumption and will confront similar energy and environmental challenges.

WHERE IS IGCC TODAY?

Gasification Worldwide

The stage is set for IGCC to play a major role in the domestic and global energy market. There are over 350 gasification units operating worldwide, producing the equivalent of about 20,000 MW. More than 300 of the units are producing synthesis gas (H_2 and CO) rather than power. The largest concentration of gasifiers is at SASOL in South Africa with about 100 fixed-bed gasifiers. China contains the next largest inventory, licensing more than 20 gasifiers and there are 14 gasifiers operating in North Dakota at the Dakota Gasification plant.

In addition to traditional coal utility IGCC applications, gasification technologies have been used in the conversion of coke, residual-oil, and biomass to power, steam, and chemicals and new facilities are being installed for additional applications. In fact, residual oil and coke account for 50 percent of the feed to gasifiers worldwide. Coal accounts for 42 percent of gasifier feedstock, and natural gas fuels 8 percent of all gasification. With the emphasis on reducing fuel costs, waste disposal costs and CO₂ emissions, a number of small projects will be using biomass as the gasifier feed and are either already operating or are near completion.

There are eight IGCC plants that are in construction or are operating in the petroleum refining industry both domestically and internationally. In these applications, the refinery residues are converted to synthesis gas to fuel a combined cycle and co-produce hydrogen for use in upgrading transportation fuel quality. There has been a great deal of activity in Europe, particularly in Italy where at least four projects are moving ahead that could add 1,500 MW to the Italian power grid before the year 2000. In the U.S., Texaco is operating a 35 MW IGCC at its El Dorado Plant in Kansas. The plant is proving that small-scale gasification combined cycle plants are economical and can convert hazardous waste streams into products. Two additional projects that integrate gasification with refining (the Motiva Refinery in Delaware and the Exxon Baytown Refinery in Texas) have awarded architectural and engineering contracts for design and construction.

Competition within Energy Markets

During the coming years, competition between the types of power systems and fuel resources will continue and as long as natural gas remains readily available and relatively inexpensive, natural gas-based power systems are likely to be the technology of choice. As natural gas becomes more expensive, lower cost energy resource options such as coal and alternative fuels will increasingly become the preferred choice and gasification the best technology to use these resources in efficient IGCC and syngas conversion technologies.

The capital cost for a natural gas-fired combined cycle plant is about one-half the cost of an IGCC plant that gasifies coal. IGCC is capital intensive; it needs economies of scale and fuel cost advantages to be an attractive investment option. However, IGCC costs can be improved by integrating processing steps and energy uses in a synergistic way with industrial applications. For example, gasifiers can operate on low-cost opportunity feedstocks, can be used to convert hazardous waste into useful products, reduce or eliminate

waste disposal costs, and can coproduce power, steam, and high-value products for use within the host plant or for export. Fluidized-bed combustors compete with IGCC in smaller cogeneration markets due to their ability to handle a wide range of feedstocks; however, IGCC has the added advantage of product flexibility, which can make it a more economical option for certain industrial applications.

Achievements

The key to commercializing technology is to demonstrate, on a commercial scale, its technical, economic, and environmental performance. DOE's Clean Coal Technology Program, a cost-shared effort with private industry, continues to be a cost effective and successful approach for moving technologies from bench scale to the marketplace. Within the structure of this program, there are three IGCC base-load power production projects and a gasification products conversion project that are relevant demonstrations of the level of commercial readiness of gasification-based technologies. These projects are individually and collectively evidencing the maturity of this technology base. The projects are:

- Wabash River Coal Gasification Repowering Project
- Tampa Electric Company IGCC Project
- Piñon Pine IGCC Power Project
- Liquid Phase Methanol (LPMEOH) Demonstration Project

IGCC PROGRAM

To meet energy market demands and to break the barriers to global commercial acceptance of gasification-based technologies, the IGCC Program strategy emphasizes increased efficiencies, cost reduction, feedstock and product flexibility, and near-zero emissions of pollutants and CO₂. As a result of the development and demonstration projects funded by the DOE's IGCC program and the CCT program achievements mentioned in the projects above, significant progress has been made to reach the capability shown at the left margin of Figure 2, namely about 40 percent efficiency and \$1,200 total plant cost per KW. It is anticipated that with the continued development of oxygen blown systems, hot gas cleaning, membranes, and advanced gasifier systems that further improvements in efficiency and reductions in cost will likely be achieved as shown in Figure 2. An overall pictorial of the FETC IGCC Product Team's view of IGCC R&D Issues is shown in Figure 3. Specific categories of R&D issues and consequent planned activity areas are identified in the figure. To achieve these goals, the strategy is broken down into four distinct areas:

● Research and Development

DOE/FETC is sponsoring a multitude of R&D contracts with industry, academia, nonprofit institutions and government laboratories that support the goals of the IGCC program. Research activities include *advanced gasifier* designs that have the potential to reduce capital and O&M costs, improve thermal efficiency, and process alternative feedstocks. The transport gasifier is being developed through a coordinated program utilizing several research facilities. One of the focus areas of this research is refractory materials and instrument development to improve gasifier performance, operational control, and reliability. Researchers are also developing fluid dynamic data and advanced computational fluid dynamic models to support the development of the transport gasifier and desulfurizer. The use of biomass and municipal waste as gasifier feedstocks for power and coproduction applications are being evaluated. Novel technologies for *gas cleaning and conditioning* are being developed to reduce capital and operating costs and to meet the stringent requirements for cogeneration and coproduction applications. These new technologies are needed to assure the supply of ultra-clean gas for fuel cell and catalytic conversion of syngas to fuels and chemicals as well as enabling advanced processes to effectively separate CO₂. These technologies focus on minimizing consumables and waste products. Research is also being conducted in the area of *advanced gas separation* technologies with the goals of reducing both capital and operating costs, improving plant efficiency, and concentrating and capturing CO₂. Researchers are investigating novel hydrogen separation technologies which are capable of operating at high temperatures and pressures and in the presence of chemical and particulate contaminants. New air separation technologies, such as mixed conducting ceramic membranes, for producing lower cost oxygen are also being developed. And lastly, technologies that can generate *value-added products* to minimize waste disposal and improve process economics are being evaluated. Processes that will improve the quality of the ash, slag, and sulfur by-products from the plant are being developed because adding value to these products will not only enhance the plant revenues, but will more effectively use all of a resource with less waste.

● Systems Engineering and Analyses

A variety of economic analyses, process performance assessments, and market studies are being conducted to provide sound engineering and economic guidance for future R&D initiatives and to support commercialization activities, both domestically and internationally. Some examples include: an IGCC

optimization study for baseload power, cogeneration of steam, and coproduction of power and transportation fuels. These studies will help to define future R&D efforts and will provide the lowest cost and highest efficiency approaches. The R&D efforts can then be aimed at: reducing material costs and consumables as well as total plant costs; a detailed market analysis and the development of a commercialization strategy tailored for coproduction applications; and system studies to assess the production, mitigation, and sequestration of CO₂ in IGCC applications for baseload power generation, cogeneration, and coproduction and concepts for achieving zero emissions and closing the carbon cycle.

- **Technology Integration/Demonstration**

Demonstrate gasification-based technologies at an industrially relevant scale of operation to confirm process scale-up, provide RAM data, and evaluate process performance. Activities would include providing DOE resources to insure the success of existing IGCC Clean Coal Technology programs through technical assistance and R&D projects. The scope of demonstrations will be expanded to incorporate fuel cell, turbine integrations, and hybrids and extend the versatility of demonstrated technology.

- **Product Outreach**

Funding for RD&D activities is becoming increasingly difficult to find in both the private and public sectors. In an effort to overcome these obstacles, DOE/FETC has implemented an aggressive outreach program to communicate, coordinate, and partner with anyone who has a stake in the outcome of IGCC RD&D efforts including: power generators; industrial firms; financial institutions; environmental groups; local, state, and Federal legislators; taxpayers, and others. As part of this activity, stakeholders will be educated on the technical, economic, and environmental benefits of the IGCC systems. Further outreach will be accomplished by coordinating activities with other Federal, state and local government programs and organizations whose programs are complementary to IGCC to avoid potential redundancies. Finally, the formation of multinational partnerships, consortia and user groups will assure a coordinated research effort and continued commercialization activities for gasification-based technologies.

ACHIEVING THE VISION

By the year 2015, gasification-based technologies will have gained global acceptance and as a result will have penetrated worldwide power generation markets, achieved widespread use in the petroleum refining market, and attained, via coproduction, deployment in the fuels and chemicals market. Gasification-based processes will be the technology of choice by being the low-cost leader and providing superior environmental performance through modularity of design and fuel flexibility for easy integration into multiple applications. Commercial guarantees and financing will be readily available, therefore, minimizing the need for government incentives. This will result in improved U.S. industrial competitiveness and enhanced U.S. energy security through increased use of domestic resources. Beyond 2015, the Federal government will continue to develop advanced low-cost technologies to achieve America's goals of economic prosperity in multiple markets, energy security and environmental quality, leading toward zero discharge of all pollutants and greenhouse gases.

Early Entrance Coproduction Plants

The versatility of coproducing power and fuels accelerates deployment of both IGCC and synthesis gas conversion technologies, increases capacity factor, and reduces risks. Coproduction would allow a reduction in oil imports by producing significant quantities of ultra-clean fuels from domestic resources with little or no carbon emissions. However, private investors and process developers are hesitant to invest in the design and construction of coproduction plants until technical, economic, and technology integration risks are acceptable. DOE is implementing a strategy to help mitigate these risks through the support of early entrance coproduction (EECP) small-scale commercial plants that will demonstrate the successful operation of the integrated technologies. They will be constructed adjacent to existing infrastructures, and be capable of processing multiple feedstocks and producing more than one product. These EECP plants will be built by an industrial consortia in partnership with state and federal governments. Once the identified risks have been shown to be acceptable by successful operation, future commercial plants would not require Federal funds for construction and deployment.

Vision 21

Ultimately, gasification will be the cornerstone technology for a new fleet of energy plants for the 21st Century, called Vision 21. These energy plants are highly efficient systems (greater than 60%) that will coproduce low-cost electric power, transportation fuels, and high-value chemicals, all tailored to the geographic energy market demands. The feedstock and product flexibility of gasification-based technologies, coupled with their high efficiency and ultra-low emissions, make them a core part of the Vision 21 concept.

Vision 21 is DOE's strategy for advancing the research and development of technologies critical to creating the integrated energy plants of the coming century. R&D by DOE and industry partners will focus on issues that are key to improving the efficiency, versatility and cost-effectiveness of IGCC components and systems, and to furthering synergies between IGCC and other advanced energy and environmental control technologies.

CONCLUSIONS

Ultimately, IGCC could become the technology of choice for electric power generation. Improvements in IGCC performance are possible through continued development and integration of advanced technologies. Thanks to investments in energy research, development, and demonstration by the Federal government and industry partners, U.S.-based companies are poised for leadership in emerging world markets for IGCC systems, positioning them at the center of a vital energy industry in the 21st century.

FIGURE 1. INTEGRATION GASIFICATION COMBINED CYCLE
Technology Options

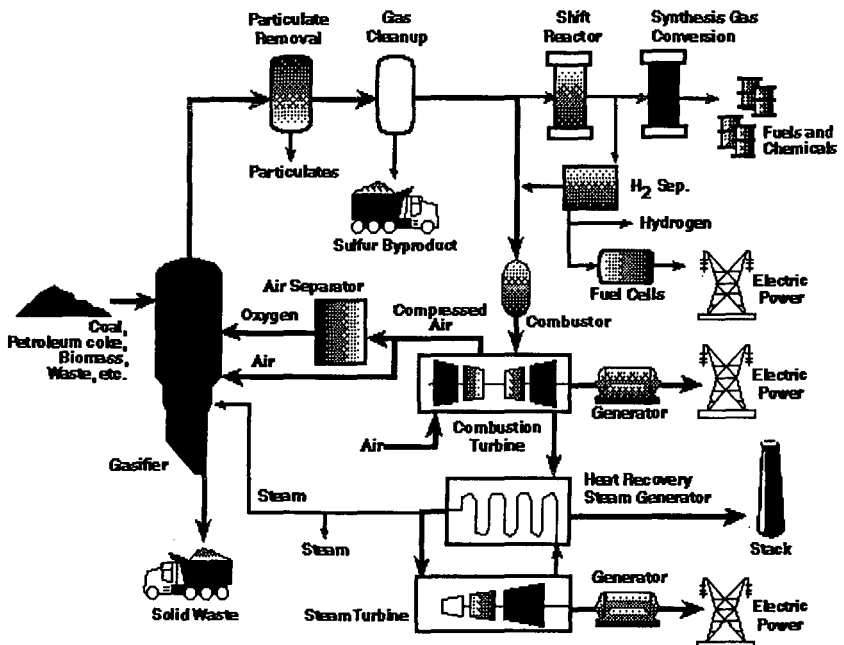


**FIGURE 2. POWER GENERATION
IGCC CAPITAL COST IMPROVEMENTS**

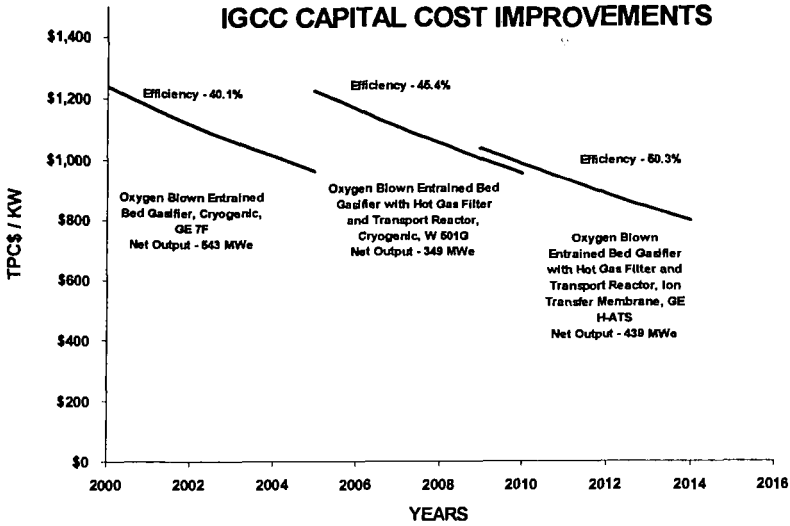
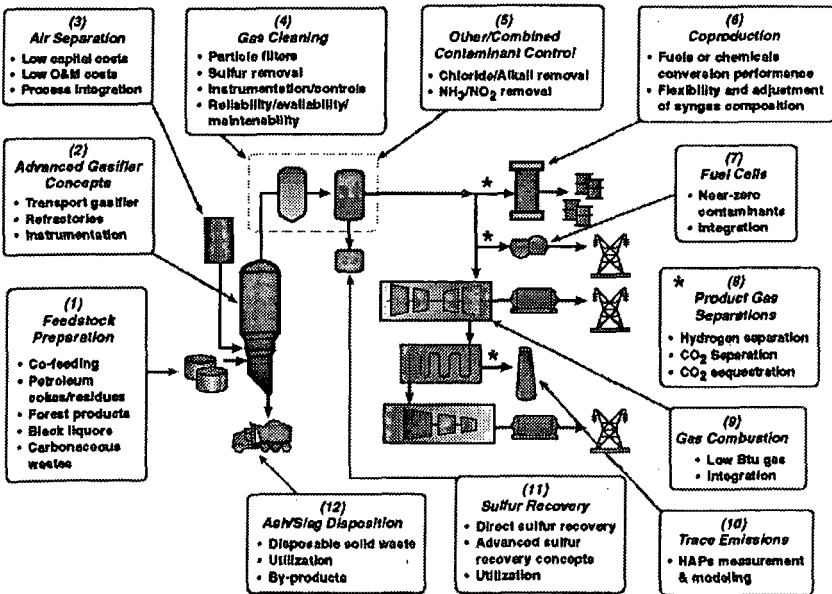


FIGURE 3. IGCC R&D ISSUES



STAGED COAL GASIFIER FOR POWER GENERATION AND FUEL PRODUCTION

**Atsushi Morihara,
Fumihiko Kiso, Tooru Akiyama and Yasuo Yoshii**
Hitachi Ltd.

Fumihiko Hanayama
Babcock-Hitachi K.K.

Satoshi Tsujiguchi and Junichi Iritani
Electric Power Development Co., LTD

ABSTRACT

As coal is the most abundant fossil fuel, coal should be used for not only power generation but also production of fuel and agriculture chemicals. Staged coal gasifier can increase production of methane by controlling the feed oxidizer ratio between stages. The gasifier can also control the ratio hydrogen and carbon monoxide by feed steam to secondary stage. The gasifier can produce di-methyl ether easily at hydrogen production equal to carbon monoxide. The 50 tons per day pilot plant of the gasifier tested at Chiba prefecture in Japan from 1990 to 1995 by NEDO (The New Energy and Industrial Technology Development Organization). The main objective is production of Hydrogen. The new 150 tons per day pilot plant has started construction from 1998 by Electric Power Development Co., LTD. EAGLE (Coal Energy Application for Gas Liquid and Electricity) project aims to increase efficiency of staged gasifier and to achieve high performance clean up system.

INTRODUCTION

Coal is the most abundant of the fossil fuels. At the end of 1990, proven world reserves of coal were estimated to be sufficient for more than 200 years at 1990 production rates. Its wide geographical distribution ensures that coal is to be found in every continent, and is fossil fuel in many countries.

Most coal used in power station. Coal-fired power stations generated almost 40% of the world's electricity. As coal is likely to remain a primary energy resource for the future environment concerns continue to dominate, these aspects will determine which technologies will be employed to convert coal in power. Therefore, that a great deal of effort is being directed into reducing the environmental impact of coal-fired generation through the environment of clean coal technologies.

Gasification processes produced fuel gas, which can be cleaned prior to firing in the turbine combustor, and suffer no such temperature constraint. In addition, there are many factors that make fuel gas easier to clean than gaseous of combustion. Coal gasification is very old technology. Before natural gas was introduced on the market, coal gasification was used to produce fuel gas for distribution in urban areas. It has also been used quite frequently in the chemical and petrochemical industries to produce raw material for chemical process. Converting coal into clean fuel gas offer a very attractive way of generating power. That is used gas and steam turbines, with minimum environment impact.

Hitachi started research on the entrained flow coal gasification process in 1980, developed the two-stage gasifier, and then researched the basic coal gasification technology of the gasifier using 1-U/d process

development unit installed at Hitachi Researcher Laboratory in 1981.

The two-stage gasifier was adopted in 1986 as the coal gasification project of Japan sponsored by NEDO as a part of the Sunshine Project of MITI. Equipment development research was started using 3-t/d gasifier. HYCOL was established in 1986; it chose Hitachi's gasification process for its pilot plant. Hitachi group designed, fabricated, and constructed the 50t/d coal gasification pilot plant 1990[3].

The present paper addresses the continuation of that effort with the focus on the IGCC performance by using two-stage gasifier. This paper refers how to deal with molten slag and sticking fly ash, and show the effect on the total system performance on the focus decreasing of recycle gas.

PRINCIPLE OF THE TWO-STAGE GASIFICATION PROCESS

The principle of the two-stage gasification process is shown in Fig. 1. Features of the process are as follows.

(1) High gasification efficiency

Pulverized coal and oxygen, the gasification agent, are fed to upper and lower burners. They are tangentially installed on the gasifier in order to create a spiral flow in the gasifier. Enough oxygen is fed to the lower burners to melt down the ash contained in the feed coal. Pulverized coal fed to the upper burners is reacted at a lower temperature with a relatively smaller amount of oxygen, compared with that fed to the lower burner, and gasified and converted to reactive and less adhesive char. The char moves down along the spiral gas flow and mixes with high temperature gas in the lower portion of the gasifier, where gasification proceeds further. The produced gas is turned over and goes up to the exit of gasifier with a small amount of char.

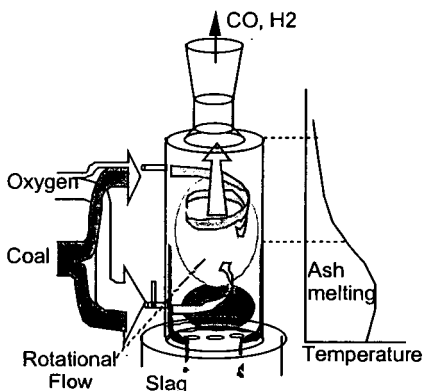


Fig. 1 Principle of the Two Stage Gasifier

The produced gas is turned over and goes up to the exit of gasifier with a small amount of char.

(2) High thermal efficiency from a pneumatic feeding system

Pulverized coal is fed to the gasifier by a dense phase pneumatic feeding system using recycled gas or nitrogen. Therefore, a high temperature can be maintained with a small amount of oxygen, compared with the slurry feed system.

(3) Reliable gasifier with a slag self-coated water-cooled tube wall.

The gasifier consists of a water-cooled tube wall, which is lined by a newly developed high temperature resistant castable. Molten slag solidifies on the inside surface of the wall at first and then molten slag flows down over the surface of the solidified slag. The slag self-coated system is more reliable and extends operation time, compared with the refractory lined gasifier.

(4) Stable slag tapping

A pressure difference between the wall side and the center of the gasifier is generated by the spiral flow. Therefore, hot gas is recycled from slag taps to a gas tap. This ensures stable slagging of molten slag without burning auxiliary fuel.

For the purpose of estimation the two-stage gasification a computational fluids code has been developed for simulating coal gasifier.

REACTION MODEL

Coal gasification is modeled as simultaneous de-volatilization and char gasification processes. The coal volatile is assumed to be a hydrocarbon mixture containing all of the coal hydrogen with the remaining mass being carbon. The volatile evolve at a rate expressed in Arrhenius form:

$$\frac{dV}{dt} = A_v \exp\left(\frac{-E_v}{T_p}\right) (V - V_{\max}) \quad (1)$$

Where A_v and E_v are kinetic rate constants, V is the fraction of coal evolved as volatile, and V_{\max} is the maximum volatile yield. Values of these parameters are shown in Table 1. Knill et al. (1989) showed that de-volatilization occurs during particle heating and is nearly instantaneous for particle temperature greater than 1300 K. Thus, the kinetic constants are chosen to ensure that de-volatilization is complete in 1 ms at 1300 K.

The remaining char is gasified with CO_2 and H_2O :

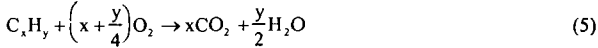


Both reactions are first order in the CO_2 and H_2O partial pressures, P_{CO_2} and $P_{\text{H}_2\text{O}}$, and they proceed in parallel. The chemical reaction rates are expressed in Arrhenius form:

$$k_{c,i} = A_{c,i} \exp\left(\frac{-E_{c,i}}{T}\right) \quad (4)$$

Where the subscript i represents either c or h .

As the volatile is released from the coal, they react with oxygen to form complete combustion products.



The volatile reaction rate, R_v , is controlled by the mixing of fuel and oxidant according to the Eddy Dissipation Model (EDM) of Magnussen and Hjertager (1976). In the EDM, reaction rate is defined as the product of a characteristic eddy lifetime, k/ϵ and the minimum of the volatile and oxygen mass fractions, Y_v and Y_o , respectively:

$$R_v = A_{edm} \frac{\epsilon}{k} \min\left(Y_v, \frac{Y_o}{r_o}\right) \quad (6)$$

Where r_o is the stoichiometry (mass O_2 /mass volatile). The volatile combustion and char gasification products are redistributed in the gas phase according to these reactions:



The water/gas shift reaction and methane-steam reforming reaction may progress in either direction depending on gas composition and temperature as determined by equilibrium[4].

CALCULATION RESULTS

Calculation results shown by fig 2. Cold gas efficiency increased with increasing upper oxygen ratio to coal, and with increasing lower oxygen ratio. The peak value of cold gas efficiency is given when addition of upper oxygen ratio to coal and lower equal 0.9. That shows cold gas efficiency is decided by total oxygen ratio of gasifier.

The outer gas temperature increase with increasing total oxygen ratio. The lower region temperature increases with increasing only lower oxygen ratio to coal.

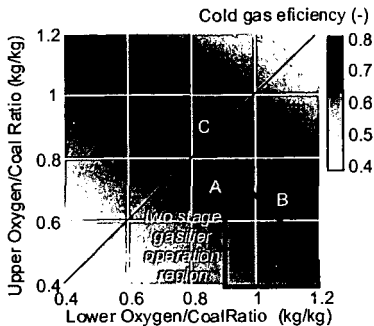


Fig. 2 Calculation Results of Two Stage Reaction

The operation region of oxygen ratio to coal at two-stage gasifier is described as below. To melt ash of coal, lower temperature need to be over ash melting point. Lower region of temperature is decided by lower oxygen ratio. Thus lower oxygen ratio need to be over the line A in figure 2.

On the other hand, the outer gas temperature is decided by total oxygen ratio. Total oxygen ratio need to be lower below the line B. Consequently operation region two-stage gasifier is shown as figure 2. The oxygen ratio to coal can be operated to be the maximum cold gas efficiency.

The oxygen coal ratio for the one stage gasifier depends on the temperature over than the melting point of coal. That is the oxygen feed operation need to be on the line C in figure 2. If the oxygen ratio to coal at the ash melting point is over than that given at the highest cold gas efficiency, the outer gas must increase. On the other hand the total oxygen ratio to coal does not have to be relate to the ash melting point at the two-stage gasifier. The two-stage gasifier can operate at lower oxygen concentration than one stage within some kinds of coal. Thus the two-stage gasifier can be operated in lower quench gas than the one stage gasifier.

EAGLE PLANT

The new 150 tons per day pilot plant has started construction from 1998 by Electric Power Development Co., LTD. EAGLE (Coal Energy Application for Gas Liquid and Electricity) project aims to increase efficiency of staged gasifier and to achieve high performance clean up system.

Figure 3 shows gasifier and heat exchanger at EAGLE Project.

The EAGLE system consists of an oxygen-blown entrained flow gasifier; dry type coal feed system and wet gas clean-up system. The heating value of the coal gas produced by the oxygen-blown gasifier is comparatively high, and the gas quantity produced by processing coal is partial produced by an air blown gasifier.

In addition, in the dry coal feed system, since the coal is transported by dry gas, the latent heat loss due to evaporation of water is nearly eliminated and the water content in the coal gas is kept to a minimum. As a result of the above, losses incurred during the process of wet gas clean-up i. e. sensible heat loss of the coal gas, H_2O and CO_2 losses are reduced. Therefore, a high heat efficiency system is expected[2].

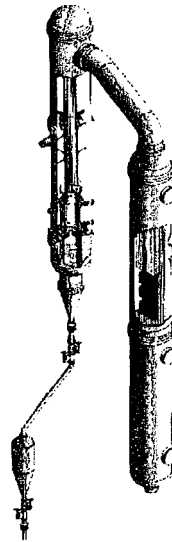


Fig3 Gasifier and Heat Exchanger

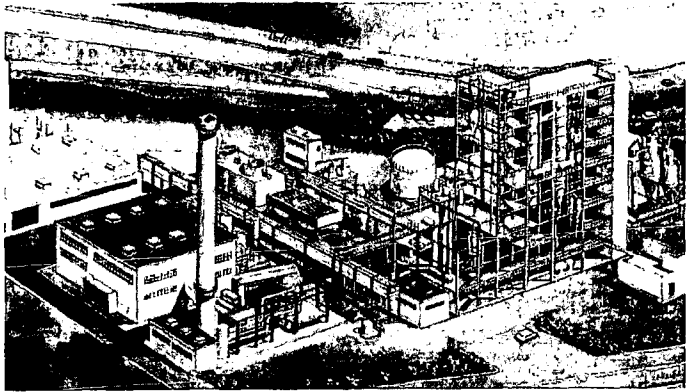


Fig4 Bird eye view of EAGLE Pilot Plant

CONCLUSIONS

This paper has described the present status of developments in the Power Plant as a part of the developments on coal usage technology. The technology strives to achieve the same aim as clean coal technology.

REFERENCES

- [1]K. Nomura et al "Development of the HYCOL Gasification Technology through Pilot Plant Operation" 13 th EPRI Conference on Gasification Power Plants, October 1994
- [2]T. Sasaki et al "Feasibility Study of an Integrated Coal Gasification Combined Cycle System with Oxygen-Blown Gasifier," Transaction of JASME 59,566(B), pp. 2660-2665(September 1993)in Japan
- [3]M. Takagi et al "Entrained flow Coal Gasification Development for a HYCOL Pilot Plant" Hitachi Review Vol. 44(1995),No. 1
- [4] FACT-Vol. 18 Combustion Modeling, Scaling and Air Toxins ASME 1994
- [5]M. Tsukamoto et al "Advances in Coal-fired Power Generation" Hitachi Review Vol. 44(1995),No. 1
- [6]H. Matsuoka et al "Development of the HYCOL Gasifier in the Pilot Plant Operation" 10 th. Annual International Pittsburgh Coal Conference(1994)

INCREASING REACTIVITY OF ILLINOIS COAL FOR USE IN IGCC PROCESSES

Anthony A. Lizzio
Illinois State Geological Survey
615 East Peabody Drive
Champaign, IL 61820

Keywords: coal gasification, IGCC processes, gasification reactivity

INTRODUCTION

Integrated gasification combined cycle (IGCC) processes are expected to become an essential component for energy production in the next century. IGCC processes are able to utilize high sulfur coal and typically achieve power generation efficiencies in excess of 40%. The Illinois State Geological Survey (ISGS) has played an important role in the commercialization of IGCC technology in the Illinois Basin region [1]. A 400 ton test of Illinois coal initiated by the ISGS and performed with Destec Energy, Inc. at the Dow Chemical Plaquemine IGCC facility [2] in 1990, showed for the first time that Illinois coal, a caking coal, could be used effectively in this process. Continued use of Illinois coal at this facility, however, was not possible since the sulfur recovery unit at this plant was designed for low sulfur coal. The results from the 400 ton test, however, were used to help design the The Wabash River Coal Gasification Repowering Project in Terre Haute, IN, initially a joint venture between Destec Energy, Inc. and PSI Energy, Inc. and currently owned and operated by Dynegy Corporation. This ongoing commercial demonstration began operation in August 1995 and currently gasifies up to 2,500 tons/day of an Indiana coal to produce 262 MW of power [3]. The Wabash River facility is the first of its kind to utilize bituminous coal having moderate amounts of sulfur (1-2%). The sulfur in the coal is recovered as elemental sulfur, a saleable byproduct.

In the majority of IGCC processes (e.g., Texaco, Shell), coal is gasified in a one stage process at relatively high temperatures (1400°C) in an oxygen rich environment. In such a process, the coal delivered to the gasifier is converted to gaseous products within seconds, therefore, the intrinsic reactivity of the coal is not an important issue since mass transfer considerations dictate how fast the coal reacts. However, in a two-stage process such as the one being commercially demonstrated by Dynegy, coal is also gasified at lower temperatures (900-1000°C) in a mostly reducing atmosphere in the second stage gasifier. Leftover heat from the oxygen blown gasifier is recovered in the second stage by gasifying additional coal, up to 30% of the total feed. Since complete char burnout is rarely achieved in this second stage, the reactivity of the coal fed into the second stage becomes an important process consideration. If partially reacted char from the second stage is reintroduced into the first stage, this could lower the overall efficiency of the process since high ash, low BTU char now replaces some of the low ash, high BTU feed coal. The development of IGCC technology that utilizes a two stage process to gasify coal provides an opportunity to optimize the reactivity of the coal added to the second stage gasifier. A more reactive coal and resultant char would lead to higher levels of conversion in the second stage gasifier and more efficient operation. The use of more reactive coals in IGCC processes should lead to even more efficient production of electricity [4, 5].

Proven methods for improving the gasification reactivity of coal include adding a catalyst, e.g., calcium, to the coal. Preoxidation of coal may also increase its gasification reactivity. Tar formation, which happens to be detrimental to IGCC process performance, could be suppressed by preoxidation as well as by the addition of calcium to the coal. The objective of this study [6, 7] was to evaluate and improve the gasification behavior of Illinois coal for use in two-stage IGCC processes. This commercial application precludes the use of alkali metal catalysts such as sodium or potassium since these may volatilize and damage the gas turbines. In this paper, we discuss various methods to increase char reactivity through coal preoxidation and/or addition of a suitable catalyst such as calcium or iron.

EXPERIMENTAL

Coal/Char Preparation

Coals were obtained from the Illinois Basin Coal Sample Program (IBCSP) [8] and from selected coal mines throughout Illinois. An Indiana coal currently being used in an IGCC two-stage gasifier was also studied. Coal chars were prepared from these coals in a 2 in. ID horizontal tube furnace (N₂, 900°C, 30°C/min, 0.5 h). After pyrolysis, agglomerated chars were ground with a mortar and pestle to a -100 mesh particle size. Some coals were preoxidized in air at 225°C for 1 h prior to gasification tests and/or catalyst addition.

Catalyst Addition

Calcium (acetate) and iron (chloride) were added to as-received coal by ion-exchange (IE) at different pHs. IE was conducted by shaking 250 mL of each metal solution with 1 g of coal for 24 h, after which the samples were filtered and the solids submitted for metal analysis. Ca and Fe were added by IE at their natural pH (5.5 and 2.0, respectively) or at pH = 10 by dropwise addition of NaOH. Gypsum was added to 250 ml of H₂O containing 20 g of preoxidized coal and stirred at 60°C for 8 h. The pH of this mixture was adjusted to pH = 11.

Coal/Char Gasification Reactivity

Two experimental procedures (isothermal and nonisothermal) were used to measure the gasification reactivity of the char or coal. The specific char gasification reactivity (g C/g C/h) as a function of char conversion (X_c) in 1 atm CO_2 at 850-940°C was determined by isothermal thermogravimetric analysis (TGA). The coal gasification rate as a function of time in 0.80 atm $\text{CO}_2/0.20$ atm H_2O was determined by nonisothermal TGA (25-1000°C, 100°C/min). A Cahn TGA (TG-131) was used to monitor changes in char or coal reactivity with conversion or time. A typical isothermal experiment proceeded as follows. A char sample (10 mg) was placed in a platinum pan suspended from the Cahn weighing unit and enclosed by a Vycor hangdown tube. High purity nitrogen (99.999%) was introduced into the system (150 cm^3/min) and allowed to displace for 0.5 h the air in the reaction chamber. After flushing the system with N_2 , the temperature was raised to 120°C and held for 15 minutes to record the dry weight. The sample was then rapidly heated (100°C/min) to the reaction temperature. Within 1 minute after reaching the setpoint, the temperature stabilized and the initial weight was recorded. High purity carbon dioxide (99.999%) was then introduced into the reaction chamber at the same flow rate (150 cm^3/min). Sample weights were recorded continuously at 30 s intervals until the run was terminated at 90-95% conversion. An ash determination was made for each sample by switching from the reactant gas to oxygen at the reaction temperature.

RESULTS AND DISCUSSION

Char Reactivity

Figure 1 presents typical reactivity profiles (specific gasification rate, R_p , versus conversion, X_c) for IBC-101 char gasified in 1 atm CO_2 at 850-940°C. Activation energies calculated from the Arrhenius plots for this char (Figure 2) increase slightly from 55.0 to 63.8 kcal/mol, well within values reported in the literature [9] for coal char gasification in CO_2 . Thus, the reactivity profiles obtained for IBC-101 under these conditions are considered to be in the chemically controlled regime and represent true variations in char reactivity with conversion.

The gasification reactivities of chars prepared from nine of the twelve coals in the IBCSP were determined in 1 atm CO_2 at 850 by isothermal thermogravimetric analysis. Chars were prepared in a tube furnace under identical pyrolysis conditions (N_2 , 30°C/min, 900°C, 0.5 h) prior to the gasification tests. Figure 3 presents reactivity profiles for these coals and two other Illinois coals, Cedar Creek and Crown II coal, and the Indiana coal. Figure 3 shows that the reactivities of IBC-103, IBC-105, IBC-106 and IBC-108 were comparable over the entire conversion range, while IBC-101, IBC-107 and IBC-109 were most reactive and the high ash IBC-104 char and Indiana coal were the least reactive. Cedar Creek coal having more than twice the sulfur content (the more sulfur the better since sulfur can be recovered as a saleable byproduct), but less ash than the Indiana coal, was more than twice as reactive as the Indiana coal char. Char made from Crown II coal was nearly four times as reactive as the Indiana coal char. Another method of measuring reactivity involving rapid heating (100°C/min) of the coal sample in a reducing atmosphere (80% CO_2 , 20% H_2O , 1 atm) was also used. The results from nonisothermal tests confirmed the order of reactivity obtained from these isothermal tests.

Effect of Preoxidation

Perhaps the most cost effective way to increase the reactivity of bituminous coal would be to add oxygen to it prior to gasification either by natural weathering or a low temperature oxidation treatment. A recent study [10] has shown improved combustion performance for naturally weathered (oxidized) coals versus deep mined (unoxidized) coals. The pretreatment of coal with oxygen is thought to promote the cross linking reactions between aromatic units in the coal structure preventing their rearrangement during pyrolysis (melting) and increasing the surface area of the resultant char, which could lead to an increase in char reactivity [11]. Figure 4 presents reactivity profiles for several as-received and preoxidized coals. Preoxidation of IBC-102 and Cedar Creek coal results in little or no increase in reactivity. Preoxidation of the Indiana coal actually leads to a decrease in reactivity. Coal preoxidation also reduces the BTU content of the coal, which would decrease overall process efficiency. Thus, coal preoxidation alone does not appear to be a viable means to increase the gasification reactivity of these candidate coals for the Wabash River gasification plant.

Catalyst Addition

Calcium and iron are appropriate catalysts for the strict corrosivity requirements of IGCC processes. Abotsi et al. [12] recently evaluated the uptake of iron by coal particles dispersed in water. A surfactant, sodium dodecylsulfate, was used to increase the dispersion and stability of iron loaded onto an Illinois #6 coal. Iron loadings up to 3 weight percent were achieved. Adsorption of iron and calcium onto coal occurs through exchange of the cations (Fe^{+2} , Ca^{+2}) with the protons on the carboxylic or phenolic acidic groups on coal. The use of a surfactant promotes the dissociation of the surface functional groups, which creates a negative charge on the surface of the coal. This will favor adsorption of Fe^{+2} through electrostatic interaction between Fe^{+2} and negatively charged active sites. Practically speaking, efficient catalyst adsorption and dispersion in the coal would need to occur during transport of a coal-water slurry to the gasifier.

The effects of calcium and iron on the gasification behavior of Illinois coal were examined. Calcium and/or iron were added to IBC-101, Crown II, IBC-102, and Indiana coal by ion exchange at various pHs (2.2, 5.6 and 10) to determine to what extent these catalysts would impact char reactivity. Figure 5 presents reactivity profiles (conversion versus time) for Ca- and Fe-catalyzed IBC-101 chars gasified in 1 atm CO₂ at 850°C. When Ca is added by IE at pH = 10, there is a three-fold increase in reactivity. Iron added by IE at pH = 2.2 (natural pH) is seen to have little impact on reactivity. On the other hand, Fe added by IE at pH = 10 increases reactivity by more than a factor of two. These results indicate the importance of using an alkaline medium for preparing Ca- and Fe- catalyzed coals by IE. To the best of our knowledge, no one has shown that adjusting pH during catalyst loading can enhance subsequent reactivity of the catalyzed char. Figure 6 presents reactivity profiles for Crown II coal chars gasified in 1 atm CO₂ at 850°C. The as-received Crown II coal was our most reactive Illinois coal (Figure 3). When Ca or Fe is added to this coal by IE (at pH = 10), char reactivity again increases by more than a factor of two. The reactivities of these coals prepared at their natural pH (either 5.6 or 2.2) are significantly lower than those at pH = 10, consistent with results obtained for the catalyzed IBC-101 coals (Figure 5). Figure 6 presents reactivity profiles for the Indiana coal char. Addition of Ca and Fe at pH = 10 leads to only a slight increase in reactivity. Addition of Ca at its natural pH (5.6) actually decreases reactivity. These results indicate that Illinois coals are not only more reactive than the Indiana coal, but also respond better to the catalyst treatments perhaps due to a more favorable surface chemistry, i.e., greater amount of carbon-oxygen groups that facilitate ion-exchange between the catalyst and the carbon surface.

Effect of Coal Preoxidation on Catalytic Activity

Crown II and IBC-102 coal were preoxidized prior to catalyst addition to determine the effect, if any, of preoxidation on catalytic activity. Although preoxidation in itself was not an effective means to increase char reactivity (Figure 4), coal preoxidation prior to catalyst addition by IE would likely provide additional ion exchange sites for calcium or iron to react with. The coal samples were preoxidized by exposure to air at 225°C for 90 min before catalyst addition by ion exchange using calcium acetate. Figure 8 shows the effects of preoxidation and pH on reactivity profiles of Ca-catalyzed IBC-102 chars gasified in 1 atm CO₂ at 850°C. The reactivity of preoxidized IBC-102 coal is similar to that of the as-received coal. When Ca is loaded by IE at pH = 11 the maximum rates for both the Ca-catalyzed raw coal and preoxidized coal chars (between 6.5 and 8.3 g/g/h) are significantly higher than that of the raw coal (1 g/g/h). The increase in reactivity is more pronounced for the preoxidized sample (8.3 g/g/h). Both Ca-catalyzed chars maintain the high reactivity over most of the conversion range ($X_c = 0.15 - 0.80$). In addition, the Ca-catalyzed chars prepared at their natural pH (5.6) was not as reactive as the one prepared at pH = 11 indicating once again the importance of pH during catalyst preparation.

Figure 9 shows the effects of preoxidation and pH on the reactivity profiles obtained for Ca-catalyzed Crown II chars gasified in 1 atm CO₂ at 850°C. The preoxidized Crown II coal was less reactive than the as-received coal. When Ca is loaded by IE at pH = 11 on the as-received and preoxidized Crown II coal, the gasification rates of both chars increase dramatically. The Ca-catalyzed preoxidized Crown II char maintains its high reactivity to higher levels of conversion compared to the Ca-catalyzed as-received coal indicating better dispersion of the catalyst in the preoxidized sample. The increases in reactivity are not as dramatic when the catalyst is loaded at its natural pH = 5.6, which is consistent with the trends observed for IBC-102 coal (Figure 8). From the data presented in Figures 8 and 9, it appears that oxidation of the coal prior to catalyst addition had a positive effect on the reactivity of both IBC-102 and Crown II coals. Figure 10 shows non isothermal reactivity profiles for raw, preoxidized, Ca-catalyzed raw, and Ca-catalyzed preoxidized IBC-101 coal. Less volatile matter is given off during the pyrolysis stage (24-45 min) for the preoxidized coal and the reactivity of the raw and preoxidized chars are comparable (56-68 min). The Ca-catalyzed chars begin to gasify at a much earlier temperature (about 200°C) than the uncatalyzed chars. The catalyzed preoxidized char produces less volatile matter during the pyrolysis stage than the catalyzed raw coal, which would be expected based on the reactivities of uncatalyzed raw and preoxidized chars.

Use of Gypsum as a Catalyst Precursor

Although calcium acetate is an effective catalyst precursor, its cost may be too high to justify its use in IGCC processes. We also attempted to load calcium onto Crown II coal by ion exchange using gypsum (calcium sulfate) instead of calcium acetate. Figure 11 shows clearly the catalytic effect imparted by gypsum to preoxidized Crown II coal at pH = 11. This result was rather unexpected given the relatively low solubility of gypsum in water (2 g/L) versus calcium acetate (> 80 g/L). Gypsum-catalyzed char is about one half as reactive as calcium acetate-catalyzed char and several times more reactive than the preoxidized coal char. One would expect very little increase in reactivity based on the solubility of gypsum, however, it appears that a significant amount of calcium was incorporated into the coal. This probably occurs because gypsum continues to solubilize as calcium is ion exchanged onto the coal, thus maintaining a sufficient driving force for the ion exchange process. This so-called "shuttling" of calcium from gypsum to coal leads to substantial loadings of calcium given a sufficient amount of time. An increase in the amount of soak time from 8 h to say 48 h as well as optimizing pH of the solution could further increase calcium loadings achieved by gypsum. Figure 12 presents non isothermal reactivity profiles for gypsum-catalyzed chars prepared at pH = 5.6 and pH = 11. The catalyzed coal prepared at pH = 11 is significantly more reactive than the raw coal or catalyzed coal prepared at pH = 5.6. Volatile matter production of the pH = 11 char during pyrolysis is also noticeably less than that of the other two chars. The effects of pH (11

versus 5.6) and catalyst precursor (gypsum versus calcium acetate) on the reactivity of Crown II coal char are shown in Figure 13. Calcium acetate loaded coal is still more reactive than gypsum loaded coal. Perhaps an increase in soak time and/or a more suitable pH will narrow the gap between CaSO₄ and CaAc. Figure 14, shows the effect of calcium precursor on so-called tar formation or volatile matter evolution. Gypsum catalyzed coal produces significantly less volatile matter (part of which is comprised of tars) than the calcium acetate loaded coal

Possible benefits to be derived from using gypsum instead of other catalyst precursors include: 1) a cheap, readily source of catalyst is made available, 2) a new use is found for gypsum, a coal combustion by-product, 3) sulfur from the gypsum could be recovered as a valuable by product in post gasification cleanup processes, 4) calcium oxide would be converted to calcium carbonate, thus reducing emissions of carbon dioxide from the gasifier, and 5) calcium would suppress tar formation, which is detrimental to the performance of some gasifier systems. Dynegy adds limestone to the coal water slurry prior to gasification to improve the slagging behavior of the ash. The limestone, however, is essentially inert with respect to increasing reactivity. Along these same lines, SASOL, the operator of the largest single train gasification plant in the world, is experimenting with adding catalysts to their feed coal to increase coal throughput in their process [13]. SASOL is using a waste stream from a power plant that contains low concentrations of calcium and sodium as the catalyst precursor solution. Note that the calcium originates from gypsum present in the power plant waste water. An up to three-fold increase in reactivity was observed when their feed coal was allowed to soak in this solution [13]. SASOL operates eighteen fixed-bed Lurgi gasifiers to produce chemicals by Fischer-Tropsch synthesis.

Potential Use of Illinois Coal in IGCC Processes

Table 1 presents key gasification properties of both Illinois and Indiana coals. The % ash, % sulfur, heating value of some of the more promising coals in these two states shows that several Illinois coals have more favorable properties than the Indiana coal presently being gasified at the Wabash River gasification plant. Cedar Creek coal apparently has the most favorable combination of properties with respect to ash content (6.00%), sulfur content (3.8%) and heating value (12,271 BTU/lb). Table 1 also lists the gasification rates at 20% char conversion in 1 atm CO₂ at 850°C. The Crown 2 coal is seen to be most reactive Illinois coal, while Pattiki is the least reactive. The Indiana coal is the least reactive among all the coals listed. Another important property of the coal is its T₂₅₀ value, which is based on the composition of the ash and gives a good indication of its slagging behavior. These values have been calculated for each coal using a graphical correlation [14] and are also listed in Table 1. Any coal having a T₂₅₀ value less than 2350°F can be gasified without having to add limestone. Dynegy typically adds limestone to their coal/water slurry feed to modify the slagging behavior of the ash. If little or no limestone needs to be added, a significant savings in operating cost could be realized. It is interesting to note that the T₂₅₀ of the Industry mine coal is less than 2150, which is quite favorable for use in the Wabash River IGCC process. It is also important that the mineral matter content of the coal feed be as low as possible. Low ash coal means less waste disposal; less energy is required to heat the coal since ash also contains water that needs to be vaporized. The sulfur content of the Indiana coal is relatively low (1.71%) compared to what would work best in the sulfur recovery system. A coal with twice the sulfur content would be easily handled by the Dynegy system. Several tests with coals other than the one presently being using are planned in the near future. The coals to be tested, however, have not been decided. High sulfur (6%) petroleum coke is also being tested.

Table 1. Comparison of Illinois and Indiana coals.

	% ash	% S	T ₂₅₀ (°F)	R _{sp} ¹ (h ⁻¹)	BTU/lb ²	FSI ³
Illinois coals						
IBC-101	10.40	4.40	---	0.25	10,764	3.8
IBC-106	8.90	3.80	---	0.13	11,796	4.3
IBC-112	10.80	2.80	---	---	12,425	6.5
Crown 2	8.72	4.14	2,500	0.35	11,022	3.5
Industry Mine	7.07	3.58	< 2,150 ³	0.16	11,500	2.5
Cedar Creek	6.00	3.68	< 2,630 ³	0.16	12,271	3.0
Monterey 2	9.63	4.20	2,500	0.14	11,183	4.0
Old Ben 25	9.36	3.12	2,460	0.12	12,163	4.5
Pattiki	9.27	3.13	2,410	0.09	11,959	4.0
Eagle 2	9.57	3.32	2,420	---	11,867	4.5
Indiana coal	10.53	1.71	---	0.06	10,805	---

¹ char gasification rate at 20% conversion in 1 atm CO₂ at 850°C.

² corrected for equilibrium moisture.

³ the predicted temperature is below the temperature of critical viscosity, thus the graphical correlation used is not applicable, actual T₂₅₀ is less than the given temperature.

SUMMARY

The goal of this study was to provide Dynegy Corporation (formerly Destec Energy) with sufficient data to perform a large scale test with Illinois coal, either as received or modified by preoxidation and/or catalyst addition. An analyses of thirty four coals obtained from active mines throughout Illinois showed that several had lower ash content, higher sulfur content and heating value than the Indiana coal presently used by Dynegy. The Indiana coal char was the least reactive of all the chars tested except one made from high ash IBC-104 coal. An Illinois coal having considerably less ash (6.00%), more sulfur (3.68% S) and a higher heating value (12,271 BTU/lb) was about four times more reactive than the Indiana coal. Coal preoxidation had minimal effect on gasification reactivity of Illinois and Indiana coals. Coal reactivity was enhanced by adding catalysts (Ca or Fe) under conditions simulating those of a coal/water slurry. Catalytic effects were strongly dependent on the pH (> 10) of the ion exchange medium. Alkaline pH was found to be most effective. Three- to five-fold increases in reactivities as a function of pH (2.2 to 10) were observed for Ca- and Fe-loaded Illinois coals. Although coal preoxidation was not an effective means to increase char reactivity, preoxidation of the coal prior to catalyst addition enhanced the reactivity of the Ca-catalyzed coal by providing additional ion exchange sites. The use of gypsum (CaSO_4), a coal combustion by-product, instead of calcium acetate (CaAc), as a catalyst precursor was studied. The reactivity of gypsum-catalyzed char was significantly greater than that of uncatalyzed char, but less than one prepared using calcium acetate. The catalytic effect imparted by gypsum was surprising given that gypsum has a relatively low solubility compared to calcium acetate. Further work is needed to modify and test Illinois coals for use in IGCC processes. Binary catalyst systems, which have shown considerable promise in lower temperature gasification systems may provide superior performance relative to equivalent loadings of a single catalyst. Large scale tests need to be performed using ton quantities of optimized Illinois coal under process conditions simulating those used in the Dynegy entrained flow gasifier. The possibility of using Illinois coal in other IGCC processes such as the one to be demonstrated at the Grand Tower Power Station built in Southern Illinois [15] also needs to be examined.

ACKNOWLEDGEMENTS

Funding for this work was provided by the Illinois Clean Coal Institute through the Illinois Department of Commerce and Community Affairs. The technical assistance of Deepak Tandon, Mark Cal, Gwen Donnals, Sheila Desai and Gwen Murphy is gratefully acknowledged. Discussions with Albert Tsang, John Lytle, Ilham Demir and Dan Banerjee are much appreciated. Special thanks to Godfried Abotsi and Gautam Saha for preparing Ca and Fe catalyzed Illinois coal chars.

REFERENCES

1. Ehrlinger, H.P., Lytle, J.M., Breton, D.L., Lizzio, A.A. and Honea, F.I., 1992, "Gasifier Feed-Tailor- Made from Illinois Coal," Final Technical Report to the Illinois Clean Coal Institute.
2. Roll, M.W., Strickland, D.T. and Payonk, R.J., "The Destec Coal Gasification Process at LTGI," 1993, Proceedings of Tenth Annual International Pittsburgh Coal Conference, p. 333.
3. Roll, M.W., "The Construction, Startup and Operation of the Repowered Wabash River Coal Gasification Project," 1995, Proceedings of Twelfth Annual International Pittsburgh Coal Conference, p. 72.
4. Ahn, D.-H., Kim, J.-J., Kim, N.-H., Park, H.-Y. and Kim, C.-Y., "A Study on the Impacts of Changes in Coal Quality on the Performances of Gasification Processes and IGCC," 1995, Proceedings of Twelfth Annual International Pittsburgh Coal Conference, p. 187.
5. Farina, G.L., "The IGCC European Scene," 1995, Proceedings of Twelfth Annual International Pittsburgh Coal Conference, p. 199.
6. Lizzio, A.A., Cal, M.P., Lytle, J.M., Demir, I., Donnals, G.L., Breton, D.L., Tsang, A. and Banerjee, D.D., 1997, "Methods to Evaluate and Improve the Gasification Behavior of Illinois Coal," Final Technical Report to the Illinois Clean Coal Institute.
7. Tandon, D., Lizzio, A.A., Abotsi, G.M.K. and Saha, G., 1997, "Increasing Reactivity of Illinois Coal for Use in IGCC Processes," Proceedings of Twenty Third Biennial Conference on Carbon, University Park, PA, p. 454.
8. Demir, I., Lizzio, A.A., Fuller, E.L. and Harvey, R.D., 1994, "Evaluation of the Surface Properties of Illinois Basin Coals," *Journal of Coal Quality* 13, p. 93.
9. Lizzio, A.A., Jiang, H. and Radovic, L.R., 1990, "On the Kinetics of Carbon (Char) Gasification: Reconciling Models with Experiments," *Carbon* 28, p. 7.
10. Pisupati, S.V., Ph.D. Thesis, The Pennsylvania State University, 1991.
11. Mahajan, O.P., Komatsu, M. and Walker, P.L. Jr., 1980, *Fuel* 59, p. 3.
12. Saha, G., Bota, K.B. and Abotsi, G.M.K., "Assessment of Catalyst-Containing Coal-Water Slurry Formulations," 1995, Proceedings of Twenty Second Biennial Conference on Carbon, San Diego, CA, p. 502.
13. Prinsloo, F.F. and Schneider, M., 1997, "Kinetics of Catalyzed CO₂ Coal Gasification Reactions, Twenty Third Biennial Conference on Carbon, The Pennsylvania State University, University Park, PA, p. 426.
14. Demir, I., Harvey, R.D., Ruch, R.R., Chaven, C., Damberger, H.H., Steele, J.D., Frankie, W.T. and Ho, K.K., 1993, "Characterization of Available Coals from Illinois Mines," Final Technical Report to the Illinois Clean Coal Institute.
15. Clean Coal Today, Newsletter published by U.S. Department of Energy, Spring 1999, p. 1.

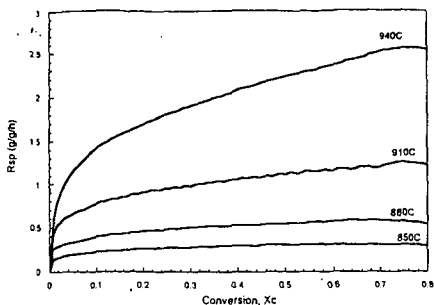


Figure 1. Reactivity profiles for IBC-101 char gasified in 1 atm CO₂.

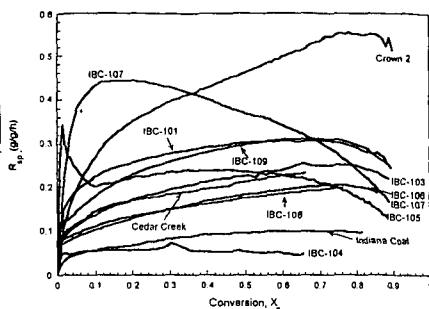


Figure 3. Reactivity profiles for Illinois and Indiana coal chars gasified in 1 atm CO₂ at 850 °C.

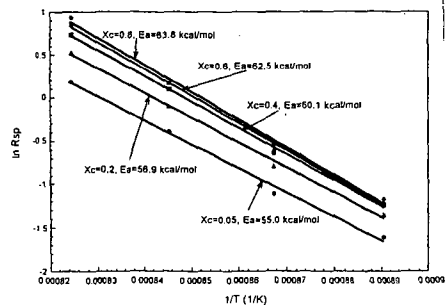


Figure 2. Arrhenius plots for IBC-101 char.

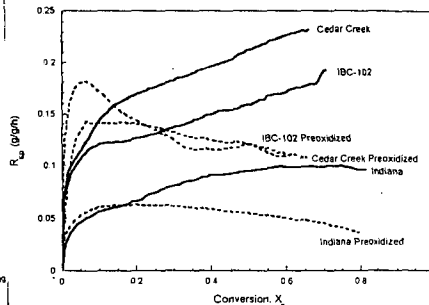


Figure 4. Effect of preoxidation (air, 225 C, 1h) on gasification reactivity.

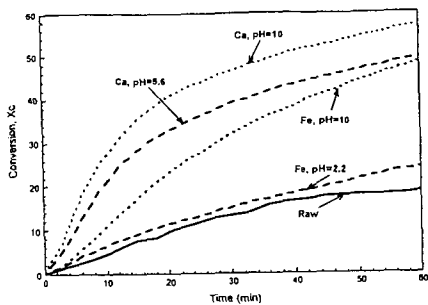


Figure 5. Effect of pH and catalyst on gasification reactivity of IBC-101 char.

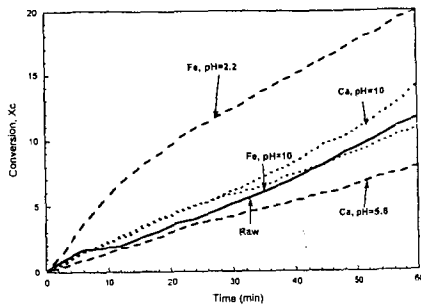


Figure 7. Effect of pH and catalyst on gasification reactivity of Indiana char.

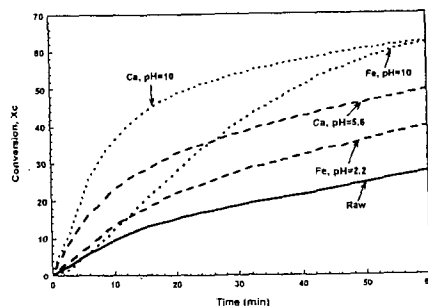


Figure 8. Effect of pH and catalyst on gasification reactivity of Crown II char.

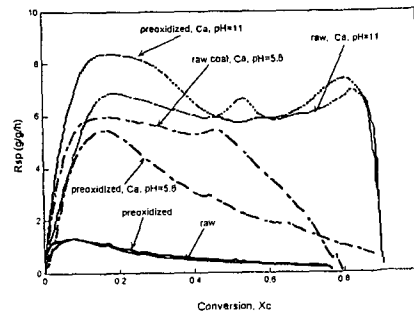


Figure 6. Effect of preoxidation and pH on reactivity of Ca-catalyzed IBC-102 char.

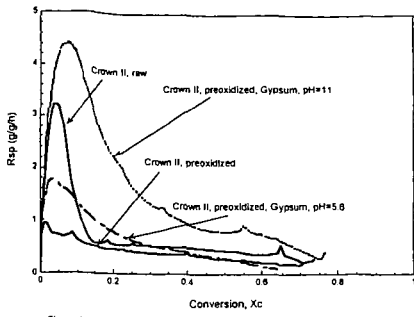


Figure 11. Use of gypsum (CaSO_4) as catalyst precursor.

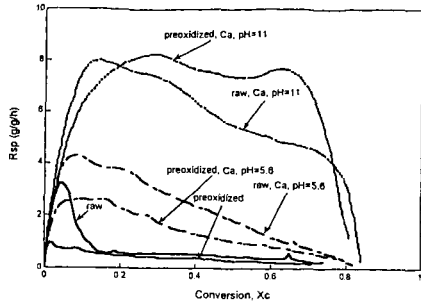


Figure 9. Effect of preoxidation and pH on reactivity of Ca-catalyzed Crown II char.

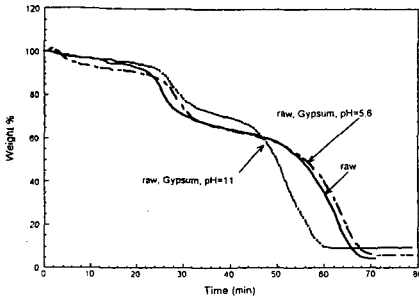


Figure 12. Effect of gypsum and pH on non isothermal reactivity of raw IBC-102 coal.

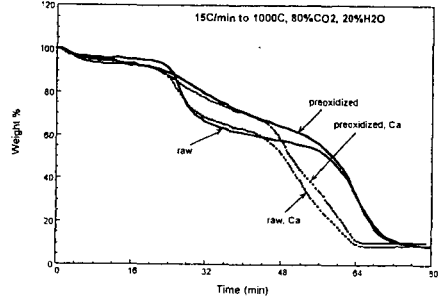


Figure 10. Effect of preoxidation and calcium addition on non isothermal reactivity of IBC-101 coal.

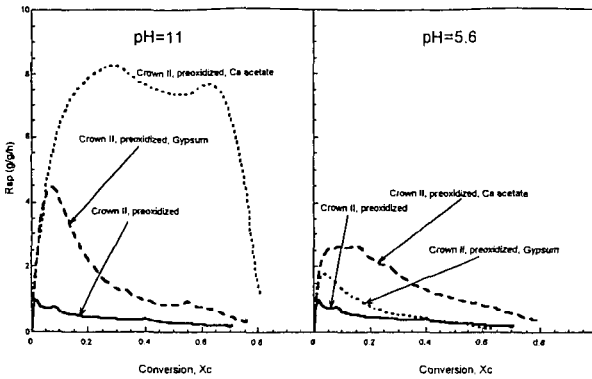


Figure 13. Comparison of gypsum and calcium acetate.

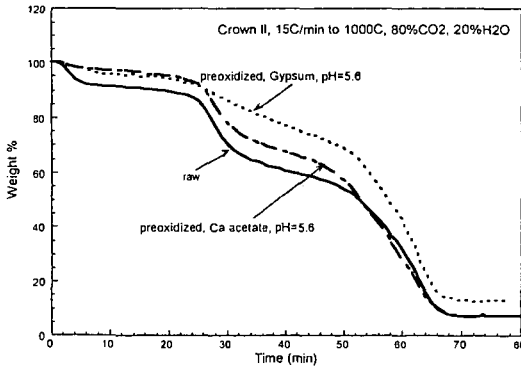


Figure 14. Effect of catalyst precursor on tar formation.

CHEMICALLY ACTIVE AEROGELS FOR HOT GAS CLEAN-UP IN A IGCC PROCESS

Uschi M. Graham and Gerald Thomas. University of Kentucky, Center for Applied Energy Research, 2540 Research Park Drive, Lexington, KY 40511 - 8410.

Abstract

To aid the development of IGCC technologies, the unique properties of aerogels were exploited to research purifying systems for H_2S , NO_x and Hg that are durable and efficient. Aerogels can be used to capture hot gases based on their high surface areas and great tendency to form composites with various other sorbents or structural supports. Silica aerogels are at the heart of the study. Sol-gel synthesis achieved chemically active silica aerogels which were used as structural supports for diverse catalysts depending on the type of gases. Carbon aerogels are also included, focusing mainly on H_2S (g) sorption. Varying the nano- and microstructure of the aerogels and supported metal catalysts further aids in the hydrogenation of CO_2 and selective catalytic reduction of NO_x . Among the sol-gel composite materials applied in this study, those being composed of both organic and inorganic components (organic-inorganic hybrid composites) are observed to have particularly strong affinities for mercury thereby achieving an effective mercury control.

Keywords: aerogels, micro-structure, adsorption

Introduction

Today, coal supplies more than 55% of the electricity consumed in the United States, and it is likely to remain the dominant source of fuel for electric-power generation well into the next century. Integrated gasification-combined-cycle (IGCC) technology is one of the most promising new prospects for electricity from coal to emerge in recent years. It is one of the cleanest methods of generating coal-fired electricity. Rather than burning coal directly, the IGCC technology begins by converting the coal into a combustible gas. The gas itself can be stripped off its impurities, a process capable of reducing about 95% of the sulfur in coal. In addition the technique removes about 90% of the nitrogen oxide pollutants. Because of the IGCC's higher efficiencies in producing electricity compared with conventional coal power plants, a given amount of fuel will produce correspondingly less greenhouse gas leading to a reduction of carbon dioxide gas by at least 35%. However, the gasified coal also contains sizable quantities of hydrogen sulfide (H_2S), a rather toxic gas that also has undesirable corrosive effects on the pipes and turbines. Various sulfidation mechanisms have been suggested during the absorption of $H_2S(g)$ by bulk sorbents, or by a novel concept involving the conversion of $H_2S(g)$ to $H_2(g)$ and elemental sulfur by applying electrochemical membranes.¹

Previous studies demonstrated different ways of cleaning the acid gas emissions prior to burning in a combustion turbine, including SO_2 , NO_x and CO_2 by converting them into marketable commodities including sulfur, sulfuric acid, gypsum and fertilizers.² Although the bulk of the pollutants can be effectively controlled, there is still much uncertainty over the technically most effective approach for controlling mercury emissions and also on how to capture those small amounts of residual $H_2S(g)$ which escaped from the primary recovery phase.

The dominant source of anthropogenic mercury emissions in the United States is derived from coal since conventional particulate control devices can not capture mercury in either of its gaseous forms (Hg^0 ; $Hg^{2+}X$) effectively. The Environmental Protection Agency (EPA) estimated that mercury from power plants accounts for 45 % of the total 158 tons/yr.³ During coal gasification mercury is completely volatilized and a promising approach for mercury control is the injection of an effective sorbent. New IGCC technologies need to address an effective mercury control and previously obtained data for mercury sorbent developments designed for coal fired boilers provide a vast source of information.⁴⁻⁵ Recent findings⁶ indicated a poor sorbent performance of mercury on activated carbon substrates in the presence of the acid gases SO_2 , HCl, NO, and NO_2 , a typical gas mixture always to be expected during gasification of coal. The interaction of SO_2 and NO_2 was observed to be particularly detrimental on the sorbent performance. For example NO_2 in a simulated flue gas inhibits $Hg^0(g)$ adsorption on activated carbon but promotes the formation of $Hg^{2+}X$ (e.g., X corresponds to $Cl_2(g)$ or $O(g)$; mercuric solids are possible in the presence of sulfate and sulfide) instead which occurs at $NO_2(g)$ concentrations as low as 20 ppmv.⁷ Although the mechanisms of the mercury-sorbent-interaction in the presence of SO_2 and NO_2 are not understood it is known that the $Hg^0(g)$ typically is converted to a volatile oxidized form and it is suggested that the sorbent's oxidized surfaces catalyze the reaction.⁸⁻⁹ Since the IGCC technology helps eliminate fly ash emissions completely, the interactions between $Hg^{2+}X$ and fly ash particle surfaces and, hence, any respective surface-catalytic effects typically occurring during flue-gas/fly ash interactions can be neglected for the purpose of this investigation. Experimental results from the sorbent-mercury-flue gas interactions may be extrapolated to the IGCC system.

In the case of mercury, carbon sorbents have been used with varying success because of the interfering reactions mentioned earlier. However, in case of $H_2S(g)$, carbon sorbents offer excellent recovery potential from the hot flue-gas stream even under a wide range of different operating conditions. It has also been suggested that the carbons may be used as an active support for either copper or zinc oxides to further enhance the sorption process.¹⁰ Instead of injecting activated carbon as a sorbent in a IGCC system this study focuses on the unique properties of advanced aerogel materials.

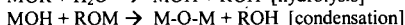
Objectives

Experiments are performed to capture both mercury and hydrogen sulfide, but not necessarily on the same aerogels. The overall objective is to identify conditions for effective capture using chemically active aerogels (and aerogel composites). Applications for aerogel materials include additives for advanced composite materials, such as more reactive sorbents. It is the study's primary objective to observe the affinity of chemically enhanced aerogels towards capturing gaseous mercury species even in the presence of a typical flue gas mixture including NO_2 and SO_2 . Another approach focuses on scrubbing dilute quantities of $H_2S(g)$.

Materials

Aerogels are highly porous, semi-transparent metal oxide materials.¹¹⁻¹² They are very light (the lightest have a density of only 3 times that of air, i.e. 0.003 g/cm^3) and are characterized by excellent heat resistance (up to 800°C), an important property allowing us to use aerogels to clean hot flue gas emissions. They have extremely high surface areas ($600\text{-}1000 \text{ m}^2/\text{g}$) and are the product of supercritical drying of a sol-gel produced alcogel.^{13, 14, 15} The combination of their properties makes them attractive for a number of reasons to be used in the adsorption and safe storage of pollutants from IGCC processes.

A thorough review of the sol-gel process used in this study, describing the transition of a system from liquid, mostly colloidal, into a solid gel phase can be found elsewhere.¹⁶⁻¹⁷ In general, the sol-gel chemistry is based on the hydrolysis and condensation of metal alkoxides $M(OR)_z$. These reactions can be generalized as follows:



The silica aerogel pore network can be characterized by an open-pore structure. The flue gas can flow from pore to pore, and eventually through the entire aerogel. It is this property that makes aerogels effective sorbents for gas phase infiltration and reaction. Although the silica aerogels possess pores in the micro, meso, and macro size range, the majority of the pores fall in the mesopore regime (diameters between 2-50 nm). The carbon aerogel also has predominantly meso pores with a slightly larger pore radius and pore sizes $>100 \text{ nm}$. The pore size distribution of the silica and carbon aerogels used in this study are shown in Figure 1.

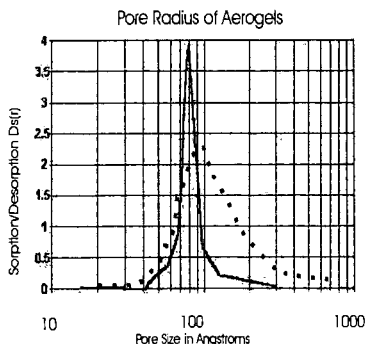


Figure 1 illustrates the distribution of pore radius for a silica aerogel (solid curve) and for a carbon aerogel (dotted curve).

Carbon aerogels are composed of covalently bonded, nanometer-sized particles that are arranged in a 3-dimensional network. Unlike conventional carbon blacks that are produced from gas phase reactions,

these materials are derived from the sol-gel polymerization of selected organic monomers in solution. After the solvent was removed, the resultant organic aerogel was pyrolyzed in an inert atmosphere at 600 °C from 45 minutes to form a carbon aerogel. This material has high porosity (>50%) due to pores that are less than 100 nm in diameter (see Figure 1). Unlike activated carbon powders, the carbon aerogels have high surface areas (ranging from 400-1000 m²/g) which are inherent to the sol-gel process and do not depend on "activation" procedures. A characterization of the primary particles that make up the aerogel network shows that they are composed of nanocrystalline, graphite-like ribbons that are intertwined to form the particles. Another very important distinction from other high surface area carbon powders is that carbon aerogels have oxygen free surfaces that can increase their effectiveness in some applications, particularly in the presence of NO₂ and SO₂ in a typical hot flue gas mixture. The gas/vapor adsorption method was used for determining this study's aerogel surface areas (silica aerogel: 980 m²/g and carbon aerogel: 750 m²/g).

Sample Preparation:

Aerogels are ideal for use in composites where the silica aerogel makes up the substrate and additional phases are added during sol-gel processing. This study used three different kinds of added materials into the silica sol-gel. The first test included spheres of preformed carbon aerogels. The second test involved a porous activated carbon (NORIT) and the third test uses a reducing gas to modify the aerogel composites formed in tests one and two. This procedure allows fabrication of chemically altered aerogel materials that also retain their structural integrity. The aerogel materials produced using this technique typically exhibit a variety of unique properties, such as enhanced chemical activity.

Experimental Setup and Discussion of Results

Mercury adsorption test on aerogels:

Mercury in a flue-gas stream is present only in trace quantities (5-12 µg/m³) and this study focused on using 10 µg/m³ at the inlet valve. The aerogel material was finely distributed on a silica filter and packed in a quartz-glass reactor (both have negligible surface areas compared with the aerogel). A mercury analyzer (Semtech 2000) was utilized to measure Hg⁰(g) on a continuous basis for up to three hours. The proportions of the different species, Hg⁰(g) and Hg²⁺X(g) in the IGCC system are not understood and, therefore, the experiments were repeated and total mercury at the outlet was monitored after passing the exiting gas over a SnCl₂ reducing unit (as was done successfully in related mercury studies⁶⁻⁷). Sorbent mass (for different aerogels) was set to range between 10-100 mg which is well beyond the range where mass transfer might be of concern, however, the pure aerogels have extremely low densities while the composites (aerogel plus active carbon) assume greater densities depending on the carbon loading ratios. A significant sorbent/mercury mass ratio of at least 1000/1 requires a minimum of 10 mg/m³ of sorbent. The transport of mercury species to the aerogel's active surface sites was facilitated using a typical flue gas mixture (Table 1) containing ~ 7 % H₂O vapor. Due to the elevated temperatures of the experiments (120-250 °C) the aerogels will not absorb any moisture. As the samples cool, however, the surfaces, which are covered with hydroxyl groups (~ 5 -OH/nm²) tend to exert strong hydrogen-bonding effects, causing the surfaces to act hygroscopic and handling procedures become more difficult. Although the aerogels's tendency to attract water can be eliminated through simple treatment with trimethylsilyl /or other non-polar aliphatic groups (-OR), this study preferred the presence of the polar acidic counter parts for the inorganic fraction of the aerogel composites.

Results of the mercury adsorption onto different aerogels are summarized in Table 2. In general, after a maximum of three hours of exposure time of the simulated hot flue gas (see flue-gas; Table 1), the chemically active silica aerogel (AERO-I), which had been pretreated with a reducing gas (H₂), adsorbed 92 % of the total mercury (58 % after 30 minutes exposure). The aerogel composite utilizing the NORIT activated carbon product (AERO-II) adsorbed 43 % of the total mercury after 3 hours and less than a third of that amount after 30 minutes. Without the SnCl₂ reducing unit, only 17 % of Hg⁰(g) was detected after the maximum exposure time suggesting that the majority of the mercury was oxidized by the sorbent interaction. Without chemically activating the silica aerogel, the active carbon/aerogel composite functioned predominantly as a catalytic surface to oxidize the Hg⁰(g) (even without the presence of chlorine species to form the thermodynamically most stable form of Hg²⁺X(g)), but did not have excellent sorption capacity for the mercury as did the AERO-I. The third aerogel utilized in this study (AERO-III), which was also prepared as a composite, but incorporated a carbon aerogel rather than the activated NORIT, had good sorption capacity towards mercury, adsorbing 71 % of the total inlet mercury concentration after 3 hours (54 % after 30 min.). However, the overall capacity was somewhat less compared with the chemically active silica aerogel (AERO-I). This study suggests that the difference in oxygen concentration on the surfaces of the NORIT carbon and carbon aerogel may significantly influence the conversion reaction of Hg⁰(g) to Hg²⁺X(g) and the dominant species for chemisorption seems to be Hg⁰.

Table 1 Flue-gas used in Hg tests

Carrier Flue Gas	% vol
H ₂ O	7
SO ₂	1000ppm
NO ₂ /NO	1000ppm
N ₂	Difference
CO ₂	12
O ₂	6
Hg	(10 µg/m ³)

Table 2 Results for Hg adsorption on aerogels*

Sorbent Type	Hg adsorption	
	30 min	180 min
AERO-I	58 %	92 %
AERO-II	11 %	43 %
AERO-III	71 %	54 %

* Table 2 shows mercury adsorption expressed as percent of the total Hg removed from the system after exposure time.

H₂S(g) adsorption tests on aerogels

The combination of in-situ desulfurization (50-60% desulfurization degree) and external desulfurization (completion until >90% sulfur capture) offers an attractive practical solution for hot sulfur abatement in IGCC systems. Work on the use of injected sorbents for in-situ gas desulfurization showed that for sorbent particles injected at high temperatures (1650°C), CaO for example preferably reacts with the silicate phase typically present in coal slag instead of the H₂S present in the gas phase. Besides carbon based sorbents, various metal oxide sorbents, either ZnO-based or CuO-based, as well as mixed metal oxides (binary and tertiary combinations) have been compared in previous works.¹⁰ In this study the H₂S was carried to the aerogel sorbent using a carrier gas (Table 3) that had a composition similar to that typically present in a IGCC system after the majority of sulfur had already been pre-scrubbed (recovered as value-added products). The simulated gas was enriched with 1000 ppm H₂S for the tests and the temperatures of the runs were fixed at 800 °C. Results are summarized in Table 4.

Table 3 Carrier gas for H₂S

Carrier gas	%vol
H ₂	30.5
CO	39.5
CO ₂	10.8 1
H ₂ S	1000ppm
N ₂	Difference
H ₂ O	1.5
T °C	800 °C

Table 4 Results for H₂S adsorption on aerogels

Sorbent type	H ₂ S adsorption
AERO-I	NA
AERO-II	complete after 1 h
AERO-III	complete after 10 min.

The chemically activated silica aerogel (AERO-I) was not used for the H₂S(g) adsorption tests. The aerogel composite with the NORIT carbon (AERO-II) had excellent adsorption capacity with all of the H₂S(g) being captured after 1 hour exposure time. The carbon aerogel-composite (AERO-III) had much faster reaction rates compared with the NORIT carbon and complete H₂S(g) capture was observed after only 10 minutes exposure time. Although both kinds of sorbents have excellent capacities, the mechanisms that control capture in the case of the carbon aerogel (AERO-III) are superior due to the rapid kinetics. To better understand the sorbent performance, experiments are required to further determine sorption rates as a function of reactor conditions.

The final experiment involved both mercury and H₂S(g). The AERO-III that was first used to chemisorb H₂S(g) was cooled to 200 °C and then a flue-gas enriched in 10 µg/m³ mercury was passed over the sorbent. The H₂S molecules which had chemisorbed onto the aerogel composite (this study was not able to tell whether the H₂S molecules attached to the silica surfaces, or to the carbon surfaces, or both) reacted with the mercury to form HgS crystallites which can be seen in a high resolution SEM shown in Figure 2.

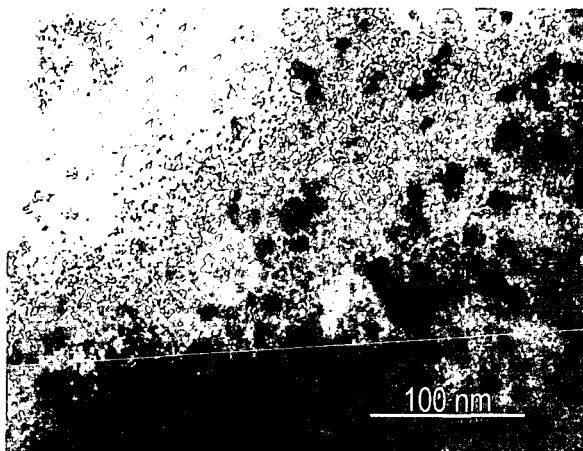


Figure 2 illustrates a high resolution SEM of the aerogel composite AERO-III after adsorption cycles involving first H₂S sorption at 800 ° C and, after cooling to 200 ° C, a second adsorption cycle with a typical flue gas enriched in mercury was performed. The dark circles represent sites where Hg₂ nucleated and grew within the composite AERO-III.

Synopsis

Ideally, new IGCC technologies provide electricity while conforming to the strictest air-quality requirements and there is a driving force to find new and enhanced sorbents. Aerogel composites through sol-gel processing including silica and carbon based aerogels were shown to have excellent potential to adsorb both mercury and H₂S(g) and future experimental work needs to focus on optimizing the conditions at which these sorbents could become economically feasible.

References

- 1 Graaf, J.M. van de, Bijl, E. van der, Stol, A, Kapteijn, F., Moulign, JA. (1998) Industrial and Engineering Chemistry Research, 37, p. 4071-4083.
- 2 Houghton, J.T., L.G. Meira Filho, J.P. Bruce, Hoesung Lee, B.T. Callander, E.F. Haites, N. Harris, and K. Maskell (1994). Cambridge University Press, Cambridge and New York, 339 pp.
- 3 U.S. Environmental Protection Agency. (1997) Office of Air Quality Planning and Standards and Office of Research and Development, EPA-452/R-97-003.
- 4 Laudal, D.L., Galbreath, K.C. and Zygarlicke, C.J. (1996) Fourth International Conference on Mercury as a Global Pollutant, Hamburg, Germany.
- 5 Galbreath, K.C and Zygarlicke, C.J. (1998) Conference Proceedings, Air Quality, Mercury, Trace Elements and Particulate Matter. McLeen, Virginia, p. 1-23 Galbreath
- 6 Miller, S.J. and Brown, T.D. (1998) Conference Proceedings, Air Quality, Mercury, Trace Elements and Particulate Matter. McLeen, Virginia, p. 1-23 Miller
- 7 Miller, S.J., Olson, E.S., Dunham, G.E. and Sharma, R.K. (1998) Air & Waste Management Association's 91st Annual Meeting & Exhibition, San Frandiego, CA, Paper 98-RA79B.07
- 8 Ghorishi, B. and Gullett, B.K (1997) Proceedings of the EPRI-DOE-EPA Combined Utility Air Pollutant Control Symposium; Washington, DC, Aug.25-29; EPRI TR--108683-V3.
- 9 Zhao, L.>, and Rochelle, G.T. (1998) Ind. Eng. Chem. Res., 37, P.380-387.
- 10 Aylett, B.J. 1975 Pergamon Texts in Inorganic Chemistry, Pergamon Press Ltd. Vol. 18.
- 11 Hunt, A.J., Ayers, M.R. and Cao (1995) Journal of Non-Crystalline Solids 189. P264-270.
- 12 Tewari, P.H., Lofftus, K.D., and Hunt, A.J. (1985) 2. Intemational conference on ultrastructure processing of ceramics, glasses and composites. Daytona Beach, FL. Lawrence Berkeley Lab, CA. pp.17
- 13 Hrubesh, L.W., and Pekala (1994) Journal of Material Research 9. P 731-738
- 14 Zeng, S.Q., Hunt, A.J., Cao, W. and Greif, R. (1994) Journal of Heat Transfer 116. P.756-759.
- 15 Hua, d.W., Anderson, J., Digeregorio, J., Smith, D.M., and Beaucage, G. (1995) Journal of Non-Crystalline Solids 186. 142-148.
- 16 Yokogawa, H. and Yokoyama, M. (1995) Journal of Non-Crystalline Solids. 186. 23-29.
- 17 Song, X.Y., Cao W.Q., Ayers, M.R., and Hunt, A.J. (1995) Journal of Materials Research 10. P. 251-254

HOT GAS DESULFURIZATION WITH Z-SORB® SORBENTS

Gyanesh P. Khare and Gil J. Greenwood

Phillips Petroleum Company
Downstream Research and Development
Bartlesville, OK 74003

Keywords: Sorbent, Clean Coal, Coal Gasification, Fuel Gas, Desulfurization, Hydrogen Sulfide, IGCC, Regenerable Sorbent, Syngas, Zinc Oxide

Introduction

Originally designed as a sorbent for tail gas cleanup [1], Phillips Z-Sorb® Sorbent has found application for the removal of hydrogen sulfide from the fuel gas that is generated in a clean coal process. For the latter technology, previous fixed bed sorbents have shown poor mechanical stability due to spalling when adsorbing hydrogen sulfide in reducing gas atmospheres or when being regenerated over many cycles [2].

Bench scale fixed-bed tests conducted at the Morgantown Energy Technology Center showed that Z-Sorb® sorbent performed better than zinc titanate [3,4]. The performance of the sorbent in a moving-bed application at General Electric was very encouraging [5]. The sorbent flowed well, H₂S was reduced to less than 50 ppm at the absorber outlet over long periods and post-test analyses of the sorbent indicated very low sulfate levels at the regenerator exit. The fluidizable version of the novel sorbent was initially tested in Research Triangle Institute's high temperature, high pressure, semi-batch, fluidized-bed reactor system [6]. In a life cycle test consisting of 50 cycles of sulfidation and regeneration, this sorbent exhibited excellent activity and regenerability. The sulfur loading was observed to be 90+ percent of the theoretical capacity. The sorbent consistently demonstrated a sharp regeneration profile with no evidence of sulfate accumulation.

Tests with Z-Sorb® sorbents for desulfurization of coal derived gases were conducted at moderate pressure (507-2027 kPa) and a broad range of operating temperatures (315-540 °C). Earlier studies emphasized the upper end of this temperature range since it is proposed for most gasification projects [4, 7, 8]; other studies have shown the new sorbent formulations operate at lower temperatures (315-425 °C) [1, 4, 9]. These sorbents fulfill the requirements of long term sorbent reactivity, chemical/mechanical stability and attrition resistance.

This paper will provide a summary of the performance of Phillips proprietary Z-Sorb® sorbents at a number of test locations in the United States and Europe. Project participants working with Phillips in this study have been the M. W. Kellogg Company, General Electric (GE), Research Triangle Institute (RTI), Morgantown Energy Technology Center (METC) and members of the European Coal and Steel Community (ECSC).

Sorbent Characteristics

A sorbent for hot gas desulfurization must demonstrate high chemical reactivity, as measured by the rate of sulfur absorption and the sulfur loading capacity, and physical integrity. In addition, for fluidized-bed/transport reactor operation the sorbent must also have good fluidizing characteristics and mechanical strength characterized by low attrition losses. Phillips Petroleum Company has developed suitable sorbent for each of the reactor types currently being developed for the hot gas desulfurization technology. Extruded, spherical, and granular Phillips sorbent formulations are now available for fixed-bed, moving-bed, and fluidized-bed/transport reactor systems, respectively. For fixed-bed reactor the sorbent used was in an extruded form consisting of 1/8" pellets having a bulk density of about 1.0 g/cc. A fluidized version of Phillips' sorbent had an average particle size of 175 micron, a particle size range of 50-300 micron and an apparent bulk density of 0.90-1.00 g/cc. For a moving-bed reactor, a spherical sorbent with an average pellet diameter of 4.1 mm and bulk density of 0.96 g/cc was used.

Bench/Pilot Scale Testing

Phillips Petroleum Company has conducted extensive testing of its proprietary Z-Sorb® sorbent with several research partners in the United States and Europe. Table I summarizes the important parameters from each of these tests. The data reveals a number of facts. It is evident that this sorbent has a high chemical reactivity for sulfur capture. Generally, a sulfur loading of 15-20 wt% is easily achieved. The most striking feature of this sorbent was its high efficiency for sulfur removal with a very sharp breakthrough. Removal of sulfur in various fuel gases to less than 10 ppm under most conditions and perhaps close to zero ppm under some conditions has been demonstrated [4, 10-15]. The data presented in Table I also show that sulfur removal ability of this sorbent is totally unaffected by the gas

composition. The sorbent appears to be effective in removing sulfur from a broad composition range of fuel gases produced by different types of gasifiers ranging from KRW to Shell.

The application of Z-Sorb® sorbent in removing sulfur from authentic gasifier product gases generated from biofuel/brown-coal was investigated by TPS Termiska Processor AB (Sweden). Of the various commercially available sorbent tested, this study found Z-Sorb® sorbent to be the most promising. The sorbent reduced the sulfur content in the effluent stream to below 10 ppm and fully reactivated after desorption at steam concentrations up to 15% at pressures up to 20 bar. Z-Sorb® sorbent was also less sensitive to steam concentration than a zinc titanate sorbent, ZT-4 [11].

Recent work with modified formulations suggests the sorbent temperature application range can be expanded to include the lower temperatures (260-430 °C) used for moderate temperature gas cleanup. Our research found that zinc oxide-based sorbents are effective in desulfurization above 315 °C. Even at temperatures of 315-430 °C the sulfur capacity retained forty to fifty percent of a typical value obtained at higher temperatures, such as 540°C. Figure 1 gives the bench scale test results for the temperature dependence of the sulfur loading capacity of Z-Sorb® sorbent. These runs were done at atmospheric pressure with 4.2% H₂S in CO₂/N₂ and a gas hourly space velocity of 1440 h⁻¹. The sorbent was a fluid bed material. Sulfur loadings of 6-22 wt% in the temperature range of 315-650 °C are quite suitable for a variety of processes currently under development in the Integrated Gasification Combined Cycle (IGCC) program. We also have Thermogravimetric Analysis (TGA) reactivity data that amplify these results. Figure 2 presents the chemical reactivity of a fresh sorbent exposed to simulated coal gases at different temperatures. There is a slight fall-off in sulfur loading as the temperature of absorption is reduced from 540 °C to 370 °C, but the rate at which hydrogen sulfide is absorbed does not suffer as much.

In the long-term bench testing at Phillips Petroleum, the sulfur loading capacity of Z-Sorb® sorbent was found to remain high over a large number of cycles. Figure 3 shows the remarkable performance of an extruded, fixed-bed formulation at an absorption temperature of 430 °C. For nearly 700 cycles of absorption and regeneration, the loadings remain at a high level, starting at 14% and ending at 8%. For most of the cycles, the sorbent picked up at least 10% sulfur, which is 50% of the theoretical loading.

Problem of Sulfate Formation

One of the major concerns in developing regenerable sorbent is formation and accumulation of sulfates in the sorbent during multi-cycle use. Accumulation of sulfates is not desirable as it not only affects the sulfur removal efficiency of the sorbent, but in some cases, for example in zinc titanate sorbents, it has been shown to cause spalling of pellets resulting in fatal failures during process. Although, this problem is not prevalent in Z-Sorb® sorbents as the total sulfur content in the regenerated samples is normally less than 0.5 weight percent, we investigated the regeneration step in detail to examine conditions for the formation of sulfates. Thermogravimetric analysis was used to investigate the regeneration kinetics of a single pellet of sulfided Z-Sorb® sorbent and corresponding x-ray photoelectron spectroscopy (XPS) analysis of the regenerated pellet was performed. A sulfided sample was used for this analysis. It had about ten weight percent sulfur on it. As drawn in Figure 4, the weight loss curves for a single pellet regenerated at different temperatures from 480 °C to 755 °C indicate that 480 °C and 540 °C are ineffective in completely regenerating the sulfided absorbent. In fact, the sample at 480 °C gained weight. XPS measurements in Figure 5 agree on this point. The binding energy data of sulfur from XPS reveal a large amount of sulfide sulfur and sulfate sulfur on the sample after regeneration at 480 °C. Apparently, zinc sulfide converted to zinc sulfate, thereby increasing the weight of the sample. The 540 °C sample showed lower sulfide and sulfate sulfur, but there still was sufficient sulfide to show that regeneration was incomplete. By 565 °C, there was no sulfide left, and by 755 °C, there was no sulfate left. This finding is in agreement with the decomposition temperature of zinc sulfate, which is 740 °C [15].

Bibliography

1. **Brinkmeyer, F. M., and G. A. Delzer**, " Z-Sorb®-A New Sulfur Removal Process", AIChE National Meeting, San Diego, CA, August (1990).
2. **Mei, J. S., L. D. Gasper-Galvin, C. E. Everitt, and S. Katta**, "Fixed Bed Testing of a Molybdenum-Promoted Zinc Titanate Sorbent for Hot Gas Desulfurization", Proceedings of the Coal-Fired Power Systems 93-Advances in IGCC and PFBE Review Meeting, DOE/METC-93/6131, NTIS/DE 93000289, Springfield, VA (1993).
3. **Campbell, W. M., J. J. O'Donnell, S. Katta, T. Grindley, G. Delzer, and G. P. Khare**, "Desulfurization of Hot Fuel Gas with Z-Sorb® III Sorbent", Proceedings of the Coal-Fired Power Systems 93-Advances in IGCC and PFBC Review Meeting, DOE/MET-93/6131, NTIS/DE 9300289, Springfield, VA (1993).
4. **Delzer, G.A., G. P. Khare, and G. J. Greenwood**, (1993). "Z-Sorb® Absorbent for Hot

- Gas Desulfurization", AIChE Annual Meeting, Symposium on Gas Purification, No. 130f, St. Louis, MO., November 7-12.
5. **Gal, E., D. Najewicz, A. H. Furnam, R. Ayala, and A. Feitelberg**, "Integrated Operation of a Pressurized Gasifier, Hot Gas Desulfurization System and Turbine Simulator", Fourteenth Annual Gasification and Gas Stream Cleanup Systems Contractors Review Meeting, Morgantown, WV, June (1994).
 6. **Gupta, R. P., and S. K. Gangwal**, "Enhanced Durability of Desulfurization Sorbents for Fluidized-Bed Applications—Development and Testing of Zinc Titanate Sorbents", Topical Report to DOE/MC/25006-3271. Morgantown Energy Technology Center, U.S. Department of Energy, Morgantown, WV. November (1992).
 7. **Khare, G. P., G. A. Delzer, D. H. Kubicek, and G. J. Greenwood**, (1994). "Hot Gas Desulfurization with Phillips Zinc Based Sorbents", AIChE Annual Meeting, Symposium on Gas Purification, No. 247e, San Francisco, CA, November 13-18.
 8. **Khare, G. P., G. A. Delzer, D. H. Kubicek, and G. J. Greenwood** (1995). "Hot Gas Desulfurization with Phillips Sorbent in Moving-Bed and Fluidized-Bed Reactors", *Environmental Progress*, Vol. 14, pp. 146-150.
 9. **Khare, G. P., G. J. Greenwood, D. H. Kubicek and G. A. Delzer**, (1995). "Regenerable Sorbents for Low Temperature Desulfurization of Coal Gas", Proceedings of the 12th Annual Pittsburgh Coal Conference, p. 1080, Pittsburgh, PA, September 11-15.
 10. **Fantom, I. R. and S. Radford**, "Performance of Regenerable Sulfur Sorbents on Coal Derived Fuel Gas", High Temperature Gas Cleaning, Ed. by E. Schmidt...-1st Ed.-Karlsruhe Institute für Mechanische und Mechanik, 1996.
 11. **Hagstrom, P. and A. Hallgren**, "Bromass for Energy and Industry", 10th European Conference and Technology Exhibition, Wurzburg, Germany, June 8, 1998.
 12. **Bevan, S, D. Najecwicz, E. Gal, A. H. Furman, R. Ayala and A. Feitelberg**, (1994). "Integrated Operation of a Pressurized Gasifier", Hot Gas Desulfurization System and Turbine Simulator, In Proceedings of the Coal-Fired Power Systems 94—Advances in IGCC and PFBC Review meeting. p. 222, DOE/METC94/1008 NTIS/DE 94012252, Springfield, VA: National Technical Service.
 13. **R. P Gupta, S. K. Gangwal and G. P Khare**, (1994). "Fluidized-Bed Testing of Z-Sorb III Sorbent", Topical Report to DOE/METC. Contract No. DE-AC21-88MC 25006, May.
 14. European Coal and Steel Community, Annual Meeting, June 1994. Cheltenham, England. Private communication.
 15. **H. R. Perry and C. H. Chilton**, 1973 Chemical Engineers' Handbook, 5th Edition, McGraw-Hill, New York, p.3-24.

Table 1. Z-Sorb® Sorbent Testing Summary for Hot Gas Cleanup

Research Partner	Process Type	Test Scale	Operating Temperature (C)	Operating Pressure (kPa)	Regeneration Temperature (C)	Coal Gas	Sulfur Loading (gS/100g Sorbent)	Effluent Sulfur (ppm)	Ref.
DOE Morgantown	Fixed Bed	Laboratory	538	1038	482-732	Simulated KRW	14	0	4
CTDD of British Coal	Fixed Bed	Pilot Plant	540	1051	540-750	Air-Blown Gasifier	10.5	<10	10
CIEMAT	Fixed Bed	Pilot Plant	400	1050-2027	550	Simulated EcoGas	15.4-16.9	<20	
TPS	Fixed Bed	Laboratory	490	1050-2027	550	Black&Brown Coal	not det.	4.7	11
General Electric	Moving Bed	Laboratory, Pilot Plant	538	2027	730	Lurgi Gasifier		<50	12
Research Triangle Institute	Fluid Bed	Laboratory	538	2027	590-790	Simulated U-Gas	10.0-20.2	10	13
CTDD of British Coal	Fluid Bed	Pilot Plant	520-540	1051	575-717	Airblown Gasifier	13-15	<10	10
Research Laboratory A	Fluid Bed	Laboratory	400	2027	600	Shell Type	17.5-20.3	<1	14
M W Kellogg	Fluid Bed	Pilot Plant	538-555	690	538	1% H ₂ S in N ₂	15.4	0	18

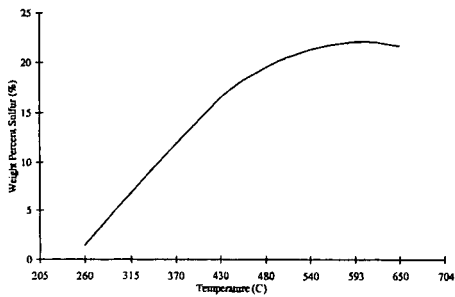


Figure 1. Sulfur Loading Capacity as a Function of Temperature

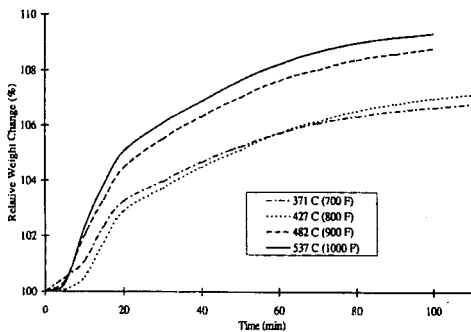


Figure 2. TGA Sulfur Loading Capacity

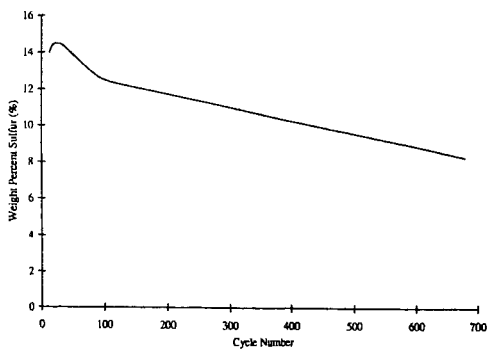


Figure 3. Sulfur Loading Capacity as a Function of Cycle

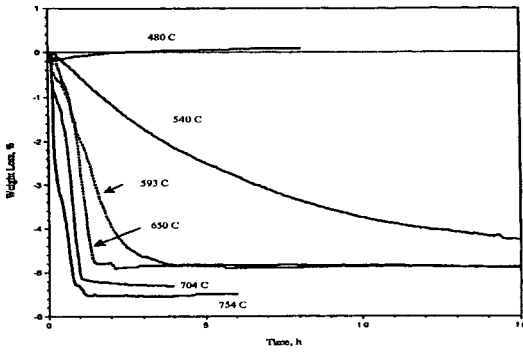


Figure 4. TGA Analysis for Sulfided Z-Sorb® Sorbent

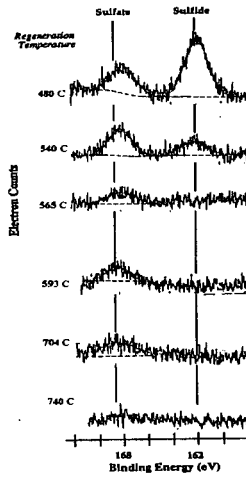


Figure 5. Z-Sorb® Sorbent XPS Analysis of Regenerated Samples

EXPERIMENTAL STUDY ON THE FLAME STABILITY AND THE NO_x EMISSION CHARACTERISTICS OF LOW CALORIFIC VALUE COAL DERIVED GAS FUEL USING FLAT FLAME BURNER

Chan Lee and Yong Chul Kim

Department of Mechanical Engineering, University of Suwon
Suwon PO Box 77, Suwon, Kyunggi-Do, Korea, 445-743

Hyung Taek Kim

Department of Energy Studies, Ajou University
Wonchon-Dong, San-5, Paldal-Gu, Suwon, Korea, 442-749

Key Words: Coal Derived Gas, Flame Stability, Fuel NO_x

ABSTRACT

Experimental studies are conducted to investigate the flame stability and the thermal/fuel NO_x formation characteristics of the low calorific value (LCV) coal derived gas fuel. Synthetic LCV fuel gas is produced by mixing carbon monoxide, hydrogen, nitrogen and ammonia on the basis that the thermal input of the syngas fuel into a burner is identical to that of natural gas. The syngas mixture is fed to and burnt with air on flat flame burner. With the variation of the equivalence ratio for specific syngas fuel, flame behaviors are observed to identify the flame instability due to blow-off or flashback and to define stable combustion range. Measurements of NO_x content in combustion gas are made for comparing thermal and fuel NO_x from the LCV syngas combustion with those of the natural gas one. In addition, the nitrogen dilution of the LCV syngas is preliminarily attempted as a NO_x reduction technique, and its effects on thermal and fuel NO_x production are discussed.

INTRODUCTION

Integrated Gasification Combined Cycle(IGCC) is emerging as a next-generation coal-based power plant because of its low fuel cost, competitive capital cost, high thermal efficiency and superior environmental performance. However, the gas fuel for gas turbine combustion in IGCC power plant is produced through oxygen-blown coal gasification and gas clean-up processes, so it is composed mainly of hydrogen, carbon monoxide and nitrogen that result in low calorific value of the fuel, 1/4-1/5 times smaller than the natural gas. In addition, due to high content of hydrogen in fuel, the LCV coal derived

gas shows very fast burning velocity, chemical reaction rate and high flame temperature[1]. As the consequence, flame instability can hardly be avoided in premixed combustion and NO_x formation rate becomes much higher than in the natural gas case. For this reason, the most of combustion tests for LCV coal derived gas are conducted on the diffusion type burners incorporating with nitrogen and/or steam dilution for NO_x control[2,3] while premix burner technology being at the first stage of development.

Therefore, for the efficient premixed combustor in IGCC power plant, fundamental characteristics of combustion stability and NO_x emission of the LCV fuel gas need to be investigated and would be useful in providing engineering guidelines for future R&D of IGCC gas turbine combustor. In the present experimental study, coal gas burner system is constructed with the flexibility in varying various fuel composition and equivalence ratio conditions, and flame behavior and stability of the coal gas are observed and furthermore thermal and fuel NO_x emission values are measured.

EXPERIMENTAL RESULTS AND DISCUSSIONS

As shown in Fig.1, experimental apparatus is composed of fuel/air feeding , premix burner and gas sampling/analysis systems. LCV fuel gas is simulated as synthetic gas that is produced by mixing carbon monoxide, hydrogen, nitrogen and ammonia. The syngas is premixed with air, fed to and burnt on flat flame burner with porous bronze water-cooled plate to produce uniform velocity distribution, and the burner does not employ the annular stream of inert gas as depicted in Fig.2. Flame behavior picture is recorded by using CCD/digital camera and image processing unit, and the NO_x emission of sampled exhaust gas is analyzed.

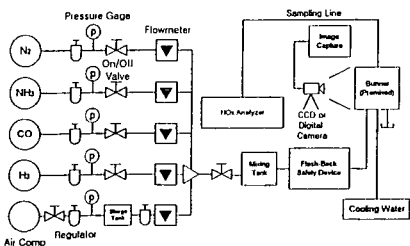


Fig.1 Schematic Diagram of Experimental Apparatus

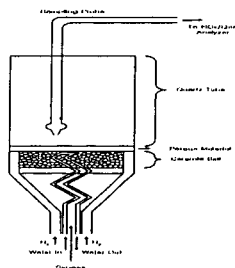


Fig.2 Flat Flame Burner

Before syngas combustion test, a reference experiment is carried out with natural gas fuel of the constant flow rate at 0.48 LPM. Flame of natural gas remains stable within the equivalence ratio range from 0.6 to 1.3, and its NO_x emission level shows lower than 50 ppm. Syngas fuel is produced by mixing carbon monoxide and hydrogen to match the composition of actual coal gas fuel derived from oxygen blown gasifier, CO: 70-90 % and H₂: 10-30% on volume basis. Fuel flow rate is determined on the basis

that the thermal input of the syngas fuel is identical to that of natural gas. In addition, the present study considers NH_3 of 0-3000 ppm in syngas fuel to investigate the effect of NH_3 on fuel NO_x formation. Table 1 represents the fuel flow rates and the compositions of three different syngas fuels used in the present study.

Table 1 Composition and Flow Rate of Syngas Fuel

Syngas No.	$\text{CO}(\%)$	$\text{H}_2(\%)$	$\text{H}_2/\text{CO}(\%)$	Flow Rate(LPM)
1	91.0	9.0	9.9	1.64
2	82.0	18.0	34.1	1.66
3	70.0	30.0 </td <td>42.8</td> <td>1.69</td>	42.8	1.69

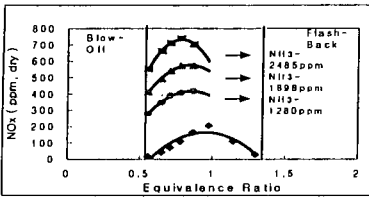


Fig.3(a) NO_x & Flame Stability of Syngas #1

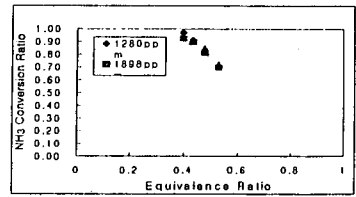


Fig.3(b) NH_3 Conversion Ratio of Syngas #1

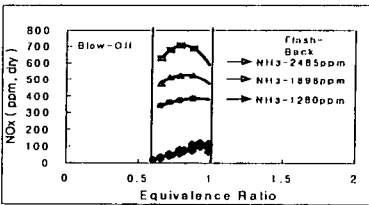


Fig.4(a) NO_x & Flame Stability of Syngas #2

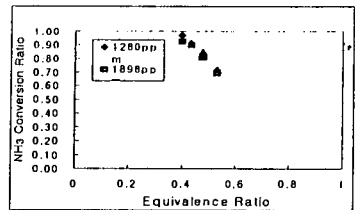


Fig.4(b) NH_3 Conversion Ratio of Syngas #2

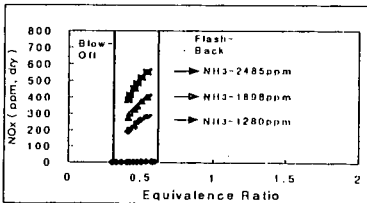


Fig.5(a) NO_x & Flame Stability of Syngas #3

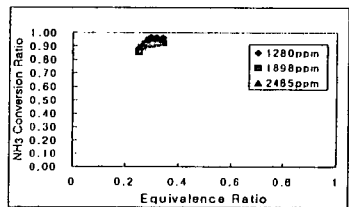


Fig.5(b) NH_3 Conversion Ratio of Syngas #3

Figs. 3(a), 4(a) and 5(a) illustrate the flame stability range and the NO_x emission of syngases with H₂/CO= 9.9, 34.1 and 42.8 % respectively. They show that the flame stability range of syngas is shrunken into narrower range at higher H₂/CO ratio. These experimental results can be explained by that flashback occurs at lower equivalence ratio point due to higher burning velocity with the increase of H₂/CO ratio of syngas[4]. It is deduced from the measured results that if coal gas firing gas turbine combustor is designed with the same burner as the natural gas case, it can be operated only at narrow combustion condition range so careful design modification must be made on air distribution in combustor. As shown also in Figs. 3(a),4(a) and 5(a), thermal NO_x emission level is lowered for higher H₂/CO ratio syngas fuel with lower flame temperature at the stable combustion range. With the addition of NH₃, NO_x emission is more produced by the order of 200-300 ppm, compared with the cases of NH₃, over entire combustion range and its peak point is shifted to lower equivalence ratio compared with the thermal NO_x. Figs. 3(b), 4(b) and 5(b) present the variation of ammonia to NO_x conversion ratio with equivalence ratio at three syngas fuel conditions, and they show ammonia is more easily converted to NO_x at lower equivalence ratio condition[5,6].

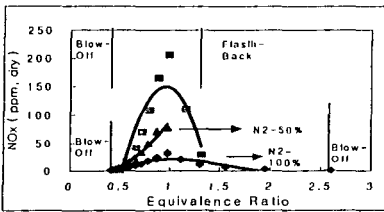


Fig.6 Effect of Nitrogen Dilution (Syngas#1)

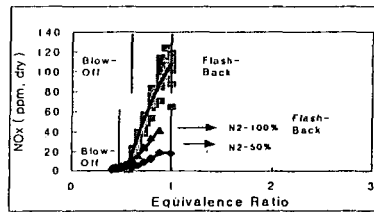


Fig.7 Effect of Nitrogen Dilution (Syngas#2)

The effects of nitrogen dilution on NO_x reduction are examined in Figs. 6 and 7. The present study employs nitrogen diluent that is blended with syngas fuel before entering burner, and its amount is considered as 50 or 100% of fuel flow rate on volume basis. Nitrogen dilution results in remarkable NO_x reduction as well as widening of flame stability range.

CONCLUSIONS

Flat flame burner tests are conducted for investigating flame stability and NO_x emission characteristics of three LCV syngas fuels with the same thermal input as the natural gas case. Flame stability range is shortened to narrower band of equivalence ratio and thermal NO_x is less produced when burning the syngas with higher H₂/CO ratio. The NH₃ content in fuel results in additional 200-300 ppm fuel NO_x formation as well as the shift of peak NO_x point to the lower equivalence ratio compared with the thermal NO_x case. The conversion ratio of NH₃ to NO_x ranges from 97 to 62% with the increase of equivalence

ratio. The effect of nitrogen dilution is very favorable both in reducing NOx emission and widening flame stability range.

ACKNOWLEDGEMENT

This work was performed by the financial support of R&D Management Center for Energy and Resources(RaCER) in Korea.

REFERENCES

1. K.Dobbeling et al., "Low-NOx Premixed Combustion of Btu Fuels Using the ABB Double Cone Burner(EV Burner)," ASME Journal of Engineering for Gas Turbines and Power, vol.118, pp.46-53, 1996
2. C.S.Cook et al., "System Evaluation and LBTU Fuel Combustion Studies for IGCC Power Generations," ASME Journal of Engineering for Gas Turbines and Power, vol.117, pp.673-677, 1995
3. B.Becker and B.Schetter, "Gas Turbine Above 150MW for Integrated Coal Gasification Combined Cycles(IGCC)," ASME Journal of Engineering for Gas Turbines and Power, vol.114, pp.660-664, 1992
4. T.G.Scholte and P.B.Vaags, "Burning Velocity of Mixtures of Hydrogen, Carbon Monoxide and Methane with Air," Combustion & Flame, vol.3, pp.511-524, 1959
5. T,Nakata et al., "A Study on Low NOx Combustion in LBG-Fueled 1500 °C-Class Gas Turbine," ASME Journal of Engineering for Gas Turbines and Power, vol.118, pp.534-540, 1996
6. R.P. Lindstedt and M.A.Selim, "Reduced Reaction Mechanism for Ammonia Oxidation in Premixed Laminar Flames," Combustion Science & Technology, vol.99, pp.277-298, 1994

A STUDY ON THE SLAGGING BEHAVIOR OF COAL ASH IN GASIFICATION/COMBUSTION ENVIRONMENT USING DTF

Hyung-Taek Kim and Byung-Chul Choi

Energy Department, Ajou University

San 5, Wonchun-dong, Paldal-gu, Suwon, Korea, 442-749

Sang-Hwan Park

Materials Science & Technology Division

Korea Institute of Science & Technology

Keywords: coal ash, slagging, gasification

ABSTRACT

The purpose of this study is to determine ash slagging behavior for the optimum ash removal in actual coal gasifier as well as combustor. DTF (drop tube furnace) was utilized for entire experiment to simulate real time and temperature history of coal particle. Pulverized particles of three different coal samples (Alaska, Cyprus and Datong) were injected into DTF with different experimental conditions. The slag samples deposited at the top of sample collector by the particle action of impacting and agglomerating. The formation shape of each deposited slag is related with physical properties of original ash such as ash fusion temperature, viscosity and surface tension. Phase diagram of main components of ash, i.e., $\text{SiO}_2\text{-CaO-Al}_2\text{O}_3$ system are analyzed to determine ash fusion behavior with different composition of the system. Shape of slag formation represents different behavior with gasification and combustion environment and also is effected by chemical composition of coal ash.

1. INTRODUCTION

Among the second-generation coal-fired power systems, IGCC (integrated gasification combined cycle) is characterized by highly efficient and environmentally sustainable technology. Since most of organic impurities of coal are converted into gas phase in gasification S- and N-containing gases can be easily separated from the product gas comparing to p.c. combustion technology. Moreover, CO_2 emission is reduced in IGCC technology because of its high electricity efficiency. Inorganic impurities of coal are also converted into slag in slagging-type coal gasifier. The volume of coal slag is reduced to 1/2~1/3 and the heavy metal compounds in coal ash is vitrified to non-leaching glass form.

In this experimental investigation, DTF is utilized to determine the characteristics and formation phenomena of ash slag generated with different coal samples. The result is analyzed for the relationship with chemical composition, ash fusion temperature and fluidity properties of coal ash. With above information, actual behavior of coal ash inside gasifier/combustor can be predicted so that optimum-operating condition for smooth slagging can be suggested.

2. EXPERIMENT

Characteristics of slag produced in slagging-type gasifier play a major factor in the continuous operation of actual gasifier. Flow properties of slag usually depend on viscosity and melting temperature, which were varied with inorganic constituents of coal ash. Ashes of three coal samples are analyzed with ICP-AAS for the inorganic constituents and the results are shown in Table 1. Generally speaking, reducing agents such as Fe_2O_3 , CaO and Na_2O behave a role in reducing viscosity and melting temperature. On the other hand, oxidizing agents such as SiO and Al_2O_3 will increase viscosity and melting temperature.

Table 1. Chemical composition of coal ash samples

Composition(%)	SiO ₂	CaO	Al ₂ O ₃	Fe ₂ O ₃	TiO ₂	Na ₂ O	K ₂ O	MgO
Datong	54.12	8.08	15.73	13.15	0.83	1.15	0.77	2.18
Alaska	44.83	20.20	19.30	7.01	1.11	0.70	1.40	3.90
Cypurus	51.60	11.37	19.30	5.73	0.84	2.71	0.83	2.11

Gas flow in the DTF reactor was arranged to laminar flow for the exact determination of reactivity and residence time of coal particles. The schematic diagram of DTF was shown in Fig. 1.

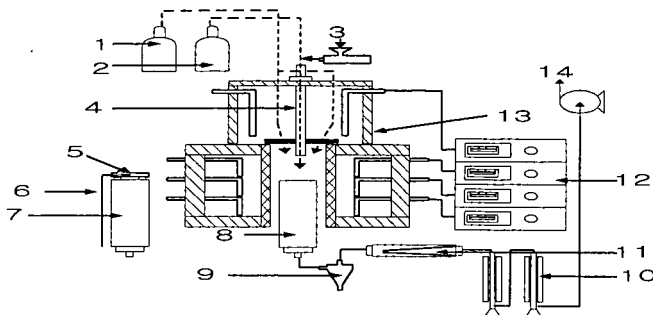


Fig. 1. Schematic diagram of Drop Tube Furnace (1: secondary gas line, 2: primary gas line, 3: coal feeder, 4: injector probe, 5: deposit disk, 6: R-type thermocouple, 7: deposit probe, 8: ash probe, 9: cyclone, 10: condenser, 11: ceramic filter, 12: PID controller, 13: furnace, 14: vent)

Coal feeding rate was fixed at 0.3g/min for entire experiment. In the combustion experiment, air were used for both primary and secondary carrier gas with the oxygen/coal weight ratio of 1.5. However, in the gasification experiment, primary gas was oxygen and secondary gas nitrogen with oxygen/coal ratio of 0.72, which is selected for maximum CO concentration in the product gas. While feeding coal particles at the top of the DTF and flowing carrier gases, reacted coal particles are collected at the top of deposit probe. Solid sample collector was installed inside deposit probe, which was made of metal substrate. Temperature was changed from 500°C to 600°C for the simulation of heat transfer surface. To investigate the reaction between coal ash and alumina refractory, solid sample collector was also made of alumina refractory that was installed at 1500°C in the deposit probe. Deposited ash samples was analyzed with photography for the shape of slag formation.

Ash fusion temperature was measured by standard ASTM method by using Ash Fusion Determinator (LECO model AF 600). Difference in FT and IDT, i.e. ΔT is a factor which shows strength of ash deposit. Generally, if ΔT is small, deposit thickness on reactor surface is thin and adhesive so that removal of ash deposit is very difficult. Table 2 shows fusion temperatures of each coal samples investigated in this study.

Table 2. Fusion Temperature of coal ash samples using ASTM method

Sample Coals	IDT(°C)	ST(°C)	HT(°C)	FT(°C)
Datong	1296	1304	1328	1359
Alaska	1205	1244	1263	1299
Cypurus	1249	1276	1301	1359

3. RESULTS AND DICUSSION

Liquid phase of coal slag behaves Newtonian fluid when flowing. When liquid phase is cooled, coal slag is transformed into pseudo-plastic solid state before solidification. Separation of solid state is dependent on composition of slag and transition temperature between liquid phase and solid phase, which is called critical viscosity temperature (T_{CV}). T_{CV} has same meaning of slag removal temperature which is ASTM fusion temperature with maximum viscosity for smooth slag removal. Slag removal temperature was identified as

temperature with viscosity of 250 poise (T_{250}) so that choice of suitable coal for slagging operation is mainly decided by the value of T_{250} . A value of T_{250} was decreased by increasing the amount of reducing agents and by decreasing the amount of oxidizing agents in coal ash. When viscosity of perfect liquid phase is determined, critical viscosity temperature (T_{CV}) can be represented as crystallization temperature. Therefore T_{CV} and T_{250} have below relationship: $T_{CV} > T_{250}$, Slag removal temperature = T_{250} , $T_{CV} < T_{250}$, Slag removal temperature = T_{CV} .

Variation of slag viscosity with different composition was calculated by Urbain equation that is based on $CaO-Al_2O_3-SiO_2$ ternary phase diagram as in Frankel equation (1).

$$\ln \eta = A \exp(B/T) \dots \dots \dots (1)$$

When calculating slag viscosity for low rank coal, equation (2) is used, where T is temperature, A and B are function of chemical composition on coal ash, η is viscosity in poise and Δ is silica percentage in slag.

$$\ln \eta = \ln A + \ln T + 10^3(B/T) - \Delta \dots \dots \dots (2)$$

When using this equation, proper classification of silica quantity is very important which is largely dependent on the B values. Calculated data of viscosity at the temperature of T_{CV} for each coal samples are illustrated in Table 3.

Table 3. T_{CV} and viscosity of ash sample

Sample Coals	Viscosity (poise)	T_{cv} (°C)
Datong	348.18	1421
Alaska	364.92	1356
Cypurus	560.71	1394

The shape of slag samples with different experimental condition is illustrated in Fig. 2. Each formed slag shows slightly different shape with the variation of coal types and reaction atmosphere. Cypurus slag was not great difference between combustion and gasification condition, but shape of gasification slag more spherical shape than combustion condition. Datong slag shaped trigonal pyramid form and melting is started at the top of the deposit. Alaska slag shows flat melting shape because of its low melting characteristics. The variation of slag shape with different coal samples can be explained with the data of ash fusion temperature, surface tension and viscosity of slag with different slag composition. Also reactivity with refractory alumina substrate of solid sample collector affects shape of slag.

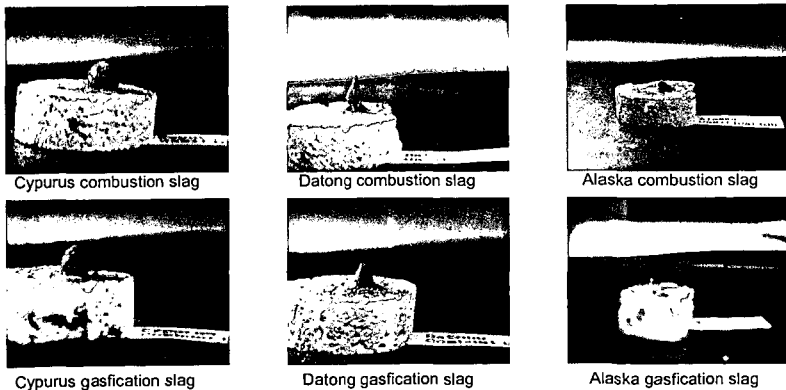


Figure. 2 Shape of ash slag with gasification/combustion condition and coal types

Coal samples in this study are classified into Alaska and Cypurus coal, which mainly consist of $SiO_2-CaO-Al_2O_3$ phase and Datong coal, which mainly consist of $CaO-SiO_2-Al_2O_3-Fe_2O_3$ phase. Mole fractions of Al_2O_3 and Fe_2O_3 in Alaska and Cypurus coals are constant but SiO_2/CaO ratio in ash components was varied from 2.07 in Alaska to 3.51 in Cypurus. For the slag samples mainly composed of $SiO_2-CaO-Al_2O_3$, viscosity is increased with increasing quantity of SiO_2 in slag.

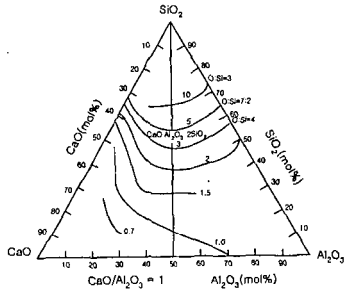


Figure 3. CaO-SiO₂-Al₂O₃ ternary diagram for coal ash samples

As shown in Fig. 3, however, Datong slag, composed of high quantity of SiO₂ and low CaO, would expected low fusion temperature and low slag viscosity. The main reason of such finding is because the reaction between high quantity of Fe₂O₃ and SiO₂ formed Fayalite(Fe₂SiO₄) which has low fusion temperature. Such finding is probably based on the fact that increasing quantity of Fe₂O₃ destroyed network structure of SiO₂. Shape of slag formation with different gasification/combustion condition was effected by chemical composition of coal ash.

However, shape of slag drop was mainly determined by surface tension value, which is subjected to wetting angle. Wetting angle between alumina refractory substrate and melting slag was represented by Young's relation as in equation (3), where O is wetting angle, r_{sv}, r_{sl} and r_{lv} are surface tension of solid-vapor, solid-liquid and liquid-vapor.

$$\cos O = (r_{sl} - r_{sv})/r_{lv} \text{-----(3)}$$

If surface tensions of solid-vapor and solid-liquid are constant, surface tension of liquid-vapor phase behave major factor in the formation of slag drop. In other words decreasing surface tension of melting slag increase wetting angle. As a result, non-wetting surface was formed so that formed slag is not penetrated into porous alumina substrate.

4. CONCLUSION

To determine optimum operation condition of ash slagging in coal gasifier/combustor, DTF is utilized, which can simulate time and temperature history of coal particle. Slagging behavior of coal ash samples was also investigated with empirical equations and the results showed that slagging behaviors of subbituminous Alaska and Datong coals were much better than Cypurus. Separation of solid state dependant on composition of slag and transition temperature between liquid phase and solid phase by experiment data. Shape of slag formation with different on gasification/combustion condition was effected by chemical composition of coal ash. Shape of slag drop was determined by surface tension value, which is subject to wetting angle.

ACKNOWLEDGEMENT

This work was performed by the financial support of R&D Management Center for Energy and Resources (RaCER) in Korea.

REFERENCE

1. S. K. Gupta et al., " Ash Fusion Temperatures and the Transformations of coal ash particles to slag," Fuel Processing Technology, vol.56, pp.33-43, 1998
2. H. B. Vuthaluru et al., " Ash Formation and Deposition from a Victorian brown coal-modeling and prevention," Fuel Processing Technology, vol.53, pp.215-233, 1998
3. J. N. Harb et al., " Use of Equilibrium Calculations To Predict the Behavior of Coal Ash in Combustion Systems," Energy & Fuels, vol.7, pp.208-214, 1993
4. Inorganic Transformations and Ash Deposition during Combustion, edited by S. A. Benson, The American Society of Mechanical Engineers, pp.121-131, 1991